Imperial College London

Copper manganese oxides as oxygen carriers for chemical looping air separation for near-zero emission power generation

Clemens Frederic Patzschke

February 2019

Supervised by Professor Paul S. Fennell

This thesis is submitted for the degree of Doctor of Philosophy in Chemical Engineering at the Department of Chemical Engineering at the Imperial College London of Science, Technology and Medicine.

Abstract

In this thesis, copper manganese oxides were evaluated as oxygen carriers for chemical looping air separation. This process allows for the production of a O_2+CO_2 mixture, which can be used for oxy-fuel combustion of biomass for near-zero emission generation of power. Unsupported oxygen carriers were prepared *via* co-precipitation at low and at high super-saturation and *via* mechanical mixing. Furthermore, TiO_2, ZrO_2 and Al_2O_3-supported oxygen carriers were prepared. The oxygen carriers were characterised to study the effect of synthesis conditions on the material properties, and experiments in the TGA and fluidised bed were performed to assess their kinetic and long-term cycling performance. The unsupported oxygen carriers showed a highly stable cycling behaviour over a high number of redox-cycles. The O_2 capacities and O_2 equilibria were measured and the data reported. Cycled oxygen carriers were characterised to study the particle evolution for different redox-cycling modes (isothermal, non-isothermal, fuelled process with CH_4) and at various conditions. The characterisation also elucidated the relevant redox-reactions and reaction pathways, as well as interactions between active phases and the supporting materials. During redox-cycling, the unsupported oxygen carriers were prone to swelling (an increase in the specific particle volume). It was demonstrated that the use of ZrO_2 as a supporting material inhibits the swelling and result in a shrinking. Kinetic parameters were isolated from experiments in the fluidised bed, and the homogeneous reaction model was found to represent the O_2 release and oxidation reaction best.

Declaration of originality

Herewith I declare that the content of this thesis is primarily my own work and work of others is appropriately referenced. I declare that I am the primary person responsible for the design, construction and preparation of this manuscript including the analysis of all the experimental data presented. Any work carried out as part of a collaborative work have been explicitly stated in the text.

Clemens F. Patzschke, January 2019

Copyright declaration

The copyright of this thesis rests with the author. Unless otherwise indicated, its contents are licensed under a Creative Commons Attribution - Non-Commercial 4.0 International Licence (CC BY-NC). Under this licence, you may copy and redistribute the material in any medium or format. You may also create and distribute modified versions of the work. This is on the condition that: you credit the author and do not use it, or any derivative works, for a commercial purpose. When reusing or sharing this work, ensure you make the licence terms clear to others by naming the licence and linking to the licence text. Where a work has been adapted, you should indicate that the work has been changed and describe those changes. Please seek permission from the copyright holder for uses of this work that are not included in this licence or permitted under UK Copyright Law.

Acknowledgements

I would like to thank my supervisor, Professor Paul S. Fennell, as well as his stand-in during the period of his sabbatical, Dr Boot-Handford, for their excellence guidance and support throughout my PhD project. I would like to thank Prof Jason Hallett and Dr Qilei Song, who always had an open door and the right advice. And, I would like to thank my girlfriend, Clarissa, and my parents, Gottfried and Teresa, for their continuous support as well as all my friends, family members and colleagues who helped me, supported me and guided me.

Table of contents

Chapter 1 – Introduction **1**

1.1 Statement of the problem 1

1.2 Aims and objectives of the research project 5

1.3 Structure of the thesis 5

Chapter 2 – Chemical looping and competing processes for electricity generation with CO_2 capture **7**

2.1 Chemical looping combustion with natural gas 8

2.2 Alternative processes for the power generation from natural gas with CO_2 capture 12

2.3 Chemical looping combustion with solid fuels 15

2.3.1 Chemical looping with oxygen uncoupling for the combustion of solid fuels 16

2.3.2 Chemical looping combustion with *ex-situ* gasification 17

2.3.3 Chemical looping combustion with *in-situ* gasification 18

2.3.4 Chemical looping for air separation with oxy-fuel combustion 18

2.4 Alternative processes for power generation from solid fuels with CO_2 capture 23

2.5 Concluding remarks 26

Chapter 3 – Desirable properties and preparation methods of oxygen carriers **27**

3.1 Desirable properties of the active phases of oxygen carriers 28

3.1.1 Reactivity, O_2 equilibria and intra-particle diffusion resistance 28

3.1.2 Mechanical resistance of oxygen carriers, attrition behaviour and support materials 34

3.1.3 Heat of the reactions and auto-thermal operation 41

3.1.4 Oxygen storage and release capacity 44

3.1.5 Solid inventory 46

3.2 Inert supporting materials 47

3.3 Cost of oxygen carriers 51

3.4 Methods for the preparation of oxygen carriers 55

3.4.1 Preparation of oxygen carrier *via* mechanical mixing 56

3.4.2 Preparation of oxygen carrier *via* impregnation 57

3.4.3 Preparation of oxygen carrier *via* co-precipitation 57

3.5 Selection of the sintering and calcination temperatures 60

3.6 Concluding remarks 62

Chapter 4 – Preparation of the oxygen carriers **67**

4.1 Preparation of oxygen carriers *via* co-precipitation 68

4.1.1 Determination of the optimal co-precipitation conditions 69

4.1.2 Development of a washing procedure for the removal of Na^+ 72
4.1.3 Construction of a rig for automated co-precipitation 73
4.1.4 Standard procedure for the co-precipitation of oxygen carriers 77
4.1.5 Preparation of oxygen carriers at high supersaturation 79
4.2 Preparation of oxygen carriers *via* mechanical mixing 80
4.2.1 Standard procedure for the preparation *via* mechanical mixing 80
4.2.2 Mechanically mixing with pore-forming agents 82
4.3 Concluding remarks 85

Chapter 5 – Material characterisation **86**
5.1 N_2 adsorption at 77 K and calculation of the BET surface area 87
5.2 Crushing force measurements 94
5.3 Helium pycnometry and mercury intrusion porosimetry 98
5.4 Determination of the crystalline phases by X-ray diffraction 103
5.4.1 Validation of the calibration and uncertainties of the XRD measurements 103
5.4.2 Calculation of the mass fractions from XRD data 108
5.4.3 Effect of calcination conditions on the crystalline phases 110
5.4.4 Effect of residual sodium in the precursor on the calcined sample 113
5.4.5 XRD patterns of the co-precipitated precursors 114
5.4.6 XRD patterns of the co-precipitated oxygen carriers 116
5.4.7 XRD patterns of the mechanically mixed oxygen carriers 123
5.5 Quantitative analysis by X-ray fluorescence 125
5.5.1 Measurement of the mass fraction of impurities in the reagents 125
5.5.2 Determination of the Cu:Mn molar ratio of the co-precipitated oxygen carriers 126
5.6 Scanning electron microscopy and the determination of the grain sizes 129
5.6.1 Grain size measurements 129
5.7 Thermo-gravimetry evolved gas analysis mass spectrometry 132
5.8 Concluding remarks 134

Chapter 6 - Thermo-gravimetric analysis of the oxygen carriers **138**
6.1 Thermo-gravimetric analysis and a screening of the reactivity 138
6.1.1 Description of the set-up of the thermo-gravimetric analyser 138
6.1.2 Rate of gas mixing in the TGA 140
6.2 External mass transfer in the TGA 141
6.3 Intra-particle diffusion resistance and tortuosity 144
6.4 Testing the reversibility of the redox-reactions at CLAS conditions 152
6.5 O_2 equilibria and enthalpy of the O_2 release 162

6.5.1 Determination of the O_2 equilibria by the 'onset-of-decomposition' method 162
6.5.2 Determination of the O_2 equilibria by the 'max-rate method' 166
6.5.3 Measurement of the O_2 equilibria using the 'max-rate method' 168
6.5.4 Results of the O_2 equilibrium measurements 170
6.6 Observed rate of oxidation and O_2 release in the TGA 173
6.7 Possible reaction pathways of the redox reactions 176
6.8 The performance of the oxygen carrier over 100 redox-cycles 177
6.8.1 Cycling of the oxygen carriers by O_2 partial pressure swing 178
6.8.2 Cycling of the oxygen carrier by temperature swing 182
6.8.3 Change of crushing strength over 100 redox-cycles 184
6.9 Redox-cycling with CH_4 186
6.9.1 Reversibility of the redox-reactions with CH_4 186
6.9.2 Long-term cycling tests with CH_4 189
6.10 Concluding remarks 195

***Chapter 7 – Redox-cycling of the oxygen carriers in the fluidised bed* 197**
7.1 Modification and operation of the fluidised bed reactor 198
7.1.1 Modification of a fluidised bed reactor 199
7.1.2 Deconvolution and calculation of the observed rates 200
7.1.3 Calculation of the minimum fluidisation velocity 203
7.1.4 Heat transfer in the fluidised bed during a reaction 204
7.2 Development of a reaction rate model assuming a well-mixed fluidised bed 207
7.2.1 Estimation of the external mass transfer coefficient 209
7.2.2 Reaction rate models 212
7.3 Long-term cycling experiments in the fluidised bed 224
7.3.1 Long-term cycling with 40 g of 1Cu-1Mn-MM 224
7.3.2 Long-term cycling of ZrO_2-supported oxygen carriers 231
7.4 Concluding remarks 235

***Chapter 8 – Conclusions and future work* 237**
8.1 Conclusions 237
8.2 Future work 247

Nomenclature 249
Appendix 254
Bibliography 267

List of Figures

Fig. 1-1 *Global CO_2 emissions ( ), national determined contributions (NDCs) for 2030 ( ), and emission pathways for an average warming of 3.2-5.4 °C ( ) and 0.9-2.3 °C ( ) in the period 2081-2100 compared to the average temperature in the period 1850-1900. The graphic is adapted from the illustration shown in Fuss et al.[20] and Pidcock[21].* 3

Fig. 1-2 *Carbon flow between the atmosphere and geological formations for different modes of power generation, adapted from Karlsson and Byström.[32]* 4

Fig. 2-1 *Schematic diagram of the conventional chemical looping combustion process.[50,72]* 9

Fig. 2-2 *Schematic diagram of the CH_4-CLC process (left), and the overall reactions in the reducer and oxidiser (right).* 9

Fig. 2-3 *A possible configuration of a 800 MW reactor system, adapted from Wolf et al.[71]* 10

Fig. 2-4 *Diagram of a conventional steam cycle with two re-heaters.* 10

Fig. 2-5 *A Grassmann diagram of a combined cycle using a reactor pressure of 13 bar, with figures in %-loss of exergy of the process, adapted from Wolf et al.[71]* 11

Fig. 2-6 *A schematic diagram of the NGCC process for electricity generation, adapted form Subramanian et al.[78]* 12

Fig. 2-7 *Grassmann diagram of a combined cycle using a reactor pressure of 13 bar, with figures in %-loss of exergy of the process, adapted from Wolf et al.[71]* 12

Fig. 2-8 *Schematic diagrams of selected pre- and post-combustion CO_2 capture technologies for gas turbine combined cycle plants that use natural gas as the fuel: (a) pre-combustion chemical adsorption, adapted from Hoffmann et al.[34]; (b) pre-combustion CO_2 capture using membranes, diagram adapted from Hoffmann et al.[34]; (c) post-combustion CO_2 capture using a calcium/carbonate looping, adapted from Berstad et al.[36]; (d) post-combustion CO_2 capture by chemical gas-liquid absorption, adapted from Cormos et al.[37]* 13

Fig. 2-9 *A diagram of the principle of chemical absorption for post-combustion CO_2 capture, based on the process illustrated by MacDowell et al.[83]* 15

Fig. 2-10 *Schematic diagram of chemical looping combustion with oxygen uncoupling (left) and the reactions in the reducer and oxidiser (right).* 16

Fig. 2-11 *Schematic of solid fuel gasification with subsequent chemical looping combustion (left) and the overall reactions in the reducer and oxidiser (right).* 17

Fig. 2-12 *Reactor configuration of chemical looping air separation with oxy-fuel combustion (left) and the relevant reactions (right). For the sake of simplicity, the fuel in the equations is assumed to consists of carbon.* 18

Fig. 2-13 *Reactor configuration of chemical looping air separation with oxy-fuel combustion (left) and the overall reactions (right).* 19

Fig. 2-14 *A flowsheet of the oxy-fuel combustion for CO_2 capture with O_2+CO_2 production via the CLAS process. A combination of the drawings from Maroto-Valer[71] and Patzschke et al.[46]* 20

Fig. 2-15 *A flowsheet of a solar powered CLAS + oxy-fuel process with arrows representing the energy and material flows (a) during the day and (b) at night. Adapted from Patzschke et al.[130]* 23

Fig. 2-16 *A schematic diagram of an integrated gasification combined cycle process, adapted from the illustration by Rhodes & Keith.[31]* 24

Fig. 2-17 *Schematic diagram of the Ca-looping process for in situ biomass combustion, based on the process illustrated by Diego et al.[136]* 25

Fig. 3-1 *A plot of log(k) against 1/T for the reduction of various metal oxides in CH_4, with k being the intrinsic reaction rate constant per unit of volume in s^{-1} and the chemical rate of CH_4 consumption, r, is given by $r = k[CH_4]$. The plot is adapted from the one shown in Mattison & Lyngfelt.[143]* 28

Fig. 3-2 *BET surface area of Cu-based oxygen carrier reported in the literature.* 29

Fig. 3-3 *Ellingham diagram for the reduction of: (a) manganese oxides, (b) copper oxides, (c) cobalt oxides and (d) iron oxides at 0.1 MPa. The lines were computed using data from FactSage.* 30

Fig. 3-4 *Ellingham diagram for common single metal oxide systems for CLOU and CLAS using the data from FactSage for the reduction of: (a) manganese oxides, (b) copper oxides, (c) cobalt oxides and (d) iron oxides, and the free energy of O_2 in an ideal gas mixture with p_{O_2} = 0.30 bar and p_{O_2} = 0.01 bar at 0.1 MPa.* 32

Fig. 3-5 *Oxygen partial pressure equilibria as a function of temperature for the systems CoO/Co_3O_4, Mn_2O_3/Mn_3O_4 and CuO/Cu_2O based on data from FactSage (solid lines), and the log-average O_2 partial pressure calculated by eq.(3-5), assuming $p_{O2,in}$ and $p_{O2,out}$ are 0.21 bar and 0.05 bar, respectively...* 34

Fig. 3-6 *Modes of attrition and their effect on the particle size distribution (PSD), adapted from Werther and Reppenhagen.[153]* 35

Fig. 3-7 *Methodology for the selection of oxygen carrier materials with a sufficiently low attrition behaviour to be used in scaled-up CLC processes, adapted from Cabello et al.[56]* 40

Fig. 3-8 *A comparison of the enthalpy of the overall reaction in the reducer for Cu-, Mn- and Co- oxides in the CLAS process and in the CLC process with biomass, CH_4, CO and H_2 as the fuel (a) per mole of O_2 release, and (b) per kg of the reduced or decomposed active metal oxide.* 43

Fig. 3-9 *The oxygen ratios of single metal oxide systems relevant for the CLC and the CLAS process, calculated from the molecular weights of the compounds and the balanced equations determined in FactSage.[139]* 45

Fig. 3-10 *Ellingham diagram for common support materials using the data from FactSage.* 48

Fig. 3-11 *Plots of the oxygen carrier lifetimes versus the cost of the solid inventory required to generate 1 MW_{th} grouped by: (a) shows the energy consumption of the oxygen carrier production and the oxygen carrier lifetimes, (b) oxygen carrier material, (b) preparation method, and (c) support material. The grey lines in (a), (b) and (c) are the iso-lines of the oxygen carrier specific cost of CO_2 capture and the dotted circles are used to highlight clusters of the same material or method.*[6075] 53

Fig. 3-12 *Block flow diagrams representing a typical process of oxygen carrier preparation via mechanical mixing with particle formation via (a) spray-drying and (b) freeze-granulation, adapted from Patzschke et al.*[75,185] 56

Fig. 3-13 *Block flow diagram representing a typical process of oxygen carrier preparation via incipient dry impregnation, adapted from Patzschke et al.*[75,185] 57

Fig. 3-14 *Simplified schematic of the process of precipitation from the solution*[195] 59

Fig. 3-15 *Block flow diagram representing a typical process of oxygen carrier preparation via co-precipitation, adapted from Patzschke et al.*[75,185] 60

Fig. 4-1 *Equilibrium diagrams of relevant Cu and Mn species for (a) 1Cu-2Mn and (b) 2Cu-1Mn as a function of the pH value at T = 25°C and P = 0.1 MPa with a total metal ion concentration and Na^+ concentration of 1 M. The Na^+ is donated by Na_2CO_3 and NaOH in molar ratios of 3:0. The software used the Helgeson-Kirkham-Flowers model to calculate the thermodynamic activity.* 70

Fig. 4-2 *Equilibrium diagrams of relevant Cu and Mn species for 1Cu-1Mn oxygen carrier as a function of the pH value at T = 25 °C and P = 0.1 MPa with a total metal ion concentration and Na^+ concentration of 1 M. The Na^+ is donated by Na_2CO_3 and NaOH in molar ratios of (a) 3:0, (b) 2:1, (c) 1:2 and (d) 0:3. The software used the Helgeson-Kirkham-Flowers model to calculate the thermodynamic activity.* 71

Fig. 4-3 *Reduction of electrical conductance with an increase of the number of centrifugations runs at 4500rpm (~2500 G) for 2 min in 90 ml centrifugation tubes of a mixture of DI water and the Cu-Mn-precipitated, precipitated with (dashed lines) Na_2CO_3 and (solid lines) NaOH.* 72

Fig. 4-4 *Schematic of the co-precipitation rig, which was constructed for the preparation of larger batches required for long-term cycling experiments in the fluidised bed.* 74

Fig. 4-5 *Diagram of the feedback loop of the PID controller*[203] 75

Fig. 4-6 *Plot of the pH value, the alkaline flow rate and the metal alkaline solution flow rate during the co-precipitation of 1Cu-1Mn-CP(3:0).* 76

Fig. 4-7 *The reduction of particle size of copper (II) oxide powder with time of milling in the planetary ball mill at 280 rpm using four steel balls and a solid:water ratio of 1:1:* 81

Fig. 4-8 *Drawings of the structure of (a) a micro-crystalline cellulose monomer, (b) a linear starch monomer, and (c) a branched starch monomer.* 83

Fig. 4-9 *Plots of the weight change during TGA experiments with 20 mg of the precursors containing different pore-forming agents. The samples are 1Cu-2Mn-MM with 10 wt% of (a) micro-crystalline cellulose (MCC), and (b) starch, heated in air (lack lines) and in 2 vol% O_2 + N_2 (grey lines).* 84

Fig. 5-1 *The BET surface area of the co-precipitated oxygen carrier.* 89

Fig. 5-2 *The results of the linear regression analysis of the BET surface area values.* 90

Fig. 5-3 *A comparison of the results of the (a) BET surface area and (b) cumulative pore volume measurements for unsupported mechanically mixed Cu-Mn oxygen carriers. The error bars indicate the uncertainty of the values from the production. This uncertainty was estimated by deconvoluting the standard deviations of three measurements of particles form the same batch and three measurements of particles from three different batches prepared using the same method as described in Appendix A.3.* 91

Fig. 5-4 *The results of BET surface area measurements of the high-surface area oxygen carrier precursor (bulk material), plotted against (a) ageing time, and (b) ageing temperature. The dotted curves/lines are the linear best fit to guide the eyes. The error bars indicate the uncertainty and were calculated as* $u(S_{BET}) = 0.046 \cdot S_{BET}$. 93

Fig. 5-5 *Change of the surface morphology of the micro-structured precursors during calcination at 600 °C for 2h in air with 1* $l \cdot min^{-1}$ *at SATP: (a) BET surface area of the precursor (□) and the calcined samples (◇); SE micrographs of (b) the precursor and (c) the calcined material.* 94

Fig. 5-6 *The data acquired during a crushing force measurement of a particle from the oxygen carrier batch 1Cu-1Mn-CP(3:0)-pH 6.0 and of particle size range 300-425 µm.* 95

Fig. 5-7 *The results of the crushing force measurements of the co-precipitated oxygen carriers with a particle diameter of 300-425 µm.* 96

Fig. 5-8 *A plot of the crushing strength against the BET surface area of the co-precipitated oxygen carriers co-precipitated, □, at a lower pH value and, ◇, at a higher pH value.* 97

Fig. 5-9 *A plot of the average crushing force against the BET surface area of the co-precipitated oxygen carriers co-precipitated using a higher pH value and, ◇, only* Na_2CO_3 *and, ◆,* $NaOH+Na_2CO_3$ *as the co-precipitation agent.* 97

Fig. 5-10 *The porosity of selected co-precipitated calcined oxygen carriers in the range between 5.5 nm and 10 µm measured by MIP, co-precipitated at (a) the lowest theoretical pH value + 0.5 at which all species precipitate, and (b) the highest theoretical pH value - 0.5 at before the formation of CuO.* 101

Fig. 5-11 *Pore size distribution determined by MIP for selected oxygen carrier from the size range 300-425 µm: (a-d) unsupported co-precipitated, (e-f) unsupported mechanically mixed, and (g-i) supported oxygen carriers.* 102

Fig. 5-12 *Schematic diagram of (a) the Bragg-Brentano geometry of an XRD instrument, adapted from the drawing shown on ywcmatsci.yale.edu,*[247] *and (b) of the two different types of sample holders used in this project.* 103

Fig. 5-13 *The results of the validation of the XRD calibration using a sintered sapphire disk: (a) the experimentally obtained XRD pattern with lines above the peaks that correspond to the peak position*

of the reference pattern (JCPDS 00-001-0787), and (b) the difference between the experimentally obtained peak position and the peak position of the reference pattern. 104

Fig. 5-14 *XRD patterns of the experiments for the determination of the uncertainties of the XRD measurements using crushed 1Cu-1Mn-CP(3:0)-pH-8.3 oxygen carriers (a) in the back-loaded mount and (b) on the disk-slide mount.* 105

Fig. 5-15 *A plot of the standard deviations against the 2θ of the three measurements obtained when using the slide disk mount (○) and the back-loaded sample holder (●) for: a) 2θ, the peak position, b) the relative intensity, I/I_{max}, c) the full width at half maximum, FWHM, and d) the integral breadth.* 106

Fig. 5-16 *Plots of the average values of three measurements obtained when using the disk slide mount against the values obtained when using the back-loaded mount for a) 2θ, the peak position and b) I/I_{max}, the relative peak intensity of the peaks larger than $I/I_{max} = 0.05$.* 107

Fig. 5-17 *Simulated copper, copper manganese and manganese oxide XRD patterns based on data from the PDF-4+ 2016 database*[212] *to show the peak used for the mass fraction calculation (☆) for Cu Kα (λ =0.1541 nm) radiation.* 109

Fig. 5-18 *XRD pattern of the 1Cu-1Mn-CP(3:0)-pH-8.3 precursor, partially calcined and calcined material. The calcination was carried out in air (1 l min^{-1} at SATP) and using a heating rate of 15 °C min^{-1}. The calcination temperatures and holding times as well as the calculated values for the FWHM and crystallite size are specified on the graph.* 110

Fig. 5-19 *XRD pattern of the mechanically mixed 1Cu-1Mn-MM oxygen carrier calcined at different conditions as specified on the plot.* 112

Fig. 5-20 *The mass fraction of CuO in the calcined 1.5Cu-1.5Mn-MM precursors as a function of calcination time, calculated by eq.(5-5a) and eq.(5-5b) from the XRD data shown in Fig. 5-19. The black line corresponds to the theoretical mass fraction of a sample containing only $CuMnO_2$ and CuO.* 112

Fig. 5-21 *XRD pattern of 1Cu-1Mn (3:0) pH 8.3 with different amounts of residual Na: (a) without the removal of Na, and removal of Na to obtain a electrical conductivity of (b) 1238 µS, (c) 256 µS, and (d) 46 µS.* 113

Fig. 5-22 *XRD pattern of the precursors of the first series of co-precipitated oxygen carriers. The samples are precursors of (a) 1Cu-2Mn-CP(3:0), (b) 2Cu-1Mn-CP(3:0), (c) 1Cu-1Mn-CP(3:0), (d) 1Cu-1Mn-CP(2:1), and (e) 1Cu-1Mn-CP(1:2).* 114

Fig. 5-23 *XRD pattern of the precursors shown of the (a) 1Cu:2Mn-CP(3:0), (b) 2Cu:1Mn-CP(3:0), (c) 1Cu:1Mn-CP(3:0) precursors (black lines), and a mixture of the precursors with 10 wt% CeO_2 as an internal standard for the determination of the mass fractions of crystalline material (blue lines).* 115

Fig. 5-24 *Mass fractions of the crystalline phase calculated from the XRD patterns from Fig. 5-23 assuming the all crystalline material is either $MnCO_3$ (■) or $Cu_2CO_3(OH)_2$ (□). For a combination $MnCO_3$ and $Cu_2CO_3(OH)_2$ the mass fraction of crystalline material is between the two dotted curves, which are drawn as guidelines.* 116

Fig. 5-25 *XRD pattern of the first series of calcined co-precipitated oxygen carriers. The samples (a, b, c) were co-precipitated with 1 M Na_2CO_3 and have the molar composition of (a) 1Cu:2Mn, (b) 1Cu:1Mn, (c) 2Cu:1Mn. The samples (c, d, e) have a molar composition of 1Cu:1Mn and were precipitated with (c) 1 M Na_2CO_3, (d) 0.66 M Na_2CO_3 + 0.66 NaOH, and 0.33 M Na2CO3 + 1.33 M NaOH. During all co-precipitation experiments, the [Na+] in the co-precipitation agent was 2 M.* 117

Fig. 5-26 *XRD pattern of the crushed co-precipitated oxygen carrier. The samples have a molar Cu : Mn ratio of 1 : 2, were calcined at 900 °C for 2 h under air, and were prepared using a 1 M Na_2CO_3 and a set pH value of (a) 8.3 and (b) 6.0; and using 0.66 M Na_2CO_3 and 0.66 NaOH and a set pH value of (c) 7.0 and (d) 6.0.* 119

Fig. 5-27 *XRD pattern of the crushed co-precipitated oxygen carrier. The samples have a molar Cu : Mn ratio of 1.25 : 1.75, were calcined at 900 °C for 2 h under air, and were prepared using a 1 M Na_2CO_3 and a set pH value of (a) 8.3 and (b) 6.0; and using 0.66 M Na_2CO_3 and 0.66 NaOH and a set pH value of (c) 6.9.* 120

Fig. 5-28 *XRD pattern of the crushed co-precipitated oxygen carrier. The samples have a molar Cu:Mn ratio of 1:1. They were calcined at 900 °C for 2 h under air, and were prepared using a 1 M Na_2CO_3 and a set pH value of (a) 8.5 and (b) 6.0; and using 0.66 M Na_2CO_3 and 0.66 NaOH and a set pH value of (c) 7.2 and (d) 6.0.* 121

Fig. 5-29 *Mass fractions of CuO (calculated from XRD data using eq.(5-5)) in the calcined co-precipitated oxygen carriers as a function of the co-precipitation pH for oxygen carriers prepared with aqueous solutions containing (a) 1 M Na_2CO_3 and (b) 0.66 M Na_2CO_3 + 0.66 M NaOH. The oxygen carriers were calcined at 900 °C for 2 h in air.* 122

Fig. 5-30 *XRD pattern of the mechanically mixed oxygen carriers with varying molar Cu:Mn ratio preapred using the standard synthesis procedure shown in Table 4-6 and calcined at 950 °C for 6 h.* 123

Fig. 5-34 *Mass fractions of CuO in the calcined mechanically mixed oxygen carriers calculated from XRD data using eq.(5-5).* 124

Fig. 5-35 *Ellingham diagram for the oxidation of Zr and Hf and the redox reactions relevant the chemical looping processes.* 126

Fig. 5-36 *The results of the XRF calibration and validation experiments: (a) a plot of the mass fractions of mechanically mixed oxygen carriers measured by XRF against the actual fractions for the determination of a calibration function; (b) the mass fraction of the 1Cu-1Mn-MM using a sample mass of 1.5 g (□) and a sample mass of 4.0 g (◇).* 127

Fig. 5-37 *Scanning electron micrograph of 1Cu-1Mn oxygen carrier calcined under 1 $l \cdot min^{-1}$ air at 980 °C and 6 h. Sample (a) and (b) were co-precipitated with 0.5 M Na_2CO_3 at a constant pH of 8.3 and are the fully oxidised and N_2-decomposed state; Sample (c) was prepared at a constant pH of 7.2 with 0.33 M Na_2CO_3 + 0.33 M NaOH, and sample (d) was co-precipitated at a constant pH of 7.0 with 0.16 M Na_2CO_3 + 0.66 M NaOH. An increase in porosity with a decreasing [Na_2CO_3]/[NaOH] is clearly visible.* 129

Fig. 5-38 *SE micrographs for and results from the grain size measurements of (a, b, c) 1Cu-1Mn-CP(3:0), (d, e, f) 1Cu-2Mn-CP(3:0), and (g, h, i) 1Cu-1Mn-MM; (a, d, g) are the SE micrographs used for this analysis, (b, e, h) are the calculated probability densities of the average grain diameter (grey bars on main graph) using a bin size of 0.25 µm, their log-normal distribution functions (solid lines) calculated by eq.(5-7) with parameter specified on the plot areas, and (c, f, i) are the probability densities of the aspect ratios of the grains with bin size of 0.9 calculated by eq.(5-8). The sample size is 75 grains per SE micrograph.* 131

Fig. 5-39 *A plot of the rate of mass change and the ion currents of the atomic masses that correspond to CO_2 and H_2O measured during the thermal decomposition of the precursor (a) 1Cu-2Mn-(2:1)pH7.0, (c) 1Cu-1Mn-CP(2:1)-pH6.0 in the TG-MS under air. A sample gas flow rate of 50 ml min^{-1} (at SATP) and a heating rate of 5 K min^{-1} was used.* 133

Fig. 6-1 *A diagram of the TGA set-up including the gas supply system.* 139

Fig. 6-2 *The change of gas concentration after switching from CO_2 to 10 vol% O_2+CO_2, measured downstream a 3-way valve (□), downstream of the gas supply system (△), and downstream of the TGA furnace at 800 °C (◇), and a best fit function for the change of gas concentration before de-convolution (thin lines) and after de-convolution (thick lines).* 141

Fig. 6-3 *Drawing of the TGA cross-section to illustrate the gas flow and the diffusion of gas from the oxygen carriers during the O_2 release.* 142

Fig. 6-4 *The rate of the external mass transfer controlled maximum rate of mass change in the TGA assuming an effective crucible height of 0.35 mm: The values reported by Hu et al.[219] for N_2 (-) and the results of the gPROMS model for N_2 (◇) and CO_2 (□).* 143

Fig. 6-5 *The effect of gas flow rate into the TGA on the maximum O_2-release rate of 2 mg 1Cu-1Mn-CP(2:1) in the TGA at 850 °C with decomposition under pure N_2. A second order polynomial trend-line is drawn to illustrate the relationship. The error bars indicate the uncertainty, which was estimated by 2·SD of the maximum rate of three redox-cycles.* 144

Fig. 6-6 *A comparison of Knudsen diffusion and molecular diffusion: (a) a schematic of the diffusion of a gas molecule (black dot) from the solid surface, through the pores to the bulk of gas; (b) values for the diffusion coefficient as a function of the pore radius.* 145

Fig. 6-7 *A plot of conversion against time during the O_2 release from 2 mg 1Cu-1Mn-MM oxygen carrier of various particle size ranges as defined by the legend on the figure. The experiments were carried out at 850 °C in the TGA using pure N_2 for the decomposition with a flow rate of 200 ml min^{-1} at SATP. The results of some particle size ranges were omitted from this graph for clarity.* 147

Fig. 6-8 *The apparent rate constant, ◯, and the calculated intrinsic rate constant, ●, for the O2 release reaction of 1Cu-1Mn-MM measured in the TGA at 850 °C under N_2 using a flow rate of 200 ml min^{-1} at SATP.* 151

Fig. 6-9 *A plot of the effectiveness factor against the mean particle radius for the O_2 release reaction of 1Cu-1Mn-MM measured in the TGA at 850 °C under N_2 using a flow rate of 200 ml min^{-1} at SATP.* 151

Fig. 6-10 *Plots of the normalised sample mass measured during T swing experiments in the TGA with alternating periods of 850 °C with 10 vol% O_2+N_2 (for the oxidation) and 950 °C with 10 vol% O_2+CO_2 (for the O_2 release) for different oxygen carriers of the size range 150-212 µm: (a) 1Cu-2Mn-CP(3:0), (b) 1Cu-2Mn-MM, (c) 1Cu-1Mn-CP(3:0), (d) 2Cu-1Mn-CP(3:0). The total gas flow rate was kept constant at 170 ml.min^{-1} at SATP.*.....154

Fig. 6-11 *Normalised weight during the redox-cycling in the TGA by (a, b) p_{O2} swing and (b, c, d) T swing: (a) by T swing: (a) O_2 release during p_{O2} swing of samples with different Cu:Mn molar ratios, (b) a comparison of the O_2 release during p_{O2} swing and T swing, (c) O_2 release during T swing of samples with different Cu:Mn molar ratios, (d) O_2 release and oxidation with different gas mixtures. During a typical p_{O2} swing experiment the oxidation occurred in 10 vol% O_2 + N_2 and the decomposition under pure N_2 at 850 °C. During a typical T swing experiment periods of 850 °C with 10 vol% O_2+N_2 (for the oxidation) and 950 °C with 10 vol% O_2+CO_2 (for the O_2 release) alternated. The total inlet gas flow rate during all experiments was 170 ml min^{-1} at SATP.*.....156

Fig. 6-12 *XRD patterns of the cycled 1Cu-2Mn-CP(3:0) oxygen carriers recovered in the seventh redox-cycled at the end of the (a) oxidation period with 10 vol% O_2 + N_2, (b) decomposition period of $pO2$ swing experiments using pure N_2, and (c) decomposition period of the T swing experiments using 10 vol% O_2 + CO_2.*.....158

Fig. 6-13 *XRD patterns of the cycled 1Cu-1Mn-CP(3:0) oxygen carriers recovered in the seventh redox-cycled at the end of the (a) oxidation period with 10 vol% O_2 + N_2, (b) decomposition period of $pO2$ swing experiments using pure N_2, and (c) decomposition period of the T swing experiments using 10 vol% O_2 + CO_2.*.....159

Fig. 6-14 *XRD patterns of the cycled 1Cu-2Mn-CP(3:0) oxygen carriers recovered in the seventh redox-cycled at the end of the (a) oxidation period with 10 vol% O_2 + N_2, (b) decomposition period of p_{O2} swing experiments using pure N_2, and (c) decomposition period of the T swing experiments using 10 vol% O_2 + CO_2.*.....160

Fig. 6-15 *The experimental data and the fitted function for the determination of T_{eq} of 40-CuMn/Zr-MM by the 'onset of decomposition method' in the TGA using 2 vol% O_2 + N_2, a heating rate of 10 °C·min^{-1}, and a total flow rate of 150 ml·min^{-1}(SATP).*.....163

Fig. 6-16 *The experimentally obtained values of T_{eq} using the 'onset of decomposition method' in the TGA under O_2+N_2 for (a) 1Cu-1Mn-CP and 1Cu-2Mn-CP, and (b) 1Cu-1Mn-CP and 40-CuMn/Zr-MM, respectively.*.....164

Fig. 6-17 *The experimentally obtained values of T_{eq} for 1Cu-1Mn-CP using the 'onset of decomposition method' in the TGA under O_2+N_2 and under O_2+CO_2.*.....165

Fig. 6-18 *Observed rate of O_2 release of ~1 mg CuO powder measured in the TGA at 925 °C under N_2-diluted O_2 with varying O_2 molar fractions, using a total gas flow rate of 200 ml·min^{-1} at SATP.*.....166

Fig. 6-19 *Results of the experiments with CuO powder to validate the 'max-rate method' for the measurements of the O_2 equilibria: (a) The maximum rate of decomposition plotted against the O_2 partial pressure at the TGA inlet, and (b) calculated points of $pO2,eq$ (markers) and $pO2,eq$-fuction from FactSage (line).*.....167

Fig. 6-20 *The measured flux of O_2 during the decomposition (black marker) and the maximum rate of external mass transfer (grey marker) for the experiments to determine the oxygen equilibria of CuO powder.* 167

Fig. 6-21 *Measured reaction rate versus conversion of 1Cu-1Mn-CP(3:0) oxygen carriers under N_2-diluted O_2 at (a) T = 800 °C, (b) T = 825 °C, (c) T = 850 °C, and (d) T = 875 °C; using a gas flow rate of 150 ml·min^{-1}. For the calculation of the conversion redox-cycling between $Cu_{1.5}Mn_{1.5}O_4$ and $CuMnO_2$ was assumed.* 168

Fig. 6-22 *Plots of (a) observed rate of O_2 release against the p_{O2} at the TGA inlet for the determination of the $p_{O2,eq}$, and (b) the calculated values of $p_{O2,eq}$ against temperature. The experiments were carried out in the TGA using 1Cu-1Mn-CP(3:0) oxygen carriers and a total flow rate of 150 ml·min^{-1}.* 169

Fig. 6-23 *The calculated maximum rate of mass transfer at, □, 800 °C, ◇, 825 °C, △, 850 °C, ○, 875 °C, and the measured rate of O_2 release at, ■, 800 °C, ◆, 825 °C, ▲, 850 °C, ●, 875 °C. The small average relative deviation of 7% shows that the experiments to measure the $pO2,eq$ were at conditions where the overall rate equals the maximum rate of external mass transfer.* 169

Fig. 6-24 *Oxygen partial pressure equilibrium ($p_{O2,eq}$) curves: plotted as (a) $p_{O2,eq}$ against T and (b) $ln(p_{O2,eq})$ against $10^4/T$ (van 't Hoff plot). The dashed lines are FactSage values for Mn_2O_3/Mn_3O_4 and CuO/Cu_2O. The markers are experimentally obtained values for $p_{O2,eq}$ using the 'onset of O_2 release' method (✱,Δ) and the 'rate-based' method (□, ■); for 1Cu-1Mn-CP(3:0) (✱,Δ, □) and for CuO powder (■); under O_2+N_2 (□, ■ ,Δ) and O_2+CO_2 (✱).* 170

Fig. 6-25 *Plots of the observed (a) O_2 release rate and (b) oxidation rate versus conversion of 1Cu-2Mn-MM at different temperatures; the O_2 release and oxidation was carried out in 0 vol% O_2 + N_2 and 10 vol% O_2 + N_2, respectively. A sample mass of 1 mg and a gas flow rate of 200 ml·min^{-1} was used. The conversion was calculated using the balanced equation in eq.(6-24a).* 173

Fig. 6-26 *The effect of Cu:Mn molar ratio on the observed rate reaction of 2 mg mechanically mixed 150-212 µm oxygen carriers measured in the TGA (average of cycles 4 to 7) at 850 °C for the (a, c, e) O_2 release under pure N_2 and (b, d, f) oxidation in 10 vol% O_2 + N_2; the plots show (a, b) the conversion against time, (c, d) the observed rate against conversion, and (e, f) the maximum observed rate against the molar Cu/(Cu+Mn) ratio. A total gas flow rate of 200 ml·min^{-1} was used during the experiments.* 174

Fig. 6-27 *XRD patterns of the 1Cu-1Mn-CP samples after redox-cycling in the TGA at 850 °C with various conversion of the oxidation reaction: (a) fully reduced (X = 0), (b) partially oxidised (X = 0.4), (c) partially oxidised (X = 0.6), and (d) fully oxidised (X = 1).* 176

Fig. 6-28 *The (a, c, e) maximum observed rate of O_2 release and (b, d, f) O_2 storage capacity over 100 cycles of 2 mg 150-210 µm (a, b) 1Cu-1Mn-CP(3:0), (c, d) 40-CuMn/Zr-MM, and (e, f) 40-CuMn/Ti-MM measured in the TGA at 850 °C. The gas during the oxidation and O_2 release was 10 vol% O_2 + N_2 and pure N_2, respectively, and the total gas flow rate was 200 ml.min^{-1} at SATP.* 178

Fig. 6-29 *SEM of a redox-cycled 1Cu-1Mn-CP(3:0) oxygen carrier (a) particle and (b) the particle surface recovered after 100 p_{O2} swing cycles in the TGA. The oxygen carriers are from a size range of 150-210 µm and 1 mg of sample was used. The gas used at a flow rate of 200 ml·min^{-1} at SATP is 10 vol% O_2 and 0 vol% O_2 balanced with N_2 for oxidation and reduction, respectively.* 179

Fig. 6-30 *SEM of a redox-cycled 40-CuMn/Zr-MM oxygen carrier (a) particle and (b) the particle surface recovered after 100 p_{O2} swing cycles in the TGA. The atom percentages in (b) were determined by EDS. The smaller and the larger black circles indicate the centre and the circumference of the area of the area measured by EDS. The oxygen carriers are from a size range of 150-210 µm and 1 mg of sample was used. The gas used at a flow rate of 200 ml·min^{-1} at SATP is 10 vol% O_2 and 0 vol% O_2 balanced with N_2 for oxidation and reduction, respectively.* 180

Fig. 6-31 *SEM with values for atom fractions quantified by EDXS of 60 wt% TiO_2/1Cu-1Mn-MM after 100 redox-cycles in the TGA. White cross and the dashed circle indicate the centre and the circumference of the area on which the X-ray detector is focused. The values in the black-transparent boxes indicate the respective atom percent. The oxygen carriers are from the size range 150-210 µm and 1 mg of sample was used. The gas used at a flow rate of 200 ml.min^{-1} at SATP is 10 vol% O_2 and 0 vol% O_2 balanced with N_2 for oxidation and reduction, respectively.* 181

Fig. 6-32 *Results of the T swing experiments in the TGA using 150-212 µm 1Cu-1Mn-CP oxygen carriers with oxidation at 800 °C in 10 vol% O_2 balanced with N_2 and decomposition at 950 °C in 10 vol% O_2 balanced with CO_2: (a) a plot of the relative mass (black lines) and the temperature (grey lines) measured during an experiment with 40 mg of the oxygen carriers for the determination of the* $R0,\exp$*, and (b-d) results of the long-term cycling experiments using 4 mg of the oxygen carriers; (b) is a plot of the O_2 release reaction rate over 100 cycles, (c) shows the O_2 release rate over the conversion during the first cycles of the long-term-cycling experiment and (d) shows averages of the O_2 release rate for cycles 11 to 100. The grey-lines in (c) and (d) show the temperature inside the TGA furnace average for the cycles 1-10 and 11-100, respectively. The gas flow rate was kept constant at 170 ml min^{-1} at SATP and the dT/dt during the temperature jumps was 200 °C min^{-1}.* 182

Fig. 6-33 *Scanning electron micrographs of fresh and cycled 1Cu-1Mn-CP(2:1)-pH7.2 oxygen carriers. The micrographs (a, b) show the fresh sample, (c, d) the sample after 10 T-swing cycles, and (e, f) the sample after 100 T-swing cycles, (a, c, e) 300 x, and (b, d, f) 10 000 x magnified. The temperature swing was carried out in the TGA between 850 °C* and *950°C using 10 vol% O_2 balanced with N_2 during the oxidation and CO_2 during the decomposition. The gas flow rate was kept constant at 200 ml.min^{-1} at SATP.* 183

Fig. 6-34 *The results of the crushing strength measurement of 1Cu-1Mn-CP(2:1)-pH7.2 cycled by different chemical looping modes in the TGA. The temperature swing was carried out between 850 °C* and *950°C using 10 vol% O_2 balanced with N_2 during the oxidation and CO_2 during the decomposition. The O_2 partial pressure swing was carried out at 850 °C using 10 vol% O_2 + N_2 during the oxidation and pure N_2 during the decomposition. The gas flow rate was kept constant at 200 ml.min^{-1} at SATP.* 184

Fig. 6-35 *Plots of the differential intrusion (DI) against pore size of 1Cu-1M-CP(2:1) oxygen carriers measured by MIP of (a) the fresh sample and the samples cycled by temperature swing, and (b) the fresh sample and the samples cycles by p_{O2}-swing.* 185

Fig. 6-36 *Plots of the particle volume against cycle number calculated as the normalised inverse of the envelope density for the oxygen carriers cycled by temperature swing and p_{O2}-swing in the TGA.* .. 186

Fig. 6-37 *Plots of the normalised sample mass of (a) 1Cu-2Mn-MM and (b) 1Cu-1Mn-MM measured during TGA experiments with alternating periods 5 vol% CH_4 + N_2 and 10 vol% O_2+N_2 at 650 °C. The*

sample mass during the experiments was 2 mg and the gas flow rate was kept constant at 200 ml·min^{-1} at SATP. 187

Fig. 6-38 *Plots of the normalised sample mass of (a) 40-CuMn-Zr and (b) 40-CuMn-Ti measured during TGA experiments with alternating periods 10 vol% CH_4 + N_2 and 10 vol% O_2+N_2 at 650 °C. A higher sample mass of 40 mg was used to study the recovered samples by XRD, and the gas flow rate during the experiment was kept constant at 200 ml·min^{-1} at SATP.* 187

Fig. 6-39 *XRD patterns of 40-CuMn/Zr-MM oxygen carriers, (a) freshly calcined, (b) recovered at the end of the 20th reduction period, and (c) recovered at the end of the 20th oxidation period. During the redox-cycling in the TGA, periods with 10 vol% CH_4 + N_2 and 10 vol% O_2+N_2 at 650 °C were alternated and the gas flow rate during the experiment was kept constant at 200 ml·min^{-1} at SATP.* 188

Fig. 6-40 *XRD patterns of 40-CuMn/Ti-MM oxygen carriers, (a) freshly calcined, (b) recovered at the end of the 20th reduction period, and (c) recovered at the end of the 20th oxidation period. During the redox-cycling in the TGA, periods with 10 vol% CH_4 + N_2 and 10 vol% O_2+N_2 at 650 °C were alternated and the gas flow rate during the experiment was kept constant at 200 ml·min^{-1} at SATP.* 189

Fig. 6-41 *The (a, c, e) rate of reduction and (b, d, f) O_2 storage capacity measured over 100 redox-cycles at 700 °C in the TGA. The samples are (a, b) 1Cu-1Mn-CP(3:0), (c, d) 40-CuMn/Zr-MM, (e, f) 40-CuMn/Ti-MM. The reduction and oxidation were carried out in 10 vol% CH_4 + N_2 and 10 vol% O_2 + N_2, respectively. A sample mass of 2 mg, a particle size range of 300-425 µm, and a total flow rate of 200 ml.min^{-1} at SATP were used.* 190

Fig. 6-42 *SE micrographs with (a) x 200 and (b) x 10 000 magnification of 1Cu-1Mn-CP-CP(3:0)-pH-8.3 after 100 redox-cycles in the TGA at 700 °C with reduction under 10 vol% CH_4 + N_2 and oxidation under 10 vol% O_2 + N_2. The total gas flow rate was 200 ml.min^{-1} at SATP.* 191

Fig. 6-43 *SE micrographs with (a) x 200 and (b) x 10 000 magnification of 40-CuMn/Zr-MM after 100 redox-cycles in the TGA at 700 °C with reduction under 10 vol% CH_4 + N_2 and oxidation under 10 vol% O_2 + N_2. The total gas flow rate was 200 ml.min^{-1} at SATP.* 191

Fig. 6-44 *SEM with atom fractions quantified by EDS of 60 wt% TiO_2/1Cu-1Mn-MM after 100 redox-cycles in the TGA with CH_4 for the reduction. White cross and the dashed circle indicate the centre and the circumference of the area on which the X-ray detector is focused. The oxygen carriers have a size range of 150-210 µm, and a sample mass of 1 mg was used. The gas used at a flow rate of 200 ml.min^{-1} at SATP is 10 vol% O_2 and 10 vol% CH_4 balanced with N_2 for oxidation and reduction, respectively.* 192

Fig. 6-45 *A diagram of the suggested mechanism for the stabilisation of the active and supporting phases by chemical reaction between the phases.* 192

Fig. 6-46 *SEM with (a, c, e) low and (b, d, f) high magnification of a 1Cu-1Mn-CP oxygen carrier particle recovered after 100 redox-cycles (a, b) by T swing, (c, d) by p_{O2} swing and (e, f) with a reduction by CH_4.* 193

Fig. 7-1 *Flow sheet of the modified fluidised bed for redox-cycling at CLAS conditions.* 198

Fig. 7-2 *Schematic diagram of the mathematical model that is used for the deconvolution of gas measurements during fluidised bed reactor experiments. The figure is adapted from Tighe.*[235] 200

Fig. 7-3 *A plot of the measured and the deconvoluted molar fraction of O_2 upon gas switching from air to N_2 in the fluidised bed containing 40 g of sand at 850 °C.* 201

Fig. 7-4 *A plot of the inlet flow rate and calculated outlet flow rate during the O_2 release of 1Cu-2Mn-MM oxygen carrier at 850 °C in the fluidised bed reactor, using an inlet flow rate of 2.53 l min^{-1} at SATP.* 202

Fig. 7-5 *Plots of the bed temperature (black line) and deconvoluted observed rate of reaction (black line) against the time after the gas switching for (a) the O_2 release and (b) the oxidation of 1Cu-2Mn-MM. The plotted values of the temperature and rate are the average values of cycle 3 to cycle 5.* ... 205

Fig. 7-6 *A drawing of the concentration gradients of O_2 in an oxygen carrier particle and its surrounding gas film.* 207

Fig. 7-7 *Validation of the gPROMS model by comparing the calculated values of the maximum rate of mass transfer (lines) with the values reported in the literature (marker): results of the gPROMS model for the particle size ranges, --- , 355-500 µm and, —, 855-1000 µm, and values reported by Chuang et al.*[238] *for the particle size ranges, ◇, 355-500 µm and ranges, □, 855-1000 µm.* 210

Fig. 7-8 *Illustration of the progression of the reaction in the (a) homogeneous reaction model, (b) shrinking grain model, and (c) shrinking core model.*[144] 212

Fig. 7-9 *Plots of (a, c, e, g) of observed conversion against time and (b, d, g, h) deconvoluted observed rate against time for the O_2 release reaction of 1000mg 1Cu-2Mn-MM at (a, b) 825 °C, (c, d) 850 °C, (e, f) 875 °C and (g, h) 900 °C. The grey markers represent the experimental data, which was measured in the fluidised bed under pure N_2 with a total gas flow rate of 2.445 l·min^{-1} at SATP. The black markers represent the modelled data.* 215

Fig. 7-10 *Plots of (a, c, e, g) of observed conversion against time and (b, d, g, h) deconvoluted observed rate against time for the O_2 release reaction of 1000mg 1Cu-2Mn-MM at (a, b) 825 °C, (c, d) 850 °C, (e, f) 875 °C and (g, h) 900 °C. The grey markers represent the experimental data, which was measured in the fluidised bed under pure N_2 with a total gas flow rate of 2.445 l·min^{-1} at SATP. The black markers represent the modelled data.* 216

Fig. 7-11 *Plots of (a, c, e, g) of observed conversion against time and (b, d, g, h) deconvoluted observed rate against time for the O_2 release reaction of 1000mg 1Cu-2Mn-MM at (a, b) 825 °C, (c, d) 850 °C, (e, f) 875 °C and (g, h) 900 °C. The grey markers represent the experimental data, which was measured in the fluidised bed under pure N_2 with a total gas flow rate of 2.445 l·min^{-1} at SATP. The black markers represent the modelled data.* 217

Fig. 7-12 *A plot of (a) k_v against temperature and ln(k) against 1/T using the intrinsic rate constants determined using the homogeneous reaction rate model.* 219

Fig. 7-13 *Plots of (a, c, e, g) of observed conversion against time and (b, d, g, h) deconvoluted observed rate against time for the oxidation reaction of 1000mg 1Cu-2Mn-MM at (a, b) 825 °C, (c, d) 850 °C, (e, f) 875 °C. The grey markers represent the experimental data, which was measured in the fluidised*

bed under pure N_2 with a total gas flow rate of 2.445 l·min^{-1} at SATP. The black markers represent the modelled data. 221

Fig. 7-14 *Plots of (a, c, e, g) of observed conversion against time and (b, d, g, h) deconvoluted observed rate against time for the oxidation reaction of 1000mg 1Cu-2Mn-MM at (a, b) 825 °C, (c, d) 850 °C, (e, f) 875 °C. The grey markers represent the experimental data, which was measured in the fluidised bed under pure N_2 with a total gas flow rate of 2.445 l·min^{-1} at SATP. The black markers represent the modelled data.* 222

Fig. 7-15 *A plot of (a) k_v against temperature and ln(k) against 1/T using the intrinsic rate constants determined using the homogeneous reaction rate model.* 223

Fig. 7-16 *O_2 concentrations during the inert cycles and during the oxidations of the first five redox-cycles of the LTC-FBR-1 experiment, the difference between those O_2 concentrations, and the averaged bed temperature.* 225

Fig. 7-17 *Observed oxidation rate during "LTC-FBR-1" experiment at 850 °C under 10 vol% O_2, balanced with N_2, with a total gas flow rate of 2.445 l·min^{-1} at SATP. The value of the bed mass used in the oxidation rate calculation was assumed to change linearly with cycle number between the values of the loaded bed mass and the recovered bed mass.* 225

Fig. 7-18 *Ratio of recovered bed mass to initial bed mass (primary axis) and cumulative mass of fines recovered from elutriate filter ($m_{fines;}$ secondary axis) of experimental series "FBR-I" using 300-425 µm 1Cu-1Mn-MM. The error bars correspond to the uncertainty, which was taken as two times the standard deviation of the first four measurements.* 226

Fig. 7-19 *XRD plot of 1Cu-1Mn-MM oxygen carrier used in the long-term cycling experiment "FBR-I" in its fully oxidised state (a) before redox-cycling, (b) after 5 redox-cycles, and (c) after 100 redox-cycles, as well as (d) fines collected in the filter.* 227

Fig. 7-20 *SE micrographs of 1Cu-1Mn-MM cycled in the fluidised bed for (a) 10 cycles, (b) 25 cycles, (c) 40 at 850 °C using 10 vol% O_2 balanced with N_2 for oxidation and pure N_2 for reduction; And (d) a plot of Mn-atom percentage against cycle number, determined by SEM-EDXS from the micrographs shown in (a), (b), and (c).* 228

Fig. 7-21 *Results from the post-cycling analysis of 300-425 µm 1Cu-1Mn-MM oxygen carriers recovered from the experiment "FBR-1": Plots of (a) the differential intrusion against pore diameter from MIP, (b) porosity and mean pore diameter against cycle number calculated from MIP and He-pycnometry, (c) the specific volume change (the specific volume is taken as the reciprocal of the envelope density), (d) particle size distribution (PSD) of the fresh sample, cycled bed material and fines recovered from the elutriate filter. A refractive index (RI) for the particles of 2.63 was selected, which corresponds to the RI of CuO, since the literature lacks data about the RI of $Cu_xMn_{3-x}O_4$. The measured size is therefore slightly larger than the actual particle size; and (e) crushing strength against cycle number.* 229

Fig. 7-22 *Results from long-term cycling experiments with 40-CuMn/Zr-MM in the fluidised bed reactor at 850 °C with oxidation in 10 vol% O_2 + N_2 and O_2 release under pure N_2: the O_2 release capacity (●), the observed oxidation rate (●) and O_2 release rate (○) over 50 redox-cycles.* 231

Fig. 7-23 *Results from long-term cycling experiments with 40-CuMn/Zr-MM in the fluidised bed reactor at 850 °C with oxidation in 10 vol% O_2 + N_2 and O_2 release under pure N_2: (a) the O_2 release capacity (●) the O_2 release rate (○), (b) the conversion measured during the O_2 release of the 1st, 3rd, 25th and 50th cycle (as indicated on the graph), (c, d) plots of the conversion vs. time measured during the 1st (--·), 3rd (—), 25th (—)and 50th (—) cycle during of the (c) oxidation and (d) O_2 release period.* 232

Fig. 7-24 *SE micrographs of 40-CuMn-Zr/MM oxygen carriers recovered from the fluidised bed reactor after 50 redox-cycles at 850 °C with oxidation in 10 vol% O_2 + N_2 and O_2 release under pure N_2: (a) particles recovered from the bed, (b) fines recovered from the elutriate filter, (c) surface morphology of a redox-cycled oxygen carrier, (d) cross-section through a grain cut with a focused Ga^+ ion beam.* 233

Fig. 7-25 *Results of the (a) XRD and (b) MIP experiments of the ZrO_2-supported oxygen carriers 40-CuMn/Zr-MM prior and after 50 cycles in the fluidised bed.* 234

List of Tables

Table 3-1 *Values of the crushing strength (larger 1 N) and preparation methods reported in the literature for oxygen carriers containing Cu and Mn.* 37

Table 3-2 *Values for the estimated average oxygen carrier lifetime and details of the oxygen carrier's composition and synthesis conditions reported in the literature.* 39

Table 3-3 *Reaction enthalpy of the O_2 release reaction of Cu, Mn and Co oxides with values form FactSage.*[139] 41

Table 3-4 *Reaction enthalpies of the metal oxide oxidation in the air reactor (AR) and fuel reduction in the fuel reactor (FR) and their ratios, based on values from FactSage.*[139] 42

Table 3-5 *Reaction enthalpy of the O_2 release reaction of Cu, Mn and Co oxides with values form FactSage.*[139] 43

Table 3-6 *Oxygen ratios for redox-systems of commonly used single metal oxides as oxygen carrier materials for the CLC and CLAS process.* 45

Table 3-7 *Literature values*[177] *for the microhardness of potential active metal oxides and inert support materials for CLC and CLAS. The testing conditions were SATP unless stated otherwise.* 47

Table 3-8 *Hüttig, Tammann, and melting point temperature of metals and metal oxides at 0.1 MPa that are used in this work for the preparation of oxygen carriers.* 49

Table 3-9 *The use of support materials for Cu-based oxygen carrier for CLC reported in the literature.* 50

Table 3-10 *Results of the economic assessment of oxygen carrier sorted by cost of carbon capture (ascending).* 52

Table 3-11 *Publications reporting the preparation of copper manganese oxides.* 55

Table 3-12 *Sintering temperatures and particle properties of Cu, Mn, and Cu-Mn oxygen carriers.* . 61

Table 3-13 *Parameters and control variables of the densification of metal oxides via sintering, adapted from German et al.*[200] 62

Table 4-1 *Elements (a-h) of the sample name for the oxygen carriers in this work.* 68

Table 4-2 *Description of chemical reagents used, where x denotes the mole fraction.* 68

Table 4-3 *The standard synthesis procedure for the co-precipitation of oxide oxygen carriers.* 77

Table 4-4 *Synthesis conditions of the oxygen carrier precursors prepared at 25 °C and 0.1 MPa using the co-precipitation standard procedure from Table 4-3.* 78

Table 4-5 *The ageing conditions of the oxygen carriers prepared at high super-saturation.* 79

Table 4-6 *Standard synthesis procedure for the preparation of oxygen carriers by mechanically-mixing of the single metal oxide powders.* 82

Table 4-7 *Oxygen carriers prepared via co-precipitation and mechanical mixing.* 85

Table 5-1 *Results of N_2-adsorption measurements of the co-precipitated oxygen carriers.* 88

Table 5-2 *Results of the BET surface area measurements of the bulk material of the high-surface area Cu-Mn oxygen carrier precursor.* 93

Table 5-3 *Results of the crushing force measurements of the co-precipitated oxygen carrier.* 95

Table 5-4 Results *from He pycnometry measurements at 25 °C and 0.1 MPa, mercury intrusion porosimetry measurements and the calculation of the envelope density of the oxygen carriers.* 100

Table 5-5 *The calculated standard deviation and uncertainties for the different sample holders for the XRD measurements.* 107

Table 5-6 *Peak data from the PDF-4+ 2016 database[212] used for mass fraction calculation and uncertainty of the mass fraction calculation.* 109

Table 5-7 *The results of the crystallite size calculation for the precursors, partially calcined and fully calcined sample 1Cu-1Mn-CP(3:0)-pH-8.3 based on the XRD data that is shown in Fig. 5-18.* 111

Table 5-8 *The mass fractions of the phases identified in the mechanically mixed unsupported oxygen carriers calculated using XRD data.* 124

Table 5-9 *Mass fractions of the powders used for the preparation of the mechanically mixed oxygen carriers and of the quartz sand used as an inert bed material during fluidised bed reactor experiments, measured by XRF.* 125

Table 5-10 *The Cu:Mn molar ratios of the crushed oxygen carriers determined by XRF.* 128

Table 5-11 *The results of the cumulative log-normal distribution function using the data from the grain size assessment.* 132

Table 6-1 *Diffusion volumes and relative molecular masses used for the calculation of the molecular diffusion.* 143

Table 6-2 *The particle size ranges used for the TGA experiments to determine the intrinsic kinetics and the tortuosity factor.* 147

Table 6-3 *The observed rate measured during TGA experiments to determine the intrinsic kinetics and the tortuosity factor.* 148

Table 6-4 *Values of $R_{0,exp}$ obtained during experiments in the TGA.* 155

Table 6-5 *The experimentally determined equilibrium temperatures, T_{eq}, using the 'onset-of-decomposition method' in O_2+N_2 and O_2+CO_2 at 0.1 MPa.* 164

Table 6-6 *Scanning electron micrographs and diagrams of the suggested growth modes for unsupported and supported copper manganese oxide oxygen carriers cycled by p_{O2}-swing and by reduction with CH_4.* 194

Table 6-7 *The kinetic parameters calculated for the oxidation and reduction reaction.* 265

Table 7-1 *Parameter and results of the mass transfer coefficient and the minimum fluidisation velocity calculation from the gPROMS model of this work for selected conditions.* 204

Table 7-2 *Results and parameter of the calculation for the maximum temperature difference between the oxygen carrier particle and the fluidised bed.* 206

Table 7-3 *Parameters and results of the calculation of the mass transfer coefficient for selected conditions using the gPROMS model of this work.* 211

Table 7-4 *Results from the calculation of the O_2 release rate using the homogeneous reaction model and assuming a well-mixed fluidised bed (CSTR).* 218

Table 7-5 *Results from the calculation of the oxidation rate using the homogeneous reaction model and assuming a well-mixed fluidised bed (CSTR).* 223

Table 7-6 *Results of the N_2-adsorption analysis of the oxidised fresh and redox-cycled oxygen carrier from the LTC-FBR-1 experiment.* 228

Chapter 1

Introduction

1.1 Statement of the problem

In recent decades, changes in the global climate, such as an increase in global mean surface temperature, average ocean temperature and melting of permafrost zones have been observed.[1] Between 1880 and 2012, the averaged ocean and land surface temperature increased by 0.85 ± 0.21 °C,[1] and there is evidence that those changes will have detrimental effects on biological cycles and environmental systems, which are not yet fully predictable.[1] The melting of glaciers, ice caps and the two ice sheets in Greenland and the Antarctic is accelerating, resulting in an increase in sea levels and a corresponding decrease in land area world-wide,[2,3] which is "expected to displace millions of people within the lifetime of many of today's children." [4] As the planet is warming, the seasons are changing: for instance, the arctic spring starts earlier and lasts longer, endangering the balance of the flora.[5,6] Further consequences include a redistribution of sea and land-based animals,[7] some of which have already moved their habitats hundreds of kilometres pole-wards.[5] This redistribution jeopardises not just the ecosystems' health, but also poses risks including those of climate feedbacks and reductions in human well-being.[7] The climate change of the 21st century is of scale comparable with the largest climate changes of the past 65 million years, but it is happening orders of magnitudes faster,[8] and is projected to result in the extinction of a high number of species that are either unable able to migrate or adapt.[8,9]

Extreme weather events are occurring more often and are increasingly more severe.[5,10] A hotter atmosphere can hold more water, which means more rain can fall, but at the same time it enhances evaporation, which in turn increases the probability of droughts.[5,10] The frequency of heat-waves has at least doubled compared to its pre-industrial level.[5] A hotter atmosphere also means that more energy is available to be converted into storms.[5] The higher temperatures increases the number of people globally exposed to floods exponentially – an increase in global surface mean temperature by

2 °C would expose 27 million people additionally to floods, while 62 million people will be additionally exposed with an increase by 4 °C.[11]

The International Panel of Climate Change (IPCC) provides evidence that this increase in global temperatures is a result of anthropogenic emissions of greenhouse gases (GHG), predominantly the emission of CO_2.[1] This is due to the 'greenhouse effect', linking the atmosphere's temperatures to the concentration of GHGs. Whilst GHGs allow short-wave sunlight to pass through, they absorb the longer-wave light that is reflected from earth, keeping it trapped within the atmosphere.[12]

Over the past four decades about 75% of emitted CO_2 has come from the combustion of fossil fuels and industrial processes.[13] Although the share of electricity generated from renewable sources increases steadily worldwide (*e.g.* has increased from 17% to 21% in the period from 2000 to 2017),[14] the main scenarios of the latest IPCC report predicts that fossil fuels will remain the major energy source throughout the 21st century.[1] An increasing number of governments and scientists are calling for a phase-out of coal-fired power generation processes, and research shows that for a successful decarbonisation the use of coal has to end around 2030-2035[15] (therefore, this thesis does not consider coal as a fuel). Coal is not so promising, as the emissions from coal are much higher than from the second most widely used fuel type[14] – natural gas. Current state-of-the-art natural gas power plants (without CO_2 capture) have specific emissions of around 350 kg(CO_2)/MWh, while coal power plants have specific emissions of 800-1000 kg(CO_2)/MWh.[16] When capturing the CO_2 from coal plants the energy-specific amount of CO_2 that needs to be captured, purified, compressed, transported and sequestered is correspondingly larger.[16] Therefore, natural gas is considered to play a key role in the strategies for a reduction in CO_2 emissions.[1] The share of electricity production from natural gas has increased from 18% to 23% from 2000 to 2017, and is predicted to increase further in the decades to come.[14]

The continued use of fossil fuels for power generation requires strategies for the reduction in CO_2 emissions.[16] The options that are commonly discussed to reduce CO_2 emissions fall typically into one of three categories, which are (i) the use of less carbon-intense energy sources, (ii) the efficiency increase of energy conversion, and (iii) carbon capture and sequestration (CCS).[13,17]

In a recent effort to limit CO_2 emissions and co-ordinate global climate change mitigation action, 195 nations signed the Paris climate change agreement, which pledges to limit "the increase in the global average temperature to well below 2 °C above pre-industrial levels" and to "pursue efforts" to keep the warming below 1.5 °C,[18] leaving us with a very limited carbon budget.[19] Projections of the 2016 CO_2 emissions (in **Fig. 1-1** below) illustrate the difficulty to follow the pathway to limit the global warming to below 1.5 °C.[20,21]

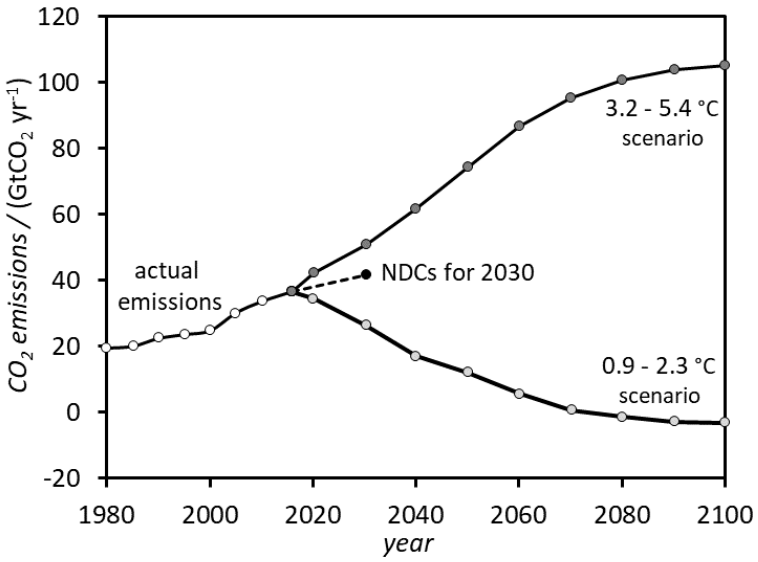


Fig. 1-1 *Global CO_2 emissions (○), national determined contributions (NDCs) for 2030 (●), and emission pathways for an average warming of 3.2-5.4 °C (●) and 0.9-2.3 °C (○) in the period 2081-2100 compared to the average temperature in the period 1850-1900. The graphic is adapted from the illustration shown in Fuss et al.[20] and Pidcock[21].*

Luderer *et al.*[22] estimated in their 'optimistic scenario' that it will be almost impossible to limit the global warming to below 1.7 °C, given the current political situation and the available global warming mitigation technologies. Since a deep decarbonisation of all energy sectors is unlikely in the near-term, technologies that result in negative CO_2 emissions become increasingly important in the global climate change mitigation strategies.[23] The use of biomass can result in such negative emissions[24] *via* at least four different routes:

(i) carbon can be sequestered in trees by conservation of forests, reforestation and afforestation, and surprisingly there has been a 7.1% net increase in the area covered by trees globally in the period from 1982 to 2016[25]. In this period, the decrease in tropical tree cover has been outweighed by the increase in extra-tropical tree cover.[25] However, the net effect on climate change is not clear, since the area specific climate change mitigation potential is believed to be in order: tropical forest > temperate forest > boreal forest,[26] since in the same order the carbon storage potential and evaporative cooling are decreasing and the albedo is increasing;[26]

(ii) fossil fuels can be replaced by fuels derived from biomass.[27,28] Though, a recent high-resolution lifecycle assessment study of an existing biofuel production chain from energy crops suggests that the global warming reduction potential is in reality lower than often anticipated[29];

(iii) carbon can be sequestered by burial of biomass, such as crop residues, in permanent storage sites such as below the seabed;[30]

(iv) biomass can be combusted for electricity production combined with CO_2 capture – a process known as bio-energy with CO_2 capture and storage (BECCS).[31]

In the process of BECCS, plants absorb atmospheric CO_2 and lock in the carbon, which is combusted in a dedicated biomass-fired power plant with CO_2 capture.[31] The CO_2 is then stored safely in geological formations. This results in a net transfer of carbon from the atmosphere to the geosphere. This transfer of carbon between the two spheres is compared with those of other common modes of power generation in **Fig. 1-2**, below.

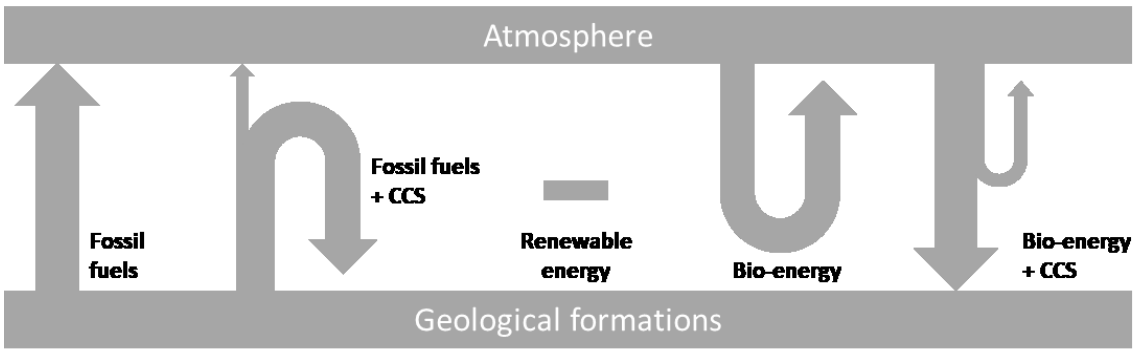


Fig. 1-2 *Carbon flow between the atmosphere and geological formations for different modes of power generation, adapted from Karlsson and Byström.*[32]

BECCS may become increasingly important, and thus the role of biomass in the decarbonisation of power generation.[24] BECCS also allows for the off-set of emissions from other sectors that are more difficult to decarbonise, such the transportation sector.[24] Rhodes and Keith[24] calculated that the mitigation potential for the transportation sector with indirect decarbonisation by BECCS bears greater potential than the utilisation of biofuels. Despite the advantages of BECCS, barriers to large-scale deployment were identified,[33] which were less technical in nature, and rather more regulatory and economical challenges. For example, governments currently do not financially incentivise negative emission technologies such as BECCS financially.[33]

Promising CO_2 capture technologies for the decarbonisation of electricity from natural gas combustion and from biomass combustion include pre-combustion capture using membranes,[34] integrated gasification combined cycle,[31] oxy-fuel combustion,[35] post-combustion capture using a calcium/carbonate looping,[36] or chemical absorption,[37,38] and chemical looping combustion (CLC).[38,39] A variant of CLC is the novel process of chemical looping air separation with oxy-fuel combustion (CLAS + oxy-fuel).[40,41] When utilising biomass in this process, it falls into the category of BECCS technologies, and negative CO_2 emissions can be achieved. This PhD project has focused on the CLAS + oxy-fuel process. For chemical looping processes (which includes the CLAS + oxy-fuel process) an expert workshop recently identified[42] the development of oxygen carriers (the metal

oxide particles used to facilitate the O_2 transport between the reactors, detailed in chapter 2) as the research area with the greatest potential for improvement. The following four key areas were identified:[42] (i) the design of "tailormade [oxygen carrier] materials", (ii) to elucidate the relationship between the surface structure of the oxygen carriers and their properties, (iii) to design oxygen carrier materials that maintain their long-term cycling performance over a high number of redox-cycles, and (iv) to elucidate the relationship between the materials and their performance in chemical looping processes. This PhD project has focused on these four aspects and has investigated the performance of copper manganese spinel oxides as oxygen carriers for the CLAS + oxy-fuel process. These oxygen carrier materials have recently been proposed for other chemical looping processes.[43,44,45] These materials were selected, as they combine promising properties that are required for the CLAS + oxy-fuel process: a relatively high oxygen carrying capacity, fast oxidation and O_2 release rates at moderate temperatures, and a stable performance over a high number of redox-cycles.[46] The specific aims and objectives of this research project are defined in the following section.

1.2 Aims and objectives of the research project

To evaluate the suitability of copper manganese oxides as oxygen carriers for the CLAS + oxy-fuel process, the following experimental objectives were specified:

- The development and characterisation of unsupported and supported copper manganese oxide oxygen carrier prepared *via* mechanical mixing and co-precipitation.
- The testing of the properties and the redox-cycling performance of the oxygen carriers in a thermogravimetric analyser and a fluidised bed reactor at conditions that are relevant for the CLAS process.
- The testing of the long-term cycling performance of the oxygen carriers in the TGA and the FBR to study the degradation of the oxygen carrier with repeated redox-cycling and elucidate the underlying degradation mechanisms.

1.3 Structure of the thesis

This thesis is comprised of eight chapters. The first chapter discussed relevant information to frame the topic: It describes the problem of climate change and explains the motive to use BECCS technologies for electricity generation with CO_2 capture to achieve negative CO_2 emissions. Furthermore, it identifies the research area of oxygen carrier development as one which bears great potential for the improvement of the process. The second chapter introduces chemical looping and competing processes for power generation with CO_2 capture. The third chapter presents a literature study on the development, performance testing and costs of oxygen carriers. The fourth chapter

details the synthesis of the oxygen carriers of this work *via* mechanical mixing and co-precipitation at high and low super-saturation. In chapter 5, the results of the material characterisation of the fresh oxygen carriers is described, to relate the preparation methods to the properties of the oxygen carriers, and to obtain data required for the reaction rate modelling in chapter 6 and chapter 7. Chapter 6 details the experimental results from thermo-gravimetric analysis of the oxygen carriers, as well as of the characterisation experiments of the redox-cycled oxygen carriers to elucidate reaction pathways, measure the O_2 release capacity and the O_2 partial pressure as a function of temperature, to study the effects of temperature and gas concentration on the observed oxidation and O_2 release rate and to study the long-term cycling performance of the oxygen carriers. Chapter 7 reports the results of redox-experiments in the fluidised bed and of characterisation experiments of redox-cycled bed material to study the rates of reaction and the long-term cycling performance. In the final chapter of this thesis (chapter 8) overall conclusions are drawn and future work is suggested.

Chapter 2

Chemical looping and competing processes for electricity generation with CO_2 capture

In this chapter the chemical looping and competing processes for power generation with CO_2 capture are introduced. This chapter focuses on technologies that utilise natural gas and biomass, as among the carbonaceous fuels these two fuels are likely to play a key role in the transition to low-carbon energy production (see the previous chapter). The differences between the two fuel types (natural gas and biomass) have led to different designs of power generation and CO_2 capture systems. This also holds true for chemical looping processes, for which process design, operating conditions and energy materials differ significantly by fuel type. Therefore, this chapter is divided into two parts with regards to the fuel type the processes utilise. Power generation using natural gas, with CO_2 capture, is discussed in the first part of this chapter (sections 2.1 and 2.2), and biomass-fired processes are evaluated in the second part (section 2.3 and 2.4). The first section of each part (section 2.1 and 2.3) discusses chemical looping, and the second section of each part (sections 2.2 and 2.4) discusses the competing processes. The fundamentals of each technology are explained using process

diagrams. Furthermore, data from literature was gathered to establish ranges of the estimated net thermal efficiencies, CO_2 capture costs, CO_2 capture rates and levelised costs of electricity (LCOE) for each process. The chapter ends demonstrating that chemical looping processes, including the chemical looping air separation are economical viable processes compared to other alternatives. For the ease of comparison all costs are stated in U.S. dollar ($), and for the conversion from euro (€) and pound sterling (£) the annual average exchange where used, which are listed in **Appendix A.1**.

2.1 Chemical looping combustion with natural gas

The process of chemical looping combustion was patented in 1954 for CO_2 production by Lewis and Gilliland[47] and was later re-discovered by Ishida and Jin for power generation with CO_2 capture.[48] In this process, solid metal oxide particles, the oxygen carriers, are cycled between two reactors, *viz.* the reducer and the oxidiser.[48] In the reducer, the oxygen carriers donate oxygen for the oxidation of the fuel, which results in a reduction of the active metal oxides phase(s).[49] The exhaust stream of the reducer contains primarily of H_2O and CO_2.[50] In subsequent process steps, residual O_2 is removed from the CO_2-rich stream, water is separated by condensation, residual impurities are removed, and the CO_2 is compressed for CO_2 sequestration.[50] The CO_2 stream is then compressed and transported *via* pipeline, truck or ship to the location of injection.[16] The reduced oxygen carriers that are leaving the reducer pass through a cyclone, which separates off the combustion products.[39] They are then transported to the oxidiser in which the active metal oxide phase(s) are oxidised.[39] The gas stream leaving the oxidiser consists of O_2 deficient air without significant amounts of by-products.[39] The oxidised oxygen carriers leave the reactor and pass through another cyclone, which separates them from the O_2 deficient air. The oxygen carriers are then transported back to the reducer and the process repeats. Typically, both reactors are circulating fluidised bed (CFB) reactors,[48] and the active metal oxides of oxygen carrier could be CuO,[51,52,53,54,55,56] Mn_2O_3,[57,58] Fe_2O_3 [59,60,61] and NiO,[39,62,63] which can be supported on Al_2O_3,[51,52,56,60,62] $NiAl_2O4$,[39] $MgAl_2O4$,[55,64] $CaAl_2O4$,[63] TiO_2,[61] ZrO_2,[57,58] SiO_2[65,66,67] to increase the particles' resistance to mechanical stresses during operation. Furthermore, natural ores[68,58] and pervoskites[69] have also been proposed as oxygen carrier materials for the CH_4-CLC process. For most materials, the reduction of the oxygen carrier is endothermic and the oxidation strongly exothermic. However, when using Cu-based oxygen carriers for the combustion of CH_4 (or natural gas) the overall reaction in the oxidiser and the reducer is exothermic.[70,54] In a chemical looping combustion system for electrical power generation, the released enthalpy is typically used to raise steam, which is used in a steam cycle to produce electricity.[50] If the reactors are operated at elevated pressure, the exhaust from the air reactor can additionally be used to drive a gas turbine.[71] Such a combined cycle has typically a higher efficiency than a conventional steam cycle with re-heat.[71]

The principle of chemical looping combustion for electrical power generation is shown in **Fig. 2-1**, below.[72,50]

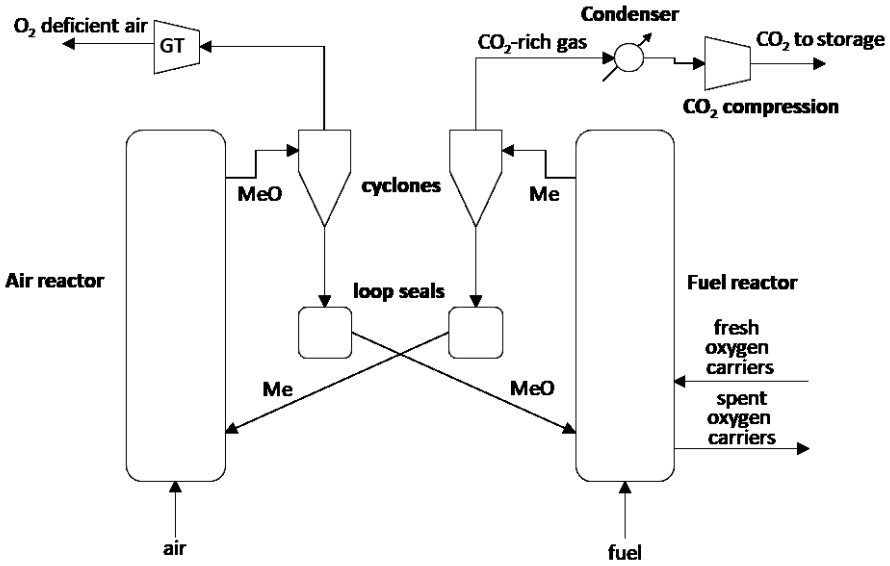
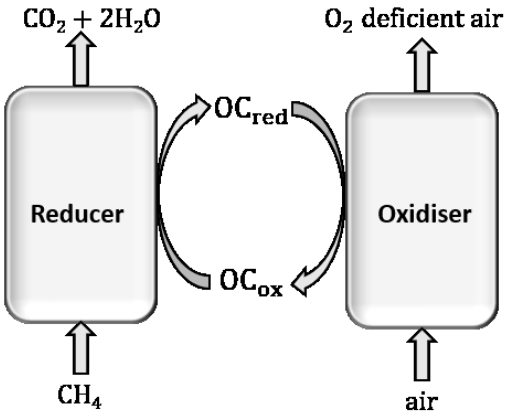


Fig. 2-1 *Schematic diagram of the conventional chemical looping combustion process.*[50,72]

The typical reactor configuration of the natural gas-fired chemical looping process together with the overall reactions are illustrated in **Fig. 2-2**, below.



Overall reaction in the reducer:

$$CH_4 + 2\,M_xO_{2y} \rightarrow CO_2 + 2\,H_2O + 2\,M_xO_{2y-2} \quad (2\text{-}1)$$

Overall reaction in the oxidiser:

$$M_xO_{2y-2} + O_2 \rightarrow M_{2x}O_{2y} \quad (2\text{-}2)$$

Fig. 2-2 *Schematic diagram of the CH_4-CLC process (left), and the overall reactions in the reducer and oxidiser (right).*

In the CH_4-fired process (**Fig. 2-2**), the gaseous fuel is oxidised in the reducer, and the active metal oxide of the oxygen carriers is reduced according to the reaction shown in eq.(2-1). In the oxidiser, the active metal oxide is oxidised according to the reaction shown in eq.(2-2). The total amount of heat released in the CLC system corresponds to the enthalpy of combustion of the fuel. However, as the exergy destruction in a chemical looping combustion process is significantly lower than in a conventional combustion process, the net power efficiency can theoretically be higher.[73]

A proposed reactor layout for the combustion of natural gas in a chemical looping process is shown in **Fig. 2-3**, below.[71]

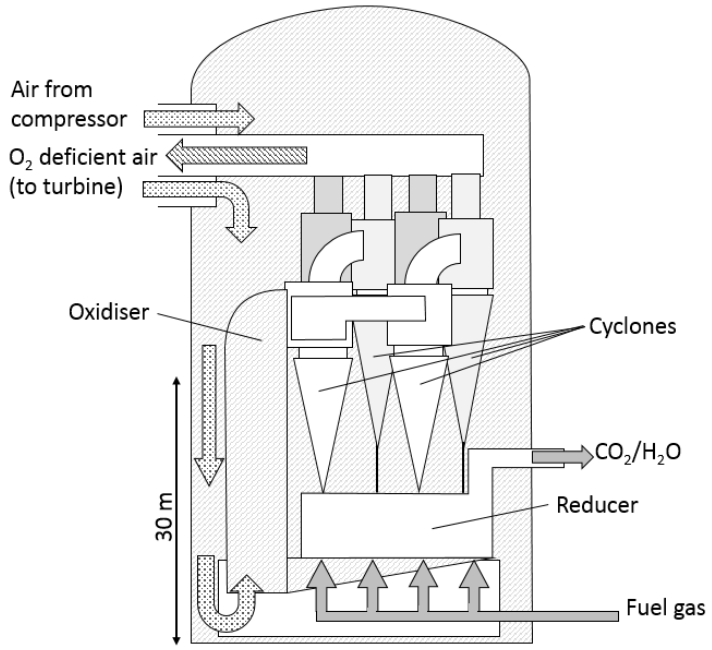


Fig. 2-3 *A possible configuration of a 800 MW reactor system, adapted from Wolf et al.*[71]

The enthalpy released in the reactors can be converted to electrical energy using (i) a steam cycle or (ii) a combination of steam cycle and gas turbine cycle (combined cycle). A state-of-the-art steam cycle configuration is comprised of a boiler, three turbines and two re-heaters.[74] This steam cycle configuration is illustrated in **Fig. 2-4**, below.[74]

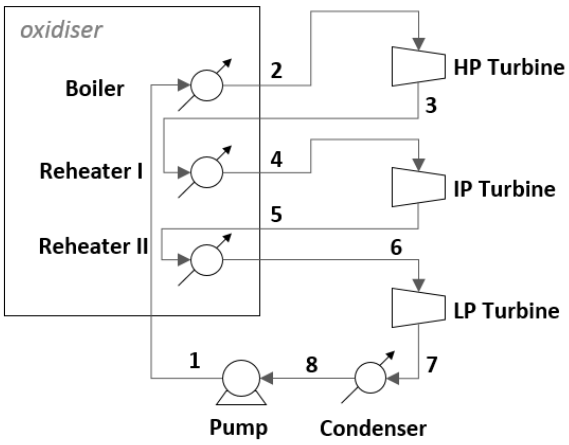


Fig. 2-4 *Diagram of a conventional steam cycle with two re-heaters.*

Patzschke *et al*.[75] simulated a 1000 MW_{th} natural gas CLC plant, which uses only a steam cycle for power conversion. They[75] calculated net plant efficiencies in the range of 35.2 - 40.1%, which vary with a change in operating conditions and oxygen carrier materials. The efficiency of the process can be increased by using a combined cycle for electricity generation. This requires both reactors to operate at elevated pressure. Though theoretically, only the air reactor has to operate at elevated pressure, significant pressure gradients between the two reactors makes it prohibitively difficult to circulate the oxygen carriers and therefore significant pressure differences between the reactors are typically not suggested.[71,76] The exhaust of the air reactor is then expanded through a gas turbine, which drives a generator. The remaining enthalpy in the gas leaving the turbine is then used to drive steam turbines, which in turn drive the generators. Such a chemical looping combustion natural gas combined cycle (CLC-NGCC) process has typically higher thermal efficiencies than a chemical looping process that uses only a steam cycle for power conversion. Wolf *et al*.[71] simulated this process and calculated an exergy efficiency of 44%.[71] The exergy destruction of this process is illustrated using a Grassmann diagram, as shown in **Fig. 2-5**, below.[71]

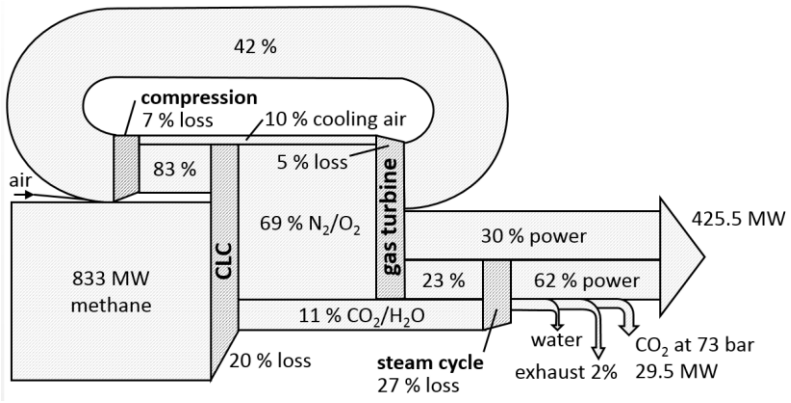


Fig. 2-5 *A Grassmann diagram of a combined cycle using a reactor pressure of 13 bar, with figures in %-loss of exergy of the process, adapted from Wolf et al.*[71]

Wolf *et al.*[71] and Petrakopoulou *et al*.[76] simulated a CLC-NGCC process and calculated a net plant efficiency (LHV) of 53.0% of 51.3%. Zhu *et al.* calculated a net plant efficiency (LHV) of 49.4% for the process.[77] The CLC-NGCC process must compete against other gas-fuelled processes for power generation with CO_2 capture, which are discussed in the next section. Since gas turbine combined cycles (without CO_2 capture) became industry standard, gas-fired processes, which use only a steam cycle for power conversion are not considered in this chapter.

2.2 Alternative processes for the power generation from natural gas with CO_2 capture

An alternative process for electricity production with CO_2 capture is a natural gas combined cycle (NGCC) with a retrofitted CO_2 capture system. The NGCC process without CO_2 capture is illustrated in **Fig. 2-6**, below.[78]

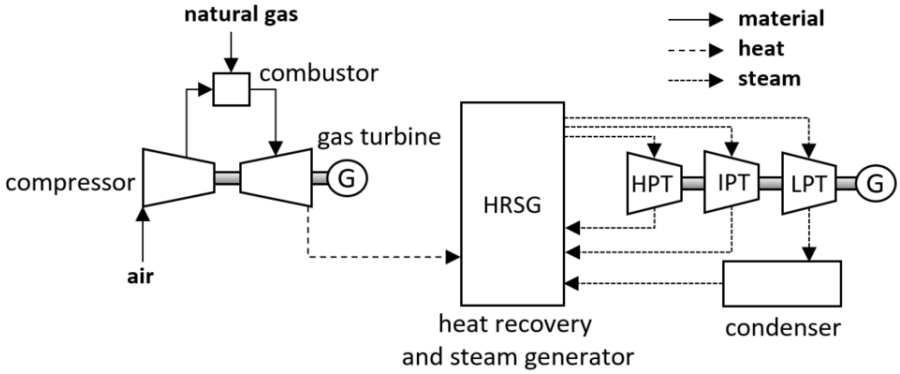


Fig. 2-6 *A schematic diagram of the NGCC process for electricity generation, adapted form Subramanian et al.*[78]

The exergy destruction of the process without CO_2 capture is illustrated in **Fig. 2-7**, below.

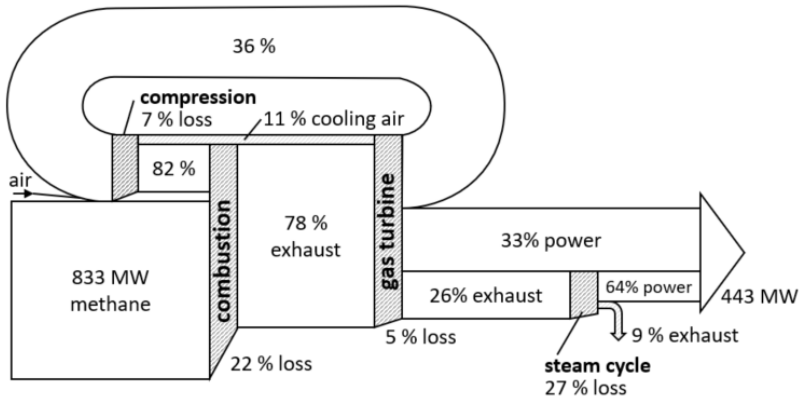
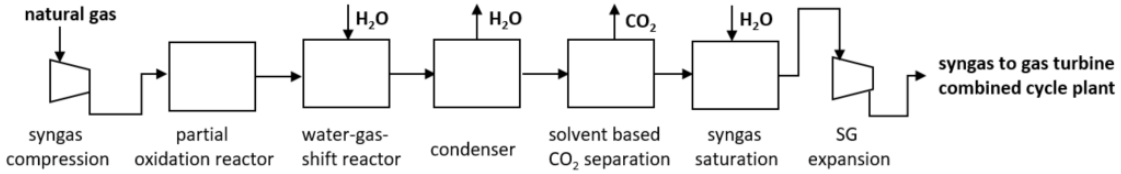


Fig. 2-7 *Grassmann diagram of a combined cycle using a reactor pressure of 13 bar, with figures in %-loss of exergy of the process, adapted from Wolf et al.*[71]

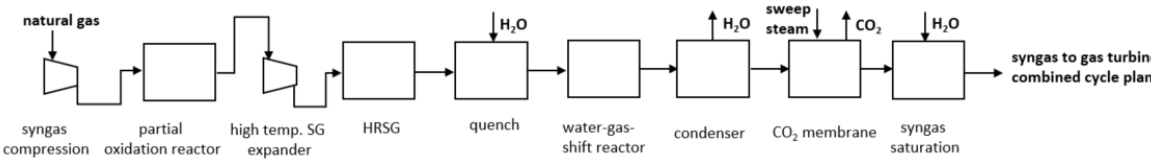
When comparing **Fig. 2-5** and **Fig. 2-7** it can be seen that 10% less exergy is lost during chemical looping combustion compared to conventional combustion. And despite accounting for the relatively energy intense CO_2 compression, the exergy efficiency of the NGCC-CLC process is 0.9% higher than of the conventional NGCC process (NGCC-CLC: 54.1% *c.f.* **Fig. 2-5**; NGCC: 53.2% *c.f.* **Fig. 2-7**).[71] Wolf *et al.* calculated a net plant efficiency (LHV) of 55.2% for the conventional NGCC process.[71] More recent simulations of state-of-the-art NGCC plants yielded net electrical efficiency (LHV) in the range 57.2% – 58.3%.[79,36,80,78,81] Cormos *et al*.[37] and Sipöcz[79] calculated a levelised cost

of electricity of (LCOE) of 49.99 $\$_{2016}$/MWh and 53.56 $\$_{2011}$/MWh (without a cost for emitting the CO_2). Various technologies exist to combine a NGCC and a CO_2 capture process. Some promising processes are illustrated **Fig. 2-8**, below.

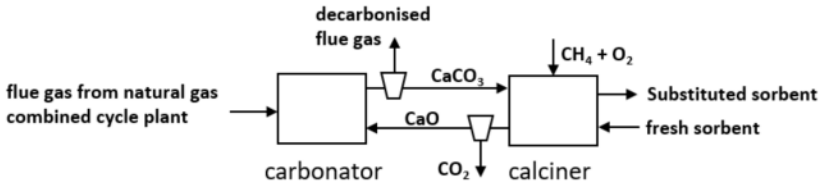
a) *pre-combustion using chemical absorption*



b) *pre-combustion CO_2 capture by using membranes*



c) *post-combustion CO_2 capture using calcium/carbonate looping*



d) *post-combustion CO_2 capture by chemical gas-liquid absorption*

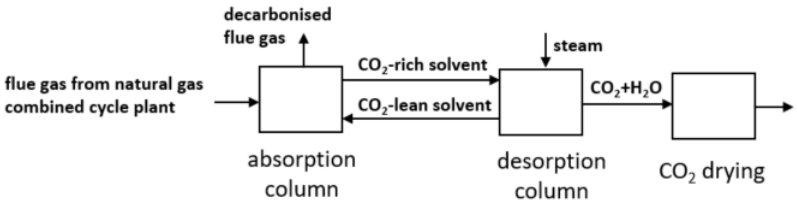


Fig. 2-8 *Schematic diagrams of selected pre- and post-combustion CO_2 capture technologies for gas turbine combined cycle plants that use natural gas as the fuel: (a) pre-combustion chemical adsorption, adapted from Hoffmann et al.[34]; (b) pre-combustion CO_2 capture using membranes, diagram adapted from Hoffmann et al.[34]; (c) post-combustion CO_2 capture using a calcium/carbonate looping, adapted from Berstad et al.[36]; (d) post-combustion CO_2 capture by chemical gas-liquid absorption, adapted from Cormos et al.[37]*

In the process of pre-combustion CO_2 capture (**Fig. 2-8a**), the natural gas is compressed and partially oxidised to syngas (H_2+CO+CO_2). The syngas is reformed to increase the mole fraction of CO_2 in a shift reactor, and the CO_2 is subsequently separated from the syngas by chemical absorption using liquid solvents (typically aqueous alkanol-amine solutions). The CO_2-lean syngas is then combusted in a gas turbine.[34] Residual CO in the CO_2-lean syngas is combusted to CO_2, resulting in relatively

low CO_2 capture rates of around 80%[34] in comparison to other CO_2 capture technologies.[76, 80] Hoffmann *et al*.[34] and Petrakopoulou *et al*.[76] calculated a net plant efficiency (HHV) of 47.5% and 50.7% (LHV, converted with a factor of 1.11), respectively. The LCOE was 102.81 $\$_{2011}$/MWh[76] and the cost of CO_2 capture 46 $\$_{2009}/t_{CO2,avoided}$.[34]

The process of pre-combustion CO_2 capture with membranes (**Fig. 2-8b**) is similar to the process using chemical absorption (**Fig. 2-8a**), though membranes instead of a liquid solvents are used for the gas separation. The CO_2 is separated at atmospheric pressure. This requires a high-temperature syngas expander, which is positioned downstream of the partial oxidiser.[34] For this process, the calculated net electrical efficiency (LHV) and cost of CO_2 capture is 50.7% and \$ 29 $/t_{CO2,avoided}$, respectively.[34]

The calcium/carbonate looping (Ca-looping) process consists of two inter-connected fluidised bed reactors that are used for the calcination of $CaCO_3$ (calcined) and the carbonation of Ca (carbonator).[77] In the process of post-combustion CO_2 capture by calcium/carbonate looping (Ca-looping, **Fig. 2-8c**) from a NGCC plant (*i.e.* **Fig. 2-6**), the flue gas is introduced into the carbonator where it is absorbed by CaO particles to form $CaCO_3$ at temperatures of around 650 °C. In the calciner, the particles release the CO_2 at higher temperatures of around 900 °C and are thus regenerated to CaO.[77,80] Hu *et al*. calculated a net plant efficiency (LHV) of 48.8% with a 93.7% CO_2 capture rate.[80] Cormos *et al.*[37] estimated a LCOE, a CO_2 capture cost, and a net electrical efficiency (LHV) of 63.10 $\$_{2015}$/MWh, 37.48 $\$_{2015}/t_{CO2,avoided}$ and 49.2%, respectively, assuming a CO_2 capture rate of 98.9%.[37]

In the process of post-combustion CO_2 capture by chemical amines (**Fig. 2-8d**), the flue gas from the NGCC plant is contacted with a liquid solvent (typically an aqueous alkanolamine solution) in a packed bed.[82,83] Upon contact, the CO_2 is absorbed by the solvent. The CO_2-rich solvent is transferred *via* a heat exchanger (where it is preheated by the returning lean solvent) to a regeneration column. Higher temperatures in this reactor result in a release of the CO_2 from the solvent. The CO_2-lean solvent is transferred back *via* the heat exchanger to the absorption column.[82,83] The acidic gas separation *via* chemical absorption is a very mature technology and was widely used in industry for sour gas sweetening since the 1930s.[84] Advances in the process design that result in a significant increase in process efficiency are therefore unlikely. Contrarily, improvements of the solvents or solvent blends bear great potential.[83,85]

The process of chemical absorption for post-combustion CO_2 capture is illustrated in **Fig. 2-9**, below.

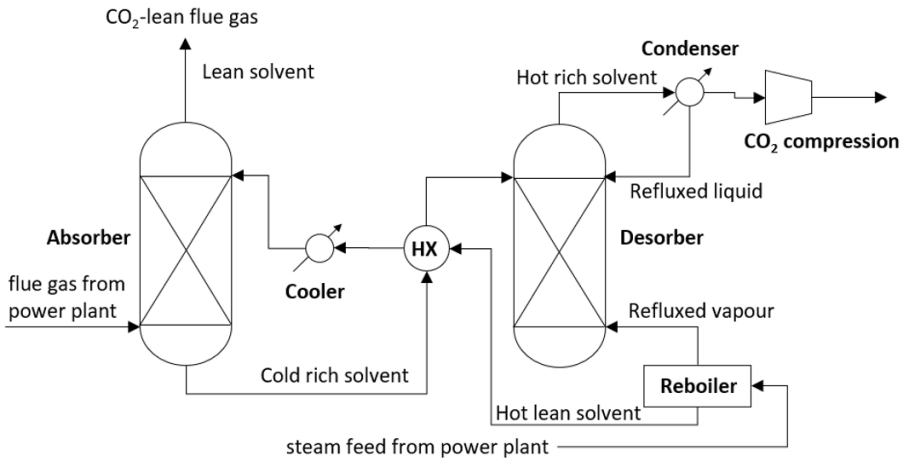


Fig. 2-9 *A diagram of the principle of chemical absorption for post-combustion CO_2 capture, based on the process illustrated by MacDowell et al.*[83]

Hu *et al*.[80] and Garcia *et al*. [81] calculated for an NGCC plant with CO_2 capture by chemical absorption with MEA a net electrical efficiencies (LHV) of 49.7% and 49.9%, respectively. When using second generation amines, the efficiency can be increased to 50.8%.[81] Cormos *et al.*[37] estimated for a process with MDEA an LCOE, a CO_2 capture cost, and a net electrical efficiency (LHV) of 73.1 $\$_{2016}$/MWh, 82.5 $\$_{2015}/t_{CO2,avoided}$ and 52.7%. Petrakopoulou *et al*.[76] calculated an LCOE, a CO_2 capture cost, and a net electrical efficiency (LHV) of 128.1 – 132.9 $\$_{2011}$/MWh, 90.4 – 108.9 $\$_{2011}/t_{CO2,avoided}$ and 45.8 – 48.2%.

Besides natural gas, biomass can be utilised in chemical looping combustion and other processes for electricity generation with CO_2 capture as discussed in the following section.

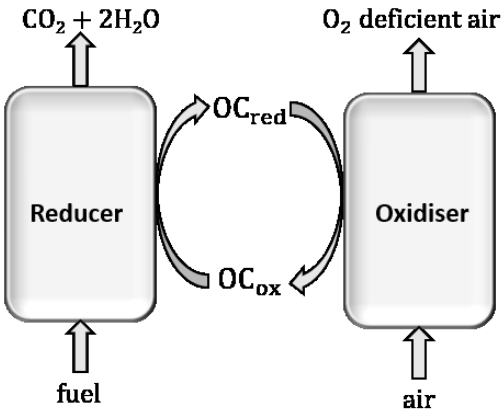
2.3 Chemical looping combustion with solid fuels

The combustion of biomass with CO_2 capture (BECCS) can result in negative CO_2 emissions (*c.f.* section 1.1), rendering these technologies highly effective tools for the reduction in CO_2 net emissions.[86,33] Biomass in general refers to mixture of organic and inorganic material produced by growing plants or contained in municipal, industrial or animal waste.[87] Arguably the most promising biomass are polymeric carbohydrates (*i.e.* wood), which are usually composed of 42-49 wt% cellulose, 16-23 wt% hemicellulose and 21-39 wt% lignin.[88, 89] An advantage, compared to coal are the typically lower ash and sulphur content and a higher volatile matter content.[90] However, compared to coal, biomass has typically a lower energy density, a more complex ash composition, and a higher content of moisture.[88, 91] The utilisation of solid fuels in the conventional CLC process (**Fig. 2-2**) is often inefficient: The reaction of non-volatile matter of the solid fuels with the lattice

oxygen of the oxygen carriers is a solid-solid reaction, which is typically very slow.[88, 92] This problem is more relavant for the solid fuels with low fractions of volatiles (*e.g.* coal). However, for solid fuels with high fractions of volatiles (*e.g.* biomass) incomplete combustion can occur do to imperfect mixing of the fuel and the oxygen carriers and a therefore resulting short residence time of the volatiles.[88, 92] Therefore, four variants of the conventional chemical looping process were suggested to avoid solid-solid reactions when utilising solid fuels. These four processes are (i) chemical looping with oxygen uncoupling (CLOU);[92] (ii) *ex-situ* gasification of biomass to syngas with subsequent syngas chemical looping combustion;[93] and (iii) *in-situ* gasification of biomass in the chemical looping process;[94] and (iv) chemical looping air separation with subsequent oxy-fuel combustion of the solid fuel.[40] The four processes are detailed in the following subsections.

2.3.1 Chemical looping with oxygen uncoupling for the combustion of solid fuels

Chemical looping combustion with oxygen uncoupling (CLOU) was proposed by Mattisson *et al.*[92] In this process, the solid fuel reacts predominantly with molecular O_2 in the gas phase, which is released by the heat of the reducer.[94] The reactor configuration together with the main reactions of the process is illustrated in **Fig. 2-10**, below.[92]



O_2 uncoupling in the reducer:

$$M_{2x}O_{2y} \rightarrow M_{2x}O_{2y-2} + O_2 \quad (2\text{-}3)$$

Solid fuel combustion in the reducer:

$$C_aH_bO_c + \left(a - \frac{b}{4} - \frac{c}{2}\right)O_2 \quad (2\text{-}4)$$

$$\rightarrow aCO_2 + \frac{b}{2}H_2O \quad (2\text{-}5)$$

Overall reaction in the oxidiser:

$$M_{2x}O_{2y-2} + O_2 \rightarrow M_{2x}O_{2y}$$

Fig. 2-10 *Schematic diagram of chemical looping combustion with oxygen uncoupling (left) and the reactions in the reducer and oxidiser (right).*

Oxygen carrier materials that are suitable for the CLOU process are materials with the ability to release O_2 into the gas phase at typical reducer conditions.[95] Suitable single metal oxide systems are Co_3O_4/CoO,[96] Mn_2O_3/Mn_3O_4[96,97] and CuO/Cu_2O[98,99,100,101]. Furthermore, Mn-Fe oxides,[102,103] $CuFe_2O_4$, $CoFe_2O_4$, $NiFe_2O_4$,[104] CuO supported on manganese oxide ore,[105] $CuMn_2O_4$,[86,45] and iron ore (containing Fe_2O_3, SiO_2, CaO and MgO)[106] were suggested as oxygen carriers for the CLOU process. Typically, the release of O_2 continues until the O_2 concentration is equal to the O_2 equilibrium concentration in the reducer.[95] Therefore, O_2 will be released in the reducer until either

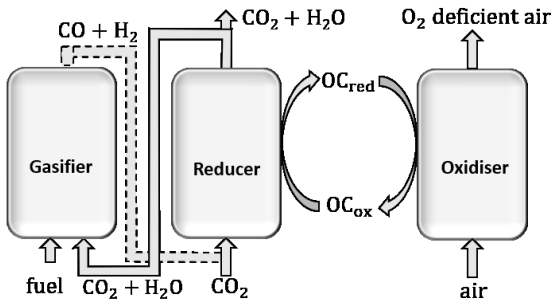
all fuel is converted or the active metal oxide has fully converted to the lowest oxidation state that is thermodynamically favourable at the reactor conditions.[95] The rate of O_2 release can thereby be controlled by the reactor temperature and the O_2 partial pressure.[107]

One drawback of the CLOU process is that the combustion rate of char in the reducer is significantly slower than the combustion of volatiles.[108] Therefore, for full combustion of all hydrocarbon compounds, either the residence times of the oxygen carriers in the reducer has to be longer than required for the combustion of volatiles, or oxygen has to be added downstream to combust the unconverted fuel, which is referred to as "oxy-polishing".[109]

Furthermore, the utilisation of solid fuels can result in the reduction of the average lifetime of the oxygen carriers owing to (i) the removal of some oxygen carrier particles *via* the ash stream owing to imperfect solid-solid separation (of oxygen carriers and ash), and (ii) the increase of the rate of degradation due to poisoning with corrosive compounds contained in the biomass.[109] The contamination of the oxygen carriers with ash can also result in a deactivation – *i.e.* reduction of the overall rates of reaction.[109]

2.3.2 Chemical looping combustion with *ex-situ* gasification

In the process of *ex-situ* gasification chemical looping combustion (*e*G-CLC), biomass is gasified in a reactor upstream of the chemical looping process. The biomass-derived syngas is then utilised in a chemical looping combustion process.[93] A schematic of the process of gasification with chemical looping combustion (gasification + CLC) is shown in **Fig. 2-11**, below.[93,110,111]



Reactions in gasifier:

$$C + H_2O \rightarrow CO + H_2 \quad (2\text{-}6a)$$

$$C + CO_2 \rightarrow 2\,CO \quad (2\text{-}6b)$$

Reactions in the reducer:

$$Me_xO_y + 2\,H_2 \leftrightarrow Me_xO_{y-2} + 2\,H_2O \quad (2\text{-}7a)$$

$$Me_xO_y + 2\,CO \leftrightarrow Me_xO_{y-2} + 2\,CO_2 \quad (2\text{-}7b)$$

Overall reaction in the oxidiser:

$$Me_xO_{y-2} + O_2 \leftrightarrow Me_xO_y \quad (2\text{-}8)$$

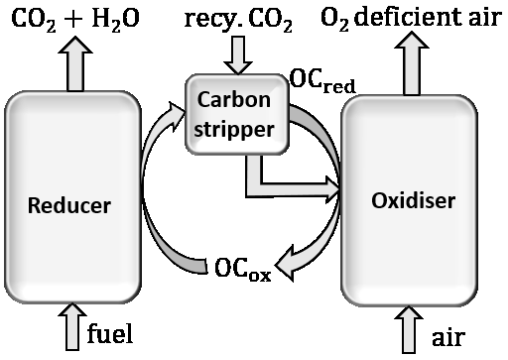
Fig. 2-11 *Schematic of solid fuel gasification with subsequent chemical looping combustion (left) and the overall reactions in the reducer and oxidiser (right).*

A drawback of this process is the relatively slow gasification reaction, which is required for the conversion of the solid fuel to syngas.[93] This results in the need of a relatively large gasification reactor.[93] Furthermore, O_2 is required for the gasification. Using air for the gasification would result in the contamination of syngas with N_2. Thus, an air separation unit for O_2 production is required,

which typically decreases the plant efficiency considerably.[108] The savings in process equipment cost due to the smaller reducer are typically offset by the additional process equipment for O_2 production and gasification.[94]

2.3.3 Chemical looping combustion with *in-situ* gasification

In the process of *in-situ* gasification chemical looping combustion (*i*G-CLC) the biomass is gasified by CO_2 or H_2O in the reducer reactor of the chemical looping system.[94] In comparison to the gasification rates of the *ex-situ* process, the rates of the *in-situ* gasification are significantly higher, since the simultaneous combustion of syngas in the reducer is removing CO and H_2. The latter gases typically inhibit gasification reactions.[94] Nevertheless, the gasification rates in the reducer are still significantly slower than the rates of combustion of a gaseous fuel in the reducer at a given temperature.[94] To achieve acceptable gasification rates, the reducer has to be operated at high temperatures than those typically selected for a gas-fired CLC reducer. Higher reactor temperatures typically increase the capital costs of the reactor.[93,110] An advantage in comparison to *e*G-CLC is that the enthalpy required for the gasification can be directly provided by the exothermic syngas oxidation reaction, which avoids the complex heat integration between the reactors that the *ex-situ* process requires.[93,110] The reactor configuration of the *i*G-CLC process is illustrated together with the relevant reactions in **Fig. 2-12**, below.[93,110, 112]



Biomass gasification in the reducer:

$$C + H_2O \rightarrow CO + H_2 \quad (2\text{-}9a)$$

$$C + CO_2 \rightarrow 2\,CO \quad (2\text{-}9b)$$

Syngas combustion in the reducer:

$$Me_xO_y + 2\,H_2 \leftrightarrow Me_xO_{y-2} + 2\,H_2O \quad (2\text{-}10a)$$

$$Me_xO_y + 2\,CO \leftrightarrow Me_xO_{y-2} + 2\,CO_2 \quad (2\text{-}10b)$$

Overall reaction in the oxidiser:

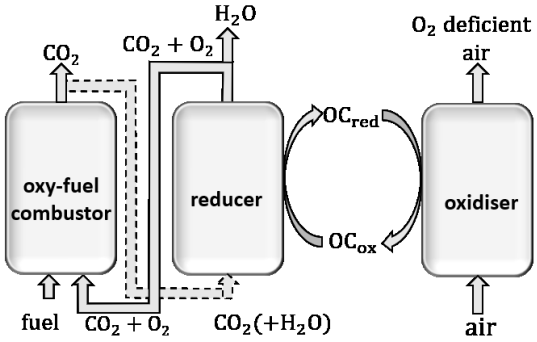
$$Me_xO_{y-2} + O_2 \leftrightarrow Me_xO_y \quad (2\text{-}11)$$

Fig. 2-12 *Reactor configuration of chemical looping air separation with oxy-fuel combustion (left) and the relevant reactions (right). For the sake of simplicity, the fuel in the equations is assumed to consists of carbon.*

2.3.4 Chemical looping for air separation with oxy-fuel combustion

In this section, the process of chemical looping air separation (CLAS) with subsequent oxy-fuel combustion (oxy-fuel) is described. This thesis focuses on the development of oxygen carriers for this process. The oxygen carriers are utilised to enrich recycled CO_2 with O_2 by oxygen uncoupling. The O_2+CO_2 mixture is then used for the combustion of biomass in an oxy-fuel reactor downstream

of the CLAS process.[40] In contrast to conventional oxy-fuel combustion, the CLAS process replaces the cryogenic air separation unit.[40] The CLAS process is illustrated together with the relevant reactions in **Fig. 2-13**, below.



oxy-fuel combustor:

$$C_aH_bO_c + \left(\frac{a}{2} + \frac{b}{8} - \frac{c}{2}\right) O_2 \leftrightarrow a\,CO_2 + \frac{b}{2} H_2O \quad (2\text{-}12)$$

reducer:

$$Me_xO_y \leftrightarrow Me_xO_{y-2} + O_2 \quad (2\text{-}13)$$

oxidiser: (2-14)

$$Me_xO_{y-2} + O_2 \leftrightarrow Me_xO_y$$

Fig. 2-13 *Reactor configuration of chemical looping air separation with oxy-fuel combustion (left) and the overall reactions (right).*

The reactions in the reducer, eq.(2-12), and in the oxy-fuel combustor, eq.(2-13), correspond to the reactions of the CLOU process shown in eq.(2-3) and eq.(2-4). Though, rather than combined in one reactor, these reactions occur in the CLAS process separately in two reactors, *viz.* the reducer and the oxy-fuel combustor. Consequently, both reactors can be operated at their individual optimal conditions and the direct contact between the fuel and the oxygen carriers is prevented. This can enhance the oxygen carriers' lifetimes significantly, as detrimental effects of fuel impurity poisoning and ash deposition are avoided.[46]

Furthermore, the combustion unit of a conventional existing power plant could be converted to operate as the oxy-fuel combustor. This would only require the CLAS unit to be retrofitted upstream, enabling construction with lower capital costs and possible construction time savings compared to a new-build CLC plant. In the following paragraph, the oxy-fuel combustion is detail.

The oxy-fuel combustion process of the CLAS + oxy-fuel system is illustrated in **Fig. 2-14**, below.[71]

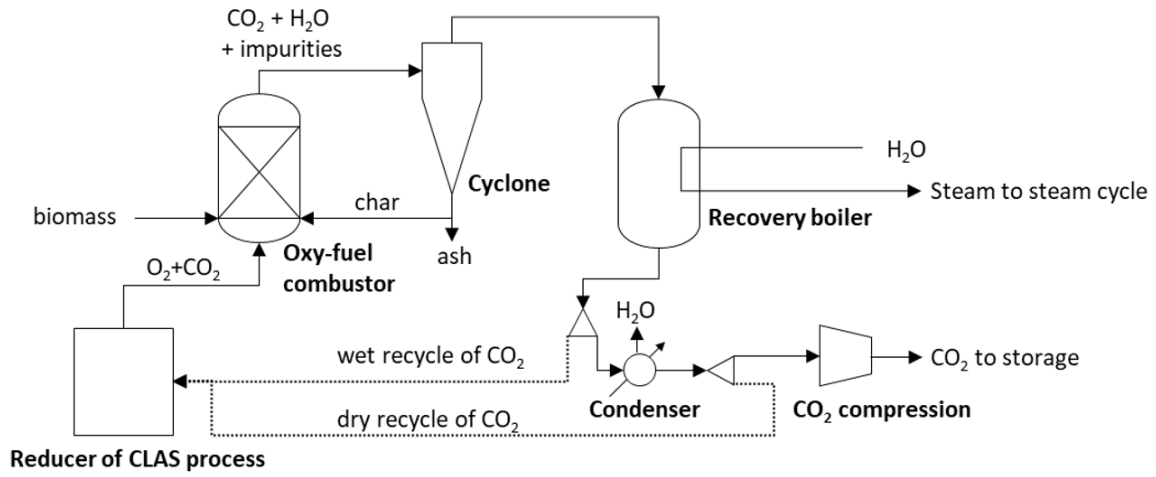


Fig. 2-14 *A flowsheet of the oxy-fuel combustion for CO_2 capture with O_2+CO_2 production via the CLAS process. A combination of the drawings from Maroto-Valer[71] and Patzschke et al.[46]*

In the oxy-fuel combustor (**Fig. 2-14**), biomass is combusted in O_2+CO_2+(H_2O). Ash and char particles are separated from the exhaust gas in a cyclone. Subsequently, the heat of the gas is transferred to the steam cycle in a boiler and the vapour from the exhaust gas is removed in a condenser. Some of the exhaust gas (wet or dry) is recycled for the production of the oxy-fuel mixture, while the remaining fraction of the dry CO_2-rich stream is compressed and transported for geological sequestration.[113] In theory, only O_2 is required for the solid fuel combustion, eq.(2-12). However, since this would result in excessive temperatures and a reduced heat transfer between the combustor and the boiler, the fuel is combusted in recycled flue gas (mainly CO_2) and hence diluted O_2, as shown in **Fig. 2-14**. The flue gas is either withdrawn upstream or downstream of the condenser, which is referred to as "wet recycle" and "dry recycle", respectively.[114] The resulting O_2 + CO_2 (+ H_2O) mixture has typically 25-35 vol% O_2,[35, 114-117] which is higher than that for conventional combustion in air (21 vol% O_2 + N_2). A higher volume fraction of O_2 is required to obtain the similar flame characteristics and adiabatic flame temperatures.[35, 40, 115] This is due to the higher specific heat capacity of CO_2 compared to N_2, and to the lower diffusivity in CO_2, which in turn results in a decrease in the propagation velocity of the flame.[35, 114] Wall *et al.*[114] calculated that 28 vol% and 35 vol% are required to achieve the same adiabatic flame temperature as during solid fuel combustion in air, for wet and dry recycle, respectively.

However, it should also be mentioned that the higher specific heat capacity of CO_2 results in an enhanced heat transfer from the combustor to the steam cycle compared to combustion in air, as the mass flow rate of hot gases leaving the combustor is increased. Though, a disadvantage of oxy-fuel combustion may be the higher rates of corrosion in the process piping owing to the presence of CO_2.[83] Detailed process simulations with data from combustion experiments and including a techno-

economic studies are therefore arguably the best way to predict the performance and the optimal operating conditions of an oxy-fuel process in comparison to an air-fuel process.

To produce an O_2+CO_2 mixture with 25 – 35 vol% (which corresponds to a p_{O_2} range of 0.25 – 0.35 bar for operation at atmospheric pressure and is hereafter referred to as $p_{O_2,\mathrm{comb}}$) the driving force of the O_2 release reaction of the oxygen carriers has to be positive. This is when the O_2 partial pressure in the reducer $p_{O_2,\mathrm{red}}$ is $p_{O_2,\mathrm{red}} < p_{O_2,\mathrm{eq}}$, where $p_{O_2,\mathrm{eq}}$ is the O_2 equilibrium pressure of the oxygen carriers. For the oxidation to occur p_{O_2} has to be lower than $p_{O_2,\mathrm{eq}}$. Since $p_{O_2,\mathrm{eq}}$ increases with temperature and the oxidation is limited to $p_{O_2} < 0.21$ when using air, the reducer has to operate at a higher temperature than the oxidiser. However, the required operating temperature of the reducer can be lowered relative to the oxidiser temperature by injecting steam into the reducer.[40] The presence of steam in the reducer affects the O_2 partial pressure of the O_2 release reaction, $p_{O_2,\mathrm{red}}$, by,[118]

$$p_{O_2,\mathrm{red}} = P \cdot \left(\frac{\dot{N}_{O_2,\mathrm{red}}}{\dot{N}_{\mathrm{steam}} + \dot{N}_{CO_2} + \dot{N}_{O_2,\mathrm{red}}} \right) \tag{2-15}$$

where $\dot{N}_{O_2,\mathrm{red}}$, $\dot{N}_{\mathrm{steam}}$ and $\dot{N}_{CO_2}$ are the molar flow rate of the produced O_2, the injected steam and the injected CO_2, respectively, and P is the absolute pressure.

The steam can be separated from the gas leaving the reducer by condensation. The flow rate of the removed water can be calculated by a dew-point calculation:[118, 119]

$$T_{dew}/°\mathrm{C} = \frac{243.12 \cdot a_1}{17.62 - a_1} \tag{2-16}$$

The parameter a_1 in eq.(2-16) is calculated by,[118, 119]

$$a_1 = \frac{\ln(\mathrm{RH}) + 17.62 \cdot T/°\mathrm{C}}{T/°\mathrm{C} + 243.12} \tag{2-17}$$

The increased O_2 partial pressure in the gas entering the combustor, $p_{O_2,\mathrm{comb}}$, can be calculated by,[118]

$$p_{O_2,\mathrm{comb}} = P \cdot \left(\frac{\dot{N}_{O_2,\mathrm{red}}}{\dot{N}_{\mathrm{steam}} + \dot{N}_{CO_2} + \dot{N}_{O_2,\mathrm{red}} - \dot{N}_{H_2O}} \right) \tag{2-18}$$

When using a steam:CO_2 molar ratio of 2:1, a gas stream with 10 vol% O_2 at the reducer outlet would result in a 25 vol% O_2 + CO_2 mixture after full condensation of the steam. The same p_{O_2} at the reducer outlet, but with fluidisation by steam and CO_2 in a molar ratio of 4:1 would result in a 36 vol% O_2 + CO_2 mixture after steam condensation. However, the amount of steam injected has to be carefully considered, since it can also lead to significant reductions in the CLAS process efficiency.

The oxygen carriers play a vital role in the CLAS process and their performance impact process efficiency significantly. Their characteristics and performances are influenced by their preparation method. Early publications focused on perovskite-type materials.[120] Yang *et al.*[120] studied a strontium-iron doped perovskite-type material and identified the slow desorption rates as well as reversible carbonate formation as major drawbacks of the perovskite-type materials. The carbonate formation is especially problematic if the CLAS process is used for CO_2 capture, since during the oxidation the carbonates decompose thereby releasing CO_2.

Contrarily, the three single metal oxides with CLOU properties (Cu, Mn and Co oxides) do not have these problems, and were thus focus of recent studies.[121, 122] CuO supported on ZrO_2[123] and $MgAl_2O_4$[100] have been reported as a promising oxygen storage material for the CLOU process.[123] Furthermore, CuO on $MgAl_2O_4$[121] and SiO_2[122] supports were identified as promising materials for the CLAS process. However, a drawback of Cu oxides is their inferior mechanical properties, which make them prone to agglomeration and attrition.[124] Another disadvantage of using Cu-based oxygen carriers for the CLAS process is the high temperature required to release gaseous O_2 in an oxygen-rich environment. The temperature at which the O_2 equilibrium partial pressure, $p_{O_2,eq}$, is 0.1 bar is 993 °C. For comparison, the temperature at which Mn_2O_3 has a $p_{O_2,eq}$ of 0.1 bar is 854 °C.

Typically, the reactor walls in a chemical looping process are protected from the heat by a refractory.[125] However, reactor walls without refractory have to be used, if heat has to be transferred through the walls to provide the enthalpy required to offset the endothermic O_2 release reaction. This exceeds the operating temperature of most common reactor materials.[126] For example, the strength of ferritic-martensitic steels reduces to critical levels in the range 600 – 700 °C.[126] Nickel-based alloys have a slightly higher maximum temperature.[126] At temperatures above 900 °C, only tungsten- and molybdenum-based systems are considered to be feasible reactor wall materials.[126]

Owing to the high cost of these materials, transfer of heat through the reactor walls at high temperatures is therefore generally not considered as feasible in the CLAS process. Heat integration among the reactors is therefore a major challenge when designing the CLAS process.[127,24,24,24,22] The O_2 release reaction is endothermic, while the combustion is highly exothermic. This requires the transfer of heat at high temperatures. Some of the heat is transported by the oxygen carrier[40] and the recycled CO_2[128]. Further heat can be provided by adding superheated steam[128] or minor amounts of CO[128] to the reducer, by integrating the reducer into the combustor[128] or by heating the reducer with concentrated solar power,[128] co-combusting methane or electrically.[40, 128] Several heat integration studies for CLAS processes can be found in the literature.[40, 128, 129]

Patzschke *et al.*[130] recently simulated a CLAS + oxy-fuel process in which concentrated solar power provides the required enthalpy to offset the endothermic reaction in the reducer. This process, which allows for solar energy storage and negative CO_2 emissions is illustrated in **Fig. 2-15**, below.

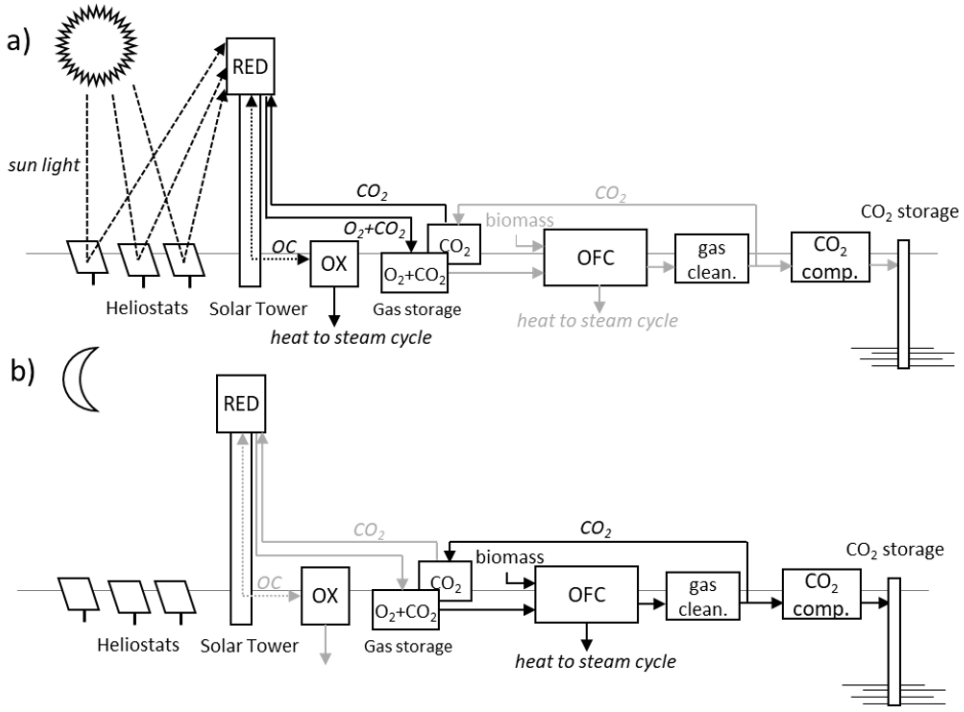


Fig. 2-15 *A flowsheet of a solar powered CLAS + oxy-fuel process with arrows representing the energy and material flows (a) during the day and (b) at night. Adapted from Patzschke et al.*[130]

During the day (**Fig. 2-15a**), solar power is used to produce a O_2+CO_2 mixture, while excess heat from the oxidiser powers a steam cycle. At night (**Fig. 2-15b**), the O_2+CO_2 mixture is used for the oxy-fuel combustion of biomass in a 100 MW_e plant. Accounting for variations in the incoming solar beam irradiance with the time of the day and year for the location of Sevilla in Spain, it was calculated that this process can capture 306 911 t(CO_2) yr^{-1}, while producing an electricity output that is proportional to electricity demand of this region considering hourly and seasonal changes of the electricity demand.

2.4 Alternative processes for power generation from solid fuels with CO_2 capture

In this section, alternative processes (other than chemical looping) for the utilisation of biomass for electricity production with CO_2 capture are discussed. Promising processes are (i) integrated gasification combined cycle (IGCC),[31] (ii) oxy-fuel combustion with O_2 production *via* cryogenic air separation, and post-combustion capture by (iii) Ca-looping[131] and (iv) chemical absorption. These processes are detailed in the following subsections.

Integrated gasification combined cycle with biomass

Rhodes and Keith[31] simulated a 123 MW_e integrated gasification combined cycled (IGCC) that utilises biomass. The process is comprised of five sub-processes: biomass drying, gasification, gas conditioning, CO_2 capture, and the combustion of a CO_2-lean syngas in a gas turbine.[31] A rotary dryer utilises the heat from the char combustor exhaust and also generates steam for the gasifier. The heat for the gasification is provided by hot sand, which is circulated between the gasifier and the char combustor. The CO_2 produced from char combustion is not captured, and therefore 30% of the carbon contained in the biomass is released as CO_2 to the atmosphere.[31] The syngas from the gasifier is conditioned to convert CH_4 and higher hydrocarbons to CO_2, CO and H_2. The CO_2 is separated from the gas, and the CO_2-lean syngas is combusted in a GE H-class gas turbine unit. The CO_2 from the exhaust gas of the gas turbine is emitted to the atmosphere. The process is illustrated in **Fig. 2-16**, below.[31]

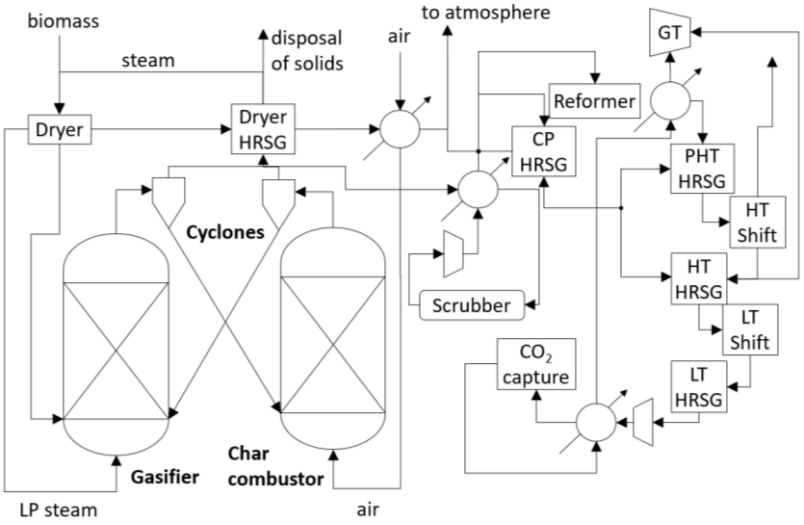


Fig. 2-16 *A schematic diagram of an integrated gasification combined cycle process, adapted from the illustration by Rhodes & Keith.*[31]

The emission of CO_2 from the exhaust of the char combustor and the gas turbine result in a relatively low rate of CO_2 capture of 44%.[31] Furthermore, the calculated thermal efficiency (HHV) of this process is only 28%.

Oxy-fuel combustion of biomass with O_2 production *via* cryogenic air separation

The principle of this technology differs from the oxy-fuel process described in section 2.3.4 only by the air separation unit, which instead of CLAS is here considered to be either a cryogenic distillation unit or a membrane system.[71] The literature lacks results of simulations from biomass fired oxy-fuel plants. However, several works have studied the coal-fired process, which provides an indication for the energy penalty of the process. For state-of-the-art technology, efficiency reductions of coal-fired

oxy-fuel plants in the range of 8-12% were reported.[132] Pressurised operation may further reduce the energy penalty, since it increases the flue gas heat recovery efficiency and decreases the energy requirements for compression.[133] A reactor pressure of around 10 bar is considered optimal.[133] Furthermore, the energy penalty can be reduced to 5-6%-points when using a membrane system instead of a cryogenic air separation system for the O_2 production, such as a four-end high-temperature oxygen transport membrane.[134,135] Mansouri *et al.*[116] calculated a net plant efficiency (HHV) for the combustion of coal in an oxy-fuel plant and a conventional plant of 38.8% and 29.5%, respectively. This 9.3%-point energy penalty contains 6.0%-points that are associated with the energy requirements due to compression of CO_2.[116] The exergy efficiency of the conventional plant and the oxy-fuel plant were calculated to be 37.9% and 31.9%, respectively.[116]

The carbonate looping process with biomass

The combination of biomass combustion and a Ca-looping is possible as either a two-step process, in which the flue gas from a biomass-fired power plant is decarbonised in a downstream Ca-looping plant or a one-step process,[131] in which biomass combustion occurs in the carbonator of the Ca-looping process. The two-step process is described in section 2.2 and will be very similar for the flue gas treatment from biomass combustion. This section therefore focuses on the novel one step process with *in-situ* biomass combustion. The process is illustrated in **Fig. 2-17**, below.

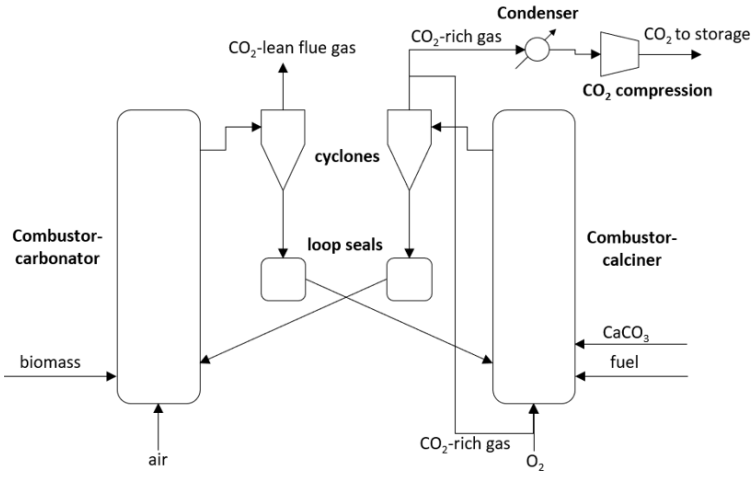


Fig. 2-17 *Schematic diagram of the Ca-looping process for in situ biomass combustion, based on the process illustrated by Diego et al.*[136]

In the process shown in **Fig. 2-17**, the biomass is fed to the carbonator, which operates at around 700 °C. The CO_2 produced by the biomass combustion reacts with the CaO particles to $CaCO_3$.[136] The $CaCO_3$ is circulated *via* a cyclone and a loop seal to the combustor, in which the $CaCO_3$ is regenerated in an oxy-fuel to CaO and CO_2 at 840 – 900 °C.[136] The CO_2-rich exhaust gas of the calciner is purified, steam is condensed out, and the dry CO_2 stream is compressed for CO_2 transport and

sequestration.[136] Ozcan[137] calculated a net thermal efficiency of 40.9% (LHV) for an air-fired biomass plant, 33.9% (LHV) for an oxy-fuel fired power plant and 35.7% (LHV) for an *in situ* biomass combustion Ca-looping plant. The levelized cost of electricity for the air fired plant was 144.6 $\$_{2014}/MW_e$, for the oxy-fuel fired biomass plant 184.4 $\$_{2014}/MW_e$ and 175.2 $\$_{2014}/MW_e$ for the *in-situ* biomass combustion Ca-looping plant.

2.5 Concluding remarks

In this chapter, chemical looping processes and alternative processes for electricity generation with CO_2 capture from natural gas and biomass were detailed. The technological aspects of all process have been explained, and data on costs and efficiencies have been compared. For the gas-fuelled processes, a combined gas turbine cycle is often possible, which results in higher efficiencies. This is also the case for CLC processes, for which the reviewed literature showed that the thermal efficiency (LHV) of a combined cycle (NGCC-CLC) is 7%-points higher.

For the competing CO_2 capture technologies, the net thermal efficiency (LHV) of these processes are (from low to high): NGCC with post-combustion capture using a Ca-looping (49.2%) < NGCC with post-combustion capture using MEA (49.9%) < GTCC with pre-combustion capture using membranes (50.7%) < NGCC with post-combustion capture using second generation solvents (50.8% – 52.7%). The reviewed literature found that NG-CLC has the second highest reported net plant efficiency, only surpassed by a NGCC process with post-combustion CO_2 capture using second generation amines.

For the combustion of solid fuels several chemical looping processes have been reviewed, which are modifications of the conventional chemical looping process to avoid slow solid-solid reactions. The *ex-situ* gasification process seems inferior to the other processes, as the need for an additional gasifier, a complex heat integration, and a source of O_2 for the gasification, which increase the capital and operating costs significantly. A high number of works were published on the CLOU process, and many works report an effective solid fuel combustion when using this process. Contrarily, the CLAS process – on which this thesis focuses – is relatively novel (the first work in which single metal oxygen carriers were proposed was published in 2008)[138] Prolonged oxygen carrier lifetimes by the process-intrinsic separation of the oxygen carriers and the fuel have been identified as an advantage. However, the slow O_2 release reaction and significant challenges of the heat integration, have been identified as major drawbacks. As alternative processes to chemical looping combustion for the utilisation of biomass for power generation with CO_2 capture, the processes of (i) integrated gasification combined cycled, (ii) oxy-fuel combustion with O_2 production by cryogenic air separation, and biomass combustion with post-combustion capture (iii) using a Ca-looping and (iii) chemical absorption were identified.

Chapter 3

Desirable properties and preparation methods of oxygen carriers

This chapter presents a literature study on the development of oxygen carriers. The review is supported with results from first principle calculations using data from FactSage.[139] In the first section (section 3.1), desirable properties of the active phase of oxygen carriers are discussed. Lower mechanical stability of the active phases requires the support with an inert material to withstand the stresses of the chemical looping process. The desirable properties of inert supports are evaluated in section 3.2. Furthermore, the preparation and operation costs associated with the oxygen carriers are important selection criteria, as discussed in section 3.3. In section 3.4, the methods that are commonly used for the preparation of oxygen carriers are reviewed. In section 3.5, the process parameters of the calcination of the oxygen carrier precursors are discussed. Finally, the findings of the literature study of this chapter are summarised in section 3.6.

3.1 Desirable properties of the active phases of oxygen carriers

The desirable properties of the active phases of oxygen carriers are evaluated in the section below, thereby focusing on materials with the ability to release gaseous O_2, as this is an essential property of oxygen storage materials in the CLAS + oxy-fuel process.[40]

3.1.1 Reactivity, O_2 equilibria and intra-particle diffusion resistance

The minimum required quantity of oxygen carrier in a reactor is inversely proportional to its reactivity.[140] The reduction and oxidation rates of the oxygen carriers need thus to be sufficiently fast to ensure that the sizes of the reducer and the oxidiser are not excessive. For an industrial-scale chemical looping process, typically the use of circulating fluidised bed reactors is proposed.[50] In those reactors, the effect of the external mass transfer on the overall rate of reaction can be rate controlling.[141,142] In this case, a further increase of the intrinsic kinetics does not result in a decrease in the required reactor size. A comparison of the reactivity of common active metal oxide system with CH_4 for chemical looping processes is shown in **Fig. 3-1**, below.

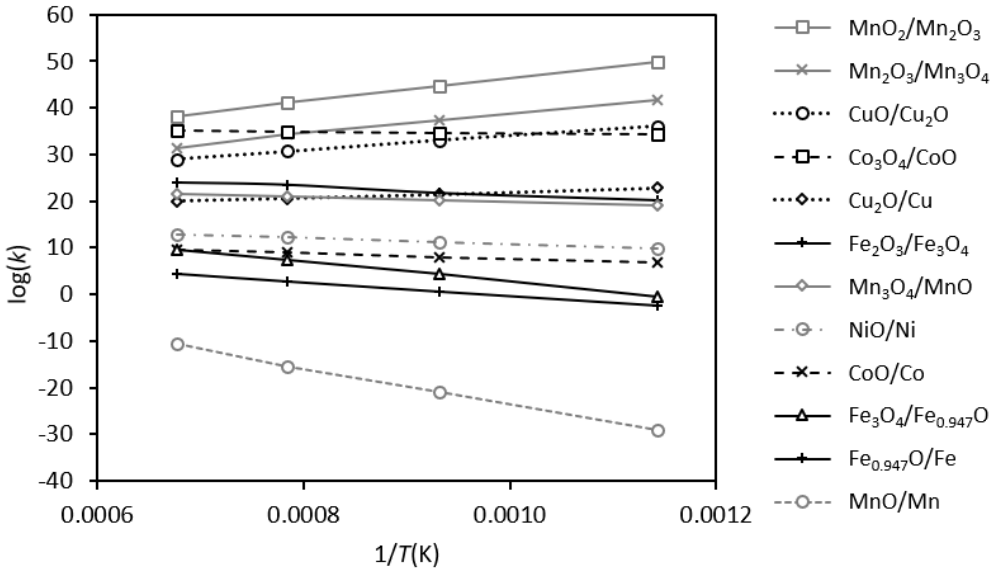


Fig. 3-1 *A plot of log(k) against 1/T for the reduction of various metal oxides in CH_4, with k being the intrinsic reaction rate constant per unit of volume in s^{-1} and the chemical rate of CH_4 consumption, r, is given by $r = k[CH_4]$. The plot is adapted from Mattison & Lyngfelt.[143]*

In **Fig. 3-1** it can be seen that the reactivity of the active metal oxides over most of the $1/T$ range of the plot follows the order (from high to low reactivity): MnO_2/Mn_2O_3 > Mn_2O_3/Mn_3O_4 > CuO/Cu_2O > Co_3O_4/CoO > Cu_2O/Cu > Fe_2O_3/Fe_3O_4 > Mn_3O_4/MnO > NiO/Ni > CoO/Co > $Fe_3O_4/Fe_{0.974}O$ > $Fe_{0.947}O/Fe$ > MnO/Mn.[143]

Besides the chemical reaction rate and the external mass transfer, the overall rate of reaction can also be limited by intra-particle diffusion resistance.[144] An overall rate, which is limited by intra-particle diffusion resistance can typically be increased by increasing the porosity (this is detailed in the chapter 6).[144] Only a few works in the literature report the value of the porosity.[145] More commonly, the BET surface area, S_{BET}, is reported, which is provides a very rough indication of the likely porosity of the particles. In the literature the reported values of S_{BET} vary significantly by preparation method. This is illustrated in **Fig. 3-2**, below.

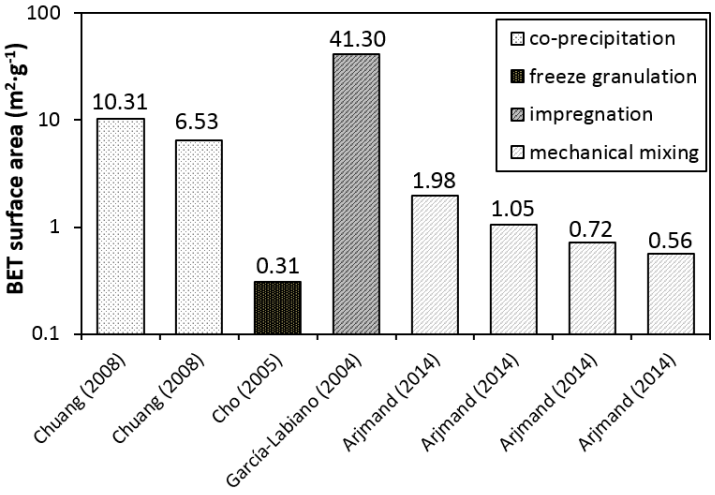


Fig. 3-2 *BET surface area of Cu-based oxygen carrier reported in the literature.*

The values of S_{BET} illustrated **Fig. 3-2** are in the range 0.31 – 41.30 m^2 g^{-1}. The oxygen carriers prepared by freeze-granulation were found to have the lowest average surface area (0.31 m^2 g^{-1}),[145] followed by those prepared *via* mechanical mixing (0.56 – 1.98 m^2 g^{-1}),[146] co-precipitation (6.53 – 10.31 m^2 g^{-1}) [147], and impregnation (41.30 m^2 g^{-1})[148]. Besides synthetic oxygen carriers, natural ores are also under investigation as oxygen carriers for chemical looping process. Sundqvist *et al.*[149] evaluated Mn ores as oxygen carrier materials, and reported values of S_{BET} in the range 0.41 – 6.10 m^2 g^{-1} (the average was 1.47 m^2 g^{-1}). The relationship between the pore morphology of the particles and the intra-particle diffusion resistance is too complex to determine optimal porosity and surface area ranges. For the oxygen carriers of this work, this matter is discussed in detail in **section 6.3**, using the results of a computer simulation of the overall reaction rate, which accounts for the chemical reaction, intra-particle diffusion and external mass transfer.

Furthermore, for the redox-reactions to occur, the Gibbs free energy of the overall reaction has to be negative. Here, it is assumed to be the case, when the sum of the Gibbs free energies of all occurring reactions is negative. This assumption holds true for compounds with activities of unity. For the solids in this section, the values of the activities are practically equal to unity. Therefore, a negative Gibbs free energy indicates that the reaction is thermodynamically favourable and will occur

spontaneously. For the overall reaction in the reducer of the CLC process, ΔG_{CLC}, to be thermodynamically favourable (*i.e.* $\Delta G_{\mathrm{CLC}} < 0$), the oxidation of the fuel has to provide enough energy for the metal oxide to decompose. The Gibbs free energies of the oxidation and of the metal oxide decomposition are denoted with $\Delta G_{\mathrm{comb.}}$ and $\Delta G_{\mathrm{decomp.}}$, respectively. The decomposition of the oxide is the reverse reaction of the oxidation: $\Delta G_{\mathrm{decomp.}} = -\Delta G_{\mathrm{oxid.}}$. These relationships can be expressed as,

$$\Delta G_{\mathrm{CLC}} = \Delta G_{\mathrm{comb.}} + \Delta G_{\mathrm{decomp.}} = \Delta G_{\mathrm{comb.}} - \Delta G_{\mathrm{oxid.}} \tag{3-1}$$

The values of $\Delta G_{\mathrm{comb.}}$ for the combustion of C, H_2 and CO are compared against the values of $\Delta G_{\mathrm{oxid.}}$ of Mn, Cu, Co and Fe oxides – commonly used single metal oxides in chemical looping processes – in **Fig. 3-3**. According to eq.(3-1), $\Delta G_{\mathrm{comb.}}$ in the plots of **Fig. 3-3** has to have a higher negative value than $\Delta G_{\mathrm{oxid.}}$ for ΔG_{CLC} to be negative, and the overall reaction to be thermodynamically favourable.

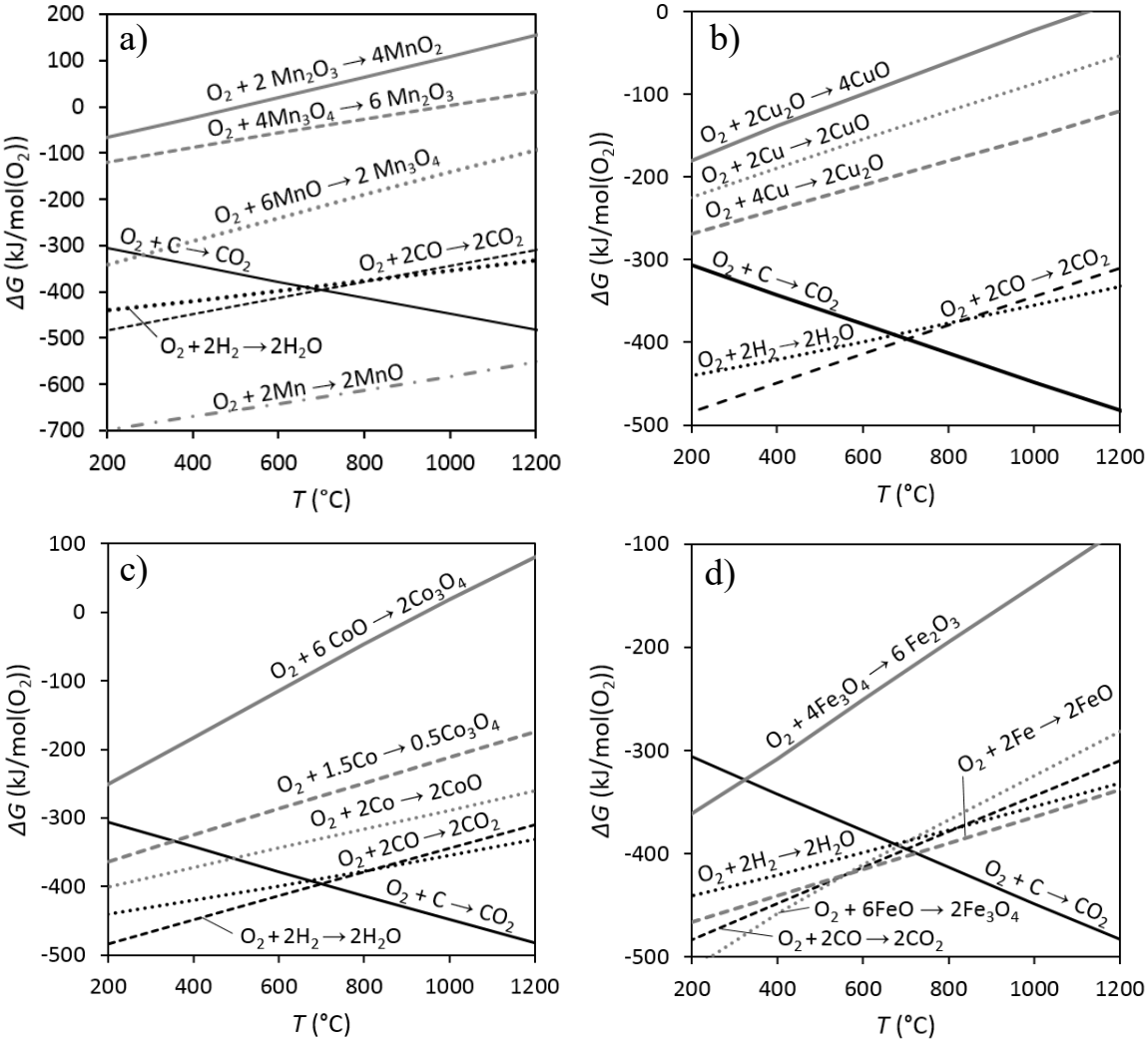


Fig. 3-3 *Ellingham diagram for the reduction of: (a) manganese oxides, (b) copper oxides, (c) cobalt oxides and (d) iron oxides at 0.1 MPa. The lines were computed using data from FactSage.*

In **Fig. 3-3a** it can be seen that the reduction from MnO_2 to Mn_2O_3, Mn_3O_4 to Mn_2O_3 and Mn_3O_4 to MnO during the combustion of C and CO to CO_2 are thermodynamically favourable over most of the plotted temperature range. However, the reduction of MnO to Mn is under the same conditions thermodynamically unfavourable. For Cu-oxygen carrier, the reduction of CuO to Cu_2O, CuO to Cu and Cu_2O to Cu with C, CO and H_2 are thermodynamically favourable across the condition range that is shown in **Fig. 3-3b**. For Co-oxygen carrier (**Fig. 3-3c**), the reduction from Co_3O_4 to CoO, Co_3O_4 to Co and CoO are thermodynamically favourable in the presence of C, CO and H_2. For Fe-oxygen carrier reduction from Fe_2O_3 to Fe_3O_4 according to **Fig. 3-3d** is thermodynamically favourable over most of the temperature range. Further reduction from Fe_3O_4 to FeO is possible in C, H_2 and CO at temperatures above ~700 °C, ~750 °C and ~600 °C, respectively. The reduction of FeO to Fe is only thermodynamically favourable with carbon at temperatures above ~700 °C.

In the oxidiser, the oxygen carriers are typically oxidised in (O_2 deficient) air, which is assumed to behave like an ideal gas. The oxidation in the oxidiser is thermodynamically favourable if the Gibbs free energy, $\Delta G_{\mathrm{oxidiser}}$, is negative. Similarly, the Gibbs free energy in the reducer of the CLAS process, ΔG_{CLAS}, has to be negative for the O_2 release to occur. The oxidation reaction in the oxidiser is the reverse reaction of the O_2 release reaction in the reducer of the CLAS process: $\Delta G_{\mathrm{CLAS}} = -\Delta G_{\mathrm{oxidiser}}$, and ΔG_{CLAS} is given by,

$$\Delta G_{\mathrm{CLAS}} = -\Delta G_{\mathrm{oxidiser}} = \Delta G_{\mathrm{O_2}} + \Delta G_{\mathrm{decomp.}} = \Delta G_{\mathrm{O_2}} - \Delta G_{\mathrm{oxid.}}, \tag{3-2}$$

where $\Delta G_{\mathrm{O_2}}$ is the free energy of O_2. The O_2 partial pressure, $p_{\mathrm{O_2}}$, can be related to the free energy of O_2 at reference conditions, $\Delta G^{\theta}_{\mathrm{O_2}}$, by,[94, 118]

$$p_{\mathrm{O_2}} = \exp\left(-\frac{\Delta G^{\theta}_{\mathrm{O_2}}}{RT}\right)\alpha \tag{3-3}$$

where, R, T and α are the ideal gas constant, the temperature and the activity respectively. The value of α is typically assumed to be unity.[94, 118] Thus, the free energy of O_2 becomes $RT \cdot \ln(p_{\mathrm{O_2}}/P)$. In **Fig. 3-4**, below, the free energy of O_2 for $p_{\mathrm{O_2}}$ = 0.01 bar and 0.30 bar, and a total pressure of P = 1 bar (or 0.1 MPa), are plotted against $\Delta G_{\mathrm{oxid.}}$ of the single metal oxides from **Fig. 3-3**.

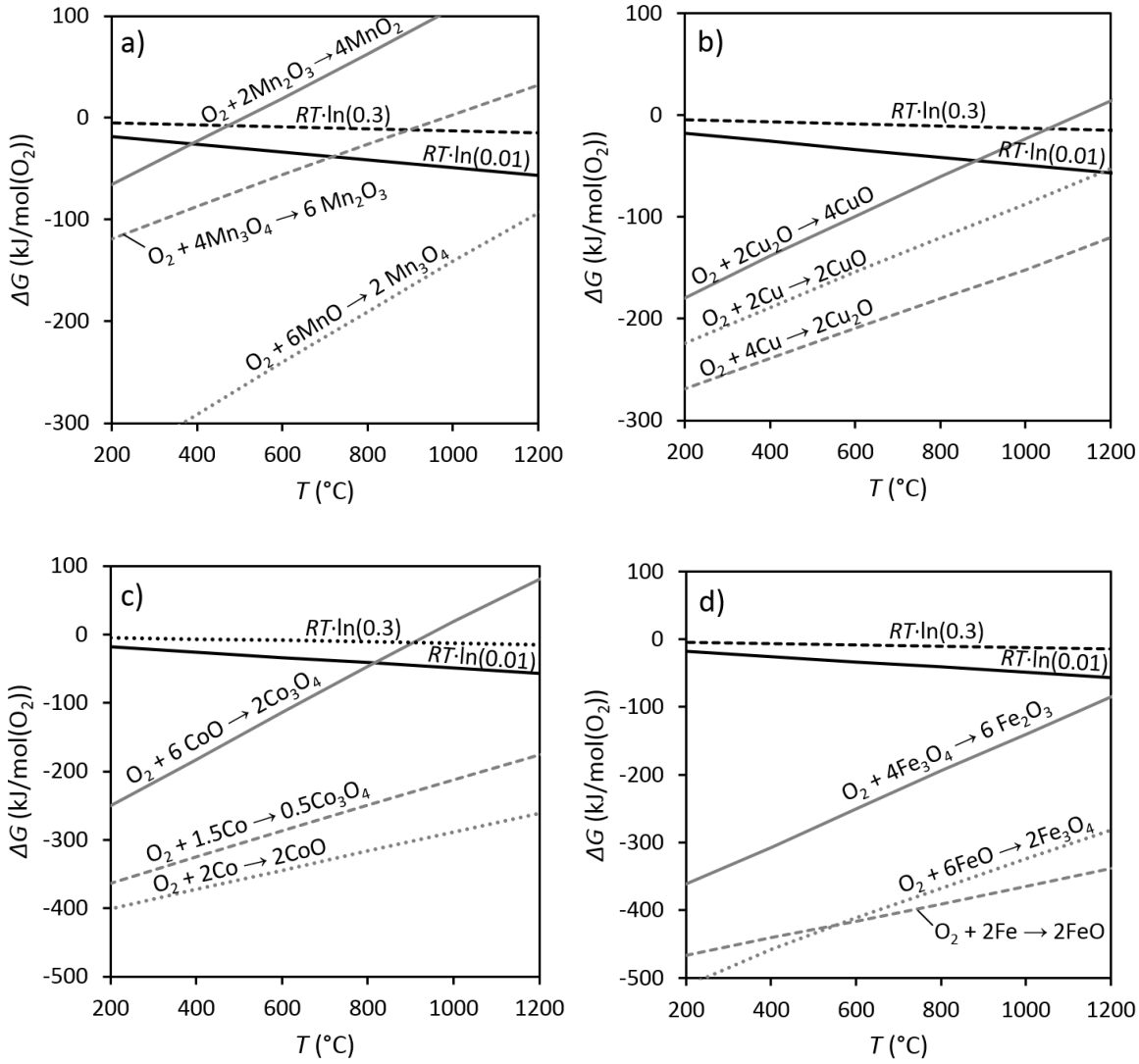


Fig. 3-4 *Ellingham diagram for common single metal oxide systems for CLOU and CLAS using the data from FactSage for the reduction of: (a) manganese oxides, (b) copper oxides, (c) cobalt oxides and (d) iron oxides, and the free energy of O_2 in an ideal gas mixture with p_{O_2} = 0.30 bar and p_{O_2} = 0.01 bar at 0.1 MPa.*

According to eq.(3-3), if the free energy of O_2 in **Fig. 3-4** has a higher negative value than the free energy of the oxidation, ΔG_{CLAS} is negative and the O_2 release is thermodynamically favourable. *Vice versa*, has the oxidation reaction a higher negative value, ΔG_{CLAS} is negative and $\Delta G_{\mathrm{oxidiser}}$ is positive, and the oxidation occurs. **Fig. 3-4a**, shows that oxidation of Mn_2O_3 to MnO_2 and of Mn_3O_4 to Mn_2O_3 at p_{O_2} > 0.01 bar and a pressure of 0.1 MPa, is favourable at temperatures below ~ 400 °C and ~700 °C, respectively. Above those temperatures the oxidation reaction reverses and gaseous O_2 is released – a process known as oxygen uncoupling. This ability is central for the CLOU and the CLAS process. The oxidation of MnO to Mn_3O_4 is thermodynamically favourable across the entire temperature range of **Fig. 3-4a**. For Cu- oxygen carrier, the oxidation of Cu_2O to CuO is favourable

at temperatures below ~800 °C. Above this temperature the reaction reverses and O_2 uncoupling occurs. The oxidation of Cu to CuO and Cu to Cu_2O is favourable across the entire condition range plotted in **Fig. 3-4b**. For Co- oxygen carrier, the oxidation of CoO to Co_3O_4 occurs at temperatures below 850 °C. Above this temperature, the reaction is reversed and O_2 uncoupling occurs. The oxidation of Co to Co_3O_4 and Co to CoO are thermodynamically favourable across the entire condition range plotted in **Fig. 3-4c**. For Fe- oxygen carrier the oxidation from Fe_3O_4 to Fe_2O_3, FeO to Fe_3O_4 and Fe to FeO is thermodynamically favourable across the entire condition range that is plotted in **Fig. 3-4d**, while O_2 uncoupling is thermodynamically unfavourable. The interceptions of ΔG and $RT{\cdot}\ln(p_{O_2})$ in **Fig. 3-4a-d** are the O_2 partial pressure equilibria ($p_{O_2,eq}$) for p_{O_2} = 0.30 bar and p_{O_2} = 0.01 bar. A multitude of these points comprise the O_2 partial pressure equilibrium function ($p_{O_2,eq}$-function). This function was computed for the systems Mn_3O_4/Mn_2O_3, Cu_2O/CuO and CoO/Co_3O_4 using FactSage data, and by setting the sum of the Gibbs free energy of the oxidation reaction and the kinetic energy of O_2 equal to zero, as shown in eq.(3-4), below.

$$0 = \Delta G^{\theta} + RT \cdot \ln\left(p_{O_2}\right) \tag{3-4}$$

In the literature, the log-mean O_2 partial pressure, $p_{O_2,\log-\mathrm{mean}}$, is used as an estimate for the p_{O_2} that the oxygen carriers are exposed to 'on average' in the oxidiser.[100, 150] In this chapter, the $p_{O_2,\log-\mathrm{mean}}$ is used for material screening purposes and was calculated by,[100, 150]

$$p_{O_2,\log-\mathrm{mean}} = \frac{p_{O_2,\mathrm{in}} - p_{O_2,\mathrm{out}}}{\ln\left(\left(p_{O_2,\mathrm{in}} - p_{O_2,eq}\right)/\left(p_{O_2,\mathrm{out}} - p_{O_2,eq}\right)\right)}\ , \tag{3-5}$$

where $p_{O_2,\mathrm{in}}$, $p_{O_2,\mathrm{out}}$ and $p_{O_2,eq}$ are the O_2 partial pressures at the inlet of the oxidiser, at the outlet of the oxidiser and the O_2 equilibrium pressure, respectively. Here, $p_{O_2,\mathrm{in}}$ and $p_{O_2,\mathrm{out}}$ were assumed to be 0.21 bar and 0.05 bar, respectively. The $p_{O_2,eq}$ and $p_{O_2,\log-\mathrm{mean}}$ were calculated according to eq.(3-4) and eq.(3-5), respectively and are plotted in **Fig. 3-5**, below.

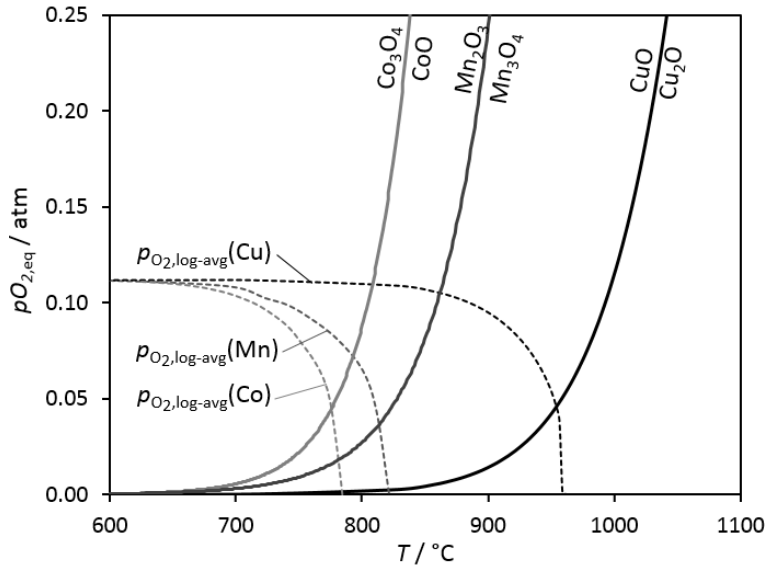


Fig. 3-5 *Oxygen partial pressure equilibria as a function of temperature for the systems CoO/Co_3O_4, Mn_2O_3/Mn_3O_4 and CuO/Cu_2O based on data from FactSage (solid lines), and the log-average O_2 partial pressure calculated by eq.(3-5), assuming $p_{O_2,in}$ and $p_{O_2,out}$ are 0.21 bar and 0.05 bar, respectively.*

Fig. 3-5 shows that the oxidation of Co to Co_3O_4, Mn_3O_4 to Mn_2O_3 and Cu_2O to CuO in the oxidiser are thermodynamically favourable at temperatures below 780 °C, 800 °C and 950 °C, respectively. Furthermore, it can be noted that $p_{O_2,\log-\mathrm{avg}}$ in **Fig. 3-5** is in the range of 0.10 ± 0.01 bar across a large temperature range – *i.e.* 600–720°C, 600–740°C and 600–910°C for the Co, Mn and Cu oxides, respectively. Therefore, a p_{O_2} of 0.10 bar is taken as the standard value for the oxidation experiments in this work.

3.1.2 Mechanical resistance of oxygen carriers, attrition behaviour and support materials

Attrition of oxygen carriers generates fines, which have to be captured to avoid emission of potentially hazardous particulates and to avoid additional costs to replace the lost bed material.[151,152] These two aspects render attrition undesirable in chemical looping processes.[151,152] Typically, two different modes of attrition occur: abrasion and fragmentation, which are both illustrated in **Fig. 3-6**, below.[153]

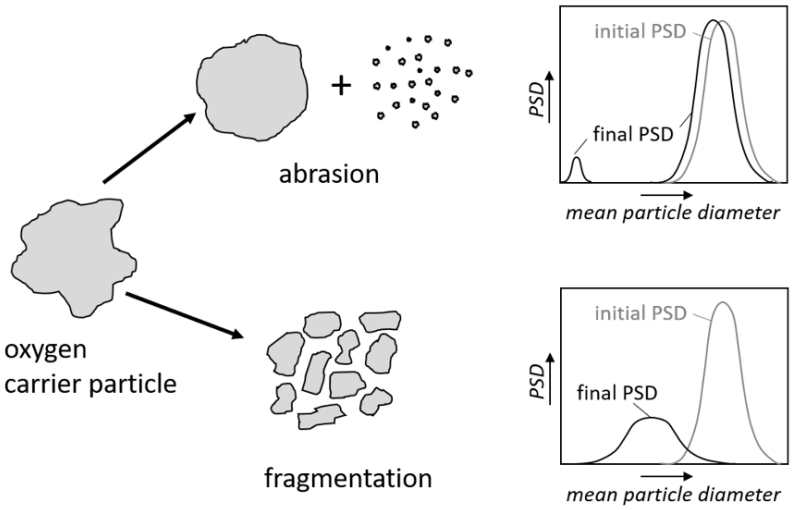


Fig. 3-6 *Modes of attrition and their effect on the particle size distribution (PSD), adapted from Werther and Reppenhagen.*[153]

Abrasion is the generation of fines from the particles' surfaces, which leads to a decrease in particle size. This results in a bimodal particle size distribution (PSD), as illustrated in **Fig. 3-6**.[153] In the process of fragmentation, the particles break up into numerous smaller particles. This typically results in a broader PSD with a smaller mean particle diameter (**Fig. 3-6**).[153] Amongst others, the particle size influences the mode of attrition. Smaller particles are more prone to abrasion owing to their larger specific surface area. For larger particles, attrition is more likely to occur due to fragmentation.[153]

In a circulating fluidised bed (CFB) system, which is typically proposed for the chemical looping process,[50] attrition is typically caused by (i) thermal, (ii) mechanical, and (iii) chemical stresses.[151] Thermal stresses are a result of rapid temperature changes, *i.e.* caused when particles with a given mean temperature are introduced into a zone of a significantly different temperature. This either results in direct stresses caused by expansion or contraction of the particle's bulk, or indirectly by a static pressure caused by expansion or contraction of gases, which are confined in the voids of the paricles.[151] Mechanical stresses occur due to the collision between particles or collision of the particles with the wall. These stresses can occur in the bubbling zone of the fluidised bed,[152,151] in risers and cyclones,[151, 153-155] or in locations where static pressure is exerted onto confined oxygen carriers, such as in the lower part of the standpipe[151] or in the screw feeders.[151] Chemical stresses occur during the redox-reaction of the oxygen carriers when the lattice structure is forced to change rapidly and thus occur predominantly during chemical reactions in the reactors.[151]

In the field of oxygen carrier research, the methods most commonly used to estimate the attrition behaviour of oxygen carriers can be categorised as follows: (i) single particle crushing tests,[123, 145-147, 156-158] (ii) ASTM 5757 tests,[159, 160] (iii) customised jet cup tests,[161, 162] and (iv) attrition tests in the fluidised bed of batch reactors[68, 163, 164] or continuous CLC systems.[163] Results of these tests that are

of relevance for this work are reviewed in the next paragraph – before though, it should be mentioned that outside chemical looping research other approaches for the determination of attrition in CFB systems exist. Theoretical models have been used to determine the rate of attrition in the bubbling zone of a fluidised bed, as a function of bed depth, gas velocities, bed density and the strength of the solids.[152] These models were not applied to chemical looping systems, probably owing to the complexity of the CFB-CLC system and because the rate of attrition is also significantly affected by the redox-reactions of the oxygen carriers.[160, 163] Furthermore, attrition models for certain parts of a CFB system do exist. For example, Reppenhangen and Werther[154] developed a theoretical model for the calculation of the attrition rate in a cyclone by estimating the surface energy of the particles. Tamjid *et al.*[155] used their model in a computational fluid dynamic (CFD) study to calculate the rate of attrition for particles at any point in a cyclone. These methods would allow for the combination of the process design of a chemical looping system and oxygen carrier development. However, so far, these advanced methods have not yet found wide application in oxygen carrier research. Therefore, the four types of attrition tests listed above will be detailed below:

Single particle crushing tests

In the single particle (crush) test a force gauge is used to determine the force required to crush a single particle. Johannson *et al.*[156] proposed to use this test for oxygen carriers according to the procedure described in the review by Bemrose and Bridegwater.[165] To determine the average crushing force, they averaged the results of 30 single particle tests, and defined this as the average crushing strength. Typically, oxygen carriers in the size range 180 - 212 µm are used for these tests.[166]

Since technically not the strength but a force is measured, this property is referred to in this work as the average crushing force, σ_{CF}. De Diego *et al.*[157] and Adánez *et al.*[158] determined σ_{CF} using the ASTM D-4179 method, which slightly differs from the Bemrose and Bridgewater method, as it also allows to test cylindrical particles (besides spherical particles), and the results are typically reported as σ_{CF}/(length of the extrudates).[167] Several works in the literature report values of σ_{CF} for Cu-based oxygen carriers in the range 0.05 – 4.6 N.[123, 145-147, 156]

The crushing strength of Cu-based and Mn-based oxygen carrier from literature are listed in **Table 3-1**. Though a few works report the preparation of copper manganese oxide oxygen carriers, their crushing strength was not reported.

Table 3-1 *Values of the crushing strength (larger 1 N) and preparation methods reported in the literature for oxygen carriers containing Cu and Mn.*

active metal loading (wt%)	supporting material	preparation method[a]	T_{calc} (°C), t_{calc} (h)	$\sigma_{CF}(N)$	Reference
Cu-based oxygen carriers:					
82.5	Al_2O_3	CP	950 °C, 2 h	3.0[a]	Chuang *et al.*[147]
60	$CuAl_2O_4$	FG	1300 °C, 4 h	4.3	Cho *et al.*[124]
40	TiO_2	MM	950 °C	4.5	Johansson *et al.*[156]
40	ZrO_2	MM	1100 °C,	2.7	Johansson *et al.*[156]
60	SiO_2	MM	1100 °C	2.6	Johansson *et al.*[156]
40	SiO_2	IM	980 °C, 7 days	4.5	Peterson *et al.*[66]
61	SiO_2	IM	980 °C, 7 days	4.1	Peterson *et al.*[66]
15	Al_2O_3	IM	850 °C, 6h	2.5	Adánez-Rubio *et al.*[123]
30	Al_2O_3	IM	850 °C, 6h	3.0	Adánez-Rubio *et al.*[123]
15	Al_2O_3	IM	850 °C, 6h	4.6	Adánez-Rubio *et al.*[123]
15	$MgAl_2O_4$	IM	850 °C, 6h	2.1	Adánez-Rubio *et al.*[123]
80	Al_2O_3	MM	1100 °C, 6h	2.6	Adánez-Rubio *et al.*[123]
60	SiO_2	MM	950 °C, 6h	1.1	Adánez-Rubio *et al.*[123]
80	TiO_2	MM	950 °C, 6h	2.2	Adánez-Rubio *et al.*[123]
40	TiO_2	MM	950 °C, 6h	2.3	Adánez-Rubio *et al.*[123]
60	$MgAl_2O_4$	MM+PP	1100 °C, 6h	1.2	Adánez-Rubio *et al.*[123]
60	$MgAl_2O_4$	MM+PP	1100 °C, 6h	1.9	Adánez-Rubio *et al.*[123]
60	$MgAl_2O_4$	MM+PP	1100 °C, 12 h	2.2	Adánez-Rubio *et al.*[123]
60	ZrO_2	MM+PP	1100 °C, 6h	2.3	Adánez-Rubio *et al.*[123]
40	ZrO_2	MM+PP	1100 °C, 6h	2.8	Adánez-Rubio *et al.*[123]
60	MgO	MM+PP	1100 °C, 6h	2.2	Adánez-Rubio *et al.*[123]
60	Sepiolite	MM+PP	1100 °C, 6h	2.2	Adánez-Rubio *et al.*[123]
20	ZrO_2	SD	1000 °C, 4 h	1.35	Jing *et al.*[166]
40	ZrO_2	SD	950 °C, 4 h	3.41	Jing *et al.*[166]
40	ZrO_2 (LSZ)	SD	950 °C, 4 h	1.39	Jing *et al.*[166]
60	Fe_2O_3	SD	950 °C, 4 h	1.0	Jing *et al.*[166]
40	ZrO_2	SD	1100 °C, 4 h	4.53	Jing *et al.*[166]
40	ZrO_2 (LSZ)	SD	1100 °C, 4 h	1.26	Jing *et al.*[166]
40	CeO_2	SD	1100 °C, 4 h	1.53	Jing *et al.*[166]
40	CeO_2 (LSC)	SD	1100 °C, 4 h	1.26	Jing *et al.*[166]
40	$MgAl_2O_4$	SD	1100 °C, 4 h	1.4	Jing *et al.*[166]
36	Al_2O_3	SD	1100 °C, 4 h	1.18	Jing *et al.*[166]
Mn-based oxygen carriers:					
60	$MnAl_2O_4$	FG	1300 °C, 4 h	0.9	Cho *et al.*[124]
37	SiO_2	SiO_2	1100 °C, 6 h	1.4	Johansson *et al.*[57]
37	ZrO_2	ZrO_2	1300 °C, 6 h	2.8	Johansson *et al.*[57]
37	ZrO_2	ZrO_2	1300 °C, 6 h	7.7	Johansson *et al.*[57]
40	$CaZrO_3$	$CaZrO_3$	1200 °C, 6 h	3.0	Johansson *et al.*[57]
40	$CaZrO_3$	$CaZrO_3$	1300 °C, 6 h	6.8	Johansson *et al.*[57]
40	Mg-ZrO_2	Mg-ZrO_2	1200 °C, 6 h	2.4	Johansson *et al.*[57]
40	Mg-ZrO_2	Mg-ZrO_2	1300 °C, 6 h	3.6	Johansson *et al.*[57]
40	Ce-ZrO_2	Ce-ZrO_2	1100 °C, 6 h	1.8	Johansson *et al.*[57]
40	Ce-ZrO_2	Ce-ZrO_2	1300 °C, 6 h	11.3	Johansson *et al.*[57]

Footnotes:(a) this value has been measured using the Zwick/Roell test.

The values of the crushing strength of Cu-based and Mn-based oxygen carriers in **Table 3-1** is in the range 1.0 – 4.6 N and 1.0 – 11.3 N, respectively. The average crushing force by preparation method of the Cu-based oxygen carriers is in the order (from low to high): spray-dried (1.8 N) < mechanically

mixed (2.3 N) < co-precipitated (3.0 N) < impregnated (3.5 N) < freeze-granulated (4.3 N). All Mn-based oxygen carriers in **Table 3-1** were prepared by mechanically mixing. Their average crushing force is 4.5 N, which is significantly higher than the average value of the Cu-based mechanically mixed oxygen carriers in **Table 3-1**. In several publications, the use of a Shimpo FGN-5X force gauge was reported.[53, 59, 166, 168] A similar instrument (a Series 3 Mark-10 force gauge with a test stand) was used for the measurements in this work. The use of the crushing strength as an indication of the resistance towards mechanical stresses has some disadvantages. It is not possible to correlate this property to the rate of attrition, because the relationship between the mechanical resistance of a particle and its attrition is highly complex.[161] Moreover, the crushing force is typically neither measured at the relevant reactor conditions nor in a reacting environment.[123, 145-147, 156] Attrition rate measurements in attrition rigs provide a better indication of the rate of attrition in an industrial-scale process.[169] One configuration, which was initially developed to quantify the rate of fines generated from catalysts in fluid catalytic cracking of refineries[159] follows the ASTM D5757 standard[170] was adapted oxygen carrier attrition tests.[162]

Attrition test according to the ASTM D5757 standard

In the ASTM D5757 method a vertical jet of gas enters, with a high-velocity (~ 490 m/s), a chamber in which the particles are fluidised.[56, 170] After five hours the bed material is weighed, and an attrition jet index (AJI) is calculated, which is equal to the mass of the bed after the experiment divided by the initial bed mass.[56] Feilen[160] measured the attrition rate using the ASTM D5757 method with three different cycling modes: (i) at ambient temperature in an inert atmosphere, (ii) at high temperature in an inert atmosphere, and (iii) at high temperature with reacting oxygen carriers. Interestingly, the average attrition rate over 700 minutes was reported to be in the order (from low to high): inert conditions at high temperature < inert conditions at ambient temperature < reacting conditions at high temperature. Drawbacks of this method include a relatively large required sample mass (50 g) and a relatively long test duration (5 h).[161] To avoid these drawbacks, Rydén *et al.*[161] developed a customised jet cup test.

Attrition test in using customised jet cup rigs

The customised jet cup rig developed by Rydén *et al.*[161] enables to perform attrition tests with a significantly lower sample mass and shorter test durations. In this customised jet cup test, a conical cup is used to hold the sample (this geometry reportedly improves particle mixing),[171] and a gas jet enters the cup tangentially to the wall with velocities of around 100 m s^{-1}.[161]

Attrition tests in the fluidised bed of batch reactors and continuous CLC systems

Several works test oxygen carriers over a high number of redox-cycles in the fluidised bed or in a continuous CLC system and calculate the rate of attrition from the mass of elutriated fines collected.

This follows the assumption that the mass of fines generated by attrition in the bed is equal to the mass of fines elutriated. Using Stokes's Law for small particle, Brown *et al.*[163] demonstrated that this assumption is valid at typical operating conditions of fluidised bed for CLC experiments (*i.e.* a terminal velocity for particles with a mean radius of 25 μm of 0.042 m s^{-1} at 850 °C and 0.1 MPa in 10 vol% O_2 + N_2, and at their conditions an elutriation rate constant of 4.22 min). Cabello *et al.*[56] proposed to estimate the lifetime of the oxygen carriers, t_{OC}, from the weight of elutriated fines, m_f, and the initial bed mass, m_t, from continuous redox-cycling tests of duration, Δt , by

$$t_{\mathrm{OC}} = \frac{100}{attrition\ (\%/\mathrm{h})} = \frac{100}{\left(\frac{\mathrm{m}_f}{\mathrm{m}_t \cdot \Delta t}\right)} \tag{3-6}$$

This method has since been used by many to estimate the average lifetime of oxygen carriers, and results of these works are presented in **Table 3-2**, below.[60, 75, 172]

Table 3-2 *Values for the estimated average oxygen carrier lifetime and details of the oxygen carrier's composition and synthesis conditions reported in the literature.*

sample name	active metal loading (wt%)	supporting material	preparation method[a]	T_{calc} (°C), t_{calc} (h)	T_{op} (°C)	t_{OC} (h)	Reference
Ni-1	18	γ-Al_2O_3	IM	900 °C, 1 h [d]	800	10 000 [g]	Adánez *et al.*[62]
Cu-3	14	γ-Al_2O_3,	IM	850 °C, 1 h	800	2 500	Adánez *et al.*[51] Forero *et al.*[52]
Cu-8	60	$MgAl_2O_4$	SD	1100 °C, 24 h	900	25 000	Adánez-Rubio *et al.*[53]
Fe-13	60	γ-Al_2O_3	FG	1100 °C, 6 h	950	10 000	Abad *et al.*[173] Gayán *et al.*[59]
Cu-3b	14	γ-Al_2O_3	IM	850 °C, 1h	900	1 100	De Diego *et al.*[54]
Cu-5	13	$NiAl_2O_4$	IM	850 °C, 1h[d]	900	2 700	Gayán *et al.* [55]
Ni-2	11	$CaAl_2O_4$	IM	950 °C, 1 h[d]	900	400 [g]	Gayán *et al.*[63]
Fe-14	15	γ-Al_2O_3	IM	950 °C, 1 h[d]	830	1 250	Gayán *et al.*[59]
Mn-ore [b]	66	-	-	-	950	1 600	Mei *et al.*[68]
Ni-3	40	$NiAl_2O_4$	FG	-	850	4 000	Fan [39]
Fe-2	20	γ- Al_2O_3	IM	800 °C, 1 h[f]	880	1 100 [g]	Cabello *et al.*[60]
Cu-6	12	$MgAl_2O_4$	IM	800 °C, 1 h[e]	900	500 [g]	Gayán *et al.*[55]
Fe-3	60	$MgAl_2O_4$	IM	950 °C, 6 h	850	1 000	Mattisson *et al.*[64] Leion *et al.*[174]
Cu-2	14	α-Al_2O_3	IM	850 °C, 1h	900	250 [g]	Forero *et al.*[52]
Fe-11	17	γ- Al_2O_3	IM	950 °C, 1 h[f]	900	700	Cabello *et al.*[60]
Cu-4b	14	γ- Al_2O_3	IM	-	900	450	Cabello *et al.*[56]
Mn-3	40	ZrO_2	FG	1150 °C, 6 h	850	2 600	Johansson *et al.*[57]
Mn-Prv [c]	-	-	SD	1300 °C, 4 h	900	1 100 [g]	Cabello *et al.*[69]
Mn-2	40	ZrO_2	SD	1200 °C, 2 h	900	400	Rydén *et al.*[58]

Footnotes: (a) the following abbreviations were used for the preparation methods: IM = impregnation; SD = spray drying; FG = freeze granulation; (b) the Mn-ore contains 65.6% Mn_3O_4; (c) this perovskite oxygen carrier has a molar composition of $CaMn_{0.9}Mg_{0.1}O_{3-\delta}$; (d-f) sintering follows a thermal decomposition of the metal nitrates at (d) 500 °C for 0.5 h, (e) 550 °C for 1 h, (f) 550 °C for 0.5 h; (g) in this case the lifetime was not estimated by the group conducting the experiments, but by Cabello et al.[56]

Table 3-2 shows that the estimates for the oxygen carrier lifetime range widely from 400 h to 10 000 h. This indicates that the choice of the materials and preparation methods as well as careful tuning of the preparation conditions can have a significant effect on the lifetime of the oxygen carriers.

Besides the above described quantitative methods, some works used qualitative methods to study the attrition behaviour. Brown *et al.*[163] targeted Fe-based and Cu-based oxygen carriers with velocities in the range 10 – 42 m s^{-1} against a plate and reported that redox-cycled oxygen carriers are more prone to fragmentation than fresh oxygen carriers.

Despite all the above reviewed methods, ultimately pilot plants tests give the best indication for the attrition in an industrial-scale process.[56, 160] However, a combination of the above described tests can be used to identify promising oxygen carriers and to refine the preparation protocols. Cabello *et al.*[56] proposed to link the methods as illustrated in **Fig. 3-7**, below.

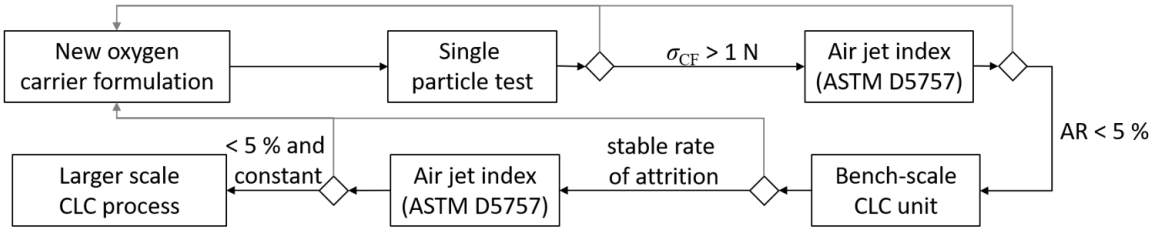


***Fig. 3-7** Methodology for the selection of oxygen carrier materials with a sufficiently low attrition behaviour to be used in scaled-up CLC processes, adapted from Cabello et al.*[56]

During the review of literature on oxygen carrier attrition it was noted that several works report an interesting anomaly. Forero *et al.*[52] studied CuO/Al_2O_3 oxygen carriers over ≤ 60 h in a continuous CLC system with methane and reported for all four tests that the attrition rate reached its minimum after ~ 20 h and then increased steadily. The cause for this phenomenon was not elucidated in detail. [52] Mei *et al.*[68] reported a similar finding for the attrition rate measurements of Mn-ores in a fluidised bed. For three of the studied four ores, the lowest attrition rate was measured in the cycle number range 18-21 (~ 450-525 min of continuous redox-cycling). After reaching this minimum the attrition rate increased again up to until cycle 60 (~ 1500 min). Brown *et al.*[163] studied Fe-based oxygen carriers over repeated redox-cycles with reduction 10 vol% CO + N_2 and reported an increase in porosity and pore size with an increasing redox-cycle number. The change of the pore-morphology of the particles might have caused this change in the observed rate of attrition. For this thesis, these findings gave reason to analyse the redox-cycled bed material from long-term cycling experiments by x-ray diffraction, Hg intrusion porosimetry, scanning electron microscopy and N_2 adsorption at 77 K. The above summarised attrition tests were all relating to a gas fuelled chemical looping process. However, this might still be of relevance for the attrition in the CLAS process (for which no detailed

attrition study was conducted). In this thesis, results from single particle tests of fresh and cycled oxygen carriers and from tests in the fluidised bed are reported, following a similar method of the tests for CLC oxygen carrier reviewed above, and parallels between attrition behaviour of the two different chemical looping processes are drawn.

3.1.3 Heat of the reactions and auto-thermal operation

In the CLC process, the overall reaction in the air reactor is typically the oxidation of the metal (oxide). For Cu-, Mn-, Fe-, Co- and Ni-based oxygen carriers this reaction is always exothermic.[94] To determine if the overall reaction in the fuel reactors is endothermic or exothermic the ratio of the enthalpies of oxygen carrier oxidation and fuel combustion can be compared.[145] Cho *et al.*[145] proposed to calculate the ratios of the enthalpy of the overall reaction in the fuel reactor, ΔH_{FR}, to the enthalpy of the reaction in the air reactor, ΔH_{AR}. Assuming full conversion of the oxygen carriers ΔH_{AR} is assumed to equal the enthalpy of the oxygen carrier oxidation ΔH_{ox}. The overall reaction in the fuel reactor, ΔH_{FR}, is assumed to equal the enthalpy of combustion ΔH_{C}. The values for commonly used fuel types are provided in **Table 3-3**, below.

Table 3-3 *Reaction enthalpy of the O_2 release reaction of Cu, Mn and Co oxides with values form FactSage.*[139]

Fuel type	Combustion reaction per mole of O_2	$\Delta H_{\mathrm{C},950\,^{\circ}C}$ (kJ)	eq.
Biomass[a]	$\mathrm{O_2} + 3.04\ \mathrm{C_{0.331}H_{0.443}O_{0.226}} \rightarrow 1\ \mathrm{CO_2} + 0.674\ \mathrm{H_2O}$	-1036.0	(3-7)
CH_4	$\mathrm{O_2} + 0.5\ \mathrm{CH_4} \rightarrow 0.5\ \mathrm{CO_2} + \mathrm{H_2O}$	-400.9	(3-8)
CO	$\mathrm{O_2} + 2\ \mathrm{CO} \rightarrow 2\ \mathrm{CO_2}$	-563.5	(3-9)
H_2	$\mathrm{O_2} + 2\ \mathrm{H_2} \rightarrow 2\ \mathrm{H_2O}$	-498.2	(3-10)

Footnotes: (a) the biomass here is beech wood and the molar composition was calculated from the ultimate analysis reported in Boot-Handford[93], who measured a C:O:H mass fraction ratio of 0.494:0.450:0.055.

A value of $\Delta H_{\mathrm{FR}}/\Delta H_{\mathrm{AR}}$ larger than unity indicates that the overall reaction in the fuel reactor is endothermic, and conversely a value smaller than unity indicates that the overall reaction in both reactors are exothermic.

This method was applied for various single metal oxide systems and fuel types using data from FactSage, and the results are presented in ***Table 3-4***.

Table 3-4 *Reaction enthalpies of the metal oxide oxidation in the air reactor (AR) and fuel reduction in the fuel reactor (FR) and their ratios, based on values from FactSage.*[139]

$\Delta H_{FR}/\Delta H_{AR}$		fuel type			
		Biomass[a] eq.(3-7):	CH_4 eq. (3-8):	CO eq. (3-9):	H_2 eq.(3-10):
metal oxide oxidation	$\Delta H_{950°C}$ kJ / mol	-1036.0	-400.9	-563.5	-498.2
$O_2 + 2\ Cu \rightarrow 2\ CuO$	-296.9	0.29*	0.74*	0.53*	0.60*
$O_2 + 2\ Cu_2O \rightarrow 4\ CuO$	-261.5	0.25*	0.65*	0.46*	0.52*
$O_2 + 6\ MnO \rightarrow 2\ Mn_3O_4$	-453.7	0.44*	1.13	0.81*	0.91*
$O_2 + 2\ Co \rightarrow 2\ CoO$	-465.7	0.45*	1.16	0.83*	0.93*

Footnotes: (*) the value of $\Delta H_{FR}/\Delta H_{AR} < 1$ implies that the reaction in both (fuel reactor and air reactor) are exothermic and no heat transfer from the air reactor to the fuel reactor is required to maintain an auto-thermal reaction; (a) the biomass is assumed to be beech wood with a molar composition of $C_{0.331}H_{0.443}O_{0.226}$, which was calculated from the ultimate analysis reported in Boot-Handford[93].

In **Table 3-4**, the values of $\Delta H_{FR}/\Delta H_{AR}$ for Cu-based oxygen carriers are smaller than unity when utilising biomass, CH_4, CO and H_2. This indicates an exothermic overall reaction in both reactors. Therefore, no heat has to be transferred from the air reactor to the fuel reactor. An exothermic reaction in both reactors also occurs during the combustion of CO and H_2 when using Mn-, Fe-, Co- and Ni-based oxygen carriers. However, when using those four oxygen carrier types for the combustion of biomass and CH_4 $\Delta H_{FR}/\Delta H_{AR}$ is larger than unity, indicating that the overall reaction in the fuel reactor is endothermic. In this case, heat can be transferred from the air reactor to the fuel reactor using the heat capacity of the circulating oxygen carriers. The oxygen carrier circulation rate can be increased until the enthalpy transferred equals the enthalpy requirement to maintain the operating temperature of the fuel reactor. However, this will reduce the average oxygen carrier conversion, and hence increase the oxygen carrier requirement beyond the minimum solid inventory at which full fuel conversion occurs. This is likely to result in an increase in capital and operating costs.[94, 95] Cycling of inert bed material in addition to the oxygen carriers might be a less expensive alternative for facilitating the heat transfer.

The enthalpies listed in **Table 3-4** can be used to calculate the enthalpy of the overall reaction in the fuel reactor, by subtracting the enthalpy of the fuel combustion from the enthalpy of the oxidation ($\Delta H_{ox} - \Delta H_{comb.}$). This value is equal to the enthalpy that is needed to be transferred to the reducer for auto-thermal operation, *e.g.* transported through increased circulation of the oxygen carriers, by pre-heating the inlet gas streams or by direct heating or cooling of the reducer. A positive value indicates that the overall reaction is exothermic, and the reactor has to be cooled, *e.g.* by raising steam. This requires an additional boiler system and is thus likely to increase the capital costs of the process.

For the CLAS process, assuming full conversion of the oxygen carriers, the enthalpy released in the reducer is equal to the enthalpy of the O_2 release reaction, $\Delta H_{O_2\mathrm{rel}}$. The values for $\Delta H_{O_2\mathrm{rel}}$ for the systems CuO/Cu_2O, Mn_2O_3/Mn_3O_4 and Co_3O_4/CoO are provided in **Table 3-5**, below.

Table 3-5 *Reaction enthalpy of the O_2 release reaction of Cu, Mn and Co oxides with values form FactSage.*[139]

Reaction to release one mole of O_2	$\Delta H_{r,950\,°C}$	Eq.
$4\,CuO \rightarrow 2\,Cu_2O + O_2$	+ 261.5 kJ	(3-11)
$6\,Mn_2O_3 \rightarrow 4\,Mn_3O_4 + O_2$	+ 143.1 kJ	(3-12)
$2\,Co_3O_4 \rightarrow 6\,CoO + O_2$	+ 393.0 kJ	(3-13)

Footnotes: The temperatures of the reducer in the CLAS process might be different in an industrial-scale process, i.e. in Fig. 3-5 it can be seen that $p_{O2,eq}$ = 0.25 for CuO, Mn_2O_3 and Co_3O_4 is ~1050 °C, ~900 °C and ~820 °C, respectively. However, the change in $\Delta H_{r,T}$ with temperature is not significant since it is only comprised of the changes in heat capacity of the gaseous reagents and products.

The values of $(\Delta H_{\mathrm{ox}} - \Delta H_{\mathrm{comb.}})$ for the utilisation of Cu-, Mn- and Co- oxides in the CLAS process are compared with the values of $\Delta H_{O_2 r.}$ in **Fig. 3-8a**. Since the materials typically release more oxygen during the fuelled reduction than during O_2 release and the different metal oxides have different molecular masses it is also meaningful to express the enthalpies per unit of mass of the reduced or decomposed active metal oxide, as shown in **Fig. 3-8b**.

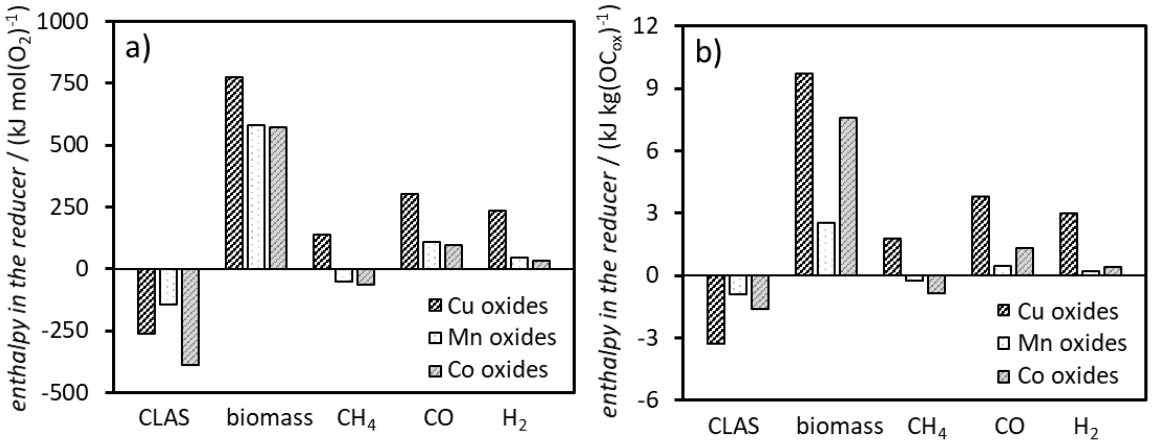


Fig. 3-8 *A comparison of the enthalpy of the overall reaction in the reducer for Cu-, Mn- and Co-oxides in the CLAS process and in the CLC process with biomass, CH_4, CO and H_2 as the fuel (a) per mole of O_2 release, and (b) per kg of the reduced or decomposed active metal oxide.*

Fig. 3-8 shows that the overall reaction in the reducers of the CLAS is negative for all three single metal oxide systems studied. The additional amount of heat required per mole of O_2 produced is in the order: Co_3O_4 (390.0 kJ·mol$(O_2)^{-1}$) > CuO (261.5 kJ·mol$(O_2)^{-1}$) > Mn_2O_3 (143.1 kJ·mol$(O_2)^{-1}$). In terms of energy required per mass of the oxidised single metal oxide, the order is: CuO (3.29 kJ/kg)

> Co_3O_4 (1.62 kJ/kg) > Mn_2O_3 (0.91 kJ/kg). When using any of the three single metal oxides additional heat has to be supplied to the reducer. In the CLAS + oxy-fuel process, this heat cannot fully be supplied by the exothermic oxidation (at least without the injected of steam into the reducer and when operating both reactors at atmospheric pressure), since the O_2 partial pressure required in the combustor, $p_{O_2,comb}$, which is in the range 0.25 – 0.35 bar is higher than the p_{O_2} in the oxidiser (*c.f.* section 2.3.4). Owing to the costs associated with required additional heat transfer it is therefore desirable to select materials with a lower additional energy requirement. Per mole of O_2 released in the reducer, the heating requirements in the reducer for the systems CuO/Cu_2O, Mn_2O_3/Mn_3O_4 and Co_3O_4/CoO are 261.5 kJ, 143.0 kJ and 393.0 kJ, respectively. From this heat integration standpoint, Mn oxides are therefore most favourable.

3.1.4 Oxygen storage and release capacity

The oxygen transport capacity, R_0, is the mass fraction of O_2 of the fully oxidised oxygen storage material that can be released during the reduction, typically in the presence of a fuel. The oxygen ratio, R_0, can be calculated by,[158]

$$R_0 = \frac{(m_{ox} - m_{red})}{m_{ox}}, \tag{3-14}$$

where m_{ox} and m_{red} is the mass of the fully oxidised and fully reduced oxygen carrier material (*i.e.* excluding the inert support), respectively. Consequently, the theoretical oxygen storage capacity can be calculated from the relative molecular masses of the oxidised, M_{ox}, and the reduce material, M_{red}, by,

$$R_{0,th} = \frac{(M_{ox} - {\nu_{ox}}/{\nu_{red}}\, M_{red})}{M_{ox}}, \tag{3-15}$$

In eq.(3-15), ν_{ox} an ν_{red} are the stoichiometric coefficients in the reduction reaction of the oxidised and reduced solid, respectively. The R_0 of the oxygen storage material is an important design criterium of the chemical looping process. The higher the R_0 for given rates of reactions, the lower is the required minimum solid inventory and the minimum reactor size. A reduction of the reactor size typically results in a reduction in the capital cost of the reactor.

Data from FactSage was used to calculate values for R_0 for single metal oxides that are commonly used in chemical looping processes. This was done by determining the thermodynamically favourable oxidation state in excess air at 800 °C for the oxidised material, and in the presence of excess biomass or CH_4 at 800 °C for the reduced material. The relevant oxidation states of the metal oxides for the CLAS process were evaluated by oxidising and decomposing the metal oxidised in the presence and the absence of O_2. Then, balanced equations were developed, and the relative molecular

masses of the materials were used to calculate the values for R_0, as proposed by Mattisson *et al.*[175] The results of this calculation are presented in **Table 3-6**, below.

Table 3-6 *Oxygen ratios for redox-systems of commonly used single metal oxides as oxygen carrier materials for the CLC and CLAS process.*

metal (oxide) system	balanced equation	R_0
redox-reaction relevant for the CLC process:		
CuO/Cu	$2CuO \leftrightarrow 2\ Cu + O_2$	0.201
Mn_2O_3/MnO	$2\ Mn_2O_3 \leftrightarrow 4\ MnO + O_2$	0.101
Co_3O_4/Co	$Co_3O_4 \leftrightarrow 3\ Co + 2\ O_2$	0.266
NiO/Ni	$2\ NiO \leftrightarrow 2\ Ni + O_2$	0.214
Fe_2O_3/Fe_3O_4	$6\ Fe_2O_3 \leftrightarrow 4\ Fe_3O_4 + O_2$	0.033
redox-reaction relevant for the CLAS process:		
CuO/Cu_2O	$4\ CuO \leftrightarrow 2\ Cu_2O + O_2$	0.101
Mn_2O_3/Mn_3O_4	$6\ Mn_2O_3 \leftrightarrow 4\ Mn_3O_4 + O_2$	0.034
Co_3O_4/CoO	$2\ Co_3O_4 \leftrightarrow 6\ CoO + O_2$	0.066

Adánez *et al.*[158] carried out redox experiments and demonstrated, that the theoretical values of R_O for the systems CuO/Cu, Mn_3O_4/MnO, Fe_2O_3/Fe_3O_4 and NiO/Ni, can be achieved in lab-scale tests. To illustrate the values from **Table 3-6**, the oxygen ratios are compared in **Fig. 3-9**, below.

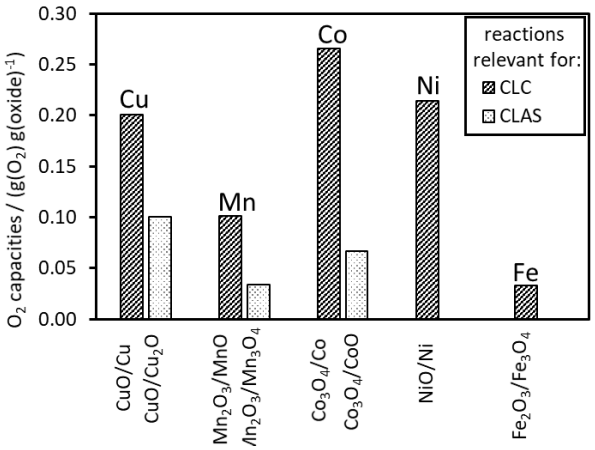


Fig. 3-9 *The oxygen ratios of single metal oxide systems relevant for the CLC and the CLAS process, calculated from the molecular weights of the compounds and the balanced equations determined in FactSage.*[139]

Fig. 3-9 shows that the values of R_0 of the reactions relevant for the CLC process (herein also referred to as the oxygen transport capacity) are in order (from high to low): Co > Ni > Cu > Mn > Fe. Since the R_0 is inversely proportional to the mass flow rate of oxygen carriers between the reactors when combusting a given amount of fuel (assuming full oxygen carrier conversion and no increased circulation rate for additional heat transfer between the reactors), the values of the oxygen carrier mass flow rate will be in the order: Fe > Mn > Cu > Ni > Co. The values of R_0 relevant for the CLAS

process are in the order: Cu > Co > Mn. The oxygen carrier mass flow rate (under the same assumptions as above) is therefore: Mn > Co > Cu. Furthermore, **Table 3-6** and **Fig. 3-9** show that the values of R_0 relevant for the CLC process are larger than those relevant for the CLAS process, with the exception of the system Fe_2O_3/Fe_3O_4. This indicates that the mass flow rate of active metal oxide between the reactors in the CLAS process will be larger than in the CLC process for the full combustion of a given amount of fuel. Arguably even more relevant for the design of the process is the overall oxygen ratio, R_0', which refers to total mass of the oxygen carrier (including the inert support) and can be calculated by,

$$R_0' = R_0 \cdot \alpha, \tag{3-16}$$

where α is the active metal oxide loading, which is the mass fraction of the active metal in the oxidised state of the oxygen carrier. As explained in section 3.1.2 and shown in **Table 3-1** and **Table 3-2**, the active metal oxide is supported on an inert material to increase the mechanical resistance of the oxygen carriers to withstand the operational stresses and to reduce the tendency of sintering and agglomeration.[39, 51-60, 62-64, 68, 69] The requirements and selection criteria of the supporting material are detailed in section 3.2.

The value of R_0' and the reactivity of the active metal oxide determines the size of the minimum solid inventory. This assumes (i) the absence of intra-particle and external mass transfer, (ii) full conversion of the active metal oxide, and (iii) no increased oxygen carrier circulation rate for the transport of heat between the reactors. The calculation of the solid inventory is explained in detail in the following section.

3.1.5 Solid inventory

The oxygen carrier inventory, m_{bed}, has a significant impact on the reactor design[94] and is one of the three process design criteria proposed by Lyngfelt *et al.*,[50] which are (i) a sufficient amount of bed material in both reactors for full fuel conversion, (ii) the oxygen carrier circulation rate, and (iii) to minimise the gas leakage between reactors. Values for m_{bed} can be calculated by,[148]

$$m_{\mathrm{bed}} = \frac{M_{\mathrm{O_2}}}{M_{\mathrm{fuel}}} \cdot b_r \cdot \frac{H_c}{R_0'} \left(\frac{1-(1-X_{\mathrm{ox}})R_0'}{(\mathrm{d}w/\mathrm{d}t)_{\mathrm{ox}}} + \frac{1-(1-X_{\mathrm{red}})R_0'}{(\mathrm{d}w/\mathrm{d}t)_{\mathrm{red}}} \right), \tag{3-17}$$

where M_{O_2} and M_{fuel} are the molecular masses of oxygen and the fuel, respectively, b_r is the stoichiometric coefficient of the combustion reaction, H_c is the heat of combustion, R_0 is the oxygen ratio, X_{ox} and X_{red} are maximum conversion of the oxygen carrier during oxidation and reduction, respectively, and $(\mathrm{d}w/\mathrm{d}t)_{\mathrm{ox}}$ and $(\mathrm{d}w/\mathrm{d}t)_{\mathrm{red}}$ are the reaction rates of the oxidation and reduction,

respectively. Circulation rate is affected by the R_0, which can be expressed as eq.(3-18) according to Abad *et al*.[176]

$$\dot{m}_{\mathrm{OC}} = \frac{b_r \, M_{\mathrm{MeO}} \, \dot{n}_{\mathrm{f}} \, \Delta X_{\mathrm{f}}}{\alpha \cdot \, \Delta X_{\mathrm{MeO}}} \tag{3-18}$$

where b_r is the stochiometric ratio of the fuel combustion reaction, M_{MeO} is the molar mass of the active metal oxide, $\dot{n}_{\mathrm{f}}$ is the molar flow rate of the fuel, ΔX_{f} is the fuel combustion efficiency, α is the mass fraction of the active metal oxide in the oxyen carrier, and ΔX_{MeO} is the conversion range of the active metal oxide.

3.2 Inert supporting materials

The copper oxides CuO and Cu_2O are relatively soft materials (see microhardness in **Table 3-7**).[177] This results in the tendency of agglomeration in the CLC process.[168] The stability of the oxygen carriers can be increased and the tendency to agglomerate decreased by supporting the active metal oxide on an inert support material.[168] The support material should (i) have a high mechanical strength, (ii) be inert (*e.g.* redox-reactions are thermodynamically not favourable at the operating conditions of the supported oxygen carriers), and (iii) be stable (*e.g.* no diffusion should occur at the operating conditions). Those three properties – high mechanical strength, inertness, and stability – will be examined in the following three paragraphs.

Firstly, the mechanical stability of potential oxygen carrier materials is evaluated. An indication for the mechanical stability of the oxygen carriers is the microhardness of their materials.[178] Some literature values[177] for the microhardness of potential oxygen carrier materials (active metal oxide as well as inert supporting material) are presented in ***Table 3-7***, below.

Table 3-7 *Literature values*[177] *for the microhardness of potential active metal oxides and inert support materials for CLC and CLAS. The testing conditions were SATP unless stated otherwise.*

metal oxide	*microhardness (MPa)*	*notes*	*metal oxide*	*microhardness (MPa)*	*notes*
CuO	2050-2491		Al_2O_3	20153 – 21487	mineral
Cu_2O	2010-2030			20448 – 20202	synthetic
Mn_3O_4	4207		MgO	7453	T = 25 °C
NiO	3922	T = 120 °C		1961	T = 650 °C
	1961	T = 450 °C	ZrO_2[a]	9807	T = 270 °C
Fe_3O_4	4678-7885			2942	T = 800 °C
Fe_2O_3	10983-6864		TiO_2	7846	T = 125 °C
SiO_2	11034			1961	T = 650 °C

Footnotes: (a) here ZrO_2 was stabilised with CaO.

Unfortunately, values for the microhardness at typical operating temperatures of CLC reactors for all metal oxides listed in **Table 3-7** were not found in the literature. However, a comparison of the microhardness at lower temperatures should give an indication of the mechanical stability of these materials. The average microhardness of the active metal oxides measured at 20 °C ≤ T ≤ 120 °C listed in **Table 3-7** is in order (from low to high): $Cu_2O < CuO < NiO < Mn_3O_4 < Fe_3O_4 < Fe_2O_3$, and the order of the microhardness of the inert supporting material is: $MgO < TiO_2 < ZrO_2$ (CaO stabilised) $< SiO_2 < Al_2O_3$. The microhardness of the two oxides of Cu is an order of magnitude lower than the microhardness of the hardest material, *viz.* Al_2O_3. Mn_3O_4 is about twice as hard as CuO and Cu_2O. The relation of the hardness of the active metal oxides containing Cu- or Mn to the hardness of the inert supporting materials from **Table 3-7**, suggests that supporting these active metal oxides with the inert materials from **Table 3-7** will result in an increase in the hardness of the resulting material.

Secondly, the 'inertness' of the potential supporting materials is evaluated. To evaluate if a material is inert at CLC process conditions, the Gibbs free energy of the oxidation of the fuels were compared to the Gibbs free energy of the formation of the supporting material, as shown in ***Fig. 3-10***, below.

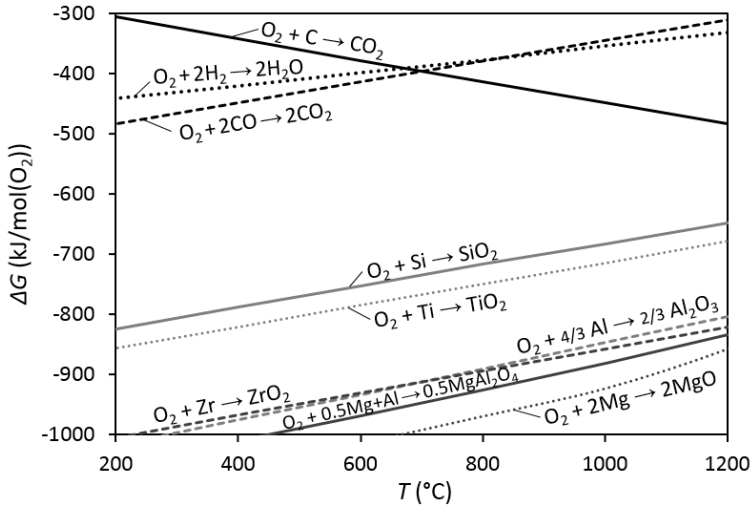


Fig. 3-10 *Ellingham diagram for common support materials using the data from FactSage.*

The values of ΔG of the oxidation reactions of all supporting materials in **Fig. 3-10** are lower (higher negative) than the values of ΔG of the combustion reactions at 0.1 MPa and 200 °C ≤ T ≤ 1200 °C. This difference corresponds to the energy that has to be added to initiate the reduction of the metal oxide. This difference is in order (from low to high): $SiO_2 < TiO_2 < ZrO_2 < Al_2O_3 < MgAl_2O_4 <$ MgO. A reduction of the metal oxides in this temperature range is therefore thermodynamically not favourable.

Thirdly, the stability of the supporting material is evaluated, which in this work is defined as the resistance towards solid-state diffusion of the ions of the supporting metal oxide. The movement of

ions requires the dissociation and the diffusion of atoms.[179] The driving force of either is proportional to the fraction of the melting point, $T_M(K)$.[179] An increase in temperature results in an increase in the mean lattice vibration of the surface atoms. At $0.3 \cdot T_M(K)$, which defines as the "Hüttig" temperature, T_H, a dissociation of the surface atoms at defect sites occurs, allowing the ions to diffuse across the surface. Above $0.5 \cdot T_M$, the Tammann temperature (T_T) the mobility of bulk atoms increases significantly and diffusion within the lattice occurs.[179] The values of T_M, T_H, and T_T for materials relevant for this work are listed in **Table 3-8**, below.[94, 177, 179, 180]

Table 3-8 *Hüttig, Tammann, and melting point temperature of metals and metal oxides at 0.1 MPa that are used in this work for the preparation of oxygen carriers.*

metal (oxide)	Hüttig temperature, T_H (°C)	Tammann temperature, T_T (°C)	melting point T_M (°C)
CuO	206	526	1326
Cu_2O	179	481	1232
Cu	134	405	1085
Mn_2O_3	91	334	888
Mn_3O_4	277	644	1567
Al_2O_3	421	884	2041
$MgAl_2O_4$	448	929	2131
ZrO_2	619	1214	2701
TiO_2	364	789	1851
SiO_2	292	669	1611
MgO	665	1290	2853
Sepolite	382	819	1911
CeO_2	529	1064	2401

Cu- and Mn-based oxygen carriers have been tested in the temperature range of 800 – 900 °C [51, 52, 54-56] and 850 – 950 °C,[57, 68, 69] respectively. The low values of T_M, T_H, and T_T (in **Table 3-8**) for Cu- and Mn- oxides indicate a high ion mobility at these temperatures, which causes sintering. Therefore, these single metal oxides are typically supported on an inert material, as summarised in **Table 3-9**, below.

Table 3-9 *The use of support materials for Cu-based oxygen carrier for CLC reported in the literature.*

Supporting material	Preparation method [a]	Active metal oxide loading, α (wt%)	σ [b] (N)	Reference
Al_2O_3	WI	15-33	2.5 - 4.6	Adánez-Rubio *et al.*[123]
	MM+E	60-80	2.6	Adánez-Rubio *et al.*[123]
	FG	60	4.3	Cho *et al.*[145]
	DI	10	-	García-Labiano *et al.*[148]
	CO	21-78	3	Chuang *et al.*[147]
	MM+E	30-82	-	Chuang *et al.*[147]
$CaZrO_3$	MM+E	40	0.7	Arjmand *et al.*[181]
$MgAl_2O_4$	WI	15-21	0.8 - 2.1	Adánez-Rubio *et al.*[123]
	MM+PP	60	1.2 - 2.2	Adánez-Rubio *et al.*[123]
Sepiolite	MM+E	80	0.8	Adánez-Rubio *et al.*[123]
SiC	MM+RE	15-61	4.1 - 4.5	Peterson *et al.*[66]
	WI	19	-	Peterson *et al.*[66]
SiO_2	MM + E	60-80	0.9 - 1.1	Adánez-Rubio *et al.*[123]
	DI	60	2.6	Johansson [156]
	MM+E	40	-	De Diego *et al.*[157]
$SrZrO_3$	MM+E	40	0.8 - 1	Arjmand *et al.*[181]
TiO_2	MM + E	40-80	2.2 - 2.3	Adánez-Rubio *et al.*[123]
	DI	40	4.5	Johansson[156]
ZrO_2	MM+E	60-80	0.7	Adánez-Rubio *et al.*[123]
	MM+PP	40-60	2.2 - 2.8	Adánez-Rubio *et al.*[123]
	DI	40	0.8 - 2.7	Johansson[156]

Footnotes: (a) the abbreviations for the preparation methods are: WI = incipient wetness impregnation, FG = freeze granulation, DI = dry impregnation, CO = co-precipitation; MM+E = mechanical mixing and extrusion, MM+PP = mechanical mixing and pressure pelletizing; (b) if several values are reported for oxygen carriers with the same composition and preparation method in the publication, then the listed value is the maximum value reported.

Cho *et al.*[124] reported a high crushing strength and a high reactivity in pilot plant tests of Cu-oxygen carrier supported on Al_2O_3. However, after repeated cycling the inert support material and the active metal oxide eventually formed $CuAl_2O_4$.

Johansson[156] used SiO_2 as support material and reported undesired formation of silicates upon sintering. Additionally, he found particles supported on TiO_2 to either produce unstable particles after sintering or de-fluidised in FBR experiments. Contrary, Adánez *et al.*[158] reported that SiO_2 and TiO_2 supported Cu-oxygen carriers, which were sintered at 950 °C, performed best of all the oxygen carriers screened.

Johansson[156] studied the effect of doping ZrO_2 with CeO_2, Y_2O_3, CaO or MgO. Generally, these dopants enable tetragonal and cubic phases of the ZrO_2 to remain stable at temperatures at which otherwise monoclinic ZrO_2 would prevail, which generally enhances the mechanical properties.[182] Mn oxides supported on doped ZrO_2 were tested as oxygen carriers for chemical looping combustion,

but no significant change in the mechanical stability and reaction rates was observed. Johansson[156] therefore concluded that this doping is not so promising and only increases the costs of the expensive support material additionally.[156,182] Furthermore, bentonite and kaolin were tested as doping agents. Although addition of these resulted in an increase in the measured crushing strength of CuO/Al_2O_3 oxygen carriers, the reactivity was found to decrease significantly. It was therefore concluded that these doping agents are not promising.[156]

Wang *et al.*[183] studied Cu-based oxygen carriers supported on SiO_2, ZrO_2 and TiO_2 by XRD, and reported that neither of these supports formed phases with the CuO. It was therefore concluded, that these three supporting materials are inert when being used for Cu-based oxygen carriers.

3.3 Cost of oxygen carriers

The cost for the replacement of the oxygen carriers is often a significant part of the total cost of a CLC process.[60, 75, 172] To enable the comparison of the costs among various oxygen carrier types as well as comparison with other CO_2 capture technologies, the costs per tonne of CO_2 captured association with the replacement of oxygen carriers, CCC_{OC}, was calculated by,[109]

$$CCC_{OC} = \frac{C_{OC} \cdot SI}{SE \cdot \eta_{CO_2} \cdot \tau_{OC}} \tag{3-19}$$

In eq.(3-19), C_{OC} is the cost of the oxygen carriers, SI, is the solid inventory per MWh_e, SE, are the fuel specific emissions, η_{CO_2} is the rate of CO_2 capture, and τ_{OC} is the average oxygen carrier lifetime. A literature value for the specific emissions of methane is 0.23 t(CO_2)/MWh.[184] The cost of the oxygen carriers, C_{OC}, can be calculated by, [60, 75, 172, 176]

$$C_{\mathrm{OC}} = m_{\mathrm{MeO}} C_{\mathrm{MeO}} + (1 - m_{\mathrm{MeO}}) C_{\mathrm{S}} + C_{\mathrm{m}}, \tag{3-20}$$

where m_{MeO} is the mass fraction of the active metal oxide of the oxygen carrier mass, and C_{MeO}, C_{S} and C_{m} is the mass specific cost of the active metal oxide, the supporting materials, and the production process. Patzschke *et al.*[75] used the cost of the reduced metal, C_{Me}, and the molecular masses of the metal oxide, M_{MeO}, and the metal, M_{Me}, to calculate the cost of the metal oxides,

$$C_{\mathrm{MeO}} = \frac{M_{\mathrm{MeO}}}{M_{\mathrm{Me}}} \cdot C_{\mathrm{Me}}. \tag{3-21}$$

Furthermore, the authors compiled an extensive table with values for SI, τ_{OC}, C_{OC} and CCC_{OC}, as reproduced in **Table 3-10**, below.[172, 185]

Table 3-10 *Results of the economic assessment of oxygen carrier sorted by cost of carbon capture (ascending).*

Sample	α (wt%)	Support	Prep.[a]	T_{calc}, t_{calc} (°C), (h)	T_{op} (°C)	*SI* (kg/MW_{th})	t_{OC} (h)	C_{Raw} ($\$_{2018}$/kg)	C_{Prep} ($\$_{2018}$/kg)	C_{OC} ($\$_{2018}$/kg)	CCC_{OC} ($\$_{2018}$/$ton_{CO2}$)	Reference
Ni-1	18	γ-Al_2O_3	IM	900, 1 [d]	800	600	10 000 [g]	1.95	0.44	2.39	0.64	Adánez *et al.*[62]
Cu-3	14	γ-Al_2O_3,	IM	850, 1	800	400	2 500	1.11	0.34	1.45	1.03	Adánez *et al.*[51], Forero *et al.*[52]
Cu-8	60	$MgAl_2O_4$	SD	1100, 24	900	670	25 000	2.56	9.25	11.81	1.40	Adánez-Rubio *et al.*[53]
Fe-13	60	γ-Al_2O_3	FG	1100, 6	950	1 200	10 000	0.34	3.81	4.15	2.21	Abad *et al.*, 2007, Gayán *et al.*, 2012
Cu-3b	14	γ-Al_2O_3	IM	850, 1	900	400	1 100	1.11	0.34	1.45	2.35	de Diego *et al.*[54]
Cu-5	13	$NiAl_2O_4$	IM	850, 1 [d]	900	450	2 700	3.70	0.45	4.15	3.07	Gayán *et al.* [55]
Ni-2	11	$CaAl_2O_4$	IM	950, 1 [d]	900	180	400 [g]	1.25	0.54	1.79	3.58	Gayán *et al.*[63]
Fe-14	15	γ-Al_2O_3	IM	950, 1 [d]	830	1 100	1 250	0.59	0.51	1.10	4.29	Gayán *et al.*[59]
Mn-ore[b]	66	-	-	-	950	683	1 600	2.57	-	2.57	4.87	Mei *et al.*[68]
Ni-3	40	$NiAl_2O_4$	FG	-	850	200	4 000	5.16	18.12	23.28	5.16	Fan[39]
Fe-2	20	γ- Al_2O_3	IM	800, 1 [f]	880	1 300	1 100 [g]	0.66	0.52	1.18	6.20	Cabello *et al.*, [60]
Cu-6	12	$MgAl_2O_4$	IM	800, 1 [e]	900	473	500 [g]	1.28	0.44	1.72	7.20	Gayán *et al.*[55]
Fe-3	60	$MgAl_2O_4$	IM	950, 6	850	500	1 000	1.39	2.15	3.54	7.85	Mattisson *et al.*[64], Leion *et al.*[174]
Cu-2	14	α-Al_2O_3	IM	850, 1	900	400	250 [g]	1.11	0.34	1.45	10.32	Forero *et al.* [52]
Fe-11	17	γ- Al_2O_3	IM	950, 1 [f]	900	1 600	700	0.62	0.51	1.13	11.42	Cabello *et al.*[60]
Cu-4b	14	γ- Al_2O_3	IM	-	900	443	450	-	-	3.04	13.28	Cabello *et al.*[56]
Mn-3	40	ZrO_2	FG	1150, 6	850	1 100	2 600	4.75	3.81	8.56	16.06	Johansson *et al.* [57]
Mn-Prv [c]	-	-	SD	1300, 4	900	700	1 100 [g]	5.77	1.96	7.73	21.81	Cabello *et al.*[69]
Mn-2	40	ZrO_2	SD	1200, 2	900	1 040	400	4.75	1.32	6.07	70.00	Rydén *et al.*[58]

Footnotes: (a) the following abbreviations were used for the preparation methods: IM = impregnation; SD = spray drying; FG = freeze granulation; (b) this Mn-ore contains 65.6% Mn_3O_4; (c) this perovskite oxygen carrier has a molar composition of $CaMn_{0.9}Mg_{0.1}O_{3-\delta}$; (d-f) the sintering follows a thermal decomposition of the metal nitrates at (d) 500 °C for 0.5 h, (e) 550 °C for 1 h, (f) 550 °C for 0.5 h; (g) here the lifetime was estimated by Cabello et al.[56]

The values from **Table 3-10** are illustrated in **Fig. 3-11**, below.[172, 185]

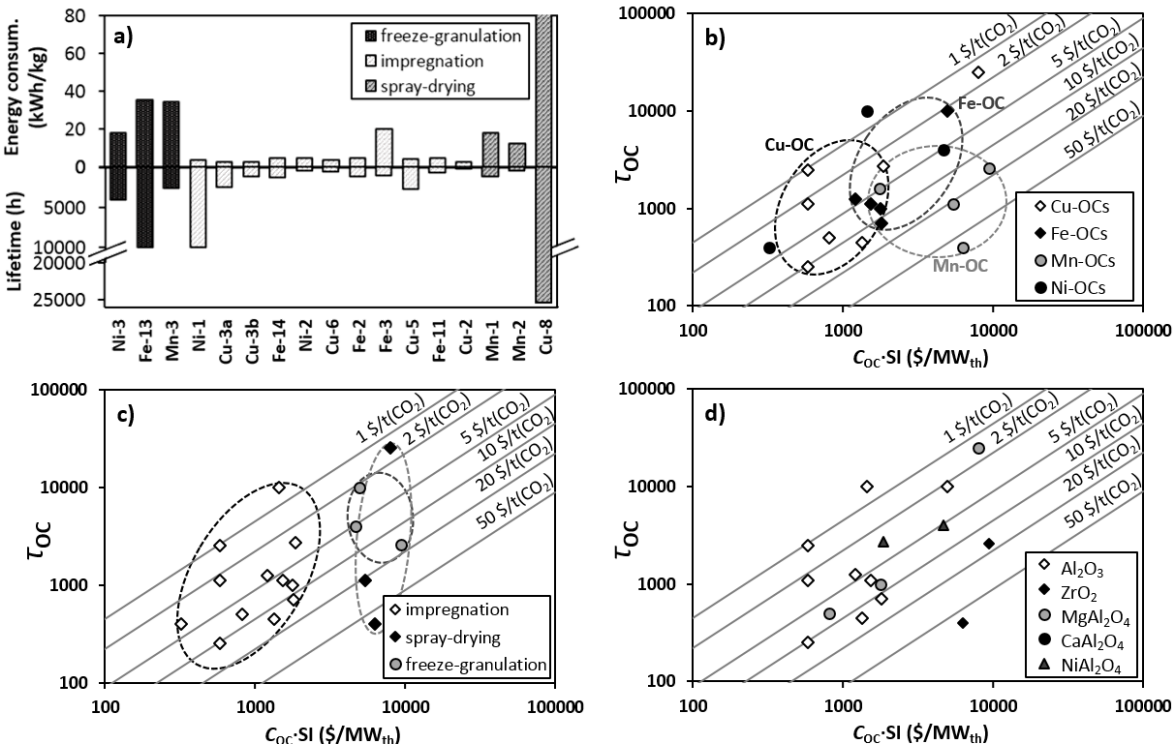


Fig. 3-11 *Plots of the oxygen carrier lifetimes versus the cost of the solid inventory required to generate 1 MW_{th} grouped by: (a) shows the energy consumption of the oxygen carrier production and the oxygen carrier lifetimes, (b) oxygen carrier material, (b) preparation method, and (c) support material. The grey lines in (a), (b) and (c) are the iso-lines of the oxygen carrier specific cost of CO_2 capture and the dotted circles are used to highlight clusters of the same material or method.*[6075]

Fig. 3-11a shows that the energy requirements for the oxygen carrier preparation vary significantly by preparation method (details for the calculation of the energy requirements are provided in Patzschke *et al.*[75]). However, in some cases oxygen carriers offset high production energy requirements with long lifetimes. The energy requirements for the preparation of the spray-dried Cu-8 (86.4 kWh kg^{-1}) are 1550% of the average of all impregnated oxygen carriers in **Fig. 3-11a**, owing to the relatively long estimated lifetime of Cu-8, the energy requirements per hour of lifetime are 51% of the average specific energy requirements of the impregnated oxygen carriers. This example shows that in some cases extensive preparation methods are justifiable.

In **Fig. 3-11b** the calculated lifetime of the oxygen carriers is plotted against the cost of the solid inventory using the data from **Table 3-10**. Additionally, iso-cost lines for the cost of CO_2 capture caused by the oxygen carrier replacement are drawn onto the graph. From **Fig. 3-11b** it can be seen that the average cost of the specific solid inventory is in the order (from low to high): Ni (1521 $\$\cdot MWth^{-1}$) < Fe (2493 $\$\cdot MWth^{-1}$) < Cu (2679 $\$\cdot MWth^{-1}$) < Mn (4673 $\$\cdot MWth^{-1}$). Using eq.(3-19) and assuming CH_4 is the fuel, the additional cost of CO_2 capture due to the replacement of oxygen

carriers is in the order (from low to high): Ni (3.1 $\$_{2017}\cdot t_{CO2}$) < Mn-ore (4.9 $\$_{2017}\cdot t_{CO2}$) < Cu (5.5 $\$_{2017}\cdot t_{CO2}$) < Fe (6.4 $\$_{2017}\cdot t_{CO2}$) < Mn (16.1 $\$_{2017}\cdot t_{CO2}$) < perovskites (21.8 $\$_{2017}\cdot t_{CO2}$).

Fig. 3-11c shows that the average specific solid inventory cost by preparation method is: impregnation (1154 $\$\cdot MWth^{-1}$) < freeze-granulation (6351 $\$\cdot MWth^{-1}$) < spray-drying (6546 $\$\cdot MWth^{-1}$), and the average ccc_{OC} is in the order impregnation (5.9 $\$_{2017}\cdot t_{CO2}$) freeze-granulation (7.8 $\$_{2017}\cdot t_{CO2}$) < spray-drying (11.6 $\$_{2017}\cdot t_{CO2}$). It can be seen that the additional cost of CO_2 capture follows the same order as the energy intensity of the preparation, indicating that the latter can affect the CO_2 capture cost, significantly. **Fig. 3-11d** shows that the average ccc_{OC} of the support material is in the order: $CaAl_2O_4$ (3.58 $\$_{2017}\cdot t_{CO2}$) < $NiAl_2O_4$ (4.12 $\$_{2017}\cdot t_{CO2}$) < $MgAl_2O_4$ (5.48 $\$_{2017}\cdot t_{CO2}$) < Al_2O_3 (5.75 $\$_{2017}\cdot t_{CO2}$) < ZrO_2 (16.1 $\$_{2017}\cdot t_{CO2}$). This indicates that the supporting material can significantly affect the cost of CO_2 capture, significantly.

3.4 Methods for the preparation of oxygen carriers

In this section, methods for the preparation of oxygen carriers are reviewed. Successful application of various techniques for oxygen carrier preparation have been reported in the literature, such as co-precipitation,[158, 186] mechanical mixing[123, 147, 181] with subsequent particle formation by drying in a rotary evaporator[66], freeze-granulation, extrusion[123, 181] or pressure pelletizing[123], incipient wet impregnation[66, 147, 187] and dry impregnation[156]. Some works report the preparation of copper manganese oxides as oxygen carriers for the CLC process and for other applications. These are summarised in **Table 3-11**, below.

Table 3-11 *Publications reporting the preparation of copper manganese oxides.*

Process/application	Preparation method	Reference
as oxygen carriers for chemical looping processes:		
CH_4 fuelled CLC	Co-precipitation using metal nitrates and Na_2CO_3.	Mungse *et al.*[44]
CLOU	Mechanical mixing of CuO, Mn_3O_4, DI water and polyvinyl alcohol with subsequent freeze-drying.	Pour *et al.*[43]
Syngas fuelled CLC	Co-precipitation with NaOH and Na_2CO_3.	Sajen *et al.*[178]
CLOU combustion of charcoal	Co-precipitation with NaOH.	Hosseini *et al.*[45]
other applications:		
Water-gas-shift catalyst	Co-precipitation with aqueous ammonia.	Tanaka *et al.*[188]
Three-way catalysts	Pechini method using manganese acetate, copper nitrate, cerium nitrate, citric acid and ethylene glycol.	Huang *et al.*[189]
Assessment of the Jahn-Teller effect	Mechanical mixing of CuO and MnO and pressure pelletising at 100 MPa (extensive calcination: 21 h at 860 °C).	Shoemaker *et al.* [190]
Semiconductor for photoelectric devices	Sol-gel method using metal acetates and melted stearic acid.	Enhessari *et al.*[191]

As shown in **Table 3-11**, copper manganese oxides have been previously proposed for CLC and CLOU processes:[43-45] Pour *et al.*[43] prepared CMO by freeze-granulation and investigated the reduction under N_2 and in the presence of wood char as the fuel, and reported no occurrence of agglomeration[43]. Mungse *et al.*[44] studied the performance of CMOs with CH_4 as the fuel and Hosseini

et al.[45] reported that for the combustion of solid fuels, CMOs with a molar Cu-Mn ratio of 1:3 performed best in the fluidised bed at 800 °C. CMOs have recently attracted interest for other applications, such as materials for three-way catalysts for the removal of CO, hydrocarbons and nitrous oxides,[189] semiconductors for photoelectric devices,[191] and water-gas-shift catalysts.[188]

3.4.1 Preparation of oxygen carrier *via* mechanical mixing

The preparation of oxygen carriers *via* mechanical mixing starts typically with the mixing of the active metal oxide(s), the supporting material and a liquid solvent (often DI water).[147,157,195] Furthermore, additives such as pore forming agents, dispersants or binders can be added to the slurry to modify the precursor properties.[157,186,195] However, Sohn *et al.*[186] recommended to abstain from using additives when preparing oxygen carriers for kinetic experiments, since products from the thermal decomposition of those additives can affect the observed rates. For mixing of the powders, the break-up of agglomerated grains, and a reduction in the mean grain size of the powders, the slurry is typically milled (*e.g.* in a planetary ball mill).[246] To obtain oxygen carrier particles, the slurry is either directly dried and calcined followed by crushing and sieving of the calcined solids into the desired size fractions, or particles are formed from the slurry, sieved in the desired particle diameter range and then calcined. [147,157,195] Commonly used methods for the particle formation include spray-drying[53,246] and freeze-granulation[100].

For the particle formation by spray-drying, the slurry is typically pumped through a nozzle located at the top of the spray-drying chamber, producing small spherules. Additionally, hot air is injected into the chamber, which result in rapid drying of the spherules. The dried particles are collected at the bottom of the spray-drying chamber.[195, 245]

In the process of freeze-granulation, the slurry is pumped through a nozzle, resulting the slurry to form small spherules, which are sprayed into liquid N_2.[100] The solvent is removed from frozen material *via* sublimation, and additives (*e.g.* dispersants and binders) are thermally decomposed during the heating of the calcination step.[112]

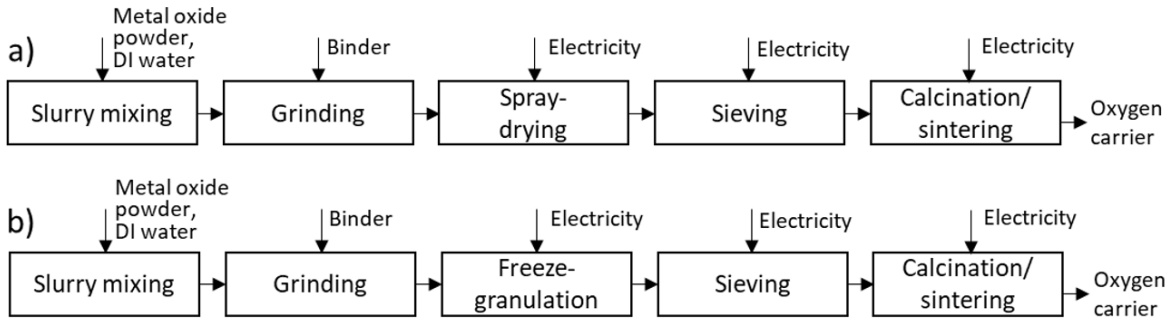


Fig. 3-12 *Block flow diagrams representing a typical process of oxygen carrier preparation via mechanical mixing with particle formation via (a) spray-drying and (b) freeze-granulation, adapted from Patzschke et al.*[75,185]

3.4.2 Preparation of oxygen carrier *via* impregnation

The preparation of oxygen carriers *via* impregnation starts commonly with the crushing and sieving of an inert supporting material. The dried crushed material is then mixed with an aqueous solution containing the salts of the active phase. Typically the volume of the solution equals the pore volume and fully deposits in the pores during drying (contrarily to the ion exchange process).[192] This method is therefore also referred to as "dry impregnation" or "incipient wetness" impregnation. The substitution of the solid-gas interface with a solid-liquid interface results in a significant reduction of the free enthalpy, which however does not affect the quality of the precursors considerably.[192] This impregnation by capillary forces is typically used for the oxygen carrier preparation.[59, 60, 148, 187] If an excess volume of liquid is used, which requires an intermediate filtration and drying step, the process is referred to as wet impregnation. Gayán *et al*. used this method for the preparation of Cu-based oxygen carriers.[55] Besides capillary impregnation, is also possible to start with the pores being initially filled with a liquid solution. In this case, the impregnation occurs by liquid phase diffusion.[192] After completion of the impregnation process, the salts (*e.g.* nitrates) that were deposited on the pore walls of the particles are thermally decomposed to the metal oxides. The process of the oxygen carrier preparation *via* co-precipitation is illustrated in **Fig. 3-13**, below.

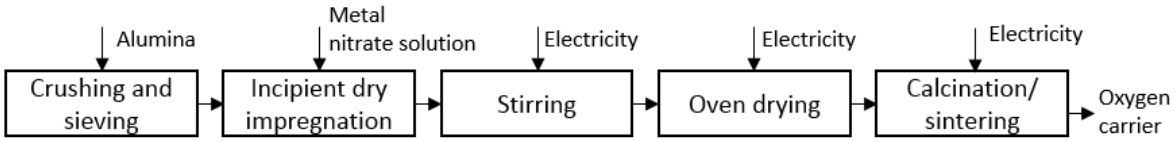


Fig. 3-13 *Block flow diagram representing a typical process of oxygen carrier preparation via incipient dry impregnation, adapted from Patzschke et al.*[75,185]

Typically used supporting materials are γ-Al_2O_3[55, 187] α-Al_2O_3, [55], $MgAl_2O_4$[55], and NiO/γ-Al_2O_3[55], and the active metal oxide loading (after calcination) is typically in the range 14-23 wt% [51, 187, 193]

3.4.3 Preparation of oxygen carrier *via* co-precipitation

In the process of co-precipitation, an aqueous solution containing dissolved metal salts is mixed with an alkaline solution, the increased *pH* value results in the precipitation of the species containing the metals.[192, 194] Commonly used salts are metal nitrates, metal sulphates and metal chlorides. For the preparation of the alkaline solution, typically Na_2CO_3, NaOH or ammonia are dissolved in DI water. The difference between the *pH* value required for the co-precipitation and actual *pH* value of the mixture corresponds to the degree of super-saturation, which is thus the driving force of the precipitation.[195] The co-precipitation can be carried out at low super-saturation or at high super-saturation. For the co-precipitation at low super-saturation, both solutions are typically added

simultaneously to a reaction vessel thereby maintaining a constant *pH* value. In the process at high super-saturation, the metal nitrate solution is typically added rapidly to the alkaline solutions.

The *pH* value of the product solution and thus the degree of super-saturation has typically a significant effect on the material properties.[195] However, although it can be predicted which phases form at a certain *pH* value,[196-198] the relationship between the material properties and the *pH* is often not clear and is therefore often determined experimentally.[195] Horn and Rieger[237] reviewed theories for the formation of complex solids *via* co-precipitation (and other methods) and concluded that many theories simplify the occurring processes. Many processes, including the molecular processes during the mixing of the two solutions to achieve supersaturation are not fully understood.[237] Keeping this in mind, some physico-chemical considerations are detailed in the following to provide a foundation that allows relating changing oxygen carrier characteristics, such as porosity, with a change in driving force, *i.e.* the degree of super-saturation.

For the precipitation to occur, nuclei have to form first. On these nuclei, solids (precursors of the precipitate) attach.[195] The change of Gibbs free energy during the formation of a particle, ΔG, is given by,[195]

$$\Delta G = \Delta G_{\text{bulk}} + \Delta G_{\text{interface}} + \Delta G_{\text{others}} \tag{3-22}$$

where ΔG_{bulk} is the difference in Gibbs free energy between the solution, $\Delta G_{\text{interface}}$, is the free energy due to the formation of the solid-liquid interface, and ΔG_{others} contains other minor contributions, *e.g.* those caused by impurities. ΔG_{others} is in the ideal case zero, and therefore here not further considered.[195] For spontaneous agglomeration to occur ΔG has to be negative, as is ΔG_{bulk} during super-saturation.[195] Contrarily, $\Delta G_{\text{interface}}$ is always positive, since the formation of an interface requires energy. With an increasing particle diameter, $\Delta G_{\text{interface}}$ increases with $4\pi r^2$, while ΔG_{bulk} energy increases with $4/3\pi r^3$. Consequently, there is a critical r beyond which ΔG is negative.[195] This point is referred to as the nucleation threshold and r at this point corresponds to the radius of the nuclei.[195] Is the precursor concentration above the nucleation threshold, new nuclei will form. The concentration of precursors decreases if their rate of production is lower than the rate of their consumption. The solids are typically consumed by nucleation and particle growth. This relationship can be simplified illustrated, as shown in **Fig. 3-14**, below.[195]

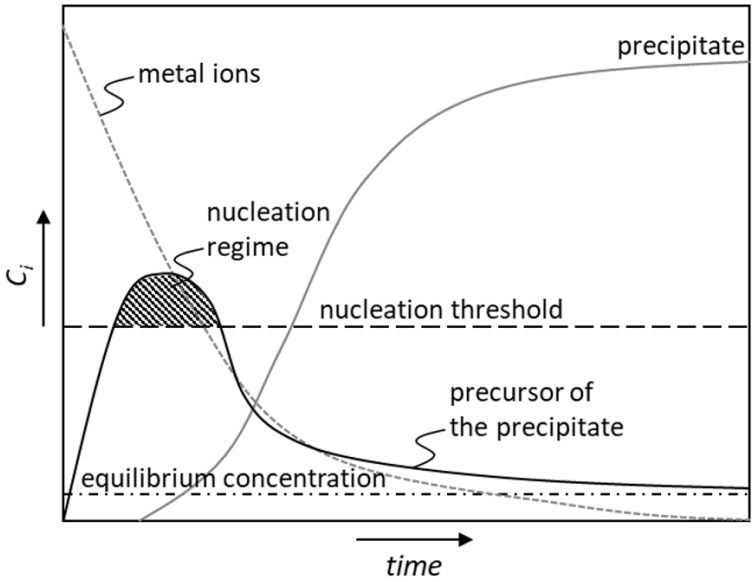


Fig. 3-14 *Simplified schematic of the process of precipitation from the solution.*[195]

Nuclei only form in the nucleation regime, and the particle size of the precipitate depends on the extend of this nucleation regime (textured area in **Fig. 3-14**). An increase in the extend of the nucleation regime typically results in a higher number of nuclei and therefore results in a smaller terminal particle size of the precipitate. *Vice versa*, a reduction results in a lower number of nuclei and thus larger precipitated particles. A higher degree of supersaturation results in a larger maximum excess of precursor of the nucleation threshold and thus likely a larger nucleation regime (though the rate of nucleation is also faster, which in turn results in a faster decrease of the precursor concentration).[195] It is therefore assumed that a higher degree of supersaturation (a higher co-precipitation *pH* value) results in a smaller terminal particle size. The less dense particles and a less dense packing of those in the dried precursor (owing to slower settling of small particles and slower evaporation of moisture from small inter-particle voids) are likely to result in oxygen carriers with a higher porosity. Contrarily, a lower degree of super-saturation (a lower co-precipitation *pH* value) results in a larger terminal particle size with fewer particles. The oxygen carriers prepared from these precursors are expected to have a lower porosity. The precipitated particles are denser, and owing to their larger particle size, will settle faster producing a denser packing, which likely produces an oxygen carrier material with a lower porosity.

After complete co-precipitation, the liquid phase (supernatant) contains excess ions. Either these ions are removed immediately by washing with DI water or the precipitated is kept in the supernatant for a certain duration (referred to as ageing) before washing. Ageing can influence the material properties significantly, often resulting in a material with a higher-crystallinity due to the following three effects:[195] Firstly, the particle size of the precipitate typically increases, which is caused by Ostwald ripening.[195] The higher curvature of smaller particles results in a higher solubility compared to larger

particles. Therefore, small particles are more likely to dissolve back into the mother solution, which in turn results in the precipitation of new material. This precipitation occurs typically on the surface of larger particles, which results in a net growth of the particles during ageing.[195] Secondly, re-crystallisation is typically favourable during ageing. In this process amorphous material turns into crystalline material, as a result of solid state diffusion.[195] Thirdly, impurities which were trapped in the precipitate, especially during fast precipitation, can dissolve back into the liquid phase.[195]

To obtain oxygen carriers from the precipitated solids, the solids are dried, calcined, crushed, and sieved into the desired particle size ranges. A diagram of the process is shown in **Fig. 3-15**, below.

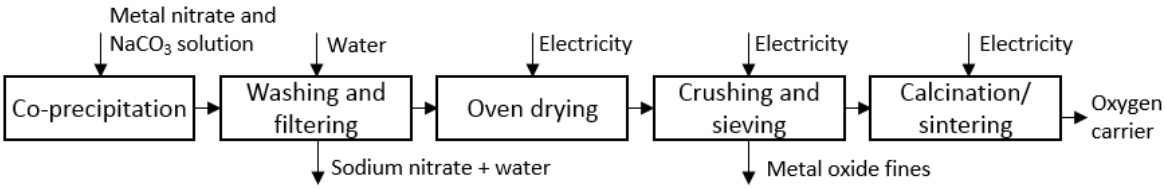


Fig. 3-15 *Block flow diagram representing a typical process of oxygen carrier preparation via co-precipitation, adapted from Patzschke et al.*[75,185]

Details on the preparation procedures of this work are provided in **chapter 4**.

3.5 Selection of the sintering and calcination temperatures

Sintering is the process of bonding metal particles, by extending their contact area, at temperatures between Tammann temperature (T_T) and their melting temperature (T_M). Metal powder has excess free energy due to the particles large surface area and defects. This is the driving force, for volume diffusion, grain boundaries diffusion and surface diffusion of atoms occur, as vibration of atoms creating more vacant lattice sites.[199-201]

The smaller the particles the shorter the diffusion ways and the larger the curvature pressure, which both accelerate the mixing of the ions due to an increase in diffusion.[201] Decreasing particle size by ball milling of CuO particles and support particles will therefore theoretically reduce sintering time and hence energy requirements of sintering. Sintering temperatures and particle characteristics of Cu-based oxygen carrier are summarised in **Table 3-12**, below.

Table 3-12 *Sintering temperatures and particle properties of Cu, Mn, and Cu-Mn oxygen carriers.*

$T_{calc.}$ (°C)	*Active phase*	σ_{CS} (N)	ρ_b (g cm^{-3})	S_{BET} (m^2 g^{-1})	*α (wt%)*	Supporting material	Preparation[a]	Work
850	CuO	4.6	2.2	-	15%	α-Al_2O_3	WI	Adánez-Rubio *et al.*[123]
		3	1.9	-	33%	γ-Al_2O_3	WI	Adánez-Rubio *et al.*[123]
		2.5	1.6	-	15%	γ-Al_2O_3	WI	Adánez-Rubio *et al.*[123]
		2.1	1.9	-	15%	$MgAl_2O_4$	WI	Adánez-Rubio *et al.*[123]
		0.8	2	-	21%	$MgAl_2O_4$	WI	Adánez-Rubio *et al.*[123]
950	Mn_2O_3	1	-	-	80%	Sepiolite	MM+E	Adánez *et al.*[158]
		1	-	-	60%	Sepiolite	MM+E	Adánez *et al.*[158]
		10	-	-	80%	SiO_2	MM+E	Adánez *et al.*[158]
		16	-	-	60%	SiO_2	MM+E	Adánez *et al.*[158]
		16	-	-	40%	SiO_2	MM+E	Adánez *et al.*[158]
		2	-	-	80%	TiO_2	MM+E	Adánez *et al.*[158]
		8	-	-	60%	TiO_2	MM+E	Adánez *et al.*[158]
		13	-	-	40%	TiO_2	MM+E	Adánez *et al.*[158]
		1	-	-	80%	ZrO_2	MM+E	Adánez *et al.*[158]
		2	-	-	60%	ZrO_2	MM+E	Adánez *et al.*[158]
950	CuO	0.7	1.63	1.98	40%	$CaZrO_3$	MM+E	Arjmand *et al.*[146]
		0.8	1.46	0.72	40%	$SrZrO_3$	MM+E	Arjmand *et al.*[146]
		2.3	-	-	40%	TiO_2	MM+E	Adánez-Rubio *et al.*[123]
		2.2	-	-	80%	TiO_2	MM+E	Adánez-Rubio *et al.*[123]
		1.1	-	-	60%	SiO_2	MM+E	Adánez-Rubio *et al.*[123]
		0.9	-	-	80%	SiO_2	MM+E	Adánez-Rubio *et al.*[123]
		0.8	-	-	80%	Sepiolite	MM+E	Adánez-Rubio *et al.*[123]
		0.7	-	-	80%	ZrO_2	MM+E	Adánez-Rubio *et al.*[123]
		<0.5	-	-	60%	ZrO_2	MM+PP[b]	Adánez-Rubio *et al.*[123]
		<0.5	-	-	60%	ZrO_2	MM+E	Adánez-Rubio *et al.*[123]
		<0.5	-	-	60%	$MgAl_2O_4$	MM+PP[b]	Adánez-Rubio *et al.*[123]
1030	CuO	1	1.51	1.05	40%	$SrZrO_3$	MM+E	Arjmand *et al.*[146]
		<0.5	1.25	0.56	40%	$CaZrO_3$	MM+E	Arjmand *et al.*[146]
1100	CuO	2.8	4.7	-	40%	ZrO_2	MM+PP[b]	Adánez-Rubio *et al.*[123]
		2.6	0	-	80%	Al_2O_3	MM+E	Adánez-Rubio *et al.*[123]
		2.3	4.9	-	60%	ZrO_2	MM+PP[b]	Adánez-Rubio *et al.*[123]
		2.2	3.4	-	60%	ZrO_2	MM+PP[b]	Adánez-Rubio *et al.*[123]
		2.2	2.9	-	60%	$MgAl_2O_4$	MM+PP[b]	Adánez-Rubio *et al.*[123]
		2.2	3	-	60%	ZrO_2	MM+PP[c]	Adánez-Rubio *et al.*[123]
		1.9	2.9	-	60%	$MgAl_2O_4$	MM+PP[b]	Adánez-Rubio *et al.*[123]
		1.2	2.4	-	60%	$MgAl_2O_4$	MM+PP[c]	Adánez-Rubio *et al.*[123]
		<0.5	-	-	60%	Al_2O_3	MM+E	Adánez-Rubio *et al.*[123]

Footnotes: (a) the nomenclature for the preparation method is: WI = Incipient wetness impregnation, MM+E = mechanical mixing and extrusion, MM+PP = mechanical mixing and pressure pelletizing; (b, c) during the preparation of the oxygen carrier precursors (b) 0.5 wt% and (c) 5.0 wt% graphite was added as a pore-forming agent.

German *et al.*[200] identified four parameters that control the sintering densification, which are presented in ***Table 3-13***, below.

Table 3-13 *Parameters and control variables of the densification of metal oxides via sintering, adapted from German et al.*[200]

parameter	effect on densification during the sintering process
density of the precursor	"initial number of neighbouring grains for bonding"
sintering temperature	"solubility, wetting and diffusivity"
grain size	"curvature, surface area and diffusion distance"
sintering time	"amount of cumulative change"

Capillary forces favour small pores to be filled over larger pores, hence the mean pore size increases with an increasing sintering duration, while the porosity decreases.[200]

The next chapter describes the production of copper manganese oxide oxygen carrier *via* co-precipitation and mechanical mixing.

3.6 Concluding remarks

The literature was reviewed to identify desirable properties of oxygen carriers. It was reported that the reactivity is inversely proportional to the minimum required active metal oxide mass in a reactor. Therefore, a higher chemical reaction rate results in a lower bed mass and thus a small minimum reactor size for a kinetic controlled reaction rate (though many works showed that in a CFB of chemical looping processes mass transfer is non-negligible). To evaluate the reactivity of single metal oxide systems, the rate constants of the redox-reactions were compared. Mn and Cu oxides were found to be most reactive (over most of the studied condition range).

Besides the reactivity, the pore morphology of oxygen carriers was identified as a tuneable property with relevance to the oxygen carriers' performance: A low internal surface area may result in a significant resistance to intra-particle diffusion, thereby potentially limiting the overall rate of reaction. Values for the BET surface area (a vague indication for the porosity) reported in the literature for Cu-based and Mn-based oxygen carriers were in the range 0.31 – 41.3 $m^2\ g^{-1}$. The average value by preparation method was found to be in the order: freeze-granulation < mechanical mixing < co-precipitation < impregnation. The reviewed data provides a first guidance for the selection of the oxygen carrier preparation method and preparation conditions.

To identify the conditions at which the reactions are thermodynamically favourable, Ellingham diagrams were computed using data from FactSage. These compare the $\Delta G(T)$ of the metal oxide oxidation reactions with the $\Delta G(T)$ of the combustion reactions (for the conventional CLC process) or with the kinetic energy of O_2 at p_{O_2}= 0.01 bar and p_{O_2}= 0.30 bar (for the CLAS process). For the

CLAS process, in the p_{O_2} range 0.01 – 0.30 bar and the temperature range 200 – 1200 °C, the only Cu, Mn and Co oxides that were found to release gaseous O_2 are CuO (at temperatures between 886 °C and 1051 °C), Mn_2O_3 (816 – 907 °C), and Co_3O_4 (721 – 901 °C). The Fe oxides were found to be unable to release gaseous O_2 within the studied condition range. In a further thermodynamic study data from FactSage was used to compute the $p_{O_2,eq}$ curves for Co_3O_4/CoO, Mn_2O_3/Mn_3O_4, CuO/Cu_2O. It was found that at typical oxidiser O_2 partial pressures (*i.e.* p_{O_2} at inlet = 0.21 bar, p_{O_2} at outlet = 0.05 bar) the oxidiser temperature has to be lower than 900 °C, 770 °C and 730 °C to ensure a positive driving force for the oxidation reaction of Cu_2O, Mn_3O_4 and CoO, respectively. These condition ranges are a (first) estimation of typical reducer and oxidiser conditions in a CLAS process when using single metal oxides, and the methods can be used to estimate the operating conditions of new combined metal oxides after experimentally obtaining their $p_{O_2,eq}(T)$ and $\Delta H\,(T)$ of the O_2 release reaction.

Furthermore, a high resistance towards attrition in the CLC process was identified as a desirable oxygen carrier property. Several methods are commonly used to measure the oxygen carriers' resistance to mechanical stresses. Arguably their accuracy for the prediction of the attrition behaviour in an industrial-scale process is in the order (from low to high): single particle tests < jet cup tests and ASTM D5757 rig tests < tests in a batch lab-scale fluidised bed reactor or lab-scale continuous CLC unit < pilot plant tests. In several works the rate of attrition was measured and this rate was used to estimate the oxygen carrier lifetime. Data from 19 works for the CH_4-CLC process were compared (relevant attrition data for the CLAS process does not exist), in which the lifetime of Cu-based and Mn-based oxygen carriers are in the range 450 h – 25 000 h and 400 h – 2600 h. The large variation demonstrates the importance of selecting of the optimal materials, preparation methods, preparation conditions, and operating conditions (and to some extent it might also demonstrate the inaccuracy of this method for the calculation of oxygen carrier lifetimes). During the review on the oxygen carrier attrition, some interesting qualitative findings were made: Several works reported an increase of the attrition rate beyond the minimum rate around 7.5 h – 20 h. Furthermore, it was reported that over extended redox-cycling the pore morphology of the oxygen carrier changes, *i.e.* the porosity and the mean pore size increased. These findings come from experiments with the conditions of a CH_4-CLC process, but to a certain extent are also relevant to the CLAS process. These findings resulted in the design of several long-term cycling experiments in the fluidised bed with up to 60 h of redox-cycling. Furthermore, these findings were a reason to carry out an in-depth material characterisation of the oxygen carriers recovered from the long-term experiments, in order to elucidate the evolution of the material morphology with an increasing number of redox-cycles and to draw parallels to the findings from the CH_4-CLC and Ca-looping experiments.

Other important parameters for the chemical looping processes design are the reaction enthalpies of the oxygen carriers. These are related to the heat balance of the reactors. If the enthalpy of the overall reaction in a reactor is negative, heat has to be added to the reactor by an enhanced circulation rate of the oxygen carriers, pre-heating the inlet gases or direct heating of the reactor in order to maintain the operating temperature. A theoretical study was performed to determine the overall heat balance in the reducer for Cu, Mn, and Co oxides. While in the fuelled CLC process most fuel types (biomass, CH_4, CO and H_2) result in an exothermic overall reaction (apart from Mn and Co oxides when using CH_4), the overall reaction in the reducer of the CLAS process was found to be strongly endothermic. The additional required enthalpy is in the order: Co_3O_4 (390.0 kJ·mol$(O_2)^{-1}$) > CuO (261.5 kJ·mol$(O_2)^{-1}$) > Mn_2O_3 (143.1 kJ·mol$(O_2)^{-1}$). This identified a significant disadvantage of the CLAS process, as vast amounts of enthalpy have to be transferred to the reducer, which might increase the operational and capital costs of the process, reduce its efficiency, or even disallow auto-thermal operation. Since heat of reaction data of the combined metal oxides of this work are not available in the literature, redox-experiments were designed to estimate the reaction enthalpy of the O_2 release. This allowed the quantification of the theoretical overall reaction enthalpy in the reducer and to conclude if auto-thermal operation is possible.

Furthermore, a large O_2 transport capacity (R_0) is a desirable oxygen carrier property as this allows for a lower solid inventory. The values of R_0 were computed using the stoichiometry of the redox-reactions relevant for the CLC and the CLAS process. In a fuelled process, the oxides of Cu, Mn, and Co, are able to release 20.1 wt%, 10.1 wt% and 26.6 wt%, respectively, while in the CLAS process, these oxides are only able to release 10.1 wt%, 3.4 wt% and 6.6 wt%, respectively. Assuming full oxygen carrier conversion and no increased oxygen carrier circulation rate for additional heat transfer, this shows that the mass flow rate in the CLAS process is higher than in the CLC process to provide O_2 for the combustion of a given amount of fuel.

The second body of this chapter focused on reviewing commonly used inert supporting materials, such as Al_2O_3, MgO, $MgAl_2O_4$, SiO_2, TiO_2, ZrO_2. The values of the micro-hardness of active and supporting materials were compared, and the values of some inert supports (*e.g.* Al_2O_3) were found to be more than an order of magnitude higher than some active metal oxides (*e.g.* CuO). Ellingham diagrams were computed using data from FactSage to confirm the 'inertness' of the supporting materials. For all evaluated support materials (Al_2O_3, MgO, $MgAl_2O_4$, SiO_2, TiO_2, ZrO_2) no reduction reactions were found to be thermodynamically favourable in the presence of excess C, H_2 or CO at 0.1 MPa and in the temperatures range 200 °C – 1200 °C. Agglomeration and phase separation was reported to be caused by sintering – a high ion mobility – which increases with an increasing temperature and occurs in the lattice of the metal oxides beyond the Tammann temperature (T_T). The values of T_T for the single metal oxides of this work are in the order of: Mn_2O_3 (334 °C) < Cu_2O (481

°C) < CuO (526 °C) < Mn_3O_4 (644 °C). It shall be noted that the decomposed form of Mn oxide and the oxidised form of Cu oxide have a lower T_T than their oxidised or decomposed counterpart. This indicates that combining Cu and Mn oxides might have a synergetic effect regarding its resistance to agglomeration. Nevertheless, the values of T_T below the estimate operating temperatures in the CLAS process indicates the need for an inert support, for which the values of T_T are: SiO_2 (669 °C) < TiO_2 (789 °C) < Sepolite (819 °C) < Al_2O_3 (884 °C) < $MgAl_2O_4$ (929 °C) < CeO_2 (1064 °C) < ZrO_2 (1214 °C) < MgO (1290 °C).

In the third body of the chapter, the costs of CO_2 capture due to the oxygen carrier replacement, ccc_{OC}, were reviewed and calculated. This was done using an equation, which relates the cost of the oxygen carriers, the minimum solid inventory, the estimated oxygen carrier lifetime, and specific O_2 demand of the fuel. The goal of this study was to find out whether more expensive materials and an energy intense preparation procedure can be economically justifiable by either reducing the solid inventory or increasing the oxygen carrier lifetimes sufficiently to result in an overall reduction in the ccc_{OC}. The average ccc_{OC} by active metal oxide was calculated to be in the order: Ni (3.1 $\$_{2017}\cdot t_{CO2}$) < Mn-ore (4.9 $\$_{2017}\cdot t_{CO2}$) < Cu (5.5 $\$_{2017}\cdot t_{CO2}$) < Fe (6.4 $\$_{2017}\cdot t_{CO2}$) < Mn (16.1 $\$_{2017}\cdot t_{CO2}$) < perovskites (21.8 $\$_{2017}\cdot t_{CO2}$). The order of the average ccc_{OC} by preparation method is: impregnation (5.9 $\$_{2017}\cdot t_{CO2}$) freeze-granulation (7.8 $\$_{2017}\cdot t_{CO2}$) < spray-drying (11.6 $\$_{2017}\cdot t_{CO2}$), which follows the same order as the energy intensity of the oxygen carrier production. This demonstrates that an energy intensive preparation might increase the costs excessively. The average ccc_{OC} by inert support material was in the order: $CaAl_2O_4$ (3.58 $\$_{2017}\cdot t_{CO2}$) < $NiAl_2O_4$ (4.12 $\$_{2017}\cdot t_{CO2}$) < $MgAl_2O_4$ (5.48 $\$_{2017}\cdot t_{CO2}$) < Al_2O_3 (5.75 $\$_{2017}\cdot t_{CO2}$) < ZrO_2 (16.1 $\$_{2017}\cdot t_{CO2}$). This indicates that expensive supporting materials can increase the ccc_{OC} significantly.

In the literature the use of various methods for the preparation of oxygen carriers has been reported, such as co-precipitation,[158, 186] mechanical mixing[123, 147, 181] and particle forming with rotary evaporator,[66] freeze granulation, with subsequent extrusion[123, 181] or pressure pelletizing[123], incipient wet impregnation[66, 147, 187] and dry impregnation[156]. In the process of co-precipitation, solutions containing the dissolved metal species (*e.g.* in form of metal nitrates) and dissolved alkalines (*e.g.* NaOH, ammonia or Na_2CO_2) are mixed. The *pH* value of the mixture facilitates an ion exchange reaction between the metal and the alkaline species, resulting in a precipitation of the metals (*e.g.* in form of carbonates). The supernatant is typically removed by washing with DI water and the liquid phase separated by decanting or centrifugation. The solid phase is dried, calcined and crushed, to obtain the oxygen carriers.

The review of the preparation methods for oxygen carriers revealed that (i) co-precipitation, (ii) mechanical mixing followed by extrusion, pressure pelletising, spray-drying, or freeze-granulation,

and (iii) impregnation of the active material on an inert support material are commonly used. These preparation methods were explained, and the effect of important control variables discussed. Furthermore, natural ores were used as oxygen carriers in various chemical looping process and proved to be promising. Some works study the performance of Cu-Mn oxides as oxygen carriers. Mungse *et al.*[44], Sajen *et al.*[178] and Hosseini *et al.*[45] prepared Cu-Mn oxides by co-precipitation for the process of CLC with CH_4, syngas and char-coal, respectively. Pour *et al.*[43] prepared Cu-Mn oxides by mechanical mixing of CuO and Mn_3O_4 with subsequent freeze-granulation and tested the O_2 release properties of the calcined material under N_2 and with wood char. However, no work was found that evaluates the performance of Cu-Mn oxides as oxygen carriers for the CLAS process.

In the last main body of this chapter, the science of sintering is reviewed, which is the increase in the contact area of the metal oxides grains during a heat treatment. Four control important variables for sintering were identified, which are (i) the density of the uncalcined sample, which controls the initial number of neighbouring grains, (ii) the sintering temperature, which controls the solubility, wetting and diffusivity, (iii) grain size, which controls the curvature, surface area and diffusion distance, and (iv) sintering time, which determines the amount of cumulative change. These findings were considered during the testing of different preparation and calcination conditions.

Chapter 4

Preparation of the oxygen carriers

This chapter is comprised of two main bodies, in which the preparation of oxygen carriers *via* co-precipitation (section 4.1) and mechanical mixing (section 4.2) is described. The section on the oxygen carrier preparation *via* co-precipitation starts by determining the optimal preparation conditions based on thermodynamic calculations (section 4.1.1), some preliminary samples were prepared to determine the required degree of washing for the reduction of sodium (4.1.2) and to find the optimal calcination conditions (4.1.2). In section 4.1.3 the construction and commissioning of rig for automated co-precipitation is reported. In section 4.1.4, a standard protocol for the preparation of oxygen carriers *via* co-precipitation at low supersaturation is presented, and the synthesis of oxygen carriers according to this protocol is detailed. In section 4.1.5, the preparation of micro-structured oxygen carriers *via* co-precipitation at high super-saturation is reported. In the second part of this chapter the preparation of unsupported, and ZrO_2, TiO_2 and Al_2O_3 supported mechanically mixed

oxygen carriers according to the standard protocol (section 4.2.1) and with the addition of pore-forming agents (section 4.2.2) is reported. Throughout this work, the notation used to describe the composition and the synthesis procedure of the oxygen carrier is as specified in **Table 4-1**, below.

Table 4-1 *Elements (a-h) of the sample name for the oxygen carriers in this work.*

(a)		**(b)**		**(c)**		**(d)**		**(e)**		**(f)**		**(h)**
40*	-	1Cu-2Mn	/	Zr	-	MM	-	950*	-	6*	-	210-300*
↓		↓		↓		↓		↓		↓		↓
mass% of active metal oxide(s)		molar Cu:Mn ratio		abbreviation of the supporting material(s)		preparation method		sintering temperature in °C		sintering time in hours		nominal particle size range in µm

Footnotes: an asterisk denotes that this part is omitted if the standard value is chosen; (c) the abbreviations of the supporting material are: Zr = ZrO_2, Ti = TiO_2, Al = Al_2O_3, (d) the abbreviations of the preparation method are: CP = co-precipitation (the standard procedure is summarised in Table 4-3) and MM = mechanical mixing (the standard procedure is summarised in Table 4-6); (e, f) the standard sintering temperature and sintering time were 950 °C and 6 h for mechanically mixed oxygen carriers and 900 °C and 2 h for co-precipitated oxygen carriers.

The development and preparation of the oxygen carriers are detailed in the following sub-sections.

4.1 Preparation of oxygen carriers *via* co-precipitation

For the preparation of the oxygen carriers *via* co-precipitation, an aqueous metal nitrate solution was prepared by dissolving metal nitrate hydrates in degassed de-ionised water (DI water). An aqueous alkaline solution was prepared by dissolving Na_2CO_3 and NaOH in DI water. The reagents used for the preparation of the two solutions are detailed in ***Table 4-2***, below.

Table 4-2 *Description of chemical reagents used, where x denotes the mole fraction.*

reagent	***purity***	***supplier***
$Cu(NO_3)_2 \cdot 2.5\ H_2O$	$x \geq 99.99\%$	Sigma-Aldrich
$Mn(NO_2)_3 \cdot 4\ H_2O$	$x \geq 97.5\%$	ACROS Organics
NaOH	$x \geq 97.0\%$	Sigma-Aldrich
Na_2CO_3	$x \geq 99.6\%$	ACROS Organics
Buffer solution *pH* 4.0	-	Fluka
Buffer solution *pH* 7.0	-	Fluka
Buffer solution *pH* 11.0[a]	-	Fluka

Footnotes: (a) according to the manufacturer's description this buffer solution has a pH value of 10.92 at 25 °C. Therefore, a pH of 10.9 has been assumed as the pH value of the solution during the calibration of the pH probe.

For each co-precipitation experiment, the metal nitrate and alkaline solutions were added drop-wise (manual co-precipitation, for the synthesis of preliminary samples) or with a constant flow rate

(automated co-precipitation using the co-precipitation rig) into a beaker (reaction vessel), in which the ion exchange reaction occured. The *pH* value of the mixture in the reaction vessel was measured, and the measured value determined the rate of addition of the solutions. The mixture was stirred at a constant rate, which was in most experiments 300 rpm. After addition of the solutions, the stirring was stopped, and the mixture was allowed to age, in this work typically for 30 min. Then, the liquid phase was decanted off, and the precipitate was repeatedly washed with DI water to remove unprecipitated ions (*e.g.* Na^+). The washing process is comprised of the mixing of the solids with DI water, the settling of the solid phase by centrifugation, and the removal of the liquid phase by decanting. The process is repeated until the measured conductivity of the liquid phase is lower than a target value. After the washing, the precipitate is dried in a well-ventilated oven at 35 °C, and then calcined in a furnace to obtain the desired combined metal oxide phases. In the following sections, the results of the calculations and experiments are discussed, which were carried out to determine the optimal co-precipitation (section 4.1.1), washing (section 4.1.2), drying and calcination (section 4.1.2) conditions and procedural steps. In section 4.1.4, the findings are combined into a standard procedure for the automated co-precipitation of oxygen carrier precursors at low super-saturation. In section 4.1.5, the preparation of micro-structured material *via* co-precipitation at high super-saturation is described.

4.1.1 Determination of the optimal co-precipitation conditions

The optimal synthesis condition were determined by calculating the equilibrium composition using the software 'Medusa-Hydra',[198] which is based on the algorithms developed by Kakolowicz *et al.*[202] and Eriksson.[196] The methods used to calculated the equilibria are detailed in Appendix A.2.

The selection of a suitable co-precipitation agents and their concentrations are important since it effects the degree of the metal ion dispersion (which in turn effects the crystallinity of the calcined material) and the micro-structure of the material. NaOH and Na_2CO_3 were used as co-precipitation agents as the procedure for the preparation of the oxygen carrier ought to be inexpensive, easily to be scaled-up and as environmentally benign as possible. The use of Na_2CO_3 enables the formation of $MnCO_3$ and $Cu_2CO_3{\cdot}(OH)_2$ (malachite). The carbonate groups decompose thermally to CO_2 during the heating phase of the calcination thereby acting as a blowing agent. The amount of CO_2 produced during this stage was thought to affect the micro-structure of the calcined material (as later confirmed by BET and SEM analysis*, c.f.* chapter 5).

The temperature was also varied; however, it decreased the range even further, in which full precipitation of dissolved Mn ions as malachite without the simulation's precipitation of CuO was possible. The results of the calculation are shown in **Fig. 4-1 a-b** and **Fig. 4-2a-d**, below.

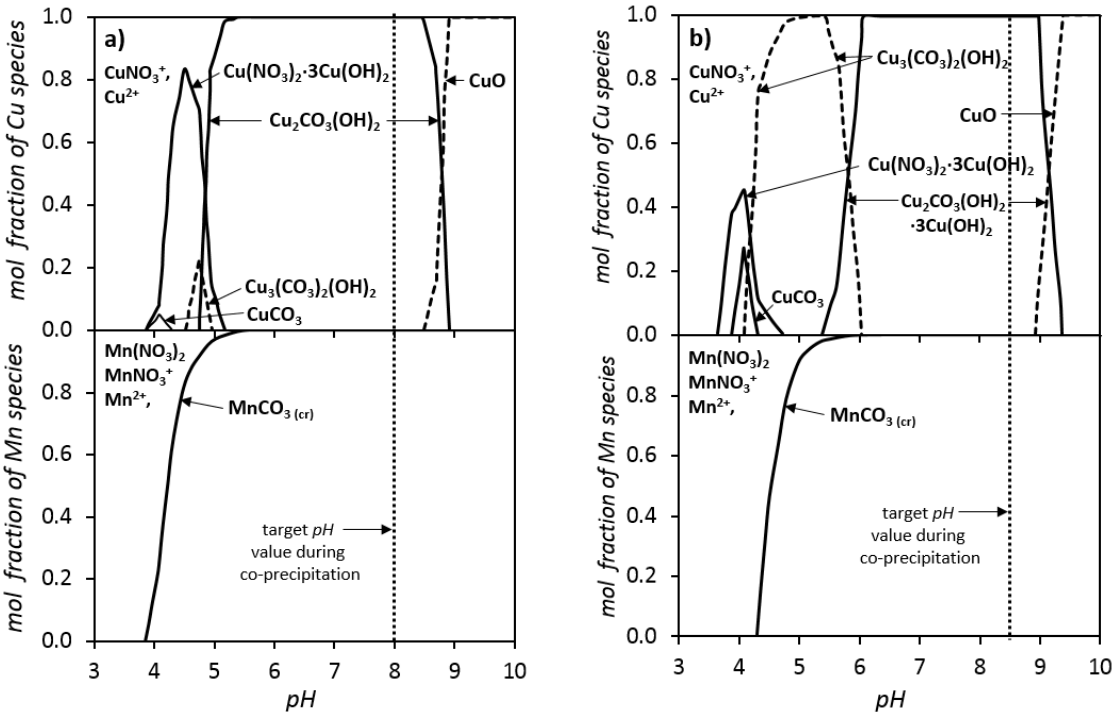


Fig. 4-1 *Equilibrium diagrams of relevant Cu and Mn species for (a) 1Cu-2Mn and (b) 2Cu-1Mn as a function of the pH value at T = 25°C and P = 0.1 MPa with a total metal ion concentration and Na^+ concentration of 1 M. The Na^+ is donated by Na_2CO_3 and NaOH in molar ratios of 3:0. The software used the Helgeson-Kirkham-Flowers model to calculate the thermodynamic activity.*

Additionally, the equilibria were calculated for the co-precipitation of 1Cu-1Mn with a Na^+ concentration of 500 mM and varying [CO_3^{2-}]. The results are shown in **Fig. 4-2**, below.

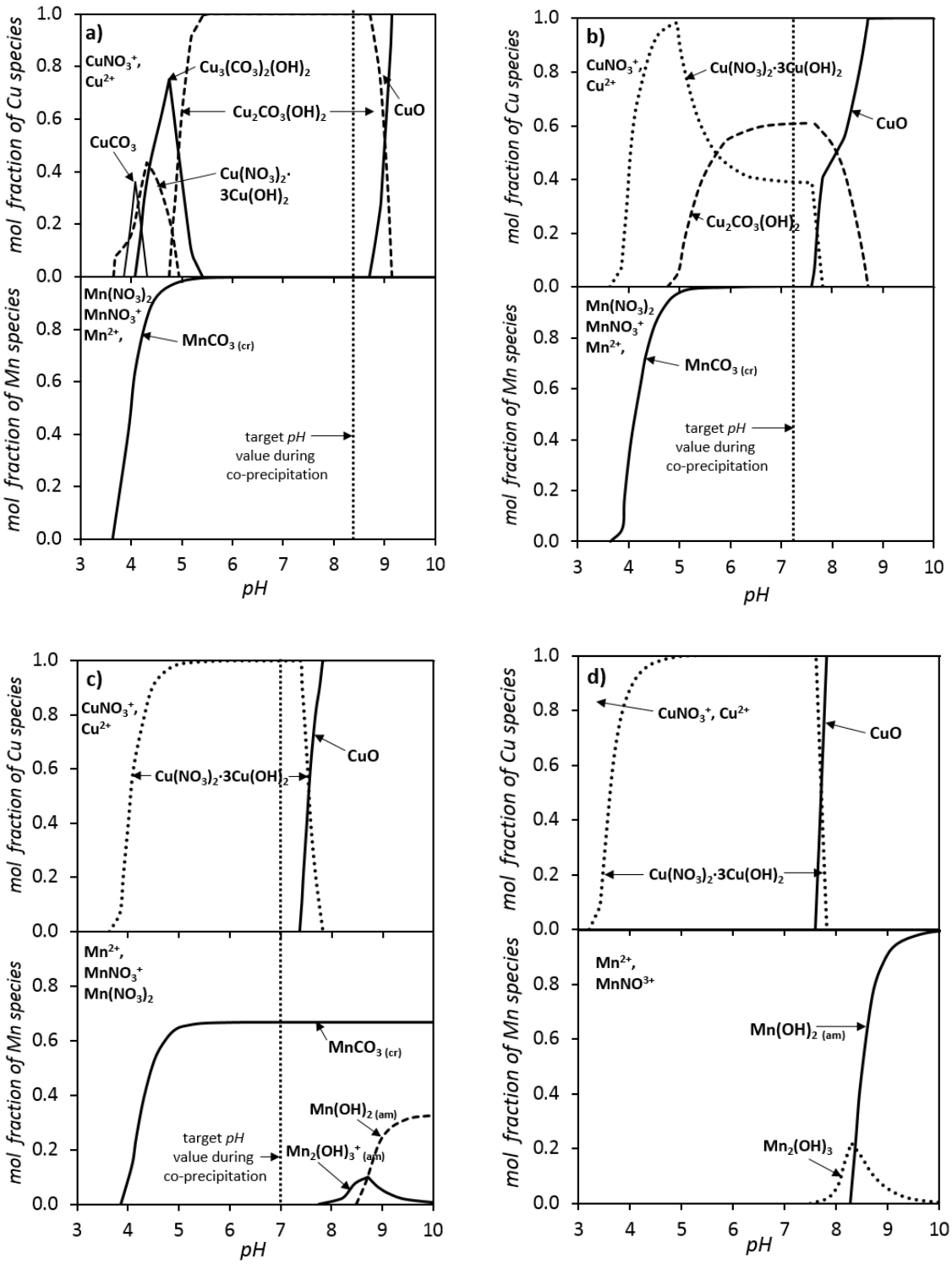


Fig. 4-2 *Equilibrium diagrams of relevant Cu and Mn species for 1Cu-1Mn oxygen carrier as a function of the pH value at T = 25 °C and P = 0.1 MPa with a total metal ion concentration and Na^+ concentration of 1 M. The Na^+ is donated by Na_2CO_3 and NaOH in molar ratios of (a) 3:0, (b) 2:1, (c) 1:2 and (d) 0:3. The software used the Helgeson-Kirkham-Flowers model to calculate the thermodynamic activity.*

The equilibrium calculations resulted in the definition of the optimal *pH* values for the preparation of samples with three different Cu-Mn ratios, but the same [CO_3^{2-}] in solution, which are used to study the effect of a changing Cu-Mn concentration. Furthermore, the conditions for the preparation of three samples with the same Cu-Mn ratio, but varying [CO_3^{2-}], were defined. These materials will be used to study the effect of carbonate concentration in the uncalcined material, as it is assumed that an increase in carbonate groups will result in an increase in surface area, owing to the production of CO_2 during thermal decomposition.

4.1.2 Development of a washing procedure for the removal of Na^+

After the fully precipitation and an aging time of 30 min, the precipitate was filled into high-G centrifuge tubes. The Na^+ concentration of the precipitate was reduced by alternating centrifugation (to separate the solid and the liquid phase) and mixing with DI water. The conductivity after each centrifugation run was measured with a PRIMO5 (Hanna Instruments) conductivity meter, which was calibrated with HI-70031 calibration solution. The decrease of conductivity with an increase in the number of centrifugations is shown in ***Fig. 4-3***, below.

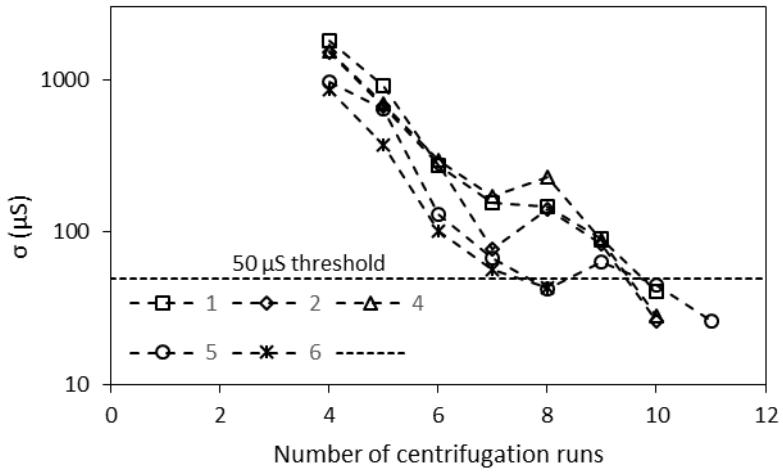


Fig. 4-3 *Reduction of electrical conductance with an increase of the number of centrifugations runs at 4500 rpm (~2500 G) for 2 min in 90ml centrifugation tubes of a mixture of DI water and the Cu-Mn-precipitated, precipitated with (dashed lines) Na_2CO_3 and (solid lines) NaOH.*

It was found that ten centrifugation runs are required to decrease the Na^+ concentration to reduce the electric conductivity to < 50 µS, which was established as the threshold. At higher residual concentrations of Na^+, Na was still detected *via* SEM-EDS analysis.

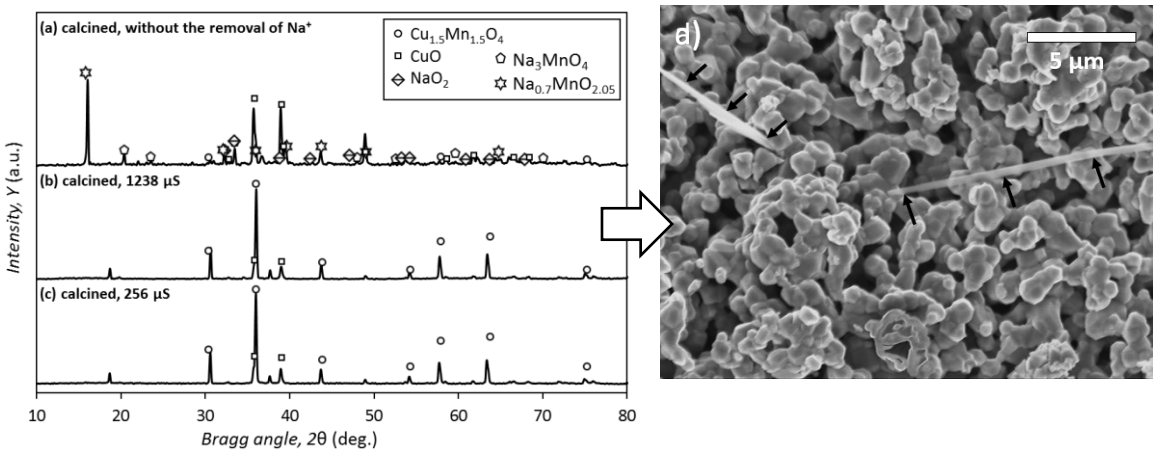


Fig. 5-3 *XRD plot for variations of 1Cu-1Mn-CP, in which the co-precipitate was dried (a) without removal of Na^+ ions, and (b, c) the removal of Na^+ ions so that the electric conductivity of the liquid phase was (b) 1238 µS and (c) 256 µS; and (d) scanning electron micrograph of the sample shown in (c) with black arrows pointing at presumably NaO_2 crystals (a high Na content was measured by SEM-EDS point analysis).*

The main phases that were identified in the unwashed sample are CuO (00-048-1548), α-Na_3MnO_4 (00-033-1268), α-MnO_2 (00-053-0633), $Na_{0.70}MnO_{2.05}$ (00-027-0751). The only phases identified in the calcined precursor with a conductivity of 1238 µS were $Cu_{1.2}Mn_{1.8}O_4$ (00-035-1029), CuO (00-041-0254) and $Cu_{1.5}Mn_{1.5}O_4$ (00-035-1172). The same three phases were identified in the material produced from the precursor with 256 µS. This variation shows that the Na^+ is inhibiting the formation of copper manganese oxide. The absence of copper manganese oxide in the unwashed sample indicates that sodium is inhibiting the formation of this spinel oxide.

4.1.3 Construction of a rig for automated co-precipitation

A co-precipitation rig was constructed as it allows for automated material synthesis (*i.e.* advantageous owing to high repeatability) and to prepare larger batches of precursors, since for some long-term cycling experiments in the fluidised bed reactor (**chapter 7**) a bed mass of ~ 40 g is required. The design of the co-precipitation rig is shown in ***Fig. 4-4***, below.

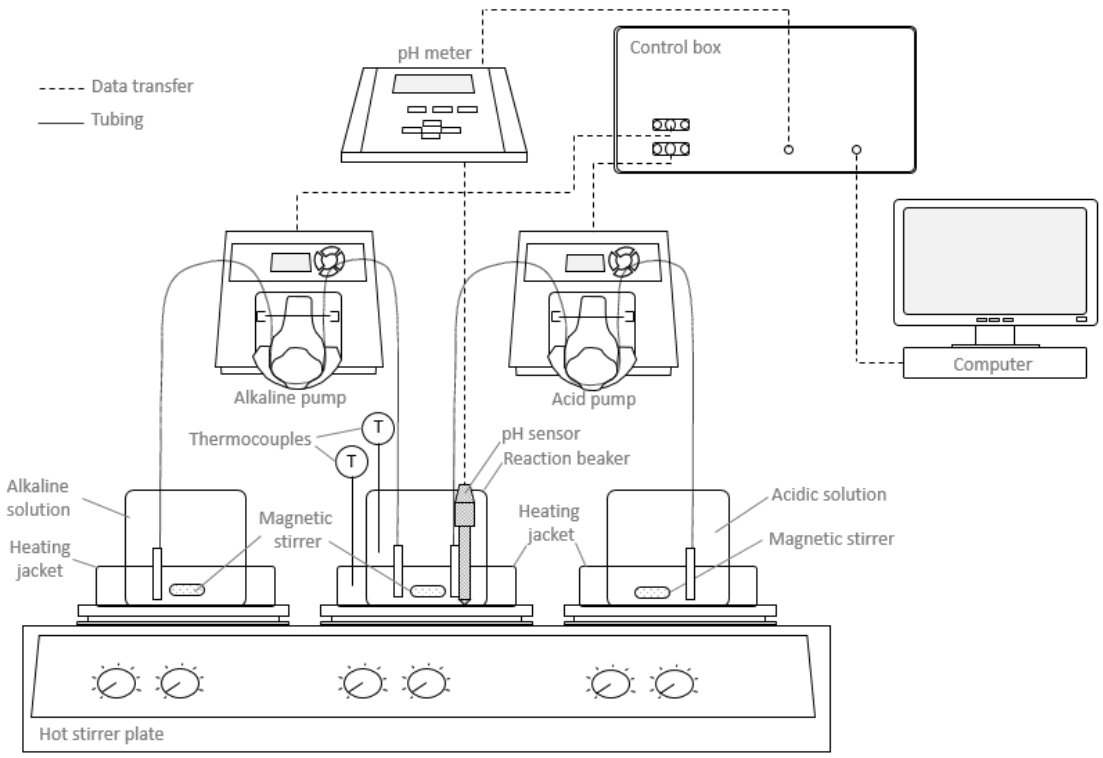


Fig. 4-4 *Schematic diagram of the co-precipitation rig, which was constructed for the preparation of larger batches required for long-term cycling experiments in the fluidised bed.*

Three beakers – for the alkaline solution, the product mixture, and the metal nitrate solution – were positioned on a triple hotplate with magnetic stirrer. Two peristaltic pumps were set up to pump the alkaline and the acidic solutions into the product beaker. The pumps are controlled *via* a control box by an Agilent VEE computer code. A *pH* probe, which is attached to the reaction beaker, measures the *pH* value of the product mixture, and feeds it through the control box into the computer. Upon standard operation of the rig, one pump is set to a steady flow rate, while the other pump is controlled by a proportional-integral-derivative controller (PID controller), which was programmed into the Agilent VEE code. The PID controller adjusts the flow rate of the second pump to maintain the set *pH value*. The output value of the PID controller, $u(t)$, is composed of the sum of three parts,[203]

$$u(t) = u_{\mathrm{P}}(t) + u_{\mathrm{I}}(t) + u_{\mathrm{D}}(t), \tag{4-1}$$

where the proportional part, $u_{\mathrm{P}}(t)$, is calculated according to,

$$u_{\mathrm{P}}(t) = k_{\mathrm{c}}(y_{\mathrm{s}}(t) - y(t)), \tag{4-2}$$

the integral part, $u_{\mathrm{I}}(t)$, according to,

$$u_{\mathrm{I}}(t) = \frac{k_{\mathrm{c}}}{\tau_{\mathrm{i}}} \int_{t_0}^{t} (y_{\mathrm{s}}(t) - y(t))\, \mathrm{d}\tau, \tag{4-3}$$

and the derivative part, $u_{\mathrm{D}}(t)$, according to,

$$u_{\mathrm{D}}(t) = k_c \tau_d \frac{\mathrm{d}(y_{\mathrm{s}}(t) - y(t))}{\mathrm{d}t}. \tag{4-4}$$

In eq.(4-2), eq.(4-3) and eq.(4-4), k_{c}, τ_{i} and τ_{d} are the proportional gain, the integral time and the derivative time, respectively. $k_{\mathrm{c}}/\tau_{\mathrm{i}}$ and $k_{\mathrm{c}}\tau_{\mathrm{d}}$ were combined to the coefficients k_{i} and k_{d}, respectively.[203] The output signal from the PID controller was taken as the input signal of the alkaline pump, with $u(t) \propto$ the flow rate of the peristaltic pump. The value of the actual flow rate, $y(t)$, was fed back into the PID controller. This feedback loop is shown in ***Fig. 4-5***, below.

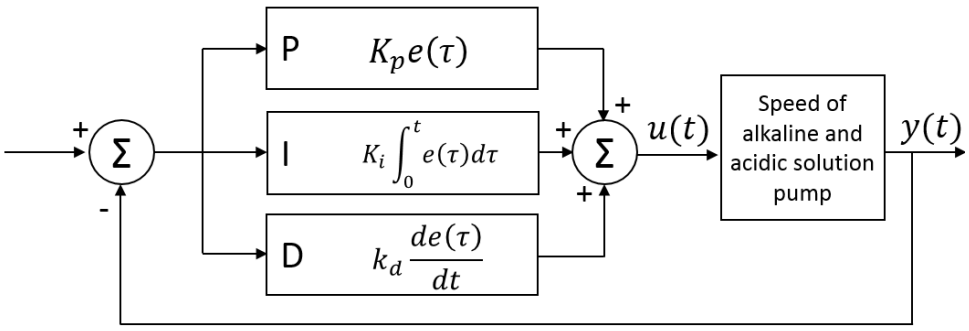


Fig. 4-5 *Diagram of the feedback loop of the PID controller*[203]

An initial value for k_{c}, k_{i} and k_{d} was estimated and then optimised by the trial-and-error method described by Sung *et al.*[203] with alternating set-points of *pH* 7.5 and *pH* 8.5. Those *pH* values were chosen, since they are in the proximity of the *pH* values of the co-precipitation. The value of k_{c} was reduced, if a large oscillation followed the set-point change – an indication for k_{c} being too large. An over-dampend response indicated that k_{c} was too small and the value was increased accordingly. After the selection of an optimal k_{c}, k_{i} and k_{d} were optimised. A set-point change with an increase in *pH* value followed by an oscillation with midpoint above the new set-point indicated that k_{i} is too large and the value was reduced. *Vice versa* an oscillation with midpoint below the set-point indicated that the integral action is too weak. Finally, the k_{d} was optimised. This parameter was reduced, if the frequency of oscillation was too high and increased if the frequency was too low.

For the preparation of the large batches of copper manganese oxide precursor using the co-precipitation rig, 1 l of the 1 M metal nitrate solution was prepared. The pumped amount was however slightly lower, as the co-precipitation was stopped before the pump drew in air and to keep a small volume for *pH* corrections during the first ten minutes of the aging period. The flow rate of the metal nitrate solution was set to 50 ml·min^{-1} and the alkaline flow rate varied controlled by the PID controller to maintain the desired *pH* value. The collected data during the co-precipitation of the 1Cu-1Mn-CP(3:0) precursor are shown in ***Fig. 4-6***, below.

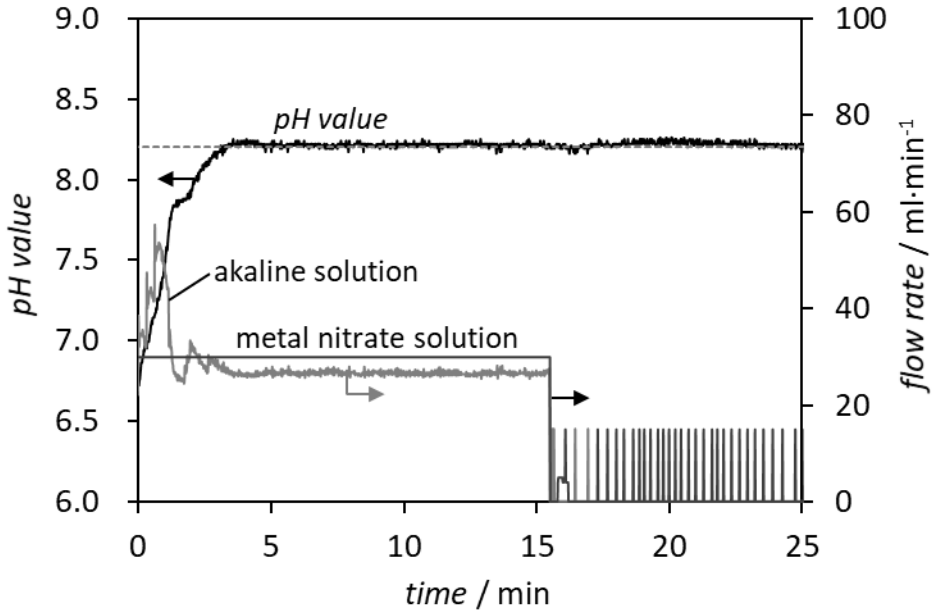


Fig. 4-6 *Plot of the pH value, the alkaline flow rate and the metal alkaline solution flow rate during the co-precipitation of 1Cu-1Mn-CP(3:0).*

After allowing the precipitate to age for 30 min, the supernatant was removed by carefully drainage, and the precipitate was washed repeatedly with DI: Two litres of DI water were added to the wet solids, the mixture was stirred for 1 min at 300 rpm and then allowed to separate without further stirring. After ~10 minutes the solid and the liquid phase had almost perfectly separated. The liquid phase was removed by decanting and the washing procedure was repeated until an electric conductivity of below 50 µS was measured. Most of the remaining water was separated from the solid phase by centrifugation at 2000 rpm for 2 minutes and the solids were then dried in a well-ventilated oven at 35 °C, calcined, crushed and sieved into the desired particle diameter range. This standard synthesis procedure for the mechanically mixed oxygen carriers is summarised in **Table 4-3**. The properties and performance of the resulting oxygen carriers of the large batch were compared against those of the small batches prepared *via* manual co-precipitation, as described in **chapter 5**. Besides co-precipitation, oxygen carriers were prepared *via* mechanical mixing, as described in the following sub-section.

4.1.4 Standard procedure for the co-precipitation of oxygen carriers

Based on the results of the above-described synthesis experiments and variations, as well as on best practices described in the literature a standard procedure for the co-precipitation of copper manganese oxide samples was developed, which is specified in **Table 4-3**, below.

Table 4-3 *The standard synthesis procedure for the co-precipitation of oxide oxygen carriers.*

	Steps	Annotations
1	$Cu(NO_3)_2 \cdot 2.5\ H_2O$ and $Mn(NO_2)_3 \cdot 4\ H_2O$ were dissolved in DI water to obtain a 1 M solution (metal nitrate solution).	It was ensured that the concentration never exceeded the calculated solubility limit.
2	NaOH and Na_2CO_3 were dissolved in DI water to obtain a 1 M Na^+ solution (alkaline solution).	-
3	A beaker (reaction vessel) was primed with 25 ml DI water.	-
4	The metal nitrate solution was added with a flow rate of 15 $ml \cdot min^{-1}$ and the alkaline solution was with a varying flow rate to keep the *pH* within ± 0.05 of the target *pH* value under constant stirring at 300 rpm.	-
5	After full addition of the acidic solution, the stirrer was switched off.	-
6	The solution was allowed to age for 30 min.	to improve the crystallinity
7	The solution was filled in 90 ml high-G centrifugation flasks and centrifuged for 2 min at 2000 rpm, then the liquid phase was decanted off and the solid phase washed with DI water. This step was repeated until the measured conductivity (σ) was below 50 µS.	-
8	The solid phase was spread-out on a petri dish and dried in an oven (Thermo Scientific) for > 12 h.	set temperature: 35 °C; Ventilation set to 50%; Fan set to 50%
9	The solids were sintered in the furnace.	heating rate: 15 $°C \cdot min^{-1}$; calcination time: 2 h; calcination temperature: 900 °C; air flow rate 1 $l \cdot min^{-1}$ at STAP
10	The solids were crushed and sieved into the desired size ranges.	-

After various preliminary 'manual' co-precipitation experiments (such as those described in section 4.1.2 and 4.1.2), three 'standard samples' were prepared using the co-precipitation rig. In these samples the molar Cu:Mn ratio was varied between 1:2 and 2:1, and the precipitation was carried out a *pH* value that was 0.3 below the value at which CuO formation was predicted to occur (*c.f.* **Fig. 4-1** and **Fig. 4-2**). Na_2CO_3 was used as the co-precipitation agent. Those conditions were selected as they were found to produce the oxygen carriers with a high mass fractions of copper manganese oxide.

Furthermore, a second series of oxygen carriers was prepared to test the effect of varying preparation conditions on the characteristics and performance of the oxygen carriers. Since the sample with a molar 2Cu:1Mn ratio was found to have excessively slow O_2 release rates (*e.g.* the time to reach a conversion of $X \geq 0.8$ was 11 min, *c.f.* chapter 6), this composition ratio was not further evaluated. Similarly, at compositions with a higher Mn content *e.g.* 1.4Cu:1.6 Mn the oxidation time was found to be significantly increased. Therefore, the molar Cu:Mn ratio range was limited in the range between 1Cu:2Mn and 1Cu:1Mn. In this series, the co-precipitation at a lower *pH* value was tested. For these experiments, a *pH* value was selected, which was 0.5 below the *pH* value at which the software 'Spana-Medusa' predicted complete precipitation of all Cu and Mn species (see section 4.1.1). The effect of a substitution of Na_2CO_3 with NaOH was also evaluated. The [Na^+] was kept constant at 2 M, and Na_2CO_3 and NaOH were mixed in amounts such that the Na^+ from Na_2CO_3 and the Na^+ from NaOH was in a ratio of 3:0 (*i.e.* 1 M Na_2CO_3 : 0 M NaOH), 2:1 (*i.e.* 0.66 M Na_2CO_3 : 0.66 M NaOH), and 1:2 (*i.e.* 0.33 M Na_2CO_3 : 1.33 M NaOH). At lower [Na_2CO_3]:[NaOH] the software predicted that full precipitation of the Mn species is not possible. This was confirmed by XRF measurements. All co-precipitated oxygen carriers that were prepared for this research project are listed in **Table 4-4**, below.

Table 4-4 *Synthesis conditions of the oxygen carrier precursors prepared at 25 °C and 0.1 MPa using the co-precipitation standard procedure from Table 4-3.*

Sample designation		$[Na_2CO_3]:[NaOH]^a$	*molar Cu:Mn ratio*	*pH*[b]
unsupported oxygen carriers (first series of co-precipitated oxygen carriers):				
1Cu-2Mn-CP(3:0)[a]	*pH* 8.3	1 M : 0 M	1:2	8.3 ± 0.1
1Cu-1Mn-CP(3:0)	*pH* 8.5	1 M : 0 M	1:1	8.5 ± 0.1
2Cu-1Mn-CP(3:0)	*pH* 8.3	1 M : 0 M	2:1	8.3 ± 0.1
unsupported oxygen carriers (additional samples to test the effect of various synthesis conditions):				
1Cu-2Mn-CP(3:0)	*pH* 6.0	1 M : 0 M	1:2	6.0 ± 0.1
1.25Cu-1.75Mn-CP(3:0)	*pH* 8.3	1 M : 0 M	1.25:1.75	8.3 ± 0.1
1.25Cu-1.75Mn-CP(3:0)	*pH* 6.0	1 M : 0 M	1.25:1.75	6.0 ± 0.1
1Cu-1Mn-CP-CP(3:0)	*pH* 6.0	1 M : 0 M	1:1	6.0 ± 0.1
1Cu-2Mn-CP(2:1)	*pH* 7.0	0.66 M : 0.66 M	1:2	7.0 ± 0.1
1Cu-2Mn-CP(2:1)	*pH* 6.0	0.66 M : 0.66 M	1:2	6.0 ± 0.1
1.25Cu-1.75Mn-CP(2:1)	*pH* 6.9	0.66 M : 0.66 M	1.25:1.75	6.9 ± 0.1
1Cu-1Mn-CP(2:1)	*pH* 7.2	0.66 M : 0.66 M	1:1	7.2 ± 0.1
1Cu-1Mn-CP(2:1)	*pH* 6.0	0.66 M : 0.66 M	1:1	6.0 ± 0.1
1Cu-1Mn-CP(1:2)	*pH* 6.0	0.33 M : 1.33 M	1:1	6.0 ± 0.1

Footnotes: (a) the concentrations and molar ratios of Na_2CO_3 and NaOH in the alkaline solution were selected to obtain a total Na^+ concentration of 2 M. The ratio in the brackets denotes the ratio of Na^+ from Na_2CO_3 to Na^+ from NaOH.

The characterisation of the oxygen carriers prepared by the standard procedure is described in the next chapter (chapter 5). Besides the preparation of the co-precipitated oxygen carriers according to the standard synthesis procedure at low super-saturation, a series of oxygen carriers has been prepared *via* co-precipitation at high super-saturation to obtain micro-structured samples with a higher surface area, as reported in the following sub-section.

4.1.5 Preparation of oxygen carriers at high supersaturation

A series of oxygen carriers was prepared *via* co-precipitation at high supersaturation. To achieve a high supersaturation, the metal nitrate solution was filled into the reaction vessel prior to the synthesis experiment. The alkaline solution was then added under vigorous stirring (600 rpm) until the *pH* value was 12.0. The duration of the addition was between 40 s and 60 s. The stirring was continued for another 15 min. The stirrer was then switched off and the mixture was allowed to age for different durations in the range 30 min to 72 hours. The ageing occurred in autoclaves at temperatures between 80 °C – 125 °C. The oxygen carrier precursors that were prepared at high supersaturation are listed in **Table 4-5**, below.

Table 4-5 *The ageing conditions of the oxygen carriers prepared at high super-saturation.*

Sample composition	*ageing time* [hours]	*ageing temperature* [°C]
1.5Cu-1.0Mn	*no ageing*	*no ageing*
	72 h	125 °C
2Cu-1Mn	*no ageing*	*no ageing*
	8 h	80 °C
	24 h	80 °C
	72 h	80 °C
	8 h	100 °C
	72 h	100 °C
	8 h	125 °C
	24 h	125 °C
	72 h	125 °C
2.5Cu-1.0Mn	*no ageing*	*no ageing*
	8 h	80 °C
	8 h	125 °C
	72 h	125 °C
3.0Cu-1.0Mn	*no ageing*	*no ageing*
	72 h	125 °C

The characterisation of the micro-structured oxygen carrier precursors is reported in chapter 5. In the following section of this chapter, the oxygen carrier preparation *via* mechanical mixing is detailed.

4.2 Preparation of oxygen carriers *via* mechanical mixing

Oxygen carriers were prepared by mechanically mixing the single metal oxide powders, which were weighted out using an analytical balance (PAS214C, Fisher Scientific), and mixed with DI water. The slurry was milled in a planetary ball mill (PM 400, RETSCH) using four steel balls. Then, the slurry was recovered and dried in a ventilated oven. After drying, the precursors were calcined in a horizontal tube furnace, crushed, and sieved into the desired size fraction. To determine the optimal synthesis conditions some preliminary experiments were carried out.

4.2.1 Standard procedure for the preparation *via* mechanical mixing

No binders or dispersants were added to the slurry to prevent contamination of the samples with those chemicals or residues of their thermal decomposition. This also reduced the number of parameters that could influence the structure and porosity of the precursor and calcined samples.

All slurries were prepared with a solid:water mass ratio of 1:1. To study the rate of particle size reduction, preliminary tests with copper (II) oxide powder were carried out. This metal oxide powder was used for the tests, as the refractive index of the material (2.63) is well known, *e.g.* contrarily to a mixture of CuO and Mn_3O_4 powders. The value for the refractive index of the inert supporting materials (*e.g.* TiO_2, ZrO_2) is also available in the literature. However, when milling the white slurry in preliminary tests, a change of colour from white to grey was observed, probably owing to a contamination with steel from the milling balls and the jar. The value of the mean particle size (D_{50}) measured by laser diffraction after 4 hours of ball milling was larger than the value of the sample recovered after 2 hours, which was attributed to the change in the refraction due to the contamination (an actual increase in size *e.g.* due to agglomeration was ruled out). The particle size reduction of the supporting materials was therefore not studied any further. From the data of laser diffraction experiments, values for D_{10}, D_{50} and D_{90} were calculated, which are in this work defined as the intercepts of the plot of cumulative particle volume against particle size for 10%, 50% and 90% of the particle size distribution, respectively. The calculated values of D_{10}, D_{50} and D_{90} for the milled slurry containing the CuO powder were plotted against the ball milling time in **Fig. 4-7**, below.

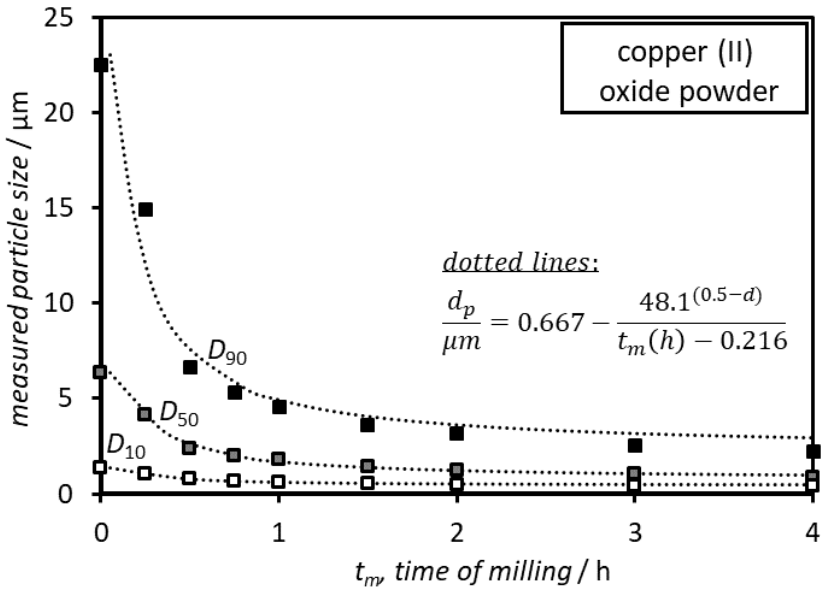


Fig. 4-7 *The reduction of particle size of copper (II) oxide powder with time of milling in the planetary ball mill at 280 rpm using four steel balls and a solid:water ratio of 1:1:*

Fig. 4-7 shows that over the first hour of ball milling the mean particle size (D_{50}) reduces rapidly to 28% (1.8 µm) of the initial particle size (6.3 µm). After four hours of ball milling, the mean particle size has reduced further to 14% (0.9 µm) of the initial value. Furthermore, the particle sizes become more uniform. The initial value of D_{90} (22.5 µm) is 16.2 times larger than the initial value of D_{10} (1.4 µm). After four hours of ball milling, this factor for D_{90} (2.2 µm) and D_{10} (0.4 µm) has reduced to 5.0. An equation for a three-parameter fit for the particle size reduction is provided on the plot area in **Fig. 4-7**, which allows to estimate the values for D_{10}, D_{50} and D_{90} at any time in the range 0 h ≤ t_m ≤ 4 h (*e.g.* to optimise the ball milling time for a minimal energy consumption in the processes of oxygen carrier production). All mechanically mixed oxygen carriers have been prepared using a ball milling time of 4 h.

After milling, for several hours at 280 rpm. XRF analysis found no traces of iron, indicating that no contamination owing to attrition of fines from the steel balls occurred. The slurry was poured onto petri dishes, dried for > 12 h at 80 °C in a well-ventilated oven and calcined for 6 h at 950 °C under air (1 l·min^{-1}, SATP) with a heating rate of 15 °C·min^{-1}. Compared to the co-precipitated oxygen carriers, a longer calcination time (6 h instead of 2 h) and a higher temperature (950 °C instead of 900 °C) was used for the calcination of the mechanically mixed oxygen carriers to obtain the maximum conversion to the bimetallic copper manganese oxide. These conditions were based on the results of a semi-factorial experiment, which was carried out to determine the optimal sintering conditions for the mechanically mixed and co-precipitated precursors (*c.f.* results of XRD analysis in **Fig. 5-18** and **Fig. 5-19**).

The standard procedure for the mechanically mixed oxygen carriers is presented in **Table 4-6**, below.

Table 4-6 *Standard synthesis procedure for the preparation of oxygen carriers by mechanically-mixing of the single metal oxide powders.*

	Steps	Annotations
1	30g of a metal powder mixture of (CuO, MnO, MgO, Al_2O3, TiO_2 and/or ZrO_2) in the desired mass fractions are mixed with DI water in a volume ratio of 1:1.	It was ensured that the concentration never exceeded the solubility limit.
2	The slurry is filled into a grinding jar of the planetary ball mill (PM 400, RETSCH) together with four steel balls (per jar), and the slurry is milled.	Standard parameter: Milling time: 4 h; Rotational speed: 280 rpm. Interval with reverse rotation: every 15 min.
3	The jars are removed from the ball mill and the steel balls are taken out.	
4	The slurry is spread-out on a petri dish and dried in an over for > 12 h.	Set temperature: 70 °C; Ventilation set to 50%; Fan set to 50%.
5	The solid is sintered in the furnace.	heating rate: 15 °C·min^{-1}; calcination time: 6 h; calcination temperature: 950 °C; air flow rate 1 l·min^{-1} at STAP.
6	The solids were crushed and sieved into the desired size ranges.	-

The standard procedure, which is presented in **Table 4-6**, was used to prepare five batches of unsupported oxygen carriers with the molar ratio: 1.0Cu:2.0Mn, 1.2Cu:1.8Mn, 1.4Cu:1.6Mn, 1.5Cu:1.5Mn, and 1.6Cu:1.4Mn. Furthermore, ZrO_2, TiO_2 and Al_2O_3-supported oxygen carriers have been prepared. The amount of supporting material added was calculated so that the weight fraction of the active phase (*e.g.* copper manganese oxide) was 40 wt%, and a 1Cu:1Mn molar ratio was used for all supported samples. The results of the material characterisation of the mechanical mixed oxygen carriers are presented in chapter 5, and the redox-performance of these samples is discussed in chapter 6 and 7. Additionally, a series of unsupported oxygen carriers has been prepared *via* mechanical mixing with the addition of pore-forming agents, as described in the following section.

4.2.2 Mechanically mixing with pore-forming agents

In the preparation of the porous materials by the sacrificing template method, a powder slurry is mixed with sponges or pore forming agents.[204] Studart *et al.*[204] used sponge replica to synthesise porous ceramics. They reported interconnected pores and porosities ranging from 0.40 to 0.95, which are promising structural properties for porous oxygen carriers. However, the pore sizes of their samples were in the range 200 – 3000 μm. Most of this range exceeds the mean particle diameter that is typically considered for oxygen carriers in chemical looping combustion.[51, 53, 56, 57, 62, 173]

Pore forming agents, such as graphite[158] and starch[124] were used for the production of oxygen carriers. Cho *et al.*[124] added 10 vol% of starch to a precursor slurry and reported an increase in pore volume by ~ 20%.

In this work, micro-crystalline cellulose (Sigma-Aldrich) and rice starch (Sigma-Aldrich) was tested as pore forming agents. Both materials are inexpensive, non-toxic and burn residue free. The later was confirmed by TGA tests. The structure of both pore forming agents is shown in **Fig. 4-8**, below.

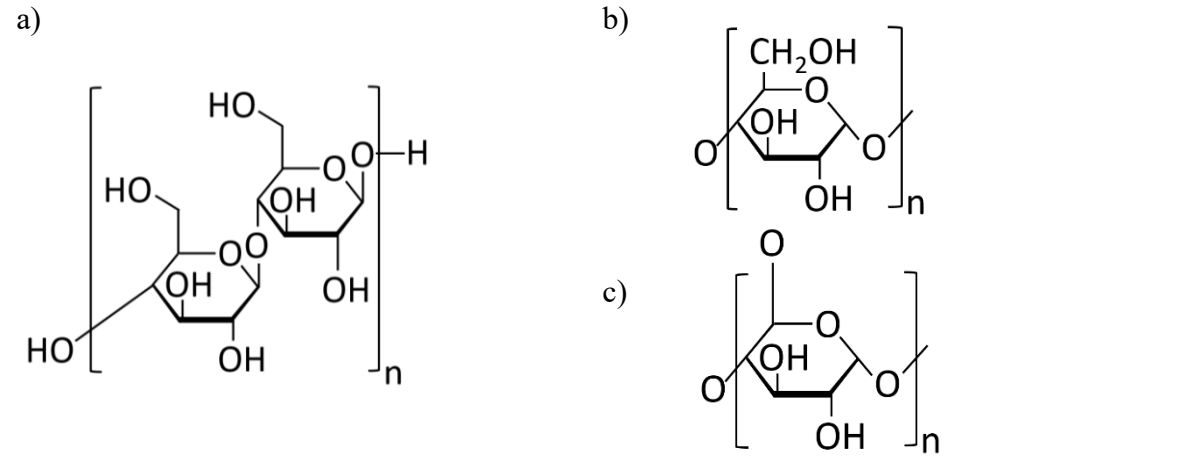


Fig. 4-8 *Drawings of the structure of (a) a micro-crystalline cellulose monomer, (b) a linear starch monomer, and (c) a branched starch monomer, adapted from the drawings on the product sheets.*

To prepare the precursors, copper and manganese oxide powders were mixed with water and the slurry was milled in the planetary ball mill, following the standard procedure for the preparation of mechanically mixed oxygen carriers in **Table 4-6**. After four hours of ball milling pore forming agents were added so that their mass percentage was 10% of the total solids. The samples were dried in an oven at 80 °C for > 12 hours.

After preparation and drying of the precursor, the burn-out characteristics of the pore forming agents were tested in a TGA. Initially, an experiment was carried out in which a heating rate of β = 15 °C min^{-1} was used and the sample was exposed to air. These are the conditions used during the heating procedure of the calcination of the non-porous mechanically mixed oxygen carrier precursors. The results of those tests are shown in **Fig. 4-9**, below.

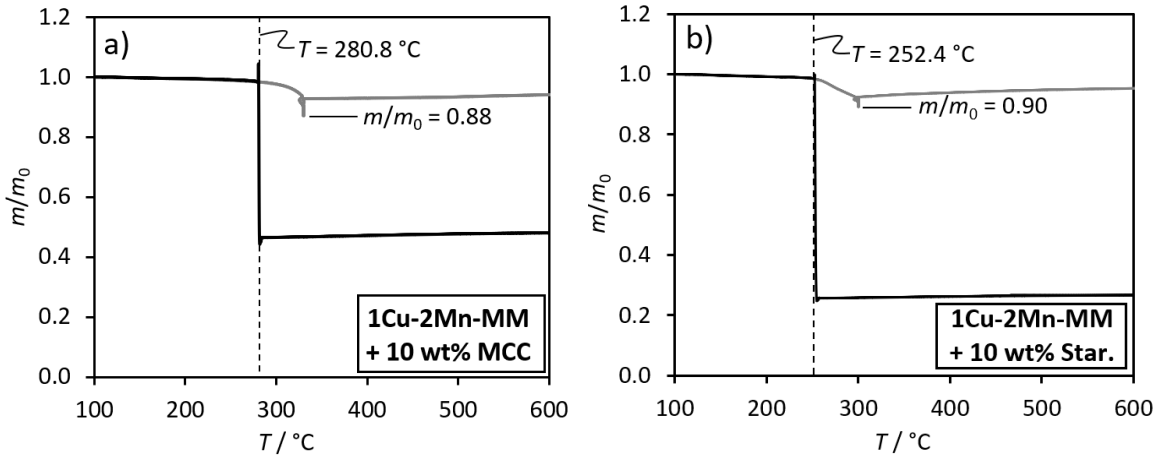


Fig. 4-9 *Plots of the weight change during TGA experiments with 20 mg of the precursors containing different pore-forming agents. The samples are 1Cu-2Mn-MM with 10 wt% of (a) micro-crystalline cellulose (MCC), and (b) starch, heated in air (lack lines) and in 2 vol% O_2 + N_2 (grey lines).*

The black lines in **Fig. 4-9a** and **Fig. 4-9b** show the burn-out of the pore-forming agents in experiments with β = 15 °C min^{-1} and p_{O2} = 0.21. The ignition of the micro-crystalline cellulose (MCC) and starch starts at 280.8 °C and 252.4 °C, respectively. Moreover, a weight loss larger than the mass fraction of the pore-forming agents (10 wt%) occurs, which can be attributed to a fuelled reduction of the metal oxides and elutriation of the sample due to the rapid production of gaseous species owing to the combustion. The recovered powder-like samples were found to have completely disintegrated during the burn-out. This shows that the standard heating procedure is not suitable for the calcination of these precursors.

The grey lines in **Fig. 4-9a** and **Fig. 4-9b** show the burn-out of the pore-forming agents in experiments, in which the sample were initially exposed to a mixture of air and N_2 resulting in p_{O2} of 0.02 bar. The temperature was increased with 15 °C min^{-1} to a temperature that was ~ 50 °C higher than the temperature at which the auto-ignition of the experiments with the standard heating procedure occurred. This temperature plateau was at 330 °C and 300 °C for the experiments with the precursors containing MCC and starch, respectively. This temperature was maintained for 20 min. The gas was then switched to pure air to prevent decomposition of the sample (*i.e.* O_2 release) during further heating, and the temperature was increased with 15 °C min^{-1} to the desired calcination temperature.

The characterisation of these oxygen carriers is detailed in the following chapter.

4.3 Concluding remarks

In this chapter, the preparation of oxygen carriers *via* co-precipitation and mechanical mixing was described. The synthesised oxygen carriers are listed in **Table 4-7**.

Table 4-7 *Oxygen carriers prepared via co-precipitation and mechanical mixing.*

sample name		abbreviated sample name[a]
co-precipitated unsupported oxygen carriers (prepared by procedure shown in Table 4-3):		
1Cu-2Mn-CP(3:0)	*p*H 8.3	1Cu-2Mn-CP
	*p*H 6.0	-
1Cu-2Mn-CP(2:1)	*pH* 7.0	-
	pH 6.0	-
1.25Cu-1.75Mn-CP(3:0)	*pH* 8.3	-
	pH 6.0	-
1.25Cu-1.75Mn-CP(2:1)	*pH* 6.9	-
1Cu-1Mn-CP(3:0)	*pH* 8.5	1Cu-1Mn-CP
	pH 6.0	-
1Cu-1Mn-CP(2:1)	*pH* 7.2	-
	pH 6.0	-
2Cu-1Mn-CP(3:0)	*pH* 8.5	2Cu-1Mn-CP
mechanically mixed unsupported oxygen carriers (prepared by procedure shown in Table 4-6):		
1.0Cu-2.0Mn-MM		1Cu-2Mn-MM
1.2Cu-1.8Mn-MM		-
1.4Cu-1.6Mn-MM		-
1.5Cu-1.5Mn-MM		1Cu-1Mn-MM
1.5Cu-1.5Mn-MM + 10 wt% starch		-
1.5Cu-1.5Mn-MM + 10 wt% MCC		-
1.6Cu-1.4Mn-MM		-
supported oxygen carriers (prepared by procedure shown in Table 4-6):		
40wt-(1Cu-1Mn)/Zr-MM		40-CuMn/Zr-MM
40wt-(1Cu-1Mn)/Ti-MM		40-CuMn/Ti-MM
40wt-(1Cu-1Mn)/Al-MM		40-CuMn/Al-MM

Footnotes: (a) this are the abbreviated sample names of the mechanically mixed and co-precipitated "standard oxygen carriers. The abbreviations were introduced, since these oxygen carriers are predominantly used in redox-experiments described in chapter 6 and chapter 7.

The next chapter details the characterisation of the oxygen carriers listed in **Table 4-7**.

Chapter 5

Material characterisation

The material characterisation of the fresh oxygen carriers, which is detailed in this chapter, has two main objectives. Firstly, to characterise the oxygen carriers and their precursors to elucidate the relationship between the composition, the preparation method, and the properties of the oxygen carriers. Precise knowledge of these relationships allows optimisation of the oxygen carrier preparation and identification of the most promising compositions. Secondly, to collect the required data for the reaction rate modelling in chapters 6 and 7.

5.1 N_2 adsorption at 77 K and calculation of the BET surface area

The specific surface area, S_{BET}, the average pore diameter, $\bar{d}_{\mathrm{pore}}$, and the cumulative pore volume, $\sum v_{\mathrm{pore}}$, were determined by physical adsorption experiments with N_2 at 77 K using a TriStar 3000 (Micrometrics). Between 0.15 g and 0.25 g of the oxygen carrier particles were degassed under N_2 at 120 °C for at least 2 h and then loaded into the TriStar inside sample tubes. After the evacuation of the sample tubes, the pressure was gradually increased by introducing N_2 at 77 K into the tubes. The pressure was recorded, and the data of the adsorption isotherm was used to calculate the BET surface area using the method developed by Brunauer, Emmett and Teller.[205] The BET surface area differs from the true specific surface area mainly due to two reasons – the intrinsic error of the experiment and the underlying assumption that monolayer adsorption occurs. In reality, the N_2 adsorbs partially as multilayers, owing to complex processes of the filling of the micro-pores and considerable adsorbent-adsorbate interactions.[206] This occurs especially at low pressures.[206]

Furthermore, the adsorption isotherms were used to calculate the specific surface area of the pores, S_{pore}, and the cumulative pore volume, $\sum v_{\mathrm{pore}}$, of pores with a diameter between 1.7 nm and 300 nm, using the method developed by Barrett, Joyner and Halenda (BJH).[207] The calculated values differ from the true ones, due to the suboptimal filling of pores, which is a result of imperfect molecular packing caused by different pore sizes and irregular pore shapes.[206] The average pore diameter, $\bar{d}_{\mathrm{pore}}$, was calculated by $\bar{d}_{\mathrm{pore}} = 4 \sum v_{\mathrm{pore}} / S_{\mathrm{pore}}$.

The uncertainties of the measured values of S_{BET}, S_{pore}, $\sum v_{\mathrm{pore}}$, $\bar{d}_{\mathrm{pore}}$ caused by the measurement (*e.g.* instrumental error), $u_{\mathrm{m}}(x)$, were estimated from the standard deviation of three repeated measurements of oxygen carriers of the same batch, $SD_{\mathrm{m}}(x)$. The combined uncertainties caused by the variations of the oxygen carrier preparation and by the instrument, $u_{\mathrm{p+m}}(x)$, were estimated from the standard deviation $SD_{\mathrm{p+m}}(x)$ of three repeated measurements with oxygen carriers from three different batches of oxygen carriers prepared following the same procedure. The uncertainty caused by the preparation of the oxygen carriers $u_{\mathrm{p}}(x)$ was calculated by a statistical deconvolution of $SD_{\mathrm{m}}(x)$ and $SD_{\mathrm{p+m}}(x)$ using a variance decomposition, assuming the combined standard deviation is related to the individual standard deviations by $SD_{\mathrm{p+m}}^2(x) = (SD_{\mathrm{m}}^2(x) + SD_{\mathrm{p}}^2(x))$. This calculation yielded a value for the uncertainty (within a 98% CI and assuming a normal distribution) in S_{BET} caused by the oxygen carrier preparation of $0.098 \cdot S_{\mathrm{BET}}$ (*c.f.* ***Appendix A.3***). This demonstrates a good reproducibility with respect of S_{BET} when preparing the oxygen carriers according to the standard synthesis method of this work.

The results of the N_2 adsorption measurements and their uncertainties are shown in **Table 5-1**, below.

Table 5-1 *Results of N_2-adsorption measurements of the co-precipitated oxygen carriers.*

sample name		S_{BET} ($\mathrm{m^2 g^{-1}}$)	$\sum v_{\mathrm{pore}}$ [a] ($\mathrm{mm^3 g^{-1}}$)	$\bar{d}_{\mathrm{pore}}$ [a] (nm)
co-precipitated unsupported oxygen carriers:				
1Cu-2Mn-CP(3:0)	*p*H 8.3	0.912 ± 0.05	2.47 ± 0.02	46.2 ± 1.4
	*p*H 6.0	0.559 ± 0.03	1.29 ± 0.01	102.5 ± 3.1
1Cu-2Mn-CP(2:1)	*pH* 7.0	0.704 ± 0.04	1.82 ± 0.02	48.1 ± 1.4
	pH 6.0	0.398 ± 0.02	0.98 ± 0.01	47.7 ± 1.4
1.25Cu-1.75Mn-CP(3:0)	*pH* 8.3	0.871 ± 0.04	1.99 ± 0.02	58.5 ± 1.8
	pH 6.0	0.116 ± 0.01	-	-
1.25Cu-1.75Mn-CP(2:1)	*pH* 6.9	0.599 ± 0.03	2.04 ± 0.02	81.9 ± 2.5
1Cu-1Mn-CP(3:0)	*pH* 8.5	0.701 ± 0.04	2.11 ± 0.02	34.3 ± 1.0
	pH 6.0	0.193 ± 0.01	1.18 ± 0.01	30.7 ± 0.9
1Cu-1Mn-CP(2:1)	*pH* 7.2	0.169 ± 0.01	0.94 ± 0.01	92.6 ± 2.8
	pH 6.0	0.392 ± 0.02	1.24 ± 0.01	19.3 ± 0.6
2Cu-1Mn-CP(3:0)	*pH* 8.5	1.477 ± 0.07	5.94 ± 0.08	26.6 ± 0.9
mechanically mixed unsupported oxygen carriers:				
1.0Cu-2.0Mn-MM		0.217 ± 0.01	1.38 ± 0.02	127.9 ± 4.2
1.2Cu-1.8Mn-MM		0.283 ± 0.01	1.46 ± 0.02	87.4 ± 2.9
1.4Cu-1.6Mn-MM		0.281 ± 0.01	1.78 ± 0.02	123.2 ± 4.1
1.5Cu-1.5Mn-MM		0.337 ± 0.02	1.52 ± 0.02	74.1 ± 2.4
1.5Cu-1.5Mn-MM + 10 wt% starch		0.348 ± 0.02	2.81 ± 0.02	133.5 ± 4.3
1.5Cu-1.5Mn-MM + 10 wt% MCC		0.444 ± 0.02	1.98 ± 0.02	76.7 ± 2.4
1.6Cu-1.4Mn-MM		0.331 ± 0.02	1.77 ± 0.02	71.0 ± 2.4
supported oxygen carriers:				
40-CuMn/Zr-MM		2.003 ± 0.09	7.84 ± 0.02	23.2 ± 0.8
40-CuMn/Ti-MM		0.306 ± 0.01	1.65 ± 0.02	96.3 ± 3.2
40-CuMn/Al-MM		0.754 ± 0.03	3.41 ± 0.02	54.3 ± 1.8

Footnotes: (a) data from the adsorption isotherms was used to calculate $\sum v_{pore}$ and $\bar{d}_{pore}$ using the BJH method.

In the following the results of the BET surface area measurements from **Table 5-1** are discussed for the oxygen carriers prepared *via* co-precipitation at low super-saturation, mechanical mixing and co-precipitation at high super-saturation.

Oxygen carriers prepared *via* co-precipitation at low super-saturation

The results for the unsupported co-precipitated oxygen carriers from **Table 5-1** are illustrated in **Fig. 5-1**, below.

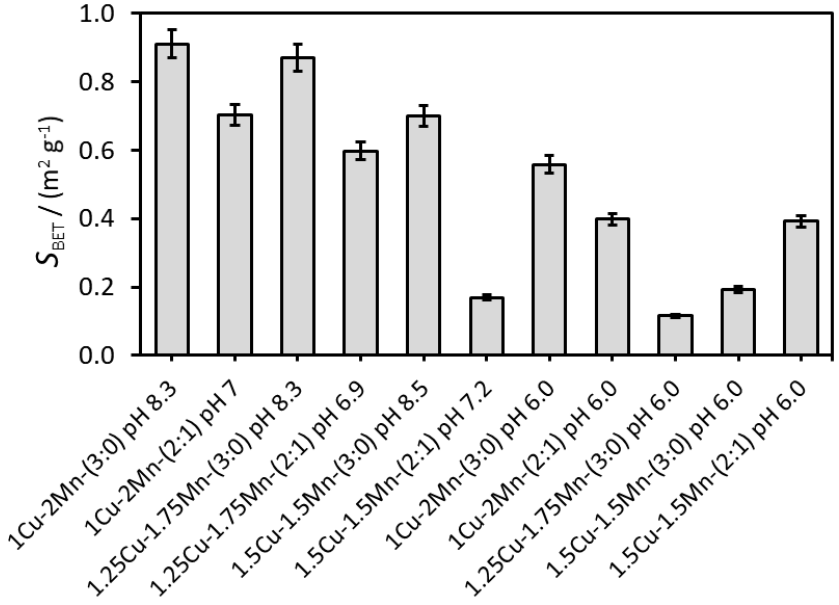


Fig. 5-1 *The BET surface area of the co-precipitated oxygen carriers. The error bars correspond to the uncertainty of the measurement, which was estimated to be 0.045·S_{BET} (c.f. Appendix A.3).*

Fig. 5-1 shows that the surface area of all oxygen carriers is in the range of 0.1 and 1.0 m^2 g^{-1}. Furthermore, it can be seen that the surface area of the oxygen carriers that were co-precipitated at a higher *pH* value have a higher surface area than those co-precipitated at a lower *pH* value.

To elucidate the reason for the differences in the BET surface area, a regression analysis was carried out using the general linear model,

$$S_{\mathrm{BET,model}} = a_{\mathrm{pH}} \cdot X_{\mathrm{pH}} + a_{\mathrm{Cu,Mn}} \cdot X_{\mathrm{Cu,Mn}} + a_{\mathrm{alkaline}} \cdot X_{\mathrm{alkaline}} + \mathrm{b}, \tag{5-1}$$

where $S_{\mathrm{BET,model}}$ is the calculated BET surface area, X_{pH}, $X_{\mathrm{Cu,Mn}}$, and X_{alkaline} are values normalised between zero and unity that depend on the *pH* value, the composition, and the co-precipitation agent, respectively, a_{pH}, $a_{\mathrm{Cu,Mn}}$, a_{alkaline} are their corresponding multipliers and *b* is the regression intercept. The *pH* value was normalised by,

$$X_{\mathrm{pH}} = \frac{pH_{set} - pH_{\mathrm{min}}}{pH_{\mathrm{max}} - pH_{\mathrm{min}}}, \tag{5-2}$$

where pH_{set} is the set *pH* value during the co-precipitation, pH_{min} is the lowest calculated *pH* value at which all Cu- and Mn- species precipitate and pH_{max} is the highest possible calculated *pH* value without the formation of CuO in the precursor. The composition was linearly normalised between

zero and unity by defining the sample with the lowest Cu content (1Cu:2Mn) and the highest Cu content (1Cu:1Mn) as $X_{\mathrm{Cu,Mn}} = 0$ and $X_{\mathrm{Cu,Mn}} = 1$, respectively. X_{alkaline} is the variable that depends on the composition of the co-precipitation agent. It was set to zero for the alkaline solution that contained no NaOH and to unity for the solution that was prepared using the highest amount of NaOH.

The square error between the experimentally obtained S_{BET} and $S_{\mathrm{BET,model}}$, which was calculated by eq.(5-1) was minimised by varying a_{pH}, $a_{\mathrm{Cu,Mn}}$, a_{alkaline} and b. This method yielded the values a_{pH} = 0.563, $a_{\mathrm{Cu,Mn}}$ = -0.205, a_{alkaline} = 0.099 and b = 0.394. The results and the agreement of S_{BET} and $S_{\mathrm{BET,model}}$ are illustrated in **Fig. 5-2a** and **Fig. 5-2b**, respectively.

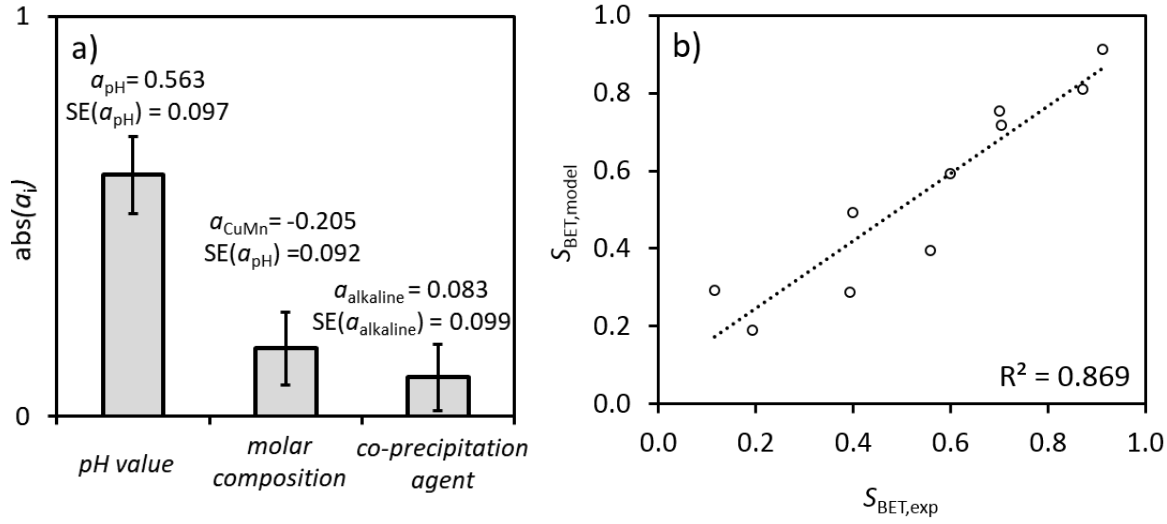


Fig. 5-2 *The results of the linear regression analysis of the BET surface area values: Plots of (a) the absolute values of the coefficients with error bars corresponding to the calculated standard error of the coefficients, and (b) the values of the modelled values against the experimentally obtained values of* S_{BET} .

Fig. 5-2a shows that the *pH* value has the largest effect on the surface area. The value is positive, indicating that an increase in the normalised *pH* value results in an increase in the BET surface area. The composition has the second largest effect. An increase in the Cu content results in a decrease of the surface area. The co-precipitation agent has the third largest effect on the surface area. A substitution of Na_2CO_3 with NaOH results in an increase in the surface area.

From **Fig. 5-2b** it can be seen that the calculated values for the specific surface are in good agreement with the experimentally obtained values. The average deviation between both is 0.07 $m^2\ g^{-1}$.

This assessment suggests that an oxygen carrier with a high Cu content (*i.e.* 1Cu-1Mn), co-precipitated with an alkaline solution with a high [NaOH]:[Na_2CO_3] (*i.e.* 0.33 M NaOH + 0.33 Na_2CO_3) and using low *pH* value during the co-precipitation (*i.e. pH* 6) has the lowest surface area

($S_{\mathrm{BET,model}} = 0.190\ \mathrm{m^2\ g^{-1}}$) in the studied condition range. In fact, the measured value at those synthesis conditions is $0.193\ \mathrm{m^2\ g^{-1}}$. Furthermore, the results of this assessment suggest that the highest surface area is achieved when selecting a low Cu content (*i.e.* 1Cu:2Mn), when using only Na_2CO_3 as the co-precipitation agent, and when using a high *pH* value during the co-precipitation. Here the values for $S_{\mathrm{BET,model}}$ and $S_{\mathrm{BET,exp}}$ are $0.912\ \mathrm{m^2\ g^{-1}}$ and $0.911\ \mathrm{m^2\ g^{-1}}$. Eq.(5-1) together with the fitted parameter allow to prepare copper manganese oxygen carriers with a desired BET surface area. This procedure can be applied for oxygen carrier development to rationally design them with desired properties.

Additionally, the surface area of the redox-cycled oxygen carriers from long-term cycling experiments in the thermogravimetric analyser and the fluidised bed rector was measured. However, as those results require the context of the experiments, they are reported in the respective sections.

Oxygen carriers prepared *via* mechanical mixing

For the unsupported mechanically mixed oxygen carriers, the values of S_{BET} and $\sum v_{\mathrm{pore}}$ from **Table 5-1** prepared with and without pore-forming agent are illustrated in **Fig. 5-4**, below.

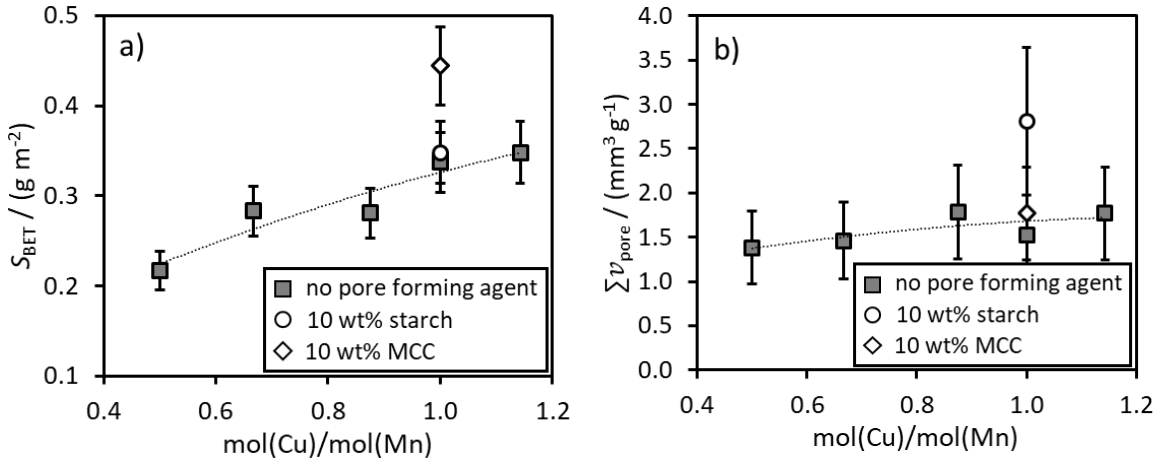


Fig. 5-3 *A comparison of the results of the (a) BET surface area and (b) cumulative pore volume measurements for unsupported mechanically mixed Cu-Mn oxygen carriers. The error bars indicate the uncertainty of the values from the production. This uncertainty was estimated by deconvoluting the standard deviations of three measurements of particles form the same batch and three measurements of particles from three different batches prepared using the same method as described in Appendix A.3.*

Fig. 5-4 and **Table 5-1** show that the S_{BET} of the unsupported mechanically mixed oxygen carriers prepared without pore-forming agents is in the range 0.217 - 0.348 g m^{-2}, and increases with an increase in the Cu:Mn molar ratio. The pore volume was found to be in the range 1.38-1.77 $mm^3 \cdot g^{-1}$ and also increases with an increase in Cu:Mn molar ratio.

The addition of 10 wt% starch did not result in a significant increase in S_{BET} (**Fig. 5-4a**). However, the mean pore diameter increased by 80% and the cumulative pore volume by 85% compared to the oxygen carriers prepared without a pore-forming agent (**Fig. 5-4a**). The increase in $\sum v_{\mathrm{pore}}$ is larger than the uncertainty in $\sum v_{\mathrm{pore}}$ due to the preparation (calculated in **Appendix A.3**), which indicates that this finding is statistically relevant. For the sample prepared with 10 wt% MCC, a 32% increase in S_{BET} was measured in comparison to the standard oxygen carrier (**Fig. 5-4a**). This difference is larger than the uncertainty in S_{BET} due to the preparation. However, the addition of the pore-forming agent did not result in a significant increase in $\sum v_{\mathrm{pore}}$ or mean pore diameter (**Fig. 5-4b**). This shows that the two pore-forming agents have different effects on the pore morphology. Starch seems to result in a pore structure with fewer larger pores, resulting in a larger cumulative pore volume, while the surface area is not affecting significantly. MCC creates smaller pores, which result in an increase in the surface area, while not changing the cumulative pore volume significantly.

The S_{BET} of the supported oxygen carriers (**Table 5-1**) are in the range 0.30 – 2.00 m^2/g and are in the order: TiO_2 (0.30 m^2/g) < Al_2O_3 (0.75 m^2/g) < ZrO_2 (2.00 m^2/g). The S_{BET} of the TiO_2-supported oxygen carriers is within the range of the S_{BET} of the mechanically mixed oxygen carriers. This indicates, that the addition of TiO_2 does not significantly affect the densification during calcination. Contrarily, the relatively high value of S_{BET} of the ZrO_2 supported oxygen carrier indicates that the preparation method might not result in a coalescence of the active metal oxide grains and the ZrO_2 grains, reasons for this could be the relatively high Tammann temperature of ZrO_2 (1214 °C, see ***Table 3-8***), which is above 950 °C – the temperature used for the calcination of the mechanically mixed oxygen carriers according to the standard synthesis procedure. For comparison, the Tammann temperatures of TiO_2 and Al_2O_3 are 789 °C and 884 °C, respectively, and are thus below the calcination temperature of 950 °C. Liquid phase sintering, during which a liquid phase (*e.g.* molten copper manganese oxide) and solid grains (*e.g.* ZrO_2 grains) co-exist,[208] could aid the densification during the calcination of the ZrO_2-supported oxygen carrier precursors, and experiments to investigate this are recommended as future work.

Oxygen carriers prepared *via* co-precipitation at high super-saturation

For the co-precipitated oxygen carrier precursors prepared at high super-saturation, the results of the BET surface area measurements are shown in **Table 5-2**, below.

Table 5-2 *Results of the BET surface area measurements of the bulk material of the high-surface area Cu-Mn oxygen carrier precursor.*

composition	*ageing time* [h]	*ageing temperature* [°C] [a]	S_{BET} [m^2 g^{-1}]
1Cu-1Mn	72	125	22.5
2Cu-1Mn	72	125	24.8
2Cu-1Mn	8	125	25.1
2Cu-1Mn	72	100	23.1
2Cu-1Mn	8	100	25.8
2.5Cu-1Mn	72	125	20.7
3Cu-1Mn	72	125	21.7
3Cu-1Mn	72	100	23.2

Footnotes: (a) for the ageing, the precipitated solids together with the supernatant were filled into autoclaves, sealed, and heated in an oven. The ageing temperature is assumed to equal the set temperature of the oven.

The results form **Table 5-2** are plotted as functions of the ageing time and temperature in **Fig. 5-4a** and **Fig. 5-4b**, below.

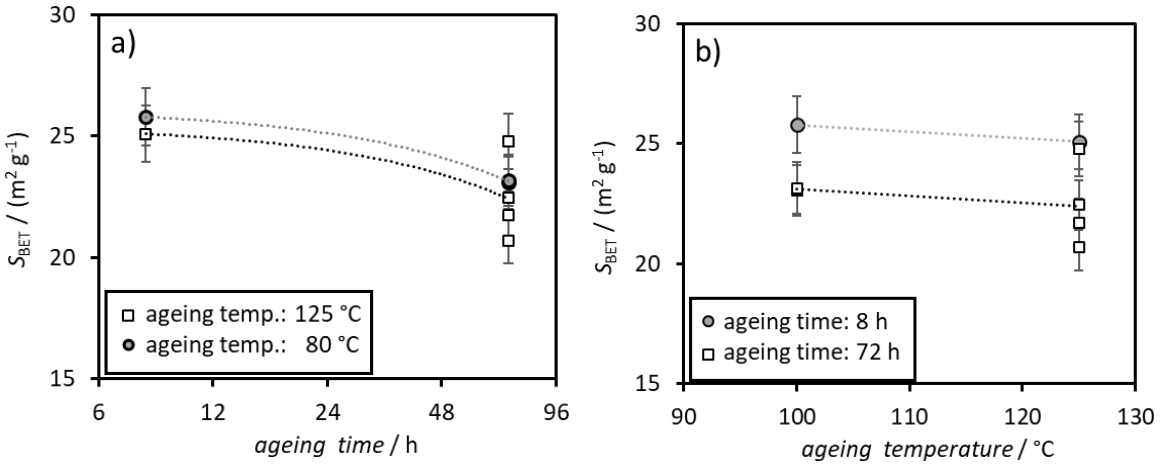


Fig. 5-4 *The results of BET surface area measurements of the high-surface area oxygen carrier precursors (bulk material), plotted against (a) ageing time, and (b) ageing temperature. The dotted curves/lines are the linear best fit to guide the eyes. The error bars indicate the uncertainty, which was estimated to be 0.046· S_{BET}.*

Contrary to the low surface area precursors, which consist predominantly of amorphous and low-crystallinity material, a high crystallinity in the precursor of the high surface area oxygen carrier is desired to achieve the platelet structure, which in turn is producing the large surface area. To improve the crystallinity of the precipitate, it was re-filled together with the supernatant (without washing)

into autoclaves. The autoclaves were placed in an oven and the precipitate inside the autoclaves was allowed to age for 8 h, 24 h or 72 h, at elevated temperatures. The results of the sensitivity experiment for the ageing of the precipitate (**Table 5-2** and **Fig. 5-4**) suggest that long ageing times at higher temperatures do not increase the surface area of the precursors.

After calcination at 600 °C and 900 °C (for 2 h in air with 1 l min^{-1} at SATP), the BET surface area of the micro-structured precursors was found to have significantly decrease, as shown in **Fig. 5-5**, below.

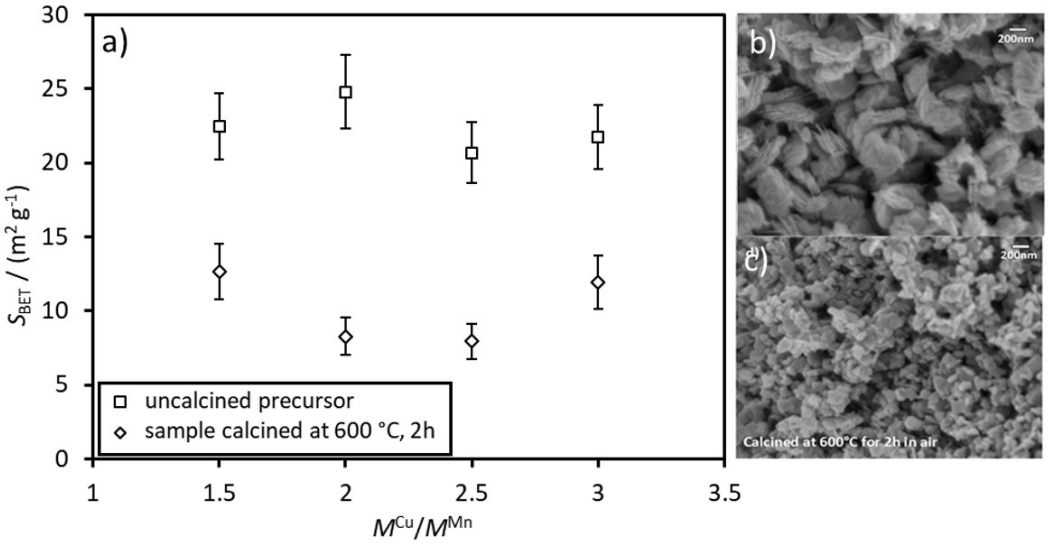


Fig. 5-5 *Change of the surface morphology of the micro-structured precursors during calcination at 600 °C for 2h in air with 1 l·min^{-1} at SATP: (a) BET surface area of the precursor (□) and the calcined samples (◇); SE micrographs of (b) the precursor and (c) the calcined material.*

As shown in **Fig. 5-5a**, the BET surface area reduced upon calcination at 600 °C to 7.94 – 12.66 m^2 g^{-1}. Furthermore, the platelet-like features of the precursors (**Fig. 5-5b**) changed into a surface morphology with grains (**Fig. 5-5c**). Calcination at 900 °C for 2 h reduced the surface area even further, *e.g.* to 2.21 m^2 g^{-1} and 5.00 m^2 g^{-1} for the samples with mol(Cu)/mol(Mn) = 2 and mol(Cu)/mol(Mn) = 3, respectively.

5.2 Crushing force measurements

The crushing force is a property that indicates the particle resistance towards mechanical stresses and was measured using a 50 N force gauge (Mark-10). A single oxygen carrier particle from the size range 300 – 425 µm was mounted on a flat steel support. The sensor was lowered onto the particle and the force increased until the particle was broken, while measuring the force exerted to the sensor with an interval of 10 s^{-1}. The force to crush an oxygen carrier particle was assumed to equal the last measured value before the first drop in the measured force, which indicates the breaking of the particle. The raw data of such a measurement is plotted in **Fig. 5-6**, below.

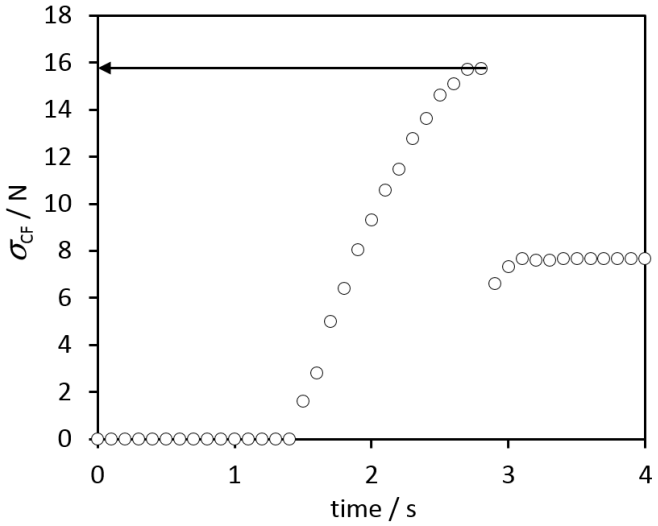


Fig. 5-6 *The data acquired during a crushing force measurement of a particle from the oxygen carrier batch 1Cu-1Mn-CP(3:0)-pH 6.0 and from the particle size range 300-425 µm.*

The reported crushing force, σ_{CF}, is an average of 36 measurements. The results of the σ_{CF} measurements of the co-precipitated oxygen carrier are shown in **Table 5-3**, below.

Table 5-3 *Results of the crushing force measurements of the co-precipitated oxygen carrier.*

Sample		σ_{CF} [b] (N)	SD_{36} [c] (N)	S_{BET} (m^2 g^{-1})[d]
unsupported co-precipitated copper manganese oxide oxygen carriers:				
1Cu-2Mn-CP(3:0)	*pH* 8.3	0.64 ± 0.04	0.46	0.91
	pH 6.0	7.97 ± 0.70	4.94	0.56
1Cu-2Mn-CP(2:1)	*pH* 7.0	0.76 ± 0.12	0.48	0.70
	pH 6.0	7.16 ± 0.94	4.10	0.40
1.25Cu-1.75Mn-CP(3:0)	*pH* 8.3	2.09 ± 0.38	0.99	0.87
	pH 6.0	8.25 ± 1.18	4.78	0.12
1.25Cu-1.75Mn-CP(2:1)	*pH* 6.9	1.55 ± 0.21	1.06	0.60
1Cu-1Mn-CP(3:0)	*pH* 8.3	3.02 ± 0.33	1.48	0.70
	pH 6.0	7.43 ± 0.83	4.55	0.17
1Cu-1Mn-CP(2:1)	*pH* 7.2	8.61 ± 1.66	4.65	0.19
	pH 6.0	9.12 ± 0.69	4.87	0.39
unsupported mechanically mixed copper manganese oxide oxygen carriers:				
1Cu-2Mn-MM		5.18 ± 0.33	1.91	0.217
1.2Cu-1.8Mn-MM		3.27 ± 0.60	1.75	0.283
1Cu-1Mn-MM		4.15 ± 0.61	1.98	0.337
supported copper manganese oxide oxygen carriers:				
40-CuMn/Zr-MM		1.84 ± 0.42	0.82	2.003
40-CuMn/Ti-MM		5.48 ± 0.28	2.37	0.306

Footnotes: (a) this is the set pH value during the co-precipitation; (b) the standard variation of σ_{CF} was determined from the average of three sets with 12 measurements each; (c) SD_{36} is the standard variation of all 36 measurements and combines the standard deviation of the σ_{CF} measurements as well as variations of the particles crushing force due to differences in shape, size and composition; (d) values of the uncertainty of S_{BET} are provided in Table 5-1.

The results of **Table 5-3** are plotted in **Fig. 5-7**. Each combination of the co-precipitation solutions was co-precipitated either at the highest possible *pH* value (minus 0.5) before formation of CuO occurred, in the Figure denoted as 'higher *pH* value' or at the lowest possible *pH* value at which all species co-precipitated (plus 0.5), in the figure denoted as 'lower *pH* value'.

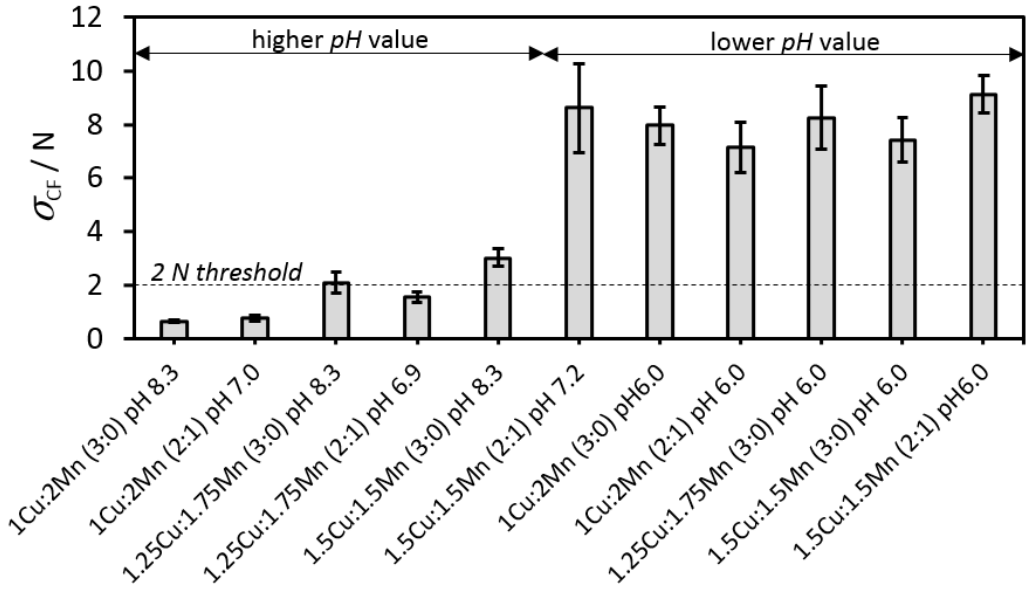


Fig. 5-7 *The results of the crushing force measurements of the co-precipitated oxygen carriers with a particle diameter of 300-425 µm.*

In **Fig. 5-7** it can be seen that all apart from three oxygen carriers have a crushing strength that is larger than the 2 N threshold. Furthermore, it becomes apparent that the oxygen carrier that were co-precipitated at the lower side of the possible *pH* value range have a significantly higher crushing strength (in average more than five times as high). The reason for this large difference becomes apparent, when plotting the crushing strength against the BET surface area, as shown in **Fig. 5-8**, below.

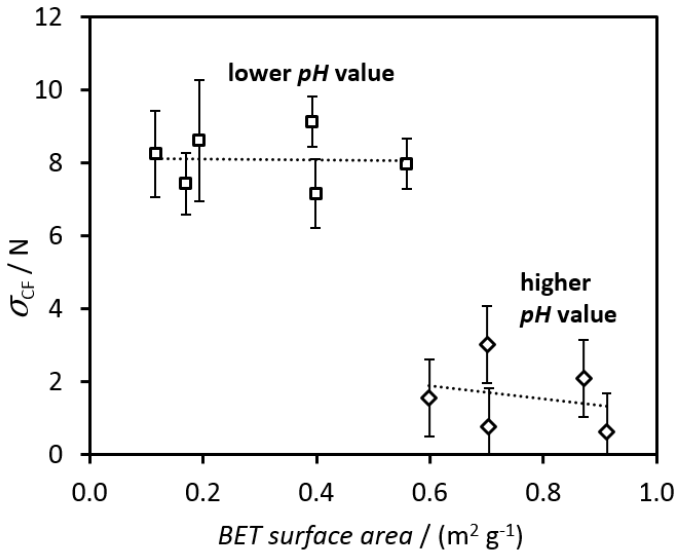


Fig. 5-8 *A plot of the crushing strength against the BET surface area of the co-precipitated oxygen carriers co-precipitated, □, at a lower pH value and, ◇, at a higher pH value.*

Fig. 5-8 shows the occurrence of two clusters. The oxygen carrier, which were co-precipitated at a lower *pH* value have a lower BET surface area and a higher crushing strength, while the oxygen carrier, which were co-precipitated at a higher *pH* value, have a higher BET surface area and a lower crushing strength.

To elucidate the reasons for the differences in crushing strength further, the 'higher *pH* value' cluster was plotted on a smaller scale in **Fig. 5-9**, below.

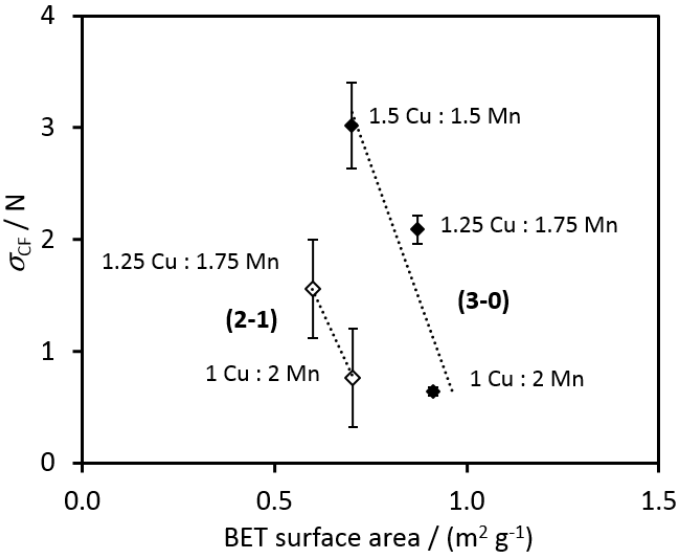


Fig. 5-9 *A plot of the average crushing force against the BET surface area of the co-precipitated oxygen carriers co-precipitated using a higher pH value and, ◇, only Na_2CO_3 and, ◆, NaOH + Na_2CO_3 as the co-precipitation agent.*

The results shown in **Fig. 5-9** indicate that a substitution of Na_2CO_3 with NaOH in the precipitation agent is resulting in a reduction of the surface area. The reason for this is elucidated in the section on the thermogravimetry evolved gas analysis mass spectrometry (section 5.7).

Furthermore, **Fig. 5-9** shows a significant increase in crushing strength with an increase in the molar Cu:Mn ratio, while the BET surface area decreases only slightly. This result indicates that a substitution of Mn with Cu results in an increase in crushing strength since the minor reduction in the surface area is insufficient to result in a three-fold increase in the crushing strength. It has been demonstrated by XRD (see section 5.4) that most of the Cu and Mn in the bulk of these oxygen carriers (1Cu-2Mn-CP(3:0), 1.25Cu:1.75Mn-CP(3:0) and 1Cu-1Mn-CP(3:0)) is incorporated in a $Cu_xMn_{3-x}O_4$ spinal phase. This suggests that substitution of Mn with Cu in the spinal structure in the molar Cu:Mn range between 1Cu:1Mn and 1Cu:2Mn results in an increase in the crushing strength of the oxygen carriers.

This analysis was not repeated for the oxygen carriers that were precipitated at a lower *pH* value, since the results of XRF experiments (*c.f.* section 5.5) suggest that some deviations between the target and the actual Cu:Mn molar ratio exists, which was attributed to incomplete precipitation of the Mn species during the co-precipitation experiment.

5.3 Helium pycnometry and mercury intrusion porosimetry

Gas displacement pycnometry with He was carried out using an AccuPyc II 1340 (Micromeritics). This technique determines the skeletal density, ρ_{sk}, of the calcined oxygen carriers, which is the density of the sample excluding the pores and including intra-particle voids.[206] The measurements were carried out at 25 °C using a sample mass of 0.6 to 1.5 g and particles of the size range 300-425 µm. In a typical experiment, the sample is loaded into the 1 cm^3 chamber and sealed. After evacuation, He is pumped into this chamber and then expanded into a second chamber of which the volume is also known. The pressure difference prior and after the expansion and the sample mass are then used to calculate ρ_{sk}.[206,209] The reported value of ρ_{sk} in this work is the average value of ten measurements. The standard deviation of a repeated measurement was multiplied by two to obtain the uncertainty within a 95% confidence interval. The results of the He pycnometry experiments are presented at the end of this section together with the results from mercury intrusion porosimetry (MIP).

MIP was carried out using an AutoPore IV 9500 (Micromeritics) to determine the particle porosity, ε, and the particle density, ρ_p. In the literature, ρ_p, is also referred to as envelope density or apparent density, and is defined following the definition of Rouquerol *et al.*[206] as the density of the particle including open (accessible and inaccessible) and closed pores. The pressure range of the MIP

experiments was in the range 0.0365 – 2272 bar, which corresponds to a pore diameter range of 342 µm – 5.5 nm. In a typical experiment between 0.10 g and 0.15 g of oxygen carriers of the size range 300 – 425 µm were filled into a penetrometer, which was then sealed and loaded into the MIP instrument. After calibration of the pressure transducers, the stem of the penetrometer is evacuated, Hg is introduced into the stem of the penetrometer, and the pressure is gradually increased. Since the wettability of the metal oxide surfaces with Hg is negligibly low, the filling of the pores does not occur by capillary action but only by the forced intrusion by an external pressure. The incremental volume, V_I, of Hg introduced into the penetrometer is assumed to be equivalent to the cumulated pore volume of a given pore size range. The pore size range is calculated from the measured pressure (theoretically, the pore size is inversely proportional to the applied pressure). In an ideal case, the Hg surrounds the particles at low pressure without intruding into the pores, and the particle density, ρ_p, is calculated as the sample mass divided by the difference between the internal volume of the empty pentameter and the intruded volume at low pressure.[210] At high pressure, when the Hg has intruded into all pores, the skeletal density, ρ_sk, is calculated as the weight of the sample divided by the difference between bulk volume of the sample and intruded volume at high pressure. [210] The porosity of the particles, ε_p, is then automatically calculated by, [210]

$$\varepsilon_\mathrm{p} = 1 - \frac{\rho_\mathrm{p}}{\rho_\mathrm{sk}}, \tag{5-3}$$

However, the automated calculation of ε_p has at least three drawbacks: (i) for the measurement of ρ_p a relatively small sample volume is used, resulting in significant uncertainties in ρ_p, (ii) at low pressures the Hg might not intrude into the voids between the particles, but only surround the perimeter of the bulk of particles, (iii) the measured value for ΣV_I (which is used to calculate ρ_sk) includes voids in the range 5 nm - 342 µm. The upper bound has the same order of magnitude as the mean particle diameter. Therefore, it is likely that the measured value of ΣV_I also includes inter-particle voids and voids at the particle circumference due to irregular curvature of the oxygen carriers' external surface. Therefore, the automatically calculated value for ρ_p, ρ_sk and ε_p were not used. Instead, the raw data for intrusion into voids < 10 µm was used and combined with the experimentally obtained values of the skeleton density, ρ_sk, from He-pycnometry to calculate ε_p and ρ_p iteratively, using eq.(5-3) and the following relationship:

$$\varepsilon_\mathrm{p} = \rho_\mathrm{p} \cdot \Sigma V_I, \tag{5-4}$$

The results of this calculation and the values of ρ_sk obtained by He pycnometry and the theoretical density of the crystalline phase calculated by density functional theory (DFT), ρ_DFT are shown in **Table 5-4**, below.

Table 5-4 Results *from He pycnometry measurements at 25 °C and 0.1 MPa, mercury intrusion porosimetry measurements and the calculation of the envelope density of the oxygen carriers.*

oxygen carrier	ρ_{sk} [a] [g cm^{-3}]	ρ_{DFT} [b] [g cm^{-3}]	ε_p	ρ_p [g cm^{-3}]
co-precipitated oxygen carriers:				
1Cu-2Mn-CP(3:0)-*pH* 8.3	5.02 ± 0.01	5.12	0.565	2.18
1Cu-2Mn-CP(3:0)-*pH* 6.0	5.56 ± 0.03	5.12	0.014	5.48
1Cu-2Mn-CP(2:1)-*pH* 7.0	5.20 ± 0.01	5.12	0.442	2.90
1Cu-2Mn-CP(2:1)-*pH* 6.0	5.36 ± 0.01	5.12	*n.d.*	*n.d.*
1Cu-1Mn-CP(3:0)-*pH* 8.3	*n.d.* [c]	5.34	0.218	4.54
1Cu-1Mn-CP(3:0)-*pH* 6.0	5.76 ± 0.01	5.34	0.013	5.68
1Cu-1Mn-CP(2:1)-*pH* 7.0	*n.d.* [c]	5.34	0.009	5.75
1Cu:1Mn-CP(2:1)-*pH* 6.0	5.80 ± 0.01	5.34	0.035	5.59
mechanically mixed oxygen carriers:				
1Cu-2Mn-MM	5.34 ± 0.01	5.21	0.359	3.42
1Cu-1Mn-MM	5.67 ± 0.01	5.34	0.492	2.88
40-CuMn/Zr-MM	5.39 ± 0.01	5.10	0.548	2.43
40-CuMn/Ti-MM	4.28 ± 0.01	3.93	0.246	3.23
40-CuMn/Al-MM	4.22 ± 0.02	4.09	0.465	2.26

Footnotes:"n.d." denotes "not determined", here the remaining sample mass was not sufficient to fill the 1 cm^3 chamber with particles; (a) the value of ρ_{sk} is the average of ten measurements and the variation range corresponds to the standard deviation of those ten experiments; (b) these values are the theoretical skeletal densities of an ideal crystal structure calculated using the DFT data from materials.project[211]; (c) the skeletal density of this sample was not measured and for the calculation of ε and ρ_p a value of 5.80 ± 0.01 is assumed, which is the result from a measurement of a similar composition.

The skeletal density of the co-precipitated oxygen carriers increases with an increase in the molar Cu:Mn ratio. This is in agreement with the values of the theoretical densities of the phase-pure copper manganese oxides from materials.project[211] – a database which contains *inter alia* results from DFT calculations. The experimentally obtained values of ρ_{sk} for the unsupported oxygen carriers are 6% higher than the theoretical density[211] of an ideal $Cu_xMn_{3-x}O_4$ crystal. As later confirmed by XRD, this deviation indicates the presence of single metal oxides in the samples, since the single metal oxides (especially CuO) have a higher density than $Cu_xMn_{3-x}O_4$. The values of ε for the co-precipitated oxygen carriers range from 0.009 to 0.565, and the average ε of the samples co-precipitated at a higher *pH* value are significantly larger (0.309) than the average of those prepared at a lower *pH* value (0.021). This is illustrated in **Fig. 5-10**, below.

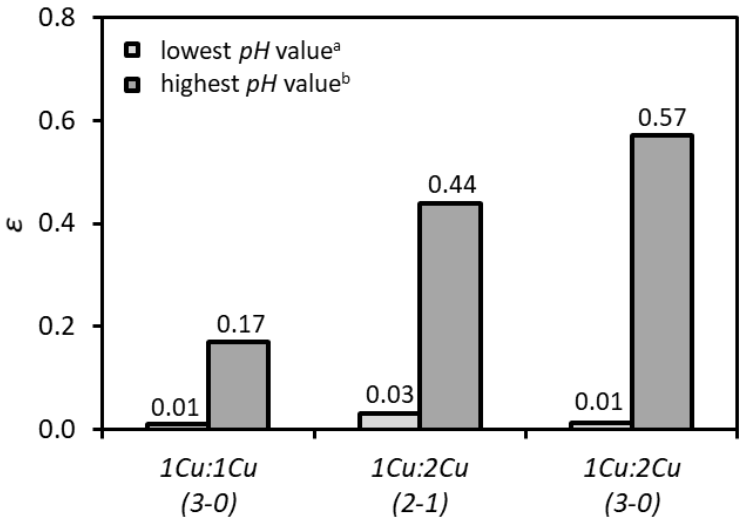


Fig. 5-10 *The porosity of selected co-precipitated calcined oxygen carriers in the range between 5.5 nm and 10 µm measured by MIP, co-precipitated at (a) the lowest theoretical pH value + 0.5 at which all species precipitate, and (b) the highest theoretical pH value - 0.5 at before the formation of CuO.*

An increase in porosity with an increase in *pH* value during the co-precipitation was expected from the results of the N_2 adsorption measurements, which found that an increase in *pH* value during the co-precipitation (in the examined range) resulted in an increase in the BET surface area. The porosity of the mechanically mixed oxygen carriers ranges from 0.255 to 0.359, and the porosity of the supported oxygen carriers is in the order: ZrO_2 ($\varepsilon = 0.548$) > Al_2O_3 ($\varepsilon = 0.465$) > TiO_2 ($\varepsilon = 0.246$).

To elucidate the nature of the pore structure in detail, the pore size distribution was measured by MIP. Selected results are shown in **Fig. 5-11**, below.

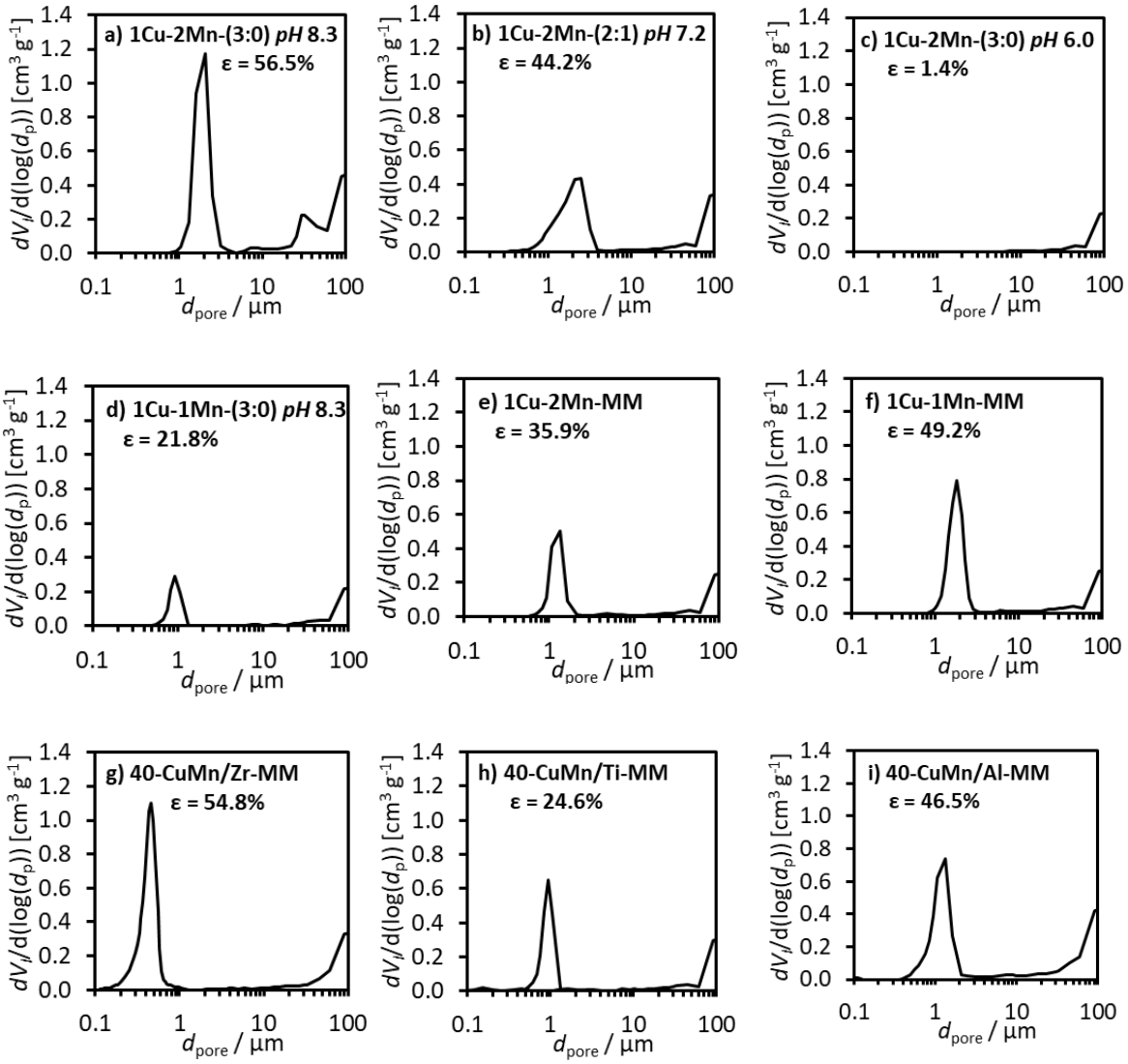


Fig. 5-11 *Pore size distribution determined by MIP for selected oxygen carrier from the size range 300-425 µm: (a-d) unsupported co-precipitated, (e-f) unsupported mechanically mixed, and (g-i) supported oxygen carriers.*

For the co-precipitated oxygen carriers, the results of the MIP experiments indicate that the mean pore diameter increases, and the porosity decreases with a decrease of the *pH* value during the co-precipitation. This is the case for 1Cu-2Mn-based oxygen carriers (**Fig. 5-11a-c**) and for (**Fig. 5-11d-e**). The pore size distribution of the mechanically mixed oxygen carriers where $DI > 0.001$ ml g^{-1} μm^{-1} is wider (0.2 µm and 100 µm) than the pore size distribution of the co-precipitated oxygen carriers. This indicates that the preparation of the oxygen carriers *via* co-precipitation can produce a material with a narrower pore-size distribution. The mechanically mixed supported oxygen carriers were found to have a porosity in the range 0.578 – 0.694. The experimentally obtained porosities will be used in the next chapter to model the diffusion inside the particle. In the following chapters, the calculated values of the envelope density ρ_p will be used for the reaction rate modelling and hydrodynamic calculations.

5.4 Determination of the crystalline phases by X-ray diffraction

Powder x-ray diffraction (XRD) was carried out in an X'Pert PRO (PANalytical) using Cu-Kα radiation with a wavelength of λ = 0.1541 nm. The instrument is set-up in the Bragg-Brentano configuration (illustrated in **Fig. 5-12a**) and two different types of sample holders were used (illustrated and **Fig. 5-12b)**.

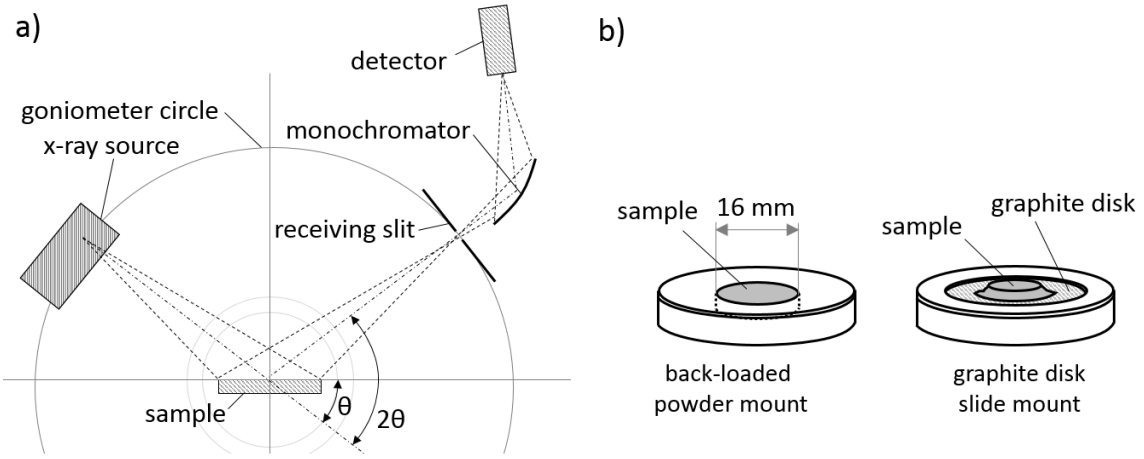


Fig. 5-12 *Schematic diagram of (a) the Bragg-Brentano geometry of an XRD instrument, adapted from the drawing shown on ywcmatsci.yale.edu,*[247] *and (b) of the two different types of sample holders used in this project.*

In a typical XRD experiment, the samples were scanned in a 2θ-range from 5° to 85° using a step size of 0.015° and a time per step of 0.25 s. Before reporting the results from XRD measurements, the validation of the XRD calibration and the determination of the uncertainties of the XRD measurements are detailed in the following subsection.

5.4.1 Validation of the calibration and uncertainties of the XRD measurements

The calibration was validated using the experimentally obtained diffraction pattern of a sintered sapphire (SiO_2) disk, which was placed onto the disk-slide mount (shown in **Fig. 5-12b**). The results of this XRD measurement are presented in **Fig. 5-13**, below.

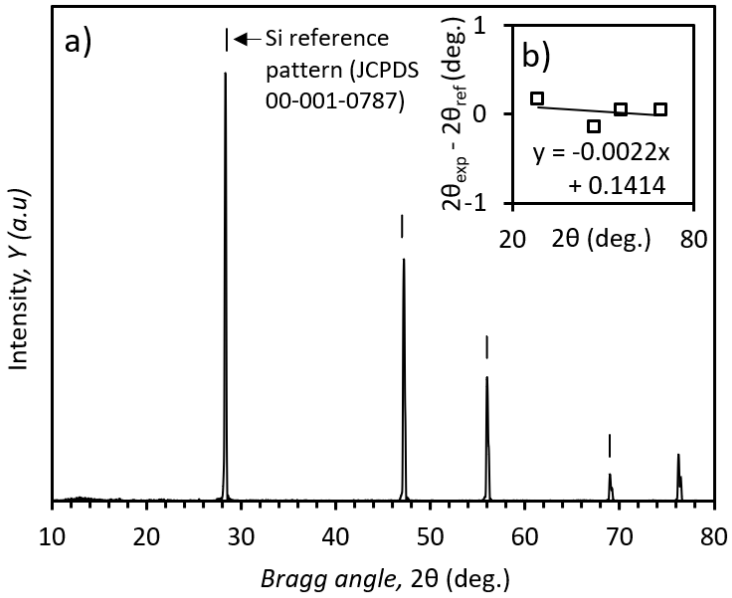


Fig. 5-13 *The results of the validation of the XRD calibration using a sintered sapphire disk: (a) the experimentally obtained XRD pattern with lines above the peaks that correspond to the peak position of the reference pattern (JCPDS 00-001-0787), and (b) the difference between the experimentally obtained peak position and the peak position of the reference pattern.*

Fig. 5-13b shows the difference between the experimentally obtained peaks of synthetic Si (JCPDS 00-001-0787) from the ICDD database.[212,213] The linear best fit of the points in **Fig. 5-13b** suggests that the shift of the XRD machine corresponds to $2\theta_{exp} = 0.0022 \cdot 2\theta_{ref} + 0.1414$. After validating the XRD calibration by demonstrating that no significant peak shift between experimental data and reference data exists, the uncertainties of the XRD measurements were determined next.

In this work, the relative intensities of the diffraction pattern peaks (I/I_{max}) are used to calculate the mass fractions of the crystalline phases, and to estimate the mass fraction of amorphous material by using CeO_2 as in internal standard. The peak position (2θ), the full width at half maximum (*FWHM*), and the integral breadth (*IB)* are used to estimate the crystallite size.

To estimate the uncertainty of the calculated mass fractions and crystallite sizes, the uncertainty of I/I_{max}, 2θ, *FWHM*, and *IB* has to be determined. Two different types of sample holders are used in this work (illustrated in **Fig. 5-12b**). The slide-disk sample holder is required for the phase determination of cycled oxygen carriers from TGA and fluidised bed reactor experiments, as the sample mass is typically insufficient to use the back-loaded sample holder. The uncertainties of the XRD measurements may vary with the type of sample holder, *inter alia* because the sample mass and thus the area of the reflection surface differs. In a typical XRD experiment a sample mass of about 1.0 ± 0.4 g was used in the back-loaded sample holder, while the sample mass of the disk-slide holder was 60 ± 20 mg. To quantify the uncertainties for each type of sample holders, three runs with

a sample from the same batch of oxygen carriers (1Cu-1Mn-CP(3:0)-*pH*-8.3) were carried out per sample holder. The diffraction patterns are presented in **Fig. 5-14**, below.

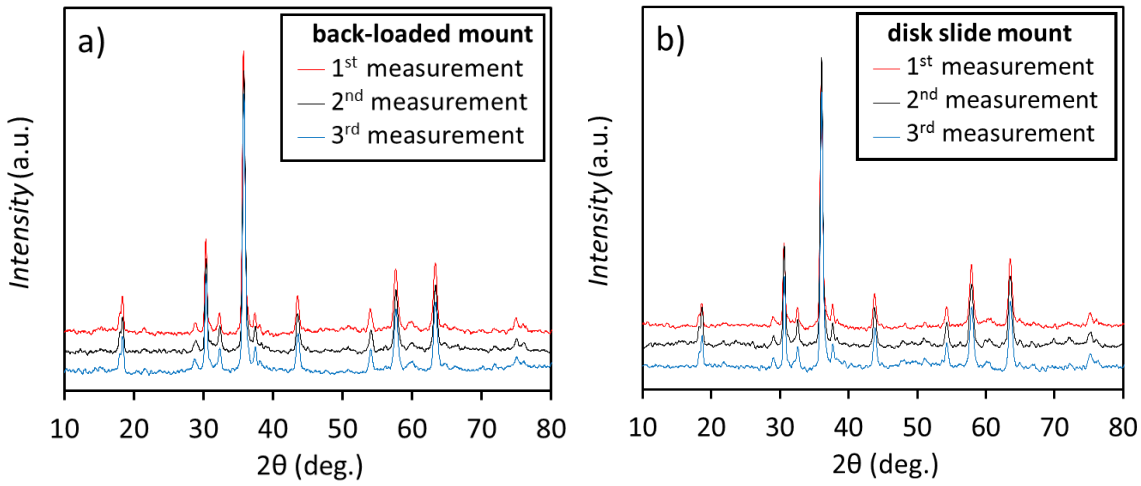


Fig. 5-14 *XRD patterns of the experiments for the determination of the uncertainties of the XRD measurements using crushed 1Cu-1Mn-CP(3:0)-pH-8.3 oxygen carriers (a) in the back-loaded mount and (b) on the disk-slide mount.*

Using the diffraction data (**Fig. 5-14**) without any smoothing, the relative uncertainties $u(x)$ and absolute uncertainties $U(x)$ of I/I_{max}, 2θ, *FWHM*, and *IB* were estimated by calculating the standard deviation of the three repeated measurements per sample holder for all peaks larger than $I/I_{max} = 0.05$ (this corresponds to eight peaks per sample). Under the assumption that the deviations follow a normal distribution, the standard deviation was multiplied by two to obtain the uncertainty within a 95% confidence interval.

The standard deviation for each peak is represented by a dot in **Fig. 5-15a-d**, below, and the uncertainties are represented by the shaded ranges.

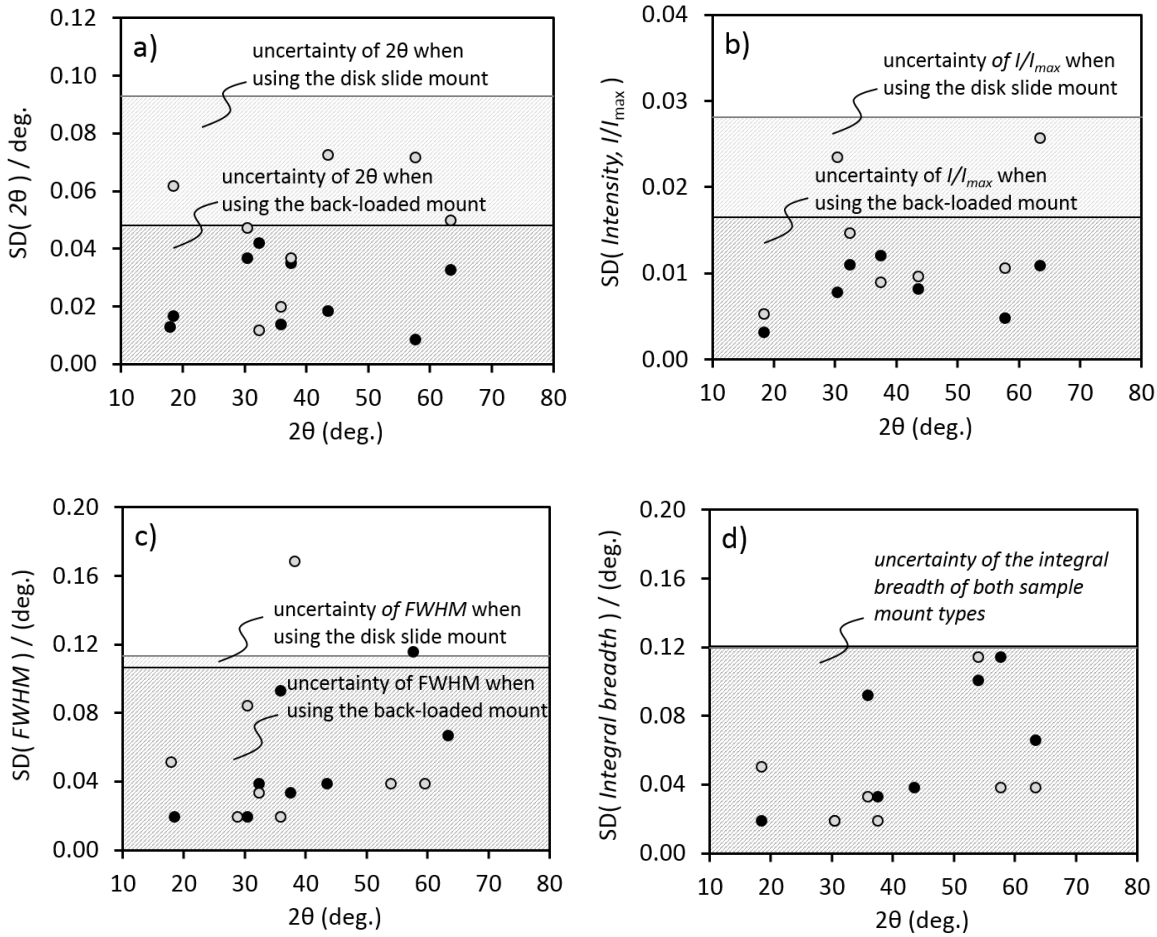


Fig. 5-15 *A plot of the standard deviations against the 2θ of the three measurements obtained when using the slide disk mount (○) and the back-loaded sample holder (●) for: a) 2θ, the peak position, b) the relative intensity, I/I_{max}, c) the full width at half maximum, FWHM, and d) the integral breadth.*

Fig. 5-15 shows that the uncertainty of *2θ* and $I/I_{\max}$ is about twice as high when using the slide-disk sample holder, while the uncertainty of the FWHM and integral breadth does not depend significantly on the sample holder type.

The deviations and uncertainties of this assessment are summarised in **Table 5-5**, below.

Table 5-5 *The calculated standard deviation and uncertainties for the different sample holders for the XRD measurements.*

property, x	standard deviation, *SD(x)*[a]		uncertainty (95% CI), *u(x)*[b]	
	back-loaded (1.0 ± 0.4 g)	slide disk (60 ± 20 mg)	back-loaded (1.0 ± 0.3 g)	slide disk (60 ± 20 mg)
peak position, 2θ (deg.)	0.024	0.046	0.048	0.093
relative intensity, I/I_{max} (-)	0.008	0.014	0.016	0.028
FWHM (deg.)	0.053	0.056	0.106	0.113
integral breadth, IB (deg.)	0.060	0.060	0.120	0.120

Footnotes: (a) the standard deviation, SD(x), was calculated from three measurements of the eight largest peaks (i.e. all peaks with $I/I_{max} > 0.05$); (b) the relative uncertainty, u(x), within a 95% confidence interval (95% CI) was calculated by 2· SD(x), assuming a normal distribution of the measurements.

The uncertainties of I/I_{max}, 2θ, *FWHM*, and *IB* from **Table 5-5** will be used to estimate the uncertainty of the mass fractions and crystallite size calculated from the XRD data (see section 5.4.2).

In addition to the determination of the uncertainties, a series of experiments was carried out to determine if the peak position is shifted when the back-loaded sample holder is used (the validation of the calibration with the sintered sapphire disk is only possible with the slide disk holder), and if the relative intensities (I/I_{max}) vary with the sample holder. For this purpose, 2θ and I/I_{max} of all peaks larger than $I/I_{max} = 0.05$ of three repeated measurements using the disk slide mount were plotted against those obtained when using the back-loaded mount.

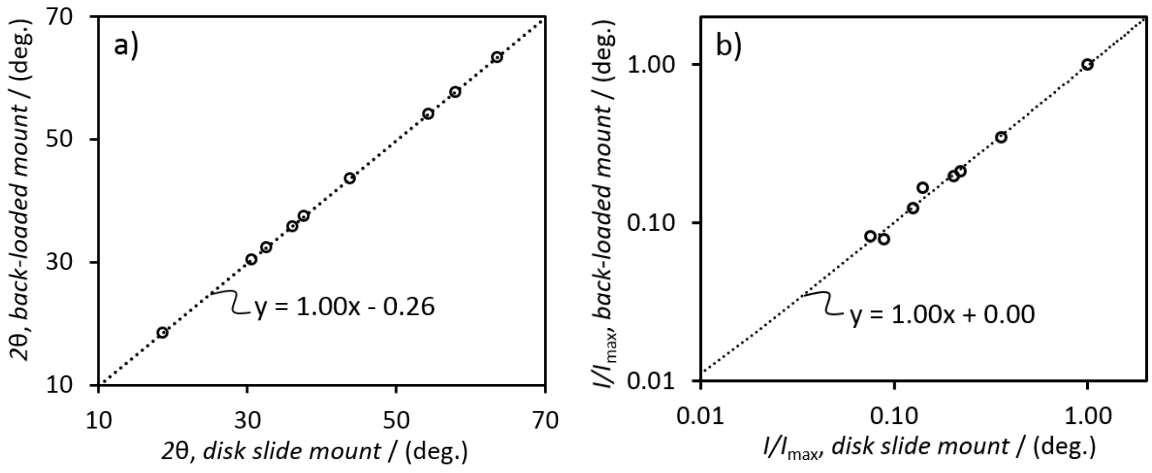


Fig. 5-16 *Plots of the average values of three measurements obtained when using the disk slide mount against the values obtained when using the back-loaded mount for a) 2θ, the peak position and b) I/I_{max}, the relative peak intensity of the peaks larger than $I/I_{max} = 0.05$.*

Fig. 5-16a shows that the peak positions obtained when using the disk slide mount are 0.26 ° higher than those obtained when using the back-loaded mount. Since the later were calibrated using the sapphire disk, the peak positions of the back-loaded holder were corrected by +0.26 °. The factor of the best fit is unity, which shows that this peak shift does not depend on the peak position. **Fig. 5-16b** shows that the calculated values of I/I_{max} do not depend on the type of sample holder.

After the validation of the calibration of the XRD equipment and determination of the uncertainties of the measurements, a method for the calculation of the mass fractions of the crystalline phases from XRD data is presented in the following section.

5.4.2 Calculation of the mass fractions from XRD data

The powder diffraction files (PFD) report relative intensity ratios $\left(I/I_c\right)$ with corundum (Al_2O_3), which is the experimentally obtained ratio of the observed intensities of the largest peak of the sample to the largest peak of corundum. These ratios are determined from experiments with a powder containing the sample and 50 wt% corundum. Chung *et al.*[214] showed that the mass fractions of a sample containing *n* phases can be estimated using the values for (I/I_c) of all phases and the following two equations:

$$x_a = \left(\frac{\left(I/I_c\right)_a}{\left(I/I_{max}\right)_a} \sum_{i=1}^{n} \frac{\left(I/I_{max}\right)_i}{\left(I/I_c\right)_i} \right)^{-1}, \tag{5-5a}$$

$$1 = \sum_{a=1}^{n} x_a, \tag{5-5b}$$

where x_a is the mass fraction of the phase *a*, I/I_c is the relative intensity ratio, I/I_{max} is the relative intensity, and *i* (with $i = 1$ to n) are all phases other than *a*. The values for the relative intensity ratios with corundum were taken from the ICDD's PDF-4+ 2016 and PDF-4+ 2019 databases.[212,213] To prevent the use of overlapping peaks for the calculation of the mass fractions, the expected phases were simulated using the phase data from the ICDD database[212], as shown in **Fig. 5-17**, below.

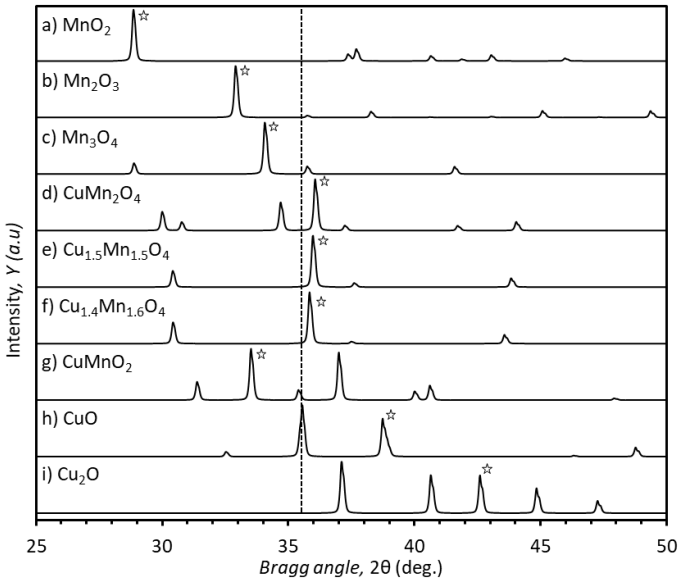


Fig. 5-17 *Simulated copper, copper manganese and manganese oxide XRD patterns based on data from the PDF-4+ 2016 database*[212] *to show the peak used for the mass fraction calculation (☆) for Cu Kα (λ =0.1541 nm) radiation.*

Fig. 5-17 shows that the largest peaks of the single metal oxides that are expected in the fully oxidised samples (*i.e.* MnO_2, Mn_2O_3 and CuO) do not overlap with the largest peaks of the combined metal oxides in the fully oxidised sample (*i.e.* $CuMn_2O_4$, $Cu_{1.4}Mn_{1.6}O_4$, $Cu_{1.5}Mn_{1.5}O_4$). The same holds true for the phases that are expected in the fully reduced form, apart from $CuMnO_2$ and Cu_2O, where the largest peaks overlap at $2\theta = 37.0°$. Therefore, the mass fraction of Cu_2O and $CuMnO_2$ are determined using the peaks at $2\theta = 42.6°$ and $2\theta = 33.5$, respectively. The values for I/I_c, the position of the peaks used, and the uncertainties of the mass fraction calculation are presented in **Table 5-6**, below.

Table 5-6 *Peak data from the PDF-4+ 2016 database*[212] *used for mass fraction calculation and uncertainty of the mass fraction calculation.*

phase, *i*	ICDD reference number[212]	*peak used for mass fraction calculation*				
		position	I/I_c	I/I_{max}	$\underline{u}_{BL}(m_i)$[a]	$u_{SID}(m_i)$[a]
MnO_2	00-043-1455	21.89	3.46	1.00	$0.03 \cdot m_i$	$0.05 \cdot m_i$
Mn_2O_3	00-041-1442	32.95	4.50	1.00	$0.02 \cdot m_i$	$0.05 \cdot m_i$
Mn_3O_4	00-024-0734	34.04	1.50	1.00	$0.06 \cdot m_i$	$0.10 \cdot m_i$
$CuMn_2O_4$	01-071-1143	36.08	4.93	1.00	$0.03 \cdot m_i$	$0.05 \cdot m_i$
$Cu_{1.5}Mn_{1.5}O_4$	01-070-0262	35.96	4.92	1.00	$0.03 \cdot m_i$	$0.05 \cdot m_i$
$CuMnO_2$	04-017-1231	33.50	3.08	1.00	$0.03 \cdot m_i$	$0.06 \cdot m_i$
CuO	00-041-0254	38.76	2.80	0.96[b]	$0.04 \cdot m_i$	$0.07 \cdot m_i$
Cu_2O	01-078-2076	42.62	8.58	0.77	$0.02 \cdot m_i$	$0.03 \cdot m_i$

Footnotes: (a) the uncertainty of the mass fractions calculated using the XRD data from the back-loaded sample holder, $u_{BL}(m_i)$, and the slide-disk sample holder $u_{SID}(m_i)$ was calculated using eq.(5-5); (b) the largest peak of CuO overlaps with the peak of Mn_3O_4, therefore the second largest peak is used for the mass fractions calculations.

In the following sections, the method for the calculation of the mass fraction of the crystalline phases will be applied when evaluating the XRD results of the preliminary oxygen carrier preparation experiments for the determination of the optimal calcination conditions (section 5.4.3) and the washing procedure (section 0), and of all co-precipitated (section 5.4.5, section 5.4.6) and mechanically mixed (section 5.4.7) oxygen carriers.

5.4.3 Effect of calcination conditions on the crystalline phases

To determine the calcination temperature and time that is required for the formation of highly crystalline copper manganese oxide, 1Cu-1Mn-CP(3:0) *pH* 8.3 precursor was calcined at different conditions, some of which are shown in **Fig. 5-18**, below.

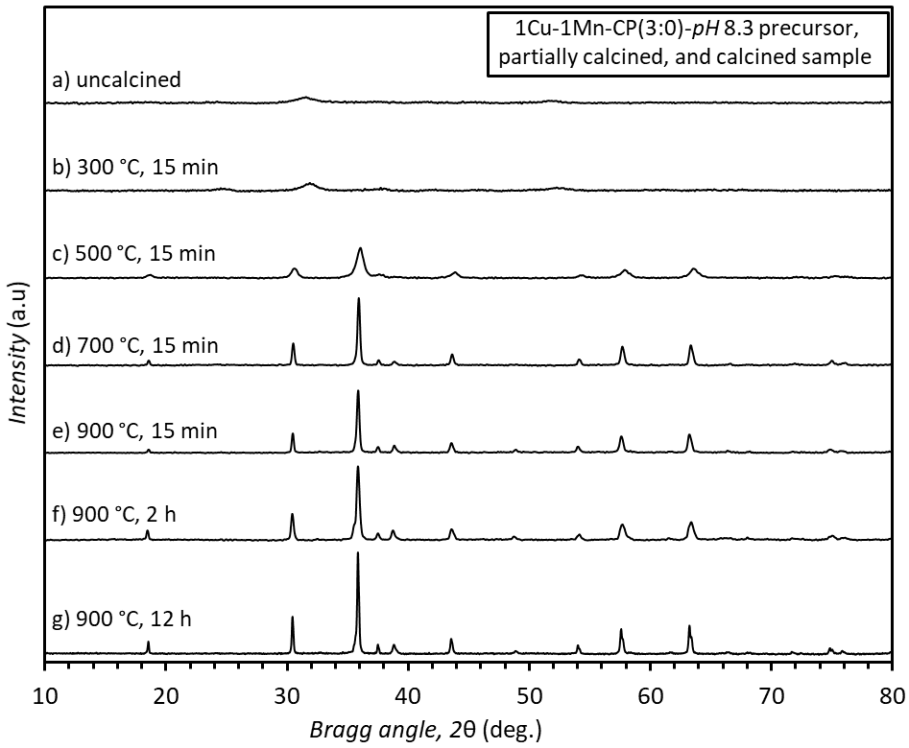


Fig. 5-18 *XRD pattern of the 1Cu-1Mn-CP(3:0)-pH-8.3 precursor, partially calcined and calcined material. The calcination was carried out in air (1 l min^{-1} at SATP) and using a heating rate of 15 °C min^{-1}. The calcination temperatures and holding times as well as the calculated values for the FWHM and crystallite size are specified on the graph.*

Fig. 5-18 shows that the formation of copper manganese oxide already occurs at calcination temperatures around 500 °C and occurs relatively fast (the holding time at 500 °C was only 15 min).

To elucidate the crystallite growth during the calcination, the Scherrer equation[215] was applied to the XRD data of the copper manganese oxide peaks at 35.86°,

$$d_c = \frac{K\,\lambda}{\beta\,\cos(B_{obs.} - B_{Si})}, \tag{5-6}$$

where K is the shape factor (here 0.9 for spherical crystals), λ is the wave-length of the Cu-Kα radiation (λ = 0.1541 nm), β is the peak position, $B_{obs.}$ is the observed peak broadening of the sample (equal to FWHM), and B_{Si} is the peak broadening of the Si (1 1 1) peak at 28.44 °C of the Si standard (from **Fig. 5-13**), assuming an indefinitely crystallite size in the Si standard so that the line broadening of the Si standard corresponds to the instrumental line broadening. The calculated value of B_{Si} is 0.102°. The uncertainty of the calculated mean crystallite size was determined using the data from **Table 5-5**. The results of the crystallite size calculation are shown in **Table 5-7,** below.

Table 5-7 *The results of the crystallite size calculation for the precursors, partially calcined and fully calcined sample 1Cu-1Mn-CP(3:0)-pH-8.3 based on the XRD data that is shown in Fig. 5-18.*

Sample	$B_{\text{obs.}}$ [FWHM (2θ)]	$B_{\text{structural}}$ ($B_{\text{obs.}}$ - B_{Si}) [FWHM (2θ)]	mean crystallite size, d_c [nm] [a]	$u(d_c)$ [nm]
500 °C, 15 min	0.595	0.493	17.0	+ 4.4 - 3.5
700 °C, 15 min	0.289	0.187	44.7	+ 38.7 - 20.7
900 °C, 15 min	0.272	0.170	49.2	+ 38.9 - 24.5
900 °C, 2 h	0.270	0.168	49.7	+ 50.4 - 25.0
900 °C, 12 h	0.184	0.082	101.9	+ 451.6 - 83.1 [b]

Footnotes: (a) the mean crystallite size was calculated assuming a shape factor, K, of 0.9, a radiation with a wave length of 0.1541 nm, and an instrumental line broadening of 0.102° (2θ); (b) the calculated uncertainty of this sample is very large, due to $B_{obs.}$ being close to the instrumental line broadening (i.e. B_{Si}).

The data in **Table 5-7** shows that higher calcination temperatures and a longer sintering time results in an increase in the calculated mean crystallite size. Though the data suggests that the sample calcined for 12 h had a significantly higher crystallite size, it was decided (also considering the crushing strength test results) that a calcination time of 2 hours at 900 °C is sufficient. These parameters were therefore used for the calcination of all co-precipitated precursors of this study.

To determine the optimal calcination conditions of the mechanically mixed samples, 1Cu-1Mn-MM precursors were calcined at different temperatures (900 °C and 950 °C) for different durations (2 h, 6 h and 12 h), and the phases of the calcined materials were studied by XRD, as shown in **Fig. 5-19**, below.

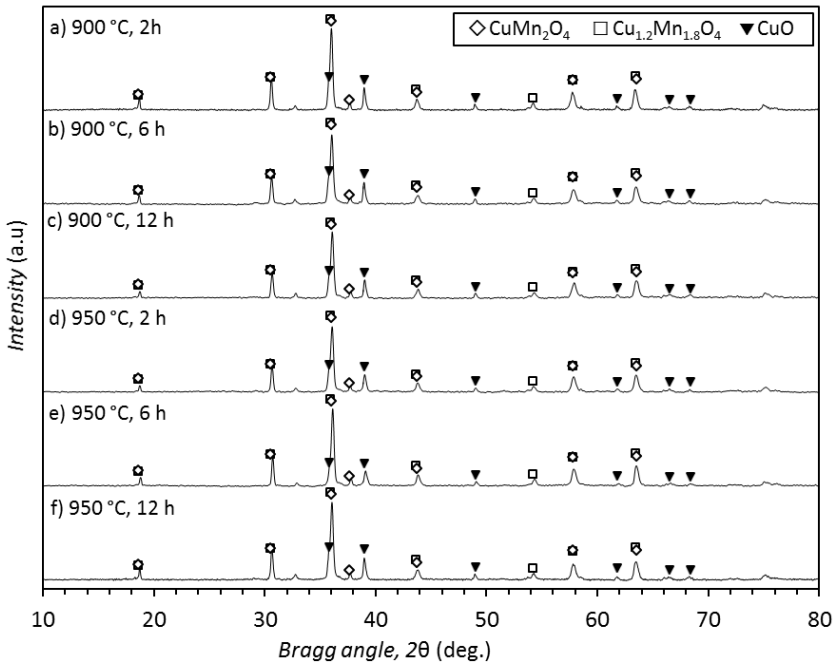


Fig. 5-19 *XRD pattern of the mechanically mixed 1Cu-1Mn-MM oxygen carrier calcined at different conditions as specified on the plot.*

The XRD plots from **Fig. 5-19** suggest that all six samples contained copper manganese oxide (identified as either $CuMn_2O_4$, JCPDS 01-071-1143, or $Cu_{1.2}Mn_{1.8}O_4$, JCPDS 01-071-1144) and CuO (JCPDS 00-45-0937). The mass fractions of the phases from **Fig. 5-19** were calculated using the 'relative intensity ratio' method (*c.f.* eq.(5-5a) and eq.(5-5b)).[214] For this calculation it is not relevant if the $Cu_xMn_{x-3}O_4$ is in the form of $CuMn_2O_4$ or $Cu_{1.2}Mn_{1.8}O_4$, since the I/I_c of all $Cu_xMn_{x-3}O_4$ are almost identical. The calculated mass fractions of CuO plotted against the sintering time in **Fig. 5-20**, below.

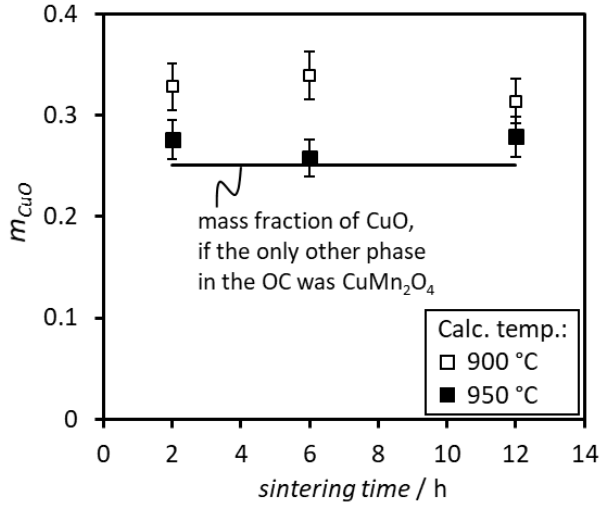


Fig. 5-20 *The mass fraction of CuO in the calcined 1.5Cu-1.5Mn-MM precursors as a function of calcination time, calculated by eq.(5-5a) and eq.(5-5b) from the XRD data shown in Fig. 5-19. The black line corresponds to the theoretical mass fraction of a sample containing only $CuMnO_2$ and CuO.*

From **Fig. 5-20** it can be seen that an increase in the calcination temperature from 900 °C to 950 °C results in a decrease in the mass fractions of CuO, m_{CuO}, for all samples. Moreover, it appears that after 6 h of calcination at 950 °C, CuO and MnO do not further combine to $Cu_xMn_{3-x}O_4$. Even after extensive sintering of 12 h it was not possible to reduce m_{CuO} to below 0.251, which corresponds to the theoretical mass fraction of CuO in a sample containing only $CuMn_2O_4$ + CuO. This finding indicates that during calcination the formation of CuO + $CuMn_2O_4$ is more favourable than the formation of $Cu_xMn_{x-3}O_4$ with $x > 1$. Therefore, it was deemed impossible to obtain a phase-pure copper manganese oxide oxygen carrier (containing only $Cu_{1.5}Mn_{1.5}O_4$) by mechanical mixing and calcination at these conditions. Since no further reduction of m_{CuO} after a calcination at 950 °C for 6 h was observed, these calcination conditions were used for the calcination of all mechanically mixed oxygen carriers in this work. In the next section, the importance of removing Na^+ from the co-precursors is demonstrated, by examining Na-rich samples.

5.4.4 Effect of residual sodium in the precursor on the calcined sample

To elucidate the effect of Na on the calcined materials, a sample that was washed according to the standard procedure (*i.e.* until the electrical conductance was below 50 µS), was compared with samples that containted higher amounts of Na (with the electrical conductance being ~250 µS and ~1250 µS, as well as a sample without the removal of the Na). The samples were calcined for at 900 °C for 2 h in air, crushed, and the crystalline phases examined by XRD. The results are shown in **Fig. 5-21**, below.

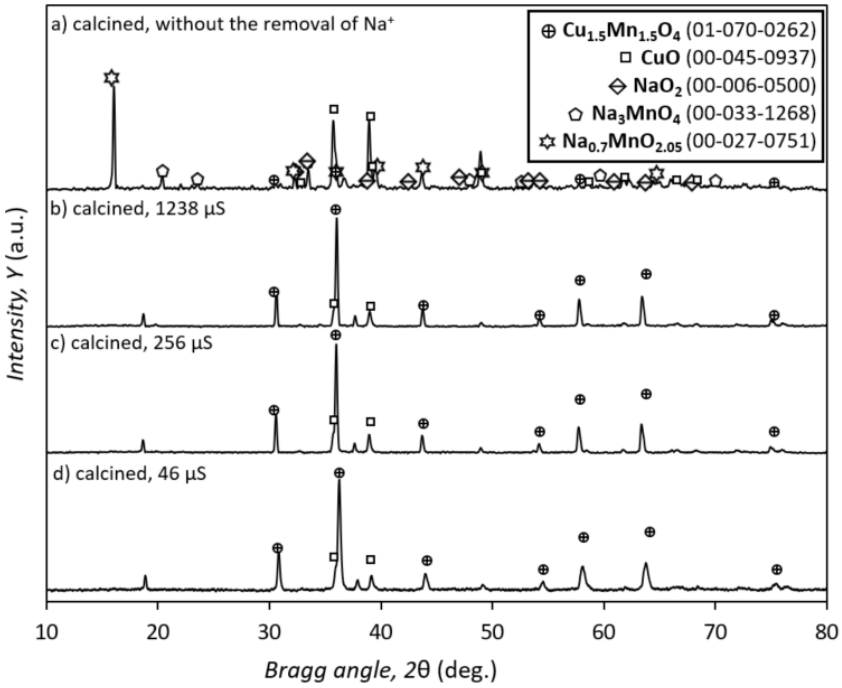


Fig. 5-21 *XRD pattern of 1Cu-1Mn (3:0) pH 8.3 with different amounts of residual Na: (a) without the removal of Na, and removal of Na to obtain a electrical conductivity of (b) 1238 µS, (c) 256 µS, and (d) 46 µS.*

The examination of the phases of the unwashed material (**Fig. 5-21**) shows that the Na reacts with the manganese species to form sodium manganese oxide, thereby reducing the amount of Mn available for the formation of copper manganese oxide. Neither manganese oxide nor copper manganese oxide was identified by XRD and the presence of NaO_2 suggests that more Na was available than required for the formation of the sodium manganese oxides. No phases were identified that suggest that the Cu species reacts with Na and CuO was the only phase found to contain Cu.

5.4.5 XRD patterns of the co-precipitated precursors

Two series of co-precipitated oxygen carriers were prepared. The results of the XRD analysis of the precursors of the first series of co-precipitated oxygen carriers is presented in **Fig. 5-22**, below.

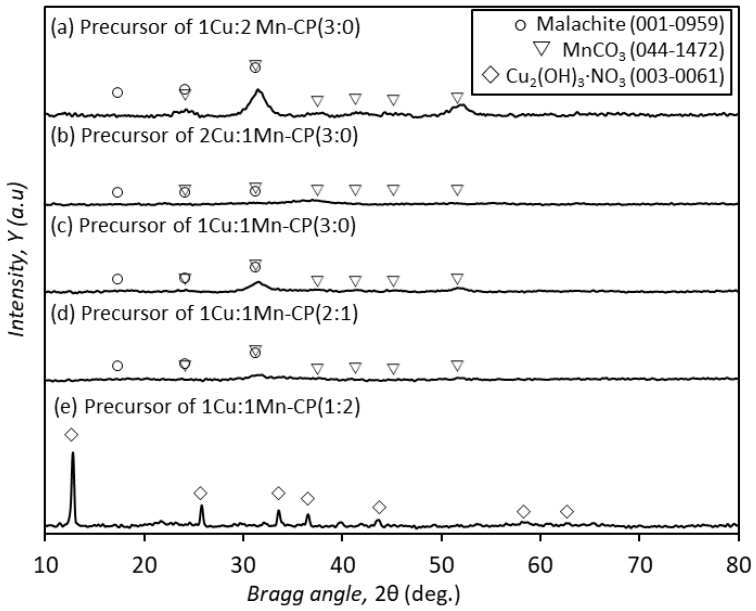


Fig. 5-22 *XRD pattern of the precursors of the first series of co-precipitated oxygen carriers. The samples are precursors of (a) 1Cu-2Mn-CP(3:0), (b) 2Cu-1Mn-CP(3:0), (c) 1Cu-1Mn-CP(3:0), (d) 1Cu-1Mn-CP(2:1), and (e) 1Cu-1Mn-CP(1:2).*

Fig. 5-22a-c show the XRD patterns of the precursors with different Cu:Mn molar ratios. The peaks agree well with the reference patterns for manganese carbonate ($MnCO_3$, JCPDS 00-044-1472) and malachite ($Cu_2CO_3(OH)_2$, JCPDS 00-001-0959). The XRD analysis of the samples shown in **Fig. 5-22c** to **Fig. 5-22e** was performed to study the effect of the substitution of Na_2CO_3 with NaOH in the precipitation agent. The phases of the samples shown in **Fig. 5-22c** (prepared with 1 M Na_2CO_3) and **Fig. 5-22d** (prepared with 0.66 Na_2CO_3 and 0.66 NaOH) do not differ significantly. However, further substitution of Na_2CO_3 with NaOH (*c.f.* **Fig. 5-22e**, prepared with 0.33 M Na_2CO_3 and 1.33 NaOH) results in the formation of a highly crystalline material containing $Cu_2(OH)_3{\cdot}NO_3$ (JCPDS 00-003-0061), as correctly predicted by the 'Spana-Medusa' calculation shown in **Fig. 4-2c**.

The relatively weak peaks indicate a low crystallinity of the material. To quantify the mass fractions of crystalline material in the co-precipitated precursor, CeO_2 powder was added to the 1Cu-2Mn-CP(3:0), 2Cu-1Mn-CP(3:0) and 1Cu-1Mn-CP(3:0) precursors as an internal standard, so that the amount of CeO_2 was 10 wt% in the mixed powders. The peak $2\theta = 31.3°$, which belongs to $MnCO_3$, $Cu_2CO_3(OH)_2$ or to a combination of both (the main peaks of these two phases are very similar) was used to calculate the ratio of the mass fractions of the crystalline phase, $x_{crystal}$, in the sample to the mass fraction of CeO_2, x_{CeO2}, using the method of the relative intensity ratios with corundum (*c.f.* eq.(5-5a) and eq.(5-5b) in section 5.4.2).[24] For this calculation, data from the three largest CeO_2 peaks was used, which are located at $2\theta = 28.7°$, ($I/I_{max} = 1.000 \pm 0.000$), 47.6° ($I/I_{max} = 0.486 \pm 0.046$) and 56.5° ($I/I_{max} = 0.388 \pm 0.050$). The method and the calculation of its uncertainties are detailed in ***Appendix A.5***. The XRD plots that were used for this calculation are shown in **Fig. 5-23**, below.

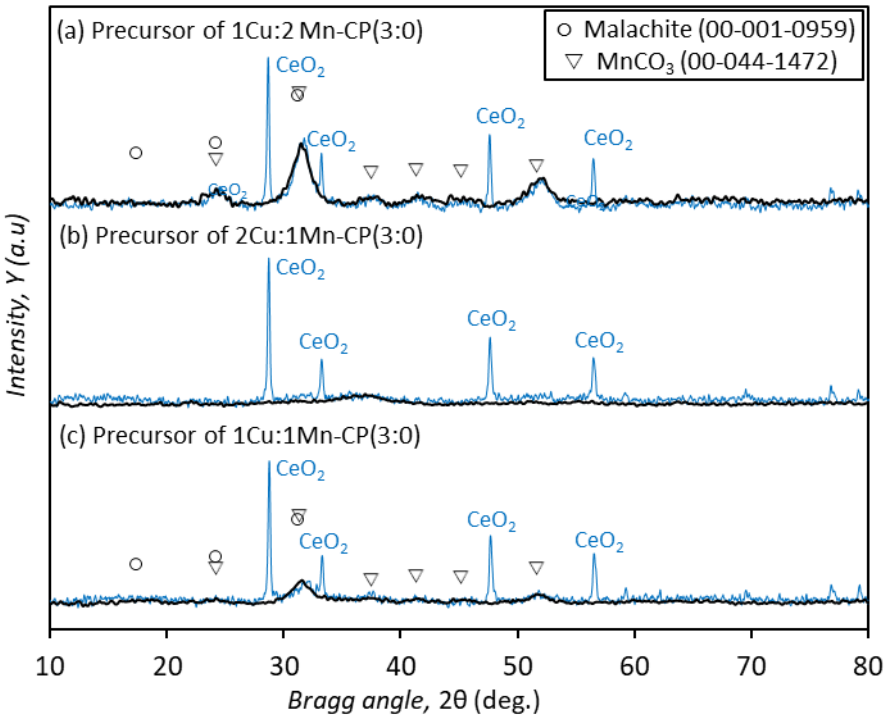


Fig. 5-23 *XRD patterns of a mixture of the precursors (90 wt%; black lines) of (a) 1Cu:2Mn-CP(3:0), (b) 2Cu:1Mn-CP(3:0), (c) 1Cu:1Mn-CP(3:0), and CeO_2 (10 wt%; blue lines) as an internal standard for the determination of the mass fractions of crystalline material.*

The calculation was carried out twice, once assuming the peak of the precursor at $2\theta = 31.3°$ belongs to $MnCO_3$ and once assuming the it belonged to $Cu_2CO_3(OH)_2$. The results of the calculation are shown in **Fig. 5-24**, below.

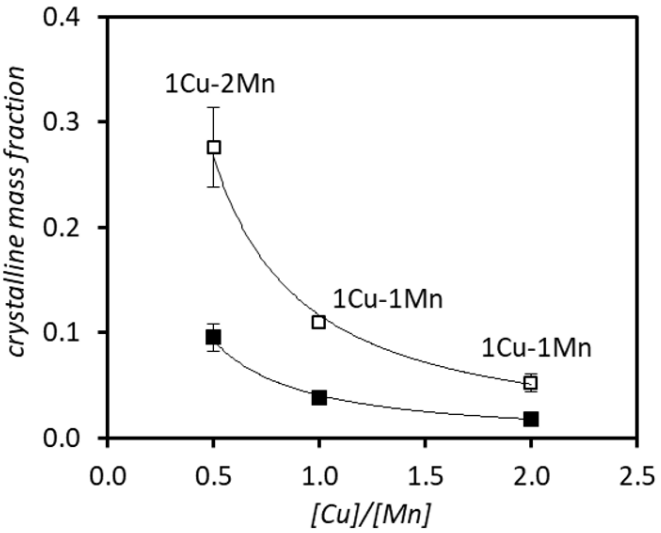


Fig. 5-24 *Mass fractions of the crystalline phase calculated from the XRD patterns from Fig. 5-23 assuming the all crystalline material is either $MnCO_3$ (■) or $Cu_2CO_3(OH)_2$ (□). For a combination $MnCO_3$ and $Cu_2CO_3(OH)_2$ the mass fraction of crystalline material is between the two dotted curves, which are drawn as guidelines.*

The results shown in **Fig. 5-24** suggest that the crystalline mass fraction for the molar 1Cu:2Mn, 1Cu:1Mn and 2Cu:1Mn ratios are in the range of 8.2 – 31.4 wt%, 3.6 – 11.5 wt% and 1.5 – 6.5 wt%, respectively. The increase of the crystalline mass fraction with an increase in [Mn] indicates that the crystalline phases consist predominantly of $MnCO_3$. In this case, the mass fraction of the crystalline material in the precursors of 1Cu-2Mn-CP(3:0), 1Cu-1Mn-CP(3:0), 2Cu-1Mn-CP(3:0) is only 9.6 ± 1.3 wt%, 3.8 ± 0.2 wt% and 1.8 ± 0.3 wt%, respectively (as shown by the black markers in **Fig. 5-24**). This shows that the samples consist predominantly of amorphous Cu and Mn species.

5.4.6 XRD patterns of the co-precipitated oxygen carriers

The precursors of co-precipitated oxygen carriers were calcined for 2 h at 900 °C under air (1 l·min^{-1} at SATP). The calcined materials were crushed and analysed by XRD. The XRD patterns are presented in **Fig. 5-25**, below.

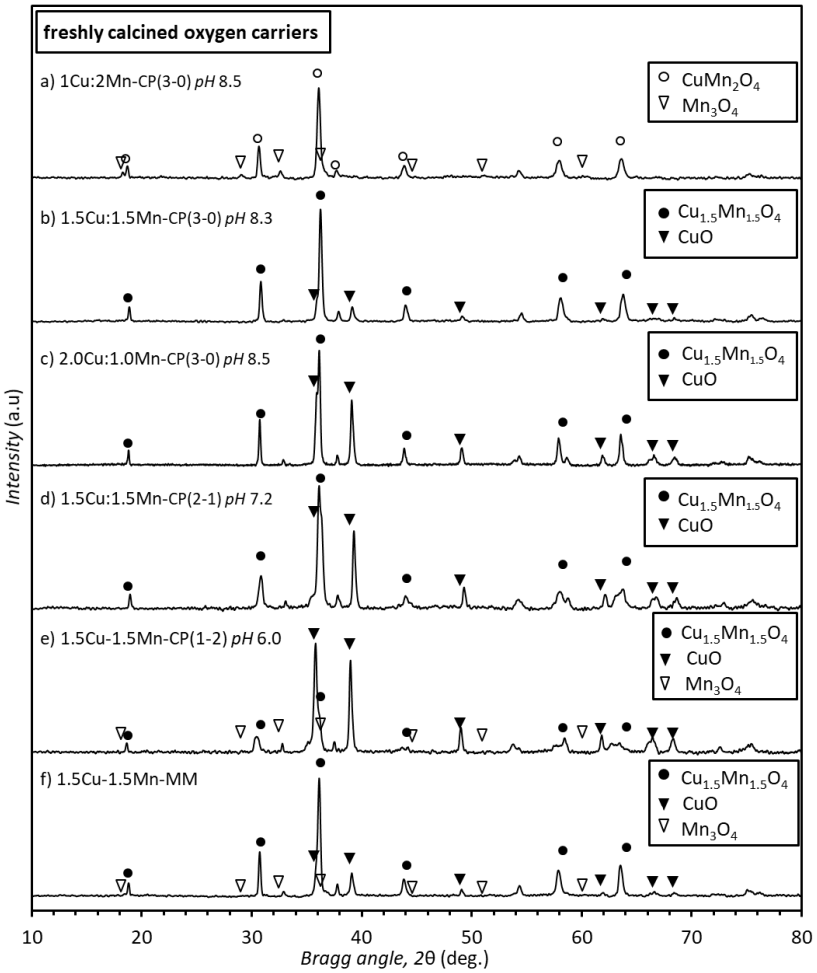


Fig. 5-25 *XRD pattern of the first series of calcined co-precipitated oxygen carriers. The samples (a, b, c) were co-precipitated with 1 M Na_2CO_3 and have the molar composition of (a) 1Cu:2Mn, (b) 1Cu:1Mn, (c) 2Cu:1Mn. The samples (c, d, e) have a molar composition of 1Cu:1Mn and were precipitated with (c) 1 M Na_2CO_3, (d) 0.66 M Na_2CO_3 + 0.66 NaOH, and 0.33 M Na2CO3 + 1.33 M NaOH. During all co-precipitation experiments, the [Na+] in the co-precipitation agent was 2 M.*

In all XRD patterns of the five samples shown in **Fig. 5-25**, copper manganese spinel oxide was identified – a face-centred cubic cell phase, which belongs to the $Fd\bar{3}m$ space group and has the general structure $A_8^{2+}\ B_{16}^{+3}\ O_{32}^{-2}$ with A being either Cu^{2+}or Mn^{2+} and being B is Mn^{3+}. In this work, the structural formula is simplified using the form AB_2O_4. Furthermore, Cu and Mn single metal oxides were identified.

The samples of the XRD patterns shown in **Fig. 5-25a-c** were prepared using the same composition of the co-precipitation agent, but different Cu:Mn molar ratios. In the crushed 1Cu-2Mn-CP(3:0) oxygen carriers (**Fig. 5-25a**), $CuMn_2O_4$ (JCPDS 01-071-1143) was identified as the main phase. Furthermore, minor amounts of Mn_3O_4 (JCPDS 00-024-0734) were identified. The sample 1Cu-1Mn-CP(3:0) (**Fig. 5-25b**) contained mainly $Cu_{1.5}Mn_{1.5}O_4$ (JCPDS 01-070-0262), and small amounts

of CuO (JCPDS 00-045-0937). In the crushed 2Cu-1Mn-CP(3:0) oxygen carriers $Cu_{1.5}Mn_{1.5}O_4$ (JCPDS 01-070-0262) and CuO (JCPDS 00-045-0937) were identified as the main phases. All three samples (**Fig. 5-25a-c**) contained predominantly copper manganese oxide. For the samples with molar ratios of 1Cu:1Mn and 1Cu:2Mn, small amounts of CuO and Mn_3O_4 were identified, while the sample with 2Cu:1Mn contained significant amounts of CuO. This indicates that formation of $Cu_xMn_{3-x}O_4$ with $x \geq 2$ is not favourable, and instead $Cu_xMn_{3-x}O_4$ with $x < 2$ and CuO co-exist in these Cu-rich samples.

The samples of the XRD patterns shown in **Fig. 5-25b**, **Fig. 5-25d** and **Fig. 5-25e** were prepared using the same molar Cu:Mn ratio, but with different compositions of the precipitation agent. The ratio of $[Na_2CO_3]$:[NaOH] was in the order 1Cu-1Mn-CP(3:0) > 1Cu-1Mn-CP(2:1) > 1Cu-1Mn-CP(1:2). In In the crushed 1Cu:1Mn-CP(2:1) oxygen carriers (**Fig. 5-25d**), $Cu_{1.5}Mn_{1.5}O_4$ (JCPDS 01-070-0262) and CuO (JCPDS 00-045-0937) were identified as the main phases. The 1Cu:1Mn-CP(1:2) oxygen carriers (**Fig. 5-25e**) contained mainly CuO (JCPDS 00-045-0937) and Mn_3O_4 (JCPDS 00-024-0734) and only minor amounts of copper manganese oxide ($Cu_{1.5}Mn_{1.5}O_4$; JCPDS 01-070-0262). The increasing substitution of Na_2CO_3 with NaOH, and the required decrease of the *pH* value (to prevent the formation of CuO in the precursor) resulted in a decrease in the fraction of copper manganese oxide, and an increase in the fractions of the single metal oxides.

A second series of co-precipitated oxygen carriers was prepared to further study the effect of the co-precipitation *pH* value, the co-precipitation agent and the molar Cu:Mn ratio. XRD analysis of the oxygen carrier precursors of the second series showed high similarity with those of the first series: predominantly amorphous species precipitated. The XRD patterns are therefore not further discussed in this chapter but are presented in the Appendix in **Fig. A-1**.

The XRD results of the calcined samples with a molar Cu:Mn ratio of 1:2, 1.25:1.75 and 1:1 are shown in **Fig. 5-26**, **Fig. 5-27**, and **Fig. 5-28**, respectively.

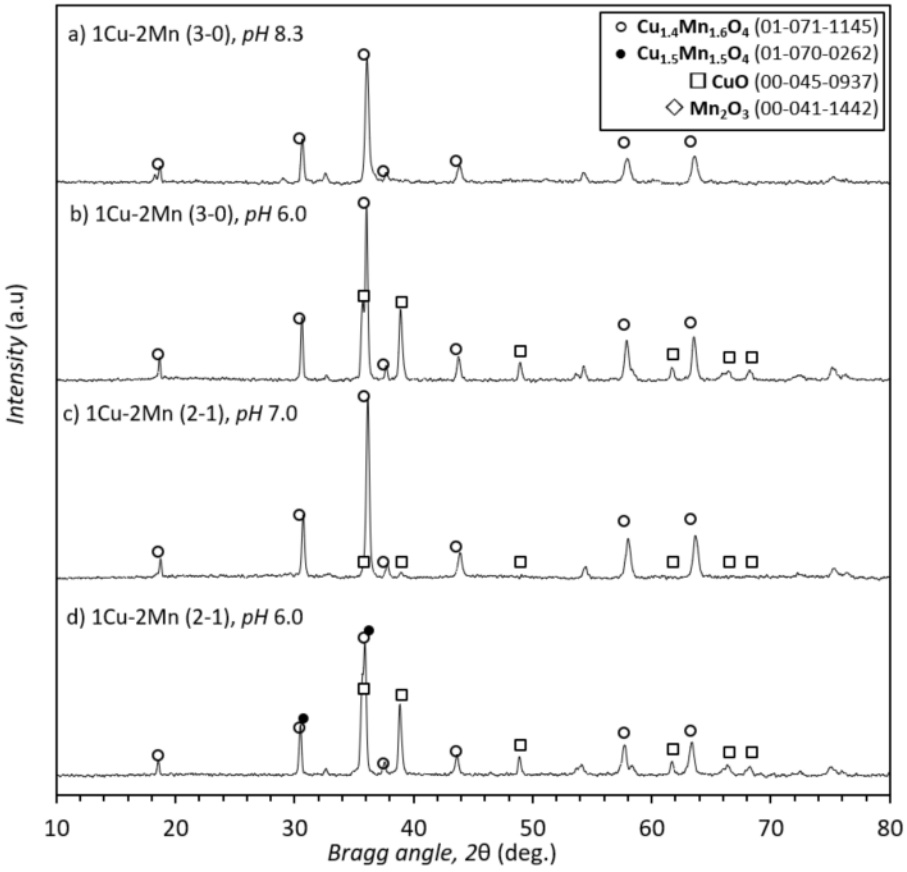


Fig. 5-26 *XRD pattern of the crushed co-precipitated oxygen carrier. The samples have a molar Cu : Mn ratio of 1 : 2, were calcined at 900 °C for 2 h under air, and were prepared using a 1 M Na_2CO_3 and a set pH value of (a) 8.3 and (b) 6.0; and using 0.66 M Na_2CO_3 and 0.66 NaOH and a set pH value of (c) 7.0 and (d) 6.0.*

In the sample, which was prepared with Na_2CO_3 at a higher *pH* of 8.3 (**Fig. 5-26a**) only $Cu_{1.4}Mn_{1.6}O_4$ (JCPDS 01-071-1145) was identified. A reduction of the *pH* value of co-precipitation (**Fig. 5-26b**) resulted in an increase in the fraction of CuO (JCPDS 00-045-0937) and a decrease in the fraction of $Cu_{1.4}Mn_{1.6}O_4$ (JCPDS 01-071-1145). The sample, which was precipitated with a solution containing $[Na^+_{Na_2CO_3}]$: $[Na^+_{NaOH}]$ = 2 and at a *pH* of 7.0 (**Fig. 5-26c**), was found to contain predominantly $Cu_{1.4}Mn_{1.6}O_4$ (JCPDS 01-071-1145) and a minor fraction of CuO (JCPDS 00-045-0937). A reduction of the *pH* value to 6.0 resulted in a substantial increase in the mass fraction of CuO JCPDS 00-045-0937). The copper manganese oxide phase of this sample was in good agreement with the reference pattern for $Cu_{1.4}Mn_{1.6}O_4$ (JCPDS 01-071-1145) and $Cu_{1.5}Mn_{1.5}O_4$ (JCPDS 01-070-0262).

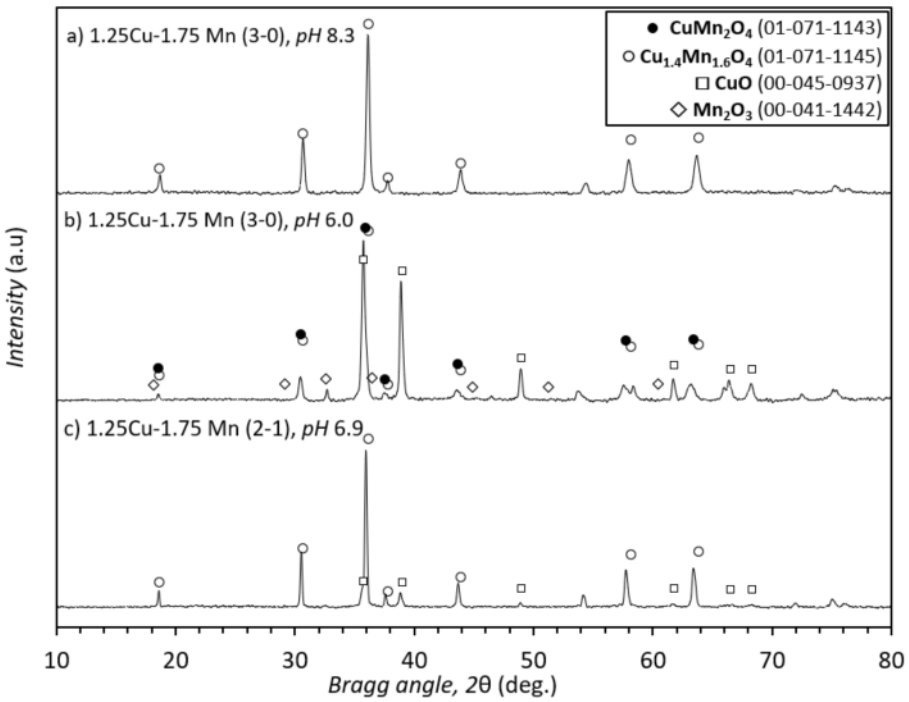


Fig. 5-27 *XRD pattern of the crushed co-precipitated oxygen carrier. The samples have a molar Cu : Mn ratio of 1.25 : 1.75, were calcined at 900 °C for 2 h under air, and were prepared using a 1 M Na_2CO_3 and a set pH value of (a) 8.3 and (b) 6.0; and using 0.66 M Na_2CO_3 and 0.66 NaOH and a set pH value of (c) 6.9.*

In the sample which was prepared with Na_2CO_3 at a higher *pH* of 8.3 (**Fig. 5-27a**) $Cu_{1.4}Mn_{1.6}O_4$ (JCPDS 01-071-1145) was identified as the only phase. A reduction of the *pH* value to 6.0 (**Fig. 5-27b**) resulted in the formation of significant amounts of CuO (JCPDS 00-045-0937) besides copper manganese oxide. The XRD pattern of the latter agrees well with either $Cu_{1.4}Mn_{1.6}O_4$ (JCPDS 01-071-1145) or $CuMn_2O_4$ (JCPDS 01-071-1143). The XRD analysis of the sample prepared with $[Na^+_{Na_2CO_3}]$: $[Na^+_{NaOH}]$ = 2 (**Fig. 5-27c**) suggests that the oxygen carriers contain predominantly $Cu_{1.4}Mn_{1.6}O_4$ (JCPDS 01-071-1145) and only a small fraction of CuO (JCPDS 00-045-0937).

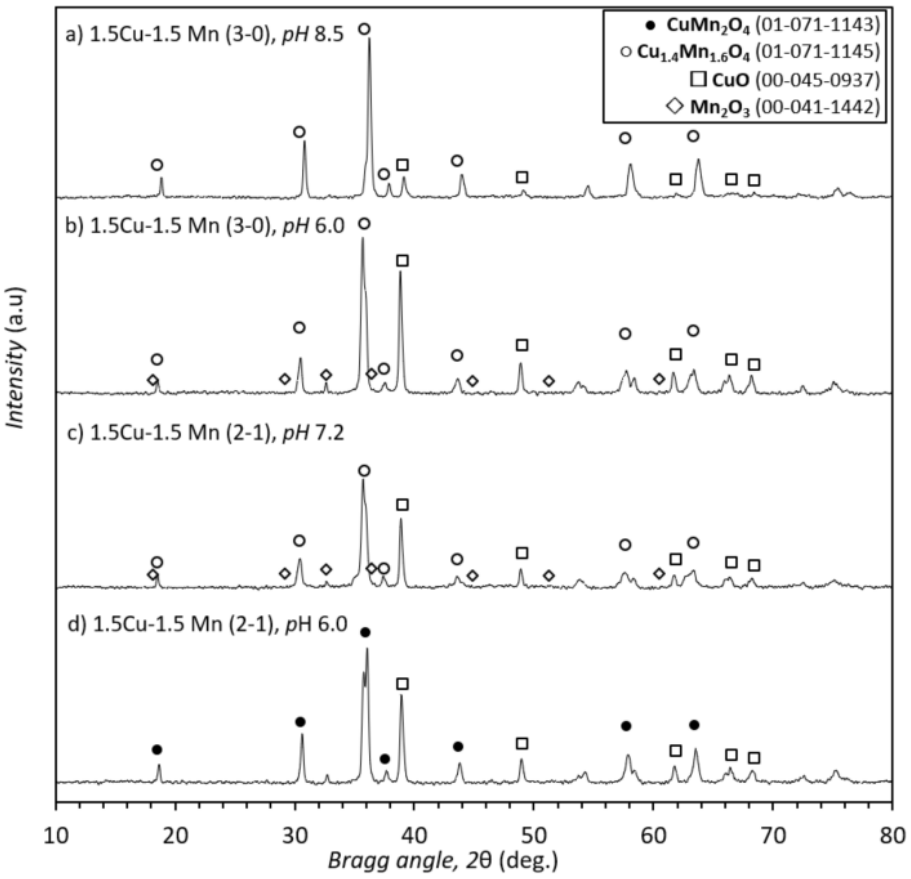


Fig. 5-28 *XRD pattern of the crushed co-precipitated oxygen carrier. The samples have a molar Cu:Mn ratio of 1:1. They were calcined at 900 °C for 2 h under air, and were prepared using a 1 M Na_2CO_3 and a set pH value of (a) 8.5 and (b) 6.0; and using 0.66 M Na_2CO_3 and 0.66 NaOH and a set pH value of (c) 7.2 and (d) 6.0.*

The XRD pattern shown in **Fig. 5-28a** indicates that the sample prepared with Na_2CO_3 at a higher *pH* contained the highest fraction of copper manganese oxide ($Cu_{1.4}Mn_{1.6}O_4$, JCPDS 01-071-1145) and only a small fraction of CuO (JCPDS 00-045-0937). A reduction of the *pH* value of co-precipitation (**Fig. 5-28b**) resulted in a decrease in the fraction of $Cu_{1.4}Mn_{1.6}O_4$ (JCPDS 01-071-1145) and an increase in the fraction of CuO (JCPDS 00-045-0937). Both samples prepared with $[Na^+_{Na_2CO_3}]$: $[Na^+_{NaOH}]$ = 2 (**Fig. 5-28c** and **Fig. 5-28d**) contained significant amounts of copper manganese oxide and CuO (JCPDS 00-045-0937). The copper manganese oxide in the sample precipitated at a *pH* of 7.2 and 6.0 was identified as $Cu_{1.4}Mn_{1.6}O_4$ (JCPDS 01-071-1145) and $CuMn_2O_4$ (JCPDS 01-071-1143), though the structures of most $Cu_xMn_{3-x}O_4$ phases are very similar, which makes their XRD patterns not always clearly distinguishable.

The XRD analysis of the crushed oxygen carriers shown in **Fig. 5-26**, **Fig. 5-27**, and **Fig. 5-28** revealed that generally co-precipitation at the lower *pH* value and the substitution of Na_2CO_3 with NaOH in the co-precipitation agent results in an increase in the fraction of CuO in the sample. The

samples prepared at a higher *pH* value using only Na_2CO_3 for the co-precipitation resulted in materials with a high copper manganese oxide content without any other phases (**Fig. 5-26a** and **Fig. 5-26b**) or with only a small fraction of CuO (**Fig. 5-26c)**.

The mass fractions of the phases form the XRD results shown in **Fig. 5-26**, **Fig. 5-27**, and **Fig. 5-28** were calculated, and the results are presented in **Fig. 5-29**, below.

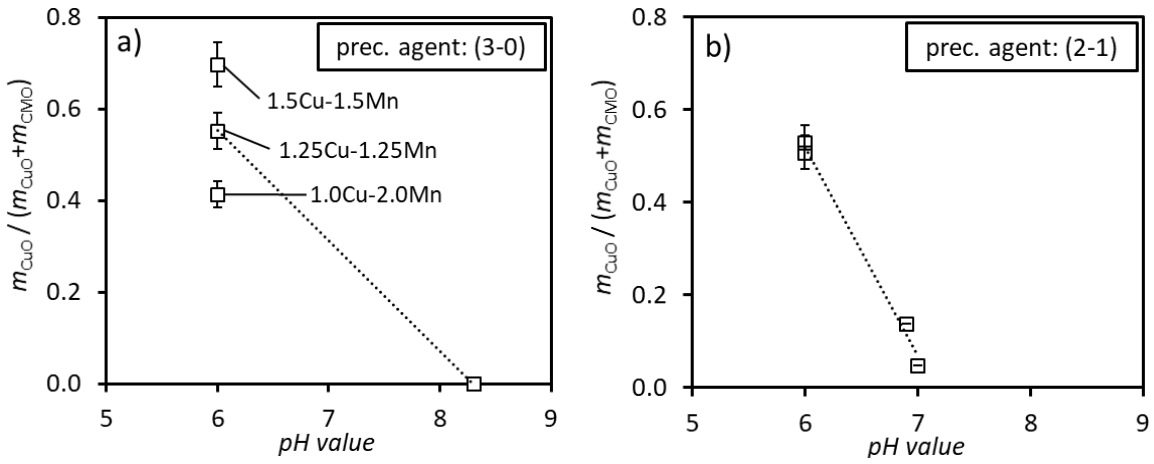


Fig. 5-29 *Mass fractions of CuO (calculated from XRD data using eq.(5-5)) in the calcined co-precipitated oxygen carriers as a function of the co-precipitation pH for oxygen carriers prepared with aqueous solutions containing (a) 1 M Na_2CO_3 and (b) 0.66 M Na_2CO_3 + 0.66 M NaOH. The oxygen carriers were calcined at 900 °C for 2 h in air.*

Fig. 5-29a shows that it was possible to produce an almost CuO-free material using the higher co-precipitation *pH* value (highest possible theoretical *pH* value without the formation of CuO in the precursor). The only phase detected in the 1Cu-1Mn-CP(3:0) *pH* 8.3 was $Cu_{1.5}Mn_{1.5}O_4$. If the initial phases were to persist over repeated redox-cycling, this co-precipitated oxygen carrier containing only $Cu_{1.5}Mn_{1.5}O_4$ would have a superior oxygen release capacity over the mechanically mixed oxygen carrier with the same molar Cu:Mn ratio (1Cu-1Mn-MM) containing $CuMn_2O_4$ and CuO. However, it is possible that the copper manganese oxides and the copper oxides in the mechanically mixed oxygen carriers combined to form $Cu_{1.5}Mn_{1.5}O_4$ during redox-cycling, which would diminish this advantage. This was tested during TGA experiments, as detailed in the next chapter.

5.4.7 XRD patterns of the mechanically mixed oxygen carriers

The oxygen carriers that were prepared by mechanical mixing according to the standard synthesis protocol (*c.f.* **Table 4-6**) were crushed and analysed by XRD. The results are shown in **Fig. 5-30**, below.

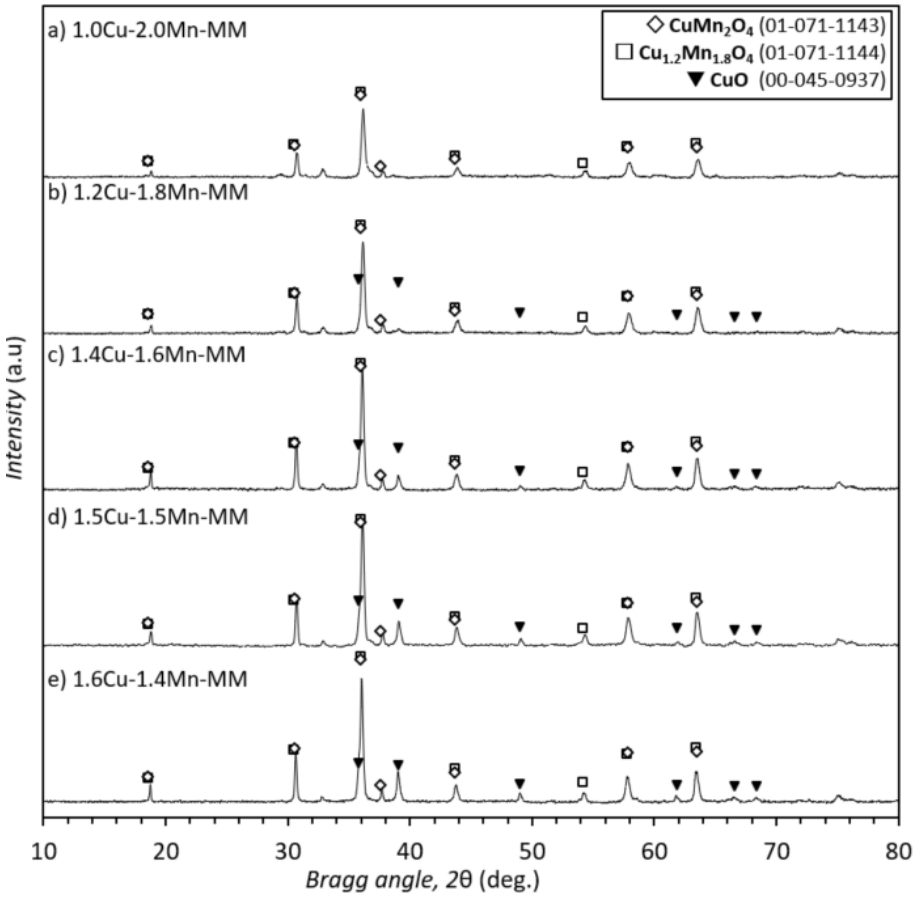


Fig. 5-30 *XRD pattern of the mechanically mixed oxygen carriers with varying molar Cu:Mn ratio preapred using the standard synthesis procedure shown in Table 4-6 and calcined at 950 °C for 6 h.*

In all mechanically mixed oxygen carriers that were studied by XRD as shown in **Fig. 5-30**, copper manganese oxide was identified with the diffraction peaks agreeing very well with $CuMn_2O_4$ (JCPDS 01-071-1143) and $Cu_{1.2}Mn_{1.8}O_4$ (JCPDS 01-071-1144). In the 1Cu-2Mn-MM oxygen carriers (**Fig. 5-30a**) no peaks of single metal oxides were identified. In all other samples (**Fig. 5-30b-e**) CuO (JCPDS 00-45-0937) was also identified, while the observed intensity of the CuO-peaks increases with an increase in the molar Cu:Mn ratio of the oxygen carriers. The mass fractions of the phases were calculated using the 'relative intensity ratios' method (*c.f.* eq.(5-5a) and eq.(5-5b) in section 5.4.2).[24] The results are presented in **Table 5-8**, below.

Table 5-8 *The mass fractions of the phases identified in the mechanically mixed unsupported oxygen carriers calculated using XRD data.*

Sample	$Cu_xMn_{3-x}O_4$[a]	Mn_2O_3	MnO_2	CuO
the results of mechanically mixed oxygen carrier calcined at 950 °C for 6 h with various Cu:Mn molar ratios:				
1Cu-2Mn, MM	1.00	-	-	-
1.2Cu-1.8Mn, MM	0.87	0.06	-	0.07
1.4Cu-1.6Mn, MM	0.70	-	0.16	0.14
1Cu-1Mn, MM	0.74	-	-	0.26
1.6Cu-1.4Mn, MM	0.68	-	-	0.32
I/I_0 of the phase:	4.93[a]	4.5	0	2.8
position of peak used for quantification, 2θ:	36.1°	32.9°	28.9°	38.7°

Footnotes: (a) The calculation of $Cu_xMn_{x-3}O_4$ in the range of $1 \leq x \leq 1.5$ is possible without the specification of x, because the relative intensities, I/I_0, of the copper manganese oxides in this x-range are almost identically (e.g. the literature values of I/I_0 of $CuMn_2O_4$ and $Cu_{1.5}Mn_{1.5}O_5$ are 4.93 and 4.92, respectively).[212]

The data in **Table 5-8** shows that the mass fraction of copper manganese oxide is decreasing with an increase in the molar Cu:Mn ratio. To elucidate the reason, the mass fraction of CuO was plotted against x in $Cu_xMn_{3-x}O_4$, in **Fig. 5-31**, below.

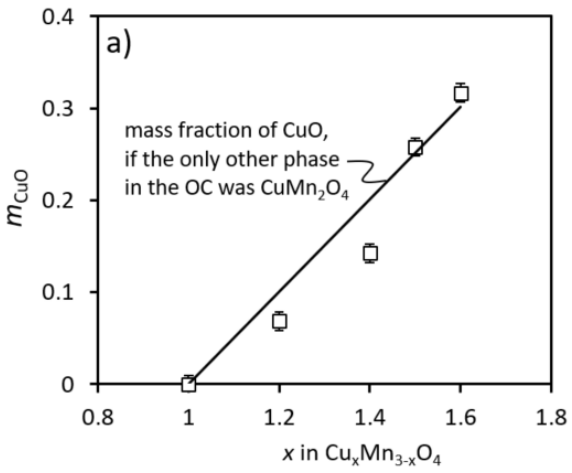


Fig. 5-31 *Mass fractions of CuO in the calcined mechanically mixed oxygen carriers calculated from XRD data using eq.(5-5).*

In addition to the calculated mass fractions of CuO in the samples, a line is drawn onto the graph (**Fig. 5-31**), which would correspond to the mass fraction of CuO if the sample contained only CuO and $CuMn_2O_4$. The good agreement between the experimentally obtained points and the line at x = 1.5 and x = 1.6 suggests that in these samples only CuO and $CuMn_2O_4$ exists. At x = 1.2 and x = 1.4

the calculated CuO mass fractions are below the line, which indicates that other copper manganese oxide phases – such as $Cu_{1.2}Mn_{1.8}O_4$, $Cu_{1.4}Mn_{1.6}O_4$, $Cu_{1.5}Mn_{1.5}O_4$ – exist. This indicates that the formation of $Cu_xMn_{3-x}O_4$ phases with $x \geq 1$ is not favourable in the molar Cu:Mn ratio range of 1:1 – 1.6:1.4 and only partially favourable for the molar Cu:Mn ratio range 1.2:1.8 – 1.4:1.6. When preparing oxygen carriers with this composition *via* co-precipitation the formation of $Cu_xMn_{3-x}O_4$ phases with $x \geq 1$ was possible (see **Fig. 5-27**, and **Fig. 5-28**) and a copper manganese oxide mass fraction of unity or close to unity was achieved. This could provide the co-precipitated oxygen carrier with a significant advantage during CLAS operation at lower temperatures, at which the CuO in the mechanically mixed oxygen carriers remains inert, thereby resulting in a significantly lower oxygen release capacity.

5.5 Quantitative analysis by X-ray fluorescence

X-ray fluorescence (XRF) analysis was carried out in an AXS S4 Explorer (Bruker) to quantify the mass fraction of the impurities in the powders used for the preparation of the mechanically mixed oxygen carrier (section 5.5.1), and to confirm the Cu:Mn molar ratios of the co-precipitated oxygen carrier (section 5.5.2).

5.5.1 Measurement of the mass fraction of impurities in the reagents

The results of the XRF analysis for the quantification of the mass fractions of impurities in powders used for the preparation of the oxygen carriers are presented in **Table 5-9**, below.

Table 5-9 *Mass fractions of the powders used for the preparation of the mechanically mixed oxygen carriers and of the quartz sand used as an inert bed material during fluidised bed reactor experiments, measured by XRF.*

CuO powder (Sigma Aldrich)		MnO powder (Sigma Aldrich)		TiO_2 powder (Sigma Aldrich)		ZrO_2 powder (Sigma Aldrich)		quartz sand	
elem.	wt% [a]	elem.	wt% [a]	elem.	wt% [a]	elem.	wt% [a]	elem.	wt% [a]
Cu	99.86	Mn	99.71	Ti	99.52	Zr	97.34	Si	98.31
Tb	0.06	Pr	0.17	K	0.25	Hf	2.47	Al	0.83
Cd	0.03	Nd	0.05	P	0.12	Ti	0.08	Fe	0.28
Tm	0.02	Lu	0.03	Sm	0.03	Al	0.04	S	0.17
Te	0.01	Lu	0.02	Bi	0.03	Fe	0.02	K	0.12
P	0.01	Hf	0.01	Nb	0.02	Pb	0.01	Cl	0.08
Si	0.01	Hg	0.01	Mn	0.01	V	0.01	Ca	0.07
-	-	Te	0.01	Te	0.01	-	-	Ti	0.07
-	-	Si	0.01	Zr	0.01	-	-	Te	0.03
-	-	-	-	-	-	-	-	Zr	0.02
-	-	-	-	-	-	-	-	Sn	0.02

Footnotes: This analysis excludes oxygen, carbon, nitrogen and hydrogen.

Table 5-9 confirms that the purity of the CuO, MnO and TiO_2 powders is > 99.5 wt%. The low mass fraction of the impurities is not expected to influence the experimental results significantly. The ZrO_2 powder contains 2.47 wt% Hf. To assess whether the Hafnium(IV) oxide participates in the redox-reactions and Ellingham diagram was generated using the data from FactSage, as shown in **Fig. 5-32**, below.

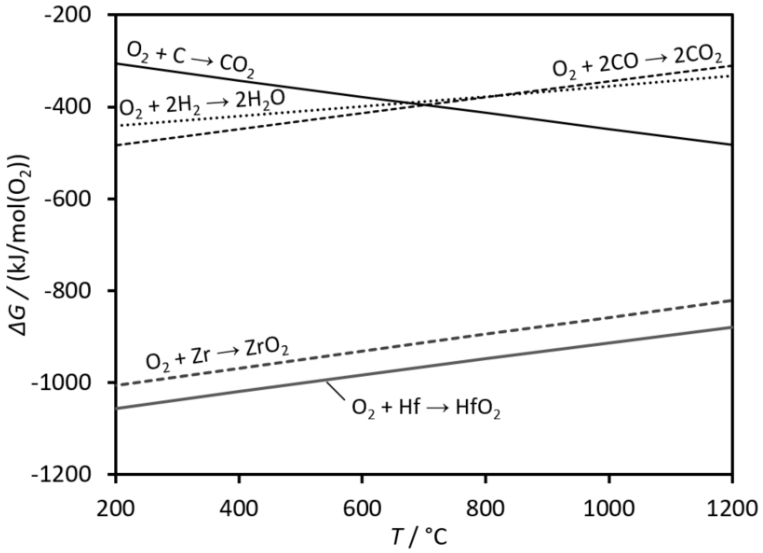


Fig. 5-32 *Ellingham diagram for the oxidation of Zr and Hf and the redox reactions relevant the chemical looping processes.*

The Ellingham diagram (**Fig. 5-32**) shows that the HfO_2 – and impurity of the ZrO_2 powder and thus of the ZrO_2-supported oxygen carriers – does not participate in the redox-reactions, since the ΔG of the oxidation of Hf is larger than the ΔG of the oxidation of the fuel across the studied condition range. Therefore, the HfO_2 remains in its fully oxidised state.

Furthermore, XRF was used to quantify the molar Cu:Mn ratio of the co-precipitated oxygen carriers. The experimental procedure and the results of these measurements are reported in the following sub-section.

5.5.2 Determination of the Cu:Mn molar ratio of the co-precipitated oxygen carriers

To quantify the Cu:Mn molar ratios of the co-precipitated oxygen carriers, a calibration was carried out using mechanically mixed oxygen carriers with a molar Cu:Mn ratio between 1:1 and 1:1.6, a sample mass of 1.5 g and a particle size range of 300 - 425 µm. The mechanically mixed oxygen carriers were prepared with known quantities of Cu and Mn and it is therefore assumed that the molar Cu:Mn ratio did not change during the preparation, *e.g.* no loss of Cu and Mn occurred during the preparation or loss of Cu and Mn during preparation was proportional to the initial molar Cu:Mn

ratio. The measured mass fraction ratios were plotted against the actual mass fraction ratios (**Fig. 5-33a**) to obtain a correlation to correct the measurements. Furthermore, it was tested whether the sample mass is sufficient to ensure that the height of the sample in the sample holder is larger than the penetration depth of the x-rays across the entire kV-range (the kV changes for the detection of different elements). If the sample bed height is insufficient (*i.e.* sample bed height < x-ray penetration depth), then x-rays escape during measurements at certain kV-range, while during other measurements all x-rays stay within the sample, which would lead to an error in the mass-fraction measurements. To ensure that the sample bed height is sufficient an experiment was carried out in which the sample mass was varied, as shown in **Fig. 5-33b**, below.

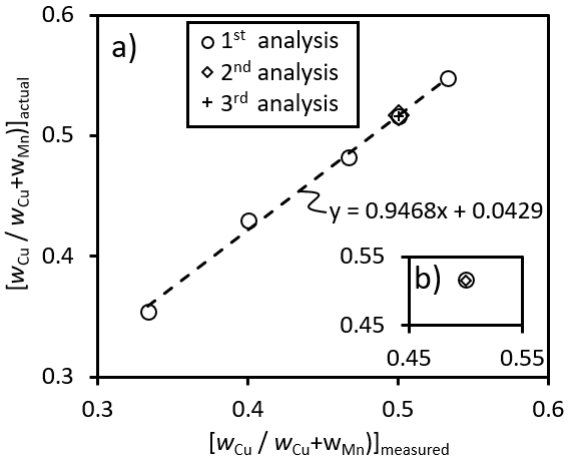


Fig. 5-33 *The results of the XRF calibration and validation experiments: (a) a plot of the mass fractions of mechanically mixed oxygen carriers measured by XRF against the actual fractions for the determination of a calibration function; (b) the mass fraction of the 1Cu-1Mn-MM using a sample mass of 1.5 g (○) and a sample mass of 4.0 g (◇).*

Fig. 5-33a shows that the relationship between the actual and the measured mass fractions can be well described (R^2 = 0.997) by a linear function. The standard deviation of three repeated measurements was 0.24%. Based on this value an uncertainty of 0.5% within a 95% confidence interval was calculated, assuming the deviation follows a normal distribution. An increase in the sample mass from 1.5 g to 4.0 g (**Fig. 5-33b**) resulted in variation of the calculated Cu:Mn ratio of 0.12%, which is below the uncertainty of the measurements and it is therefore assumed that the distance between the top and the bottom of the sample is larger than the penetration distance of the x-rays. Following this calibration and validation of the experimental set-up, the mass fractions of the co-precipitated samples were analysed by XRF. The data was corrected using the linear correlation (**Fig. 5-33a**) and converted to molar fractions using the relative molecular masses of Cu and Mn.

The results of the measurements are shown in **Table 5-10**, below.

Table 5-10 *The Cu:Mn molar ratios of the crushed oxygen carriers determined by XRF.*

sample	*pH* value[a]	Cu:Mn molar ratio[b,c]	sample	Cu:Mn molar ratio[b,c]
co-precipitated unsupported oxygen carrier:			*mechanically mixed oxygen carrier:*	
1Cu-2Mn-CP(3:0)	8.3	1.024 : 1.976	1Cu-2Mn-MM	1.020 : 1.980
1Cu-1Mn-CP(3:0)	8.3	1.469 : 1.531	1.2Cu-1.8Mn-MM	1.243 : 1.757
2Cu-1Mn-CP(3:0)	8.3	2.040 : 0.960	1.4Cu-1.6Mn-MM	1.400 : 1.600
1Cu-2Mn-CP(2:1)	7.0	1.345 : 1.655	1Cu-1Mn-MM	1.501 : 1.499
1Cu-1Mn-CP(2:1)	7.0	1.588 : 1.412	1.4Cu-1.6Mn-MM	1.595 : 1.405
1Cu-1Mn-CP(2:1)	6.0	2.049 : 0.951		

Footnotes: (a) this is the pH value set during the co-precipitation, which was maintained within ± 0.1; (b) the measured molar fractions were corrected using the equation shown in Fig. 5-33a; (c) the uncertainty of the measured molar fractions is 0.5%, and was determined by repeating the measurement for 1Cu-1Mn-MM three times.

The Cu:Mn molar ratio of the three co-precipitated standard oxygen carriers of this work 1Cu-2Mn-CP(3:0), 1Cu-1Mn-CP(3:0) and 2Cu-1Mn-CP(3:0) differ from the target composition by 4-6 % (three first entries in **Table 5-10**), which is deemed acceptable. However, the Cu:Mn molar ratio of the oxygen carriers co-precipitated with a lower $[Na_2CO_3]$:[NaOH] and at a lower *pH* differ significantly from the target molar ratio. This indicates that the driving force was insufficient for the precipitation of all Mn species during the duration of the precipitation experiment. Using the theory of co-precipitation that was introduced in section 3.4.3 and the equilibrium plots for the precipitation experiments in 4.1.1, it becomes apparent that at a lower *pH* value the driving force for the precipitation of Cu species is larger than of the Mn species. This might thermodynamically favour the precipitation of Cu species over that of Mn species on the nuclei, which were formed during a probably short nucleation regime (*c.f.* textured area in **Fig. 3-14**). A reduction in the precipitation of Mn species is likely to cause a reduction of the surface area of the calcined samples, as less carbonates are formed, which function as a blowing agent. They release gaseous CO_2 during the heating process of the calcination, which forms pores. While Cu species were found to predominantly precipitate as amorphous material, Mn precipitates as a combination of amorphous material and $MnCO_3$ (*c.f.* section 5.4.5). Therefore, less precipitated Mn species result in less $MnCO_3$, and thus a material with a lower porosity. However, deviations of the composition from the target composition are never ideal. Therefore, samples in which the Cu:Mn molar ratio (measured by XRF) deviated from the target by more than 6% (*e.g.* owing ot incomplete precipitation) were not further considered in the following chapters.

5.6 Scanning electron microscopy and the determination of the grain sizes

The surface morphology of the oxygen carriers was studied by scanning electron microscopy (SEM) using a LEO Gemini 1525 at 10 kV. Particles were loaded onto an SEM stub using double sided carbon tape and sputter coated with gold for 30 s at 20 mA to improve their conductivity, which corresponds to a thickness of about 5 nm. SEM was also used to conduct electron-dispersive spectroscopy (EDS) to examine the ion dispersion by elemental mapping. The freshly calcined oxygen carriers were examined by SEM. Selected SE micrographs are shown in **Fig. 5-34**, below.

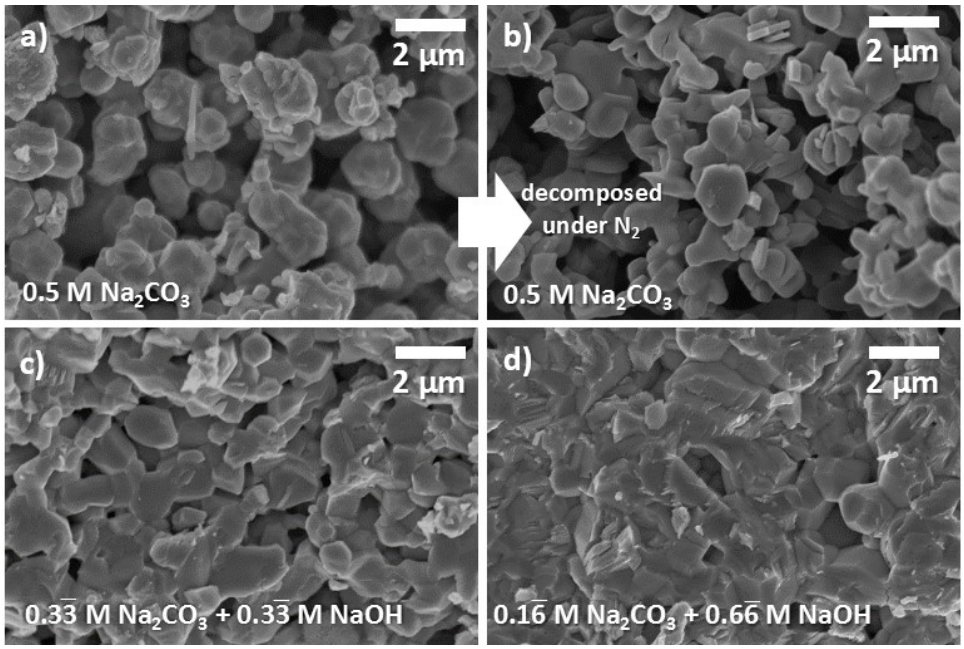


Fig. 5-34 *Scanning electron micrograph of 1Cu-1Mn oxygen carrier calcined under 1 l·min^{-1} air at 980 °C and 6 h. Sample (a) and (b) were co-precipitated with 0.5 M Na_2CO_3 at a constant pH of 8.3 and are the fully oxidised and N_2-decomposed state; Sample (c) was prepared at a constant pH of 7.2 with 0.33 M Na_2CO_3 + 0.33 M NaOH, and sample (d) was co-precipitated at a constant pH of 7.0 with 0.16 M Na_2CO_3 + 0.66 M NaOH. An increase in porosity with a decreasing [Na_2CO_3]/[NaOH] is clearly visible.*

5.6.1 Grain size measurements

The distribution of the average diameter of the metal oxide grains was measured using the ASTM E1382-97 method,[216] for which ten diagonal lines from the top-right to the bottom-left and from the top-left to the bottom-right are drawn. The size of the grain at which the diagonal lines crossed was measured. To evaluate the uncertainty of this method three different SE micrographs of the same sample (1Cu-1Mn-CP(3:0)) were analysed, one of which is shown in **Fig. 5-35a**. The mean grains size, d_g, of the three repeats were 1.566 µm, 1.490 µm and 1.572 µm. The standard deviation of the

results is 2.9%, and the relative uncertainty of the measurement, $u(d_g)$, was therefore estimated to be $0.06 \cdot d_g$. The relatively low value of $u(d_g)$ suggests that this method is well suited for the estimation of the mean grain size. However, it should be noted that the mean grain size might vary by area across the sample. These grain size measurements should therefore only be taken as an approximation of the samples mean grain size.

As the grain-size was found not to follow a normal distribution, other distribution functions were tested. The log-normal distribution[217],

$$p(d_g) = \frac{1}{\sqrt{2\pi}\sigma_{lm} d_g} \cdot \exp\left(- \frac{\ln\left({d_g}/{(d_g)_{lm}} \right)^2}{2 \cdot \sigma_{lm}^2} \right), \tag{5-7}$$

was found to represent the probability density of the grains' characteristic length best. In eq.(5-7) d_g is the average diameter of a grain in µm calculated by $d_g = (d_{g,max} + d_{g,min})/\,2$, $(d_g)_{lm}$ is the mean deviation and σ_{lm} the standard deviation of $\ln(d_g)$. The aspect ratio (R_A) was calculated by,

$$A_R = \frac{d_{g,min}}{d_{g,max}}, \tag{5-8}$$

where $d_{g,min}$ and $d_{g,max}$ are the minimum and maximum diameter of a grain. The log-normal distribution of the different samples was used to determine the most probable range of the characteristic length of the platelets, with 95% confidence for the grain models of the reaction rate, discussed later in chapter 7. The results of the measurements are shown in **Fig. 5-35**, below.

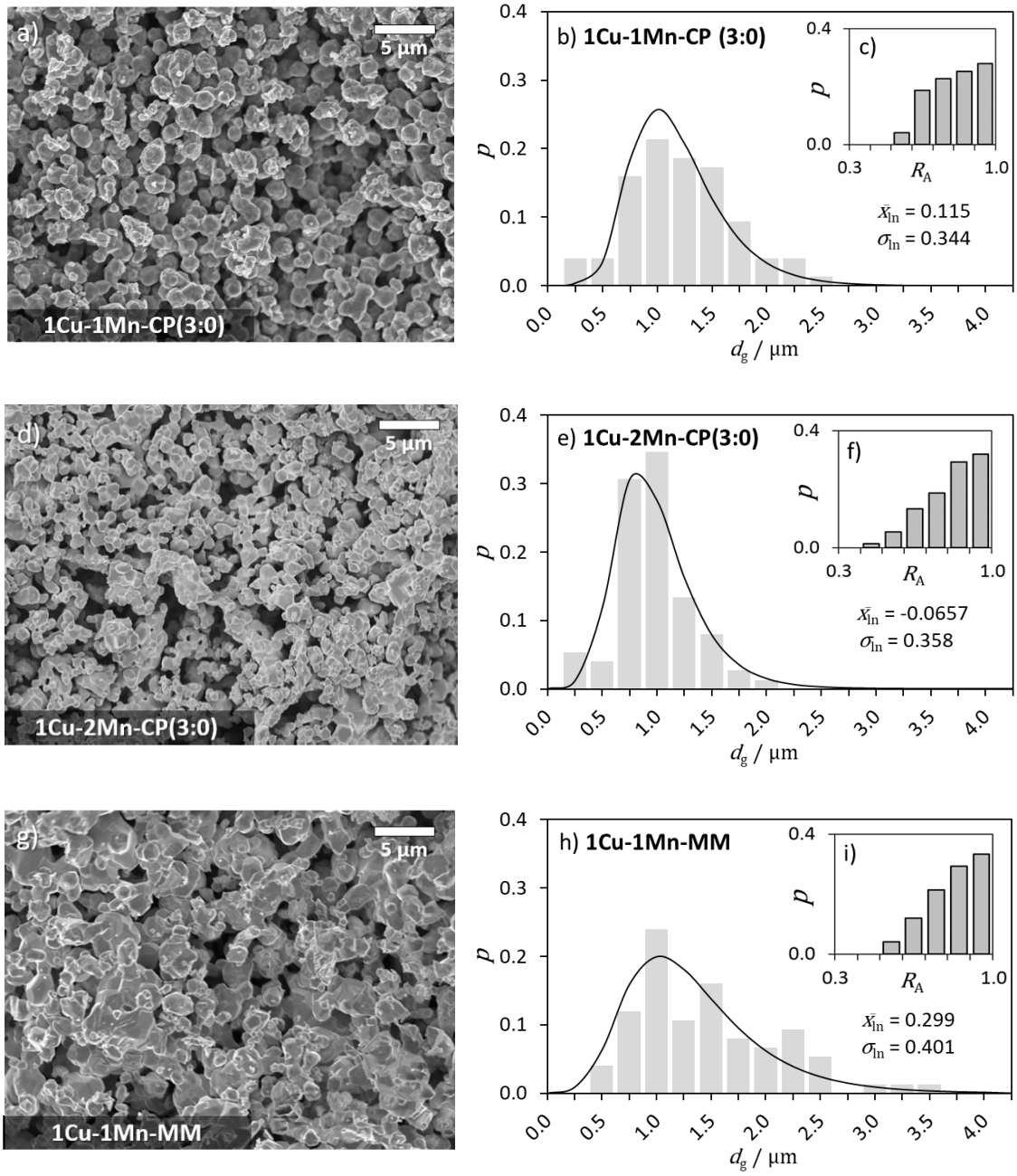


Fig. 5-35 *SE micrographs for and results from the grain size measurements of (a, b, c) 1Cu-1Mn-CP(3:0), (d, e, f) 1Cu-2Mn-CP(3:0), and (g, h, i) 1Cu-1Mn-MM; (a, d, g) are the SE micrographs used for this analysis, (b, e, h) are the calculated probability densities of the average grain diameter (grey bars on main graph) using a bin size of 0.25 µm, their log-normal distribution functions (solid lines) calculated by eq.(5-7) with parameter specified on the plot areas, and (c, f, i) are the probability densities of the aspect ratios of the grains with bin size of 0.9 calculated by eq.(5-8). The sample size is 75 grains per SE micrograph.*

The cumulative variant of the log-normal distribution was used to calculate the average grain diameter, below which statistically 2% ($d_{g,0.02}$), 50% ($d_{g,0.50}$), 98% ($d_{g,0.98}$) of the grains are fall. The results are summarised in **Table 5-11**, below.

Table 5-11 *The results of the cumulative log-normal distribution function using the data from the grain size assessment.*

Sample	$d_{g,0.02}$ / µm	$d_{g,0.50}$ / µm	$d_{g,0.98}$ / µm	$d_{g,0.98} - d_{g,0.02}$ / µm
1Cu-1Mn-CP	0.551	1.122	2.270	1.719
1Cu-2Mn-CP	0.452	0.936	1.949	1.497
1Cu-1Mn-MM	0.587	1.349	3.076	2.489

The grains of the mechanically mixed samples have the largest grain diameter ($d_{g,0.50}$ = 1.349 µm) and the widest distribution ($d_{g,0.98}$ - $d_{g,0.02}$ = 2.489 µm), this might be a result of imperfect grinding and mixing in the planetary ball mill. The smallest mean grain size and narrowest grain size distribution has the sample 1Cu-2Mn-CP(3:0). This indicates that the co-precipitation at these conditions is relatively effective in controlling the grain size diameter. The results of this grain size assessment will be used in chapter 7 to model the reaction rate function using the grain model.

Further SEM results of fresh and cycled oxygen carriers are presented and discussed in the following chapters in the sections on long-term cycling tests in the thermogravimetric analyser and in the fluidised bed.

5.7 Thermo-gravimetry evolved gas analysis mass spectrometry

Mass spectrometry (MS) was used in combination with a TGA type TG 209F1 Libra (NETZSCH) to determine the gas species that are released during the thermal decomposition of the precursor to elucidate the process of the formation of the copper manganese oxide. About 30 mg of the precursor were loaded into an alumina crucible. In a typical TGA-MS experiment, the sample was exposed to air (50 ml min^{-1} at SATP) and the temperature was increased to 950 °C with a heating rate of 5 K min^{-1}. During the experiment, the TGA measured the mass of the sample and the MS measured the ion current of the gas species with the atomic mass 12 u, 18 u, 28 u, 30 u, 32 u, 44 u, and 46 u, which correspond to the masses of the atoms or molecules C, H_2O, CO, NO, O_2, CO_2 and NO_2. The signal of the ion currents (IC) were normalised with $(IC\text{-}IC_{min})/(IC_{max}\text{-}IC_{min})$. The results of the experiments are shown in **Fig. 5-36**, below.

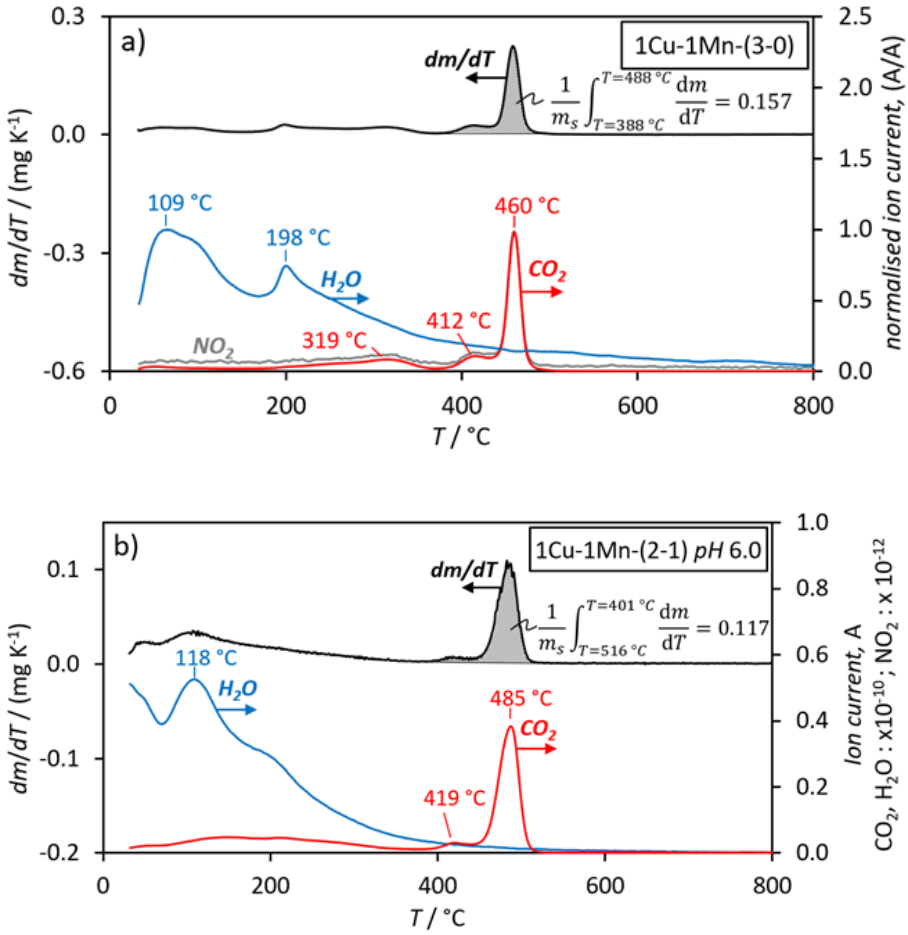


Fig. 5-36 *A plot of the rate of mass change and the ion currents of the atomic masses that correspond to CO_2 and H_2O measured during the thermal decomposition of the precursor (a) 1Cu-2Mn-(2:1)pH7.0, (c) 1Cu-1Mn-CP(2:1)-pH6.0 in the TG-MS under air. A sample gas flow rate of 50 ml min^{-1} (at SATP) and a heating rate of 5 K min^{-1} was used.*

Fig. 5-36a shows that the precursor releases H_2O mainly at temperatures below 400 °C. The ion current that corresponds to the atomic mass of H_2O has a peak at 109 °C and 198 °C, which are attributed to the evaporation of moisture and the thermal decomposition of Cu and Mn hydroxides. Though, the rate of mass change (black line in **Fig. 5-36a**) shows that these are rather minor quantities. The ion current that corresponds to the atomic mass of CO_2 peaks at 412 °C and 460 °C, which is attributed to the release of CO_2 due to the thermal decomposition of Cu and Mn carbonates. The mass lost during this decomposition (*c.f.* Integral in **Fig. 5-36a**) corresponds to 15.7 wt% of the initial precursor mass. **Fig. 5-36b** shows the evaporation of water (peak at 118 °C) and the decomposition of Cu and Mn carbonates (peaks at 419 °C and 485 °C). Here the integrated area corresponds to only 11.7 wt% of the initial precursor mass. This supports the theory from section 4.1.1, 5.1, 5.4.5 and 5.5 that a lower co-precipitation *pH* value and a lower $[Na_2CO_3]$:[NaOH] resulted in less $MnCO_3$, which in turn releases less CO_2 during the thermal decomposition, resulting in a lower pore volume.

5.8 Concluding remarks

The BET surface area, S_{BET}, of the oxygen carriers were measured by N_2 physisorption experiments at 77 K. The values of S_{BET} for the oxygen carriers from the twelve co-precipitated batches prepared using the standard synthesis procedure were in the range 0.17 - 0.91 m^2/g. The *pH* value during the co-precipitation was found to have the largest effect on S_{BET} (a higher *pH* value results in a higher S_{BET}). The second largest effect on S_{BET} had the molar Cu:Mn ratio (a higher Cu-content resulted in a lower S_{BET}), and the least large effect on S_{BET} had the co-precipitation agent (a substitution of Na_2CO_3 with NaOH reduced S_{BET} only slightly). A correlation has been developed to forecast the S_{BET} based on these three co-precipitation variables.

The S_{BET} of the series of micro-structured oxygen carriers, which was prepared *via* co-precipitation at higher super-saturation (a deviation from the standard synthesis procedure) was in the range of 20.7 – 25.8 m^2/g. Some unwashed precursors were re-filled into auto-claves, and were kept in their supernatant for 8 to 72 h to study the effect of ageing at temperatures between 80 °C and 125 °C. An increase in ageing time from 8 h to 72 h was found to decrease the surface area from an average of 25.1 m^2/g to 22.7 m^2/g, and an increase in the ageing temperature was found to decrease the surface area from an average of 24.0 m^2/g to 23.4 m^2/g. It was concluded that the ageing at those conditions does not increase the S_{BET}. During calcination at 600 °C and 900 °C the surface area of the micro-structured oxygen carrier was reduced to 7.9 – 12.7 m^2/g and 2.3 – 5.0 m^2/g. The crushing force of all calcined high-surface area oxygen carriers was below the minimum limit of the measurements at 0.5 N. This low mechanical stability would have been insufficient to withstand stresses in the fluidised bed reactor and would have caused disintegration of the oxygen carriers over the first cycles in the fluidised bed reactor. Therefore, these high-surface oxygen carriers were not investigated any further.

The values of S_{BET} for the unsupported mechanically mixed oxygen carriers was found to be in the range 0.22 - 0.34 m^2/g and increased with an increase in the molar Cu:Mn ratio. The effect of two pore-forming agents (microcrystalline cellulose (MCC) and starch) were tested. The addition of MCC resulted in a pore structure with more smaller pores, which resulted in an increase in the surface area, while leaving the cumulative pore volume mostly unchanged. The addition of starch resulted in a pore structure with fewer larger pores, resulting in a larger cumulative pore volume, while not affecting the surface area significantly.

The S_{BET} of the TiO_2, Al_2O_3 and ZrO_2-supported oxygen carriers was found to be 0.30 m^2/g, 0.75 m^2/g, 2.00 m^2/g, respectively. The values of the particle porosities follow the same order, as do the Tammann temperatures of these supporting materials: TiO_2 (789 °C) < Al_2O_3 (884 °C) < calcination temperature (950 °C) < ZrO_2 (1214 °C). An insufficient rate of solid-state diffusion of ZrO_2 might

have inhibited the densification of the ZrO_2-supported oxygen carriers during calcination. It is suggested for future work to test liquid phase sintering (LPS) for ZrO_2-supported oxygen carriers.

The average force required to crush an oxygen carrier particle, σ_{CF}, of the unsupported co-precipitated oxygen carriers (prepared by the standard synthesis procedure) was measured to be in the range of 0.76 – 9.12 N. The σ_{CF} was found to increase with a decrease in S_{BET}, and it was demonstrated that careful selection of the co-precipitation conditions can result in an increase of σ_{CF} by more than an order of magnitude. The values of σ_{CF} for the mechanically mixed unsupported oxygen carriers were found to be in the range between 3.27 – 5.18 N. The crushing strength of the supported oxygen carriers was: TiO_2 (5.48 ± 0.28 N) > ZrO_2 (1.84 ± 0.28 N). An increase in σ_{CF} due to the introduction of a supporting material was not observed. It might be worthwhile testing higher calcination temperatures (*i.e.* for liquid phase sintering) to increase the wettability and the bonding between the copper manganese oxide and the inert phase.

Pycnometry experiments with He were carried out to calculate the skeletal density of the samples, which ranged between 5.02 – 5.80 $cm^3\ g^{-1}$ and 4.22 – 5.39 $cm^3\ g^{-1}$ for the unsupported and supported oxygen carriers, respectively. The values of the densities were on average 6% higher than the values for ideal $Cu_xMn_{x-3}O_4$ materials calculated using DFT theory.[211] The deviations suggest that not all single metal oxides had fully combined into copper manganese oxides. The measured values were combined with data from mercury intrusion porosimetry (MIP) to iteratively calculate the porosity for pores in the size range 5.5 nm – 10 µm and the envelope density. The porosity of the unsupported co-precipitated and mechanically mixed oxygen carriers was found to be in the range 0.009 – 0.565 and 0.255 – 0.359, respectively. This shows that the preparation of CMO oxygen carriers by co-precipitation allows control of the porosity over a relatively wide range. Plots of the differential intrusion (*DI, with DI* > 0.001 ml g^{-1} μm^{-1}) against the pore size showed that the co-precipitation allowed the preparation of materials with a relatively narrow pore size range. All co-precipitated oxygen carriers with a porosity larger than 0.05 were found to have > 99% of their pore volume within pores with a difference in pore size of one magnitude or less. All of these pores were in the range of 0.38 – 3.8 µm and the highest differential intrusions (peaks of curves) was between 0.94 – 2.09 µm. Contrary, the unsupported mechanically mixed oxygen carriers had pores (*DI* > 0.001 ml g^{-1} μm^{-1}) across the entire studied range above 0.18 – 0.31 µm, though, with peaks in the DI (highest differential intrusion) between 0.83 – 1.33 µm. The ZrO_2- and TiO_2-supported oxygen carriers were found to have a bi-modal pore distribution. The smaller pores were found at 0.10-1.62 µm (ZrO_2 supported samples) and 0.28 – 2.08 µm (TiO_2 supported samples) and the larger pores d_{pore} > 1.62 µm (ZrO_2 supported samples) and d_{pore} > 4.84 µm (TiO_2 supported samples).

X-ray diffraction (XRD) experiments were carried out to identify the optimal calcination conditions for the co-precipitated and mechanically mixed oxygen carriers with a molar 1Cu:1Mn ratio. It was

revealed that the co-precipitated precursors react directly to copper manganese oxide, without the formation of single metal oxides as intermediates. Copper manganese oxide was identified in the co-precipitated samples even after short calcination (15 min holding time) and temperatures as low as 500 °C. The mean crystallite size, *d*, was found to increase with calcination temperature (*e.g.* calcined at 500 °C for 15 min: $d = 17.0$ nm; calcined at 900 °C for 15 min: $d = 49.2$ nm), and with calcination time (*e.g.* calcined at 900 °C for 15 min: $d = 49.2$ nm; 900 °C for 12 h = 101.9 nm). Based on this sensitivity study, it was decided to use for the standard synthesis procedure of the co-precipitated oxygen carriers a calcination temperature and holding time of 900 °C and 2 h, respectively.

A similar study was carried out for the mechanically mixed oxygen carriers, though here the objective was to identify calcination conditions with the maximum conversion of CuO and MnO to copper manganese oxide. The mechanically mixed precursors were calcined at different temperatures and for different durations. An increase in calcination temperature from 900 °C to 950 °C was found to increase the mass fraction of $Cu_xMn_{3-x}O_4$ significantly. The effect of the holding time was studied, and a decrease in the mass fraction of CuO was measured when increasing the holding time from 2 h to 6 h. A further increase in the calcination time did not result in a further decrease in the measured CuO mass fraction. Therefore, a calcination time and duration of 950 °C and 6 h, respectively, were selected for the standard synthesis procedure of the mechanically mixed oxygen carriers. The samples that were calcined at 950 °C for 6 h and for 12 h, had a CuO mass fraction of close to 25.1 wt%, which is mass fraction of a CuO of a sample with a molar 1Cu:1Mn ratio that contains only CuO and $CuMn_2O_4$. This finding indicates that the mechanically mixed precursors do not form $Cu_xMn_{3-x}O_4$ with $x > 1$ (*e.g.* no $Cu_{1.5}Mn_{1.5}O_4$) during calcination – contrary to the samples prepared by co-precipitation. This finding was confirmed when studying the effect of a varying molar Cu:Mn ratio. At (lower) temperatures at which CuO remains inert, a sample that contains a mixture of $CuMn_2O_4$ and CuO is disadvantageous compared to a sample containing $Cu_{1.5}Mn_{1.5}O_4$ (with the same molar Cu:Mn ratio), since the O_2 release capacity is significantly reduced.

To find the optimal washing procedure during co-precipitation, samples with varying residual amounts of Na were prepared. XRD analysis of a sample, which was calcined without washing revealed that all Mn had reacted with Na to sodium manganese oxides. Furthermore, NaO_2 and CuO were identified. The sample contained neither copper manganese oxide nor was its resistance to mechanical stresses detectable (the average force to crush a particle was below 0.5 N – the lower limit of force measurements) and was therefore not considered promising. Samples with lower Na concentrations were studied: in the samples with an electrical conductance (the indirect measure of the Na concentration) of 46 µS, 256 µS and 1238 µS, no significant amounts of sodium manganese oxides were detected. However, SEM images of the 256 µS and 1238 µS samples identified Na-rich

needle-like features in the sample, which were not found in the 46 µS sample. It was therefore descried to wash the co-precipitated precursors until the electrical conductance is < 50 µS.

The co-precipitated precursors were analysed by XRD using CeO_2 as an internal standard, and it was found that those prepared with only Na_2CO_3 had a mass fraction of crystalline material in the range 1.5 – 10.9 wt%, which is very likely $MnCO_3$. Upon calcination, the highly amorphous material formed a material with a mass fraction of $Cu_xMn_{3-x}O_4$ close to unity. Co-precipitation with different mixtures of Na_2CO_3 and NaOH were tested. At low [Na_2CO_3]:[NaOH] the formation of a highly crystalline material containing $Cu(NO_3)_2{\cdot}3Cu(OH)_2$ occurred, which was previously correctly predicted by the 'Spana-Medusa' software (see **Fig. 4-2**). The highly crystalline material formed a material with a low copper manganese oxide content during the calcination. The results of this study suggest that crystalline phases in the precursor inhibit the formation of $Cu_xMn_{3-x}O_4$. Further co-precipitation conditions were tested, and the XRD analysis of the calcined material revealed that a lower *pH* value and the substitution of Na_2CO_3 with NaOH resulted in an increase in the CuO mass fraction.

In all mechanically mixed oxygen carriers, either $CuMn_2O_4$ or $Cu_{1.2}Mn_{1.8}O_4$ was identified as the main phase by XRD. Apart from 1Cu-2Mn-MM, all samples contained CuO, and the mass fraction of CuO was found to increase with an increase in the molar Cu:Mn ratio.

Quantitative elemental analysis by XRF confirmed that the CuO, MnO and TiO_2 powder had a purity in excess of 99.5 wt%. In the ZrO_2 powder, 2.47 wt% Hf was identified. Zr and Hf accounted for 99.8 wt% of tested elements (metals and alkaline). XRD analysis confirmed that the Hf occurred as HfO_2, and a calculation using data from FactSage showed that the HfO_2 remains inert across the entire condition range of the redox-experiments.

The data obtained from the material characterisation is used for hydrodynamic calculations and reaction rate modelling, as described in the following sections.

Chapter 6

Thermo-gravimetric analysis of the oxygen carriers

6.1 Thermo-gravimetric analysis and a screening of the reactivity

In the following sections, the set-up of the thermo-gravimetric analyser (section 6.1.1) and the experiments for the determination of the gas mixing time (6.1.2) are described.

6.1.1 Description of the set-up of the thermo-gravimetric analyser

The experiments of this chapter were performed in a thermo-gravimetric analyser (TGA) of type Q5000 (TA Instruments). The gas supply to the TGA was controlled by three external mass flow controllers (MFC). Furthermore, two TGA-internal MFCs controlled the sample and balance purge flow, respectively. TGA set-up, including the gas supply system, is illustrated in **Fig. 6-1**, below.

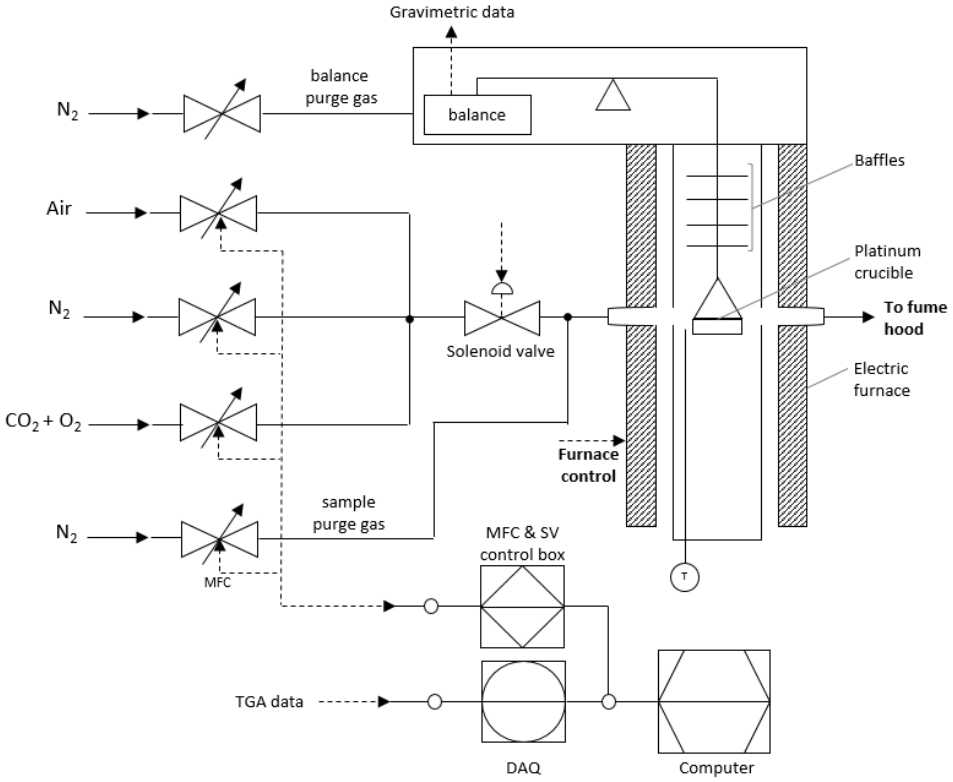


Fig. 6-1 *A diagram of the TGA set-up including the gas supply system.*

The TGA software from TA Instruments controlled the furnace temperature, and the gas flows of the two TGA-internal MFCs. Furthermore. the software measured the sample mass with 0.2 – 0.5 data points per second and communicated with a binary signal with the control box of the external MFC. A second software, Agilent VEE, controlled the external MFCs of the gas supply system. An Agilent VEE code for a gas switching sequence with the four phases for (i) reduction, (ii) N_2 purge, (iii) oxidation and (iv) N_2 purge already existed and was used for CH_4-fuelled experiments. For experiments relevant for CLAS, a two-phase gas switching sequence was required, in which the degree of dilution of N_2 or CO_2 with O_2 during the O_2 release and oxidation phase is adjustable. Such a programme did not exist and was therefore programmed in Agilent VEE. The calibration of the MFCs of the gas supply system and the calculation of the uncertainties of their mass flows is described in ***Appendix A.6***. A gas analyser was used to validate the calibration by comparing the O_2 volume fractions that were set in the Agilent VEE computer programme with the actual (measured) O_2 volume fractions in the range 0 – 20 vol%. The average absolute relative deviation and the maximum relative deviation between the set and the measured values were 0.12% and 0.60% (= 0.10 vol%), respectively.

6.1.2 Rate of gas mixing in the TGA

The change of the actual gas concentration upon gas switching from an oxidative to a reductive atmosphere, or *vice versa*, is not a step-function. This is due to the time required for the mass flow controllers to assume their new target flow rate, and for gas mixing in the tubing and inside the TGA furnace to occur. Substantial differences between the actual gas concentration inside the TGA furnace and the set gas concentration during the measurement of a reaction would result in misleading results. To determine the time required for the gas concentration to reach the set value three experiments were carried out using a gas analyser and 20 cm of 1/8-inch nylon tubing:

(i) The O_2+CO_2 and CO_2 gas lines with 1.3 bar line pressure were connected to a 3-way valve with a subsequent needle valve. The flow rate of this needle valve was set to 200 ml·min^{-1} (*i.e.* the gas flow rate used for most TGA experiments) using a rotameter, which was removed after calibration. Then, the needle valve was connected to the 20 cm tubing of the gas analyser, and the gases were manually repeatedly switched.

(ii) The outlet of the TGA gas supply system was connected to the gas analyser, and the gases were switched automatically using the Agilent VEE standard code.

(iii) A 5 cm ¼-inch steel tubing was connected to the outlet of the TGA furnace (to cool the exhaust gas). This steel tubing was connected to the 20 cm nylon tubing of the gas analyser, and the gases were switched automatically at a furnace temperature of 800 °C.

The data of five gas switching events were averaged and de-convoluted by,

$$y_{\mathrm{O}_2} = \tau_{\mathrm{r}} \frac{y_{\mathrm{O}_{2,\mathrm{m}}}}{dt} + y_{\mathrm{O}_{2,\mathrm{m}}}\,, \tag{6-1}$$

where y_{O_2} and $y_{\mathrm{O}_{2,\mathrm{m}}}$ are the deconvoluted and measured O_2 molar fractions, respectively. The response time, τ_{r}, for the three cases described above was calculated by minimising the mean square error, which was taken as the difference between $y_{\mathrm{O}_{2,\mathrm{m}}}$ and the set gas molar fraction. The response time for case (i), in which the gas analyser was directly connected to a 3-way valve, was assumed to correspond to the response time of the gas analyser and was found to be 3.8 s. The response times measured downstream of the TGA gas supply system and downstream of the TGA furnace were found to be 4.2 s and 5.3 s, respectively. The response time of the gas analyser was subtracted from the other two response times. A response time delay caused by the TGA gas supply system of 0.4 s was calculated. The response time across the entire TGA (including the TGA gas supply, the TGA furnace and the tubing between those parts) was found to be 1.1 s. The values of y_{O_2} and $y_{\mathrm{O}_{2,\mathrm{m}}}$ for the three cases are plotted against time in **Fig. 6-2**, below.

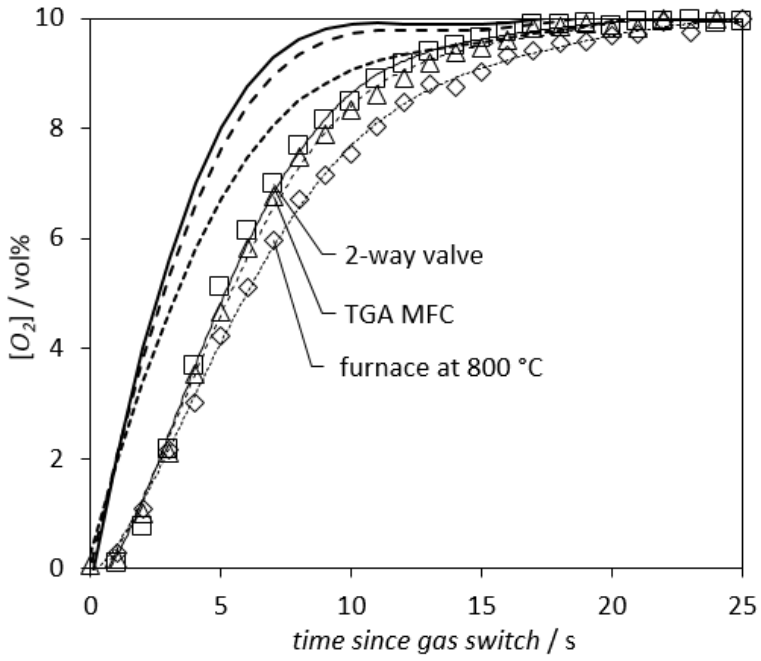


Fig. 6-2 *The change of gas concentration after switching from CO_2 to 10 vol% O_2+CO_2, measured downstream a 3-way valve (□), downstream of the gas supply system (△), and downstream of the TGA furnace at 800 °C (◇), and a best fit function for the change of gas concentration before de-convolution (thin lines) and after de-convolution (thick lines).*

This finding suggests that the gas concentration during the first 1.1 s increases exponentially, and thus initially differs significantly from the change in set gas concentration (which is almost a step function). Therefore, the data obtained during this period will neither be used for the calculation of the kinetic parameter nor the fitting to a reaction function. The fastest CLAS-relevant reaction measured in the TGA (the oxidation of 1Cu-2Mn-based oxygen carriers at 900 °C in 10 vol% O_2 + N_2) required ~15 sec to reach a conversion of $X = 0.8$. Since this interval is an order of magnitude larger than the response time of the gas concentration in the furnace, it is assumed that the gas mixing is rapid enough for the TGA to be a suitable instrument for the experiments.

After completing the calibrations, validations and calculations for the experimental set-up, a model for the quantification of the external mass transfer in the TGA was developed, as described in the following section.

6.2 External mass transfer in the TGA

The measured rate of reaction during TGA experiments may be significantly influenced by external mass transfer. Therefore, the maximum rate of external mass transfer was calculated for all TGA according to the method proposed by Hu *et al*.[219] During the O_2-release, this method assumes that

the molar flow of oxygen from the oxygen carrier to the bulk of the TGA furnace, N_r, can be calculated by,

$$N_\mathrm{r} = \frac{C \cdot D_{\mathrm{M},ij}}{l_\mathrm{c}} \cdot \ln\left(\frac{1 - y_{O_2,b}}{1 - y_{O_2,s}}\right), \tag{6-2}$$

where C is the calculated molar gas concentration calculated and $D_{\mathrm{M},ij}$ the diffusivity of gas species i in gas species j, with i being O_2 and j being either CO_2 or N_2. In eq.(6-2), l_c is the height of the crucible, and $y_{O_2,b}$ and $y_{O_2,s}$ are the molar fractions in the bulk and at the surface, respectively. This relationship is illustrated in **Fig. 6-3**, below.

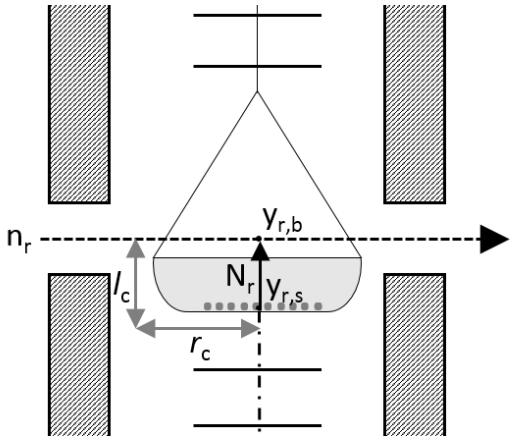


Fig. 6-3 *Drawing of the TGA cross-section to illustrate the gas flow and the diffusion of gas from the oxygen carriers during the O_2 release.*

The diffusivity in eq.(6-2) is calculated with the empirical correlation proposed for simple molecules by Fuller, Schettler and Gidding:[220]

$$D_{\mathrm{M},ij}/(cm^2/s) = \frac{0.00143 \cdot (T/K)^{1.75} \left(1/M_i + 1/M_j\right)^{1/2}}{P \cdot \left[(\Sigma_v)_i^{1/3} + (\Sigma_v)_j^{1/3}\right]^2} \tag{6-3}$$

Eq.(6-3) is a correlation for the diffusion of gas species *i* in *j*. In this equation *T* is the temperature in Kelvin, M_i and M_j are the relative molecular masses, $(\Sigma_v)_i$ and $(\Sigma_v)_j$ are the diffusion volumes, and *p* is the pressure in atm. The values for M and (Σ_v) that were used in this work are listed in **Table 6-1**, below.

Table 6-1 *Diffusion volumes and relative molecular masses used for the calculation of the molecular diffusion.*

Molecule, i or j	$(\Sigma_v)_{i\ or\ j}$	$M_{i\ or\ j}$ [g mol^{-1}]
O_2 [a]	16.3	15.999
N_2 [a]	18.5	28.013
CO [a]	18.0	28.010
CO_2 [a]	26.9	44.010
CH_4 [b]	25.14	16.040
H_2 [a]	6.12	2.016
H_2O [a]	13.1	18.015

Footnotes: The values are taken from (a) Poling [221] and (b) Kleiber et al.[222]

Values of the maximum rate of external mass transfer in the TGA were reported by Hu *et al*.[219] The results of their calculation were reproduced by using the same input data, and the results of the gPROMS calculation of this work were compared with the values reported in Hu *et al*.[219] to validate the model. The results are shown in **Fig. 6-4**, below.

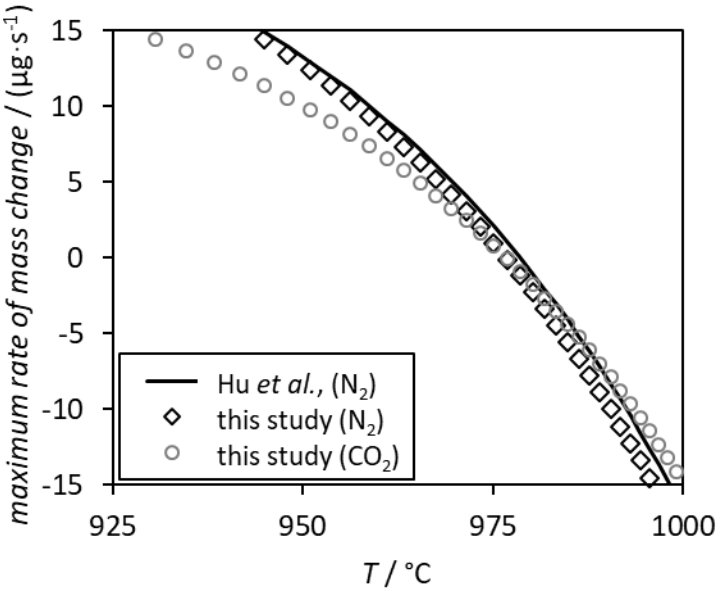


Fig. 6-4 *The rate of the external mass transfer controlled maximum rate of mass change in the TGA assuming an effective crucible height of 0.35 mm: The values reported by Hu et al.[219] for N_2 (-) and the results of the gPROMS model for N_2 (◇) and CO_2 (□).*

The result of the gPROMS calculation is in good agreement with the values calculated by Hu *et al*.[219] The small deviation could derive from a slightly different correlation to calculate the molar diffusivity and/or the O_2 equilibrium partial pressure (both are not further specified in their study).[219]

In eq.(6-2), a value of $y_{O_2,b}$ is required for the calculation of the diffusion. To test if $y_{O_2,b}$ can be assumed to be equal to the y_{O_2} at the inlet of the TGA, the total TGA sample gas flow rate was

varied, and the change of the maximum rate of O_2 release was observed. The maximum rates are plotted against the TGA inlet gas flow rate in **Fig. *6-5***, below.

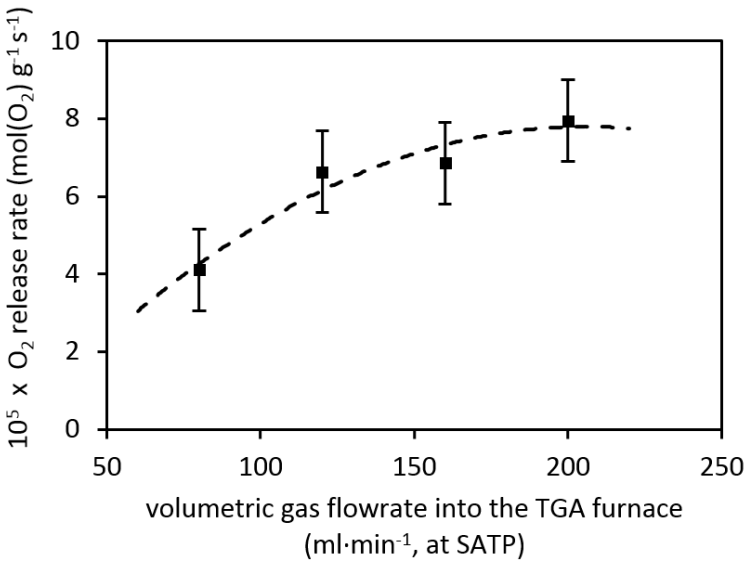


Fig. 6-5 *The effect of gas flow rate into the TGA on the maximum O_2 release rate of 2 mg 1Cu-1Mn-CP(2:1) in the TGA at 850 °C with decomposition under pure N_2. A second order polynomial trend-line is drawn to illustrate the relationship. The error bars indicate the uncertainty, which was estimated by 2·SD of the maximum rate of three redox-cycles.*

Fig. *6-5* shows that the maximum observed rate of O_2 release increases with increasing gas flow rate in the range between 80 ml·min^{-1} and 150 ml·min^{-1}. However, the rate of increase of the maximum rate is decreasing with increasing gas flow rate. At around 200 ml·min^{-1} the slope of the fitted curve is almost zero. This indicates that at 200 ml·min^{-1} the inlet concentration of O_2, $y_{r,0}$, is approximately equal to the O_2 concentration inside the furnace – or in this case the bulk concentration of O_2 in the furnace, $y_{r,b}$ in eq.(6-2), is ~ zero. For these experiments (**Fig. 6-5**) the highest temperature and lowest [O_2] of all TGA experiments were used. Since the rate of O_2 release is expected to be lower at lower temperatures and higher [O_2], the assumption $y_{r,0} = y_{r,b}$ is assumed to be valid for all other conditions as well.

6.3 Intra-particle diffusion resistance and tortuosity

During the O_2 release reaction, gas molecules are desorbed from the metal oxide surface and have to diffuse through the pores of the particle to the bulk of the gas. During the oxidation, the direction of transport reverses, and the O_2 molecules diffuse from the gas bulk, through the pores, to the metal oxide surface. This diffusion occurs due to Brownian motion and due to concentration gradients. The pore size can thereby affect the rate of diffusion and results in the classification of two diffusional modes – Knudsen diffusion and molecular diffusion.

Knudsen diffusion occurs in pores where the mean free path, λ, is relatively long compared with the diameter of the pores, *i.e.* $\lambda >> d_{pore}$. It is typically dominant for 2 nm < d_{pore} < 50 nm. Molecular diffusion occurs in larger pores, where $\lambda << d_{pore}$. In this diffusional mode the movements of the molecules are not significantly influenced by the walls of the pores. In both cases the driving force is concentration gradient and the molecules move owing to Brownian motion. The two diffusional modes are illustrated in **Fig. 6-6**, below.

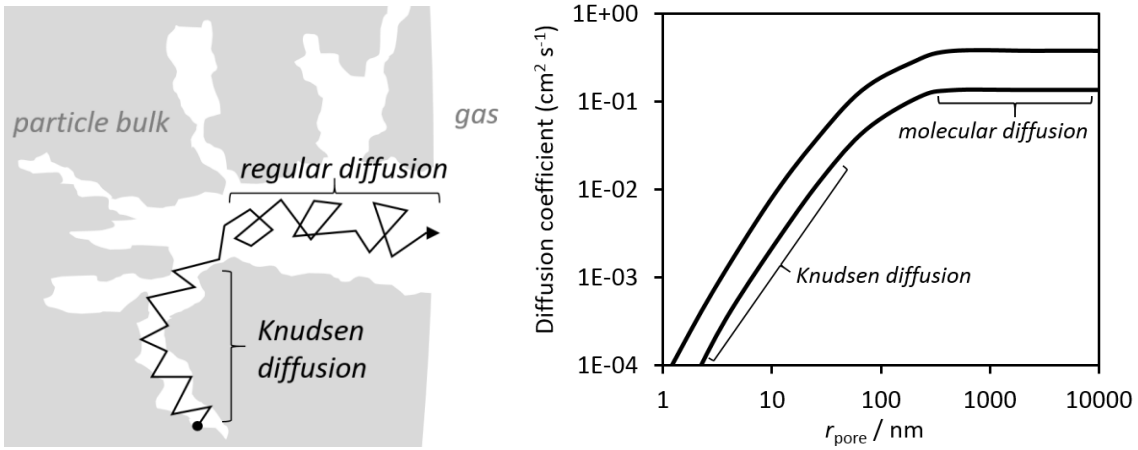


Fig. 6-6 *A comparison of Knudsen diffusion and molecular diffusion: (a) a schematic of the diffusion of a gas molecule (black dot) from the solid surface, through the pores to the bulk of gas; (b) values for the diffusion coefficient as a function of the pore radius.*

The N_2 adsorption analysis at 77 K (*c.f.* section 5.1) revealed that a substantial part of the pore volume lies in pores with r_p < 50 nm, *e.g.* 38% of the volume for mechanically mixed 1Cu-1Mn-MM. Thus, the two diffusional modes have to be considered.

The Knudsen diffusion was calculated by,[199]

$$D_K = \frac{4}{3}\sqrt{8RT/\pi M_{O_2}} \cdot \frac{\varepsilon_p \bar{d}_{\text{pore}}}{4}, \tag{6-4}$$

where M_{O_2} is the molecular mass of the diffusing O_2 molecule, ε_p is the porosity of the particle calculated from MIP and He pycnometry, $\bar{d}_{\text{pore}}$ is the mean diameter of the pores. The value of $\bar{d}_{\text{pore}}$ can be approximated by,

$$\bar{d}_{\text{pore}} = \frac{4}{S_{\text{BET}} \cdot \rho_p}, \tag{6-5}$$

where S_{BET} is the specific surface area determined by N_2 adsorption at 77 K and ρ_p is the envelope density of the particle determined by MIP and He pycnometry.

The combination of eq.(6-4) and eq.(6-5) yields,

$$D_{\mathrm{K}} = \frac{8 \cdot \varepsilon_{\mathrm{p}}}{3 \cdot S_{\mathrm{BET}} \cdot \rho_{\mathrm{p}}} \sqrt{2RT/\pi M_{\mathrm{O_2}}}. \tag{6-6}$$

The molecular diffusion was estimated using eq.(6-3), which was introduced in the previous section. The Knudsen diffusion and the molecular diffusion were assumed to occur in series. This can be expressed by,

$$\frac{1}{D_{\mathrm{p}}} = \left(\frac{1}{D_{\mathrm{K}}} + \frac{1}{D_{\mathrm{M}}}\right), \tag{6-7}$$

where D_{p}, D_{K}, and D_{M} are the diffusion coefficients for the combined diffusion inside the particle, the Knudsen diffusion, and the molecular diffusion, respectively. Wakao[223] demonstrated that the effective diffusion also depends on the porosity of the particle, ε_p, and proposed to calculate the effective diffusion inside the particle, D_e, by,

$$D_{\mathrm{e}} = \varepsilon_{\mathrm{p}}^2 \, D_{\mathrm{p}} \tag{6-8}$$

Satterfield[224] later refined Wakao's model by considering additionally a tortuosity factor, τ_p:

$$D_{\mathrm{e}} = \frac{\varepsilon_{\mathrm{p}}}{\tau_{\mathrm{p}}} D_{\mathrm{p}} \tag{6-9}$$

The tortuosity accounts for the curvature of the pores. A simple definition of τ_p is that it corresponds to the ratio of the actual length of the diffusion path to the shortest length between the beginning and the end of the diffusion path.[224] Eq.(6-9) was used in this work to calculate D_{e} for all TGA and fluidised bed reactor experiments. However, in this work τ_p is a fitted parameter which, in contrast to the true tortuosity factor, accounts for errors in the particle characterisation measurements.[91, 225] It was determined iteratively, by measuring the rate of reaction of oxygen carriers from eight different particle size ranges. The calculation of k_{i} and τ_{p} is possible, since neither of the two variables depend on the particle radius. The experiments were carried out in the TGA at 850 °C using 10 vol% O_2 + N_2 for the oxidation and pure N_2 for the decomposition. The particle size ranges that were used for this experiment are shown in **Table 6-2**, below.

Table 6-2 *The particle size ranges used for the TGA experiments to determine the intrinsic kinetics and the tortuosity factor.*

$d_{p,min}$ [µm]	$d_{p,max}$ [µm]	RMS(r_p) [µm]
90	150	58
150	212	89
212	300	126
300	425	179
425	500	230
500	710	298
710	850	388
850	1000	461
1000	1250	559

The results of the first five cycles were ignored, as the measured rate during those initial cycles is potentially lower than the average rate that is achieved during long-term cycling. This is because initially the particles might not be fully activated. The data of the remaining cycles was averaged. The results of this experimental series are shown in **Fig. 6-7**, below, where the conversion is plotted against the time of the O_2 release reaction to show the effect of a variation in the particle size range.

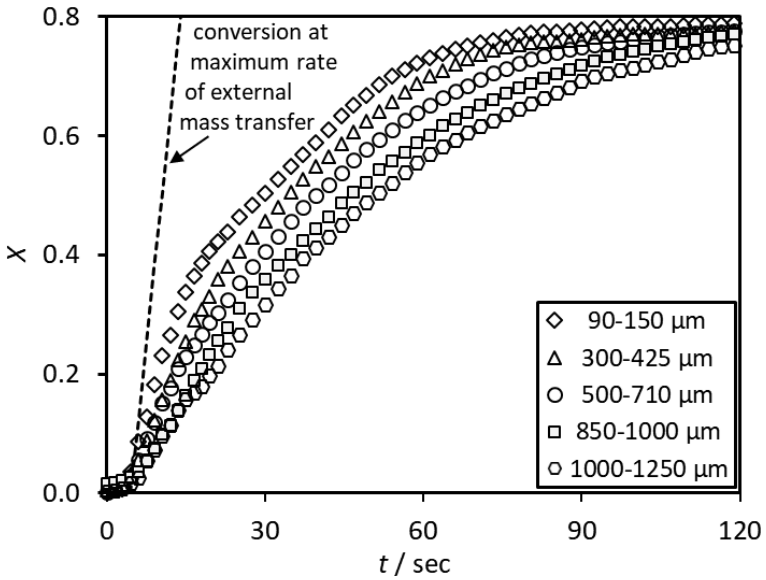


Fig. 6-7 *A plot of conversion against time during the O_2 release from 2 mg 1Cu-1Mn-MM oxygen carrier of various particle size ranges as defined by the legend on the figure. The experiments were carried out at 850 °C in the TGA using pure N_2 for the decomposition with a flow rate of 200 ml min^{-1} at SATP. The results of some particle size ranges were omitted from this graph for clarity. The conversion at maximum rate of external mass transfer (dashed line) was calculated using eq.(6-2) and eq.(6-3) with $y_{O_2,b} = 0$ and $y_{O_2,s} = y_{O_2,eq}$, and was shifted by 4.5 s to account for the initiation period.*

Fig. 6-7 shows that the time to reach a given conversion (lower than the final conversion) increases with an increase in particle size, thus indicating that intra-particle diffusion resistance is affecting the overall rate of reaction. The measured values of the maximum observed rate, *r'*, are presented in **Table 6-3**, below.

Table 6-3 *The observed rate measured during TGA experiments to determine the intrinsic kinetics and the tortuosity factor.*

particle diameter range group	$d_{p,min}$ - $d_{p,max}$ [μm]	*RMS(r_p)* [μm]	*max observed rate, r'* [mmol(O_2) g^{-1} s^{-1}]
1	90-150	58	0.0699
2	150-212	89	0.0519
3	212-300	126	0.0611
4	300-425	179	0.0436
5	425-500	230	0.0343
6	500-710	298	0.0308
7	710-850	388	0.0284
8	850-1000	461	0.0263
9	1000-1250	559	0.0242

It was assumed that the oxidation and the O_2 release reaction have a reaction order close to unity (this was later confirmed during kinetic experiments). The observed rate constant, k, can therefore be calculated by,

$$k = r' \cdot \frac{\rho_p}{C_{O_2}^S} \, [s^{-1}], \tag{6-10}$$

where $C_{O_2}^S$ is the concentration of O_2 at the solid surface and ρ_p (g m^{-3}) is the envelope density (determined by MIP and He pycnometry).

Assuming pseudo steady-state conditions, Fan *et al.*[91] demonstrated that the observed maximum rate of carbonation of CaO, r, can be related to the external mass transfer coefficient, k_g, the intrinsic rate constant, k_i, and an effectiveness factor, η, that accounts for effect of the intra-particle diffusion resistance on the overall rate by,[91]

$$r = kC_r \, , \tag{6-11a}$$

$$\frac{1}{k} = \frac{r_p}{3k_g} + \frac{1}{\eta k_s}, \tag{6-11b}$$

where k is the observed rate constant, C_r the concentration of the reagent, and r_p the mean radius of an oxygen carrier particle. This equation was slightly modified for the oxygen carriers in this work,

to account for the dependence of k_i on both, the O_2 surface concentration, $C_{O_2}^S$, as well as on the O_2 equilibrium concentration, $C_{O_2,eq}$, using additionally the equations suggested by Hu *et al.*[219] The diffusion of O_2 in N_2 from the bulk to the oxygen carriers in the crucible was assumed to occurs according to the Stefan's tube model, as detailed in section 6.2 (*c.f.* eq.(6-2)).

The diffusion in eq.(6-2) can be approximated by linearizing the natural logarithm with a Taylor expansion, which yields: [219]

$$N_r \approx \frac{C \cdot D_{M,ij}}{l_c}(y_s - y_b) \approx \frac{D_{M,ij}}{l_c}\left(C_{O_2}^s - C_{O_2}^b\right) \tag{6-12}$$

The maximum error of N_r when using this approximation for the extreme case (y_s = y_{eq} = 0.04) is 7%. This approximation allows definition of the mass transfer coefficient as $k_g \approx D_{M,ij}/l_c$, and the diffusional flux of O_2 as,[219]

$$N_r \approx k_g\left(C_{O_2}^s - C_{O_2}^b\right) \tag{6-13}$$

Assuming quasi steady-state conditions, the reaction rate inside the particle has to be equal to the external diffusion:

$$\eta k_v(C_{O_2,eq} - C_{O_2}^s) \approx k_g\left(C_{O_2}^s - C_{O_2}^b\right) \tag{6-14}$$

This equation can be solved for the surface concentration, C_s:

$$C_{O_2}^s = \frac{\eta k_v\left(C_{O_2,eq} - C_{O_2}^b\right)}{\left(\eta k_v + k_g\right)} + C_{O_2}^b \tag{6-15}$$

The derivation of eq.(6-15) is detailed in **Appendix A.9**. Re-substituting eq.(6-15) into eq.(6-13) yields,

$$r_{O_2} = \frac{\eta k_v k_g}{\eta k_v + k_g}\left(C_{O_2,eq} - C_{O_2}^b\right), \tag{6-16}$$

or,

$$r_{O_2} = \left(\frac{1}{k_g\left(C_{O_2,eq} - C_{O_2}^b\right)} + \frac{1}{\eta k_v\left(C_{O_2,eq} - C_{O_2}^b\right)}\right)^{-1} \tag{6-17}$$

The intrinsic rate constant per unit of surface area, $k_s[\mathrm{m}\cdot\mathrm{s}^{-1}]$ and the intrinsic rate constant per unit volume, $k_\mathrm{v}[\,\mathrm{s}^{-1}]$ are related by,

$$k_\mathrm{s} = V_\mathrm{p}\frac{1}{S_\mathrm{p}}k_\mathrm{v} = \frac{4}{3}\pi r_\mathrm{p}^3 \cdot \frac{1}{4\pi r_\mathrm{p}^2}k_\mathrm{v} = \frac{r_\mathrm{p}}{3}k_\mathrm{v} \tag{6-18}$$

where V_p, S_p and r_p are the volume, the external surface area (assuming spherical particles), and the radius of an oxygen carrier particle, respectively. The observed rate in terms of k_s is,

$$r_{O_2} = \left(\frac{r_\mathrm{p}}{3k_\mathrm{g}\left(C_{\mathrm{O_2,eq}} - C_{\mathrm{O_2}}^\mathrm{b}\right)} + \frac{1}{\eta k_s\left(C_{\mathrm{O_2,eq}} - C_{\mathrm{O_2}}^\mathrm{b}\right)}\right)^{-1} \tag{6-19}$$

The value of $p_{\mathrm{O_2,eq}}$ was calculated using eq.(6-30), and $C_{\mathrm{O_2,eq}}$ was calculated from $p_{\mathrm{O_2,eq}}$ using the ideal gas law,

$$C_{\mathrm{O_2,eq}} = \frac{p_{\mathrm{O_2,eq}}}{RT}, \tag{6-20}$$

The effectiveness factor, η, in eq.(6-20) was calculated by,[91, 144]

$$\eta = \frac{3}{\phi^2}\cdot(\phi\cdot\coth(\phi) - 1), \tag{6-21}$$

where ϕ is the Thiele modulus, which in turn can be calculated by,[91, 144]

$$\Phi = r_\mathrm{p}\sqrt{\frac{k_\mathrm{i}}{D_\mathrm{e}}} \tag{6-22}$$

The values of τ_p and k_i were determined iteratively using eq.(6-9), eq.(6-19), eq.(6-21) and eq. (6-22). This was done by minimising the square error of k_i for a given mean particle radius and the average value of k_i by varying τ_p.

The results are plotted in **Fig. 6-8**, below.

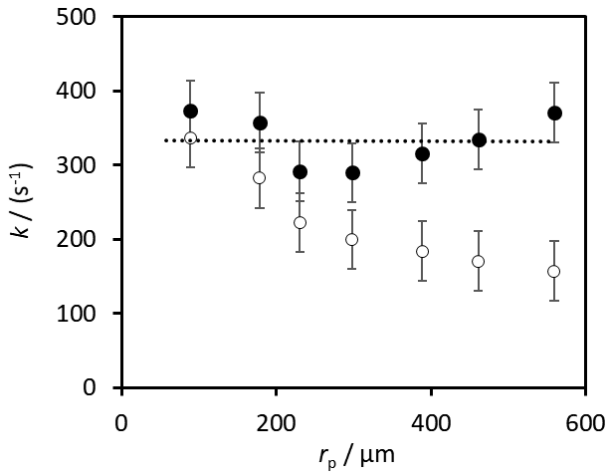


Fig. 6-8 *The apparent rate constant, ○, and the calculated intrinsic rate constant, ●, for the O_2 release reaction of 1Cu-1Mn-MM measured in the TGA at 850 °C under N_2 using a flow rate of 200 ml min^{-1} at SATP.*

This procedure yields the value of τ_p of 2.21, when using a porosity $\varepsilon_p = 0.492$ amd an envelope density $\rho_p = 2.88$ g cm^{-3} (*c.f.* MIP results in chapter 5). The effectiveness factor decreases with an increasing r_p, as shown in **Fig. 6-9**, below.

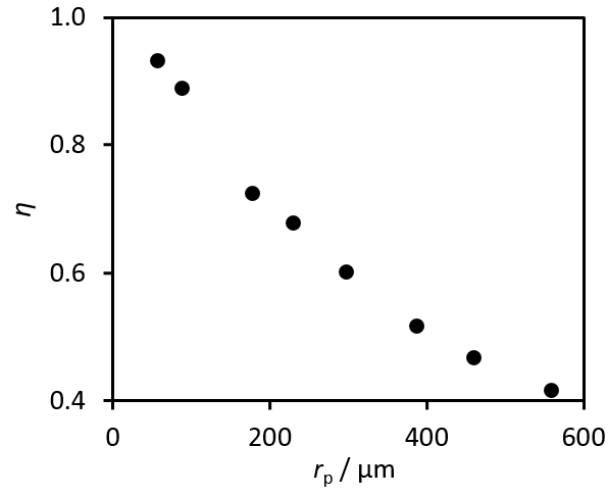


Fig. 6-9 *A plot of the effectiveness factor against the mean particle radius for the O_2 release reaction of 1Cu-1Mn-MM measured in the TGA at 850 °C under N_2 using a flow rate of 200 ml min^{-1} at SATP.*

The calculated value of τ_p and the diffusion model of this section were used in the following sections to calculate the intra-particle diffusion resistance during TGA and fluidised bed reactor experiments.

6.4 Testing the reversibility of the redox-reactions at CLAS conditions

To assess if the redox-reactions of the oxygen carriers at conditions relevant to the CLAS process are fully reversible (*i.e.* no deactivation occurs with an increasing cycle number), the oxygen carriers were tested over several redox-cycles in the TGA. Preliminary experiments had shown that an activation process with slightly different rates and O_2 capacities over the first two to four cycles can occur. To ensure that the data contained at least three cycles after full activation, a total of seven redox-cycles was selected for a typical experiment. Furthermore, the experiments were performed at different conditions and in different cycling modes (isothermal and non-isothermal).

In the literature, the O_2 release behaviour is often studied in isothermal experiments under pure N_2.[43, 66, 102, 123, 168, 226] Only a few works have studied the O_2 release in the presence of CO_2 during isothermal experiments.[227] In the CLAS process, however, the inert gas is CO_2, not N_2, the oxidation and decomposition are facilitated by a temperature swing (T swing) rather than an O_2 partial pressure swing (p_{O_2} swing) – or by a combination of both. Furthermore, the decomposition of the oxygen carriers in the CLAS process occurs in the presence of substantial amounts of O_2, *i.e.* with p_{O_2} being presumably in the range 0.25 - 0.35 bar without the injection of steam and in the order 0.10 bar when using steam as an inert (*c.f.* section 2.3.4) Those three differences might change the results of repeated redox-cycling experiments significantly. When substituting N_2 by CO_2, different metal oxide phases might form as well as carbonates, and elemental carbon deposition might occur. The formation of phases might also be significantly influenced by the presence of O_2 as well as by the rapid temperature changes and the temperature differences (between the redox-phases) in the T swing process.

For the evaluation of the oxygen carriers for the CLAS process, T swing experiments were carried out in which 10 vol% O_2 balanced with N_2 was used during the oxidation and 10 vol% O_2 balanced with CO_2 during the decomposition. A successful O_2 release in an atmosphere of 10 vol% O_2 demonstrates the feasibility to produce an oxy-fuel mixture with this O_2 volume percentage. Though generally the optimal p_{O_2} of the O_2+CO_2 mixture for oxy-fuel combustion is considered to be in the range 0.30 – 0.35 bar,[114, 116] it is not reasonable to take this p_{O_2} range as the target for gas leaving the reducer of the CLAS process.[40] This would require the reducer to operate at a significantly higher temperature than the oxidiser, which in turn would require enormous amounts of heat to be transferred.[40] Instead, a mixture of CO_2 and steam is assumed as the fluidising gas in the reducer. In section 2.3.4 it was shown that when producing a 10 vol% O_2 mixture at the reducer outlet, a mixture with 25 vol% and 36 vol% O_2 + CO_2 would be obtained after condensation of all H_2O, when using a fluidisation gas with a steam:CO_2 molar ratio of 2:1 and 4:1, respectively. Though, an increase in the

steam injected (and condensed) can result in a significant reduction in the CLAS process efficiency. Arguably, the best way to predict the optimum is to perform process simulations.

For the TGA experiments in this section, a p_{O_2} of 0.1 bar was used for all T swing experiments. Besides the T swing experiments, some isothermal (p_{O_2} swing) experiments were carried out with decomposition under pure N_2 to allow direct comparison between the two cycling modes.

In most experiments (unsupported) co-precipitated oxygen carriers were used, since XRD analysis of those samples (*c.f.* section 5.4) revealed that the copper manganese oxide mass fractions are higher than those of the mechanically mixed oxygen carriers. The 1Cu-2Mn-MM oxygen carriers are an exception to this (XRD indicated copper manganese mass fractions close to unity), and these oxygen carriers were therefore also studied during the experiments of this section. The oxygen carriers were repeatedly oxidised at 850 °C in 10 vol% O_2 + N_2 and decomposed at 950 °C in 10 vol% O_2 + CO_2. After seven redox-cycles, the samples were recovered at the end of the oxidation and reduction period and analysed by XRD. Selected results for the unsupported oxygen carriers are shown in **Fig. 6-10**, below.

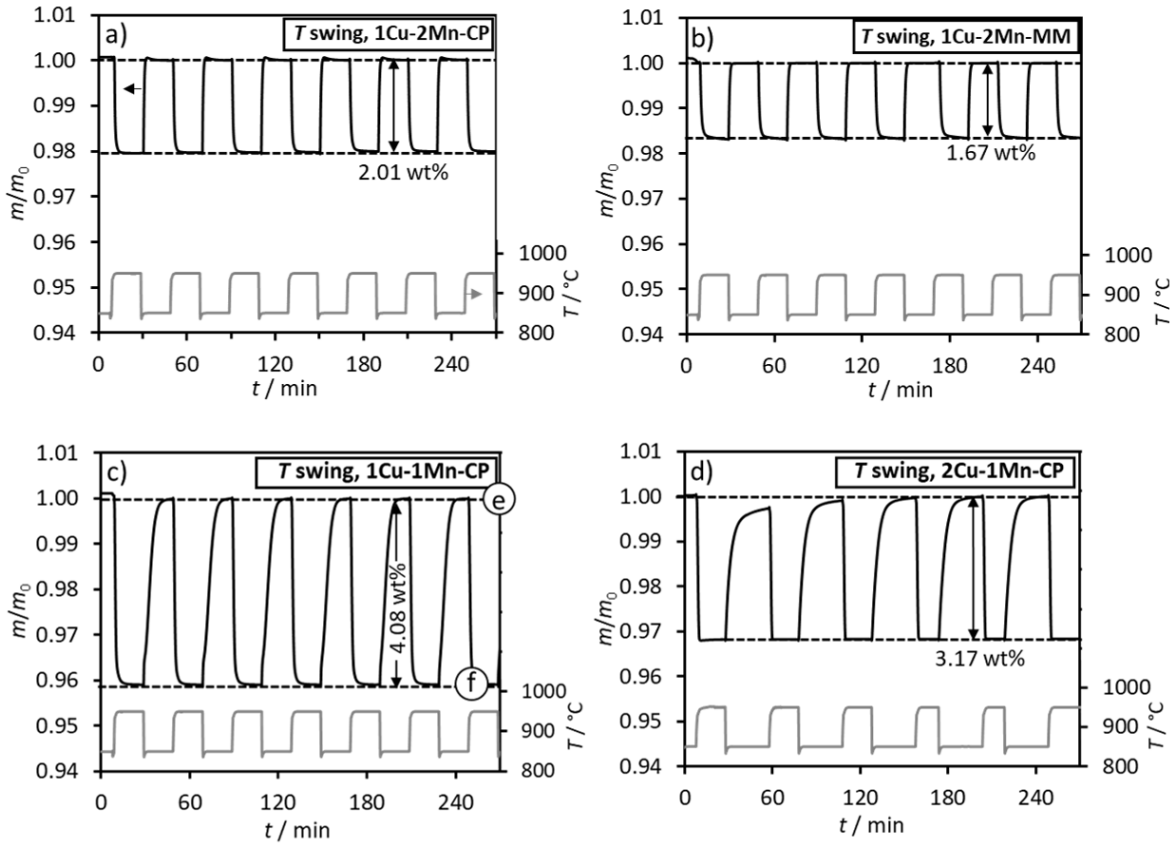


Fig. 6-10 *Plots of the normalised sample mass measured during T swing experiments in the TGA with alternating periods of 850 °C with 10 vol% O_2+N_2 (for the oxidation) and 950 °C with 10 vol% O_2+CO_2 (for the O_2 release) for different oxygen carriers of the size range 150-212 µm: (a) 1Cu-2Mn-CP(3:0), (b) 1Cu-2Mn-MM, (c) 1Cu-1Mn-CP(3:0), (d) 2Cu-1Mn-CP(3:0). The total gas flow rate was kept constant at 170 ml.min^{-1} at SATP.*

A second series of experiments was carried out in which the oxygen carriers were cycled by p_{O_2} swing at 850 °C, using 10 vol% O_2 + N_2 during the oxidation period and pure N_2 during the reduction period. In addition, further experiments were carried out with various gas compositions during the oxidation and the decomposition to study the effect of substituting O_2+N_2 with O_2+CO_2 during the redox-cycling. For all isothermal and non-isothermal experiments, the O_2 release capacity for cycle i, $R_{0,\mathrm{exp}}$, was calculated using the average sample mass of the last 30 s of the oxidation period, $m_{\mathrm{ox,avg}}$, and decomposition period, $m_{\mathrm{red,avg}}$, by,

$$R_{0,\mathrm{exp}} = \frac{(m_{\mathrm{ox,avg}} - m_{\mathrm{red,avg}})}{m_{\mathrm{ox,avg}}} \tag{6-23}$$

The values of $R_{0,\mathrm{exp}}$ calculated for cycles five to seven were averaged and the values are reported as $\bar{R}_{0,\mathrm{exp}}$. The calculated values are shown in **Table 6-4**, below.

Table 6-4 *Values of $\bar{R}_{0,\mathrm{exp}}$ obtained during experiments in the TGA.*

oxygen carrier	***T* swing** (T = 850 °C ↔ 950 °C) oxidation: 10 vol% O_2 + N_2 O_2 rel.: 10 vol% O_2 + CO_2	$\boldsymbol{p_{O_2}}$ **swing** (T = 850 °C) oxidation: 10 vol% O_2 + N_2 O_2 rel.: 10 vol% O_2 + CO_2
1Cu-2Mn-CP(3:0)	2.01	4.31
1Cu-1Mn-CP(3:0)	4.08	4.81
2Cu-1Mn-CP(3:0)	3.17	6.55
1Cu-2Mn-MM	1.67	4.14
1.2Cu-1.8Mn-MM	*n.d.*	4.39
1Cu-1Mn-MM	*n.d.*	4.90

Footnotes: The experimentally obtained O_2 release capacity was calculated by eq.(6-23); "n.d." denotes "not determined".

The results presented in **Table 6-4** are discussed together with **Fig. 6-11**, which shows a selection of the results from the isothermal and non-isothermal experiments.

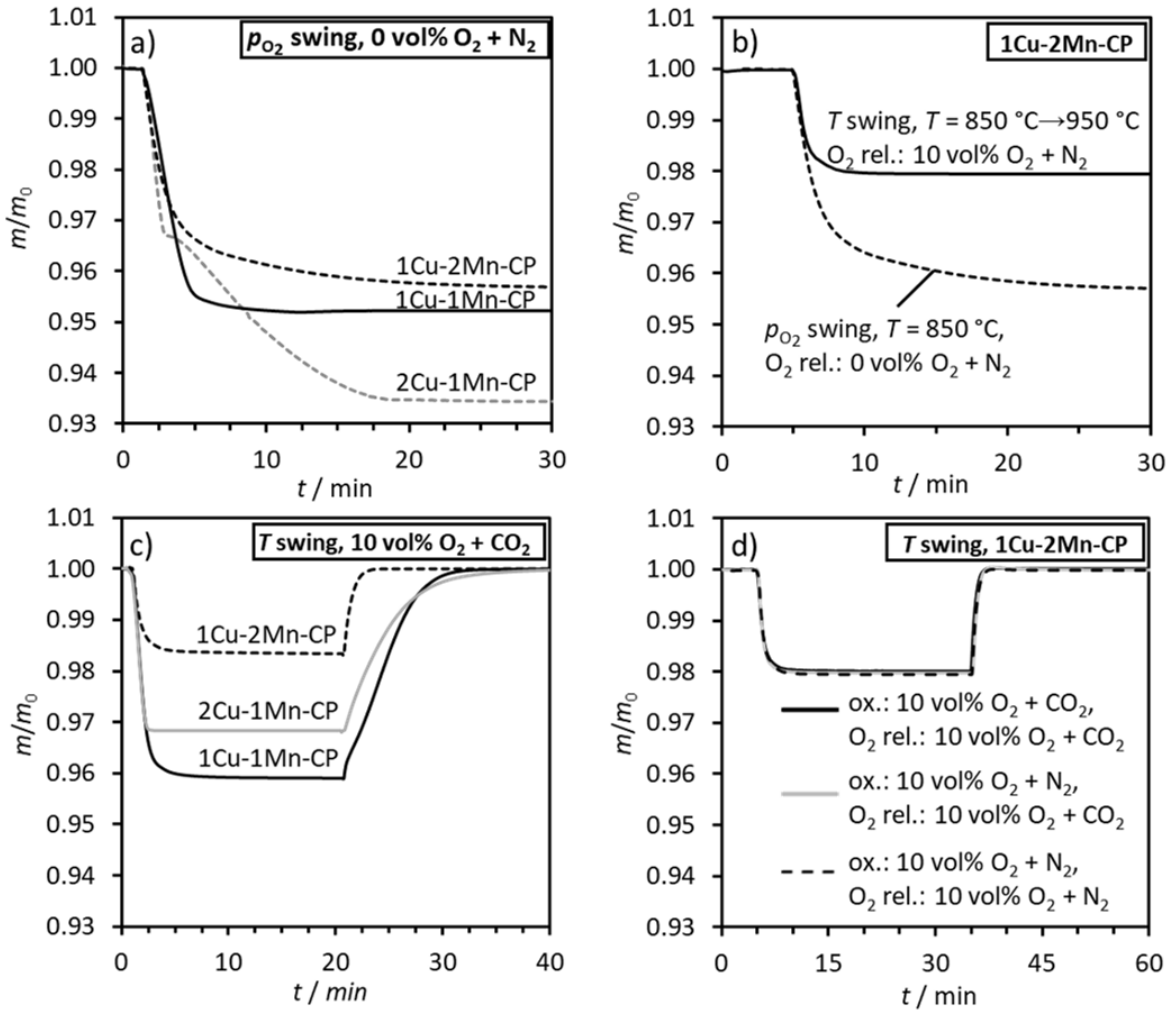


Fig. 6-11 *Normalised weight during the redox-cycling in the TGA by (a, b) p_{O2} swing and (b, c, d) T swing: (a) by T swing: (a) O_2 release during p_{O2} swing of samples with different Cu:Mn molar ratios, (b) a comparison of the O_2 release during p_{O2} swing and T swing, (c) O_2 release during T swing of samples with different Cu:Mn molar ratios, (d) O_2 release and oxidation with different gas mixtures. During a typical p_{O2} swing experiment the oxidation occurred in 10 vol% O_2 + N_2 and the decomposition under pure N_2 at 850 °C. During a typical T swing experiment periods of 850 °C with 10 vol% O_2+N_2 (for the oxidation) and 950 °C with 10 vol% O_2+CO_2 (for the O_2 release) alternated. The total inlet gas flow rate during all experiments was 170 ml min^{-1} at SATP.*

Fig. 6-11a shows that the $\bar{R}_{0,\mathrm{exp}}$ varies with the Cu:Mn molar ratio during isothermal experiments at 850 °C under pure N_2 for the decomposition. For 1Cu-2Mn-CP, 1Cu-1Mn-CP and 2Cu-1Mn-CP, the measured values for $\bar{R}_{0,\mathrm{exp}}$ are 4.31 wt%, 4.81 wt%, and 6.55 wt%, respectively. A substitution of Mn with Cu resulted in an increase in the $R_{0,\mathrm{exp}}$.

Fig. 6-11b shows that for 1Cu-2Mn-CP the O_2 release under pure N_2 at 850 °C results in a significantly larger $\bar{R}_{0,\mathrm{exp}}$ (4.31 wt%) than the $\bar{R}_{0,\mathrm{exp}}$ measured during the *T* swing between 850 °C and 950 °C at p_{O_2} = 0.1 bar (2.01 wt%). This is attributed to incomplete reduction to crednerite (as

confirmed later in this section by XRD data). This phenomenon was also observed when comparing the results of the p_{O_2} and T swing experiments with 1Cu-1Mn-CP and 2Cu-1Mn-CP.

Fig. 6-11c shows that during the T swing, $\bar{R}_{0,\mathrm{exp}}$ of 1Cu-1Mn-CP (4.08 wt%) is larger than $\bar{R}_{0,\mathrm{exp}}$ of 1Cu-2Mn-CP (2.01 wt%), and larger than the $\bar{R}_{0,\mathrm{exp}}$ of 2Cu-1Mn-CP (3.17 wt%). The latter finding is at odds with the results from isothermal cycling experiments with N_2, in which the $\bar{R}_{0,\mathrm{exp}}$ of 2Cu-1Mn-CP was higher the $\bar{R}_{0,\mathrm{exp}}$ of 1Cu-2Mn-CP. The reason for the relatively small $\bar{R}_{0,\mathrm{exp}}$ of 2Cu-1Mn-CP during T swing experiments is attributed the relatively large fraction of CuO in the sample (~ 60 mol% CuO), which remains inert during the T swing cycling (later confirmed by XRD). Contrarily, the CuO decomposes to Cu_2O during the p_{O_2} swing experiments, owing to the lower p_{O_2}.

Fig. 6-11d shows that a substitution of N_2 with CO_2 during the oxidation and the O_2 release during T swing experiments did not affect the redox-behaviour of the samples, and the values of the $\bar{R}_{0,\mathrm{exp}}$ changed only marginally. The following values of $\bar{R}_{0,\mathrm{exp}}$ were measured: 2.06 wt% during oxidation and decomposition under O_2+N_2, 2.03 wt% during oxidation under O_2+N_2 and decomposition under O_2+CO_2, and 1.99 wt% during oxidation and decomposition under O_2+CO_2 (repeats with a higher sample mass indicated that this deviation is caused by the experimental equipment, *e.g.* by a slightly changing buoyancy force exerted at the crucible when changing between O_2+N_2 and O_2+CO_2, since this error did not scale with the sample mass).

To further elucidate the reason for the differences in $R_{0,\mathrm{exp}}$ between the T swing and p_{O_2} swing experiments, the oxygen carriers recovered from the TGA experiments were analysed by XRD. To minimise phase changes during the cooling of the sample, a rapid temperature drop (of initially -200 °C min^{-1}) was programmed as the last step of each TGA experiment. The results of the XRD analysis for the recovered oxygen carriers 1Cu-2Mn-CP, 1Cu-1Mn-CP and 2Cu-1Mn-CP are shown in **Fig. 6-12**, **Fig. 6-13**, and **Fig. 6-14**, respectively.

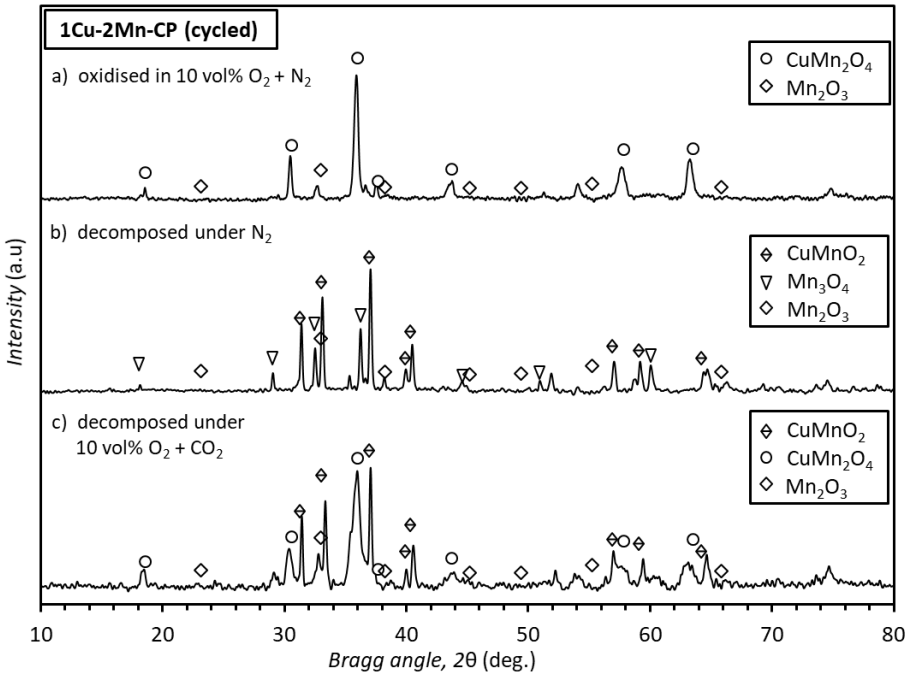


Fig. 6-12 *XRD patterns of the cycled 1Cu-2Mn-CP(3:0) oxygen carriers recovered in the seventh redox-cycled at the end of the (a) oxidation period with 10 vol% O_2 + N_2, (b) decomposition period of p_{O_2} swing experiments using pure N_2, and (c) decomposition period of the T swing experiments using 10 vol% O_2 + CO_2.*

XRD analysis of the 1Cu:2Mn-CP oxygen carriers recovered after the seventh oxidation period from *T* swing experiments (**Fig. 6-12a**) identified $CuMn_2O_4$ (JCPDS 01-071-1143) and $Cu_{1.5}Mn_{1.5}O_4$ (JCPDS 01-070-0262) as the main phases. Additionally, minor amounts of Mn_2O_3 (JCPDS 00-041-1442) were identified. The XRD patterns are very similar to those of freshly calcined materials, and the absence of significant amounts of Cu and Mn oxides demonstrates that no phase separation of the copper manganese oxide during the redox-cycling at these conditions occurs. In the sample recovered at the end of the seventh decomposition period of the p_{O_2} swing experiment $CuMnO_2$ (JCPDS 04-017-1231) and Mn_3O_4 (JCPDS 00-024-0734) were identified as the main phase by XRD (**Fig. 6-12b**). Furthermore, minor amounts of Mn_2O_3 (JCPDS 00-041-1442) and Cu_4O_3 (JCPDS 00-033-0480) were detected. In the decomposed sample recovered from *T* swing experiments the $CuMnO_2$ (JCPDS 04-017-1231) and Mn_2O_3 (JCPDS 00-041-1442) were identified by XRD. Based on the identified phases, it is proposed that the redox-reactions during the p_{O_2} swing and *T* swing experiments correspond to the reactions shown in eq.(6-24a) and eq.(6-24b), respectively.

$$3\ CuMn_2O_4 \leftrightarrow 3\ CuMnO_2 + 1\ Mn_3O_4 + O_2 \quad (6\text{-}24a)$$

$$4\ CuMn_2O_4 \leftrightarrow (4-n)\ CuMnO_2 + n\ CuMn_2O_4 \quad (6\text{-}24b)$$

Using the molecular masses of the phases shown in eq.(6-24a) a theoretical O_2 release capacity, $R_{0,th}$, of 4.49 wt% was calculated. This is close to the experimentally obtained value of 4.31 wt%.

Contrarily, the $R_{0,\mathrm{th}}$ for eq.(6-24b) cannot be determined from the balanced equation, as the equation has an infinite number of possible solutions, since *n* can assume any value between zero and four. The $R_{0,\mathrm{exp}}$ for this reaction is 2.01 wt% (*c.f.* **Fig. 6-10a**). The rate of weight change at the end of the decomposition period (after 30 min) in **Fig. 6-10a** is ~ zero, which indicates that this is the maximum conversion at this condition (when not considering very slow reactions). $R_{0,\mathrm{th}}$ equals $R_{0,\mathrm{exp}}$ if n = 1.61, which demonstrates that the two forms of copper manganese oxide on the right-hand side of eq.(6-24b) co-exist in considerable quantities.

Next, the recovered 1Cu-1Mn-CP(3:0) samples were studied by XRD, and the results are shown in **Fig. 6-13**, below.

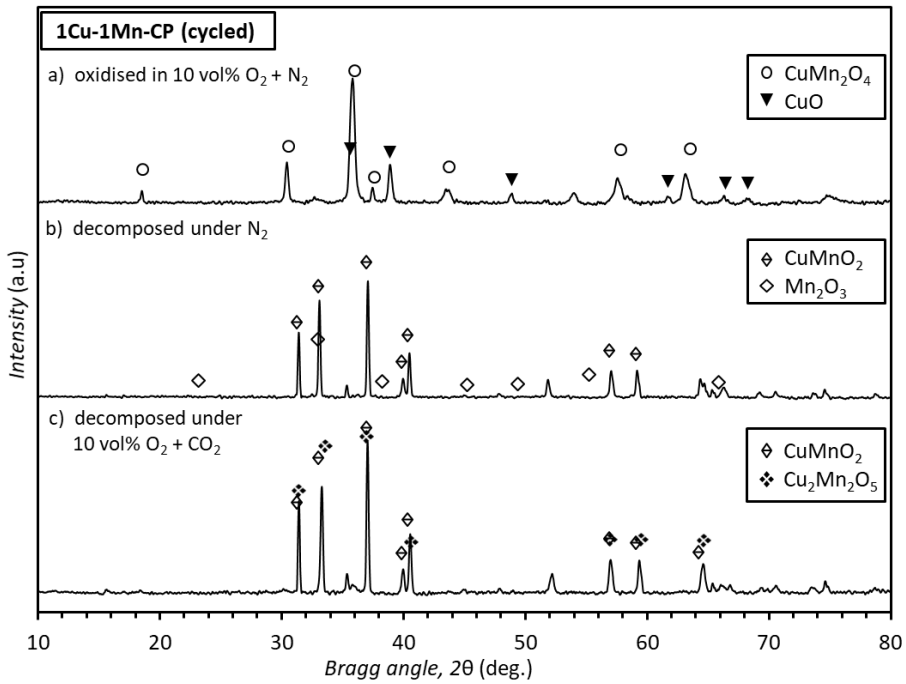


Fig. 6-13 *XRD patterns of the cycled 1Cu-1Mn-CP(3:0) oxygen carriers recovered in the seventh redox-cycled at the end of the (a) oxidation period with 10 vol% O_2 + N_2, (b) decomposition period of p_{O_2} swing experiments using pure N_2, and (c) decomposition period of the T swing experiments using 10 vol% O_2 + CO_2.*

During the XRD analysis of the redox-cycled 1Cu:1Mn-CP(3:0) oxygen carriers recovered at the end of the seventh oxidation period (**Fig. 6-13**) predominantly $CuMn_2O_4$ (JCPDS 01-071-1143) and minor amounts of CuO (JCPDS 00-045-0937) were identified. The fresh sample contained mainly $Cu_{1.5}Mn_{1.5}O_4$ (**Fig. 5-25b**). This finding suggests that the $Cu_{1.5}Mn_{1.5}O_4$ is separating into $CuMn_2O_4$ and CuO during the *T* swing and p_{O_2} swing experiments. In the reduced sample recovered from p_{O_2} swing cycling, $CuMnO_2$ (JCPDS 04-017-1231) was the only phase identified by XRD (**Fig. 6-11b**). Contrarily, in the reduced samples recovered from *T* swing experiments, $CuMnO_2$ (JCPDS 04-017-1231) and a defected perovskite-like structure with the composition $Cu_2Mn_2O_5$ (JCPDS 00-010-

0364) were identified (**Fig. 6-11c**). Based on the phases identified by XRD, it is proposed that the reactions shown in eq.(6-25a) and eq.(6-25b) occur during the redox-cycling by p_{O_2} and T swing cycling, respectively.

$$2\ CuMn_2O_4\ + 2\ CuO \leftrightarrow 4\ CuMnO_2\ +\ O_2 \tag{6-25a}$$

$$2\ CuMn_2O_4\ + 2\ CuO \leftrightarrow n\ CuMnO_2\ + \frac{4-n}{2} Cu_2Mn_2O_5 + \frac{n}{4} O_2 \tag{6-25b}$$

The theoretical O_2 release capacity, $R_{0,\mathrm{th}}$, calculated from eq.(6-25a) was 5.05 wt%. The experimentally obtained value during the p_{O_2} swing experiments was 4.81 wt%. Eq.(6-25b), which represents the redox-reactions during the *T* swing cycling has an infinite number of solutions, since *n* can assume any value between zero and four. For $R_{0,\mathrm{th}}$ to assume a value of 4.08 wt%, which is the experimentally obtained $R_{0,\mathrm{exp}}$, *n* has to be equal to 3.28. This shows that the sample consists predominantly of $CuMnO_2$. Further decomposition of $Cu_2Mn_2O_5$ to 2 CuO and Mn_2O_3 would be possible without affecting the R_0. However, this did not occur in this case, demonstrated by the absence of CuO and Mn_2O_3 peaks on the XRD plot (**Fig. 6-13c**). Decomposition of CuO to Cu_2O under 10 vol% O_2 + CO_2 at 850 °C and 0.1 MPa is thermodynamically not favourable since p_{O_2} (0.100 bar) is larger than the $p_{O_2,\mathrm{eq}}$ of CuO/Cu_2O at these conditions (0.042 bar).

The XRD plots of recovered 2Cu:1Mn-CP(3:0) oxygen carriers are shown in **Fig. 6-14**, below.

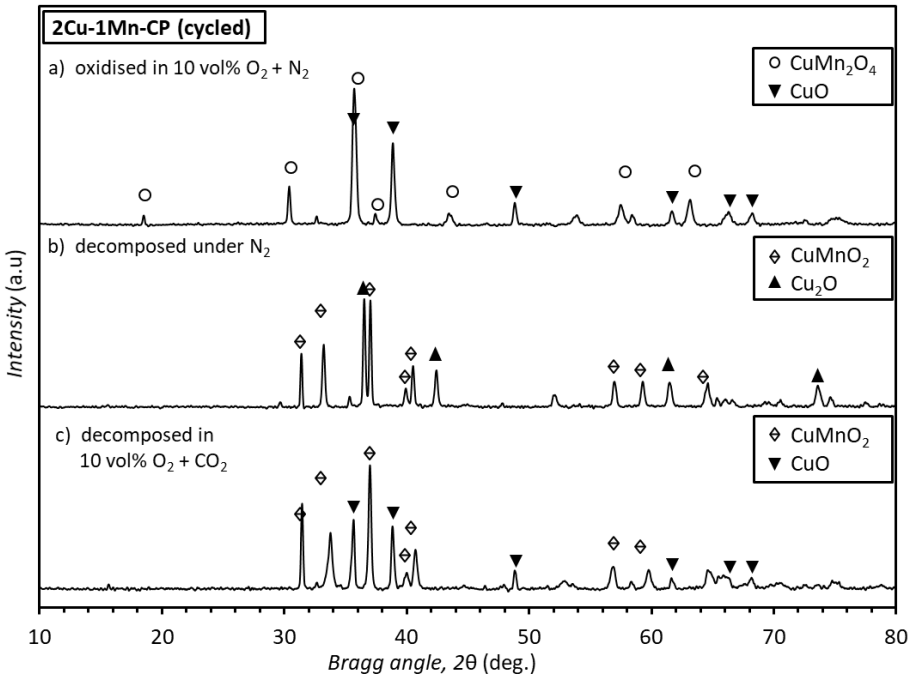


Fig. 6-14 *XRD patterns of the cycled 1Cu-2Mn-CP(3:0) oxygen carriers recovered in the seventh redox-cycled at the end of the (a) oxidation period with 10 vol% O_2 + N_2, (b) decomposition period of p_{O2} swing experiments using pure N_2, and (c) decomposition period of the T swing experiments using 10 vol% O_2 + CO_2.*

During XRD analysis of the oxidised 2Cu-1Mn-CP(3:0) oxygen carriers that were recovered from *T* swing experiments (Fig. 6-14a) $CuMn_2O_4$ (JCPDS 01-071-1143) and CuO (JCPDS 00-045-0937) were identified. XRD analysis of the fresh oxygen carriers (**Fig. 5-25c**) identified $Cu_{1.5}Mn_{1.5}O_4$ as the main phase. This indicates that over the seven redox-cycles, $Cu_{1.5}Mn_{1.5}O_4$ separates into $CuMn_2O_4$ and CuO. The decomposed oxygen carriers recovered from p_{O_2} swing experiments (**Fig. 6-14b**) contained $CuMnO_2$ (JCPDS 01-071-1143) and Cu_2O (JCPDS 00-005-0667), while the decomposed samples recovered from *T* swing experiments (**Fig. 6-14c**) contained $CuMnO_2$ (JCPDS 04-017-1231) and CuO (JCPDS 00-045-0937). It is therefore proposed that the redox-reactions during p_{O_2} swing and *T* swing cycling correspond to the reactions shown in eq.(6-26a) and eq.(6-26b), respectively.

$$CuMn_2O_4 + 3\,CuO \leftrightarrow 2\,CuMnO_2 + 1\,Cu_2O + O_2 \quad (6\text{-}26a)$$

$$2\,CuMn_2O_4 + 6\,CuO \leftrightarrow 4\,CuMnO_2 + 4\,CuO + O_2 \quad (6\text{-}26b)$$

From eq.(6-26a) and eq.(6-26b) an $R_{0,th}$ of 6.72 wt% and 3.36 wt% can be calculated for the p_{O_2} swing and *T* swing, respectively. These values are within 6% of the experimentally obtained values of 6.55 wt% and 3.17 wt% for the p_{O_2} swing and *T* swing, respectively.

The values of $R_{0,th}$ calculated from eq.(6-24a), eq.(6-25a), eq.(6-26a), and eq.(6-26b) are on average merely 4.4 wt% higher than the experimentally obtained values. This indicates that the proposed balanced equations are generally correct. The (relatively small) difference between the values of $R_{0,th}$ and $R_{0,exp}$ might be attributed to an unreacted core at the centre of the oxygen carrier particles, the loss of bed material during the experiments, or the formation of minor amounts of single metal oxides that were not considered in the stoichiometric equations – or a combination of all. Eq.(6-24a) and eq.(6-25a) represent linear combinations of reactions in different amounts. For the two equations, the value of *n* was determined experimentally at 850 °C in 10 vol% O_2 + N_2. It shall be noted that at different conditions *n* might assume different values. For the equations shown in eq.(6-24a) and eq.(6-25a), the value of $R_{0,exp}$ was found to be significantly lower than the value of $R_{0,th}$ for $n = 0$. This finding suggests that during a decomposition in the presence of O_2, the oxygen release capacities of the materials with Cu:Mn molar ratios in the range 1:1 – 1:2 are significantly reduced in comparison to a decomposition in the absence of O_2. This should be considered in future works on materials for the CLAS process when measuring the $R_{0,exp}$ of mixed metal oxides.

6.5 O_2 equilibria and enthalpy of the O_2 release

Precise knowledge of the O_2 equilibrium partial pressure, $p_{O_2,eq}$, of an oxygen carrier is important as the $p_{O_2,eq}$ is typically part of the reaction rate expression of the O_2 release and oxidation reaction.[228] Furthermore, it allows for the calculation of the enthalpy for the O_2 release reaction, as demonstrated by Patzschke *et al.*[46] For single metal oxides, the $p_{O_2,eq}$ can be determined by placing the oxygen carrier into an atmosphere with known p_{O_2}, followed by a slow increase (or decrease) in temperature. In theory, the temperature at which the first weight change due to the oxidation or decomposition of the oxygen carrier occurs is equal to the equilibrium temperature, T_{eq}. At this temperature $p_{O_2,eq}$ is equal to p_{O_2}.[46] In this work, a positive heating rate is used, and this method is referred to as the 'onset-of-decomposition' method. It was applied in section 6.5.1 to determine $p_{O_2,eq}(T)$. A disadvantage of this method is that it only measures the $p_{O_2,eq}(T)$ of the phase with the lowest, or the highest, T_{eq} for experiments with a positive heating rate or a negative heating rate, respectively. Therefore, a new rate-based method was developed, which allows determination of the $p_{O_2,eq}$ of a single phase system (*i.e.* combined metal oxide) or an effective $p_{O_2,eq}$ for a multi-phase system (*i.e.* mixed metal oxide), as described in section 6.5.2. This method was then applied to the oxygen carriers of this work (section 6.5.3).

6.5.1 Determination of the O_2 equilibria by the 'onset-of-decomposition' method

The $p_{O_2,eq}$ function of several oxygen carriers of this work was determined by measuring the equilibrium temperature, T_{eq}, for a given O_2 partial pressure, p_{O_2}. This was done by exposing 10 mg of fully oxidised oxygen carriers to a mixture of either O_2+N_2 or O_2+CO_2 with a known p_{O_2}. The temperature was then increased using a heating rate of 10 °C·min^{-1}. At temperatures where p_{O_2} = $p_{O_2,eq}$ was exceeded the O_2 release occurred. The temperature at the onset of the decomposition was assumed to equal T_{eq}. In this work, the method is therefore referred to as the 'onset-of-decomposition' method. A similar method was used by Li *et al.*[138] to compute the $p_{O_2,eq}$ curve for CoO/Co_3O_4. The values of T_{eq} can be identified manually, by identifying the temperature beyond which the relative mass (m/m_0) begins to decline or the measured rate of mass change (dm/dT) deviates from zero. However, an automated method has the advantage that it prevents biased results. Furthermore, it allows for faster data analysis. To determine T_{onset} a discontinuous function consisting of a linear fit for $T \geq T_{onset}$ and being zero below T_{onset} was used,

$$\left(\frac{\mathrm{d}m}{d\mathrm{T}}\right)_{model} = \begin{cases} 0, & \text{for } x = T_{\mathrm{eq}} \\ a \cdot (T - T_{\mathrm{eq}}) & \text{for } x \geq T_{\mathrm{eq}} \end{cases}, \tag{6-27}$$

where a is the slope of the function. Eq.(6-27) was fitted to the experimental data in a 40 °C temperature range around the assumed T_{eq}. Then the temperature range above T_{eq} was reduced so that only data points with $0 \leq \mathrm{d}m/\mathrm{d}T < 0.3$ µg °C^{-1} are considerd. A larger temperature range with $\mathrm{d}m/\mathrm{d}T > 0.3$ µg °C^{-1} would require fitting of a polynomial function to obtain a good fit, rather a linear function. Using a polynomial function instead of a linear function in eq.(6-27) for $x \geq T_{\mathrm{eq}}$ would result in a larger uncertainty in T_{eq}, hence the additional range restriction. For the fitting, T_{eq} and a in eq.(6-27) where varied using a mathematical solver to minimise the square error between the modelled and the experimental values for $\mathrm{d}m/\mathrm{d}T$. The data and the fitted function for a typical experiment are shown in **Fig. 6-15**, below.

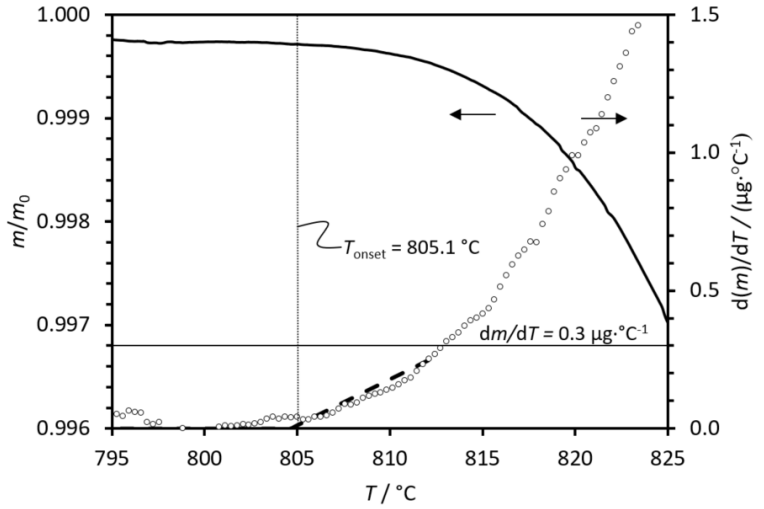


Fig. 6-15 *The experimental data and the fitted function for the determination of T_{eq} of 40-CuMn/Zr-MM by the 'onset of decomposition method' in the TGA using 2 vol% O_2 + N_2, a heating rate of 10 °C·min^{-1}, and a total flow rate of 150 ml·min^{-1}(SATP).*

For the data shown in **Fig. 6-15** the calculated value of T_{eq} is 805.1 °C. The experimentally determined for values of T_{eq} for 1Cu-1Mn-CP, 1Cu-2Mn-CP, and 40-CuMn/Zr-MM are presented in **Table 6-5**, below.

Table 6-5 *The experimentally determined equilibrium temperatures, T_{eq}, using the 'onset-of-decomposition method' in O_2+N_2 and O_2+CO_2 at 0.1 MPa.*

O_2+N_2						O_2+CO_2	
1Cu-2Mn-CP(3:0)		1Cu-1Mn-CP(3:0)		40-CuMn/Zr-MM		1Cu-1Mn-CP(3:0)	
p_{O_2}	T_{eq} (°C)[a]	p_{O_2}	T_{eq} (°C)	p_{O_2}	T_{eq} (°C)	p_{O_2}	T_{eq} (°C)
0.025	-	0.025	825	0.0025	725.6	0.0025	726
0.050	853.8	0.050	860.4	0.005	752.4	0.005	754
0.075	879.9	0.075	885.4	0.010	778.9	0.010	781
0.100	898.21	0.100	900.9	0.020	805.1	0.020	813
0.125	911.18	0.125	916.6	0.040	845.2	0.040	850
0.150	925.0	0.150	928.0	0.080	881.0	0.060	875
0.175	934.4	0.175	935.2	0.160	927.0	0.080	892
0.200	936.4	0.200	943.6	-	-	0.100	907

Footnotes: (a) the uncertainty in T_{eq}, $U(T_{eq})$ is ± 6.6 °C and was determined by 2·SD of the deviation between the measured values of T_{eq} and a best fit (power), (b) the uncertainty in y_{O2} is $u(y_{O2})$= 0.0047·y_{O2} and was determined using a gas analyser as described in Appendix A.6.

The results from **Table 6-5** are illustrated in **Fig. 6-16** and **Fig. 6-17**, below.

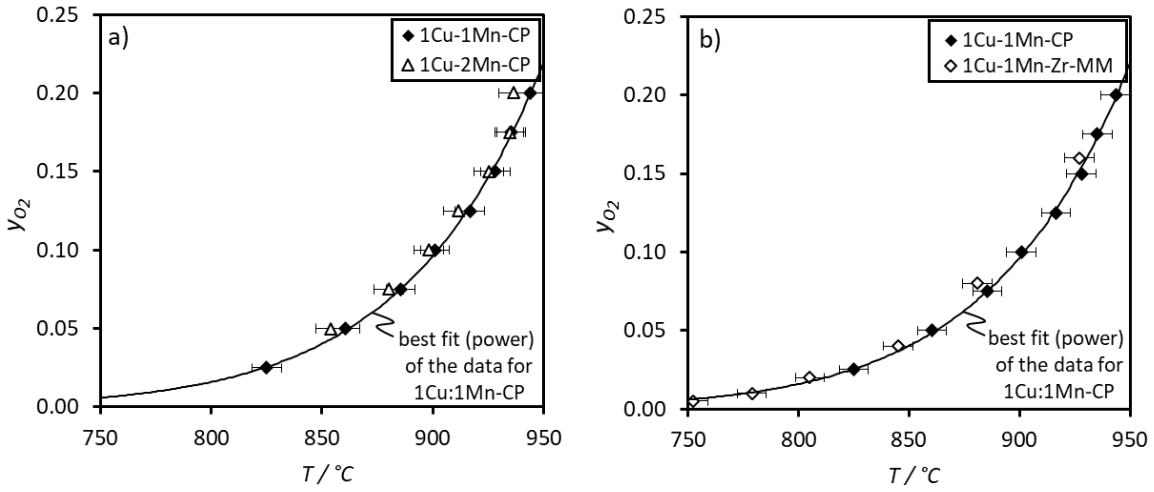


Fig. 6-16 *The experimentally obtained values of T_{eq} using the 'onset of decomposition method' in the TGA under O_2+N_2 for (a) 1Cu-1Mn-CP and 1Cu-2Mn-CP, and (b) 1Cu-1Mn-CP and 40-CuMn/Zr-MM, respectively.*

Fig. 6-16a shows that despite having different Cu:Mn molar ratios, the measured T_{eq} points of 1Cu-2Mn-CP and 1Cu-1Mn-CP agree within the experimental error. **Fig. 6-16b** compares the measured T_{eq} points of unsupported and ZrO_2-supported oxygen carriers with a 1Cu:1Mn molar ratio. The good agreement between the data points of the ZrO_2-supported oxygen carrier and the best fit for 1Cu:1Mn-CP indicates that the introduction of a supporting material does not affect the $p_{O_2,eq}$ significantly. Additionally, an experiment was carried out using O_2+CO_2, to study the effect of

substituting O_2+N_2 with O_2+CO_2. The results of the experiments with O_2+N_2 and O_2+CO_2 for 1Cu-1Mn-CP(3:0) are illustrated in **Fig. 6-17**, below.

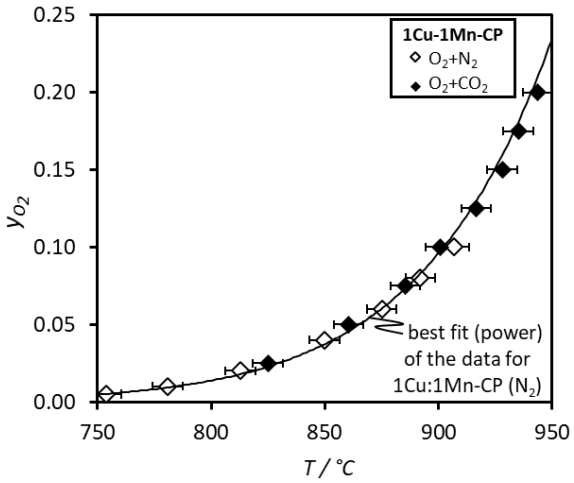


Fig. 6-17 *The experimentally obtained values of T_{eq} for 1Cu-1Mn-CP using the 'onset of decomposition method' in the TGA under O_2+N_2 and under O_2+CO_2.*

The measured points of T_{eq} in O_2+CO_2 deviate less than the uncertainty of the measurement, $U(T_{\mathrm{eq}})$, from the curve fitted to the points of T_{eq} measured in O_2+N_2 (black line in **Fig. 6-17**). This indicates that the $p_{\mathrm{O_2,eq}}$ is not significantly affected by a substitution of O_2+N_2 with O_2+CO_2 within the studied condition range.

The 'onset of decomposition' method has a significant drawback when being applied to multi-phase mixture. In a system with several phases with different $p_{\mathrm{O_2,eq}}(T)$, the method would only allow to determine the $p_{\mathrm{O_2,eq}}(T)$ of the material with the lowest or the highest T_{eq} when using oxidised samples with a positive or decomposed samples with a negative heating rate, respectively. The oxygen carriers that were studied in the experiments shown in **Fig. 6-16** and **Fig. 6-17** have an active phase with copper manganese oxide mass fractions close to unity (according to XRD analysis). In theory, the results of the experiments with these single phase combined metal oxides should result in the calculation of a $p_{\mathrm{O_2,eq}}(T)$, which leads to a correct result when being used in the typical reaction rate function for the O_2 release from oxygen carriers in a chemical looping process, *i.e.* $r = f(P, T, p_{\mathrm{O_2}}, p_{\mathrm{O_2,eq}})$.[228]

To test this assumption, a new method was developed, which measures an apparent $p_{\mathrm{O_2,eq}}(T)$ 'across' all phases. If the above assumption is correct, this new method should yield the same values for $p_{\mathrm{O_2,eq}}$ those obtained using the 'onset-of-decomposition method' when testing the materials from **Fig. 6-16** and **Fig. 6-17**. Since the new method is based on the observed maximum O_2 release rate, it is referred to hereafter as 'max-rate' method. The method is detailed in the following section.

6.5.2 Determination of the O_2 equilibria by the 'max-rate method'

In this section, a method for the calculation of $p_{O_2,eq}$ based on the maximum rate of O_2 release observed during TGA experiments is developed, validated with CuO powder, and used to determine the $p_{O_2,eq}$ of the copper manganese oxide oxygen carriers. The maximum O_2 release rate of a CLOU/CLAS oxygen carrier material is typically a function of $p_{O_2,eq}$, such as,[228]

$$r' = k \cdot \exp\left(\frac{-E_a}{RT}\right) \cdot [CuO]^{n_1} \cdot \left(p_{O_2,eq}(T) - p_{O_2}\right)^{n_2}, \tag{6-28}$$

where k is the pre-exponential factor, E_a the activation energy and n_1 and n_2 the orders of reaction with respect to the CuO concentration and $\left(p_{O_2,eq} - p_{O_2}\right)$, respectively. The results of a series of experiments in which p_{O_2} is varied at a given temperature should therefore produce a linear series of points on a plot on which p_{O_2} is plotted against r', provided that n has a value of unity, and for the case that the influence of the external mass transfer on the overall rate does not significantly change within the studied condition range. To prevent transitioning from a mass transfer-controlled to a kinetic-controlled rate regime, the studied p_{O_2} was limited to the range $(p_{O_2,eq} - 0.03\ \text{bar}) < p_{O_2} < p_{O_2,eq}$. The method was validated with CuO powder. This was done by comparing the experimentally obtained values of $p_{O_2,eq}$ for the system CuO/Cu_2O with data from FactSage[139] at temperatures in the range 900 °C – 975 °C. The O_2 release rate vs. conversion measured during such an experiment is shown in **Fig. 6-18a-b**, below.

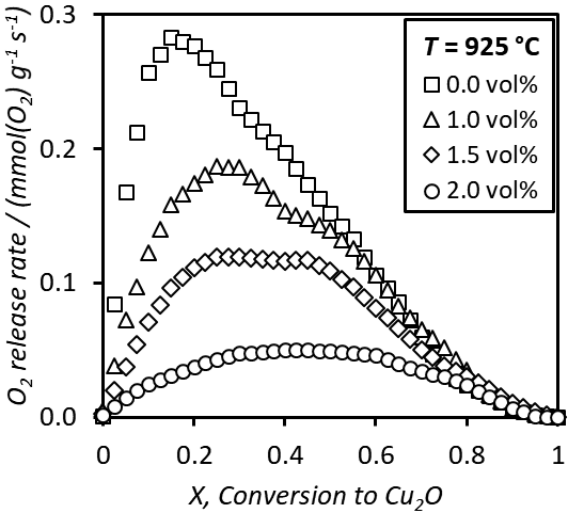


Fig. 6-18 *Observed rate of O_2 release of ~1 mg CuO powder measured in the TGA at 925 °C under N_2-diluted O_2 with varying O_2 molar fractions, using a total gas flow rate of 200 ml·min^{-1} at SATP.*

After processing the raw data, the maximum measured rates of O_2 release of a given temperature were plotted against the inlet O_2 partial pressure that was set during each experiment. Then, a linear

fit was plotted through the experimental points of a given temperature. The *x*-axis intercept of each line corresponds to the O_2 partial equilibrium pressure at this temperature under the above discussed assumptions. This method is illustrated in **Fig. 6-21**, below.

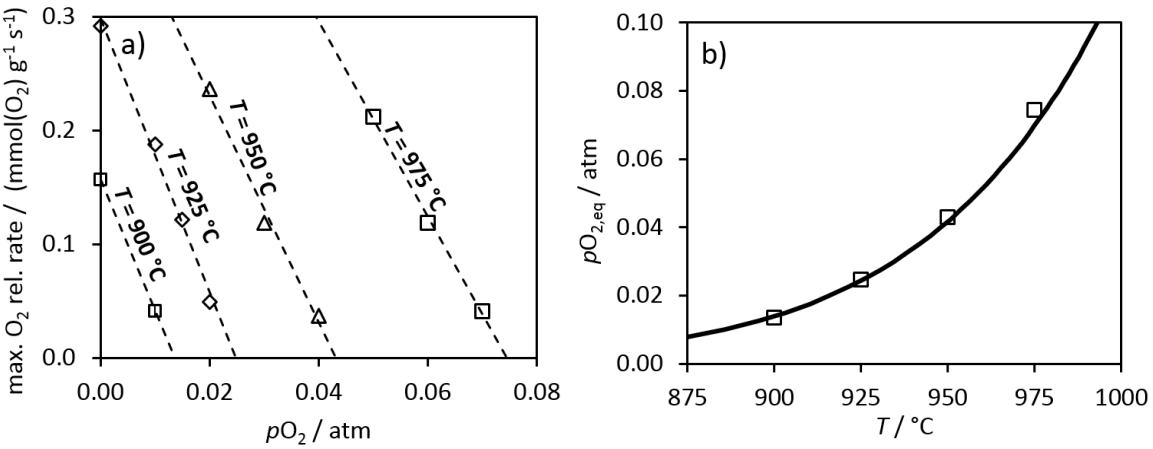


Fig. 6-19 *Results of the experiments with CuO powder to validate the 'max-rate method' for the measurements of the O_2 equilibria: (a) The maximum rate of decomposition plotted against the O_2 partial pressure at the TGA inlet, and (b) calculated points of $p_{O_2,eq}$ (markers) and $p_{O_2,eq}$-fuction from FactSage (line).*

The rate of external mass transfer for each condition was calculated using eq.(6-2) and eq.(6-3) to determine the influence of the mass transfer and compared against the measured rates, as shown in **Fig. 6-20**, below.

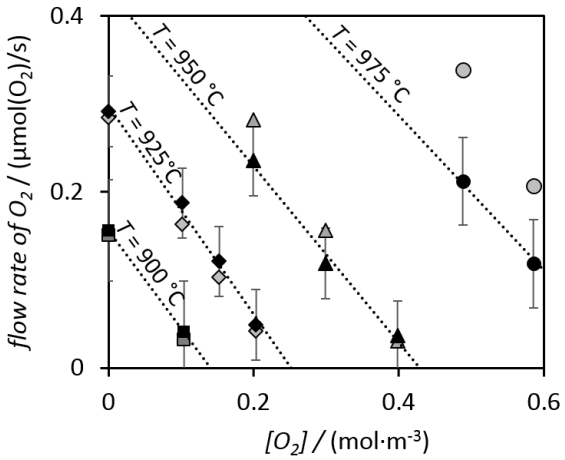


Fig. 6-20 *The measured flux of O_2 during the decomposition (black marker) and the maximum rate of external mass transfer (grey marker) for the experiments to determine the oxygen equilibria of CuO powder.*

From **Fig. 6-20** it becomes apparent that the rate measured during the experiments to obtain the O_2 equilibrium function is mainly controlled by external mass transfer. In the temperature range 900 °C – 950 °C, the maximum rate of mass transfer was within the uncertainty of the observed O_2 release rate, which was determined by repeated experiments. (*c.f.* error bars in **Fig. 6-20a**). This indicates

that the O_2 release in this temperature range is external mass transfer controlled. Only at 975 °C the rate of external mass transfer was significantly larger than the observed mass transfer. This also explains the deviation of the data point in **Fig. 6-20b** for 975 °C. As the intrinsic kinetics at 975 °C were lower than the rate of maximum mass transfer, the measure rate of O_2 release is lower as well, especially at lower partial pressures of oxygen. This decreases the slope of the best fit and shifts the *y*-axis interception to the right, *i.e.* to a higher oxygen partial pressure.

The 'max-rate method' to determine the $p_{O_2,eq}$ function was validated by the experiments with CuO powder and the comparison of the results with FactSage values. However, it demonstrates the importance of calculating the effect of the external mass transfer on the observed rate for each point.

6.5.3 Measurement of the O_2 equilibria using the 'max-rate method'

Experiments for the calculation of the $p_{O_2,eq}$ using the 'max-rate method' were carried out with 1Cu-1Mn-CP(3:0) oxygen carriers in the temperature range 800°C – 875 °C. The results of these experiments are shown in **Fig. 6-21**, below.

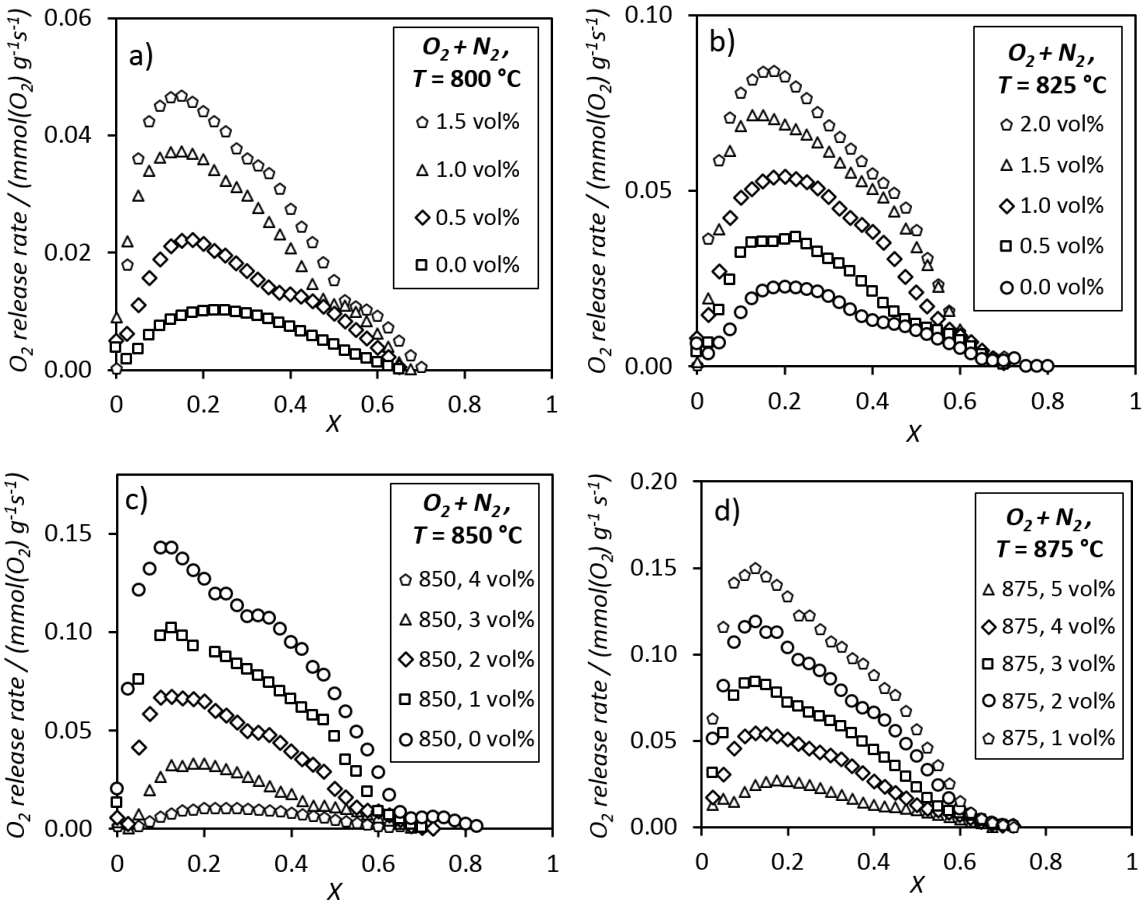


Fig. 6-21 *Measured reaction rate versus conversion of 1Cu-1Mn-CP(3:0) oxygen carriers under N_2-diluted O_2 at (a) T = 800 °C, (b) T = 825 °C, (c) T = 850 °C, and (d) T = 875 °C; using a gas flow rate of 150 ml·min^{-1}. For the calculation of the conversion redox-cycling between $Cu_{1.5}Mn_{1.5}O_4$ and $CuMnO_2$ was assumed.*

The maximum rates from **Fig. 6-21** were plotted against the set O_2 partial pressure. As detailed in the previous section, the *x*-axis interception of the linear best fit corresponds to the calculated $p_{O_2,eq}$ at a given temperature (**Fig. 6-22a**). Those equilibrium partial pressures are plotted against temperature, as shown in **Fig. 6-22b**, below.

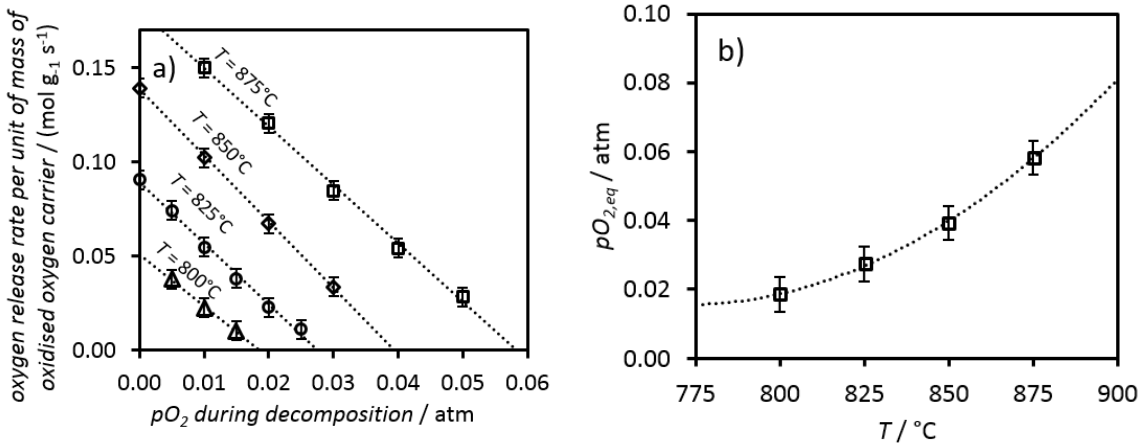


Fig. 6-22 *Plots of (a) observed rate of O_2 release against the p_{O2} at the TGA inlet for the determination of the $p_{O2,eq}$, and (b) the calculated values of $p_{O2,eq}$ against temperature. The experiments were carried out in the TGA using 1Cu-1Mn-CP(3:0) oxygen carriers and a total flow rate of 150 ml·min^{-1}.*

To test, if all points of the experiments illustrated in **Fig. 6-22a** were obtained in the same mass transfer regime, the observed rate of O_2 release was compared maximum rate of external mass transfer. The rate of mass transfer was calculated using eq.(6-2), and the results are illustrated in **Fig. 6-23**, below.

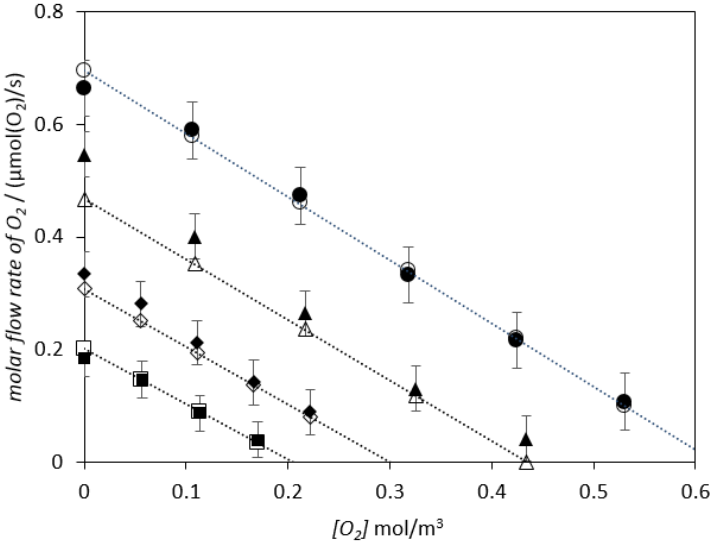


Fig. 6-23 *The calculated maximum rate of mass transfer at, □, 800 °C, ◇, 825 °C, △, 850 °C, ○, 875 °C, and the measured rate of O_2 release at, ■, 800 °C, ◆, 825 °C, ▲, 850 °C, ●, 875 °C. The small average relative deviation of 7% shows that the experiments to measure the $p_{O_2,eq}$ were at conditions where the overall rate equals the maximum rate of external mass transfer.*

Fig. 6-23 shows that the difference between the maximum rate of mass transfer and the maximum observed rate of O_2 release across the condition range shown in **Fig. 6-23** is within the experimental error of each other – this means that the observed rate is controlled by external mass transfer. The calculated values of $p_{O_2,eq}$ of this experimental series are detailed in the following section.

6.5.4 Results of the O_2 equilibrium measurements

The results of the $p_{O_2,eq}$ measurements for CuO and the copper manganese oxide oxygen carriers are shown in **Fig. 6-24**, below.

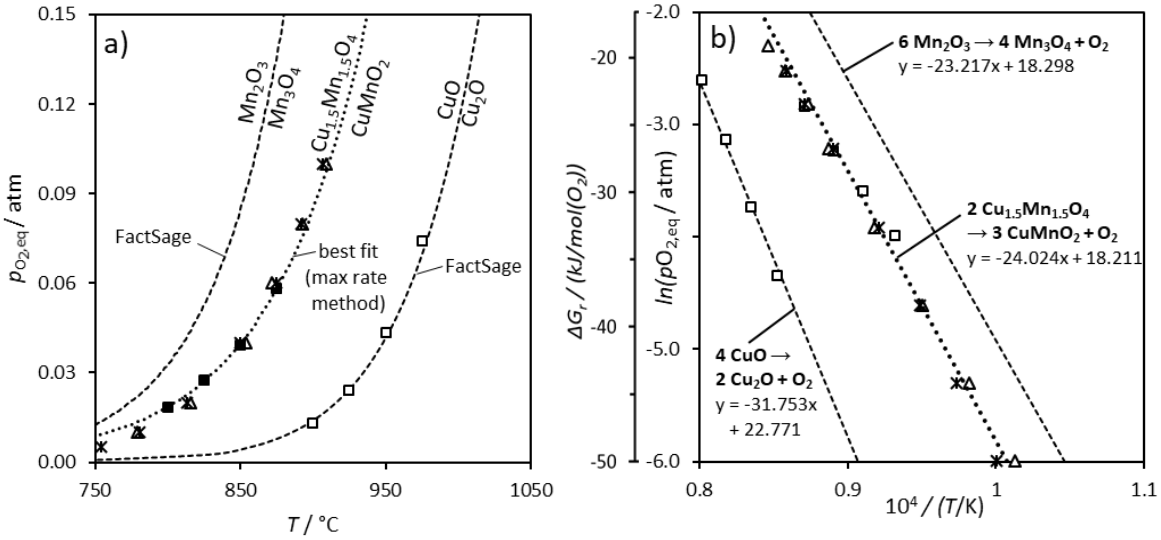


Fig. 6-24 *Oxygen partial pressure equilibrium ($p_{O2,eq}$) curves: plotted as (a) $p_{O2,eq}$ against T and (b) ln($p_{O2,eq}$) against 10^4/T (van 't Hoff plot). The dashed lines are FactSage values for Mn_2O_3/Mn_3O_4 and CuO/Cu_2O. The markers are experimentally obtained values for $p_{O2,eq}$ using the 'onset of O_2 release' method (✱,Δ) and the 'rate-based' method (□, ■); for 1Cu-1Mn-CP(3:0) (✱,Δ, □) and for CuO powder (■); under O_2+N_2 (□, ■ ,Δ) and O_2+CO_2 (✱).*

Fig. 6-24a shows good agreement between the results of the onset-of decomposition method and the results of the max-rate method. However, the onset-of decomposition method tends to underestimate the $p_{O_2,eq}$ at values below 0.03 bar slightly. Furthermore, comparison of the results of the onset-method for O_2+N_2 (Δ in **Fig. 6-24**) and for O_2 + CO_2 (✱ in **Fig. 6-24**) indicate that the $p_{O_2,eq}$ does not change when substituting O_2+N_2 with O_2+CO_2.

The calculated points of $p_{O_2,eq}$ were correlated using an Antoine type equation, which has the form,[229]

$$\ln\left(\frac{p_{O_2}}{atm}\right) = A - \frac{B}{\left({}^{T}/_{K}\right) + C}, \tag{6-29}$$

where $(T\ /\ \mathrm{K})$ is the temperature in Kelvin, and A, B and C are fitted parameters. When fitting the experimental data from **Fig. 6-24** to the three-parameter equation in eq.(6-35), *C* assumes a value of 0.0018 and the average deviation (0.854%) was only slightly lower than when fitting a two-parameter equation (0.853%). Therefore, the following two-parameter correlation is suggested for this work:

$$\ln\left(\frac{p_{O_2}}{atm}\right) = 16.960 - \frac{22710}{\left({}^{T}/_{K}\right)}, \tag{6-30}$$

For the experimental data from **Fig. 6-24** and the values calculated by eq.(6-30), the absolute average relative deviation, Δ_{AARD}, calculated by ${}^{1}/_{N}\,\Sigma(|p_{O_2,eq_{exp}} - p_{O_2,eq_{exp}}|)/p_{O_2,eq_{exp}}$ and the maximum average relative deviation, Δ_{MARD}, calculated by $\max(|p_{O_2,eq_{exp}} - p_{O_2,eq_{model}}|)/p_{O_2,eq_{exp}}$ are 0.852% and 5.6%, respectively.

The heat of O_2 release is an important parameter for the design of a CLAS process.[46] To determine this value, the results shown in **Fig. 6-24a** are replotted in **Fig. 6-24b** as a van 't Hoff plot (*i.e.* $\ln(p_{O_2,eq})$ is plotted against $10^4/T$).[46] During the O_2 release reaction, the energy of the material changes due to (i) the change of entropy ($\Delta S_{r,T}$), which is typically governed by the restructuring of the crystal structure upon the removal of lattice oxygen, and due to (ii) the heat that is thereby released ($\Delta H_{r,T}$). The total energy balances the kinetic energy of one mole of O_2 at its equilibrium point. This can be explained by the fundamental thermodynamic concept of the Gibbs free energy as:[27]

$$\mathrm{d}G = -S\mathrm{d}T + V\mathrm{d}P, \tag{6-31}$$

where *G* is the Gibbs free energy and *S, V* and *P*, are the entropy, the volume, and the pressure, respectively. During an isothermal O_2 release, d*T* is zero, and integration of both sides of eq.(6-31) yields,[230]

$$\Delta G = G^{\theta} + \int_{P\theta}^{P} V_m \mathrm{d}p, \tag{6-32}$$

where *p* is the pressure at which the O_2 release occurs, *i.e.* $p_{O_2,eq}$, P^{θ} is the reference pressure, *i.e.* the pressure of the surroundings, and V_m is the molar volume of O_2.

According to the ideal gas law, $V_m = RT/p$, and eq.(6-32) can therefore be rewritten as,[230]

$$\Delta G = G^{\theta} + RT \int_{P\theta}^{P} \mathrm{d}p = RT \ln\left(\frac{P}{P\theta}\right), \tag{6-33}$$

At the equilibrium, the Gibbs free energy is by definition zero. Furthermore, the Gibbs free energy is also a function of the entropy and the enthalpy:[230]

$$\Delta G^{\theta} = \Delta H^{\theta} - T\Delta S^{\theta}. \tag{6-34}$$

The eq.(6-33) and eq.(6-34) can be combined to,

$$T\Delta S^{\theta} - \Delta H^{\theta} = RT \ln\left(\frac{p_{O_2,eq}}{P^{\theta}}\right). \tag{6-35}$$

With P^{θ} = 0.1 MPa, the pressure at which experiments were carried out, the equation becomes,

$$\frac{\Delta S^{\theta}}{R} - \frac{\Delta H^{\theta}}{R} \cdot \frac{1}{T} = \ln\left({p_{O_2,eq}}/{0.1\ \mathrm{MPa}}\right) \tag{6-36}$$

Thus, when plotting $\ln(p_{O_2,eq})$ against $1/T$ (the van 't Hoff plot) the intercept is equal to $\Delta S^{\theta}/R$ and the slope is equal to $\Delta H^{\theta}/R$.

The derivation above[230] demonstrates, that when assuming O_2 behaves like an ideal gas, the energy of one mole is equal to *RT*, where *R*, the ideal gas constant, which has a value of 8.314 kJ/mol(O_2)/K. This relationship allows the addition of a second *y*-axis scale with the values of $\Delta G_{r,T}$ to the plot in **Fig. 6-24b**, which were obtained by multiplying $\ln(p_{O_2,eq})$ with *RT*. When using the $\Delta G_{r,T}$,-scale in **Fig. 6-24b**, the gradient of a line fitted to the experimental data points corresponds to $\Delta H_{r,T}$, while the y-axis interception is $\Delta S_{r,T}$ of the oxygen carrier. The values of $\Delta H_{r,T}$ and $\Delta S_{r,T}$ of the oxygen carriers are equal to those of the decomposition of $CuMn_2O_4$ to crednerite (*c.f.* (6-25a)) if the crystal structure of the samples is free of defects. The stable cycling performance that is reached after typically two to four activation cycles indicates that the activate crystal structure is mainly free of defects. Thus, it can be assumed that $\Delta H_{r,T}$ and $\Delta S_{r,T}$ of the activated oxygen carriers is approximately equal to $\Delta H_{r,T}$ and $\Delta S_{r,T}$ of the redox-reaction shown in eq.(6-25a).

The method of the calculation of $\Delta H_{r,T}$ and $\Delta S_{r,T}$ was validated with the data obtained for CuO powder (for the transition between CuO and Cu_2O; □ in **Fig. 6-24**). When using the correlation for the best fit of the data (the values of the correlation are shown on the graph in **Fig. 6-24b**), the calculated values for $\Delta H_{r,800°C}$ and $\Delta S_{r,800°C}$ are 264.0 kJ, and 189.3 J/mol/K, respectively. This is in good agreement with the values from FactSage ($\Delta H_{r,800°C}$ = 264.7 kJ and $\Delta S_{r,800°C}$ = 190.2 J/mol/K). For the 1Cu-1Mn-CP(3:0) oxygen carriers (■ in **Fig. 6-24**), the calculated values for the release of one mole of O_2 from 2 moles of $Cu_{1.5}Mn_{1.5}O_4$ are $\Delta H_{r,800°C}$ = 199.7 kJ and $\Delta S_{r,800°C}$ = 151.4 J/mol/K,

respectively. The positive value of $\Delta H_{r,800°C}$ indicates the endothermic nature of the reaction. To maintain the heat of the reducer in a CLAS process, heat has to be provided either by direct heating of the reactor or by indirect heating using hotter gases or hotter solids. The mass specific amount of heat that has to be transferred when using the 1Cu-1Mn-CP(3:0) oxygen carriers for the O_2 release can be estimated from $\Delta H_{r,800°C}$ and the molar mass of the compound (241.74 g/mol). Assuming full conversion, the heat of reaction is 413.1 kJ/kg(oxidised oxygen carriers). The values for Mn_2O_3/Mn_3O_4 and CuO/Cu_2O are 203.8 kJ/kg(Mn_2O_3) and 829.7 kJ/kg(CuO), respectively. This demonstrates that the 1Cu-1Mn-CP oxygen carrier material has a lower mass specific heat of O_2 release than CuO.

6.6 Observed rate of oxidation and O_2 release in the TGA

The observed rate of oxidation and O_2 release of the copper manganese oxide oxygen carriers was measured in the TGA to elucidate the effect of the temperature, the preparation method, the Cu:Mn molar ratio, and the gas composition (O_2+N_2 or O_2+CO_2) on the observed reaction rate and conversion. The results of the rate of O_2 release and oxidation observed during experiments in which the temperature was varied between 800 °C and 875 °C are shown in **Fig. 6-25**, below.

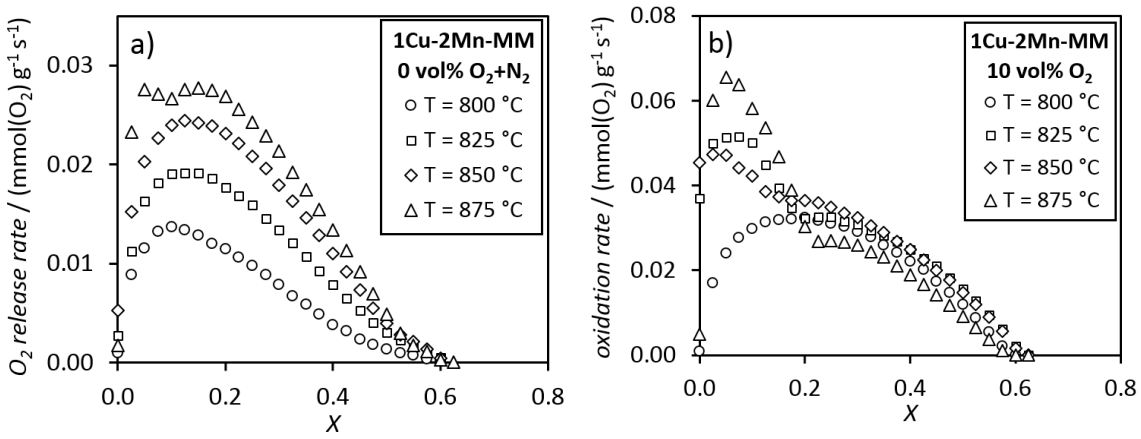


Fig. 6-25 *Plots of the observed (a) O_2 release rate and (b) oxidation rate versus conversion of 1Cu-2Mn-MM at different temperatures; the O_2 release and oxidation was carried out in 0 vol% O_2 + N_2 and 10 vol% O_2 + N_2, respectively. A sample mass of 1 mg and a gas flow rate of 200 ml·min^{-1} was used. The conversion was calculated using the balanced equation in eq.(6-24a).*

The maximum observed rate of oxidation of copper manganese oxide in 10 vol% O_2 (**Fig. 6-25b**) was around twice as high as the maximum observed O_2 release rate under N_2 at temperatures between 800 °C and 875 °C. The rate of oxidation peaks around $X = 0.1$ and falls rapidly until $X = 0.2$, after which the rate falls steadily with approximately the same profile for each temperature. This discontinuity of the profile might be attributed to the occurrence of two reactions with different reaction times - the fast oxidation of Mn_3O_4 to Mn_2O_3, and the slower oxidation of $CuMnO_2$ to $CuMn_2O_4$ with simultaneous incorporation of the manganese oxides into the lattice.

To study the effect of the Cu:Mn molar ratio on the observed rate of reaction mechanically mixed oxygen carriers with five different compositions have been tested at 850 °C. The results are shown in **Fig. 6-26**, below.

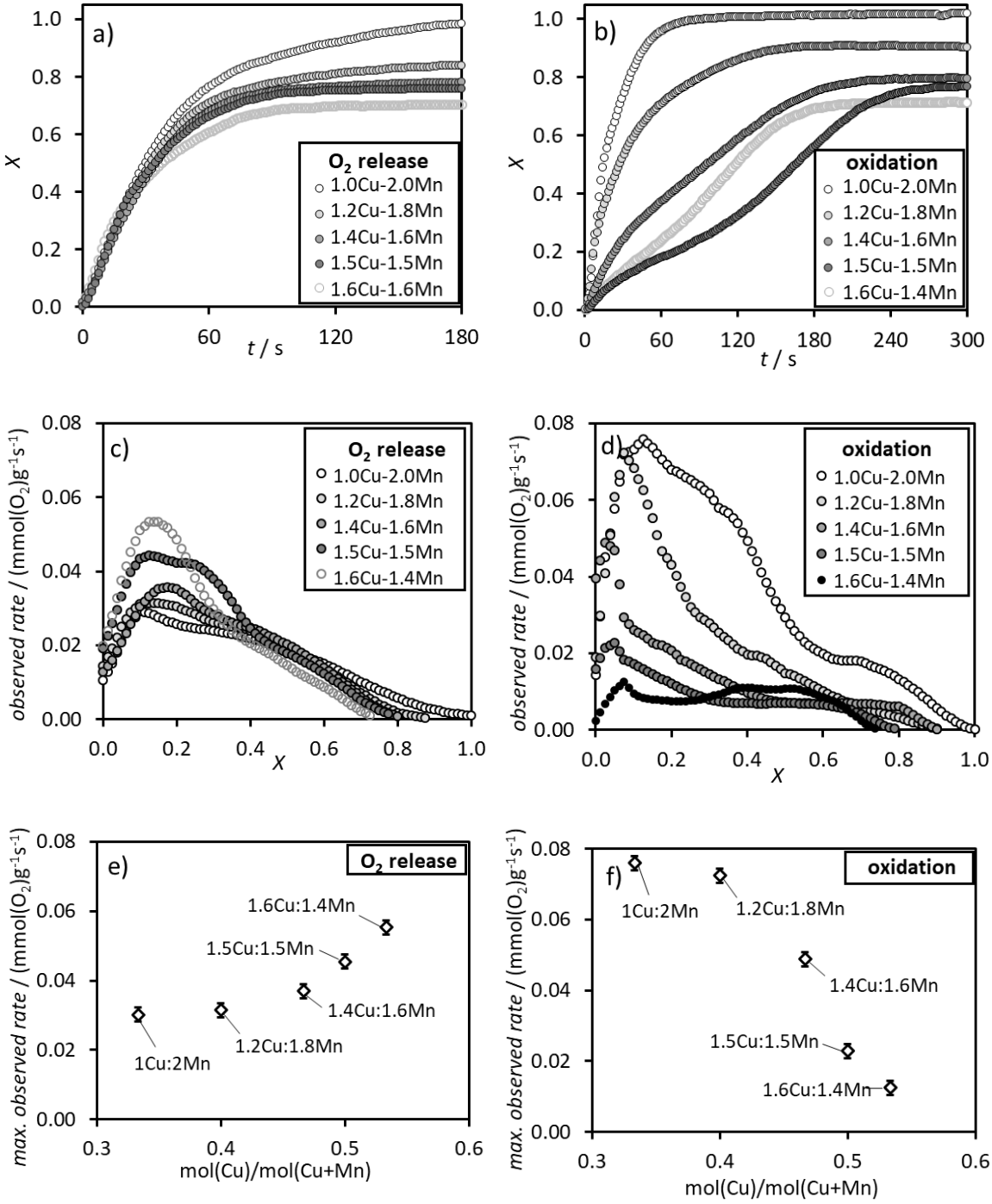


Fig. 6-26 *The effect of Cu:Mn molar ratio on the observed rate reaction of 2 mg mechanically mixed 150-212 µm oxygen carriers measured in the TGA (average of cycles 4 to 7) at 850 °C for the (a, c, e) O_2 release under pure N_2 and (b, d, f) oxidation in 10 vol% O_2 + N_2; the plots show (a, b) the conversion against time, (c, d) the observed rate against conversion, and (e, f) the maximum observed rate against the molar Cu/(Cu+Mn) ratio. A total gas flow rate of 200 ml·min^{-1} was used during the experiments.*

Fig. 6-26a shows that the oxygen carriers with a lower Cu content require less time to reach a conversion of X = 0.6 during the O_2 release. The order was found to be: 1.0Cu:2.0Mn (38 s) < 1.2Cu:1.8Mn (43 s) < 1.4Cu:1.6Mn (46 s) < 1.5Cu:1.5Mn (48 s) < 1.6Cu:1.6Mn (59 s). Contrarily, as shown in **Fig. 6-26b**, the oxygen carriers with a lower Cu content oxidised slower. The time to reach a conversion of X = 0.6 was in the order: 1.0Cu:2.0Mn (20 s) < 1.2Cu:1.8Mn (39 s) < 1.4Cu:1.6Mn (124 s) < 1.5Cu:1.50Mn (141 s) < 1.6Cu:1.4Mn (190 s). Presumably, the Cu oxides in the sample inhibit the oxidation rate.

The maximum observed rates of O_2 release (**Fig. 6-26c** and **e**) decreased with a decrease in Cu content. The order was: 1.0Cu:2.0Mn (0.030 mmol$(O_2)g^{-1}s^{-1}$) < 1.2Cu:1.8Mn (0.031 mmol$(O_2)g^{-1}s^{-1}$) < 1.4Cu:1.6Mn (0.037 mmol$(O_2)g^{-1}s^{-1}$) < 1.5Cu:1.50Mn (0.045 mmol$(O_2)g^{-1}s^{-1}$) < 1.6Cu:1.4Mn (0.055 mmol$(O_2)g^{-1}s^{-1}$). Contrarily, the observed rate of oxidation increased with a decrease in the Cu content: 1.0Cu:2.0Mn (0.076 mmol$(O_2)g^{-1}s^{-1}$) > 1.2Cu:1.8Mn (0.072 mmol$(O_2)g^{-1}s^{-1}$) > 1.4Cu:1.6Mn (0.049 mmol$(O_2)g^{-1}s^{-1}$) > 1.5Cu:1.50Mn (0.023 mmol$(O_2)g^{-1}s^{-1}$) < 1.6Cu:1.4Mn (0.012 mmol$(O_2)g^{-1}s^{-1}$).

Kinetic parameters were not calculated from the results of the TGA experiments owing to significant external mass transfer effects. The fluidised bed reactor (chapter 7) was used for measurements of the rates of reactions.

6.7 Possible reaction pathways of the redox reactions

To elucidate the reaction mechanism, partially reacted samples were analysed by XRD. A fully reduced sample was oxidised under 10 vol% O_2 + N_2, when reaching the desired conversion, which was calculated from the TGA reading of the actual sample mass, the reaction was slowed down by setting the $p_{O_2} = p_{O_2,eq}$ and the sample was rapidly cooled, with an initial cooling rate of -200 °C min^{-1}. During the cooling, the p_{O_2} was constantly adjusted to correspond to the $p_{O_2,eq}$ at a given temperature, which were calculated using eq.(6-30). The results for the experiments with 1Cu-1Mn-CP are shown in ***Fig. 6-27***, below.

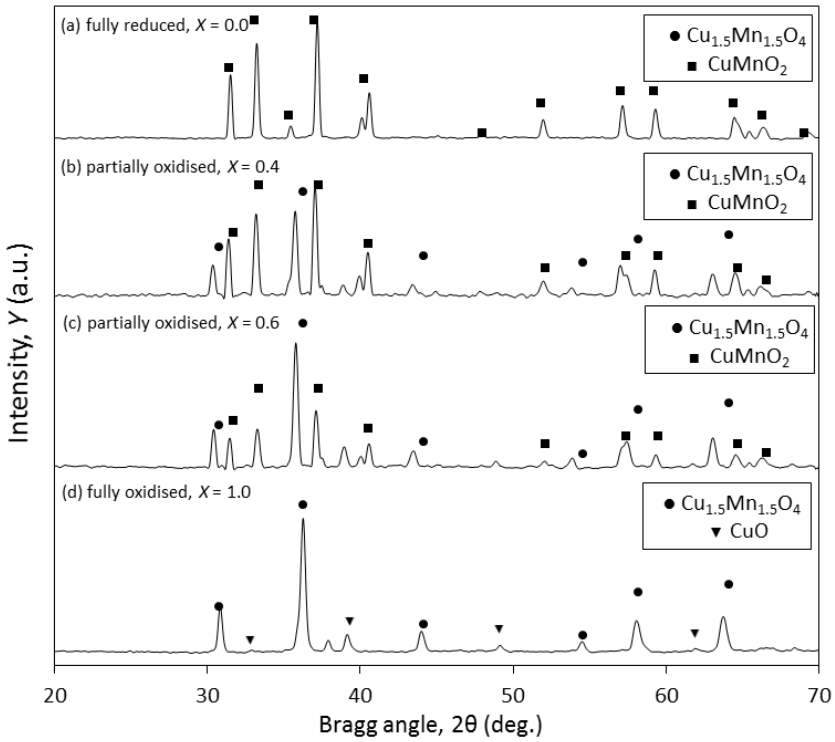


Fig. 6-27 *XRD patterns of the 1Cu-1Mn-CP samples after redox-cycling in the TGA at 850 °C with various conversion of the oxidation reaction: (a) fully reduced (X = 0), (b) partially oxidised (X = 0.4), (c) partially oxidised (X = 0.6), and (d) fully oxidised (X = 1).*

In the fully reduced sample (**Fig. 6-27a**) the only peaks that were identified belong to crednerite ($CuMnO_2$, JCPDS 04-017-1231). During the oxidation (**Fig. 6-27b→c →d)**, the two main phases that were identified belong to $CuMnO_2$ (JCPDS 01-071-1143) and $Cu_{1.5}Mn_{1.5}O_4$ (JCPDS 01-070-0262). The absence of significant amounts of the single metal oxides suggests that $CuMnO_2$ reacts directly to $Cu_xMn_{3-x}O_4$, without the formation of single metal oxide intermediates. However, HighScore did identify some minor amounts of a defected perovskite like compound with structure $Cu_2Mn_2O_5$ (JCPDS 00-010-0364). The absence of single metal oxides during the reaction suggests that phase separation is thermodynamically not favourable. Formation of single metal oxides during the reaction could have resulted in the undesired migration of one metal species relative to the other *via* solid state diffusion.

6.8 The performance of the oxygen carrier over 100 redox-cycles

The long-term cycling performance of the oxygen carriers was tested over 100 redox-cycles in the TGA. The reduction of the oxygen carriers was carried out (i) by O_2 partial pressure swing (*e.g.* relevant for packed-bed reactors) and (ii) by temperature swing. The aim of this study is to assess if the reaction rates and O_2 capacities are stable over 100 cycles, and to identify differences in the kind and rate of oxygen carrier deterioration due to the chemical stresses in the TGA. The observed rate of reaction (which includes external mass transfer effects and intra-particle diffusion effects) was determined by calculating the observed rate of reaction between each recorded weight measurement by,

$$\mathrm{r}'(t)/\ (\mathrm{mol}(\mathrm{O_2})\mathrm{g}^{-1}\mathrm{s}^{-1}) = \frac{\mathrm{d}m}{\mathrm{d}t} \cdot \frac{1}{m_{\mathrm{ox}} \cdot M_{\mathrm{O_2}}}, \tag{6-37}$$

where m is the mass of the sample at time t, m_{ox} is the mass of the fully oxidised sample, and $M_{\mathrm{O_2}}$ is the relative molecular mass of O_2. The sampling rate was 0.2 s^{-1}, and the maximum observed rate was calculated from the three highest values of $\mathrm{r}'(t)$ and corrected by the method presented in **Appendix A.7**. The oxygen capacities, $R_{0,\mathrm{exp}}$, were calculated using the method that was presented in section 6.4 (*c.f.* eq.(6-23)), using the average mass of the sample in the last 30 s of the oxidation period and of the reducing period, respectively. The calculated values for $R_{0,\mathrm{exp}}$ are reported without any smoothing.

In the following sections the results of experiments with redox-cycling by O_2 partial pressure swing (section 6.8.1) and temperature swing (section 6.8.2) are presented.

6.8.1 Cycling of the oxygen carriers by O_2 partial pressure swing

The result of the TGA long-term experiments for the redox-cycling by p_{O_2} swing with oxidation under 10 vol% O_2 + N_2 and decomposition under N_2 at 850 °C are shown in **Fig. 6-28**, below.

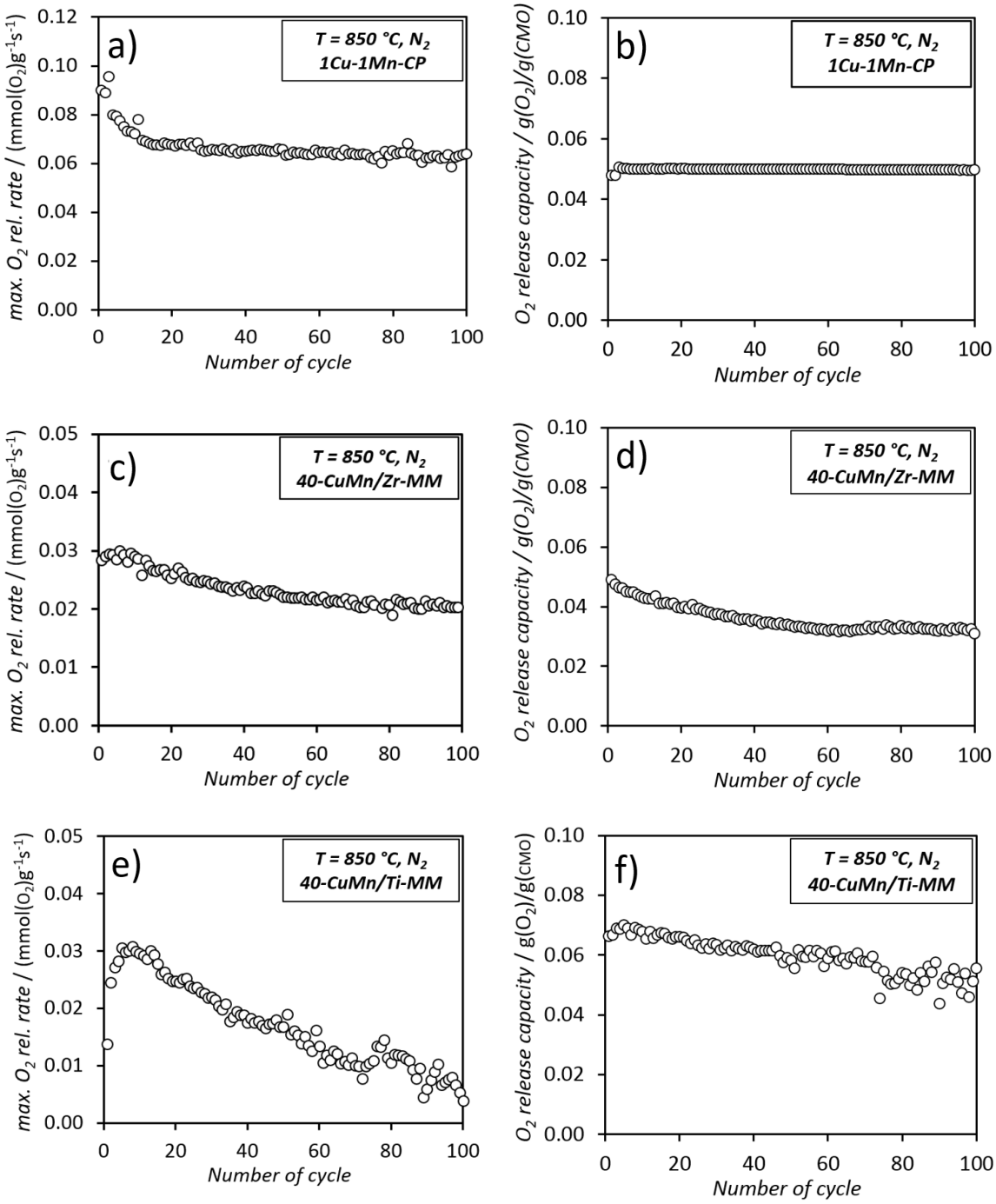


Fig. 6-28 *The (a, c, e) maximum observed rate of O_2 release and (b, d, f) O_2 storage capacity over 100 cycles of 2 mg 150-210 µm (a, b) 1Cu-1Mn-CP(3:0), (c, d) 40-CuMn/Zr-MM, and (e, f) 40-CuMn/Ti-MM measured in the TGA at 850 °C. The gas during the oxidation and O_2 release was 10 vol% O_2 + N_2 and pure N_2, respectively, and the total gas flow rate was 200 ml.min^{-1} at SATP.*

Fig. 6-28a shows that the observed maximum rate of O_2 release of 1Cu-1Mn-CP decreased over the first 15 cycles by 24% (from 0.088 to 0.067 mmol(O_2)$g^{-1}s^{-1}$). Then, over the cycles 15 to 100 the rate decreased by 5% (from 0.067 to 0.064 mmol(O_2)$g^{-1}s^{-1}$), which was determined from the slope of a linear best fit over this cycle number range. XRD analysis in the previous section (**Fig. 6-13**) had revealed that the $Cu_{1.5}Mn_{1.5}O_4$ initially present in the (oxidised) fresh oxygen carriers is converted to $CuMn_2O_4$ and CuO over the few redox-cycles, which presumably is the reason for the initial decrease in the O_2 release rate. The $R_{0,\mathrm{exp}}$ of the sample was stable at 4.99 wt% over the 100 redox-cycles (**Fig. 6-28b**).

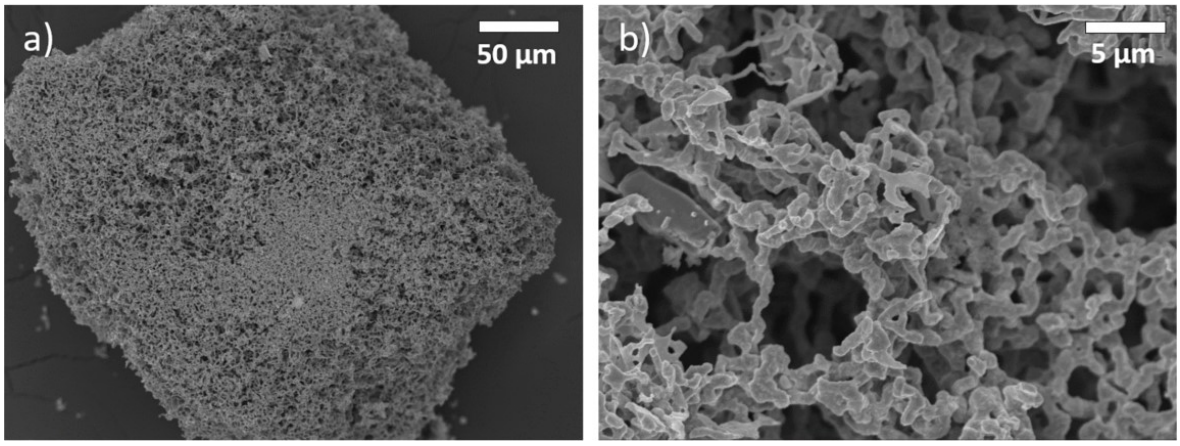


Fig. 6-29 *SEM of a redox-cycled 1Cu-1Mn-CP(3:0) oxygen carrier (a) particle and (b) the particle surface recovered after 100 p_{O2} swing cycles in the TGA. The oxygen carriers are from a size range of 150-210 µm and 1 mg of sample was used. The gas used at a flow rate of 200 ml·min^{-1} at SATP is 10 vol% O_2 and 0 vol% O_2 balanced with N_2 for oxidation and reduction, respectively.*

Fig. 6-28c shows that the O_2 release rate of the ZrO_2 supported oxygen carriers decreased over the first 70 cycles by 29% (from 0.029 to 0.021 mmol(O_2)$g^{-1}s^{-1}$) before being stable. The O_2 release capacity (**Fig. 6-28d**) showed a similar behaviour. It decreased by 32% (from 4.7 to 3.2 wt%) over the first 61 cycles, and then remained almost stable (-0.2 wt%) over the cycles 61 to 100. To elucidate the reason for the reduction in the maximum observed O_2 release rate, the cycled oxygen carriers were analysed by SEM and the results are shown in **Fig. 6-30**, below.

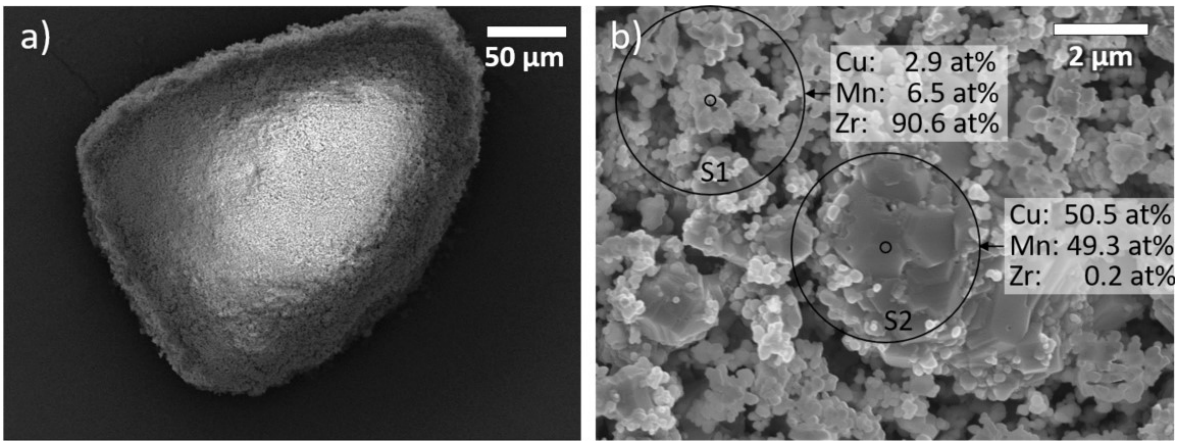


Fig. 6-30 *SEM of a redox-cycled 40-CuMn/Zr-MM oxygen carrier (a) particle and (b) the particle surface recovered after 100 p_{O2} swing cycles in the TGA. The atom percentages in (b) were determined by EDS. The smaller and the larger black circles indicate the centre and the circumference of the area of the area measured by EDS. The oxygen carriers are from a size range of 150-210 µm and 1 mg of sample was used. The gas used at a flow rate of 200 ml·min^{-1} at SATP is 10 vol% O_2 and 0 vol% O_2 balanced with N_2 for oxidation and reduction, respectively.*

Fig. 6-30a shows a ZrO_2-supported oxygen carrier particle recovered after 100 p_{O_2} swing cycles in the TGA, which appears to have densified in the presence of ZrO_2 (this theory is later studied in detail during FBR experiments and confirmed, *c.f.* section 7.3.2). Furthermore, large CMO grains can be seen in **Fig. 6-30b**. The longest visible length of the CMO grain in **Fig. 6-30b** on which the EDS spectra S2 points measures 7.61 µm. The mean diameter of the CMO grains in the fresh mechanically mixed oxygen carrier is 1.35 µm and the log-normal distribution of the grain size suggests that 98% of the grains have a diameter below 3.08 µm. This indicates that CMO grain growth occurred over the 100 redox-cycles of the experiment. The decrease in rate with increasing cycle number was attributed to this growth of the CMO grains. A larger grain size requires the ions to migrate a longer average distance by solid-state diffusion through the lattice to reach before they desorb at the solid-gas interface of the CMO grain. Since the intrinsic rate of reaction (*i.e.* a series of chemical reaction rate, diffusion through the lattice and diffusion across grain boundaries) is affecting the overall rate of reaction (*c.f.* section 6.3), a slower intrinsic rate owing to coalescence of the CMO grains results in a lower observed rate.

The O_2 release rate of 40-CuMn/Ti-MM oxygen carriers in **Fig. 6-28e** increased over the first five redox-cycles, which was attributed to activation processes. A second-order polynomial fit through the experimental points of cycle 6 to cycles 100 showed that over this range the maximum observed O_2 release rate decreased by 77% (from 0.031 to 0.007 mmol(O_2)g^{-1}s^{-1}). Over the same range, the O_2 release capacity decreased by 26% (from 6.8 wt% to 5.0 wt%; **Fig. 6-28f**). The cycled sample was analysed by SEM-EDS, as illustrated in **Fig. 6-31**, below.

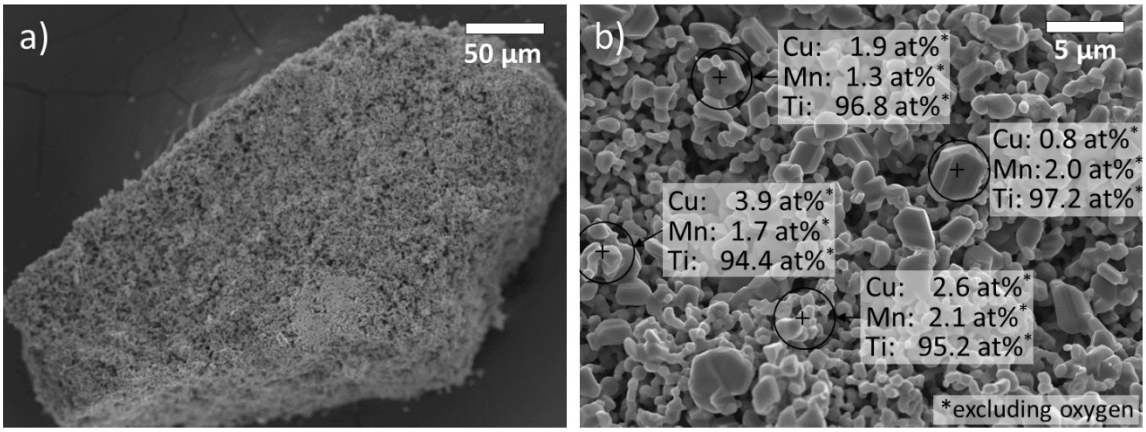


Fig. 6-31 *SEM with values for atom fractions quantified by EDXS of 60 wt% TiO_2/1Cu-1Mn-MM after 100 redox-cycles in the TGA. White cross and the dashed circle indicate the centre and the circumference of the area on which the X-ray detector is focused. The values in the black-transparent boxes indicate the respective atom percent. The oxygen carriers are from the size range 150-210 µm and 1 mg of sample was used. The gas used at a flow rate of 200 ml.min^{-1} at SATP is 10 vol% O_2 and 0 vol% O_2 balanced with N_2 for oxidation and reduction, respectively.*

The cycled TiO_2-supported oxygen carrier particle shown in **Fig. 6-31a** does not appear as densified as the ZrO_2-supported cycled particle (**Fig. 6-30a**). The large reduction in the O_2 release rate and O_2 release capacity due to structural changes (*e.g.* a loss of pores due to sintering) is therefore unlikely. The atom percentages in **Fig. 6-31b** indicate that the grains on the surface of the particle contain predominantly TiO_2. This in turn indicates that the TiO_2 migrated outwards relative to the copper manganese oxide. Generally, the formation of a core-shell with harder supporting material being in the shell might be desirable, since this might further reduce the rate of attrition and the agglomeration tendency. However, it seems that this separation between active phase and supporting material and possibly a phase change inside the particle have cause a significant deactivation (*e.g.* due to the formation of parasitic phases). The sample mass was too low for the determination of the phases by XRD. When repeating the experiment in the FBR and studying the phases of the recovered particles by XRD it was found that most Mn had formed $TiMnO_3$.

6.8.2 Cycling of the oxygen carrier by temperature swing

Temperature swing experiments were carried out to assess the cycling-behaviour of the oxygen carriers at conditions that better approximate the operation in the CLAS process. The oxygen carriers were oxidised at 800 °C in 10 vol% O_2 balanced with N_2. The temperature was then rapidly increased to 950 °C and O_2 release occurred in 10 vol% O_2 balanced with CO_2. The maximum rate of temperature change between the periods was 200 °C min^{-1}. The results of the temperature swing experiments are shown in **Fig. 6-32**, below.

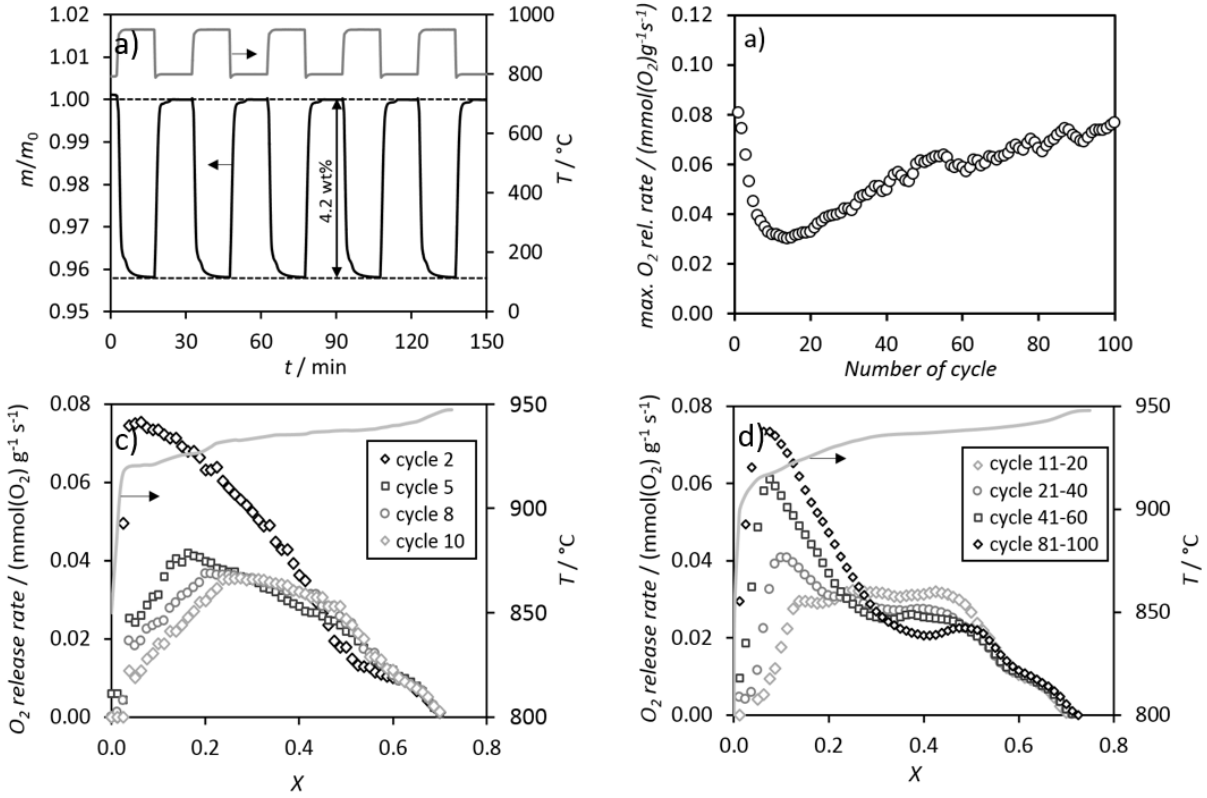


Fig. 6-32 *Results of the T swing experiments in the TGA using 150-212 µm 1Cu-1Mn-CP oxygen carriers with oxidation at 800 °C in 10 vol% O_2 balanced with N_2 and decomposition at 950 °C in 10 vol% O_2 balanced with CO_2: (a) a plot of the relative mass (black lines) and the temperature (grey lines) measured during an experiment with 40 mg of the oxygen carriers for the determination of the $R_{0,exp}$, and (b-d) results of the long-term cycling experiments using 4 mg of the oxygen carriers; (b) is a plot of the O_2 release reaction rate over 100 cycles, (c) shows the O_2 release rate over the conversion during the first cycles of the long-term-cycling experiment and (d) shows averages of the O_2 release rate for cycles 11 to 100. The grey-lines in (c) and (d) show the temperature inside the TGA furnace average for the cycles 1-10 and 11-100, respectively. The gas flow rate was kept constant at 170 ml min^{-1} at SATP and the dT/dt during the temperature jumps was 200 °C min^{-1}.*

Fig. 6-32a shows that stable redox-cycling by *T* swing is possible, and that a O_2+CO_2 mixture with 10 vol% O_2 can be produced at these conditions. **Fig. 6-32b** shows that over the first 10 cycles the maximum O_2 release rate decreased by 62% (from 0.08 mol(O_2) g^{-1} s^{-1} to 0.03 mol(O_2) g^{-1} s^{-1}), and

then increased steadily to reach its initial value (0.08 mol(O_2) g^{-1} s^{-1}) around cycle 100. **Fig. 6-32 c** and **Fig. 6-32 d** show the reaction rate profiles during the long-term cycling experiments. The conversion range remains stable over the course of the experiment. The decreases and subsequent recovery of the maximum O_2 release rate is most likely due to changes in the structure of the oxygen carrier (*e.g.* the blocking of micro-pores during the first 10 cycles and subsequent re-opening). To test this hypothesis, fresh and cycled samples were analysed by SEM, as shown in **Fig. 6-33**, below.

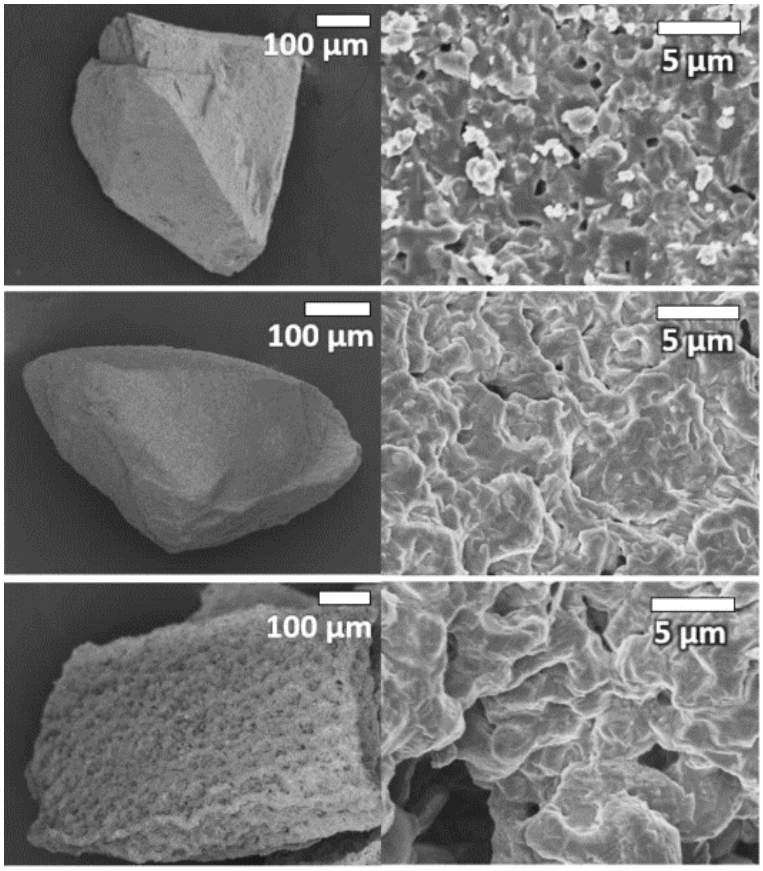


Fig. 6-33 *Scanning electron micrographs of fresh and cycled 1Cu-1Mn-CP(2:1)-pH7.2 oxygen carriers. The micrographs (a, b) show the fresh sample, (c, d) the sample after 10 T-swing cycles, and (e, f) the sample after 100 T-swing cycles, (a, c, e) 300 x, and (b, d, f) 10 000 x magnified. The temperature swing was carried out in the TGA between 850 °C* and *950°C using 10 vol% O_2 balanced with N_2 during the oxidation and CO_2 during the decomposition. The gas flow rate was kept constant at 200 ml.min^{-1} at SATP.*

Fewer pores on the surface of the sample can be seen after 10 cycles (**Fig. 6-33c** and **d**) compared to the fresh sample (**Fig. 6-33a** and **b**), which might indicate that the rapid initial decrease in the observed rate is a result of an increase in intra-particular diffusion resistance due to 'clogging' of the pores. After 100 cycles (**Fig. 6-33e** and **f**) pores at the surface of the sample are visible, which co-inside with the increase in the observed rate. The sample mass was insufficient to demonstrate the absence of pores after 10 cycles by MIP. The experiments have therefore been repeated with a larger sample mass. Though direct comparison is not possible, since contribution of external mass transfer

is significantly larger, MIP analysis of the sample recovered after 10 *T* swing cycles confirmed the absence of micro-pores (no pores with d_{pore} < 4 µm were measured). Contrarily, the smallest pore size measured by MIP in the samples after 10 p_{O_2} swing cycles was 0.4 µm, as detailed in the next section. Besides the ability to study the differences in the changes in pore morphology over 100 cycles by *T* swing and p_{O_2} swing, the experiments with a larger sample mass were also conducted to recover sufficient material for crushing strength tests.

6.8.3 Change of crushing strength over 100 redox-cycles

Understanding the relationship between the change of mechanical properties over extended redox-cycling and the redox-cycling mode (*T* swing or p_{O_2} swing) allows the estimation of the effect of the redox-cycling mode on the average oxygen carrier lifetime (and thus the resulting changes in cost due to the renewal of oxygen carriers), which in turn can be a further consideration for the process design. For this reason, oxygen carriers from the same batch (1Cu-1M-CP(2:1) *pH* 7.0) were cycled by p_{O_2} swing (*e.g.* rather relevant for O_2 production in a packed bed reactor) and by *T* swing (*e.g.* relevant for conventional dual fluidising bed reactor set-up). Oxygen carriers with a relatively high crushing strength (10.0 ± 0.8 N) were chosen so that the reduction in crushing strength becomes more apparent. Experiments were carried out over 10 and 100 redox-cycles, and the crushing strength of the fresh and cycled oxygen carriers was measured. The results are shown in **Fig. 6-34**, below.

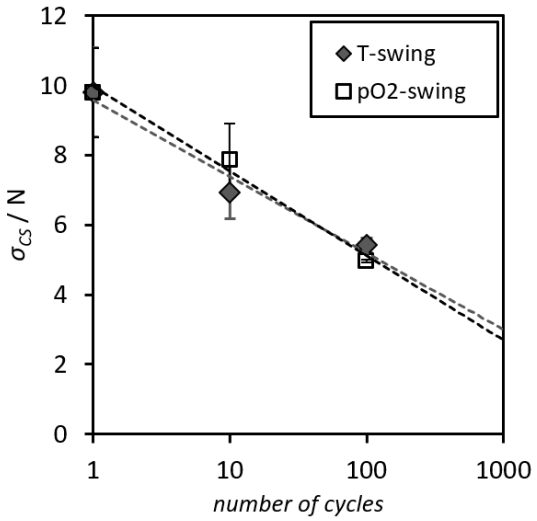


Fig. 6-34 *The results of the crushing strength measurement of 1Cu-1Mn-CP(2:1)-pH7.2 cycled by different chemical looping modes in the TGA. The temperature swing was carried out between 850 °C* and *950°C using 10 vol% O_2 balanced with N_2 during the oxidation and CO_2 during the decomposition. The O_2 partial pressure swing was carried out at 850 °C using 10 vol% O_2 + N_2 during the oxidation and pure N_2 during the decomposition. The gas flow rate was kept constant at 200 ml.min^{-1} at SATP.*

Fig. 6-34 shows that the crushing strength of the sample cycled by the two different modes decreases steadily with an increase in cycle number. After 10 cycles the sample cycled by *T* swing has a slightly lower crushing strength (6.9 ± 0.7 N) than the sample cycled by p_{O_2} swing (7.9 ± 1.8 N). However, the difference is smaller than the uncertainty (*c.f.* error bars in **Fig. 6-34**). After 100 cycles the sample cycled by *T* swing was found to have a slightly higher crushing strength (5.4 ± 0.2 N) than the sample cycled by p_{O_2} swing (4.9 ± 0.1 N), though the difference is only slightly larger than the uncertainty. This suggests that the rate of the decrease of crushing strength beyond cycle 10 is slightly slower when cycling the sample by *T* swing instead of p_{O_2} swing. Mercury intrusion porosimetry (MIP) was carried out to elucidate the reason for decrease in crushing strength. The results are plotted in **Fig. 6-35**, below.

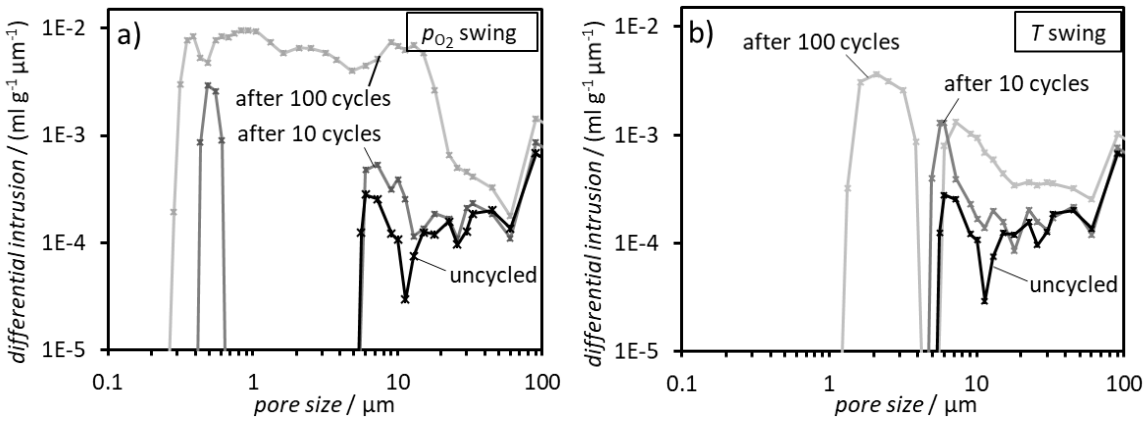


Fig. 6-35 *Plots of the differential intrusion (DI) against pore size of 1Cu-1M-CP(2:1) oxygen carriers measured by MIP of (a) the fresh sample and the samples cycled by temperature swing, and (b) the fresh sample and the samples cycles by p_{O2}-swing.*

Only pores larger than 4.9 µm with $DI \geq 0.01$ µl g^{-1} µm^{-1} were identified in the fresh sample (black markers in **Fig. 6-35a** and **b**). After 10 cycles, the differential intrusion over most of this pore size range (5 µm – 40 µm) had increased during the *T* swing and p_{O_2} swing experiments (dark grey markers in **Fig. 6-35a** and **b**). However, in the sample cycled by p_{O_2} swing, pores in the range between 0.3 µm and 0.5 µm were additionally detected after 10 cycles (dark grey markers in **Fig. 6-35a**). After 100 p_{O_2} swing cycles this bi-modal distribution of pores that was identified after 10 cycles had combined into a wide pore size distribution with $DI > 1$ µl g^{-1} µm^{-1} between 0.3 µm and 22 µm (light grey markers in **Fig. 6-35a**). Conversely, no pores with DI ≥ 0.01 µl g^{-1} µm^{-1} smaller than 1.1 µm were identified in the oxygen carriers recovered after 100 *T*-swing cycles (light grey markers in **Fig. 6-35b**). The wider pore size range of the sample after 100 cycles by p_{O_2} swing (compared to the pore size range of the sample after 100 cycles by *T* swing) might result in a reduction in oxygen carrier lifetime. From He-pycnometry and MIP data, the change of the specific particle

volume (normalised inverse of the envelope density) was calculated and is plotted against cycle number in **Fig. 6-36**, below.

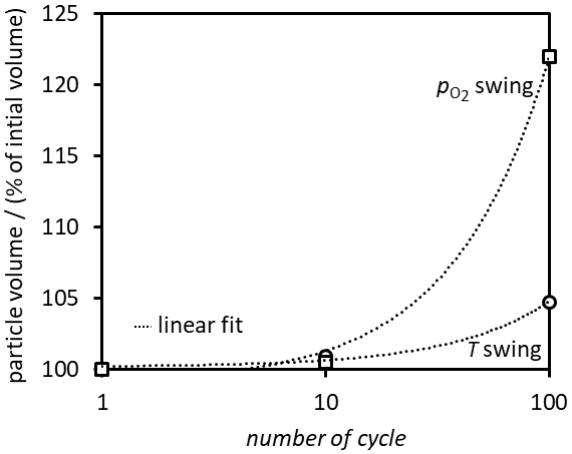


Fig. 6-36 *Plots of the particle volume against cycle number calculated as the normalised inverse of the envelope density for the oxygen carriers cycled by temperature swing and p_{O2}-swing in the TGA.*

Fig. 6-36 shows that over the course of the experiment the average swelling of the oxygen carriers during p_{O_2} swing was significantly faster (0.22 vol%/cycle) than during *T* swing (0.05 vol%/cycle). It is likely that this swelling, which typically results in an increase in porosity, results in a decrease in the resistance of mechanical stresses and results ultimately in either an excessive rate of attrition or a particle fragmentation. This swelling and its relationship with the rate of attrition as well as the particle's lifetime will be studied in further detail during experiments in the fluidised bed (section 7.3).

6.9 Redox-cycling with CH_4

The performance of selected oxygen carriers was tested with CH_4 to obtain parameters that allow for a direct comparison to the oxygen carriers cycled at CLAS conditions. The objective of this study was to find out (i) if the redox-reactions are fully reversible (section 6.9.1), (ii) how fast the reduction and oxidation reactions are – the results were used to estimate the minimum required solid inventory by the method proposed by García-Labiano[148] – and (iii) if the oxygen carriers (unsupported and supported) withstand the chemical stresses of the reactions. Ultimately, these results were used to benchmark the performance of the copper manganese oxygen carriers in the CLAS process against the performance in the CH_4-CLC process.

6.9.1 Reversibility of the redox-reactions with CH_4

This section presents data from experiments that evaluate if stable redox-cycling of the oxygen carriers with a reduction under CH_4+N_2 is possible. The reversibility of the redox-reactions with CH_4

of the unsupported oxygen carriers was tested over 10 cycles in the TGA at 650 °C. The results are illustrated in **Fig. 6-37**, below.

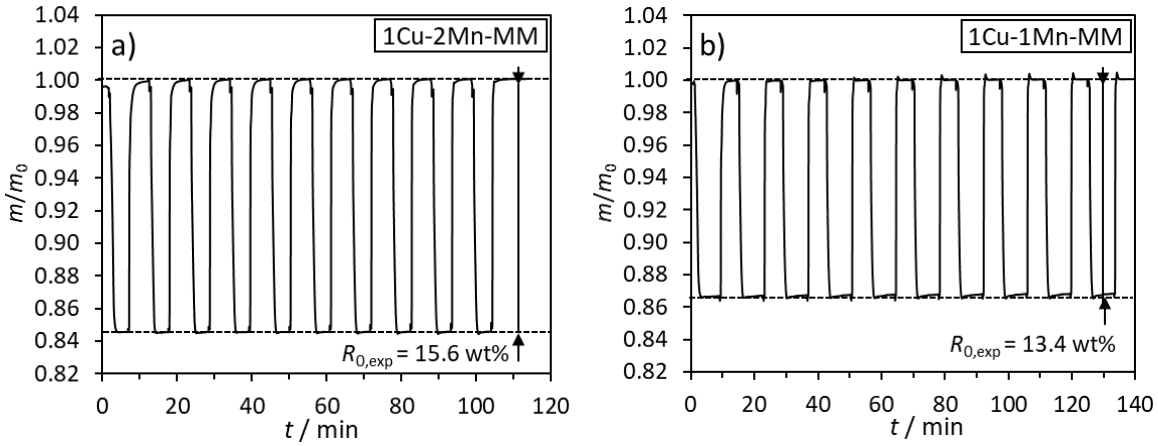


Fig. 6-37 *Plots of the normalised sample mass of (a) 1Cu-2Mn-MM and (b) 1Cu-1Mn-MM measured during TGA experiments with alternating periods 5 vol% CH_4 + N_2 and 10 vol% O_2+N_2 at 650 °C. The sample mass during the experiments was 2 mg and the gas flow rate was kept constant at 200 ml·min^{-1} at SATP.*

Fig. 6-37a and **Fig. 6-37b** show that the 1Cu-2Mn-MM and the 1Cu-1Mn-MM react reversibly with an $R_{0,exp}$ of 15.6 wt% and 13.4 wt%, respectively. Owing to these results, it was decided to continue testing of the unsupported oxygen carriers with CH_4 to assess their reactivity and long-term cycling performance. Furthermore, the ZrO_2 and TiO_2 supported oxygen carriers were tested over 20 redox-cycles with CH_4. The higher cycle number was selected to be able to even observe slower deactivation due to interactions between the active phase and the supporting material. The results of the experiment are shown in **Fig. 6-38**, below.

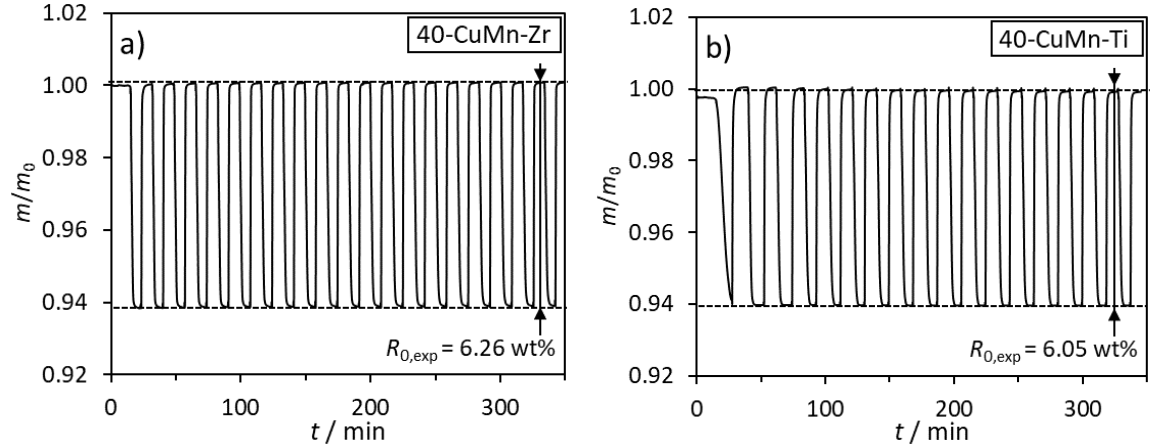


Fig. 6-38 *Plots of the normalised sample mass of (a) 40-CuMn-Zr and (b) 40-CuMn-Ti measured during TGA experiments with alternating periods 10 vol% CH_4 + N_2 and 10 vol% O_2+N_2 at 650 °C. A higher sample mass of 40 mg was used to study the recovered samples by XRD, and the gas flow rate during the experiment was kept constant at 200 ml·min^{-1} at SATP.*

Fig. 6-38 shows that the ZrO_2 and the TiO_2 supported samples react reversibly with CH_4 and the measured values of $R_{0,exp}$ were 6.26 wt% and 6.05wt%, respectively. After the end of the 20th reduction period and 20th oxidation period, the samples were quenched by cooling the furnace with an initial rate of -200 °C min. After the cool-down, the samples were recovered, and their phases analysed by XRD. The results of this characterisation together with the diffraction patterns of the fresh oxygen carriers is shown for the ZrO_2 supported samples in **Fig. 6-39**, below.

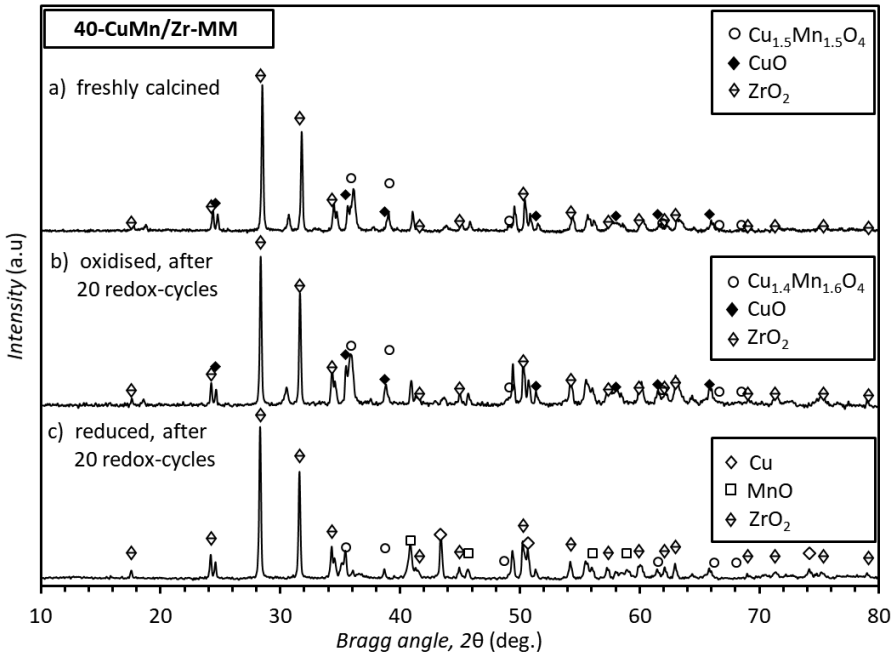


Fig. 6-39 *XRD patterns of 40-CuMn/Zr-MM oxygen carriers, (a) freshly calcined, (b) recovered at the end of the 20th reduction period, and (c) recovered at the end of the 20th oxidation period. During the redox-cycling in the TGA, periods with 10 vol% CH_4 + N_2 and 10 vol% O_2+N_2 at 650 °C were alternated and the gas flow rate during the experiment was kept constant at 200 ml·min^{-1} at SATP.*

In the oxidised sample recovered after 20 redox-cycles, the phases CuO (JCPDS 00-005-0661), $Cu_{1.4}Mn_{1.6}O_4$ (JCPDS 00-035-1030), ZrO_2 (JCPDS 00-013-0307) and $CuMn_2O_4$ (JCPDS 00-034-1322) were identified. Furthermore, some weak peaks matched $CuZrO_3$ (JCPDS 00-043-0953) well. In the reduced sample recovered after 20 redox-cycles, the phases ZrO_2 (JCPDS 00-013-0307), Cu (α-brass, 00-004-0836), MnO (JCPDS 00-001-1206) were identified.

The results of the XRD analysis of the fresh and redox-cycled TiO_2-supported oxygen carriers is shown in **Fig. 6-40**, below.

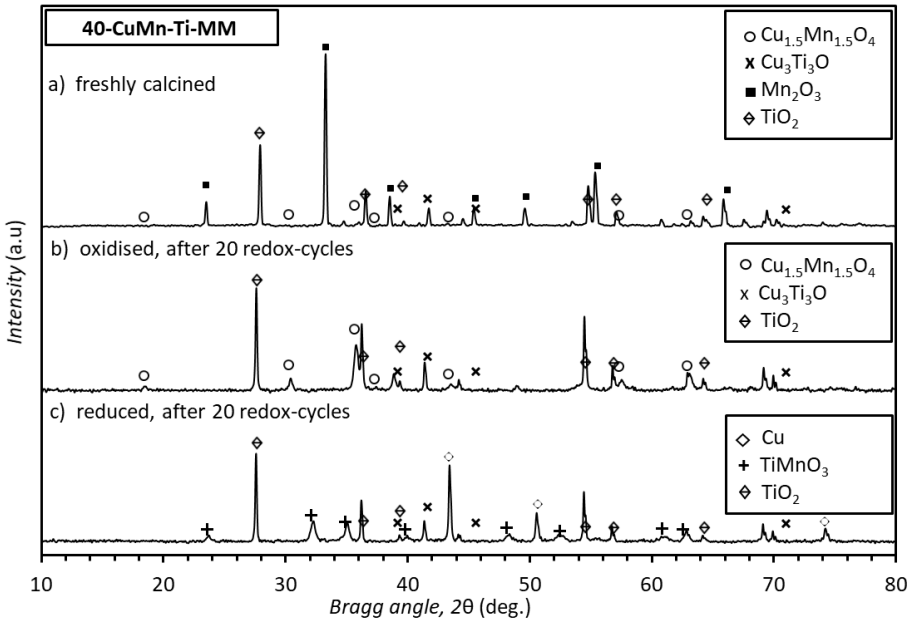


Fig. 6-40 *XRD patterns of 40-CuMn/Ti-MM oxygen carriers, (a) freshly calcined, (b) recovered at the end of the 20th reduction period, and (c) recovered at the end of the 20th oxidation period. During the redox-cycling in the TGA, periods with 10 vol% CH_4 + N_2 and 10 vol% O_2+N_2 at 650 °C were alternated and the gas flow rate during the experiment was kept constant at 200 ml·min^{-1} at SATP.*

XRD analysis identified Mn_2O_3 (JCPDS 00-041-1442), Cu_3Ti_3O (JCPDS 00-049-0665), TiO_2 (JCPDS 00-034-0180) and minor amounts of $Cu_{1.5}Mn_{1.5}O_4$ (JCPDS 01-070-0262) in the fresh sample. This indicates that the presence of TiO_2 is inhibiting the formation of copper manganese oxide. In the oxidised sample recovered after 20 redox-cycles, the phases TiO_2 (JCPDS 00-034-0180), $CuMn_2O_4$ (JCPDS 00-034-1400), CuO (JCPDS 00-048-1548), and Cu_3Ti_3O (00-049-0665) were identified. No Mn oxides were identified. This shows that during the redox-cycling with CH_4 copper manganese oxidised is formed. In the reduced sample recovered after 20 redox-cycles, the phases $MnTiO_3$ (JCPDS 00-012-0435), Cu (α-brass, 00-004-0836), TiO_2 (JCPDS 00-034-0180), and Mn_2TiO_4 (JCPDS 00-016-0241). In all three samples, combined metal oxides containing Ti and Mn or Cu were identified. This shows that TiO_2 is not inert, but forms combined phases with the active phase. Furthermore, kinetic parameters (activation energy and pre-exponential factor) as well as the reaction order of several oxygen carriers were calculated from TGA experiments to allow estimation of the minimum solid inventory or process simulation of the CH_4-CLC process. This in turn allows direct of the performance of a CLAS process. The results are provided in **Appendix A.10**.

6.9.2 Long-term cycling tests with CH_4

As a third type of test, long-term cycling experiments in the TGA were performed to assess the chemical stability of the oxygen carriers in the CH_4-CLC process. In a typical experiment 2 mg of the oxygen carriers in the size range 300-425 μm were redox-cycled 100 times at 700 °C with

reduction in 10 vol% CH_4 + N_2 and oxidation in 10 vol% O_2 + N_2. The results of this assessment are shown in **Fig. 6-41**, below.

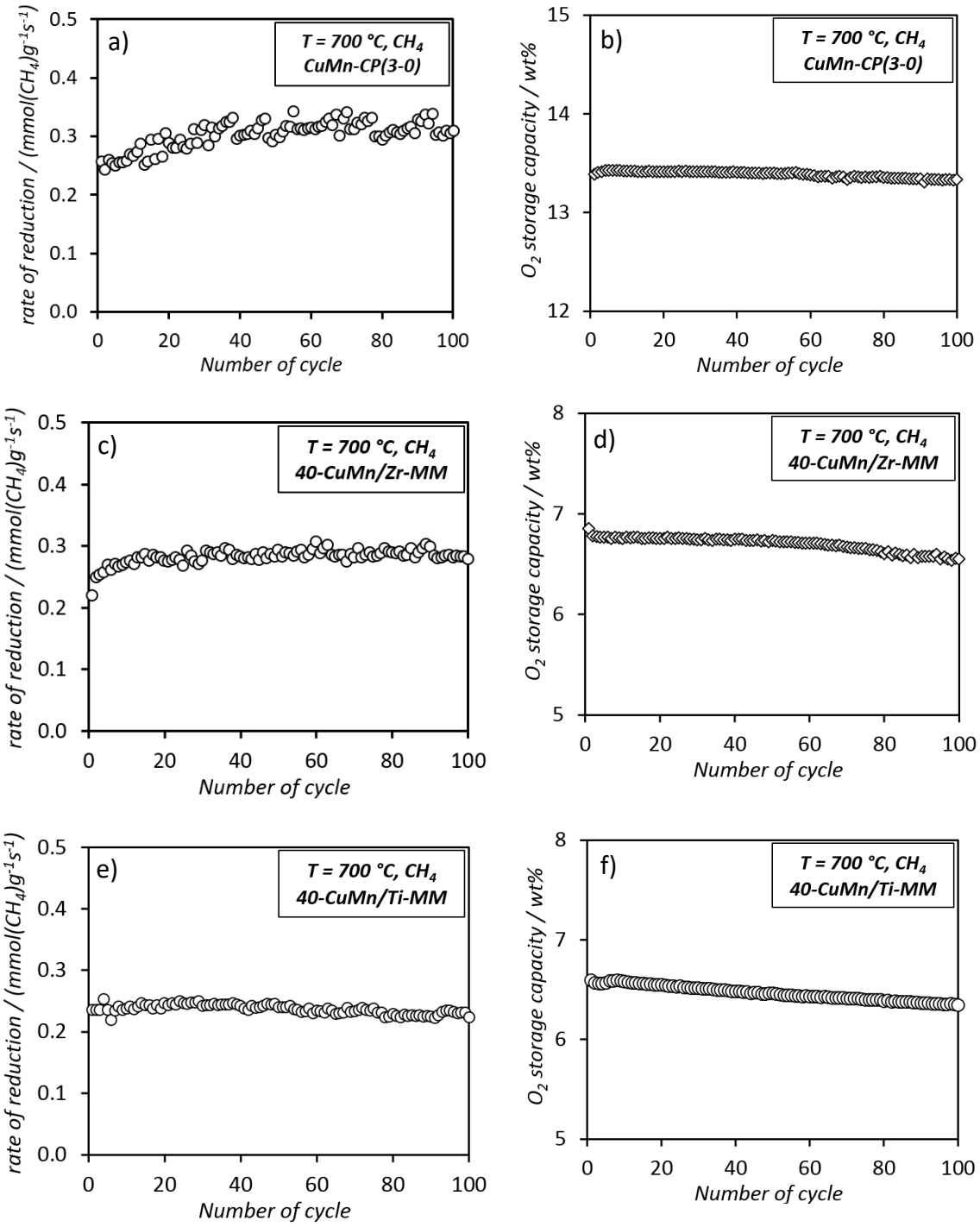


Fig. 6-41 *The (a, c, e) rate of reduction and (b, d, f) O_2 storage capacity measured over 100 redox-cycles at 700 °C in the TGA. The samples are (a, b) 1Cu-1Mn-CP(3:0), (c, d) 40-CuMn/Zr-MM, (e, f) 40-CuMn/Ti-MM. The reduction and oxidation were carried out in 10 vol% CH_4 + N_2 and 10 vol% O_2 + N_2, respectively. A sample mass of 2 mg, a particle size range of 300-425 µm, and a total flow rate of 200 ml.min^{-1} at SATP were used.*

The cycled samples were analysed by SEM-EDS. The micrographs are shown in **Fig. 6-42**, below.

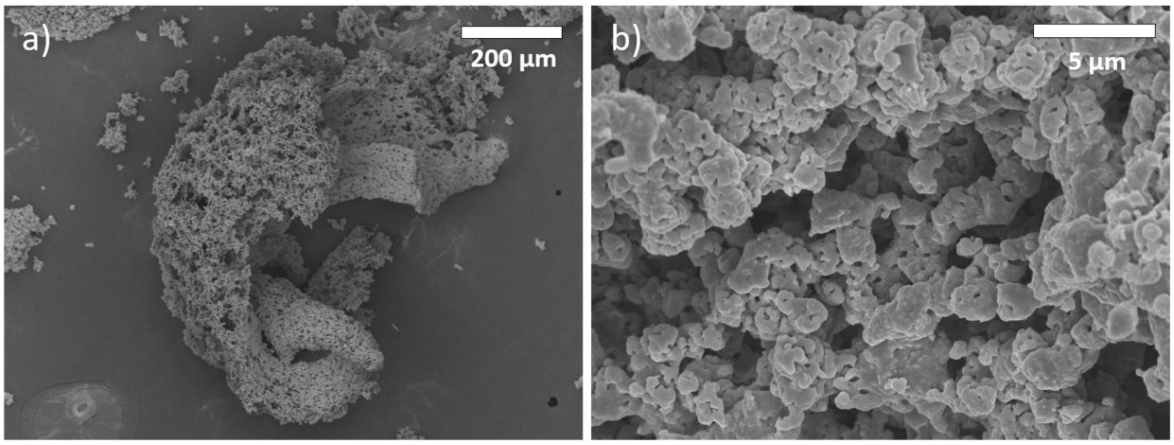


Fig. 6-42 *SE micrographs with (a) x 200 and (b) x 10 000 magnification of 1Cu-1Mn-CP-CP(3:0)-pH-8.3 after 100 redox-cycles in the TGA at 700 °C with reduction under 10 vol% CH_4 + N_2 and oxidation under 10 vol% O_2 + N_2. The total gas flow rate was 200 ml.min^{-1} at SATP.*

Fig. 6-42a shows that the unsupported particle disintegrated during the redox-cycling with CH_4. The micrograph with higher magnification (***Fig. 6-42b***) shows that a highly porous structure had formed.

Scanning electron micrographs of the ZrO_2 supported oxygen carriers, which were recovered after 100 redox-cycles are shown in ***Fig. 6-43***, below.

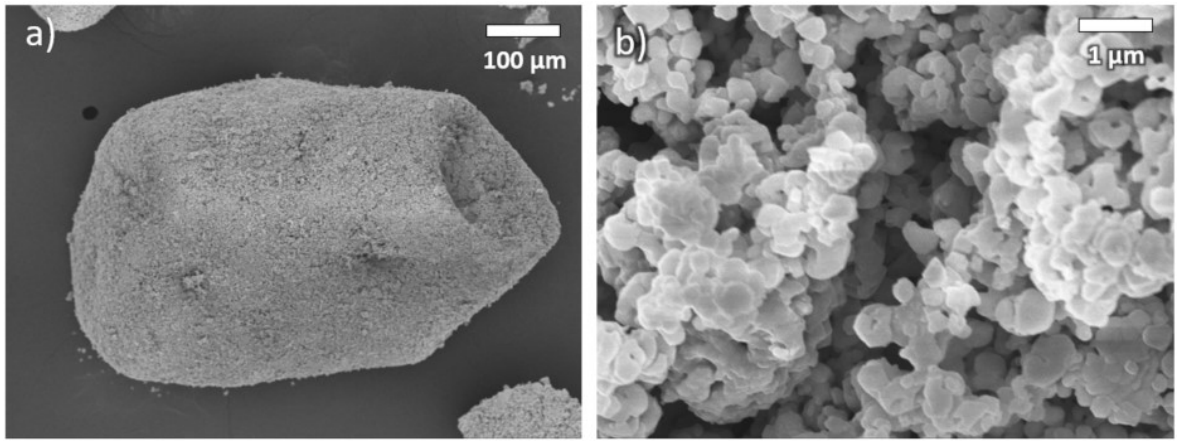


Fig. 6-43 *SE micrographs with (a) x 200 and (b) x 10 000 magnification of 40-CuMn/Zr-MM after 100 redox-cycles in the TGA at 700 °C with reduction under 10 vol% CH_4 + N_2 and oxidation under 10 vol% O_2 + N_2. The total gas flow rate was 200 ml.min^{-1} at SATP.*

Fig. 6-43 shows that the oxygen carriers maintained their integrity over 100 cycles. Scanning electron micrographs of the TiO_2 supported oxygen carriers, which were recovered after 100 redox-cycles are shown in **Fig. 6-44**, below.

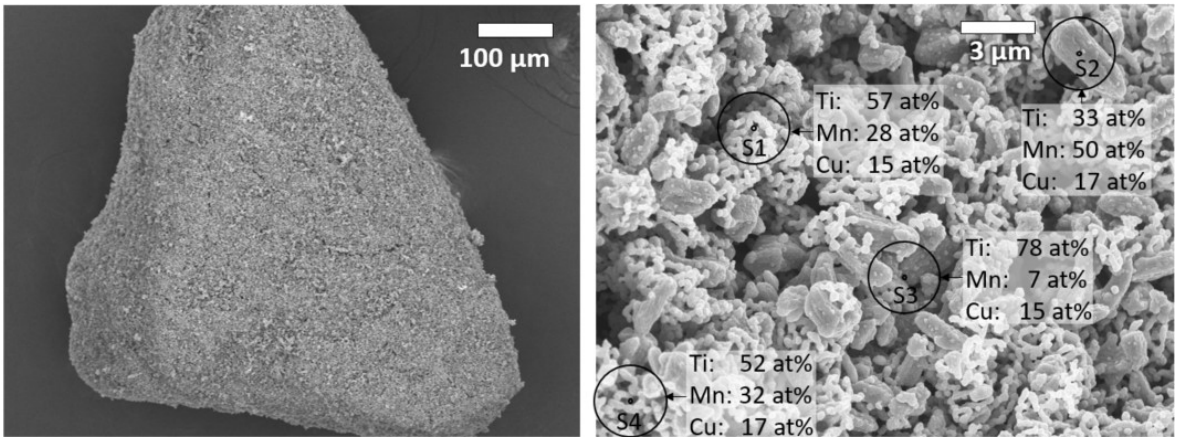


Fig. 6-44 *SEM with atom fractions quantified by EDS of 60 wt% TiO_2/1Cu-1Mn-MM after 100 redox-cycles in the TGA with CH_4 for the reduction. White cross and the dashed circle indicate the centre and the circumference of the area on which the X-ray detector is focused. The oxygen carriers have a size range of 150-210 µm, and a sample mass of 1 mg was used. The gas used at a flow rate of 200 ml.min^{-1} at SATP is 10 vol% O_2 and 10 vol% CH_4 balanced with N_2 for oxidation and reduction, respectively.*

The scanning electron micrograph of the surface of the TiO_2 supported oxygen carrier after 100 redox-cycles (**Fig. 6-44**) shows a mixture of smaller slab-like grains (brighter) and larger slab-like grains (darker). To elucidate the difference between those two different types of grains, elemental surface analysis by EDS was carried out at four points (**Fig. 6-44b**)– two in areas with predominantly brighter grains and two in areas with darker grains.

The fact that significant amounts of each metal is found at the surface confirms that redox-cycling with a reduction by CH_4 does not result in a separation between the active material and the inert support, in contrast to inert cycling, where predominantly Ti species were found at the surface.

The two spectra S1 and S4 that are targeted at an area with predominantly brighter grains have the average composition 54 at% Ti, 30 at% Mn, 16 at% Cu, which is almost identical to the average composition of the spectra S2 and S3 that are targeted at the darker grains, which have the average composition 55 at% Ti, 28 at% Mn, 17 at% Cu.

Combining the findings from XRD, SEM and EDS analysis a mechanism is suggested that inhibits the separation of the active material and the supporting phase that is illustrated in **Fig. 6-45**, below.

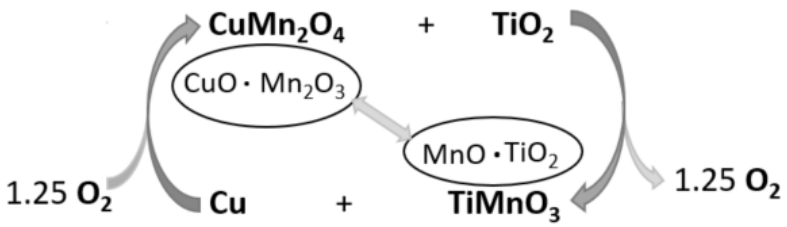


Fig. 6-45 *A diagram of the suggested mechanism for the stabilisation of the active and supporting phases by chemical reaction between the phases.*

The unsupported oxygen carriers disintegrated over 100 cycles, while the ZrO_2 and TiO_2 supported oxygen carriers maintained the shapes of particles. Although the O_2 release rate and O_2 release capacity over 100 redox-cycles with a reduction under CH_4+N_2 for the unsupported as well as the ZrO_2- and TiO_2-supported oxygen carriers is stable (**Fig. 6-41**), the SE micrographs of the cycled oxygen carriers (**Fig. 6-42**, **Fig. 6-43, Fig. 6-44**) showed that the degree of deterioration was very different. The unsupported oxygen carriers had disintegrated, while the supported oxygen carriers maintained their shape. To demonstrate the effect of the different magnitudes of thermal and chemical stresses during the different cycling modes on the particle morphology and the resulting differences in the degree of deterioration, micrographs of the redox-cycled unsupported oxygen carriers (1Cu-1Mn-CP) recovered after 100 redox-cycles from the TGA are compared in **Fig. 6-46**, below.

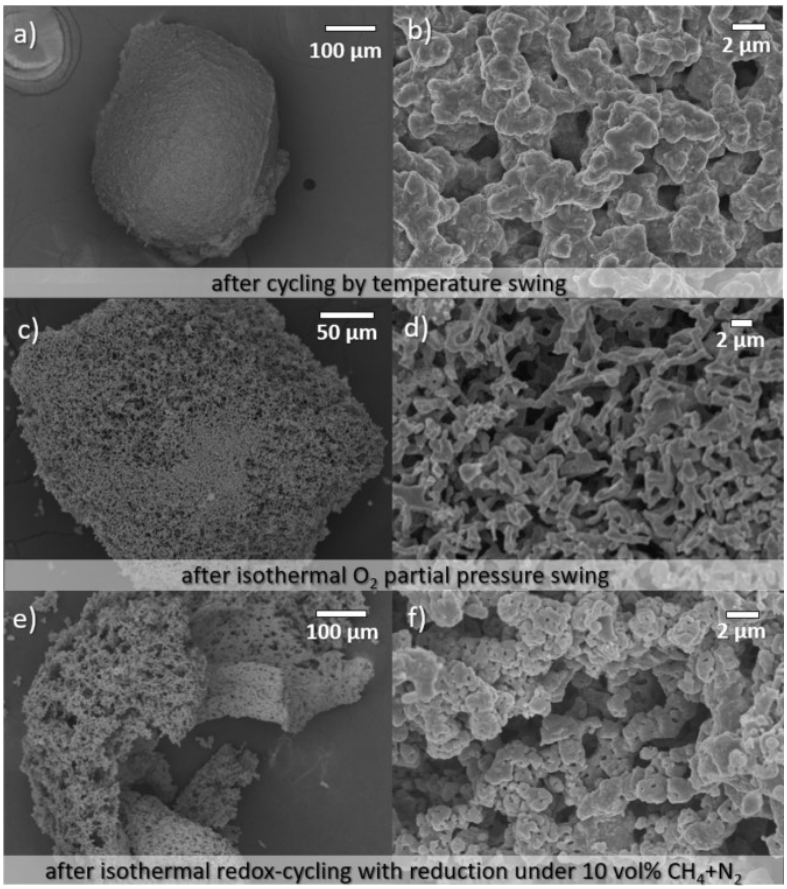
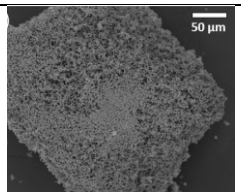
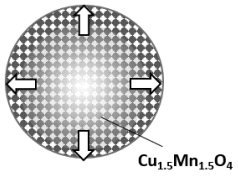
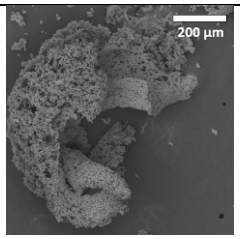
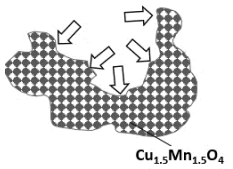
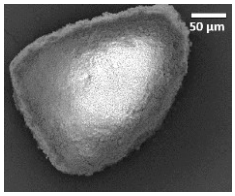
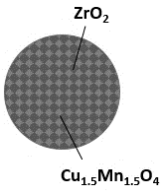
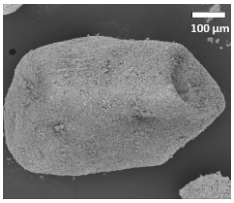
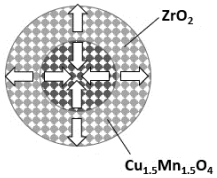
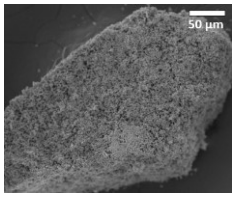
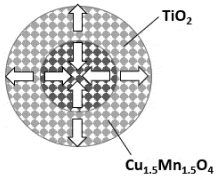
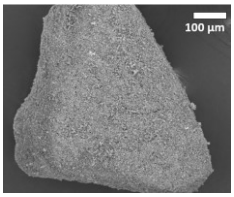
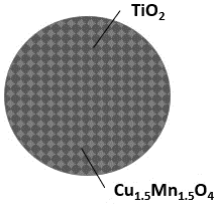


Fig. 6-46 *SEM with (a, c, e) low and (b, d, f) high magnification of a 1Cu-1Mn-CP oxygen carrier particle recovered after 100 redox-cycles (a, b) by T swing, (c, d) by p_{O2} swing and (e, f) with a reduction by CH_4.*

Furthermore, the characterisation of the long-term cycled samples indicated that the unsupported and supported samples evolve differently during redox-cycling with and without CH_4, as illustrated in **Table 6-6**, below.

Table 6-6 *Scanning electron micrographs and diagrams of the suggested growth modes for unsupported and supported copper manganese oxide oxygen carriers cycled by p_{O2}-swing and by reduction with CH_4.*

supporting material	cycling by p_{O_2} swing		redox-cycling with CH_4	
	micrograph	diagram	micrograph	diagram
no				
ZrO_2				
TiO_2				

The sample mass of the TGA experiments was insufficient to analyse the pore structure by MIP, He porosimetry or N_2 adsorption to further support the theories for the particle evolutions shown in **Table 6-6**. Therefore, some redox-cycling experiments were repeated in the fluidised bed (with a larger sample mass), and in fact, an increase of the specific particle volume was measured for the unsupported and TiO_2-supported oxygen carriers after long-term cycling by p_{O_2} in the fluidised bed, while the specific volume of the ZrO_2-supprted oxygen carriers decreased. The results of the fluidised bed reactor experiments are reported in full detail in the following chapter.

6.10 Concluding remarks

In this chapter, the TGA set-up, the calibration and validation of the flow rates of the gas supply system, and the experiments that were conducted to determine the response time of the TGA system are described. Then a model was presented, which has been developed to calculate the external mass transfer during the O_2 release inside the TGA. The model was validated with data from the literature and showed very good agreement. Another model was developed to estimate the effective intra-particle diffusion. This model was used to determine an apparent tortuosity factor. This factor was found to have a value of τ = 2.21 and was used in the reaction rate models of this thesis. The reversibility of the redox-reactions and the oxygen release capacity, $R_{0,\mathrm{exp}}$, was determined for $p_{\mathrm{O_2}}$ and T swing experiments. It was demonstrated that the substitution of O_2+N_2 with O_2+CO_2 affects neither the redox-behaviour nor the $R_{0,\mathrm{exp}}$. However, the precence of O_2 during the O_2 release resulted in a significant reduction in $R_{0,\mathrm{exp}}$, which was attributed to the occurrence of phases with higher oxidation states compared to the samples decomposed in the absence of O_2. Balanced equations for the redox-reactions of the $p_{\mathrm{O_2}}$ and T swing experiments were developed and presented. Furthermore, the O_2 equilibria were determined by a series of TGA experiments and expressed as an Antoine type correlation. The equilibrium data was then used to calculate the enthalpy of the O_2 release, which is essential for the CLAS process design, and an equation to correlate the $p_{\mathrm{O_2,eq}}$ of the oxygen carriers of this work was presented. This correlation was used to calculate the enthalpy of the O_2 release reaction of the oxygen carriers. During the TGA experiments for the determination of $p_{\mathrm{O_2,eq}}$, the observed rate of O_2 release was predominantly mass transfer controlled. This indicates the problems in calculating the intrinsic rate of reactions of the CLAS process (rate of O_2 uncoupling and oxidation) from TGA experiments, which was the reason that in this thesis kinetic parameters were only calculated from fluidised bed reactor experiments. Furthermore, partially reacted (quenched) oxygen carriers were studied by XRD to elucidate the reaction pathways. The absence of single metal oxides suggests that these do not form as intermediates. Moreover, experiments with CH_4 were carried out to test the reversibility of the redox-reactions, the interactions between the active phase and the support material, the rate of reactions and the long-term cycling performance. All samples reacted reversibly with CH_4 and the rate of reduction was in the order: 40-CuMn/Zr-MM > 1Cu-1Mn-CP > 1Cu-1Mn-MM > 40-CuMn/Ti-MM, indicating that ZrO_2 and TiO_2 enhances and inhibits the rate of reduction. The inhibition of the reaction rate was attributed to the formation of $TiMnO_3$ during the reduction. In contrast to the CLAS experiments, the O_2 capacities during redox-cycling with CH_4. Furthermore, it was found that the different magnitudes of thermal and chemical stresses during the different cycling modes has a significant impact on the morphology of the sample and result in different degrees of deterioration.

The sample mass during most TGA experiments was too low for MIP, He porosimetry and N_2 adsorption analysis to support some of the observations made from the SE micrographs. Thus, some redox-cycling experiments were repeated in the fluidised bed, and the observation from the TGA experiments regarding the swelling and the shrinking of the oxygen carriers during p_{O_2} when being unsupported or TiO_2-supported and ZrO_2-supported, respectively, were confirmed by calculating the change in the specific volume from MIP data. The results of the fluidised bed reactor experiments are reported in full detail in the following chapter.

Chapter 7

Redox-cycling of the oxygen carriers in the fluidised bed

In this chapter, the modification of a fluidised bed reactor is described and the results of the FBR experiments are reported to fulfil the objectives described in section 1.1, which are (i) to measure the rates of reactions, and (ii) to determine the long-term cycling performance of the oxygen carriers of this research project.

A 1.5 kW_e bench-top fluidised bed reactor (FBR) was used for the experiments of this chapter. The reactor is illustrated in **Fig. 7-1**, below.

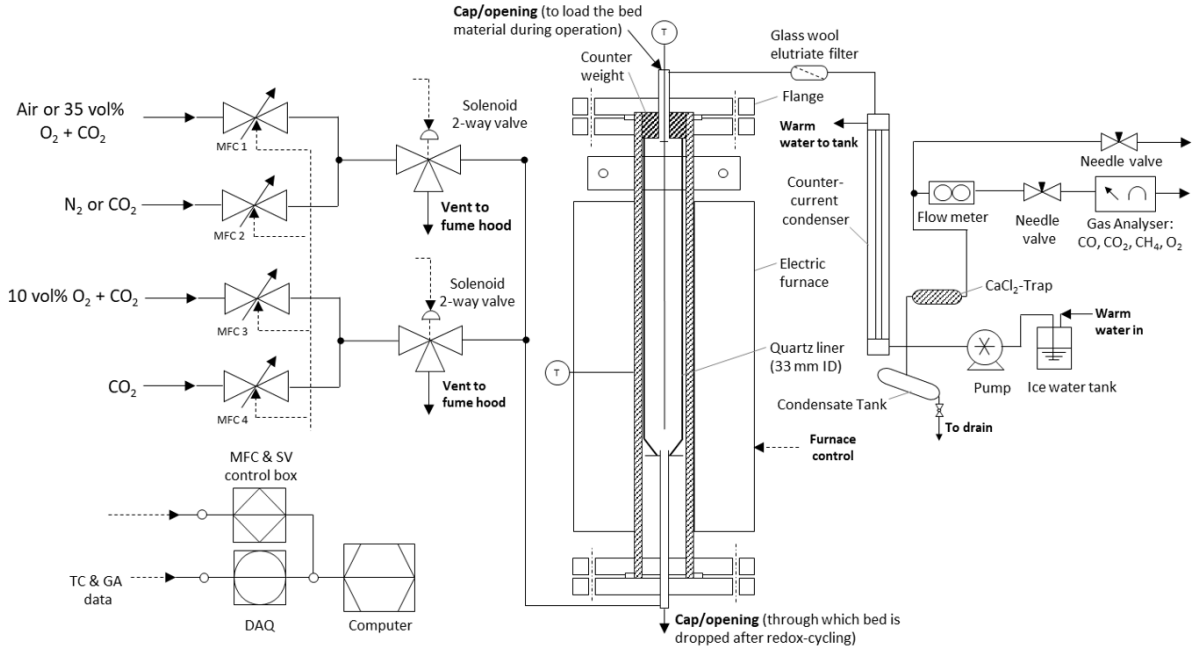


Fig. 7-1 *Flow sheet of the modified fluidised bed for redox-cycling at CLAS conditions.*

The fluidised bed reactor shown in **Fig. 7-1** has no distributor (typically a porous sintered disk at the bottom of the liner). The gas enters the reactor instead through a single orifice at the bottom of the reactor vessel. This results in the formation of an "open cylindrical cavity that penetrates to the bed surface",[231] which is referred to as the spout. Therefore, this type of fluidised bed reactor is also called a spouting bed reactor. A spouted bed has typically a lower pressure drop than a fluidised bed.[231] Furthermore, in a spouted bed reactor the contacting between the gas and the solids over a wide condition range is superior compared to a fluidised bed reactor with a distrubutor.[231] The following section describes the modification of a fluidised bed reactor (to reach the status shown in **Fig. 7-1**) as well as the principles of reactor operation.

7.1 Modification and operation of the fluidised bed reactor

This section starts by outlining the modifications to the fluidised bed reactor that have been done to allow for automated redox-cycling (section 7.1.1). Then, the deconvolution of the gas sampling system and the calculation of the observed rate of reaction from the measured O_2 volume fraction is detailed (section 7.1.2). The minimum fluidisation velocity was calculated for the determination of the feasible gas flow rate range (section 7.1.3). Finally, a heat balance around a reacting particle in the fluidised bed has been done to determine if temperature gradients inside the particle exists and to

estimate the difference between the mean particle temperature and the bed temperature during the reaction (section 7.1.4).

7.1.1 Modification of a fluidised bed reactor

The reactor that is used for the experiments of this chapter (illustrated in **Fig. 7-1**) was previously used to evaluate the performance of sorbents for enhanced reforming in batch mode.[232,244] To allow continuous redox-cycling of the oxygen carriers at the relevant conditions the following modifications had to be made:

(i) The gas supply system was previously used for steady-state operation (batch mode) and therefore consisted of manual valves and rotameters. It was automated to allow redox-cycling by replacing the rotameter with four mass flow controllers (MFCs) as well as two solenoid valves. The calibration of the MFC is detailed in **Appendix A.11**.

The solenoid valves were used for rapid gas switching, since the MFCs were found to have a definite ramp-up time before they reach the set value. This gradual increase in flow rate could impact the reaction rate measurements. Therefore, the MFC that controlled the gas of the next redox-phase were set to the target rate a few seconds before the end of a redox-phase. This allowed the MFC to reach the new target rate, while the gas was vented through the flare stack. At the end of the redox-phase the two solenoid valves were switched to vent the gas that was flowing into the reactor, and to route the gas of the new redox-phase – which was routed to the flare stack – into the reactor.

(ii) A new Agilent VEE code was written, which enables an automated sequence with predefined gas compositions and redox-phase duration for the oxidation and decomposition phase. The new code allowed to either set a total inlet gas flow rate or a value for the ratio of the gas velocity to the minimum fluidisation velocity at reactor temperature, u/u_{mf}. To code automatically calculates the minimum fluidisation velocity from the envelope density, ρ_{p}, the mean particle diameter, $\bar{d}_{\mathrm{p}}$, the specified gas composition (using density and viscosity correlations based on RefProp (NIST)[233] data), and the measured bed temperature (or wall temperature, if the bed thermocouple is disconnected, *e.g.* during the loading of the oxygen carriers). This automated gas flow rate mode was used during most fluidised bed reactor experiments. It reduced the probability of selecting an improper flow rate and simplified the operation during heating and cooling.

(iii) The piping at the bottom of the reactor vessel (where the gases enter) was changed to have an opening directly below the centre of the reactor liner. This allowed to unload the bed particles by "dropping the bed" during the cool-down phase after experiments. This enabled repeated unloading and re-loading of the bed particles during long-term cycling tests.

(iv) A U-shaped ½-inch tubing was installed downstream of the reactor vessel. It was packed with glass wool and functioned as a trap to collect elutriated particles for characterisation by SEM, EDS and XRD. The U-shape simplified the de-installation and re-installation of the elutriates trap.

(iv) A smaller $CaCl_2$-vapour trap was built for operation without steam. The reduction in size resulted in a reduction in gas mixing inside the trap. This is demonstrated in the following section about the de-convolution of the gas sampling measurements. The new vapour trap consists of a $^3/_8$-inch tubing with cross-overs to ¼-inch tubing on both ends. The calculated internal volume of the unpacked and packed vapour trap is ~5.7 cm^3 and ~2.2 cm^3, respectively. The trap was packed with dry $CaCl_2$ granules and a sheet of fine steel wire mesh was placed inside the larger side of each cross-over to prevent granules (or their fragments) leaving the device.

After completion of the modifications and calibration of the MFCs, a method for the deconvolution of the gas sampling system was applied and the model for the calculation of the observed rates from the deconvoluted O_2 molar fractions was developed, as described in the following section.

7.1.2 Deconvolution and calculation of the observed rates

The gas sampling system was deconvoluted following the method proposed by Fennell *et al.*,[234] which was subsequently used elsewhere in the literature.[225,235] The path of the gas from the fluidised bed to the gas analyser is finite, which results in a time difference between C_i, the concentration inside the fluidised bed of species i, and $C_{i,m}$, the measured concentration of i. This time difference is the dead time, t_d. Additionally, gas mixing along the path occurs, and the sensitive elements of the gas analyser have an intrinsic response time.[234, 235] Those phenomena can be modelled by a dead time followed by two well-stirred tanks with the residence times $\tau_{\mathrm{r,R}}$ and $\tau_{\mathrm{r,GA}}$ to account for the gas mixing along the path from the reactor to the gas analyser, and for the response time of the gas analyser, respectively.[235] This model is illustrated in ***Fig. 7-2***, below.

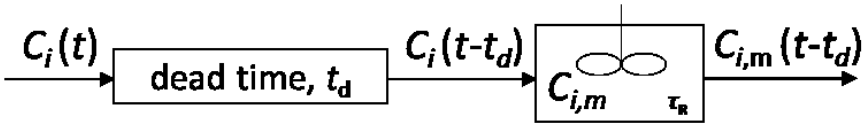


Fig. 7-2 *Schematic diagram of the mathematical model that is used for the deconvolution of gas measurements during fluidised bed reactor experiments. The figure is adapted from Tighe.*[235]

The model shown in **Fig. 7-2** can be expressed by,[235]

$$C_i(t - t_\mathrm{d}) = C_{i,m} + \tau_\mathrm{r}\frac{d(C_{i,m})}{dt} \tag{7-1}$$

Eq.(7-1) can also be expressed in terms of molar fractions as,

$$y_{O_2}(t - t_d) = y_{O_2,\mathrm{m}} + \tau_\mathrm{r} \frac{d(y_{O_2,\mathrm{m}})}{dt} \tag{7-2}$$

The measured molar fraction of O_2, $y_{\mathrm{O_2,m}}$, consisted of the signal and the noise. The latter was assumed to be random. Since deconvolution is typically amplifying the noise, the noise in $y_{\mathrm{O_2,m}}$ was reduced prior to the deconvolution by, firstly, averaging the $y_{\mathrm{O_2,m}}(t)$ of three cycles (either inert or with the sample) and, secondly, by applying the filter developed by Savitzky and Golay[236]. The method is detailed in **Appendix A.12**.

To determine τ_r in eq.(7-2) the gas going into the FBR was switched repeatedly from air to N_2. The fluidised bed contained 40 g of inert bed material, was at a temperature of 850 °C, and the inlet gas flow rate was 2.537 l min^{-1} as SATP. The sampling flow rate into the gas analyser was choked to 300 ml min^{-1} (at SATP) using a needle valve. These conditions corresponded to operating conditions of the fluidised bed during a typical experiment. At $t = t_\mathrm{d}$, with the dead time, t_d, = 15.94 s, the measured molar fraction of O_2 started to decrease. This decrease in $y_{\mathrm{O_2}}$ was compared to a step-function, in which rapid gas switching from $y_{O_2} = 0.1$ to $y_{O_2} = 0$ was assumed. Then, the square error between the deconvoluted O_2 fraction in eq.(7-2) and the step-function was minimised by varying τ_r. The measured and the deconvoluted signal are shown in **Fig. 7-3**, below.

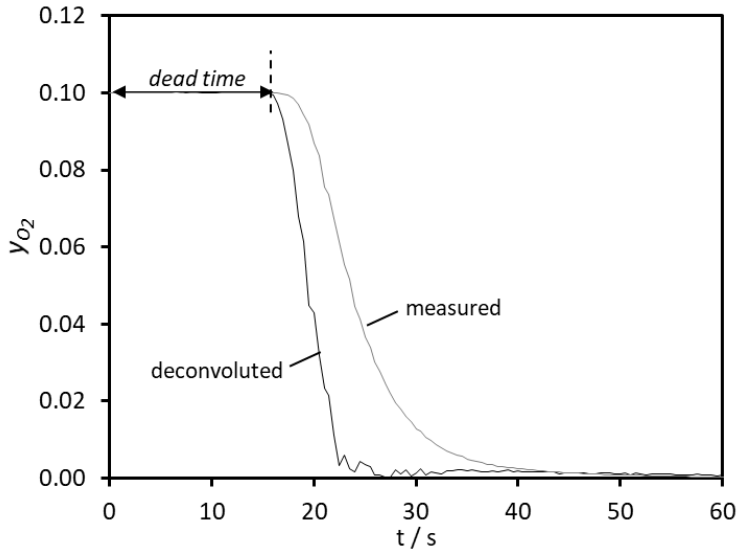


Fig. 7-3 *A plot of the measured and the deconvoluted molar fraction of O_2 upon gas switching from air to N_2 in the fluidised bed containing 40 g of sand at 850 °C.*

This procedure yielded a value of τ_r = 4.55 s for the optimised fluidised bed reactor system, in which the volume of the vapour trap and the tubing downstream of the reactor vessel was reduced to minimise gas mixing.

The observed rate of reaction (oxidation and O_2 release) per unit of oxygen carrier mass, r', was calculated from the deconvoluted O_2 molar fractions from inert cycles, $y_{O_2,\mathrm{inert}}$, and cycles with the sample, $y_{O_2,\mathrm{sample}}$, by,

$$\frac{\mathrm{d}m}{\mathrm{d}t} = r'\left[\frac{\mathrm{mol(O_2)}}{\mathrm{g_{OC}\cdot s}}\right] = \frac{y_{O_2,\mathrm{inert}} - y_{O_2,\mathrm{sample}}}{dt} \cdot \frac{\dot{v}_{\mathrm{g,out}}}{m_{\mathrm{sample}} \cdot V_{\mathrm{m}}} \tag{7-3}$$

In a typical experiment, the data of the first two redox-cycles with the sample were ignored and $y_{O_2,\mathrm{sample}}$ was calculated from the averaged measured O_2 molar fractions of cycle 3 to cycle 5. In eq.(7-3), m_{sample} [g] is mass of oxygen carriers loaded into the reactor and v_{m} is the molar volume at SATP. For v_{m} a value of 24.790 l·mol^{-1} was assumed, which was calculated using the ideal gas law. The deconvoluted volumetric flow rate of gas at SATP leaving the reactor, $\dot{v}_{\mathrm{gas,out}}$, was calculated from the inlet flow rate and the deconvoluted molar fraction of O_2 by,[100]

$$\dot{v}_{\mathrm{g,out}} = \frac{\dot{v}_{\mathrm{g,in}}}{1 - y_{O_2}}, \tag{7-4}$$

During a redox-experiment, $\dot{v}_{\mathrm{g,out}}$, differs slightly from $\dot{v}_{\mathrm{g,in}}$, as the production or consumption of O_2 results in an increase and decrease of $\dot{v}_{\mathrm{g,out}}$, respectively. This is illustrated in **Fig. 7-4**, below.

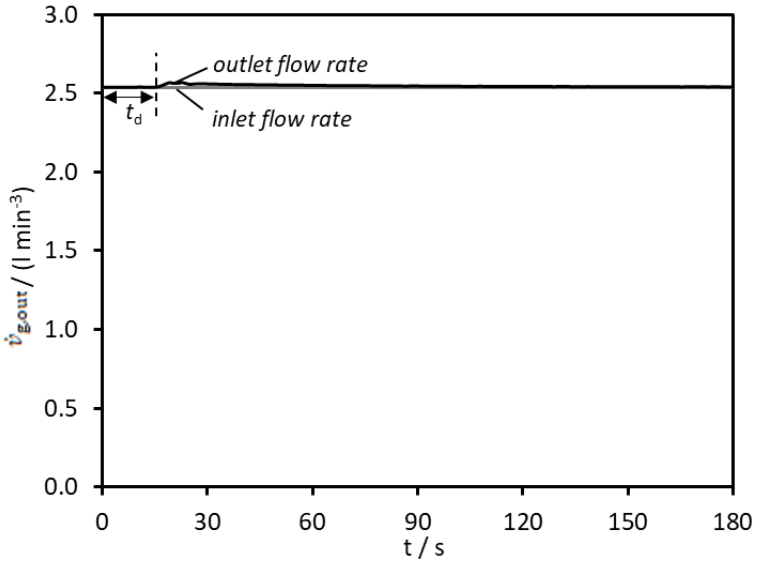


Fig. 7-4 *A plot of the inlet flow rate and calculated outlet flow rate during the O_2 release of 1Cu-2Mn-MM oxygen carrier at 850 °C in the fluidised bed reactor, using an inlet flow rate of 2.53 l min^{-1} at SATP.*

It is important to consider this subtle difference between $\dot{v}_{\mathrm{g,in}}$ and $\dot{v}_{\mathrm{g,out}}$ during a reaction, as otherwise $y_{\mathrm{O_2,inert}}$ and $y_{\mathrm{O_2,sample}}$ would not be correctly aligned over time.

The conversion was calculated from the rate using eq.(7-3) by,

$$X = \int_{t_0}^{t} \frac{\mathrm{d}m}{\mathrm{d}t} \cdot \frac{M_{\mathrm{O_2}}}{R_{0,\mathrm{th}}}\ , \tag{1}$$

where $M_{\mathrm{O_2}}$ is the relative molecular mass of O_2 (32 g mol^{-1}) and $R_{0,\mathrm{th}}$ is the theoretical oxygen release capacity. For $R_{0,\mathrm{th}}$, values of 4.49 w%, 5.35 wt% and 6.62 wt% were assumed for the oxygen carriers with a molar ratio of 1Cu:2Mn, 1.2Cu:1.8Mn and 1Cu:1Mn, respectively. This was determined from the balanced equations in section 6.3.

To determine a suitable flow rate for the experiments, the minimum fluidisation velocity was calculated, as described in the next section.

7.1.3 Calculation of the minimum fluidisation velocity

For the calculation of the minimum fluidisation velocity, the density, ρ_{gas}, and viscosity, η_{gas}, of the gas mixture have to be known.[144] For the calculation of these properties correlations for O_2 + N_2 and O_2 + CO_2 mixtures were developed using data RefProp (NIST) – a software for the calculation of thermodynamic and transport properties of fluid mixtures.[233] These correlations are valid at 0.1 MPa, for 500 °C ≤ T ≤ 1000 °C, and for the O_2 volume fraction range 0 – 30 vol%. The development of the correlations and the calculation of the uncertainties of ρ_{gas} and η_{gas} are detailed in **Appendix A.8**. The minimum fluidisation velocity, u_{mf}, was calculated by,

$$u_{\mathrm{mf}} = \frac{\mu_{\mathrm{g}} \cdot Re_{\mathrm{mf}}}{\rho \cdot d_{\mathrm{p}}}, \tag{7-5}$$

where Re_{mf} is the Reynolds number at minimum fluidisation and d_{p} is the mean particle diameter, which was assumed to equal the average of the minimum and the maximum nominal diameter of a given size range. In eq.(7-5), Re_{mf}, was correlated by,

$$Re_{\mathrm{mf}} = \sqrt{(33.7^2 + 0.0408\ Ar)} - 33.7 \tag{7-6}$$

In eq.(7-6), Ar is the Archimedes number, which was calculated by,

$$Ar = \frac{d_{\mathrm{p}}^3 \cdot \rho_{\mathrm{g}}(\rho - \rho_{\mathrm{g}}) \cdot \mathrm{g}}{\mu_{\mathrm{g}}^2}, \tag{7-7}$$

where g is the standard gravity (= 9.8067 m s^{-2}). The density, ρ, in eq.(7-5) and eq.(7-7) was assumed to equal the envelope density (determined by MIP and He porosimetry) for the calculation with oxygen carriers, and to equal ρ_{sand} for the calculation with the inert bed material. To determine the density of the sand, ρ_{sand}, the weight of a bed of closely packed 300-425 µm sand grains in a 25 ml measuring cylinder was measured and used to calculate the density of the bed, ρ_{bed}. Assuming a bed voidage, $\varepsilon_{\mathrm{bed}}$, of 0.38, the density of the sand was estimated by,

$$\varepsilon_{\mathrm{bed}} = 1 - \frac{\rho_{\mathrm{bed}}}{\rho_{\mathrm{sand}}}, \tag{7-8}$$

This method yielded a value of $\rho_{\mathrm{sand}} = 2628\ \mathrm{kg\,m^{-3}}$. The equations for the calculation of the minimum fluidisation velocity are a part of the FBR gPROMS model of this work. Using this model relevant fluidisation variables were computed (as an example) and are presented in **Table 7-1**, below.

Table 7-1 *Parameter and results of the mass transfer coefficient and the minimum fluidisation velocity calculation from the gPROMS model of this work for selected conditions.*

T [°C]	ρ_g [kg m^3]	μ_{g} [$m\ s^{-1}$]	Ar [−]	Re_{mf} [−]	u_{mf} [m s^{-1}]	$\dot{v}_{\mathrm{g},T}$ [l min^{-1}]	$\dot{v}_{\mathrm{g,SATP}}$ [l min^{-1}]
100 vol% CO_2:							
800	0.500	$0.867\cdot10^{-4}$	81.39	0.0492	0.0236	1.211	0.337
900	0.461	$1.008\cdot10^{-4}$	55.30	0.0335	0.0203	1.044	0.265
1000	0.422	$1.155\cdot10^{-4}$	38.74	0.0234	0.0177	0.911	0.213
10 vol% O_2 + CO_2:							
800	0.486	$0.907\cdot10^{-4}$	72.37	0.0438	0.0227	1.163	0.323
900	0.445	$1.053\cdot10^{-4}$	49.17	0.0298	0.0195	1.002	0.255
1000	0.410	$1.207\cdot10^{-4}$	34.45	0.0208	0.0170	0.874	0.205
100 vol% N_2:							
800	0.318	$1.368\cdot10^{-4}$	20.84	0.0126	0.0150	0.769	0.214
900	0.291	$1.584\cdot10^{-4}$	14.24	0.0086	0.0129	0.664	0.169
1000	0.268	$1.813\cdot10^{-4}$	10.01	0.0061	0.0113	0.580	0.136
10 vol% O_2 + N_2:							
800	0.323	$1.375\cdot10^{-4}$	21.67	0.0131	0.0151	0.777	0.216
900	0.296	$1.593\cdot10^{-4}$	14.81	0.0090	0.0131	0.672	0.171
1000	0.272	$1.823\cdot10^{-4}$	10.41	0.0063	0.0114	0.587	0.137

Footnote: the following parameter were used in addition to those shown above: d_{liner} = 0.034 mm, d_p = $3.625\cdot10^{-4}$ m, ε_{mf} = 0.42, ρ_p = 2628 kg m^{-3}. The table above only shows selected conditions. The model was re-run for each experiment with the relevant conditions.

7.1.4 Heat transfer in the fluidised bed during a reaction

The change of the measured temperature in the fluidised bed was studied during the 3rd to 5th redox-cycle of 1Cu-2Mn-MM for 10 vol% O_2 + N_2 during the oxidation and N_2 and $u/u_{\mathrm{mf}} = 4$. The bed temperature fell during the O_2 release period by 1.3 °C below the temperature that was measured

during the beginning of the period. During the oxidation period, the measured temperature increased by up to 1.9 °C in comparison to the initial temperature. This is illustrated in ***Fig. 7-5***, below.

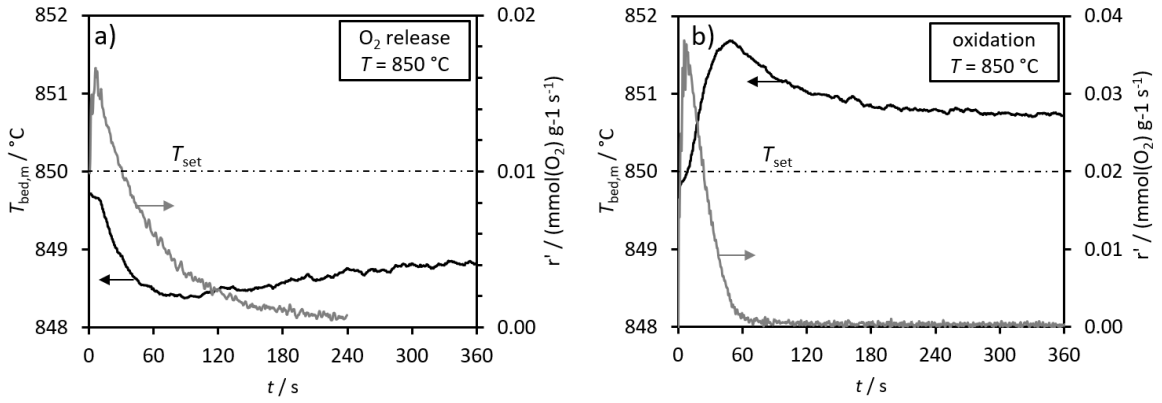


Fig. 7-5 *Plots of the bed temperature (black line) and deconvoluted observed rate of reaction (black line) against the time after the gas switching for (a) the O_2 release and (b) the oxidation of 1Cu-2Mn-MM. The plotted values of the temperature and rate are the average values of cycle 3 to cycle 5.*

In addition to the change in the bed temperature, the mean particle temperature might change significantly during the redox-reactions. The maximum difference of the temperature between the particle and the fluidised bed was calculated using correlations of the Nusselt number, the Biot number and a heat balance of a single oxygen carrier particle similar to the method proposed by Zhang.[107] The heat transfer coefficient of the gas was calculated using the equation for the Nusselt number,

$$Nu = \frac{convective\ heat\ transfer}{conductive\ heat\ transfer} = \frac{h}{\lambda_g / L}\ , \tag{7-9}$$

where h is the heat transfer coefficient, λ_g is the thermal conductivity of the gas and L is a characteristic length. Subsequently, the Biot number, N_{Bi}, was calculated by,[144]

$$N_{Bi} = \frac{heat\ transfer\ resistance\ inside\ the\ particle}{heat\ transfer\ resistance\ in\ the\ gas\ film} = \frac{h_g \cdot d_p}{\lambda_p}\ , \tag{7-10}$$

where h_g is the heat transfer coefficient of the gas and λ_p is the thermal conductivity of the particle. The Biot number relates the heat transfer resistance inside the particle to the heat transfer resistance of the gas phase and allows to assess whether the assumption can be made that during the reaction the particle behaves isothermally. For $N_{Bi} << 1$ the main resistance to the heat transfer lies in the gas phase. During the O_2 release, the gas composition at the surface of the particle is assumed to be N_2+O_2 or CO_2+O_2 with an C_{O_2} corresponding to $C_{O_2,eq}$. During the oxidation and under the assumption that the FBR behaves as a CSTR, the gas composition at the surface of the particle is

assumed to equal the composition of the gas leaving the reactor. Therefore, the heat balance around a single particle can be written as,[107]

$$r' \Delta H_T^{\theta} \rho_{\mathrm{p}} V_{\mathrm{p}} = h_{\mathrm{g}}\, S_{\mathrm{p}} (T_{\mathrm{P}} - T_{\infty}) \tag{7-11}$$

where the left-hand side accounts for the generation or consumption of heat owing to the exothermic oxidation reaction or the endothermic O_2 release reaction, respectively, and the right-hand side accounts for the transfer of heat between the particle and the gas bulk. In eq.(7-11), r' (s^{-1}) is the rate of reaction, ΔH_T^{θ} is the enthalpy released during the reaction, V_p and S_p are the particle volume and the external surface area (assuming spherical particles), respectively. In eq.(7-11), T_P and T_∞ are the temperature of the particle and of the fluidised bed, respectively. The equation was written in terms of the mean particle diameter, $\bar{d}_p$, and then solved for T_{p}, in eq.(7-12a) and eq.(7-12b), respectively.

$$r' \Delta H_T^{\theta} \rho_{\mathrm{p}} \frac{1}{6} \pi\, \bar{d}_{\mathrm{p}}{}^{3} = h_g\, \pi\, \bar{d}_{\mathrm{p}}{}^{2} (T_{\mathrm{P}} - T_{\infty}) \tag{7-12a}$$

$$T_P = \frac{r' \Delta H_T^{\theta} \rho_{\mathrm{p}} \bar{d}_{\mathrm{p}}}{6\, h_g} + T_{\infty} \tag{7-12b}$$

The parameters used for this calculation and the results are shown in **Table 7-2**, below.

Table 7-2 *Results and parameter of the calculation for the maximum temperature difference between the oxygen carrier particle and the fluidised bed.*

T_∞ [°C]	r'^{a} [mmol(O_2)$g^{-1}s^{-1}$]	y_{O_2} [-]	λ_{g} [mW m^{-1} K^{-1}]	h_{g} [$Wm^{-1}K^{-1}$]	ΔT_{p} [°C]
oxygen release in N_2:					
825 °C	0.020	0.018	68.93	377.7	- 1.16
850 °C	0.021	0.027	70.15	384.4	- 1.20
875 °C	0.039	0.040	71.39	391.2	- 2.18
oxygen release in CO_2:					
825 °C	0.020	0.018	75.35	412.9	- 1.06
850 °C	0.021	0.027	76.92	421.5	- 1.09
875 °C	0.039	0.040	78.49	430.1	- 1.99
oxidation in 10 vol% O_2 + N_2:					
825 °C	0.037	0.027	70.60	386.8	+ 2.10
850 °C	0.041	0.040	71.77	393.3	+ 2.28
875 °C	0.046	0.058	72.95	399.7	+ 2.52

Footnotes: (a) these are the observed rates taken from experiments with O_2+N_2.

The results presented in **Table 7-2** suggests that the temperature of the particle decreases during the O_2 release under N_2 and CO_2 by up to 2.2 °C and 2.0 °C, respectively. The maximum increase in temperature during the oxidation is 2.5 °C. This temperature difference together with the correction for the variation in bed temperature (-1.3 °C during the O_2 release and +1.9 °C during the oxidation) was considered during the calculation of the kinetic parameters.

7.2 Development of a reaction rate model assuming a well-mixed fluidised bed

In this section, the intrinsic kinetics are determined by fitting reaction rate models to the (deconvoluted) observed rate of reaction, r', under the assumption that the fluidised bed is well mixed (*i.e.* no concentration gradients exist inside the reactor). This simplification allows to model the fluidised bed reactor as a continuously stirred tank reactor (CSTR). In a CSTR, the deconvoluted outlet concentration of O_2 is assumed to be equal to the concentration of O_2 anywhere in the reactor.[144] All equations introduced below were combined into one gPROMS model, which was used to compute the observed rate of reactions. The mass specific O_2 release rate, r'_{O_2}, calculated by eq.(7-3) was converted to the volumetric rate, r_{O_2}, using the envelope density of the particle, ρ_p,

$$r'_{O_2}\left[\frac{\text{mol}}{\text{g}\cdot\text{s}}\right] = \frac{r_{O_2}}{\rho_p} \tag{7-13}$$

In the absence of intra-particle diffusion, the observed volumetric rate of the O_2 release was assumed to depend on the intrinsic reaction rate and the mass transfer through the gas film surrounding the particle. It was assumed that the intrinsic rate depends on the concentration gradient between the O_2 equilibrium concentration, $C_{O_2,eq}$, and O_2 surface concentration, $C^s_{O_2}$. This assumption is based on the finding from section 6.5, in which results of experiments indicated that the reaction order of the copper manganese oxygen carriers is ~ 1 with respect to $(C_{O_2,eq} - C_{O_2})$. The rate of external mass transfer was assumed to depend on $C^s_{O_2}$ and the O_2 concentration in the gas bulk, $C^b_{O_2}$. These concentration gradients in the particle and the surrounding gas film during the O_2 release reaction, in **Fig. 7-6**, below.

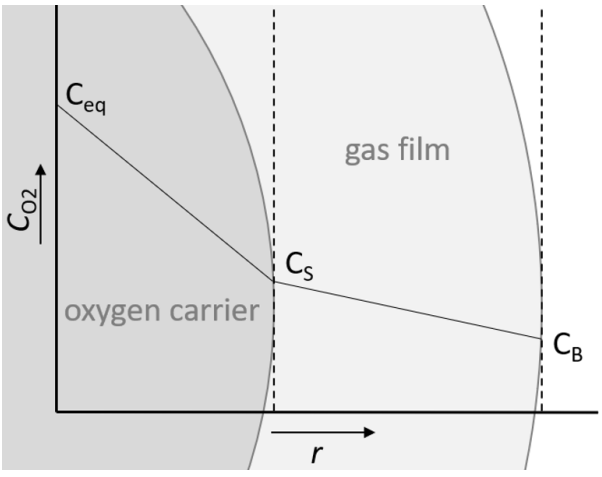


Fig. 7-6 *A drawing of the concentration gradients of O_2 in an oxygen carrier particle and its surrounding gas film.*

Based on the above stated assumptions, the chemical reaction rate was modelled by,

$$r_{\mathrm{O_2}}\left[\frac{\mathrm{mol}}{\mathrm{m^3 \cdot s}}\right] = k_s(C_{\mathrm{O_2,eq}} - C^{\mathrm{S}}_{\mathrm{O_2}}) \cdot f(X), \tag{7-14}$$

where $k_v[\mathrm{s^{-1}}]$ is the intrinsic reaction rate constant per unit of volume and $f(X)$ is a reaction rate function. When accounting for intra-particle diffusion, eq.(7-14) becomes,

$$r_{\mathrm{O_2}} = \eta \cdot k_s(C_{\mathrm{O_2,eq}} - C^{S}_{\mathrm{i}}) \cdot f(X), \tag{7-15}$$

where η is the effectiveness factor, which is calculated as detailed in section 6.3, using the following set of equations:[144, 224]

$$\eta = \frac{3}{\phi^2} \cdot (\phi \cdot \coth(\phi) - 1), \tag{7-16a}$$

$$\Phi = r_{\mathrm{p}}\sqrt{\frac{k_{\mathrm{i}}}{D_{\mathrm{e}}}}, \tag{7-16b}$$

$$D_{\mathrm{e}} = \frac{\varepsilon_{\mathrm{p}}}{\tau_{\mathrm{p}}}\left(\frac{1}{D_{\mathrm{K}}} + \frac{1}{D_{\mathrm{M}}}\right)^{-1}, \tag{7-16c}$$

The Knudsen diffusion, D_{K}, and the molecular diffusion in eq.(7-16c) were calculated by eq.(6-4)[199] and eq.(6-3)[220], respectively.

Assuming quasi-steady-state conditions to eliminate transient terms, the rate of O_2 production at the surface of the oxygen carrier given by eq.(7-14) has to balance the diffusion of O_2 away from the particle through the gas film, which is proportional to the concentration gradient of $C^{\mathrm{s}}_{\mathrm{O_2}}$ and $C^{\mathrm{b}}_{\mathrm{O_2}}$. This can be written as,

$$r_{\mathrm{O_2}} = \eta k_{\mathrm{s}}(C_{\mathrm{O_2,eq}} - C^{\mathrm{S}}_{\mathrm{O_2}})f(X) = k_{\mathrm{g}}(C^{\mathrm{s}}_{\mathrm{O_2}} - C^{\mathrm{b}}_{\mathrm{O_2}}) \tag{7-17}$$

where k_{g} is the mass transfer coefficient and $k_s[\mathrm{m \cdot s^{-1}}]$ is the intrinsic rate constant per unit of surface area, which in turn is related to the intrinsic rate constant per unit volume, $k_{\mathrm{v}}[\,\mathrm{s^{-1}}]$, by:

$$k_{\mathrm{s}} = V_{\mathrm{p}}\frac{1}{S_{\mathrm{p}}}k_{\mathrm{v}} = \frac{4}{3}\pi r_{\mathrm{p}}^3 \cdot \frac{1}{4\pi r_{\mathrm{p}}^2}k_{\mathrm{v}} = \frac{r_{\mathrm{p}}}{3}k_{\mathrm{v}} \tag{7-18}$$

where V_{p}, S_{p} and r_{p} are the volume, the external surface area (assuming spherical particles), and the radius of an oxygen carrier particle, respectively. Therefore, eq.(7-17) can be expressed as,

$$r_{\mathrm{O_2}} = \eta k_{\mathrm{v}}(C_{\mathrm{O_2,eq}} - C^{\mathrm{s}}_{\mathrm{O_2}})f(X) = \frac{3k_{\mathrm{g}}}{r_p}(C^{\mathrm{s}}_{\mathrm{O_2}} - C^{\mathrm{b}}_{\mathrm{O_2}}) \tag{7-19}$$

Re-arranging eq.(7-17) and solving for the surface concentration, $C^{s}_{\mathrm{O_2}}$, yields:[219]

$$C^{\mathrm{s}}_{\mathrm{O_2}} = \frac{\eta k_{\mathrm{s}} \cdot f(X) \cdot k_{\mathrm{g}}}{\eta k_{\mathrm{s}} \cdot f(X) + k_{\mathrm{g}}}\left(C_{\mathrm{O_2,eq}} - C^{\mathrm{b}}_{\mathrm{O_2}}\right) + C^{\mathrm{b}}_{\mathrm{O_2}} \tag{7-20}$$

The calculation is detailed in Appendix A.9. When re-substituting the expression for $C^{s}_{\mathrm{O_2}}$ from eq.(7-20) into eq.(7-14), the equation for the observed rate becomes:

$$r_{\mathrm{O_2}} = \left(\frac{1}{k_{\mathrm{g}}\left(C_{\mathrm{O_2,eq}} - C^{\mathrm{b}}_{\mathrm{O_2}}\right)} + \frac{1}{\eta k_s\left(C_{\mathrm{O_2,eq}} - C^{\mathrm{b}}_{\mathrm{O_2}}\right) \cdot f(X)}\right)^{-1} \tag{7-21}$$

The calculation of the mass transfer coefficient, k_{g}, in eq.(7-21) is detailed in the next section.

7.2.1 Estimation of the external mass transfer coefficient

The external mass transfer coefficient, k_{g}, was estimated using the Sherwood number, Sh, by,[238]

$$k_{\mathrm{g}}\left[\frac{m_f^3}{m_s^3 \cdot s}\right] = Sh \cdot \frac{D_{\mathrm{M}}}{d_{\mathrm{p}}} \tag{7-22}$$

The Sherwood number was estimated using a correlation proposed by La Nauze and Jung,[239]

$$Sh\,[-] = 2\varepsilon_{\mathrm{mf}} + 0.69\left(\frac{Re_{\mathrm{p}}}{\varepsilon_{\mathrm{mf}}}\right)^{\frac{1}{2}} Sc^{\frac{1}{3}} \tag{7-23}$$

The Reynolds number in eq.(7-23) was calculated using a correlation of the minimum fluidisation velocity, u_{mf}, and the kinematic viscosity of fluidising gas, μ_{g},[238]

$$Re_{\mathrm{p}}\,[-] = u_{\mathrm{mf}} \cdot \frac{d_p}{\mu_{\mathrm{g}}} \tag{7-24}$$

The Schmidt number in eq.(7-23) was calculated by,[144]

$$Sc\ \ [-] = \frac{\mu_g}{\rho_g\, D_M} \tag{7-25}$$

Chuang *et al.*[238] used the same method and reported data that allows validation of the correlated values of this work. They[238] calculated the maximum rate of mass transfer for a single particle (ρ_{p} = 1820 kg m^{-3}) in the size range 355-500 µm and 850-1000 µm during the oxidation in the fluidised bed under 1.22 vol% $O_2 + N_2$.

The authors[238] assumed that the particle is spherical, so that its mass and external surface area is given by eq.(7-25) and eq.(7-26), respectively.

$$S_{\mathrm{p}}\ [\mathrm{m}^2] = \pi \bar{d}_p{}^2 \tag{7-26}$$

$$m_{\mathrm{p}}\ [\mathrm{g}] = 1/6\pi \bar{d}_{\mathrm{p}}{}^3 \rho_{\mathrm{p}} \tag{7-27}$$

The maximum rate of mass transfer was estimated for $C_{O_2}^s = 0$ – the extreme case in which the O_2 surface concentration, $C_{O_2}^s$, is zero – using the relation,

$$r' \cdot m_{\mathrm{p}} \left[\frac{\mathrm{mol}}{\mathrm{s}}\right] = k_{\mathrm{g}} S (C_{O_2}^b - C_{O_2}^s) \tag{7-28}$$

The gPROMS model of this work was run with the values reported in Chuang *et al.*,[238] and the results are compared with the values of their work in **Fig. 7-7**, below.[238]

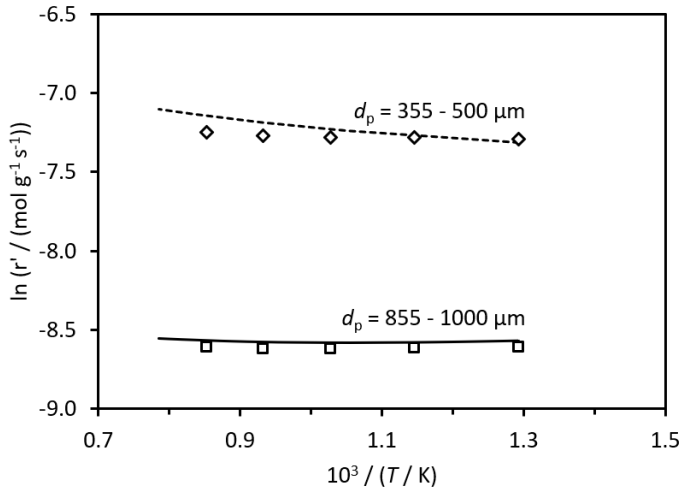


Fig. 7-7 *Validation of the gPROMS model by comparing the calculated values of the maximum rate of mass transfer (lines) with the calculated values reported in the literature (marker): results of the gPROMS model for the particle size ranges, --- , 355-500 µm and, —, 855-1000 µm, and calculated values reported by Chuang et al.[238] for the particle size ranges, ◇, 355-500 µm and ranges, □, 855-1000 µm.*

Fig. 7-7 shows a good agreement between the values reported by Chuang *et al.*[238] and those calculated using the gPROMS model of this work. The average relative deviations were 5%, and 4% for the smaller and the larger oxygen carrier particles, respectively. Such minor deviations might be due to differences in the correlations used for the calculation of the molecular diffusivity and viscosity of the fluidising gas.

Table 7-3 *Parameters and results of the calculation of the mass transfer coefficient for selected conditions using the gPROMS model of this work.*

T [°C]	D_M [$m^2 s^{-1}$]	Sc [−]	Sh [−]	Re_p [−]	k_g [$m\ s^{-1}$]
100 vol% CO_2:					
800	$1.961 \cdot 10^{-4}$	0.89	1.19	0.117	0.644
900	$2.292 \cdot 10^{-4}$	0.96	1.14	0.080	0.719
1000	$2.644 \cdot 10^{-4}$	1.04	1.09	0.056	0.799
10 vol% O_2 + CO_2:					
800	$1.961 \cdot 10^{-4}$	0.96	1.18	0.104	0.638
900	$2.292 \cdot 10^{-4}$	1.04	1.13	0.071	0.712
1000	$2.644 \cdot 10^{-4}$	1.12	1.09	0.050	0.792
100 vol% N_2:					
800	$1.961 \cdot 10^{-4}$	2.20	1.08	0.030	0.584
900	$2.292 \cdot 10^{-4}$	2.38	1.04	0.021	0.660
1000	$2.644 \cdot 10^{-4}$	2.56	1.01	0.014	0.740
10 vol% O_2 + N_2:					
800	$1.961 \cdot 10^{-4}$	2.14	1.08	0.031	0.585
900	$2.292 \cdot 10^{-4}$	2.31	1.05	0.021	0.661
1000	$2.644 \cdot 10^{-4}$	2.49	1.02	0.015	0.742

Footnote: the following parameters were used in addition to those shown above: $d_p = 3.625 \cdot 10^{-4}$ m, $\varepsilon_{mf} = 0.42$, $\rho_p = 2628$ kg m^3. Though the table above show only a few conditions, this model was re-run for every experimental condition individually.

Until here, all variables in eq.(7-21) were determined, apart from the reaction rate function, $f(X)$, which is introduced in the next section.

7.2.2 Reaction rate models

In this section, three different reaction models are introduced, and it is tested if these models are suitable to represent the experimental data. The three reaction models are the homogeneous reaction model, the shrinking grain model, and the shrinking core mode, which are illustrated in **Fig. 7-8**, below.

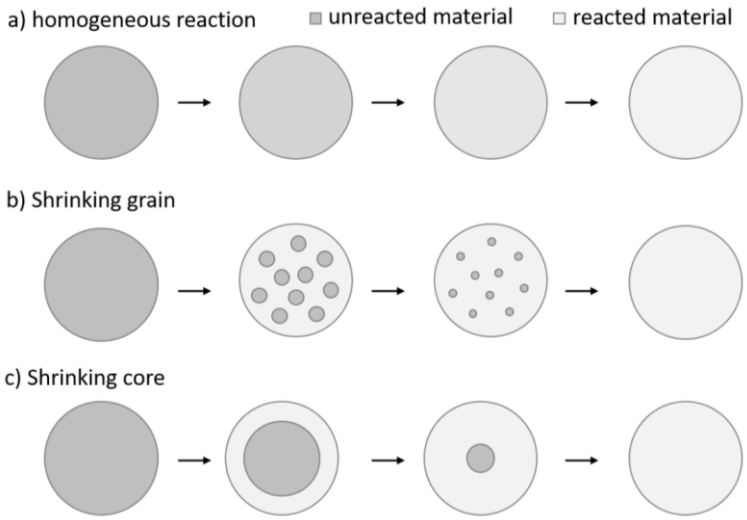


Fig. 7-8 *Illustration of the progression of the reaction in the (a) homogeneous reaction model, (b) shrinking grain model, and (c) shrinking core model.*[144]

In the reaction rate equation, the rate function, $f(X)$, accounts for the change in surface area that is available for the reaction.[235] A simple relationship of the initial surface area, $S_{OC,0}$, and the surface area at a given conversion, S_{OC}, is,[235]

$$S_{\mathrm{OC}} = S_{\mathrm{OC},0}(1-X)^{m} \,. \tag{7-29}$$

For a homogeneous reaction, the rate of reaction is assumed to be spatially uniform across the oxygen carrier particle, and thus m assumes a value of unity. In the case of the shrinking grain model, an oxygen carrier particle is assumed to consist of an agglomeration of grains with gas species being able to diffuse in the macro-pores between the grains.[240] The concentration of the diffusion species is thus typically assumed spatially uniform across the particle. This allows the volume of the grains and the volume of the pores to be treated as one combined volume each. During the reaction, the grains shrink, with the surface area available for reaction being proportional to $(1-X)^{2/3}$. Therefore, m in eq.(7-29) assumes a value of $2/3$ for this reaction type. [235]

The third reaction model illustrated in **Fig. 7-8**, is the shrinking core model, which assumes a shrinking unreacted core surrounded by a growing product layer during the reaction. Owing to considerable diffusion resistance in the product layer, the concentration of the diffusing species

varies exponentially with the difference between the radius of the particle and the radius of the product layer.[144] The reaction model is obtained from a material balance of O_2 across the reacted shell. Assuming no reaction in the product layer, the material balance of O_2 through this layer can be expressed by,[238, 241]

$$\frac{1}{r^2}\frac{d}{dr}\left(r^2 N_{O_2}\right) = 0 \tag{7-30}$$

where N_{O_2} is the molar flow of O_2, and is modelled as series of intrinsic reaction, diffusion through the product layer and mass transfer through the gas film surrounding the particle. Chuang *et al.*[238] modified the shrinking core model presented by Levenspiel[144] accordingly, by also accounting for a surface reaction that is proportional to $(C_{\mathrm{O_2,eq}} - C_{O_2}^S)$. In this model, the diffusion of O_2 through the gas film can be expressed by,[144,238]

$$N_{O_2} = 4\pi r_0^2 k_{\mathrm{g}}\left(C_{O_2}^B - C_{O_2}^S\right), \tag{7-31}$$

the diffusion through the product layer by, [144,238]

$$N_{O_2} = \frac{4\pi D_e\left(C_{O_2}^B - C_{O_2}^S\right)}{\left(\frac{1}{r} - \frac{1}{r_0}\right)}, \tag{7-32}$$

and the surface reaction by, [144,238]

$$N_{O_2} = 4\pi r^2 k_{\mathrm{s}}(C_{O_2}^B - C_{\mathrm{O_2,eq}}) \tag{7-33}$$

As demonstrated in Levenspiel[144] the three individual resistances can be combined into one equation. Chuang *et al.*[238] did this for the oxidation of Cu. When modifying this model for the O_2 release reaction (by swapping $C_{O_2}^B$ and $C_{\mathrm{O_2,eq}}$), the expression for the rate of O_2 release becomes, [238]

$$N_{\mathrm{O_2}} = \frac{(C_{O_2}^B - C_{\mathrm{O_2,eq}})}{\frac{1}{4\pi D_{\mathrm{e}}}\left(\frac{1}{r} - \frac{1}{r_0}\right) + \frac{1}{4\pi r^2 k_{\mathrm{s}}} + \frac{1}{4\pi r_0^2 k_{\mathrm{g}}}} \tag{7-34}$$

In this work, the radius of the unreacted core, r_0, as a value of $1.785 \cdot 10^{-04}$ m and r in eq.(7-34) is the radius of the unreacted core at any given time. This was combined by,[238]

$$t = -\frac{\rho_{\mathrm{OC}}}{4\left(C_{O_2}^B - C_{\mathrm{O_2,eq}}\right)}\left(\frac{(r_1^2 - r_0^2)}{2D_{\mathrm{eff}}} - \frac{(r_1^3 - r_0^3)}{3r_0 D_{\mathrm{eff}}} + \frac{(r_1 - r_0)}{k_{\mathrm{s}}} + \frac{(r_1^3 - r_0^3)}{3r_0 k_{\mathrm{g}}}\right) \tag{7-35}$$

where ρ_{m} is the molar density of the copper manganese oxide ($\rho_m = 12305$ mol($CuMn_2O_4$) m^{-3}).

The conversion of this model is given by,[144,238]

$$X = 1 - \left(\frac{r}{r_0}\right)^3 \tag{7-36}$$

Using this model, the conversion calculated by eq.(7-36) was fitted to the observed conversion over the first 180 s of the reaction by varying k_s.

The gPROMS model was used to minimise the square error between the observed conversion and the calculated conversion by varying k_s in eq.(7-21) for the homogeneous reaction model (with $f(X) = (1 - X)$), and the shrinking grain model (with $f(X) = (1 - X)^{2/3}$), as well as eq.(7-35) and eq.(7-36) for the shrinking core model.

The results for the homogeneous reaction model are illustrated in **Fig. 7-9**, below.

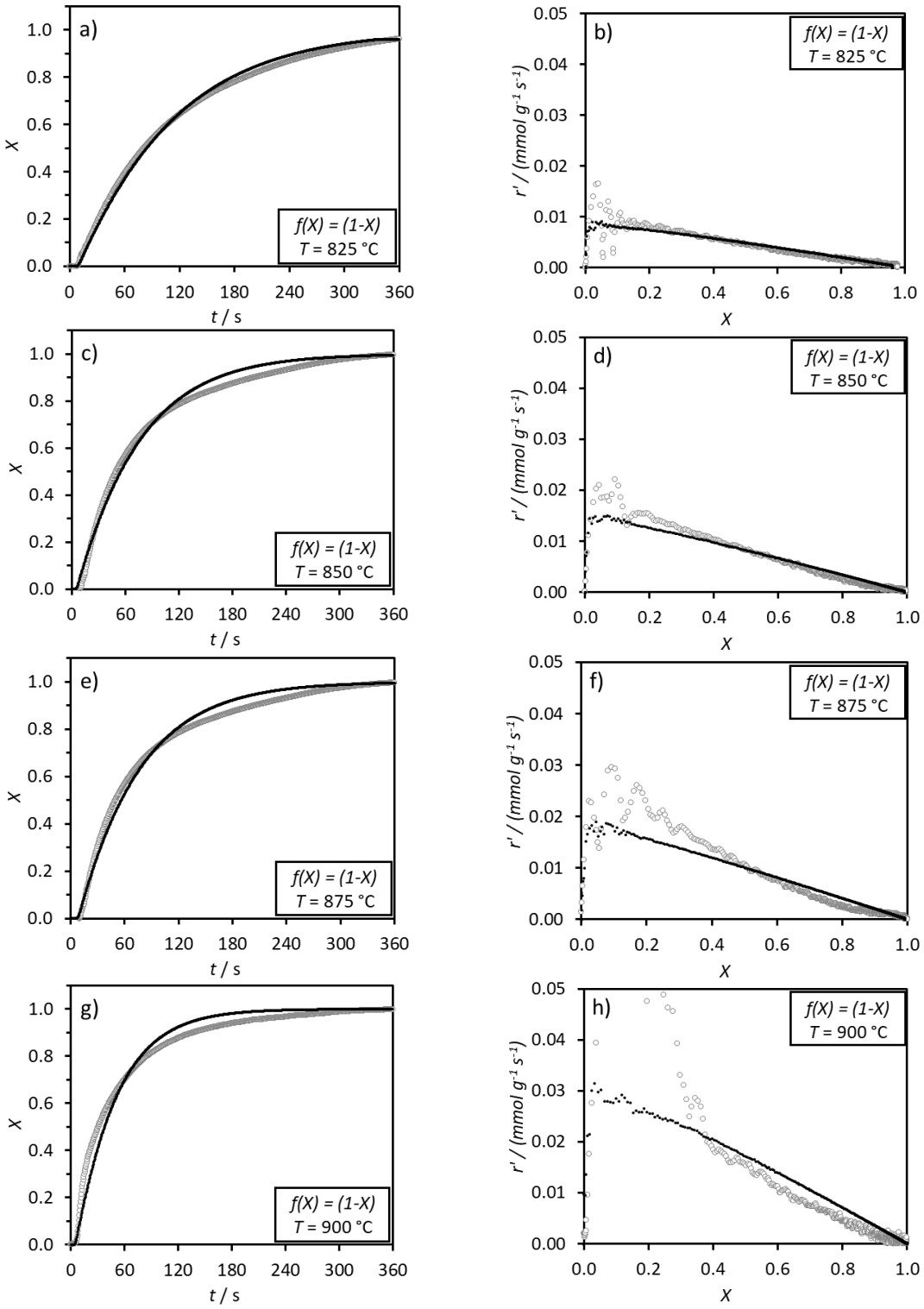


Fig. 7-9 *Plots of (a, c, e, g) of observed conversion against time and (b, d, g, h) deconvoluted observed rate against time for the O_2 release reaction of 1000mg 1Cu-2Mn-MM at (a, b) 825 °C, (c, d) 850 °C, (e, f) 875 °C and (g, h) 900 °C. The grey markers represent the experimental data, which was measured in the fluidised bed under pure N_2 with a total gas flow rate of 2.445 l·min^{-1} at SATP. The black markers represent the modelled data.*

The results for the shrinking grain model are illustrated in **Fig. 7-10**, below.

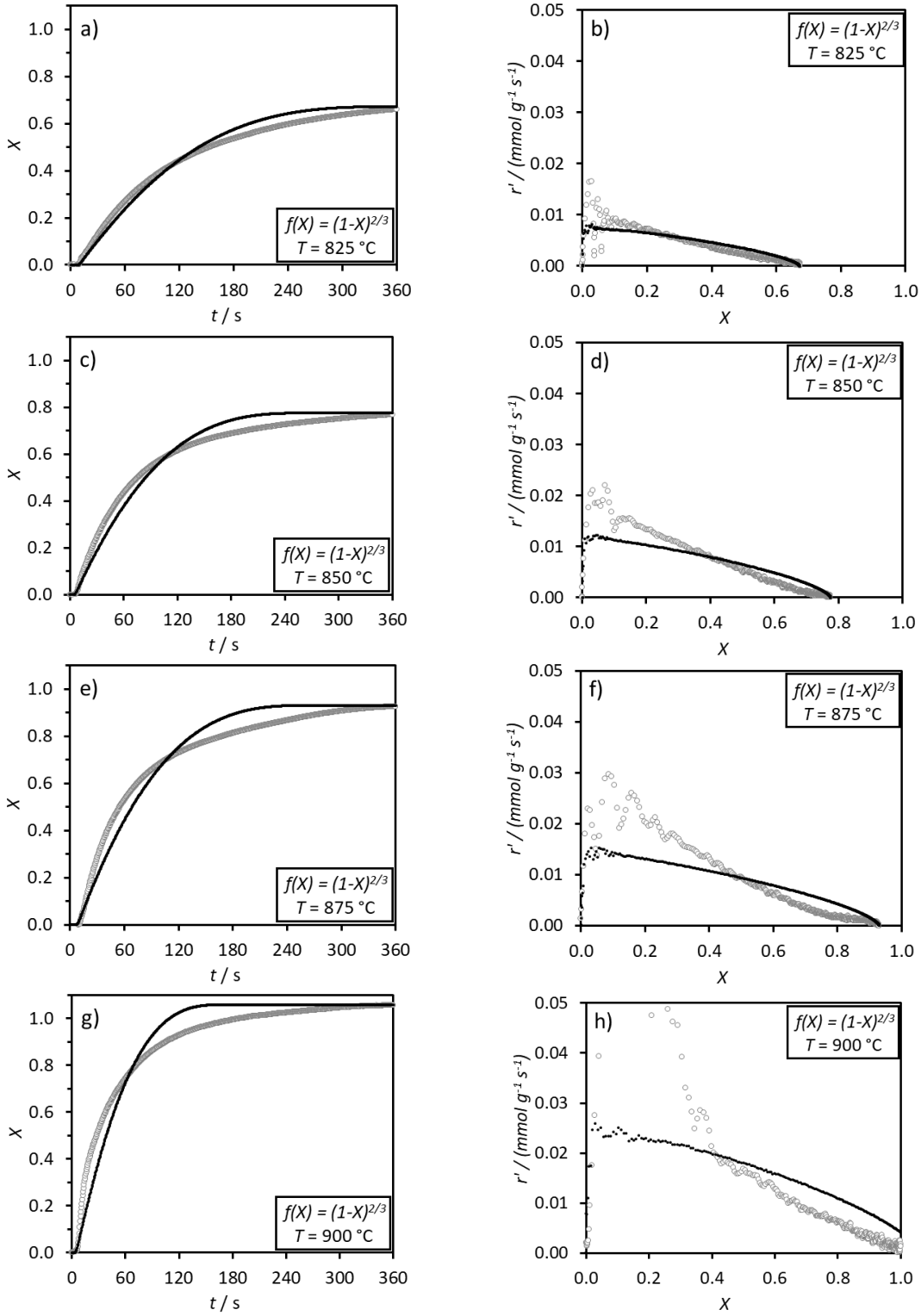


Fig. 7-10 *Plots of (a, c, e, g) of observed conversion against time and (b, d, g, h) deconvoluted observed rate against time for the O_2 release reaction of 1000mg 1Cu-2Mn-MM at (a, b) 825 °C, (c, d) 850 °C, (e, f) 875 °C and (g, h) 900 °C. The grey markers represent the experimental data, which was measured in the fluidised bed under pure N_2 with a total gas flow rate of 2.445 l·min^{-1} at SATP. The black markers represent the modelled data.*

The results for the shrinking core model are illustrated in **Fig. 7-11**, below.

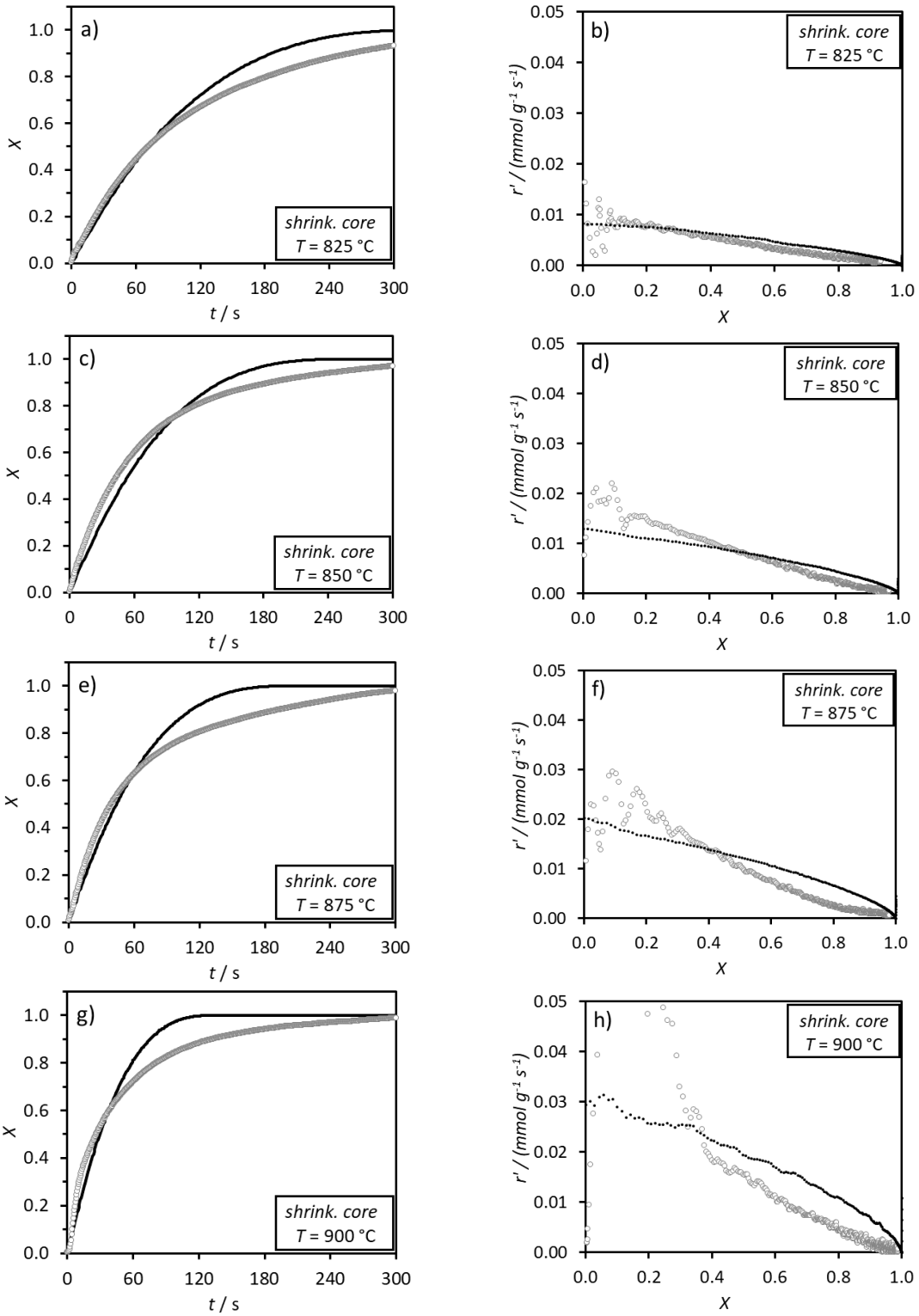


Fig. 7-11 *Plots of (a, c, e, g) of observed conversion against time and (b, d, g, h) deconvoluted observed rate against time for the O_2 release reaction of 1000mg 1Cu-2Mn-MM at (a, b) 825 °C, (c, d) 850 °C, (e, f) 875 °C and (g, h) 900 °C. The grey markers represent the experimental data, which was measured in the fluidised bed under pure N_2 with a total gas flow rate of 2.445 l·min^{-1} at SATP. The black markers represent the modelled data.*

The results of the parameter estimation illustrated in **Fig. 7-9**, **Fig. 7-10**, and **Fig. 7-11** are presented in **Table 7-4**, below.

Table 7-4 *Results from the calculation of the O_2 release rate using the homogeneous reaction model and assuming a well-mixed fluidised bed (CSTR).*

	825 °C	850 °C	875 °C	900 °C
Homogeneous reaction model:				
k_v [s^{-1}]	113.35	115.77	88.58	98.19
k_s [m s^{-1}]	$6.746 \cdot 10^{-03}$	$6.889 \cdot 10^{-03}$	$5.272 \cdot 10^{-03}$	$5.844 \cdot 10^{-03}$
$\Delta_{AARD,X}$ [a]	0.01	0.02	0.03	0.04
$\Delta_{MARD,X}$ [b]	0.03	0.04	0.05	0.12
Shrinking grain model:				
k_v [s^{-1}]	95.69	92.95	70.92	78.60
k_s [m s^{-1}]	$5.695 \cdot 10^{-03}$	$5.531 \cdot 10^{-03}$	$4.220 \cdot 10^{-03}$	$4.678 \cdot 10^{-03}$
$\Delta_{AARD,X}$ [a]	0.03	0.05	0.06	0.07
$\Delta_{MARD,X}$ [b]	0.06	0.08	0.09	0.15
Shrinking core model:				
k_v [s^{-1}]	91.70	83.67	52.34	62.49
k_s [m s^{-1}]	$5.457 \cdot 10^{-03}$	$4.98 \cdot 10^{-03}$	$3.11 \cdot 10^{-03}$	$3.719 \cdot 10^{-03}$
Δ_{AARD,X_n} [a]	0.047	0.055	0.12	0.15
Δ_{MARD,X_n} [b]	0.07	0.08	0.07	0.10
$p_{O_2,eq}$ [bar]	0.0256	0.0416	0.0663	0.1036
$C_{O_2,eq}$ [mol m^3]	0.2839	0.4518	0.7041	1.0760

Footnotes: (a) the average absolute relative deviation between the observed conversion and the modelled conversion was calculated by $\frac{1}{N}\Sigma(|X_{exp,t} - X_{model,t}|)/X_{exp,t}$ *and (b) the maximum absolute relative deviation was calculated by* $max(|X_{exp,t} - X_{model,t}|)/X_{exp,t}$.

The homogeneous reaction rate model represents the experimental data best. The average absolute relative deviation between the observed and the modelled conversion, $\Delta_{AARD,X}$, was in the range $\Delta X = 0.03 - 0.12$. The values of $\Delta_{AARD,X}$ for the shrinking grain model were in the range $0.05 - 0.15$ and for the shrinking core model in the range $0.06 - 0.15$. The homogeneous reaction model **Fig. 7-9** shows that the model overestimates the conversion in the first stage of the reaction (until X = 0.5-0.7).

The shrinking core mechanism describes the rate of O_2 release not as good as the other two models. The calculated conversion differed on average from the observed conversion by ΔX = 0.10. The maximum deviation was ΔX = 0.19.

To evaluate the fit of correlations for the rate constants calculated using the homogeneous reaction model (best fitting model, *c.f.* **Table 7-4**), the rate constants were plotted against temperature and into an Arrhenius plot in **Fig. 7-12a** and **Fig. 7-12b**, respectively.

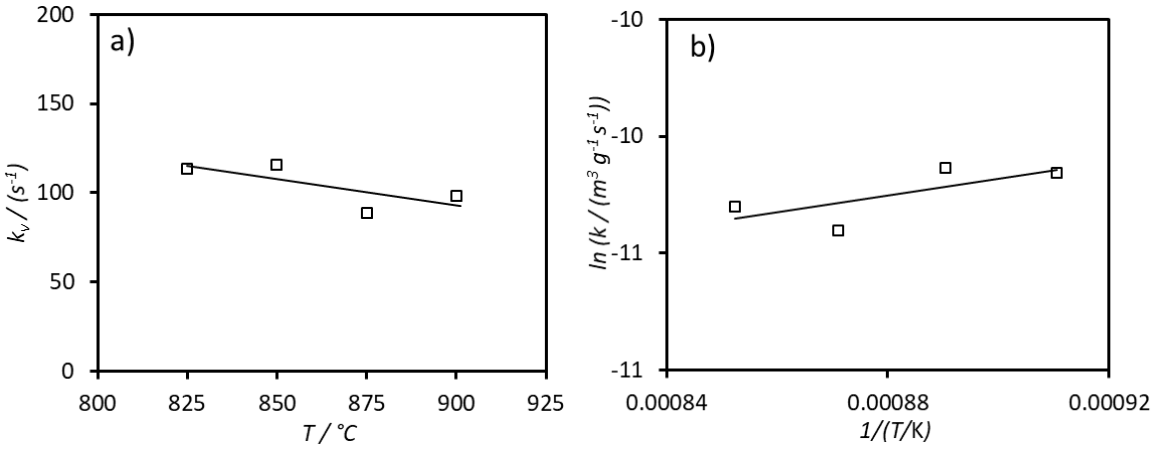


Fig. 7-12 *A plot of (a) k_v against temperature and ln(k) against 1/T using the intrinsic rate constants determined using the homogeneous reaction rate model.*

Fig. 7-12a shows that the calculated rate constant decreases with an increasing temperature. Commonly, the rate constants are correlated with a pre-exponential factor, A, and an activation energy, E_a, using an Arrhenius type expression:

$$k[\mathrm{m^3 g^{-1} s^{-1}}] = A \exp\left(\frac{-E_a}{R(T/K)}\right), \tag{7-37}$$

where R is the real gas constant and T/K is the temperature in Kelvin. The values of A and E_a can be directly taken from the Arrhenius plot in **Fig. 7-12b**, in which the slope and the intercept of the fitted line correspond to -E_a/R and ln(A), respectively. This method yields values for the apparent activation energy and the apparent pre-exponential factor of $E_a = -30.06\ \mathrm{kJ/mol}$ and $A = 2.87 \cdot 10^{-6}\ \mathrm{m^3 g^{-1} s^{-1}}$, respectively. However, when testing the data using the student-t method, the result suggests that the correlation has no statistical significance, and the prediction range for a 95% confidence interval is $2.27 \cdot 10^{-6}\ \mathrm{m^3 g^{-1} s^{-1}} < A < 3.61 \cdot 10^{-6}\ \mathrm{m^3 g^{-1} s^{-1}}$. The reason for this large confidence interval is that when using an Arrhenius type expression to correlate the O_2 release rates for the oxygen carriers of this work, the fitted values contain at least two functions of temperature – one to correlate the equilibrium concentration and the Arrhenius expression to correlate k, since the complete O_2 release rate expression is,

$$r'[\mathrm{mol\ g^{-1} s^{-1}}] = A \exp\left(\frac{-E_a}{R\left(T/_K\right)}\right)\left[C_{eq} - C\right] \cdot f(X) \tag{7-38}$$

Within the tested temperature range, p_{O_2} varies between 0.0256 bar and 0.1036 bar, and the uncertainty in the correlation of p_{O_2} amplifies the uncertainty in the correlated values of A and E_a. Therefore, the use of eq.(7-37) should be limited to the evaluated temperature range. The aim of this kinetic study was to provide data that allows estimation of a minimum solid inventory.

The kinetic study was not the focus of this work. For in-depth process design it is therefore recommended to carry out a kinetic study with more experimental data points.

The same procedure was carried out for the oxidation. The conversion was normalised by dividing it by the maximum conversion, $X_{\max}$, which was for all three experiments in the range 0.76 – 0.79. When varying the intrinsic reaction rate to minimise the square error between the modelled conversion and the experimental conversion, this change is accounted for by calculating the modelled conversion from the modelled observed rates (which include kinetics, intra-particle diffusion and external mass transfer limitations) by division with the experimental O_2 capacity (*i.e.* 0.76 – 0.79) , instead of division by the theoretical O_2 capacity (since $R_{0,\mathrm{th}} \cdot X_{\max} = R_{0,\mathrm{exp}}$. The results for the oxidation reaction using the homogeneous reaction model are illustrated in **Fig. 7-9**, below.

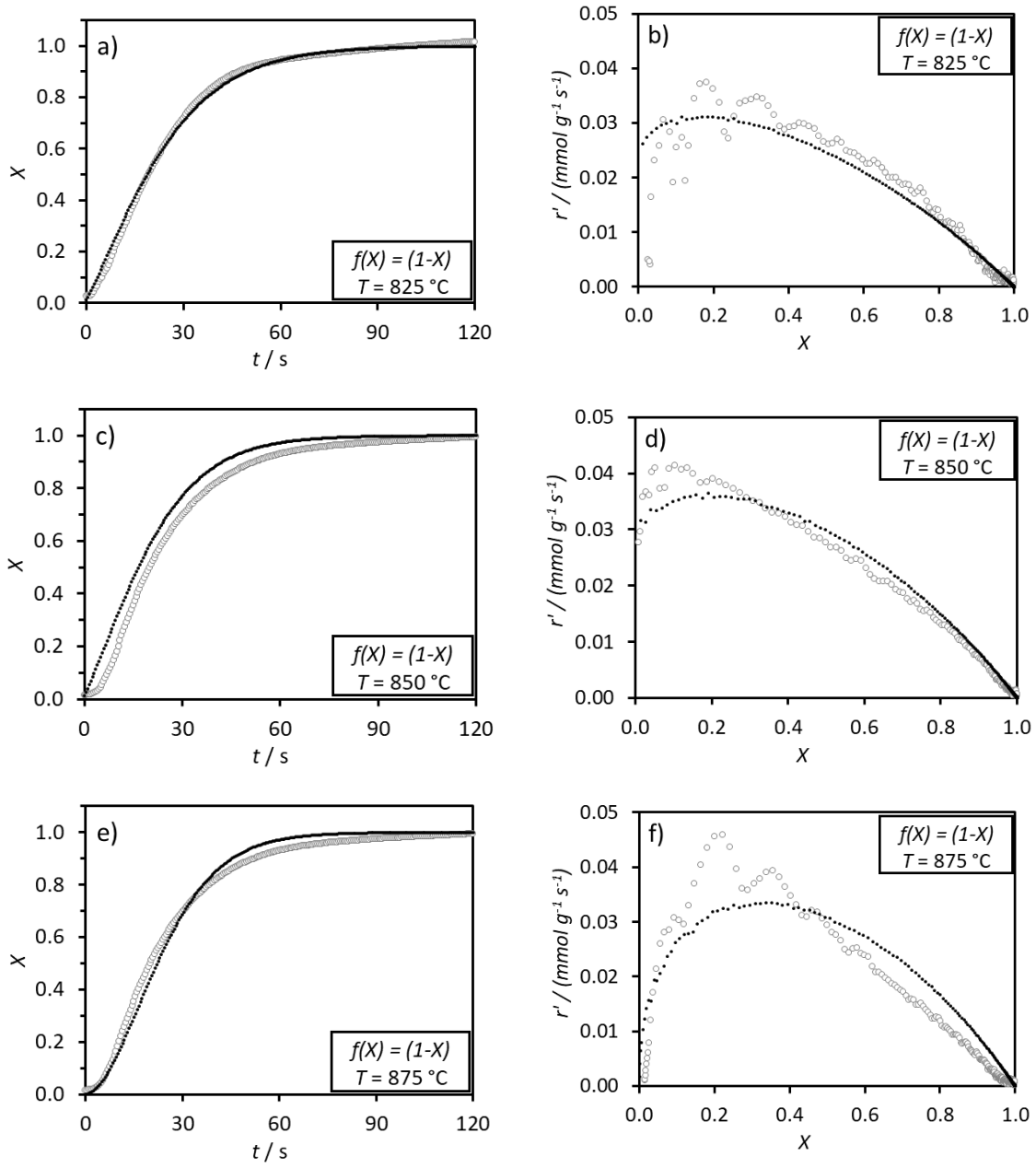


Fig. 7-13 *Plots of (a, c, e, g) of observed conversion against time and (b, d, g, h) deconvoluted observed rate against time for the oxidation reaction of 1000mg 1Cu-2Mn-MM at (a, b) 825 °C, (c, d) 850 °C, (e, f) 875 °C. The grey markers represent the experimental data, which was measured in the fluidised bed under pure N_2 with a total gas flow rate of 2.445 l·min^{-1} at SATP. The black markers represent the modelled data.*

The results for the oxidation reaction using the homogeneous reaction model are illustrated in **Fig. 7-9**, below.

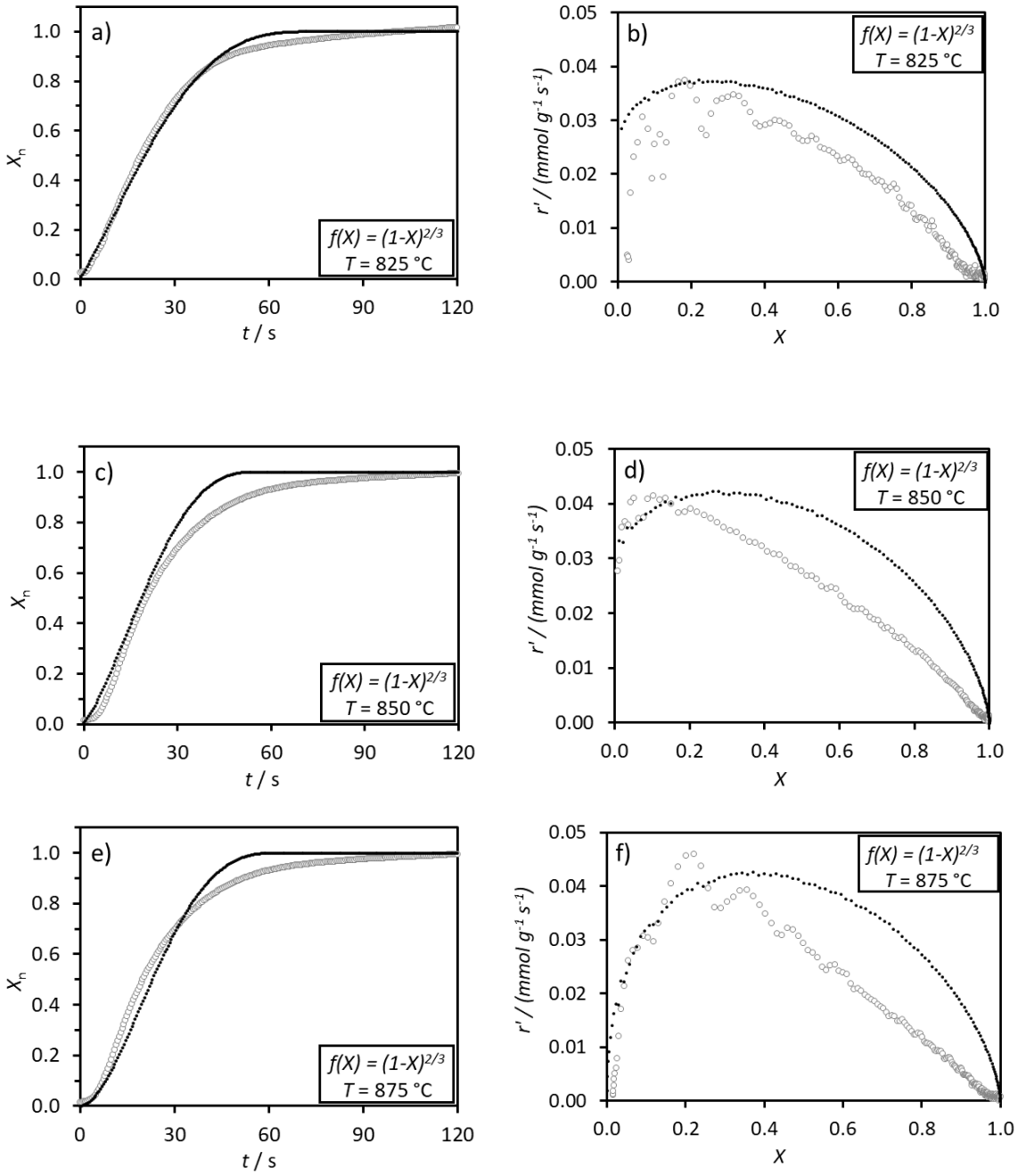


Fig. 7-14 *Plots of (a, c, e, g) of observed conversion against time and (b, d, g, h) deconvoluted observed rate against time for the oxidation reaction of 1000mg 1Cu-2Mn-MM at (a, b) 825 °C, (c, d) 850 °C, (e, f) 875 °C. The grey markers represent the experimental data, which was measured in the fluidised bed under pure N_2 with a total gas flow rate of 2.445 l·min^{-1} at SATP. The black markers represent the modelled data.*

The results of the parameter estimation illustrated in **Fig. 7-16** and **Fig. 7-17** are presented in **Table 7-5**, below.

Table 7-5 *Results from the calculation of the oxidation rate using the homogeneous reaction model and assuming a well-mixed fluidised bed (CSTR).*

	825 °C	850 °C	875 °C
Homogeneous reaction model:			
k_v [s^{-1}]	234.30	407.74	880.59
k_s [$\mathrm{m\ s}^{-1}$]	$1.394 \cdot 10^{-02}$	$2.427 \cdot 10^{-02}$	$5.241 \cdot 10^{-02}$
$\Delta_{\mathrm{AARD},X}$ [a]	0.012	0.024	0.028
$\Delta_{\mathrm{MARD},X}$ [b]	0.050	0.059	0.066
Shrinking grain model:			
k_v [s^{-1}]	190.08	385.69	636.98
k_s [$\mathrm{m\ s}^{-1}$]	$1.131 \cdot 10^{-02}$	$2.295 \cdot 10^{-02}$	$3.791 \cdot 10^{-02}$
$\Delta_{\mathrm{AARD},X}$ [a]	0.020	0.019	0.041
$\Delta_{\mathrm{MARD},X}$ [b]	0.046	0.044	0.090
$p_{\mathrm{O_2,eq}}$ [bar]	0.0256	0.0416	0.0663
$C_{\mathrm{O_2,eq}}$ [$\mathrm{mol\ m}^3$]	0.2839	0.4518	0.7041

Footnotes: (a) the average absolute relative deviation between the observed conversion and the modelled conversion was calculated by $\frac{1}{N}\Sigma(|X_{exp,t} - X_{model,t}\ |)/X_{exp,t}$ *and (b) the maximum absolute relative deviation was calculated by* $max(|X_{exp,t} - X_{model,t}\ |)/X_{exp,t}$.

The homogeneous reaction rate model represents the experimental data best. The average absolute relative deviation between the observed and the modelled conversion, $\Delta_{\mathrm{AARD},X}$, was in the range 1.2 – 2.8%. The values of $\Delta_{\mathrm{AARD},X}$ for the shrinking grain model were in the range 1.9 – 4.1%. This shows that the homogeneous reaction model represents the experimental data of the oxidation function better than the shrinking grain model.

To evaluate the fit of correlations for the rate constants calculated using the homogeneous reaction model (best fitting model, *c.f.* **Table 7-5**), the rate constants were plotted against temperature and into an Arrhenius plot in **Fig. 7-15**, respectively.

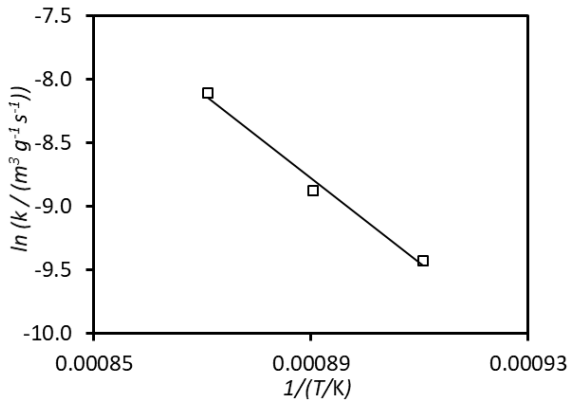


Fig. 7-15 *A plot of (a) k_v against temperature and ln(k) against 1/T using the intrinsic rate constants determined using the homogeneous reaction rate model.*

Fig. 7-15 shows that the calculated rate constant decreases with an increasing temperature. Using the Arrhenius equation in eq.(7-37) values for the apparent activation energy and the apparent pre-exponential factor of $E_a = 277.2\,\mathrm{kJ/mol}$ and $A = 8.46 \cdot 10^{-10}\,\mathrm{m^3 g^{-1} s^{-1}}$, respectively, were calculated. Though, it should be mentioned again, that the calculated values of E_a and A contain uncertainties owing to the uncertainties of the correlation of C_{eq}. Besides this screening of the intrinsic kinetic, long-term cycling experiments have been performed in the fluidised bed, as detailed below.

7.3 Long-term cycling experiments in the fluidised bed

In this section, the results from long-term redox-cycling experiments in the fluidised bed are reported at conditions similar to those expected in a CLAS process. The aim was to study the attrition of the oxygen carriers. In contrast to the long-term cycling experiments in the TGA (which are detailed in section 6.8), the long-term cycling experiments in the fluidised bed reactor allowed to study the mechanical stability of the oxygen carriers in addition to their chemical stability. Attrition tests were carried out with a low bed mass (using 750 mg of the active metal oxide) and a high bed mass (40 g of the active metal oxide). The low bed mass tests allowed to study the change of oxidation and O_2-release rate in a kinetics-controlled regime. High bed mass tests, in which the observed rate was controlled by the external mass transfer, allowed to study the agglomeration tendencies and attrition rate. The results of the long-term cycling tests are detailed in the following sections.

7.3.1 Long-term cycling with 40 g of 1Cu-1Mn-MM

After four gas switching cycles with an empty reactor liner (with neither inert nor sample) at 850 °C, 40 g of 1Cu-1Mn-MM were loaded into the reactor. In the kinetic experiments described in section 7.2, sand was added in a ratio of 40 g of sand per 1 g of the active metal oxide to: (i) disperse the samples spatially and (ii) to disperse the heat of reaction. During kinetic experiments, the maximum increase in bed temperature, T_{bed}, during oxidation was 1.4 °C (*c.f.* section 7.1.4). Without sand and a relatively high sample mass, the temperature during this long-term cycling experiments increased on average by 9.8 °C, as shown in **Fig. 7-16**, below. Owing to the significant temperature changes during the redox-reactions as well as an excessive effect of external mass transfer on the observed rate, the observed rate of reaction shall only be taken as an indication of its trend.

The observed rate was calculated following the same procedure outlined for the kinetic experiments. The difference between y_{O_2} during the cycles with and without sample was significantly larger, owing to the larger sample mass. The y_{O_2} measured during the empty cycles and the first cycles with sample, is shown in **Fig. 7-16**, below.

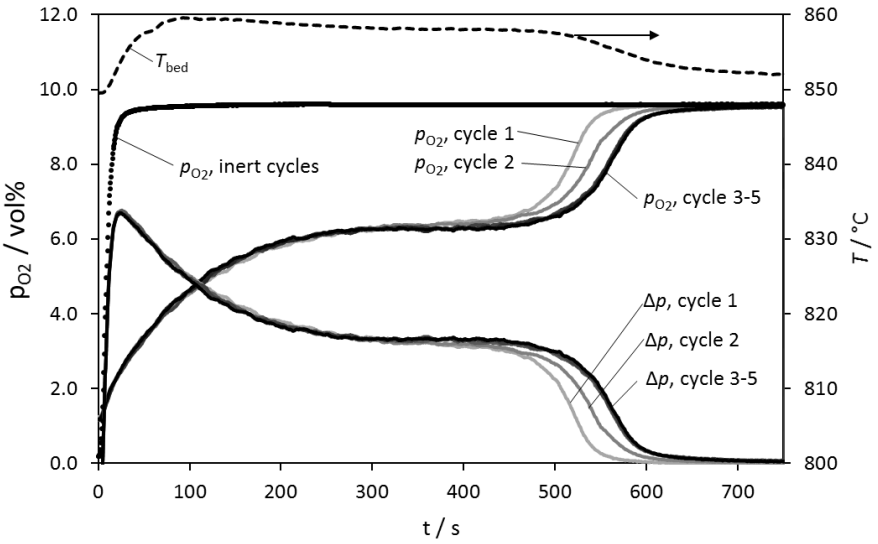


Fig. 7-16 *O_2 concentrations during the inert cycles and during the oxidations of the first five redox-cycles of the LTC-FBR-1 experiment, the difference between those O_2 concentrations, and the averaged bed temperature.*

The maximum oxidation rate of each redox-cycle plotted against the cycle number in ***Fig. 7-17***, below.

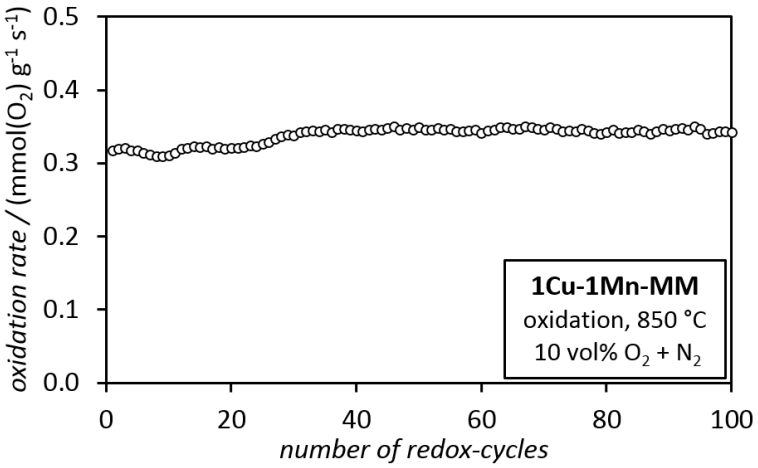


Fig. 7-17 *Observed oxidation rate during "LTC-FBR-1" experiment at 850 °C under 10 vol% O_2, balanced with N_2, with a total gas flow rate of 2.445 l·min^{-1} at SATP. The value of the bed mass used in the oxidation rate calculation was assumed to change linearly with cycle number between the values of the loaded bed mass and the recovered bed mass.*

The maximum overall rate of oxidation remained relatively stable at $0.34 \cdot 10^{-3}$ mol(O_2)g^{-1}s^{-1} over 100 redox-cycles – it has to be noted that this rate is mainly the rate of O_2 diffusion from the bulk to the particle surface rather than the rate of intrinsic kinetics. After the 5th , 10th , 25th , 40th , 60th , 80th and 100th redox-cycle, the bed was cooled down to 550 °C and then dropped by opening a cap at the bottom of the reactor body. From the recovered bed material, 300 mg was withdrawn for XRD, MIP, BET, and SEM-EDS analysis. The remaining oxygen carriers were loaded back into the reactor and

the next redox-cycling interval was started. The mass fraction of oxygen carriers lost due to attrition, w_a, was calculated by,

$$w_a = 1 - (m_{\text{bed}} - \sum_0^n m_{\text{removed}})/m_{\text{bed,0}}\,, \tag{2}$$

where w_a is the sample mass attrited, $m_{\text{bed,0}}$ is initial sample mass, m_{bed} is the recovered bed mass after the last interval, and m_{removed} is the cumulated mass of samples removed for the material characterisation (300 mg per sampling). The calculated values for m_{bed} / $m_{\text{bed,0}}$ and the mass of fines collected from the elutriate filter, m_{fines}, are plotted over the number of cycles in **Fig. 7-18**, below.

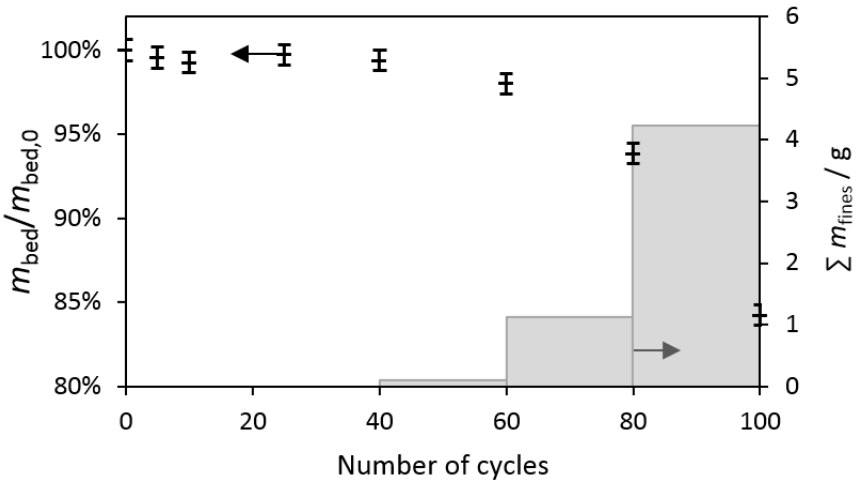


Fig. 7-18 *Ratio of recovered bed mass to initial bed mass (primary axis) and cumulative mass of fines recovered from elutriate filter ($m_{\text{fines;}}$ secondary axis) of experimental series "FBR-I" using 300-425 µm 1Cu-1Mn-MM. The error bars correspond to the uncertainty, which was taken as two times the standard deviation of the first four measurements.*

Over the first 40 redox-cycles, the loss of sample was only 0.6 wt%. The rate of loss increased and amounted to 2.0 wt%, 6.2 wt% and 15.8 wt% after the 60th, 80th and 100th cycle. No fines were collected from the filter until the 40th redox-cycle. Then, the cumulated mass of fines collected increased to 0.10 g, 1.03 g and 3.11 g after the 60th, 80th and 100th cycles. This shows that extrapolation of the weight-loss to estimate the lifetime of the oxygen carrier can be misleading, when selecting short cycling durations.

To elucidate the reasons for the sudden increase in attrition rate the cycled materials were characterised by means of XRD, SEM and N_2-adsorption and the crushing force was measured. The results of the XRD analysis are shown in **Fig. 7-19**, below.

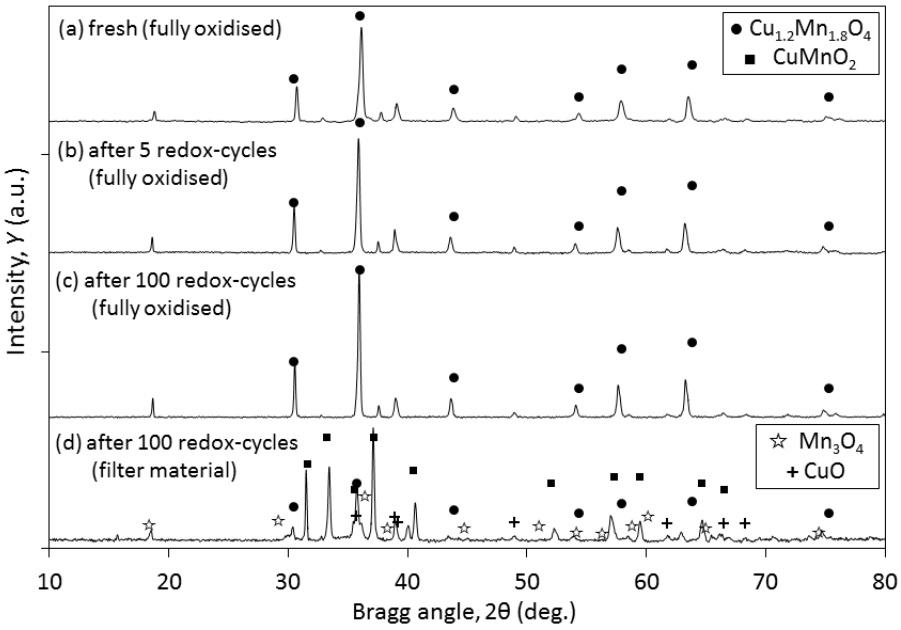


Fig. 7-19 *XRD plot of 1Cu-1Mn-MM oxygen carrier used in the long-term cycling experiment "FBR-I" in its fully oxidised state (a) before redox-cycling, (b) after 5 redox-cycles, and (c) after 100 redox-cycles, as well as (d) fines collected in the filter.*

XRD analysis (**Fig. 7-19**) shows that $Cu_xMn_{3-x}O_4$ and CuO are the main phases of the fresh and redox-cycled oxidised oxygen carriers. Here $Cu_{1.2}Mn_{1.8}O_4$ was identified, however, the peaks of the $Cu_xMn_{3-x}O_4$ with $1 < x < 1.5$ are very similar and hence are not clearly distinguishable. In fact, the peak position of the largest copper manganese oxide XRD peak (at $2\theta \sim 36°$) in **Fig. 7-19** of the cycled material (after 5 and 100 redox-cycles) is shifted slightly to the left ($2\theta = 35.9°$) in comparison to the fresh oxygen carrier ($2\theta = 36.1°$). This indicates a reduction of the value of x in $Cu_xMn_{3-x}O_4$, *e.g.* formation of $CuMn_2O_4$ from $Cu_{1.2}Mn_{1.8}O_4$. Furthermore, an increase in 'sharpness' of the peaks can be observed in **Fig. 7-19**. This indicates an increase in the crystallite size. This was confirmed using the Scherrer equation, eq.(5-6), which yielded values of the mean crystallite size of 47.8 nm, 50.3 nm and 76.0 nm, for the oxygen carriers analysed before the first cycle, after the fifth cycle and after the 100th cycle, respectively. This demonstrates that CMO does not separate into its single metal oxides during extended cycling. XRD analysis of the filter material **Fig. 7-19d** identified mainly $Cu_{1.2}Mn_{1.8}O_4$, CuO and $CuMnO_4$ and minor amounts of Mn_3O_4. Since these phases are mixture of the oxidised and decomposed oxygen carrier material, this finding indicates that none of the oxidation states has higher attrition rates compared to the other. In addition to the XRD analysis, the cycled oxygen carriers were studied by SEM-EDS, as shown in **Fig. 7-20**, below.

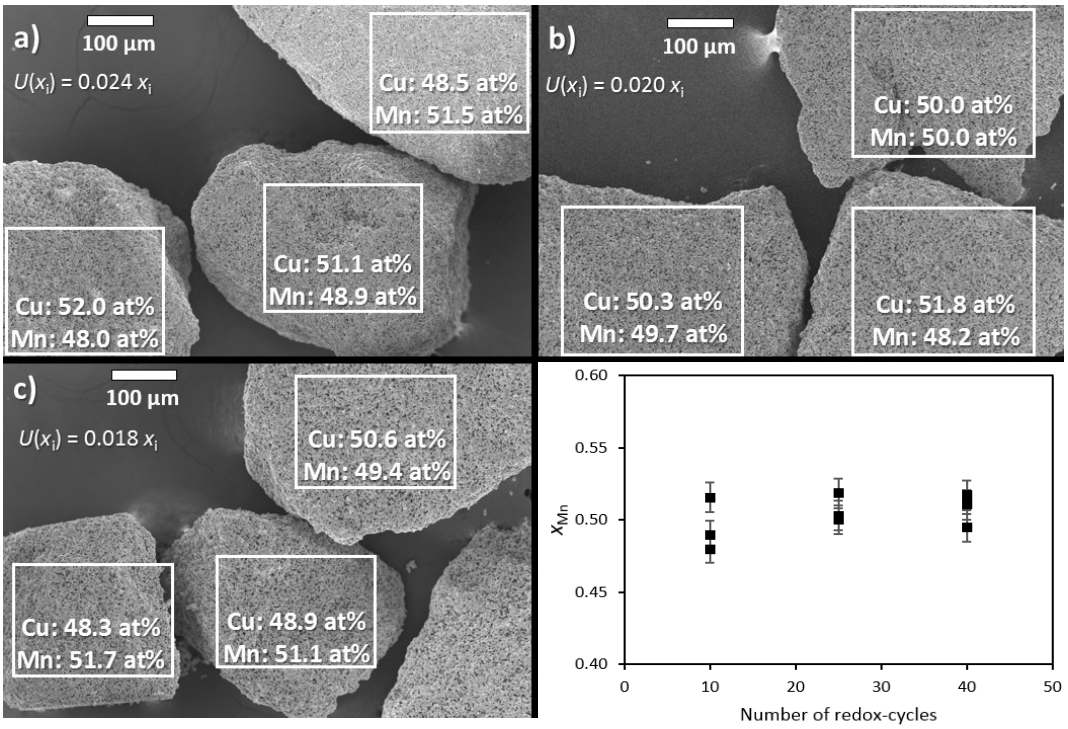


Fig. 7-20 *SE micrographs of 1Cu-1Mn-MM cycled in the fluidised bed for (a) 10 cycles, (b) 25 cycles, (c) 40 at 850 °C using 10 vol% O_2 balanced with N_2 for oxidation and pure N_2 for reduction; And (d) a plot of Mn-atom percentage against cycle number, determined by SEM-EDXS from the micrographs shown in (a), (b), and (c).*

The SE micrographs in **Fig. 7-20** show no significant change of the surface morphology (at this magnification). Furthermore, the Cu:Mn molar ratio at the surface of the oxygen carriers measured by SEM-EDS did not change with an increasing cycle number. This confirms the findings from the XRD analysis that a phase separation of copper manganese oxide and migration of single metal oxides does not occur. Overall the XRD and SEM-EDS analysis demonstrated high chemical stability of the oxygen carriers during this long-term cycling experiment. To evaluate the change of the pore structure, N_2-adsorption analysis at 77 K was performed, and the results are shown in **Table 7-6**.

Table 7-6 *Results of the N_2-adsorption analysis of the oxidised fresh and redox-cycled oxygen carrier from the LTC-FBR-1 experiment.*

Recovered after redox-cycle number	BET surface area [m^2/g] [a, b]	Pore volume [mm^3/g] [c]	BJH pore diameter [nm] [d]
0	0.332 ± 0.02	1.563 ± 0.01	82.6 ± 2.1
25	0.270 ± 0.02	1.334 ± 0.01	96.7 ± 2.1
40	0.278 ± 0.02	2.184 ± 0.01	96.0 ± 2.1
60	0.222 ± 0.02	1.717 ± 0.01	114.0 ± 2.1
100	0.208 ± 0.02	1.354 ± 0.01	103.3 ± 2.1

Footnotes: (a) the uncertainties of the BET surface area measurements were assessed by conducting three separate measurements of the same batch (c.f. Appendix A.3), (b) the correlation coefficients of the surface area $1/[Q(P_0/P-1)]$ vs. P/P_0 plot was > 0.993 for all measurements, (c) the pore volumes were calculated during adsorption for 1.7nm < d_{pore} < 300 nm; (d) the BJH pore diameter is based on data obtained during adsorption.

The data in **Table 7-6** indicates an increase in the BJH pore diameter and a reduction in the BET surface area with an increasing cycle number. To elucidate further the structural changes, the samples were additionally characterised by MIP, laser diffraction and crushing strength tests. The laser diffraction experiments were performed with a Mastersizer 2000 (Malvern Instruments), using a refractive index of 2.63 and 1.33 for the particles and the dispersant (water), respectively. The results of the characterisation are illustrated in **Fig. 7-21**, below.

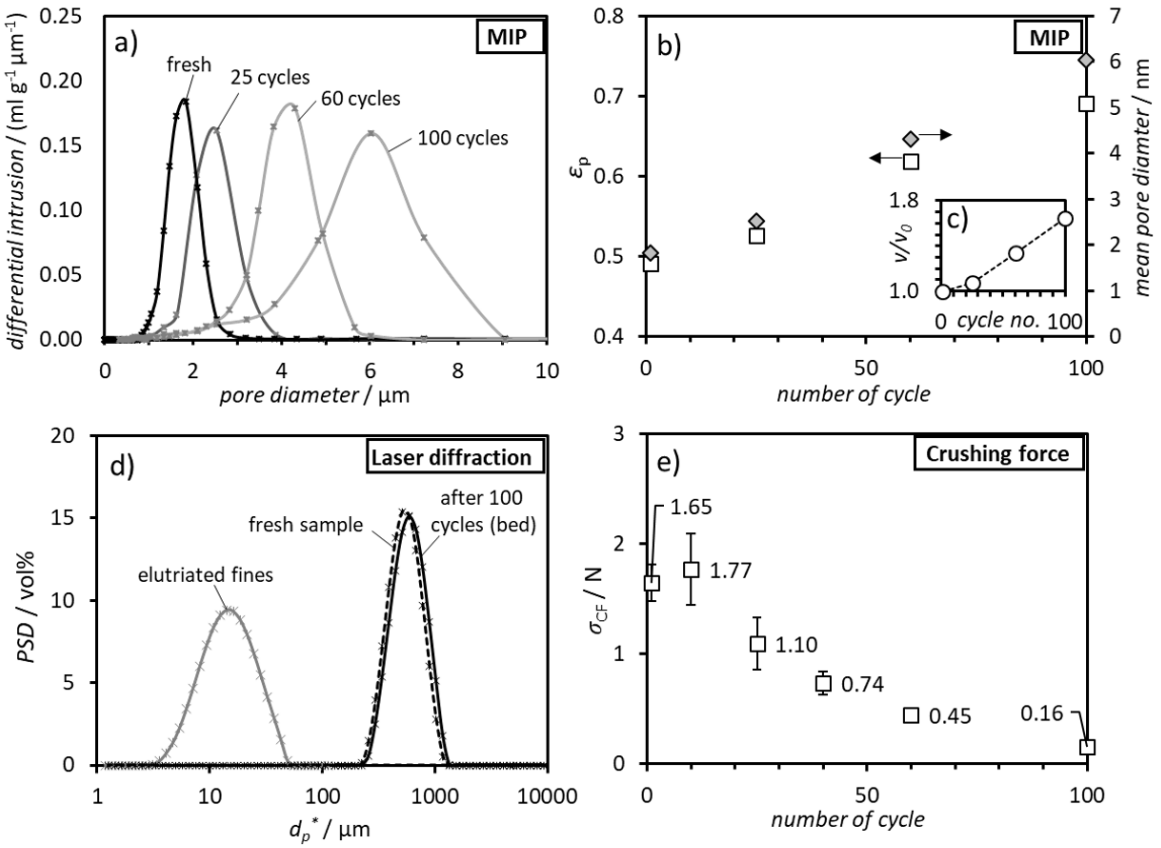


Fig. 7-21 *Results from the post-cycling analysis of 300-425 µm 1Cu-1Mn-MM oxygen carriers recovered from the experiment "FBR-1": Plots of (a) the differential intrusion against pore diameter from MIP, (b) porosity and mean pore diameter against cycle number calculated from MIP and He-pycnometry, (c) the specific volume change (the specific volume is taken as the reciprocal of the envelope density), (d) particle size distribution (PSD) of the fresh sample, cycled bed material and fines recovered from the elutriate filter. A refractive index (RI) for the particles of 2.63 was selected, which corresponds to the RI of CuO, since the literature lacks data about the RI of $Cu_xMn_{3-x}O_4$. The measured size is therefore slightly larger than the actual particle size; and (e) crushing strength against cycle number.*

Fig. 7-21a and **Fig. 7-21b** show that over the course of 100 redox-cycles the porosity and the mean pore diameter of the oxygen carriers increased from 0.492 to 0.691 and from 1.8 µm to 6.0 µm, respectively. Brown *et al.*[163] studied Fe-based oxygen carriers over repeated redox-cycles with reduction 10 vol% CO + N_2 and reported an increase in porosity and pore size with an increasing

redox-cycle number as well. This suggests that the evolution of the pore morphology of oxygen carriers during the CLAS process is to a certain extent similar to those of oxygen carriers during the conventional CLC process. The specific volume (**Fig. 7-21c**) increased over the 100 cycles by 64.5%, demonstrating a swelling of the particles. **Fig. 7-21d** shows that the particle size distribution (PSD) of the cycled bed material was very similar to the PSD of the fresh oxygen carriers. In fact, the value of the mean particle diameter, $\bar{d}_{\mathrm{p}}$, of the bed material after 100 cycles was 14.8% larger than the $\bar{d}_{\mathrm{p}}$ of the fresh material. The increase can be attributed to the swelling of the particle. The swelling of 64.5 vol% (*c.f.* **Fig. 7-21c**) corresponds, for spherical particles, to an increase in diameter by 18.0%. Without swelling, the theoretical $\bar{d}_{\mathrm{p}}$ of the cycled bed material would be 2.8% lower than the $\bar{d}_{\mathrm{p}}$ of the fresh bed material. This relatively small decrease over 100 cycles in the fluidised bed, as well as the PSD of the fines recovered from the elutriate filter, indicate that attrition occurred due to abrasion. **Fig. 7-21d** shows that over the course of the experiment, the average force to crush a particle decreased almost steadily from 1.65 N (fresh particle) to 0.16 (after cycle 100), with the decrease being approximately inversely proportional to the cycle number.

Conclusion of the long-term cycling "FRB-1" experiment

The purpose of this experiment was to investigate whether unsupported copper manganese oxide oxygen carriers withstand the chemical and mechanical stresses at conditions typical to oxidiser conditions over a high number of redox-cycles, with gas-solid ratios being similar to those of a scaled-up CLAS process. However, it has to be mentioned that in a dual circulating fluidised bed reactor system of a chemical looping process, the stresses in the cyclone and in the piping between the reactor vessels can also considerably attribute to attrition or can even be the main cause of attrition.[151] The overall rate of oxidation and O_2 release – which was external mass transfer limited – remained stable over the 100 redox-cycles, which corresponded to a duration of 58 hours (the reaction periods were set sufficiently long to allow full oxidation and reduction in the mass transfer-controlled regime). The swelling of the particle and the increase in the mean crystallite size resulted in an increase in porosity and therefore a decrease in the crushing strength. This in turn resulted in a rapid increase in attrition rate, which becomes apparent after ~ 40 redox-cycles. It is positive for the material development programme of this project that the copper manganese oxide phases are thermodynamically stable, and no phase separation occurs. However, the swelling of the particles appears to lead to a decrease in their mechanical stability, and after 60 cycles excessive attrition rates resulted in a substantial loss of bed material. A strategy to mitigate this issue is to support the oxygen carriers on a material that inhibits the particle swelling.

7.3.2 Long-term cycling of ZrO_2-supported oxygen carriers

Long-term cycling experiments with 40-CuMn/Zr-MM were performed with oxidation at conditions which are assumed to be typical for the oxidiser of the CLAS process (*i.e.* oxidation in 10 vol% O_2 + N_2 at 850 °C). The loss of bed material was determined by weighing the glass wool of the elutriate filter prior and after the experiments together with fines that were collected. The difference between the two measurements, which is assumed to equal the elutriated bed material, amounted to 5.3 mg during the long-term cycling experiment with the ZrO_2-supported oxygen carriers. This corresponds to a bed mass of 0.28 wt%. The oxidation and O_2 release rates as well as the $R_{0,\mathrm{exp}}$ were calculated for each cycle, and the results are presented in **Fig. 7-22** and **Fig. 7-23**.

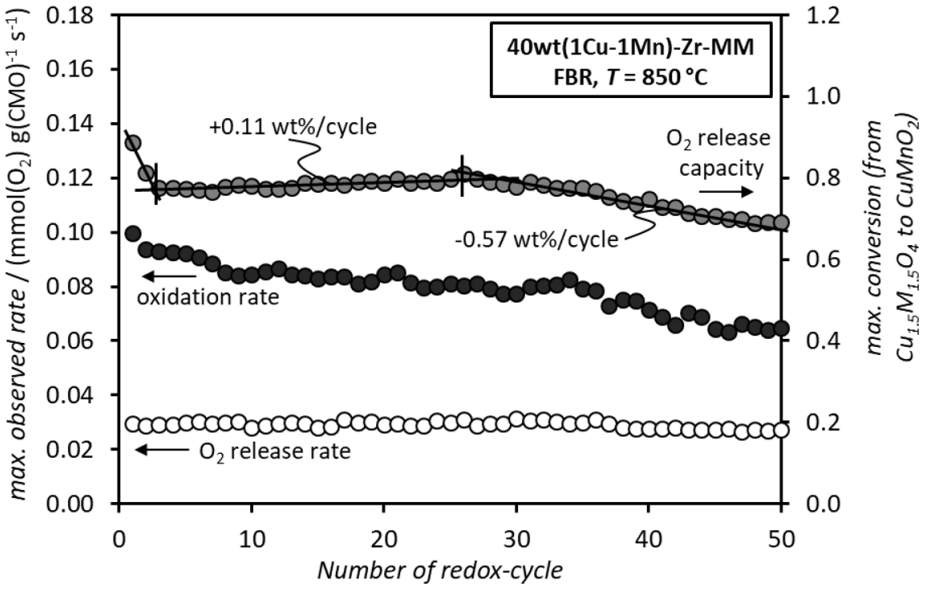


Fig. 7-22 *Results from long-term cycling experiments with 40-CuMn/Zr-MM in the fluidised bed reactor at 850 °C with oxidation in 10 vol% O_2 + N_2 and O_2 release under pure N_2: the O_2 release capacity (●), the observed oxidation rate (■) and O_2 release rate (○) over 50 redox-cycles.*

Fig. 7-22 shows that the measured maximum conversion decreased over the first three cycles (from X = 0.89 to X = 0.78), which might be attributed to sharp edges chipping off and being elutriated. From cycle 3 to cycle 25, the maximum conversion increased by +0.11%/cycle. This is possibly due to the reduction of the mass fraction of CuO and an increase in the mass fraction of $Cu_xMn_{3-x}O_4$, owing to single metal oxides combining to copper manganese oxide. A trend change is observed around cycle number 26, after which the maximum conversion almost steadily decreased until cycle 50 (on average by 0.57%/cycle). Later in this section it is shown that a minor fraction of $CuZrO_3$ had formed, which might have been the main reason for this deactivation.

The observed rates of reaction and the conversion of the oxidation and O_2 release during selected cycles are plotted in **Fig. 7-23**, below.

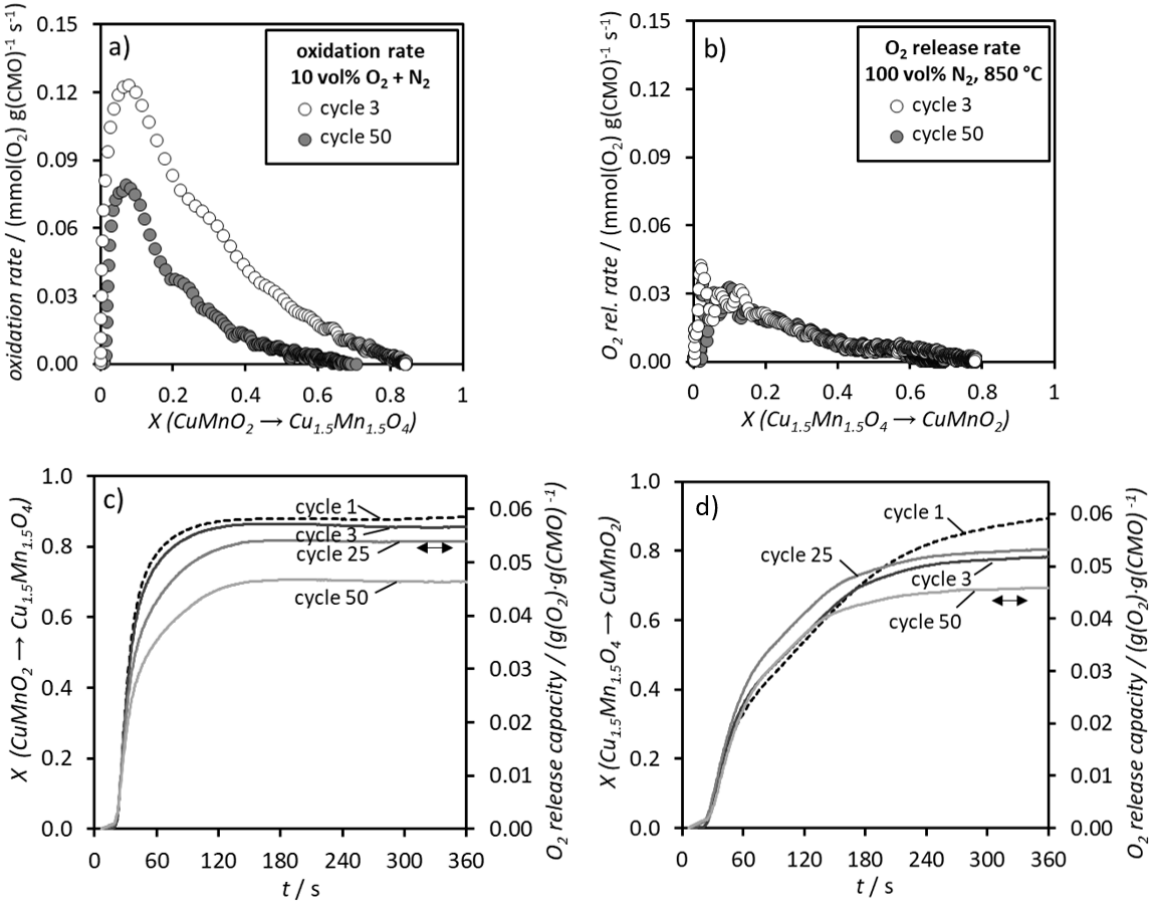


Fig. 7-23 *Results from long-term cycling experiments with 40-CuMn/Zr-MM in the fluidised bed reactor at 850 °C with oxidation in 10 vol% O_2 + N_2 and O_2 release under pure N_2: (a) the O_2 release capacity (●) the O_2 release rate (○), (b) the conversion measured during the O_2 release of the 1st, 3rd, 25th and 50th cycle (as indicated on the graph), (c, d) plots of the conversion vs. time measured during the 1st (---), 3rd (—), 25th (—)and 50th (—) cycle during of the (c) oxidation and (d) O_2 release period.*

Fig. 7-23a shows that the time-deconvoluted maximum observed rate of oxidation for cycle 3 (first cycle with stable O_2 release capacity) is significantly higher than of cycle 50 (last cycle of the experiment). A significant change of the maximum O_2 release rate (**Fig. 7-23b**) is not observable. However, the maximum conversion decreases from $X = 0.84$ in cycle 1 to X = 0.71 in cycle 50 (**Fig. 7-23c-d**), and the reaction rate function of the cycles shown in **Fig. 7-23d** differs in the latter stage ($X > 0.6$) of the O_2 release. The difference between cycle 3 and cycle 50 in the shape of the curve of conversion against time (**Fig. 7-23d**) for $X > 0.6$ indicates that the overall O_2 release rate in this stage for cycle 50 is lower than the rate in cycle 3. In this range, the intra-particle diffusion is commonly controlling the overall rate at lower porosities. Therefore, this reduction in rate indicates an increase in the intra-particle diffusion resistance, *e.g.* caused by decrease in porosity in smaller pores (later

confirmed by MIP). The recovered materials were studied by XRD, MIP and SEM-EDS to elucidate the reason for the decrease in the maximum oxidation rates and maximum conversions, as well as the decrease in the O_2 release rate at $X > 0.6$ with an increase in cycle number. The results of the material characterisation are shown in **Fig. 7-24** and **Fig. 7-25**.

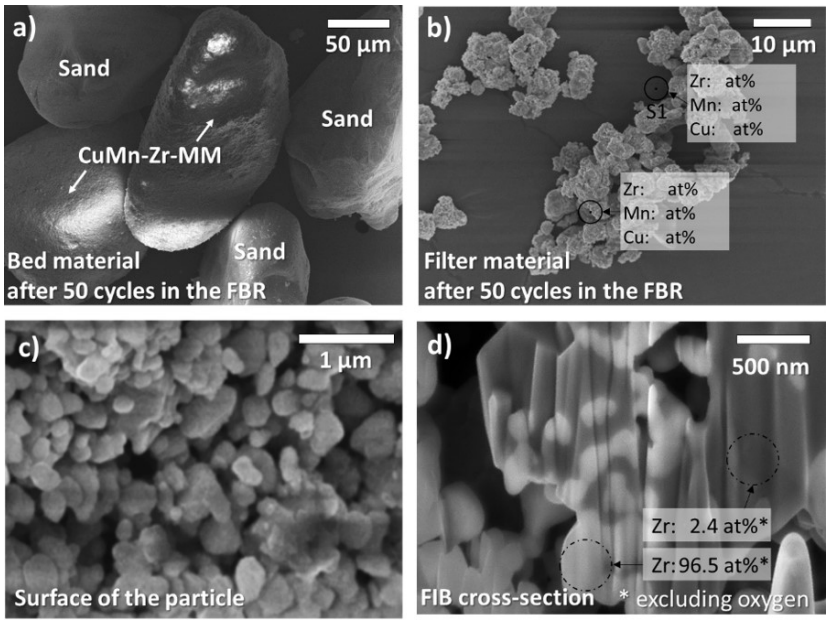


Fig. 7-24 *SE micrographs of 40-CuMn-Zr/MM oxygen carriers recovered from the fluidised bed reactor after 50 redox-cycles at 850 °C with oxidation in 10 vol% O_2 + N_2 and O_2 release under pure N_2: (a) particles recovered from the bed, (b) fines recovered from the elutriate filter, (c) surface morphology of a redox-cycled oxygen carrier, (d) cross-section through a grain cut with a focused Ga^+ ion beam.*

Fig. 7-24a shows that the oxygen carriers did not fragmentate over the course of the experiments, indicating that the main reason for the attrition was abrasion. Furthermore, only small particles (< 20 µm) were found in the sample recovered from the elutriate filter (**Fig. 7-24b**), supporting that abrasion was the main reason for the attrition. The surface structure of the cycled particle (**Fig. 7-24c**) is well-defined, without excessive pores, and resembles the surface morphology of the fresh particle (section 5.6). The change of the surface morphology of the unsupported oxygen carriers was significantly larger, which indicates that the ZrO_2 support inhibits this structural change. The cut through a metal oxide grain using a focused ion beam (**Fig. 7-24d**) shows that the ZrO_2 and copper manganese oxide phases remains well combined. The mean diameter of the grain measured 2.4 µm, which is 85% larger than the average copper manganese oxide grain prior to the cycling, indicating that coalescence and grain growth of the active phase occurs.

Furthermore, characterisation by XRD and MIP of the recovered oxygen carriers was performed. The results are compared with the data from the fresh oxygen carriers in **Fig. 7-25**, below.

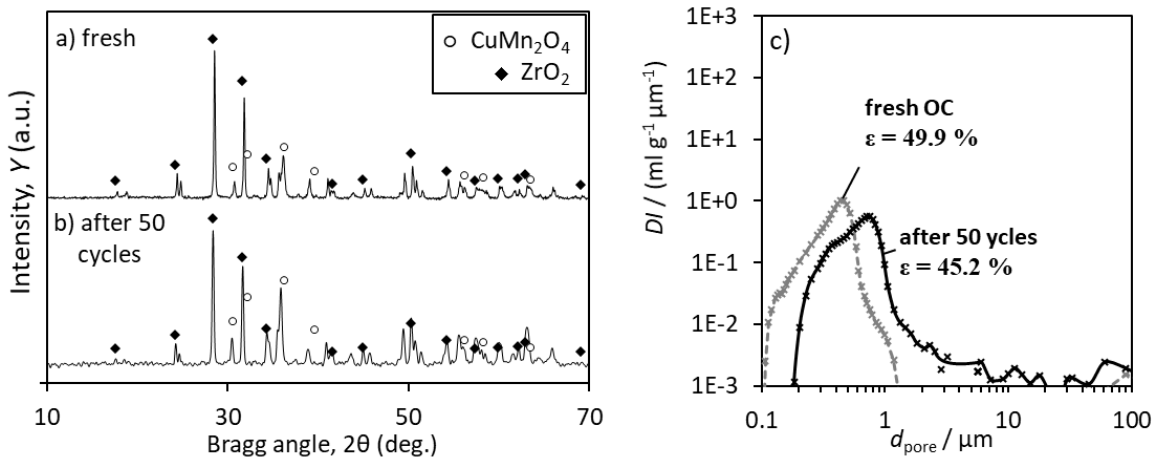


Fig. 7-25 *Results of the (a) XRD and (b) MIP experiments of the ZrO_2-supported oxygen carriers 40-CuMn/Zr-MM prior and after 50 cycles in the fluidised bed.*

In the fresh oxygen carriers $CuMn_2O_4$ and ZrO_2 were the only phases identified by XRD (**Fig. 7-21a** and **b**) in the fresh and cycled oxygen carriers. However, structural changes become apparent from MIP results (**Fig. 7-21c**). Pores with $d_{pore} < 0.2$ µm disappeared during the redox-cycling. This might have resulted in a larger unreacted fraction of the material, which resulted in the observed decrease in the maximum conversion from $X = 0.84$ in cycle 3 to X = 0.71 in cycle 50 (**Fig. 7-23**). The loss of bed materials was (0.28 wt%) almost two orders of magnitude lower than required to explain this reduction in conversion and was thus ruled out as the main reason. **Fig. 7-21c** shows that the porosity decreased, despite an increase in the mean pore size. Furthermore, smaller pores below 200 nm disappeared almost entirely and the intrusion into pores smaller than 1 µm decreased from 0.23 ml g^{-1} to 0.16 ml g^{-1} (a 27% reduction). This reduction in porosity of smaller pores is likely to be the reason for an increase in intra-particle diffusion resistance, which is indicated by plot of conversion against time (**Fig. 7-23d**).

This long-term cycling experiment demonstrates that supporting copper manganese oxide on ZrO_2 aids to maintain the surface structure and inhibits the particle swelling. In fact, the specific volume of the particle decreased by 9 vol% over the 50 cycles, based on the envelope density, which was calculated from He porosimetry and MIP data. Some deactivation was observed (*i.e.* a reduction in the O_2 release capacity and oxidation rate in **Fig. 7-22**) and it is worthwhile to test the performance of the ZrO_2-supported oxygen carriers over a higher cycle number to elucidate if the increase in deactivation continues or stable capacities and rates are achieved over the long-run. The results of this long-term cycling experiment indicate that ZrO_2 is a suitable support material for Cu-Mn oxygen carriers in the CLAS process.

7.4 Concluding remarks

A 1.5 kW_e fluidised bed reactor was modified for the experiments of this work, *inter alia* by adding a gas supply system, which allows for computer-controlled redox-cycling. Suitable gas flow rates have been determined by hydrodynamic calculations and a heat balance around a single oxygen carrier particle has been developed, which uses the reaction enthalpies calculated from TGA experiments. The heat balance has been used to demonstrate that during the redox-reactions temperature gradients within the particles are negligible (*i.e.* the main resistance to the heat transfer lies in the gas film surrounding the particle) and that the maximum temperature difference compared to the temperature of the fluidised bed during the O_2 release and the oxidation is - 2.2 °C and + 2.5 °C, respectively.

Based on the observed rates of reaction, a model for the calculation of the intrinsic kinetics of the O_2 release and oxidation reaction was developed assuming the fluidised bed is well-mixed. The observed rate of reaction was thereby assumed to be a result of a series of chemical reaction rate, intra-particle diffusion and diffusion through the gas film surrounding the particle. Based on previous experimental results, the chemical rate of reaction was assumed to be first order with respect to the difference of O_2 equilibrium concentration and O_2 surface concentration. Reaction rate functions of the homogeneous reaction model, the shrinking grain model and the shrinking core model were tested. The homogeneous reaction model represented the experimental data best. For this model, the calculated intrinsic rate constant, k_v, for the temperature range 825 – 900 °C was in the range 88.6 – 115.8 s^{-1} and was found to decrease with increasing temperature. The same procedure was followed to calculate the rate constant for the oxidation reaction. The homogeneous reaction model represented the experimental data of the oxidation reaction best as well and the kinetic parameter were presented.

In addition to the kinetic experiments, long-term cycling experiments were carried out in the fluidised bed to elucidate the particle (and pore) evolution over extended redox-cycling. 40 g of oxygen carriers without inert bed material were redox-cycled over 100 cycles (58 hours). Over the first 40 cycles no fines were recovered from the elutriate filter. Then, an increase in generation of fines was measured. After 60 cycles, 80 cycles and 100 cycles, the fines accumulated in the filter corresponded to 0.25 wt%, 2.58 wt%, and 7.78 wt% of the sample mass, respectively. XRD analysis of the recovered bed and filter material suggested that no separation of the copper manganese oxide into the single metals occurred. This was confirmed by EDS analysis of the particles surface, which demonstrated that the Cu:Mn molar ratio at the particle surface was close to unity. In fact, the values of the crystallite size calculated from XRD data increased with an increasing cycle number. Therefore, further post-cycling material characterisation was carried out to elucidate the reason for the disintegration of the oxygen carriers. It was found that during the redox-cycling the surface area

had decreased, while the BJH pore diameter, the mean pore diameter (MIP) and the porosity had increased. Furthermore, a decrease in crushing strength was measured. Laser diffraction experiments indicated that abrasion is the main mechanism for attrition. Furthermore, a swelling of the particles (+64.5 vol% after 100 redox-cycles) was measured by MIP. This swelling and the resulting increase in porosity is probably the reason for the increase in attrition rate with an increasing cycle number.

Furthermore, ZrO_2 supported oxygen carriers were tested over a high redox-cycle number in the fluidised bed (TiO_2-supported oxygen carriers were not tested, since the TGA experiments indicated that their performance is less promising). Here aim was to examine if the support material inhibits the particle swelling and increases the particle stability. The results from TGA experiments have suggested that a consolidation (or shrinkage) occurs. The particles were tested over 50 redox-cycles and only 0.28 wt% of the initial bed mass was collected in the elutriate filter. Until cycle number 26, the ZrO_2-supported oxygen carriers showed a stable O_2 release capacity corresponding to 78% of the theoretical conversion from $CuMn_2O_4$ to $CuMnO_2 + Mn_3O_4$. Between cycle 26 and cycle 50, the O_2 release capacity decreased by 0.57% per cycle. MIP analysis showed that in fact a decrease in porosity had occurred. Furthermore, it showed that pores below 0.2 µm had disappeared. The slight deactivation of the material was attributed to this clogging of smaller pores. Nevertheless, the ZrO_2 supported particles performance was promising and the ZrO_2 remained inert over the course of the experiment (contrarily to TiO_2 and Al_2O_3). The redox-cycling with ZrO_2 demonstrated that the support can influence the pore evolution of the particles (change it from swelling to shrinking). A well-balanced mass ratio of copper manganese oxide and ZrO_2 might result in particles that maintain their initial porosity (or assume a desired porosity over the long-term) by balancing the effects causing the swelling and shrinking, and thus allow for very long oxygen carrier lifetimes.

Chapter 8

Conclusions and future work

8.1 Conclusions

In this thesis, copper manganese oxides as oxygen carriers for chemical looping air separation were evaluated. In the first chapter, the topic is framed by presenting evidence from the literature that anthropogenic emissions of CO_2 owing to the burning of fossil fuels are the main driver of global warming. CO_2 capture and storage (CCS) allows to minimise the CO_2 emissions from power generation processes that utilise carbonaceous fuels. The utilisation of sustainably produced biomass can even result in a net transfer of carbon from the atmosphere to the geosphere. Chemical looping processes allow for power generation with CCS from gaseous and solid fuels (including biomass). A novel variant is chemical looping air separation, which is used to enrich CO_2 with O_2, which can be used for oxy-fuel combustion or gasification (*e.g.* IGCC with CO_2 capture). A review of the literature identified important properties for oxygen carriers in the CLAS process, which are *inter alia* a high reactivity and O_2 release capacity, the ability to release gaseous O_2 at reducer conditions, as well as sufficient mechanical stability to withstand a high number of redox-cycles in a CFB system. Copper manganese oxides were identified as promising oxygen carrier materials that fulfil these requirements. Co-precipitated oxygen carriers were prepared at low and at high super-saturation. Furthermore, unsupported mechanically mixed oxygen carriers were prepared with and without the

addition of starch and micro-crystalline cellulose as pore-forming agents. Furthermore, supported oxygen carriers were prepared using Al_2O_3, TiO_2 and ZrO_2 as the inert supporting material. The oxygen carriers were characterised to study the effect of synthesis conditions on the material properties and experiments in the TGA and fluidised bed were performed to assess the performance of the oxygen carriers. Important findings of these experiments are summarised in the paragraphs below.

Preparation of highly pure copper manganese oxide from co-precipitated amorphous precursors

Copper manganese oxygen carriers were developed, which were prepared *via* co-precipitation at low super-saturation. Most co-precipitation experiments were carried out using an alkaline solution with a high [Na_2CO_3]:[NaOH]. This resulted in the precipitation of predominantly amorphous species with the crystalline mass fraction presumably consisting of $MnCO_3$ and being in the range 1.5 – 10.9 wt% (this was determined by XRD using CeO_2 as an internal standard). The calcination of the amorphous precursors was studied by XRD and it was found that the precursors react directly to pure copper manganese oxide with a mass fraction close to unity without the formation of single metal oxides as intermediates. Copper manganese oxide was identified in the samples even after short calcination (15 min holding time) and temperatures as low as 500 °C, though the mean crystallite size was only 17.0 nm. The crystallite size was found to increase with an increase in calcination temperature, *e.g.* from 17.0 nm (500 °C, 15 min) to 49.2 nm (900 °C, 15 min), and with an increase in holding time, *e.g.* from 49.2 nm (900 °C, 15 min) to 101.9 nm (900 °C, 12 hours). The results of this calcination sensitivity resulted in the selecting of 900 °C and 2 hours as the calcination temperature and holding time for standard experiments.

Poor performance of highly crystalline precursors prepared by co-precipitation with a low Na_2CO_3 content

During preliminary co-precipitation experiments two other types of materials were prepared *via* co-precipitation using a low [Na_2CO_3]:[NaOH] at low super-saturation, and at high super-saturation resulting in materials with low and high surface areas respectively. The precursors precipitated using a low [Na_2CO_3]:[NaOH] contained a high mass fraction of crystalline material, which was identified as $MnCO_3$ and $Cu(NO_3)_2{\cdot}3Cu(OH)_2$ as predicted in advance by *in silico* experiments. The highly crystalline precursor formed upon calcination a material with a low copper manganese oxide mass fraction (*i.e.* mainly CuO + Mn_2O_3), which suggested that a high fraction of crystalline material inhibits the formation of $Cu_xMn_{3-x}O_4$. The development of the low surface area materials was discontinued, since their performance was inferior compared to the (low surface area) oxygen carriers prepared from the amorphous precursors: The O_2 release rates observed during TGA experiments at

850 °C was an order of magnitude lower, which was attributed to a low mass fraction of $Cu_xMn_{3-x}O_4$ and a very low porosity which resulted in a high intra-particle diffusion resistance. However, the high surface area materials co-precipitated at a high supersaturation and a low $[Na_2CO_3]$:[NaOH] were investigated further, to test if the large internal surface areas offset the disadvantages of a lower $Cu_xMn_{3-x}O_4$ mass fraction. SE micrographs showed that the precursors had a well-defined micro-structure, and BET surface areas in the range 20.7 – 25.8 m^2/g were measured. Different ageing conditions were tested to try to enhance the micro-structure and increase the surface area. However, all aged precursors had a lower BET surface area than the un-aged materials. During calcination at 600 °C and 900 °C, the surface area of the micro-structured materials reduced to the range 7.9 – 12.7 m^2/g and 2.3 – 5.0 m^2/g, respectively. The crushing force of these oxygen carriers was below the minimum limit of the measurements (0.5 N). Owing to this poor stability, they were ruled out as promising oxygen carriers. Therefore, the development of oxygen carriers prepared *via* co-precipitation with a low $[Na_2CO_3]$:[NaOH] at low and high super-saturation was therefore not continued and the material development focused on the oxygen carrier preparation from amorphous precursors.

Effect of residual Na on the oxygen carrier properties

Next, the effect of residual Na from the supernatant was studied, by analysing the calcined material by XRD and SEM-EDS. In the sample prepared from the unwashed precursor all Mn had reacted to sodium manganese oxides. In addition, NaO_2 and CuO were detected. The crushing strength of the sample was below the 0.5 N limit of measurement. The poor mechanical stability and the apparent inhibition of copper manganese oxide formation suggested that larger amounts of Na in the sample were undesirable. Lower Na concentrations were also studied, for which the electrical conductance, σ, was taken as an indirect measure of the Na concentrations. In precursors which were removed from the supernatant at σ = 46 µS, 256 µS, 1238 µS, and subsequently calcined, no sodium species were detected by XRD. However, SE micrographs identified needle-like features, determined by EDS as Na-rich were found in the 256 µS and 1238 µS precursors, while no Na contamination was found in the 46 µS sample. It was therefore decided to wash the co-precipitated precursors so that σ < 50 µS.

Tuning the oxygen carrier properties by adjusting the co-precipitation conditions

At this point, all synthesis conditions for the standard co-precipitation procedure were complete and twelve oxygen carrier batches with varying (i) co-precipitation *pH* value, (ii) Cu:Mn molar ratio and (iii) co-precipitation agent composition were prepared. It has been demonstrated that the variation of these three co-precipitation parameters affect the BET surface area (0.17 - 0.91 m^2/g), porosity (0.009 – 0.565), envelope density (2.18 – 5.75 g cm^3), and the crushing strength (0.76 – 9.12 N) of the

calcined particles. In the listed order, the effect of the three co-precipitation variables on the four properties decreased. XRD analysis revealed that a lower co-precipitation *pH* value and the substitution of Na_2CO_3 with NaOH in the precipitation agent resulted in an increase in the CuO mass fraction in the calcined material.

The calcination of CuO and MnO to copper manganese oxide

To identify conditions with a high conversion of CuO and MnO contained in the mechanically mixed precursors to copper manganese oxide, a sensitivity analysis with different sintering temperatures and durations was carried out. An increase in calcination temperature from 900 °C to 950 °C was found to increase the mass fraction of $Cu_xMn_{3-x}O_4$ for all studied sintering durations significantly. The effect of the holding time was also studied, and a decrease in the mass fraction of CuO was observed when increasing the holding time in the range 2 – 6 h. Longer holding times than 6 hours did not result in a further decrease in the measured CuO mass fraction. Therefore, a calcination time and duration of 950 °C and 6 h was selected for the calcination of all mechanically mixed oxygen carriers. In the range 6 – 12 h the mass fraction of CuO was never below 25.1 wt%, which corresponds to the mass fraction of CuO in a sample with a 1Cu:1Mn molar ratio that contains only CuO and $CuMn_2O_4$. This finding indicates that the mechanically mixed precursors do not form $Cu_xMn_{3-x}O_4$ with $x > 1$ (*e.g.* no $Cu_{1.5}Mn_{1.5}O_4$) during calcination, contrarily to the samples prepared by co-precipitation. This finding was confirmed when studying the effect of a varying Cu:Mn molar ratio. For redox-cycling at (lower) temperatures at which CuO remains inert, a sample that contains a mixture of $CuMn_2O_4$ and CuO is disadvantageous compared to a sample containing $Cu_{1.5}Mn_{1.5}O_4$ (with the same Cu:Mn molar ratio), since the O_2 release capacity is significantly reduced.

In all mechanically mixed oxygen carriers, either $CuMn_2O_4$ or $Cu_{1.2}Mn_{1.8}O_4$ was identified as the main phase by XRD. 1Cu-2Mn-MM contained only $CuMn_2O_4$, while all other samples contained CuO in addition. The mass fraction of CuO was found to increase with an increase in the Cu:Mn molar ratio.

Characterisation of oxygen carriers prepared *via* mechanically mixing

The unsupported mechanically mixed oxygen carriers were characterised, and values for the BET surface area (0.22 - 0.34 m^2/g), porosity (0.255 – 0.359), envelope density (3.42 and 4.22 g cm^3) and crushing strength (3.27 – 5.18 N) determined. The addition (+ 10 wt%) of microcrystalline cellulose (MCC) as a pore forming agent resulted in an increase in surface area but had no significant effect on the cumulative pore volume. It was thus concluded that MCC results in a pore structure with smaller pores. Contrarily, the use of starch as a pore-forming agent resulted in a pore structure with fewer larger pores, resulting in a larger cumulative pore volume, while not affecting the BET surface area significantly.

The BET surface area of the TiO_2, Al_2O_3 and ZrO_2-supported oxygen carriers was measured to be 0.30 m^2/g, 0.75 m^2/g, 2.00 m^2/g, respectively. In the listed order, the Tammann temperatures of the supporting materials increased, indicating that especially in the case of ZrO_2, an insufficient rate of solid-state diffusion of ZrO_2 might have inhibited the densification of these oxygen carriers during calcination. Liquid phase sintering was not tested in this work, as the melting of one phase typically increases the energy requirements for the preparation excessively. However, if low energy requirements of the preparation are not an objective, sintering at temperatures around or above the Tammann temperature of ZrO_2 (1214 °C) may result in highly stable oxygen carriers.

Reversibility of the O_2 release reaction and measurement of the O_2 release capacity

To assess if the redox-reactions of the oxygen carrier at CLAS conditions are fully reversible, the samples were cycled over seven redox-cycles by T swing between 850 °C and 950 °C at a constant p_{O_2} of 0.1 bar and by p_{O_2} swing between 0.1 bar and zero bar at a constant temperature of 850 °C. The measured O_2 release capacity, $R_{0,\mathrm{exp}}$, during all p_{O_2} swing and T swing experiments of the unsupported oxygen carriers was stable – *i.e.* no deactivation was observed. Furthermore, it has been demonstrated that substitution of O_2+CO_2 with O_2+N_2 during the oxidation and decomposition of the oxygen carriers does not result in a change in the redox-behaviour or $R_{0,\mathrm{exp}}$. It has been also demonstrated that the oxygen release capacity during *T* swing experiments was significantly lower than during p_{O_2} swing experiments: During the p_{O_2} swing experiments a R_0 for the co-precipitated oxygen carriers 1Cu:2Mn-CP(3:0), 1Cu:1Mn-CP(3:0), and 2Cu:1Mn-CP(3:0) of 4.31 wt%, 4.81 wt%, and 6.55 wt% was measured, while during *T* swing experiments the experimental values of R_0 for 1Cu:2Mn-CP(3:0), 1Cu:1Mn-CP(3:0), and 2Cu:1Mn-CP(3:0), were 2.01 wt%, 4.08 wt%, and 3.17 wt%, respectively. XRD analysis of the cycled samples recovered after the seventh oxidation revealed that $Cu_xMn_{3-x}O_4$ remains the main phase in all mechanically mixed and co-precipitated oxygen carriers in the molar Cu:Mn ratio range 0.5 – 2.0. Interestingly, the phases identified by XRD analysis in the decomposed samples recovered from T swing and after p_{O_2} swing experiments differed significantly. The samples decomposed under pure N_2 reduced to $CuMnO_2$ in the sample with a molar Cu:Mn ratio of 1, while the Mn-richer and Cu-richer samples contained additionally Mn_3O_4 and Cu_2O, respectively. The samples decomposed by *T* swing and at p_{O_2} = 0.1 bar contained different copper manganese oxide phases with higher oxygen mass fractions, *i.e.* a defected perovskite-like structure $Cu_2Mn_2O_5$. The single metal oxide phases in the oxygen carriers recovered from T swing experiments were also in a higher oxidation state than those in the samples recovered from p_{O_2} swing experiments: *i.e.* CuO instead of Cu_2O, and Mn_2O_3 instead of Mn_3O_4 were identified.

Quantifying the intra-particle diffusion

The intra-particle diffusion was modelled as a function of the porosity, the tortuosity, and series of Knudsen and molecular diffusion. Since the two unknown variables of this model – the tortuosity, τ, and the intrinsic rate constant – do not depend on the particle diameter, values for those have been determined interactively from results of TGA experiments with varying particle size ranges. This calculation yielded a value of $\tau = 2.21$, which was used in the reaction rate models of this work.

Determination of the O_2 equilibria and heat of reaction from TGA experiments

The O_2 partial pressure equilibria of the unsupported oxygen carriers were first determined by a series of experiments in which the temperature was increased gradually (dT/dt = 3 °C min^{-1}) while maintaining a constant p_{O_2}. The temperature at which the decrease in mass began (owing to a release of O_2) was assumed to be the temperature where $p_{O_2} = p_{O_2,eq}$. The temperature was determined automatically by fitting a function to the experimental data. This 'onset-method' was applied to various copper manganese oxide oxygen carriers with an O_2 release under O_2+N_2 and O_2+CO_2. It was found that the substitution of N_2 with CO_2 does not affect the $p_{O_2,eq}$. However, a disadvantage of this method when applied to samples containing a mixture of phases is that it detects only the $p_{O_2,eq}$ of the phase that decomposes first when increasing the temperature. The use of the results of this 'onset method' for multi-phase materials would be misleading when using those in process calculations (*e.g.* the reaction rate expressions). Therefore, a new 'rate-based' method was developed, in which experiments at different temperatures and O_2 partial pressures were carried out. Since the chemical rate of reaction and the maximum rate of mass transfer for materials with the ability to release O_2, contain at least one term that depends on $p_{O_2,eq}$, the rate expression for a rate controlled or a mass transfer-controlled regime can be solved for $p_{O_2,eq}(T)$. In a regime in which the rate is neither controlled by mass transfer nor by the intrinsic kinetics, the isolation of the $p_{O_2,eq}(T)$ is more difficult. To test the effect of mass transfer on the observed rate, the maximum rate of external diffusion was calculated using the Stefan's tube model. The values of the calculated maximum rates of diffusion were within the experimental error of the observed rates, which led to the conclusion that the rates are controlled by external mass transfer and thus allowed to extract $p_{O_2,eq}(T)$ from the TGA data.

Very good agreement between the results of the two methods was achieved. A van 't Hoff plot was used to determine the reaction enthalpy and entropy from the $p_{O_2,eq}$ data. The calculation yielded values of $\Delta H_{r,800\,°C}$ = 199.7 kJ and $\Delta S_{r,800\,°C}$ = 151.4 J/mol/K, respectively. This confirms that the O_2 release reaction is of endothermic nature. The calculated heat of the O_2 release translates to a mass

specific heat of reaction of 413.1 kJ/kg($Cu_{1.5}Mn_{1.5}O_4$). This value lies between the calculated values for Mn_2O_3/Mn_3O_4 and CuO/Cu_2O: 203.8 kJ/kg(Mn_2O_3) and 829.7 kJ/kg(CuO), respectively.

Observed rates of oxidation and O_2 release in the TGA

A series of experiments was carried out to measure the observed rates of reaction of mechanically mixed and co-precipitated oxygen carriers. An increase in the Cu content was found to decrease the O_2 release rate slightly. The time to reach a conversion of $X = 0.6$ was 38 s and 48 s for 1Cu-2Mn-MM and 1Cu-1Mn-MM, respectively. Contrarily, the oxidation rate decreased drastically when increasing the Cu content. The time to reach a conversion of $X = 0.6$ was 20 s and 141 s for 1Cu-2Mn-MM and 1Cu-1Mn-MM. This demonstrated that the presence of CuO inhibits the rate of oxidation significantly.

Reaction pathways

To elucidate the reaction pathways, the p_{O_2} was set to $p_{O_2,eq}$ during the oxidation and the O_2 release reaction before complete conversion was reached to stop (or at least minimise) the progression of the reaction. This was followed by a rapid temperature decrease (with initially -200 °C·min^{-1}) while continuously adjusting p_{O_2} to equal $p_{O_2,eq}$ to 'freeze' the phases by quenching. The phases of the recovered partially reacted oxygen carriers were studied by XRD, and $Cu_{1.5}Mn_{1.5}O_4$ and $CuMnO_2$ were identified as the main phases. Furthermore, some identified peaks correspond to a defect perovskite with structure $Cu_2Mn_2O_5$, which suggests that upon oxidation O_2 is first absorbed into the space between the crystal structure and then incorporated into the crystal. The absence of significant amounts of the single metal oxides (*e.g.* CuO, Mn_3O_4 and Mn_2O_3) suggests they do not occur as intermediates in the reaction. This prevents the separate solid-state diffusion of Cu and Mn species in the lattice and thus an undesirable phase separation.

Differences in the particle evolution during T swing and p_{O2} swing experiments

A series of experiments with low porosity high strength oxygen carriers (10.0 ± 0.6 N) was carried out by p_{O_2} swing and T swing, to allow direct comparison of the particle evolution between the cycling modes. Over 100 redox-cycles the average crushing strength of the p_{O_2} swing and T swing cycled material reduced by 51 ± 1% and 44 ± 2%, respectively. The higher crushing strength of the material cycled by T swing indicates that the thermal stress during the rapid temperature changes of the experiments (*i.e.* -200 °C min^{-1} $\leq \mathrm{d}m/\mathrm{d}T \leq$ +200 °C min^{-1}) did not result in a faster particle deterioration. In fact, the crushing strength of the T swing cycled material was slightly (7%-points) higher than those cycled by p_{O_2}. The smallest pores of the fresh oxygen carriers (with $DI \geq 0.01$ µl g^{-1} µm^{-1}) were 4.9 µm. During the T swing experiments, the pore size range increased slightly, with

the smallest pores being 1.1 μm, while during the p_{O_2} cycling, the increase in pore size range was larger with the smallest pores being 0.3 μm. The formation of smaller pores during the p_{O_2} cycling resulted in a faster increase in porosity and specific particle volume (0.22 vol%/cycle) compared to (0.05 vol%/cycle) during *T* swing. The lower rate of swelling and lower rate of increase in porosity during *T* swing cycling in comparison to p_{O_2} swing favourably affects the oxygen carrier lifetimes. As summarised in the next paragraphs, it has been shown that supporting copper manganese oxides on ZrO_2 resulted in a change of the growth mode from swelling to shrinking (*i.e.* a decrease of porosity).

Long-term cycling experiments in the TGA

Unsupported oxygen carriers and ZrO_2 and TiO_2-supported oxygen carriers were tested over 100 p_{O_2} swing cycles in the TGA. For the unsupported co-precipitated oxygen carriers, a stable O_2 release capacity ($R_{0,\mathrm{exp}}$ = 5.1 wt%) and (after a slight loss over the first 15 cycles) a stable maximum O_2 release rate (0.06 mmol(O_2)$g^{-1}s^{-1}$) was measured.

The O_2 release rate and $R_{0,\mathrm{exp}}$ of the ZrO_2 supported oxygen carriers decreased from 0.029 mmol(O_2)$g^{-1}s^{-1}$ to 0.021 mmol(O_2)$g^{-1}s^{-1}$ and from 4.7 wt% to 3.2 wt% over the duration of the experiment. Which was later attributed to the clogging of smaller pores, a coalescence of ZrO_2 and CMO grains, and the formation of some $CuZrO_3$.

The results from long-term cycling experiments with TiO_2 supported oxygen carriers was less promising. Their O_2 release rate decrease from 0.032 mmol(O_2)$g^{-1}s^{-1}$ (cycle 5) by 77% and the O_2 release capacity by 26% over the 100 cycles. XRD analysis showed that the support and the active phase formed $MnTiO_3$. SEM-EDS analysis identified neither significant amounts of Cu nor of Mn on the surface of the particle, which suggests that separation between the active and supporting material occurred, with TiO_2 migration to the surface of the particle.

Long-term cycling by *T* swing of unsupported co-precipitated oxygen carriers showed an initial rapid decrease of the observed rate of O_2 release from 0.08 mol(O_2) g^{-1} s^{-1} to 0.03 mol(O_2) g^{-1} s^{-1} over the first 10 cycles, which was attributed to a 'clogging' of the pores (confirmed by SEM). After ~10 cycles, the rate of O_2 release increased steadily to 0.08 mol(O_2) g^{-1} s^{-1} at cycle 100. Scanning micrographs of the sample recovered after 100 cycles showed a well-defined pore structure.

Heat balance of a particle in the fluidised bed

By conducting a heat balance around a single oxygen carrier particle in the fluidised bed, using the reaction enthalpies calculated from TGA experiments, it was demonstrated that temperature gradients within the particles are negligible during the redox-reactions, *i.e.* the main resistance to the

heat transfer lies in the gas film surrounding the particle. It was calculated that in relation to the fluidised bed, the temperature of the particles is slightly lower (-1.1 – 2.2 °C) during the O_2 release and slightly higher (+ 2.1 – 2.5 °C) during the oxidation. The lower value and the higher value of the ranges occurred at lower and higher temperatures, respectively, which is mainly due to the differences in the maximum observed reaction rates. In addition to this temperature difference, the observed bed temperature decreased by 1.3 °C during the O_2 release and increased by 1.9 °C during the oxidation. The calculated effective particle temperature was used for the calculation of the kinetic parameter.

Development of a reaction rate model and calculation of the intrinsic rate of reaction

For the calculation of the kinetic rate constants from the observed rates of reaction, a model was developed based on the assumption that the fluidised bed is well-mixed. The observed rate of reaction was thereby assumed to be a result of a series of chemical reaction rate, intra-particle diffusion and diffusion through the gas film surrounding the particle. Based on previous experimental results, the chemical rate of reaction was assumed to be first order with respect to the difference of O_2 equilibrium concentration and O_2 surface concentration. Reaction rate functions representing the homogeneous reaction model, the shrinking grain model and the shrinking core model were tested. The homogeneous reaction model represented the experimental data best. For this model, the calculated intrinsic rate constant, k_v, for the temperature range 825 – 900 °C was in the range 88.6 – 115.8 s^{-1} and was found to decrease with increasing temperature. It was suggested not to correlate the rate constant by a temperature dependent correlation (*e.g.* an Arrhenius expression), since the reaction rate expression already contains a strong temperature dependence due to the correlation of the O_2 equilibrium concentration.

Long-term cycling in the fluidised bed

In addition to the kinetic experiments, long-term cycling experiments were carried out in the fluidised bed to elucidate the particle (and pore) evolution over extended redox-cycling. 40 g of oxygen carriers without inert bed material were redox-cycled over 100 cycles (58 hours). Over the first 40 cycles no fines were recovered from the elutriate filter. Then, an increasing production of fines was observed. After 60 cycles, 80 cycles and 100 cycles, the fines accumulated in the filter corresponded to 0.25 wt%, 2.58 wt%, and 7.78 wt% of the sample mass, respectively. XRD analysis of the recovered bed and filter material suggested that no separation of the copper manganese oxide into the single metals occurred. This was confirmed by EDS analysis of the particles surface, which demonstrated that the Cu:Mn molar ratio at the particle surface was unity. In fact, the values of the crystallite size calculated from XRD data increased with an increasing cycle number. Therefore, further post-cycling material characterisation was carried out to elucidate the reason for the

disintegration of the oxygen carriers. The BET surface area was found to decrease from 0.332 ± 0.02 $m^2\ g^{-1}$ (fresh sample) to 0.208 ± 0.02 $m^2\ g^{-1}$ (after 100 redox-cycles). Over the same cycle-range, the BJH pore diameter increased from 82.6 ± 2.1 nm to 103.3 ± 2.1 nm. MIP analysis showed an increase in the mean pore diameter size and an increase in porosity from 0.492 to 0.691. Furthermore, a decrease in the crushing strength was measured. Laser diffraction experiments indicated that abrasion is the main mechanism for attrition. The particle size distribution of the bed material did not change excessively over the 100 cycles. In fact, the measured mean diameter (D_{50}) increased by 9.3%, which is attributed to the particle swelling (confirmed by MIP). However, in addition to the PSD of the bed material, fines accumulated in the elutriate filter, with a calculated mean diameter of 14 µm. The attrition tests with the unsupported mechanically mixed copper manganese oxide oxygen carriers showed a weakness of the material. Swelling occurred, resulting in an increase in porosity, which after 40 redox-cycles had compromised the mechanical stability of the particle sufficiently for increased abrasion to occur. This resulted in a significant loss of bed material after 100 cycles.

Two supported oxygen carriers (supported on ZrO_2 and TiO_2) were tested to examine if the support material inhibits the particle swelling and increases the particle stability. The particles were tested over 50 redox-cycles and only 0.28 wt% of the initial bed mass was collected in the elutriate filter. Until cycle number 26, the ZrO_2-supported oxygen carriers showed a stable O_2 release capacity corresponding to 78% of the theoretical conversion from $CuMn_2O_4$ to $CuMnO_2 + Mn_3O_4$. Between cycle 26 and cycle 50, the O_2 release capacity decreased by 0.57% per cycle. MIP analysis showed a decrease in porosity from 0.499 to 0.452 and a clogging of smaller pores. The latter was proposed as the reason for the observed deactivation.

8.2 Future work

In this last section, future work is proposed. Such work did not form part of this thesis as either it was outside the scope or considered unreasonable with respect to the principle and assumptions of this work. These ideas are detailed in the section below.

Improvement of the oxygen carrier properties

In the work, emphasis was placed on the material development of oxygen carriers using non-complex synthesis routes with lower energy requirements (*i.e.* < 20 kWh per kg of the calcined oxygen carriers, *c.f.* **Fig. 3-11a**). However, another local minimum of the CO_2 capture cost and total CO_2 emissions might be located in a zone that justifies energy intense multi-step synthesis procedures of oxygen carriers, which offset high costs and CO_2 emissions of the production with significantly prolonged oxygen carrier lifetimes. Under those circumstances, liquid phase sintering of TiO_2 and ZrO_2 supported oxygen carriers might be reasonable, to maximise the bonding between the active phase (*e.g.* copper manganese oxide) and the support. Even a synthesis procedure involving two calcination steps might be justifiable under these circumstances. Such a two-step synthesis procedure could involve the sintering of the supporting material at temperatures well above their Tammann temperatures, which are 789 °C, 884 °C and 1214 °C for Al_2O_3, TiO_2 and ZrO_2, respectively. In a second step, the active phase is then deposited onto the porous Al_2O_3, TiO_2 or ZrO_2 support by impregnation, followed by a second calcination at lower temperatures. Such a procedure might result in oxygen carriers with an exceptionally high mechanical stability.

Experiments with steam, fixed-bed reactors, and pressure swing

Furthermore, O_2 release and oxidation experiments could be performed with fluidisation by steam and CO_2 to test the effect of steam on the evolution and performance of the particle. Carrying out pressurised tests is reasonable to a lesser extent, since the O_2 release reaction is typically the 'bottleneck' of the redox-reactions. A pressurised operation at a given temperature is likely to result in slower O_2 release and faster oxidation rates, which is not necessarily required. Operation of the reducer and oxidiser at different pressures was reported as prohibitively difficult in a CFB system, owing to oxygen carrier transport problems. However, fixed-bed reactor configuration would allow this. Such a system with redox-cycling by p_{O_2} swing and the O_2 release occurring at sub-atmospheric pressure will shift the operation to lower temperatures and might simplify or even eliminate the need for additional heat transfer into the reactor during the endothermic O_2 release.

Continuation of the study of the relationship between redox-reactions and particle evolution

In this work, a faster swelling of the unsupported oxygen carriers during the p_{O_2} swing cycling (0.22 vol%/cycle) was measured compared to that during T swing cycling (0.05 vol%/cycle). The lower rate of swelling and lower rate of increase in porosity during T swing cycling in comparison to p_{O_2} swing will likely result in extended oxygen carrier lifetimes. When supporting the copper manganese oxides on ZrO_2, a shrinking has been observed over extended p_{O_2} swing cycling. As future work, it is worthwhile elucidating how the material and the cycling conditions such as T and $|C_{O_2}^b - C_{O_2}^s|$ during the oxidation and the O_2 release affect the evolution of the pore structure over a high number of p_{O_2} swing and T swing cycles. Here, research should focus on the influence of the material composition (including dopants and supporting materials) and operating conditions on the solid-state diffusion of ions in the lattice and the gas diffusion in the pores. Careful tuning of the material composition and rational selection of operating conditions could allow for the oxygen carriers assuming an optimal pore structure over the long-term. Precise knowledge of the relationships would also allow for a new kind of rational process design. Currently, process simulations typically optimise for a maximum net plant efficiency or minimum in exergy destruction.[74] Precise knowledge of the effect of the cycling conditions on the long-term mechanical properties of the oxygen carriers would allow to optimise for the minimum oxygen-carrier replacement cost, minimum operating cost or even minimum LCOE. Recently, CFD simulations were performed in which the mechanical properties were used to calculate the attrition of particles at any point in a cyclone.[155] The combination of these new computational particle fluid dynamics (CPFD) tools for CFB systems with insights into particle evolution would enable this new promising kind of rational process design for chemical looping process research.

Nomenclature

Roman letters

A_{R}	Aspect ratio, defined by eq.(5-8) [-].
A_{pp}	Projected area of a particle in the fluidised bed [m^2].
Ar	Archimedes number, defined by eq.(7-7) [-].
$B_{obs.}$	Observed broadening of XRD peak (equal to *FWHM* of this peak) [°2θ].
B_{Si}	Instrumental line broadening, which in this work was determined with an Si standard.
b_r	Stoichiometric ratio [-].
C_{D}	Drag coefficient of a particle in the fluidised bed [-].
CCC_{OC}	Cost of CO_2 capture induced by cost of oxygen carriers, defined by eq.(3-19) [$ X].
C_i	Concentration of *i* in the gas phase [mol m^{-3}].
C_i^b	Concentration of *i* in the gas phase in the bulk [mol m^{-3}].
C_i^s	Concentration of *i* in the gas phase at the surface of the oxygen carrier particle [mol m^{-3}].
$C_{\mathrm{O_2,eq}}$	Equilibrium concentration of O_2 in the gas phase, defined by eq.(6-20) [mol(O_2)/m^3].
C_{OC}	Cost of the oxygen carriers [$/t].
d_c	Mean crystallite size calculated from XRD measurements [nm].
D_{e}	effective diffusion inside the particle, defined by eq.(6-9)
d_{g}	grain diameter determined from SE micrographs using the ASTM E1382-97 method
D_K	Knudsen diffusivity, defined by eq.(6-6) [m2/s?].
D_{p}	diffusion inside the particle, a series of Knudsen diffusion and molecular diffusion, defined by eq.(6-7)
d_{p}	Mean particle diameter [m].
d_{pore}	mean pore diameter, defined by eq.(6-5) [m].
$\mathrm{d}w/\mathrm{d}t$	Rate of reaction.
f_b	Fraction in the fluidised bed occupied by bubbles [-].
F_{D}	Drag exerted on a particle in the fluidised bed [N].
G^0	Gibbs free energy.
g	Acceleration due to gravity (g = 9.81 m s^{-1}).

H^{θ}	Enthalpy.
h_{g}	Heat transfer coefficient of the gas [W $m^{-1}K^{-1}$].
$H_{i,T}$	Heat of reaction in the fuel reactor (i = FR), the air reactor (i = AR); heat of combustion (i = C).
H_T^{θ}	Enthalpy of reaction [kJ mol].
I/I_{max}	Observed intensity of an XRD peak (also I_{obs}) [-].
K	Shape factor for the crystallite size calculation (0.9 is typically assumed for spherical crystals).
k	Reaction rate constant per unit of oxygen carrier mass [$\mathrm{m^3\ g^{-1}\ s^{-1}}$].
k_s	Intrinsic reaction rate constant per unit of surface area [$\mathrm{m \cdot s^{-1}}$].
k_v	Intrinsic reaction rate constant per unit of volume [$\mathrm{s^{-1}}$].
k_{c}	Proportional gain of the PID controller.
k_{g}	External mass transfer coefficient, defined by eq.(7-22) [m/s].
l_{c}	height of a crucible that holds the sample during TGA experiments (*i.e.* length from the bottom to the top) [m].
L_{f}	Height of the fluidised bed [m].
L_{mf}	Height of the fluidised bed at minimum fluidisation [m].
M_i	Relative molecular mass of i [g mol^{-1}].
m_{p}	Theoretical mass of an oxygen carrier particle, calculated by eq.(7-27) [kg].
m_{ox}	Mass of the fully oxidised oxygen carrier [g].
m_{red}	Mass of the fully reduced oxygen carrier [g].
m_{sample}	Mass of the sample [g].
$m_{OC,i}$	Mass of the oxygen carriers in the fuel reactor (i = FR) and in the air reactor (i = AR).
$\dot{m}_{\mathrm{OC}}$	Oxygen carrier circulation rate, defined in eq.(3-18).
n	Order of the reaction
N_{Bi}	Biot number, defined by eq.(7-10) [-].
N_{r}	Molar diffusional flux [mol s^{-1} m^{-2}]
$\dot{n}_{\mathrm{i}}$	Molar flow rate of i [mol s^{-1}].
Nu	Nusselt number, defined by eq.(7-9) [-].
$[O_2]_{\mathrm{c}}$	Calculated O_2 concentration [mol m^3].

$[O_2]_{\mathrm{m}}$	Measured O_2 concentration [mol m^3].
P	Total pressure [bar].
$p(x)$	probability density of x [-].
p_{O_2}	O_2 partial pressure [bar].
$p_{O_2,\mathrm{eq}}$	O_2 equilibrium partial pressure [bar].
R	Universal gas constant (= 8.314 J $\mathrm{mol^{-1}K^{-1}}$).
r	Observed rate of reaction per unit of oxygen carrier volume $[\mathrm{mol}(O_2)\ \mathrm{m^{-3}\cdot s^{-1}}]$.
r'	Observed rate of reaction per unit of oxygen carrier mass $[\mathrm{mol}(O_2)\ \mathrm{g^{-1}\cdot s^{-1}}]$.
r_{p}	Mean particle radius [m].
R_0	Oxygen ratio with respect to the weight of the active metal oxide [-].
R_0'	Oxygen ratio with respect to the weight of the oxygen carrier [-].
Re_{mf}	Reynolds number at minimum fluidisation [-].
Re_{p}	Reynolds number of a particle in the fluidised bed, defined by eq.(7-24) [-].
S_{r}^{θ}	Entropy of reaction [J K^{-1} mol^{-1}].
S_{p}	External surface area of a particle, defined by eq.(7-26) [m^2].
Sc	Schmidt number, defined by eq.(7-25) [-].
Sh	Sherwood number, defined by eq.(7-23) [-].
SI	Specific solid inventory [kg MW_{th}^{-1}].
SE	Fuel specific emissions [t(CO_2) MW_{th}^{-1}].
T	Temperature [°C].
t	Time [s].
t_d	Dead time in the gas sampling system of the fluidised bed [s].
T_{eq}	Equilibrium temperature, *i.e.* T at which $p_{O_2} = p_{O_2,\mathrm{eq}}$ [°C].
t_{OC}	Lifetime of the oxygen carriers, defined by eq.(3-6) [h].
T_{P}	Temperature of a particle in the fluidised bed [°C].
$U(x)$	Absolute uncertainty of the property x within a 95% confidence interval [-].
$u(x)$	Relative uncertainty of the property x within a 95% confidence interval [-].
u_{g}	Superficial gas velocity with respect to a particle in the fluidised bed [m s^{-1}].
u_{mf}	Minimum fluidisation velocity, defined by (7-5) [m s^{-1}].

u_0	Gas velocity entering the fluidised bed reactor [m s^{-1}].
u_t	Terminal velocity of a particle in the fluidised bed [m s^{-1}].
V	Volume [m^3].
$\dot{v}_{g,in}$	Volumetric flow rate of the gas leaving the fluidised bed reactor [l min^{-1}].
$\dot{v}_{g,out}$	Volumetric flow rate of the gas leaving the fluidised bed reactor, defined by eq.(7-4) [l min^{-1}].
V_I	Volume intrude by Hg during MIP measurements at a given pressure (ΣV_I denotes the cumulative intrusion) [mm^3].
V_p	Volume of an oxygen carrier particle [m^3].
w_a	Mass fraction of a in the solid phase [-].
x_a	Molar fraction of a in the solid phase. *E.g.* determined by XRD by eq.(5-5a) and eq.(5-5a) [-].
X_{ox}	Degree of conversion during the oxidation reaction (i = ox), the reduction or O_2 release reaction (i = red), and the fuel combustion (i = f) [-].
y_{O_2}	Molar fraction of O_2 in the gas phase [mol mol^{-1}].

Greek letter

α	Active metal loading: The mass fraction of the active metal [-].
β	Position of the peak that is used for the crystallite size calculation from XRD data or peak position of the observed peak broadening [°2θ].
ε_b	Fractions of bubbles in fluidised bed, defined by eq. [-].
ε_{mf}	Porosity of the bed at incipient fluidisation [-].
ε_p	Porosity of the particle in pores between 5.5 nm and 10 µm measured by MIP [-].
η_{CO_2}	CO_2 capture rate [t(CO_2) h^{-1}].
η	Effectiveness factor of the intra-particle diffusion, defined by eq.(6-21) [-].
η_g	Dynamic viscosity of the gas mixture [Pa s].
λ	Wave length of the x-ray radiation (for Cu-Kα radiation λ = 0.1541 nm)
λ_g	Thermal conductivity of the gas [mW m^{-1} K^{-1}].
λ_p	Thermal conductivity of the particle [mW m^{-1} K^{-1}].
μ_g	Kinematic viscosity of a gas mixture [m^2 s^{-1}].

ρ_{p}	Particle or envelope density, defined by eq.(5-3) and eq.(5-4) [g m^{-3}].
ρ_{sk}	Skeletal density determined by He pycnometry [kg m^{-3}].
ρ_{g}	Density of the gas mixture [g m^{-3}].
ρ_{m}	Molar density of the active metal oxide [mol m^{3}]
ρ_{DFT}	Density of the crystal phase based on DFT calculation [kg m^{-3}].
$(\Sigma_v)_i$	Diffusion coefficients for gas molecules of species i [-].
σ	Electrical conductance [μS].
σ_{CF}	Average crushing force calculated from single particle tests [N].
τ_{r}	Response time (6-1) of the TGA system
τ_i	Integral time (i = i), and derivative time (i = d) of the PID controller [s].
τ_{p}	Tortuosity factor of the oxygen carrier particle [-].
ν_i	Stoichiometric coefficient of the component i [-].
ϕ	Thiele modulus, defined by eq.(6-22) [-].

Superscripts

b	Value of the parameter at the bulk condition.
s	Vaule of the parameter at the particle surface condition.

Abbreviations

CFB	Circulating fluidised bed.
CFD	Computational fluid dynamics.
CMP	Copper manganese oxide.
CPFD	Computational particle fluid dynamics.
DFT	Density functional theory.
LCOE	Levelised cost of electricity.
SD	Standard deviation.
TGA	Thermo-gravimetric analyser.

Appendix

Appendix A.1 *- The annual average currency exchange rates used for the conversion of costs*

The currency exchange rates that were used for the conversion of euro (€) and pound sterling (£) denominated costs to U.S. dollar ($) are listed below.

year	GBP/USD	EUR/USD	year	GBP/USD	EUR/USD
2000	0.6614	1.0859	2010	0.6475	0.7549
2001	0.6946	1.1171	2011	0.6236	0.7188
2002	0.6680	1.0644	2012	0.6311	0.7783
2003	0.6121	0.8834	2013	0.6396	0.7530
2004	0.5459	0.8047	2014	0.6074	0.7536
2005	0.5500	0.8039	2015	0.6544	0.9017
2006	0.5434	0.7967	2016	0.7406	0.9042
2007	0.4998	0.7308	2017	0.7767	0.8868
2008	0.5446	0.6831	2018	0.7497	0.8473
2009	0.6412	0.7190			

Source: www.ofx.com/en-gb/forex-news/historical-exchange-rates/yearly-average-rates/

Appendix A.2 *– The methods used by 'Medusa-Hydra' for the calculation of the CP equilibria*

The software calculates the equilibrium constant, $K°$, from the equation[198] of the Gibbs free energy of reaction $\Delta G_r°$,[198,196]

$$\Delta G_r° = -RT \ln K° , \tag{A-1}$$

where R and T the gas constant and the temperature in K, respectively. $\Delta G_r°$, is calculated from the free energies of formation of the individual species by the equation [198],

$$\Delta G_r° = \sum v_i \, \Delta G_f°(i), \tag{A-2}$$

where υ_i and $\Delta G_f°(i)$ are the stoichiometric coefficient and the free energy of formation of the species *i*, respectively. For example, $\Delta G_r°$ of the nitrate-carbonate anion exchange reaction using copper nitrate and sodium carbonate,

$$Cu(NO_3)_2 + Na_2CO_3 \rightleftharpoons CuCO_3 + 2NaNO_3, \tag{A-3}$$

is calculated according to,

$$\Delta G_r° = \Delta G_f°(CuCO_3) + 2\Delta G_f°(NaNO_3) - \Delta G_f°(Cu(NO_3)_2) - \Delta G_f°(Na_2CO_3)\ , \tag{A-4}$$

The equilibrium constant $K°$ is calculated based $\Delta G_r°$ on using the relation,

$$\log K° = \Delta G_r°/[-RT\ \ln(10)]. \tag{A-5}$$

The simplified Helgeson-Kirkham-Flowers (HKF) model was selected for all calculations to calculate the activity of the reactions, where the activity coefficient γ_i (which is related to the thermodynamic activity, a_i, by $a_i = m_i\ \gamma_i$, with γ_i being the molality) for the species i is calculated according to,

$$\log \gamma_i = -A\ Z_i^2 \left(\frac{\sqrt{I}}{1 + å\ B_\gamma \sqrt{I}}\right) - \log\left(1 + 0.018 \sum m_k\right) + b\ I, \tag{A-6}$$

where *A* is the Debye-Hückel slope, Z_i the electric charge, å the effective ionic radii, B_γ is the Debye-Hückel constant, and *b* is a parameter that is specific to the solute. The first term on the right-hand side is the Debye-Hückel model that accounts for long-range electrostatic interactions between the species. The model is simplified by using NaCl, an approximation which is legitimate owing to the similar nature with the sodium compounds used in the experiments. The software uses the values for *A*, B_γ, *å*, and *b* from literature[242,197,243]. The activity of H_2O is calculated by,

$$\log a_{H_2O} = -\phi\ \frac{\sum m_k}{\ln(10)\ 55.508}, \tag{A-7}$$

where ϕ is the correlated osmotic coefficient. The 'Spana' software also allows to calculate the activity coefficients using the Davies equation and a model based on specific ion interaction theory. Those two other models were tested, and the results were compared to the HKF model. As the calculated molar fraction of all species did not notably differed, the recommendation of the software was followed[198] and the HKF model used for all calculations.

Appendix A.3 *– The determination of the uncertainty of N_2 adsorption measurements*

The uncertainty of the values calculated from N_2 adsorption experiments is mainly due to the instrumental uncertainty and due to variations during the oxygen carrier preparation, and were determined by comparing the calculated values of three measurements of particles from the same oxygen carrier batch and of three measurements of particles from three different oxygen carrier batches (prepared by the same method). The standard deviation was multiplied with two to obtain the uncertainty within a 95% confidence interval under the assumption that the deviation of the results follows a normal distribution. The results of the measurements and the calculated values for the standard deviation and the uncertainty are shown in **Table A.3**, below.

Table A.3 *Results of N_2-adsorption experiments to calculate standard deviations and estimate uncertainties of the measuring method and synthesis procedure using the standard procedure for the preparation of 1Cu-1Mn-MM, which was calcined at 950 °C for 6 h in air (1 l min^{-1} at STAP).*

	S_{BET} (m^2 g^{-1})		Internal surface area (m^2 g^{-1})		$\sum v_{pore}$ [a] (mm^3 g^{-1})		$\bar{d}_{pore}$ [a] (nm)	
	S_{BET}	Langmuir	adsorption	desorption	adsorption	desorption	adsorption	desorption
results of the three repeat measurements of the same oxygen carrier batch:								
A1	0.3316	0.4238	0.0829	0.0935	1.513	1.514	73.05	64.75
A2	0.3333	0.4305	0.0811	0.0935	1.530	1.530	75.44	65.46
A3	0.3456	0.4408	0.0827	0.1037	1.529	1.644	73.93	63.41
$SD_m(x)$	0.008	0.009	0.001	0.006	0.010	0.071	1.209	1.041
$u_m(x)$ [b]	0.045·x	0.040·x	0.024·x	0.122·x	0.013·x	0.091·x	0.033·x	0.032·x
results of the measurements of three different oxygen carrier batches:								
A1	0.3316	0.4238	0.0829	0.0935	1.513	1.514	73.05	64.75
B1	0.2984	0.3792	0.0719	0.0901	1.757	1.757	97.69	78.04
C1	0.3236	0.4170	0.0878	0.1086	2.038	2.038	92.87	75.06
$SD_{m+p}(x)$	0.017	0.024	0.008	0.010	0.263	0.262	13.06	6.97
$u_{p+m}(x)$ [b]	0.109·x	0.118·x	0.201·x	0.202·x	0.297·x	0.296·x	0.297·x	0.192·x
Calculated standard deviation and uncertainty of x due to the preparation of the oxygen carriers [c]								
$SD_p(x)$	0.016	0.022	0.008	0.008	0.263	0.252	13.00	6.90
$u_p(x)$ [c]	0.098·x	0.110·x	0.200·x	0.162·x	0.297·x	0.285·x	0.296·x	0.190·x

Footnotes: (a) The BJH cumulative volume of pore measured during adsorption and desorption was calculate for pore diameters ranging between 1.7 and 300 nm; (b) The relative uncertainties of the instrument and of instrument + preparation were calculated from the standard deviations of repeated measurements of samples of the same batch (A1, A2, A3), and of repeated measurements of samples of different batches (A1, B1, C1), respectively, by multiplying the SD by two assuming a normal distribution of the results of an uncertainty within a 95% confidence interval; (c) the standard deviation and uncertainty caused by variations in the oxygen carrier preparation were calculated by a statistical combination of the SD_{p+i} and SD_i by $SD_p^2 = (SD_{p+i}^2 - SD_i^2)$.

The calculated values of the relative uncertainties of the measurement, $u_m(x)$, were used to calculate the uncertainties of all measurements of S_{BET}, S_{pore}, $\sum v_{pore}$ and $\bar{d}_{pore}$ in this chapter, and to size the error bars when presenting the results from the N_2 adsorption measurements.

Appendix A.4 *– XRD pattern of all co-precipitated precursors*

The reference pattern of all co-precipitated precursors is shown in **Fig. A-1**, below.

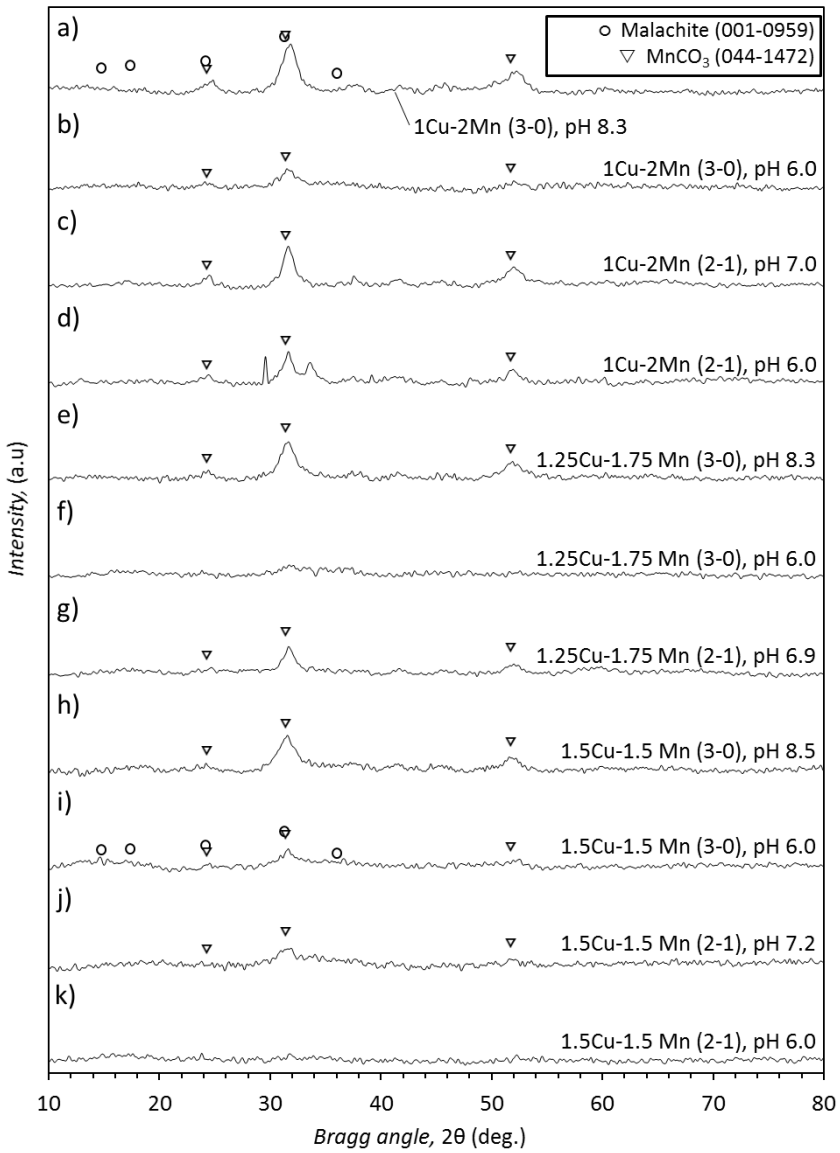


Fig. A-1 XRD pattern of the precursors of all co-precipitated oxygen carriers of this work.

Appendix A.5 *– Estimation of the uncertainty of the crystalline mass fraction calculation.*

The uncertainty of the crystalline mass fractions in the precursors of the co-precipitated oxygen carriers was assumed to be a combination of (i) the observed peak intensity, I_{obs}, of CeO_2 and (ii) the uncertainty of the reference pattern data. The uncertainty of I_{obs} of CeO_2, was estimated based on the standard deviation of I_{obs} of the three largest CeO_2 peaks (at 2θ = 28.7°, 47.6° and 56.5°). The uncertainty in I/I_c and I/I_{max} of the reference patterns for $MnCO_3$, $Cu_2CO_3(OH)_2$, and CeO_2 was determined by calculating the standard deviation from five reference patterns* per phase. For I/I_c the average value and the uncertainty (twice the standard deviation of five reference patterns) for $MnCO_3$, $Cu_2CO_3(OH)_2$, and CeO_2 were 3.52 ± 0.10, 1.22 ± 0.34 and 14.66 ± 0.62, respectively. The mass fraction of CeO_2 was determined using I/I_{max} of the three largest peaks, which are located at 2θ = 28.7 (I/I_{max} = 1.000 ± 0.000), 47.6° (I/I_{max} = 0.486 ± 0.046) and 56.5 (I/I_{max} = 0.388 ± 0.050).

Appendix A.6 *– Calibration and mass flow uncertainties of the TGA mass flow controllers*

The mass flow controllers were calibrated with a 250 ml bubble column from Soham Scientific. A gas regulator set pressure of 1.3 bar was used during the calibrations. A flow rate was set and mixture of DI water and detergent created a horizontal liquid film across the cylindrical column, which moved upwards. The real gas flow rate, $\dot{v}_{\mathrm{real}}$, was calculated by,

$$\dot{v}_{\mathrm{real}} = \frac{v_{t_2} - v_{t_1}}{t_2 - t_1}, \tag{A-8}$$

where v_{t_2} and v_1 is the volume between the upwards rising liquid film at the time t_2 and t_1, respectively. The real gas flow rate was potted against the set flow rate, as shown in **Fig. A-2a-d**, below.

* For the determination of the mass fraction of the crystalline phases the reference patterns for $MnCO_3$ are JCPDS 00-044-1472, JCPDS 01-073-4352, JCPDS 04-011-3970, JCPDS 04-011-3971, JCPDS 04-015-6715; for $Cu_2CO_3(OH)_2$ are JCPDS 04-019-0177, JCPDS 04-019-0178, JCPDS 04-019-0179, JCPDS 04-019-0180, JCPDS 04-019-0181; for CeO_2 are JCPDS 00-067-0121, JCPDS 00-067-0121, JCPDS 00-067-0123 and JCPDS 01-075-8371 and JCPDS 01-075-9470 were used.

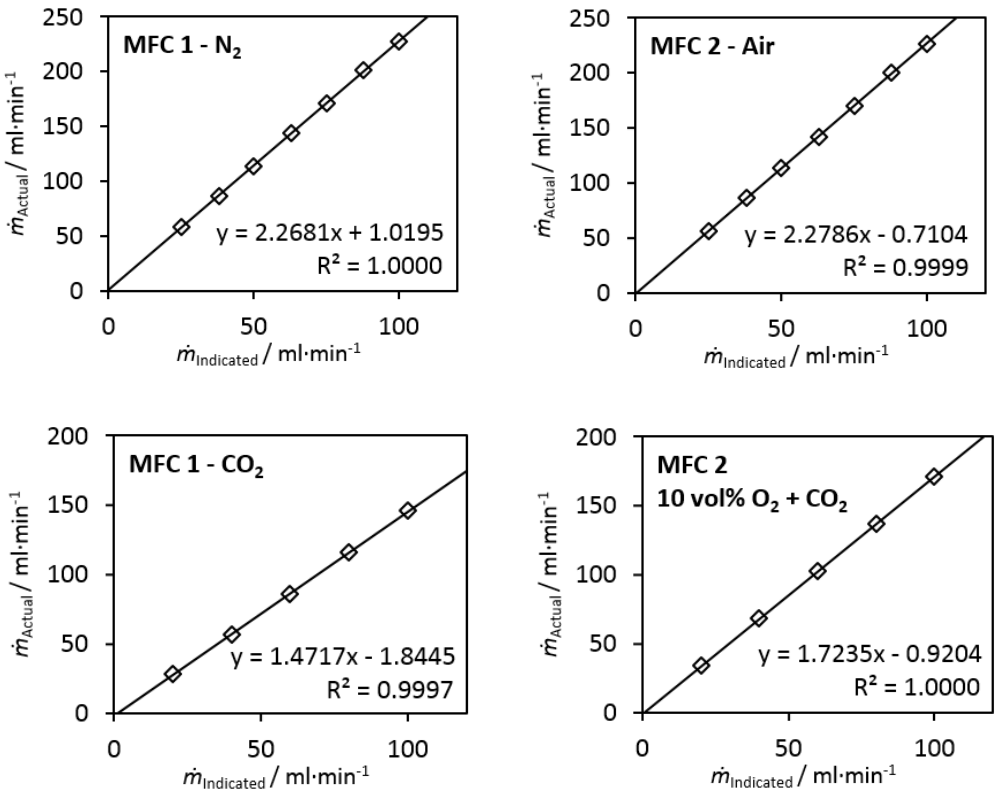


Fig. A-2 *Calibration plots of the MFCs for (a) N_2, (b) air, (c) CO_2 and (d) 10 vol% O_2 + CO_2.*

The experimental points were found to be very well represented by a linear fit. Those correlations were used to control the flow rates of the MFC. To validate the calibration, a gas analyser was connected to the outlet of the gas supply system, and volume fractions of O_2 set in the Agilent VEE code compared with the measured volume fractions. The results are shown in **Fig. A-3**, below.

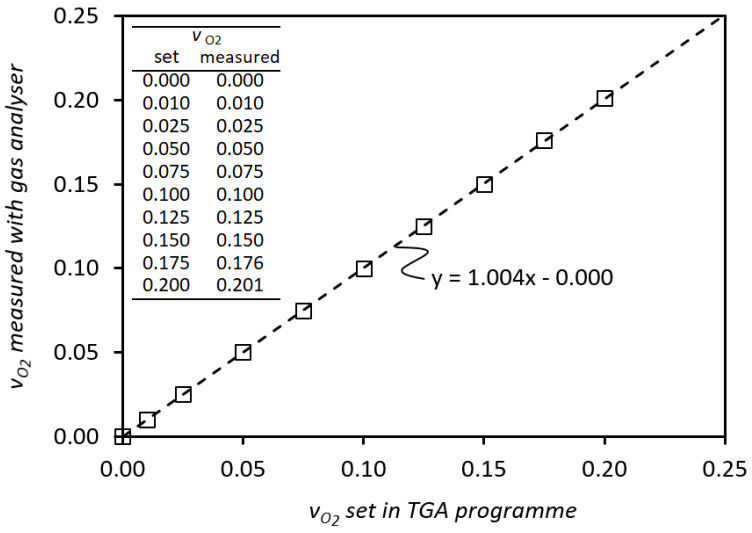


Fig. A-3 *A plot of the set volume fraction of O_2 against the volume fraction of O_2 measured with a gas analyser at a flow rate of 150 ml·min^{-1} at SATP using air and N_2.*

The average absolute relative deviation and the maximum relative deviation between the set and the measured volume fraction of O_2 (using the values listed in **Fig. A-3**) is 0.12% and 0.6%, respectively. The deviation was found to be proportional to y_{O2}, a standard deviation, *SD*, of 0.0024(y_{O2}) was calculated, and an uncertainty within a 95% confidence interval (assuming a normal distribution and hence u(y_{O2})=2*SD*) of 0.0047(y_{O2}) is assumed.

Appendix A.7 – Smoothing of the maximum rate of reaction during TGA experiments.

The observed rate of reaction was calculated by eq.(6-37), and the maximum rate was determined from the three largest values of r′ and corrected as described below. It was found that when taking solely one maximum value of r′, this maximum value would vary significantly by cycle. Therefore, the data was smoothed by averaging the three largest values of the calculated rate ($r_{\mathrm{max1},i}, r_{\mathrm{max2},i}, r_{\mathrm{max3},i}$) and correcting this average rate so that the average of the average rate over 100 cycles is equal to the average of the maximum rate, which can be written as,

$$r_{\mathrm{max,calc}} = \frac{r_{\mathrm{max1},i} + r_{\mathrm{max2},i} + r_{\mathrm{max3},i}}{3} \cdot \frac{\sum_{i=1}^{n}(r_{\mathrm{max1},i})}{\sum_{i=1}^{n}\{(r_{\mathrm{max1},i} + r_{\mathrm{max2},i} + r_{\mathrm{max3},i})/3\}}, \tag{A-9}$$

where $r_{\mathrm{max,calc}}$ is the calculated maximum observed rate, $r_{\mathrm{max1},i}$, $r_{\mathrm{max2},i}$, and $r_{\mathrm{max3},i}$ are the first, second and third highest value of $r'(t)$ within one reaction period of a redox-cycle, and n is the number of redox-cycles.

Appendix A.8 – The correlations used for the calculation of the viscosity and density of gas mixtures, and their uncertainties.

The density of pure N_2 was modelled by,

$$\rho_{N_2}/(kg \cdot m^3) = -0.33685 \left(T/T_0\right)^3 + 1.3745 \left(T/T_0\right)^2 - 2.0803 \left(T/T_0\right) + 1.3837, \tag{A-10}$$

and the density of pure CO_2 by,

$$\rho_{CO_2}/(kg \cdot m^3) = -0.53130 \left(T/T_0\right)^3 + 2.1667 \left(T/T_0\right)^2 - 3.2770 \left(T/T_0\right) + 2.1775, \tag{A-11}$$

where T is the temperature of the gas in K and T_0 is the reference temperature 1000 K. The division of *T* by T_0 aided to keep the parameter closer to unity.

The density of the mixture containing O_2 and N_2 or CO_2, ρ_g,was correlated by,

$$\rho_g/\rho_{N_2 \text{ or } CO_2}/(kg \cdot m^3) = 1 + \mathrm{a}_1\, y_{O_2} + \frac{\mathrm{a}_2\, y_{O_2}}{T/T_0} + \mathrm{a}_3\, y_{O_2}(T/T_0) + \mathrm{a}_4\, y_{O_2}(T/T_0)^2, \tag{A-12}$$

where y_{O_2} is the molar fraction of O_2, and a_i with *i* = 1 to 4 are parameter, which are listed in **Table A.1**. The values for a_i were found by minimising the sum of the square errors between the correlated values and the values calculated with RefProp.[233]

Table A.1 *Parameter for eq.(A-12) and eq.(A-15) to correlate the density and viscosity of the gas mixtures containing O_2 and CO_2 or N_2.*

property	*mixture*	*parameter*			
		a_1	a_2	a_3	a_4
ρ	$N_2 + O_2$	$1.4091 \cdot 10^{-1}$	$4.8109 \cdot 10^{-4}$	$1.9290E \cdot 10^{-3}$	$-9.1980 \cdot 10^{-4}$
	$CO_2 + O_2$	$-2.6881 \cdot 10^{-1}$	$-2.1574 \cdot 10^{-3}$	$-2.5245 \cdot 10^{-3}$	$4.9914 \cdot 10^{-4}$
η	$N_2 + O_2$	$2.0783 \cdot 10^{-1}$	$-3.8712 \cdot 10^{-3}$	$-5.9836 \cdot 10^{-3}$	$-1.6331 \cdot 10^{-2}$
	$CO_2 + O_2$	$1.3800 \cdot 10^{-1}$	$4.4185 \cdot 10^{-3}$	$2.8151 \cdot 10^{-2}$	$2.1966 \cdot 10^{-2}$

The deviations of the calculated densities for the mixtures containing O_2 and CO_2 or N_2 are illustrated in **Fig. A-4**, below.

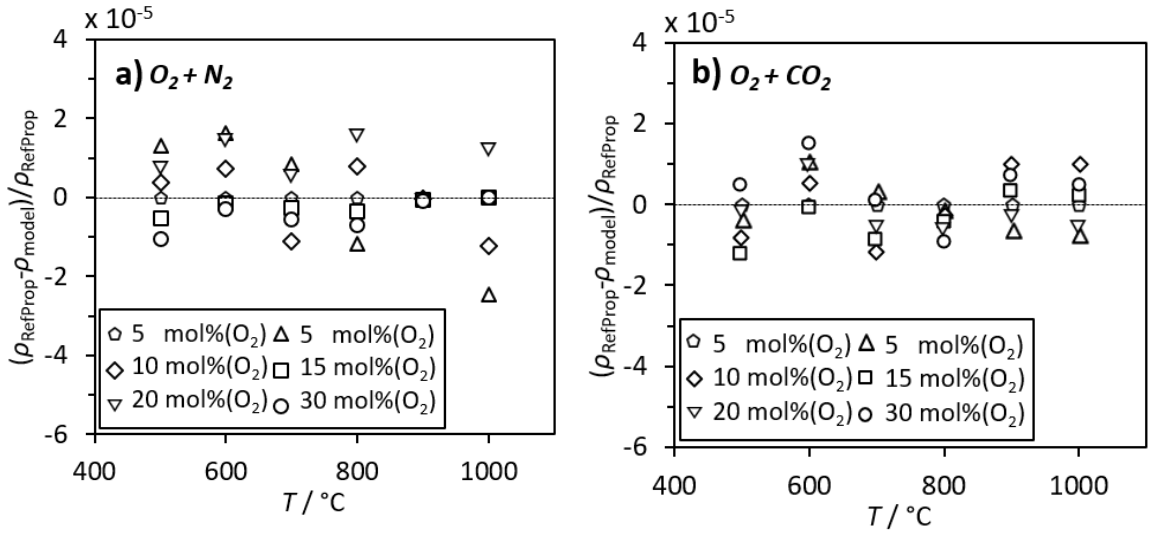


Fig. A-4 *The relative deviations between the calculated density with RefProp*[233] *and the density correlated using eq.(A-12), a) for the mixture containing O_2 and N_2, and b) for the mixture containing O_2 and CO_2.*

Fig. A-4 shows neither a clear trend of deviations with a variation in temperature nor with a variation in the oxygen concentration. The average absolute relative deviations ($\Delta_{\mathrm{AARD},X}$) and the maximum absolute relative deviation ($\Delta_{\mathrm{MARD},X}$) were calculated by $1/n \sum\{(|X_{\mathrm{RefProp}} - X_{\mathrm{model}}|)/X_{\mathrm{RefProp}}\}$ and $\max\{(|X_{\mathrm{RefProp}} - X_{\mathrm{model}}|)/X_{\mathrm{RefProp}}\}$, respectively, with n being the total number of values and X denotes the property ρ or η. For the mixture containing CO_2 and O_2, $\Delta_{\mathrm{AARD},\rho}$ is 0.0005% and $\Delta_{\mathrm{MARD},\rho}$ is 0.0015%. For the mixture containing N_2, $\Delta_{\mathrm{AARD},\rho}$ is 0.0006% and $\Delta_{\mathrm{MARD},\rho}$ is 0.0025%. The dynamic viscosity of a mixture was correlated similarly as the density of a mixture.

Firstly, the viscosity of pure N_2 was correlated with,

$$\eta_{N_2}/(\text{uPa}\cdot\text{s}) = -5.2375\left(T/T_0\right)^2 + 37.704\left(T/T_0\right) + 9.0743, \quad \text{(A-13)}$$

for pure CO_2 with,

$$\eta_{CO_2}/(\text{uPa}\cdot\text{s}) = -8.153571\left(T/T_0\right)^2 + 45.530\left(T/T_0\right) + 3.8815, \quad \text{(A-14)}$$

with T_0 = 1000 K. The viscosity of the gas mixtures containing O_2 + (N_2 or CO_2), η_g, were correlated by,

$$\eta_g/\eta_{N_2 \text{ or } CO_2}/(\text{uPa}\cdot\text{s}) = 1 + a_1\, y_{O_2} + a_2\, y_{O_2}\left(T/T_0\right) + a_3\, y_{O_2}\left(T/T_0\right)^2 + a_4\, y_{O_2}{}^2. \quad \text{(A-15)}$$

The parameter for eq.(A-15) are listed in **Table A.1** and the deviations of this correlation compared to the values from RefProp are illustrated in **Fig. A-5**, below.

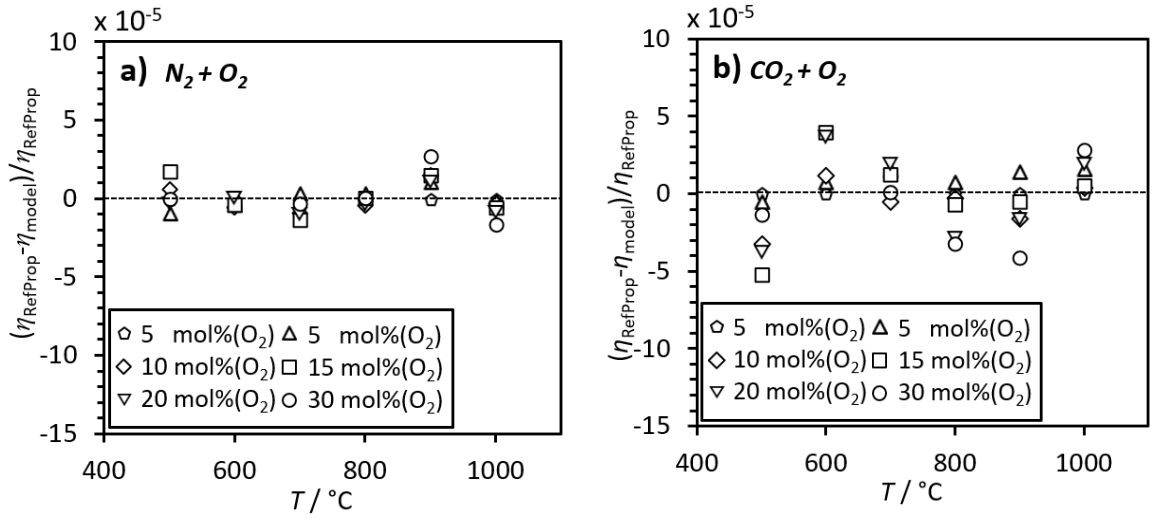


Fig. A-5 *The relative deviations between the calculated viscosity with RefProp*[233] *and the viscosity correlated using eq.(A-15), for mixtures containing (a) O_2 and N_2, and (b) O_2 and CO_2.*

Fig. A-5 shows no significant trend in the deviations with a change in T or [O_2], which suggests that the correlations are suitable. For the mixture containing N_2 and O_2, a $\Delta_{AARD,\rho}$ of 0.0006% and a $\Delta_{MARD,\rho}$ of 0.0027% were calculated. For the mixture containing CO_2 and O_2, the $\Delta_{AARD,\rho}$ is 0.0017% and the $\Delta_{MARD,\rho}$ is 0.0075% were calculated. The deviations together with the deviations published by RefProp[233] were used to calculate the uncertainty in estimated parameter, such as the minimum fluidisation velocity and the external mass transfer coefficient.

Appendix A.9 *– Solving eq.(6-14) for the surface concentration*

In eq.(6-14), quasi steady-state conditions are assumed and therefore the external diffusion has to balance the rate of reaction inside the particle:

$$\eta k_i(C_{eq} - C_s) \approx k_{\mathrm{g}}(C_s - C_b) \tag{A-16}$$

Expansion of the bracket yields,

$$\eta k_i C_{\mathrm{eq}} - \eta k_i C_s \approx k_{\mathrm{g}} C_s - k_{\mathrm{g}} C_b \tag{A-17}$$

Bringing all terms that depend on C_s to the l.h.s. and expanding again, yields:

$$\eta k_i C_S + k_{\mathrm{g}} C_s \approx \eta k_i C_{\mathrm{eq}} + k_{\mathrm{g}} C_b + \eta k_i C_b - \eta k_i C_b \tag{A-18}$$

When factoring out the terms in eq.(A-18) yields,

$$C_S(\eta k_i + k_{\mathrm{g}}) = \eta k_i(C_{\mathrm{eq}} - C_{\mathrm{b}}) + C_{\mathrm{b}}(\eta k_i + k_{\mathrm{g}}) \tag{A-19}$$

Division by $(\eta k_i + k_{\mathrm{g}})$ yields:

$$C_S = \frac{\eta k_i(C_{\mathrm{eq}} - C_{\mathrm{b}})}{(\eta k_i + k_{\mathrm{g}})} + C_{\mathrm{b}} \tag{A-20}$$

Eq.(A-20) is used in section 6.3 to eliminate C_S form the reaction rate function to model the observed rate of reaction during the experiments to measure the effect of the intra-particle diffusion resistance.

Appendix A.10 *– Kinetic parameters and reaction order for the reduction with CH_4*

From the experiments After demonstrating that stable redox-cycling with a reduction in $CH_4 + N_2$ is possible, experiments were performed to determine the reaction order and kinetic parameter, as shown in **Fig. A-6**, below.

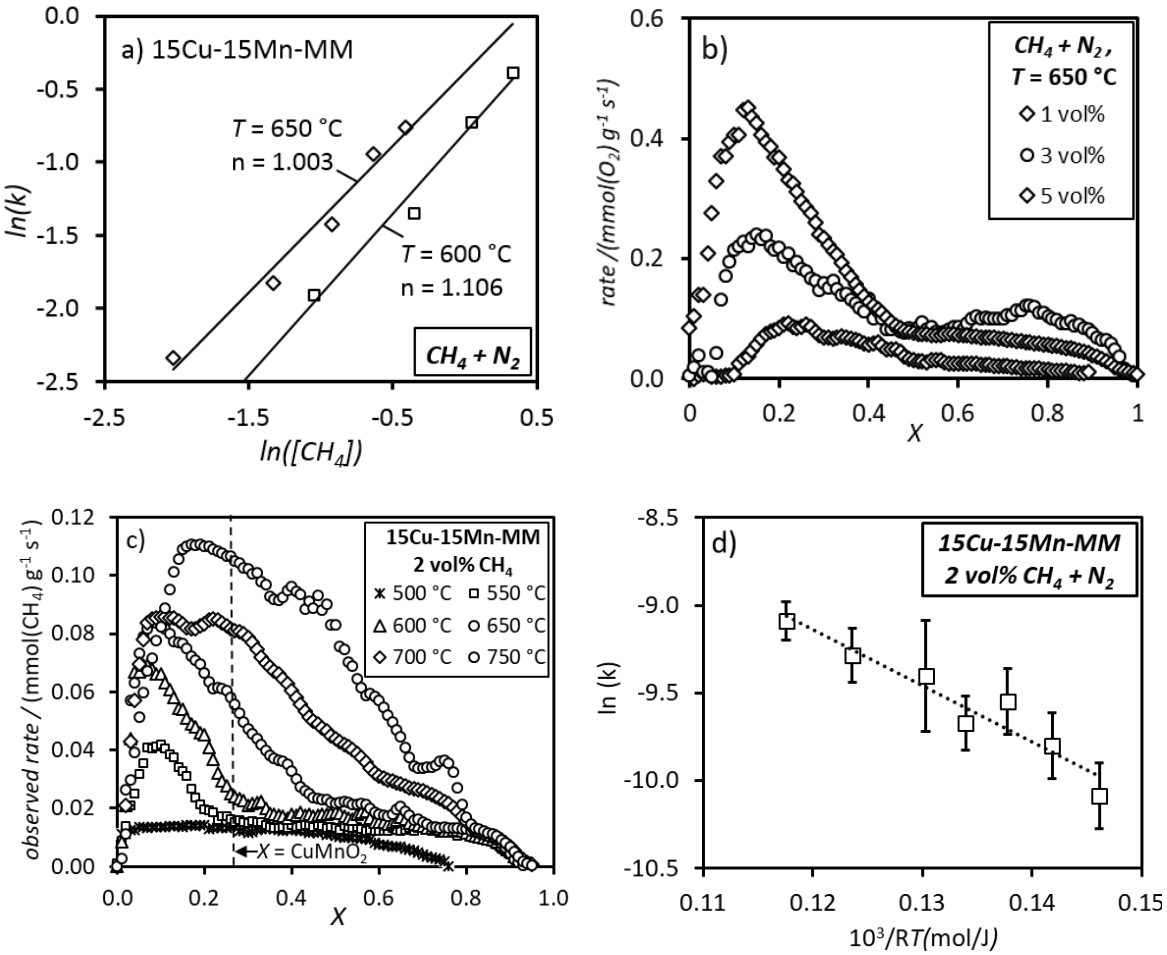


Fig. A-6 *Plots (a) of the reaction rate against conversion at varying [CH_4], (b) for the determination of the reaction order, (c) of the reaction rate against conversion for different temperatures, and (d) for determination of the pre-exponential factor and activation energy of 1Cu-1Mn-MM oxygen carriers measured in the TGA using a total gas flow rate of 200 ml·min^{-1}. The full conversion is calculated assuming a reaction between $Cu_{1.5}Mn_{1.5}O_4$ and ($Cu+Mn_2O_3$).*

The fitted line in **Fig. A-6a** is in good agreement with the experimental data. The gradient of this line corresponds to a reaction order of n = 1.003 and n = 1.106 with respect to the molar CH_4 concentration for the reduction reaction at 600 °C and 650 °C, respectively. **Fig. A-6b** shows the reaction rate profile of the reactions that were used for the determination of the maximum rates in **Fig. A-6a**. **Fig. A-6c** shows the reaction rate profiles of the observed rate of reaction, r, during experiments with

various temperatures. The maximum observed rates were related to the observed rate constant, k, and the molar CH_4 concentration, C_{CH4}, by,

$$r = kC_{\mathrm{CH_4}} \tag{A-21}$$

The observed rate constant was then related to the particle radius, r_{p}, the external mass transfer, k_{g}, an effectiveness factor to account for the reduction of the intrinsic rate due to the intra-particle diffusion resistance, η, and an intrinsic rate constant, k_i, by, [91]

$$\frac{1}{k} = \frac{r_{\mathrm{p}}}{3k_{\mathrm{g}}} + \frac{1}{\eta k_i} \tag{A-22}$$

The intrinsic rate constant was expressed by an Arrhenius equation,

$$k_i = \mathrm{A} \cdot \exp\left(-\frac{\mathrm{E_a}}{\mathrm{RT}}\right) \tag{A-23}$$

The calculated values for k were plotted as an Arrhenius plot to determine the activation energy and rate constants. The calculated kinetic parameters are shown in **Table 6-7**, below.

Table 6-7 *The kinetic parameters calculated for the oxidation and reduction reaction.*

oxygen carrier	*reduction in CH_4 + N_2*		
	A	E_A	*n*
1Cu-1Mn-MM	6.628 ± 1	33.91 ± 1	1.003 ± 0.1
1Cu-1Mn-CP	6.738 ± 1	33.42 ± 1	*n.d.*
1Cu-2Mn-MM	6.738 ± 1	33.42 ± 1	1.000 ± 0.1
40-CuMn/Zr	8.027 ± 1	25.57 ± 1	*n.d.*
40-CuMn/Ti	6.628 ± 1	31.48 ± 1	*n.d.*

The kinetic parameters from **Table 6-7** allow calculation of the minimum solid inventory for the CH_4-CLC process or process simlulation, which both can be used as a benchmark for the estimated minimum solid inventory of the oxygen carriers for the CLAS process.

Appendix A.11 *– Calibration and mass flow uncertainties of the FBR mass flow controllers*

The MFCs of the gas supply system of the fluidised bed reactor have been calibrated following the same procedure that has been used for the calibration of the TGA MFCs. The calibration plots are shown in **Fig. A-7**, below.

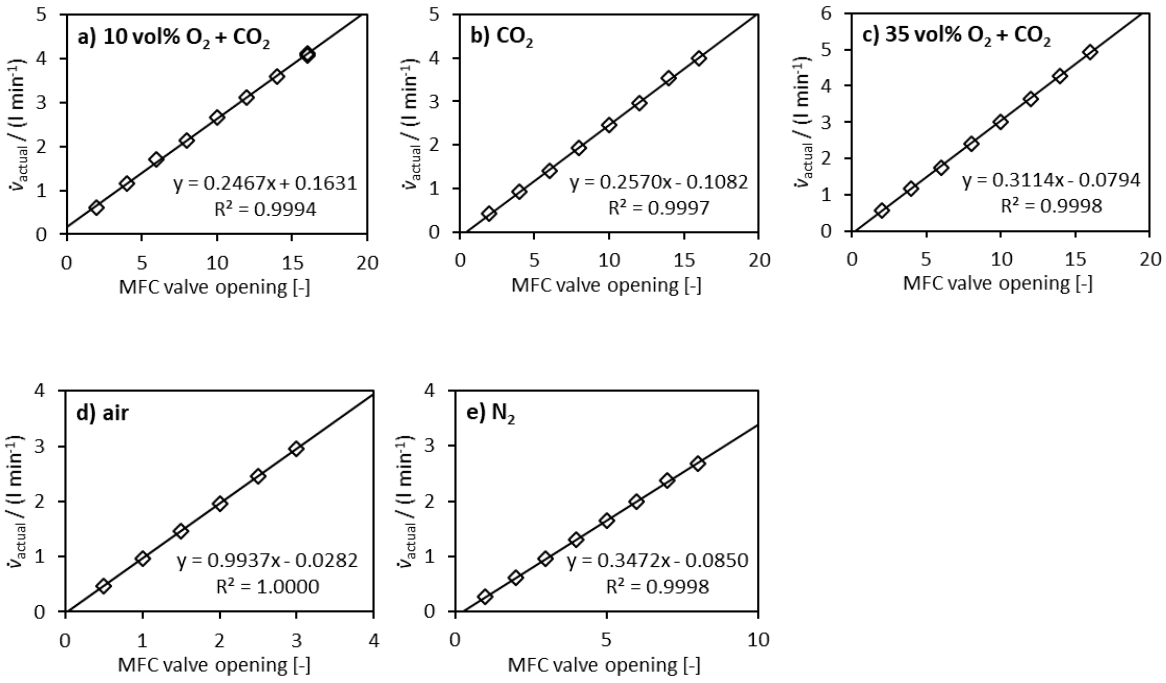


Fig. A-7 *Calibration plots of the mass flow controllers of the fluidised bed reactor. The calibration was carried out at 3 barg.*

Appendix A.12 – Reduction of the noise-to-signal ratio of the measured gas volume fractions using the algorithm proposed by Savitzky and Golay.

The data was smoothed using the algorithm proposed by Savitzky and Golay with 11 data points.[236] The gas sampling interval was 0.5 s^{-1} during all experiments. Therefore, the data in the range between $t - 2.5\text{s}$ and $t + 2.5\text{s}$ was used for the smoothing, and the smoothed molar fraction of O_2, $(y_{O_2})_{\text{smoothed}}$, was calculated by,

$$(y_{O_2})_{\text{smoothed}} = \frac{\sum_{i=0}^{10} a_i \, y_{O_2}(t - 2.5\text{s} + \frac{i\,\text{s}}{2})}{429} \qquad \text{(A-24)}$$

The values for a_i in eq.(A-24) are listed in **Table A.2**, below.

Table A.2 Parameter used for the Savitzky and Golay algorithm.

i	0	1	2	3	4	5	6	7	8	9	10
a_i	-36	9	44	69	84	89	84	69	44	9	-36

Bibliography

1 IPCC (2014). Climate Change 2014: Synthesis Report. Contribution of Working Groups I, II and III to the Fifth Assessment Report of the Intergovernmental Panel on Climate Change [Core Writing Team, R.K. Pachauri and L.A. Meyer (eds.)]. IPCC, Geneva, Switzerland, 151 pp.

2 M. F. Meier; M. B. Dyurgerov; U. K. Rick; S. O'Neel; W. T. Pfeffer; R. S. Anderson; S. P. Anderson; A. F. Glazovsky (2007). Glaciers dominate eustatic sea-level rise in the 21st century. *Science,* 317, 1064-7.

3 J. A. Church; N. J. White (2006). A 20th century acceleration in global sea-level rise. *Geophysical Research Letters,* **33**, 1-4.

4 T. Moon (2017). Saying goodbye to glaciers. *Science*, **356**, 580-581.

5 M. Le Page; J. Brown (2017). Living with climate change: The new normal. *New Scientist,* **234**, 28-31.

6 E. Post; J. Kerby; C. Pedersen; H. Steltzer (2016). Highly individualistic rates of plant phenological advance associated with arctic sea ice dynamics. *Biol Lett,* **12**, 1-5.

7 G. T. Pecl; M. B. Araujo; J. D. Bell; J. Blanchard; T. C. Bonebrake; I. C. Chen; T. D. Clark; R. K. Colwell; F. Danielsen; B. Evengard; L. Falconi; S. Ferrier; S. Frusher; R. A. Garcia; R. B. Griffis; A. J. Hobday; C. Janion-Scheepers; M. A. Jarzyna; S. Jennings; J. Lenoir; H. I. Linnetved; V. Y. Martin; P. C. McCormack; J. McDonald; N. J. Mitchell; T. Mustonen; J. M. Pandolfi; N. Pettorelli; E. Popova; S. A. Robinson; B. R. Scheffers; J. D. Shaw; C. J. Sorte; J. M. Strugnell; J. M. Sunday; M. N. Tuanmu; A. Verges; C. Villanueva; T. Wernberg; E. Wapstra; S. E. Williams (2017). Biodiversity redistribution under climate change: Impacts on ecosystems and human well-being. *Science,* **2017**, 355.

8 N. S. Diffenbaugh; C. B. Field (2013). Changes in ecologically critical terrestrial climate conditions. *Science (New York, N.Y.),* **341**, 486.

9 W. Jetz; D. S. Wilcove; A. P. Dobson (2007). Projected impacts of climate and land-use change on the global diversity of birds. *PLoS Biol,* 5, e157.

10 IPCC (2012). *Managing the Risks of Extreme Events and Disasters to Advance Climate Change Adaptation*. A Special Report of Working Groups I and II of the Intergovernmental Panel on Climate Change [Field, C. B., V. Barros, T. F. Stocker, D. Qin, D. J. Dokken, K. L. Ebi, M. D. Mastrandrea, K. J. Mach, G.-K. Plattner, S. K. Allen, M. Tignor, and P. M. Midgley (eds.)]. Cambridge University Press, Cambridge, UK, and New York, NY, USA, 582 pp.

11 Y. Hirabayashi; R. Mahendran; S. Koirala; L. Konoshima; D. Yamazaki; S. Watanabe; H. Kim; S. Kanae (2013). Global flood risk under climate change. *Nature Climate Change,* **3**, 816.

12 C. H. Hsu; H. Chu; C. M. Cho, Absorption and Reaction Kinetics of Amines and Ammonia Solutions with Carbon Dioxide in Flue Gas. *Journal of the Air & Waste Management Association,* **2012**, 53, 246-252.

13 IPCC (2014). Climate Change 2014: Synthesis Report. Contribution of Working Groups I, II and III to the Fifth Assessment Report of the Intergovernmental Panel on Climate Change [Core Writing Team, R.K. Pachauri and L.A. Meyer (eds.)]. IPCC, Geneva, Switzerland, 151 pp.

14 IEA (2018). Atlas of Energy (energyatlas.iea.org). 21 Dec 2018.

15 J. Rockstrom; O. Gaffney; J. Rogelj; M. Meinshausen; N. Nakicenovic; H. J. Schellnhuber (2017). A roadmap for rapid decarbonization. *Science,* **355**, 1269-1271.

16 IPCC (2005). *IPCC special report on carbon dioxide capture and storage*. B. Metz; O. Davidson; H. d. Coninck; M. Loos; L. Meyer (Eds.) Cambridge University Press, UK.

17 C. M. White; B. R. Strazisar; E. J. Granite; J. S. Hoffman; H. W. Pennline (2003). Separation and Capture of CO_2 from Large Stationary Sources and Sequestration in Geological Formations—Coalbeds and Deep Saline Aquifers. *J. Air & Waste Manage. Assoc.,* **53**, 645-715.

18 United Nations (2015). Paris Agreement. Treaty Collection (treaties.un.org). 06 Dec 2018.

19 J. Rogelj; M. Schaeffer; P. Friedlingstein; N. P. Gillett; D. P. van Vuuren; K. Riahi; M. Allen; R. Knutti (2016). Differences between carbon budget estimates unravelled. *Nature Climate Change,* **6**, 245.

20 S. Fuss; J. G. Canadell; G. P. Peters; M. Tavoni; R. M. Andrew; P. Ciais; R. B. Jackson; C. D. Jones; F. Kraxner; N. Nakicenovic; C. Le Quéré; M. R. Raupach; A. Sharifi; P. Smith; Y. Yamagata (2014). Betting on negative emissions. *Nature Climate Change,* **4**, 850.

21 R. Pidcock (2016). Analysis: What global emissions in 2016 mean for climate change goals. Carbon Brief (www.carbonbrief.org).

22 G. Luderer; R. C. Pietzcker; C. Bertram; E. Kriegler; M. Meinshausen; O. Edenhofer (2013). Economic mitigation challenges: how further delay closes the door for achieving climate targets. *Environmental Research Letters,* **8**, 1-8.

23 J. Rogelj; G. Luderer; R. C. Pietzcker; E. Kriegler; M. Schaeffer; V. Krey; K. Riahi (2015). Energy system transformations for limiting end-of-century warming to below 1.5 °C. *Nature Climate Change,* **5**, 519.

24 J. S. Rhodes; D. W. Keith (2008). Biomass with capture: negative emissions within social and environmental constraints: an editorial comment. *Climatic Change,* **87**, 321-328.

25 X.-P. Song; M. C. Hansen; S. V. Stehman; P. V. Potapov; A. Tyukavina; E. F. Vermote; J. R. Townshend (2018). Global land change from 1982 to 2016. *Nature,* **560**, 639-643.

26 G. B. Bonan (2008). Forests and climate change: forcings, feedbacks, and the climate benefits of forests. *Science,* **320**, 1444-1449.

27 S. K. Rose; E. Kriegler; R. Bibas; K. Calvin; A. Popp; D. P. van Vuuren; J. Weyant (2013). Bioenergy in energy transformation and climate management. *Climatic Change,* **123**, 477-493.

28 G. Sorda; M. Banse; C. Kemfert (2010). An overview of biofuel policies across the world. *Energy Policy,* **38**, 6977-6988.

29 J. L. Field; S. G. Evans; E. Marx; M. Easter; P. R. Adler; T. Dinh; B. Willson; K. Paustian (2018). High-resolution techno–ecological modelling of a bioenergy landscape to identify climate mitigation opportunities in cellulosic ethanol production. *Nature Energy,* **3**, 211-219.

30 R. A. Metzger; G. Benford; M. I. Hoffert (2002). *Climatic Change,* **54**, 369-374.

31 J. S. Rhodes; D. W. Keith (2005). Engineering economic analysis of biomass IGCC with carbon capture and storage. *Biomass and Bioenergy,* **29**, 440-450.

32 H. Karlsson; L. Byström (2011). Global Status of BECCS Projects 2010. Global CCS Institute: Canberra, Australia.

33 A. Bhave; R. H. S. Taylor; P. Fennell; W. R. Livingston; N. Shah; N. M. Dowell; J. Dennis; M. Kraft; M. Pourkashanian; M. Insa; J. Jones; N. Burdett; A. Bauen; C. Beal; A. Smallbone; J. Akroyd (2017). Screening and techno-economic assessment of biomass-based power generation with CCS technologies to meet 2050 CO_2 targets. *Applied Energy,* **190**, 481-489.

34 S. p. Hoffmann; M. Bartlett; M. Finkenrath; A. Evulet; T. P. Ursin (2009). Performance and Cost Analysis of Advanced Gas Turbine Cycles with Precombustion CO_2 Capture. *Journal of Engineering for Gas Turbines and Power,* 131.

35 J. Riaza; M. V. Gil; L. Álvarez; C. Pevida; J. J. Pis; F. Rubiera (2012). Oxy-fuel combustion of coal and biomass blends. *Energy,* **41**, 429-435.

36 D. Berstad; R. Anantharaman; R. Blom; K. Jordal; B. Arstad (2014). NGCC post-combustion CO_2 capture with Ca/carbonate looping: Efficiency dependency on sorbent properties, capture unit performance and process configuration. *International Journal of Greenhouse Gas Control,* **24**, 43-53.

37 C.-C. Cormos (2015). Assessment of chemical absorption/adsorption for post-combustion CO_2 capture from Natural Gas Combined Cycle (NGCC) power plants. *Applied Thermal Engineering,* **82**, 120-128.

38 P. Fennell; B. Anthony (2015). *Calcium and Chemical Looping Technology for Power Generation and Carbon Dioxide (CO_2) Capture*. Woodhead: **2015**.

39 L.-S. Fan (2010). *Chemical looping systems for fossil energy conversions*. Wiley Wiley-AIChE: Hoboken, N.J.

40 B. Moghtaderi (2010). Application of Chemical Looping Concept for Air Separation at High Temperatures. *Energy & Fuels,* **24**, 190-198.

41 C. Tagliaferri; R. Görke; S. Scott; J. Dennis; P. Lettieri (2017). Life cycle assessment of optimised chemical looping air separation systems for electricity production. *Chemical Engineering Research and Design,* **131**.

42 T. Niass; J. Kislear; M. Buchanan; J. Svalestuen; A. Park; D. DePaolo; J. Powell (2017). Accelerating Breakthrough Innovation in Carbon Capture, Utilization, and Storage. *Report of the Mission Innovation Carbon Capture, Utilizsation, and Storage Experts' Workshop*.

43 N. Mohammad Pour; H. Leion; M. Rydén; T. Mattisson (2013). Combined Cu/Mn Oxides as an Oxygen Carrier in Chemical Looping with Oxygen Uncoupling (CLOU). *Energy & Fuels,* **27**, 6031-6039.

44 P. Mungse; G. Saravanan; T. Uchiyama; M. Nishibori; Y. Teraoka; S. Rayalu; N. Labhsetwar (2014). Copper-manganese mixed oxides: CO_2-selectivity, stable, and cyclic performance for chemical looping combustion of methane. *Phys Chem Chem Phys,* **16**, 19634-42.

45 D. Hosseini; Q. Imtiaz; P. M. Abdala; S. Yoon; A. M. Kierzkowska; A. Weidenkaff; C. R. Müller (2015). CuO promoted Mn_2O_3-based materials for solid fuel combustion with inherent CO_2 capture. *J. Mater. Chem. A,* **3**, 10545-10550.

46 C. F. Patzschke; M. E. Boot-Handford; Q. Song; P. S. Fennell (*in preparation*). The development and performance testing of copper manganese oxides prepared via co-precipitation as oxygen carrier for chemical looping air separation (CLAS).

47 W. K. Lewis; E. R. Gilliland (1954). Production of pure carbon dioxide. Patent: US 2665972 A.

48 M. Ishida; H. Jin (1994). A new advanced power-generation system using chemical-looping combustion. *Energy,* **19**, 415-422.

49 Z. Cheng; L. Qin; J. A. Fan; L.-S. Fan (2018). New Insight into the Development of Oxygen Carrier Materials for Chemical Looping Systems. *Engineering,* **4**, 343-351.

50 A. Lyngfelt; B. Leckner; T. Mattisson (2001). A fluidized-bed combustion process with inherent CO_2 separation; application of chemical-looping combustion. *Chemical Engineering Science,* **56**, 3101-3113.

51 J. Adánez; P. Gayán; J. Celaya; L. F. de Diego; F. García-Labiano; A. Abad (2006). Chemical Looping Combustion in a 10 kW_{th} Prototype using a CuO/Al_2O_3 Oxygen Carrier: Effect of Operating Conditions on Methane Combustion. *Industrial & Engineering Chemistry Research,* **45**, 6075-6080.

52 C. R. Forero; P. Gayán; F. García-Labiano; L. F. de Diego; A. Abad; J. Adánez (2011). High temperature behaviour of a $CuO/\gamma Al_2O_3$ oxygen carrier for chemical-looping combustion. *International Journal of Greenhouse Gas Control,* **5**, 659-667.

53 I. Adánez-Rubio; P. Gayán; A. Abad; L. F. de Diego; F. García-Labiano; J. Adánez (2012). Evaluation of a Spray-Dried $CuO/MgAl_2O_4$ Oxygen Carrier for the Chemical Looping with Oxygen Uncoupling Process. *Energy & Fuels,* **26**, 3069-3081.

54 L. F. de Diego; F. Garcı´a-Labiano; P. Gayán; J. Celaya; J. M. Palacios; J. Adánez (2007). Operation of a 10kW_{th} chemical-looping combustor during 200 h with a $CuO–Al_2O_3$ oxygen carrier. *Fuel,* **86**, 1036-1045.

55 P. Gayán; C. R. Forero; A. Abad; L. F. de Diego; F. García-Labiano; J. Adánez (2011). Effect of Support on the Behavior of Cu-Based Oxygen Carriers during Long-Term CLC Operation at Temperatures above 1073 K. *Energy & Fuels,* **25**, 1316-1326.

56 A. Cabello; P. Gayán; F. García-Labiano; L. F. de Diego; A. Abad; J. Adánez (2016). On the attrition evaluation of oxygen carriers in Chemical Looping Combustion. *Fuel Processing Technology,* **148**, 188-197.

57 M. Johansson; T. Mattisson; A. Lyngfelt (2006). Investigation of Mn_3O_4 with stabilized ZrO_2 for Chemical-Looping Combustion. *Chemical Engineering Research and Design,* **84**, 807-818.

58 M. Rydén; P. Moldenhauer; T. Mattisson; A. Lyngfelt; M. Younes; T. Niass; B. Fadhel; J.-P. Ballaguet (2013). Chemical-Looping Combustion with Liquid Fuels. *Energy Procedia.* **37**, 654-661.

59 P. Gayán; M. A. Pans; M. Ortiz; A. Abad; L. F. de Diego; F. García-Labiano; J. Adánez (2012). Testing of a highly reactive impregnated Fe_2O_3/Al_2O_3 oxygen carrier for a SR–CLC system in a continuous CLC unit. *Fuel Processing Technology,* **96**, 37-47.

60 A. Cabello; C. Dueso; F. García-Labiano; P. Gayán; A. Abad; L. F. de Diego; J. Adánez (2014). Performance of a highly reactive impregnated Fe_2O_3/Al_2O_3 oxygen carrier with CH_4 and H_2S in a 500W_{th} CLC unit. *Fuel,* **121**, 117-125.

61 Y.-C. Liu; Y. Ku; Y. Tseng; H.-Y. Lee; Y.-L. Kuo (2016). Fabrication of Fe_2O_3/TiO_2 Oxygen Carriers for Chemical Looping Combustion and Hydrogen Generation. *Aerosol and Air Quality Research*, 16, 2023–2032.

62 J. Adánez; C. Dueso; L. F. de Diego; F. García-Labiano; P. Gayán; A. Abad (2009). Methane Combustion in a 500 W_{th} Chemical-Looping Combustion System using an impregnated Ni-Based Oxygen Carrier. *Energy & Fuels,* **23**, 130-142.

63 P. Gayán; A. Cabello; F. García-Labiano; A. Abad; L. F. de Diego; J. Adánez (2013). Performance of a low Ni content oxygen carrier for fuel gas combustion in a continuous CLC unit using a CaO/Al_2O_3 system as support. *International Journal of Greenhouse Gas Control,* **14**, 209-219.

64 T. Mattisson; M. Johansson; A. Lyngfelt (2004). Multicycle Reduction and Oxidation of Different Types of Iron Oxide Particles – Application to Chemical-Looping Combustion. *Energy & Fuels,* **18**, 628-637.

65 Q. Zafar; T. Mattisson; B. Gevert (2006). Redox Investigation of Some Oxides of Transition-State Metals Ni, Cu, Fe, and Mn Supported on SiO_2 and $MgAl_2O_4$. *Energy & Fuels,* **20**, 34-44.

66 S. B. Peterson; G. Konya; C. K. Clayton; R. J. Lewis; B. R. Wilde; E. M. Eyring; K. J. Whitty (2013). Characteristics and CLOU Performance of a Novel SiO_2-Supported Oxygen Carrier Prepared from CuO and β-SiC. *Energy & Fuels,* **27**, 6040-6047.

67 H. Song; K. Shah; E. Doroodchi; T. Wall; B. Moghtaderi (2014). Analysis on Chemical Reaction Kinetics of CuO/SiO_2 Oxygen Carriers for Chemical Looping Air Separation. *Energy & Fuels,* **28**, 173-182.

68 D. Mei; T. Mendiara; A. Abad; L. F. de Diego; F. García-Labiano; P. Gayán; J. Adánez; H. Zhao (2015). Evaluation of Manganese Minerals for Chemical Looping Combustion. *Energy & Fuels,* **29**, 6605-6615.

69 L. F. de Diego; A. Abad; A. Cabello; P. Gayán; F. García-Labiano; J. Adánez (2014). Reduction and Oxidation Kinetics of a $CaMn_{0.9}Mg_{0.1}O_{3-\delta}$ Oxygen Carrier for Chemical-Looping Combustion. *Industrial & Engineering Chemistry Research,* **53**, 87-103.

70 T. Mattisson; A. Lyngfelt; P. Cho (2001). The use of iron oxide as an oxygen carrier in chemical-looping combustion of methane with inherent separation of CO_2. *Fuel,* **80**, 1953-1962.

71 J. Wolf; M. Anheden; J. Yan (2005). Comparison of nickel- and iron-based oxygen carriers in chemical looping combustion for CO_2 capture in power generation. *Fuel,* **84**, 993-1006.

72 B. Zheng; J. Xu (2014). Carbon Capture and Storage Development Trends from a Techno-Paradigm Perspective. *Energies,* **8**, 5221-5250.

73 M. Ishida; D. Zheng; T. Akehata (1987). Evaluation of a chemical-looping-combustion power-generation system by graphic exergy analysis. *Energy,* **12**, 147-154.

74 S. Mukherjee; P. Kumar; A. Yang; P. Fennell (2015). Energy and exergy analysis of chemical looping combustion technology and comparison with pre-combustion and oxy-fuel combustion technologies for CO_2 capture. *Journal of Environmental Chemical Engineering,* **3**, 2104-2114.

75 C. F. Patzschke; X. Wenzhao; H. Bahzad; M. E. Boot-Handford; N. M. Dowell; P. S. Fennell (in preparation). Life cycle assessment of oxygen carrier preparation, use and recycling or disposal for chemical looping combustion with CH_4.

76 F. Petrakopoulou; G. Tsatsaronis; A. Boyano; T. Morosuk (2011). Exergoeconomic and exergoenvironmental evaluation of power plants including CO_2 capture. *Chemical Engineering Research and Design,* **89**, 1461-1469.

77 L. Zhu; H. Chen; J. Fan; P. Jiang (2016). Thermo-economic investigation: an insight tool to analyze NGCC with calcium-looping process and with chemical-looping combustion for CO_2 capture. *International Journal of Energy Research,* **40**, 1908-1924.

78 A. S. R. Subramanian; K. Jordal; R. Anantharaman; B. A. L. Hagen; S. Roussanaly (2017). A Comparison of Post-combustion Capture Technologies for the NGCC. *Energy Procedia,* **114**, 2631-2641.

79 N. Sipöcz; A. Tobiesen; M. Assadi (2011). Integrated modelling and simulation of a 400 MW NGCC power plant with CO_2 capture. *Energy Procedia,* **4**, 1941-1948.

80 Y. Hu; H. Ahn (2017). Process integration of a Calcium-looping process with a natural gas combined cycle power plant for CO_2 capture and its improvement by exhaust gas recirculation. *Applied Energy,* **187**, 480-488.

81 S. Garcia; E. S. Fernandez; A. J. Stewart; M. M. Maroto-Valer (2017). Process Integration of Post-combustion CO_2 Capture with Li_4SiO_4/Li_2CO_3 Looping in a NGCC Plant. *Energy Procedia,* **114**, 2611-2617.

82 M. E. Boot-Handford; J. C. Abanades; E. J. Anthony; M. J. Blunt; S. Brandani; N. Mac Dowell; J. R. Fernández; M.-C. Ferrari; R. Gross; J. P. Hallett; R. S. Haszeldine; P. Heptonstall; A. Lyngfelt; Z. Makuch; E. Mangano; R. T. J. Porter; M. Pourkashanian; G. T. Rochelle; N. Shah; J. G. Yao; P. S. Fennell (2014). Carbon capture and storage update. *Energy Environ. Sci.,* **7**, 130-189.

83 N. MacDowell; N. Florin; A. Buchard; J. Hallett; A. Galindo; G. Jackson; C. S. Adjiman; C. K. Williams; N. Shah; P. Fennell (2010). An overview of CO_2 capture technologies. *Energy & Environmental Science,* 3, 1645-1669.

84 R. B. Robert (1930). Process for separating acidic gases. Patent: US1783901.

85 A. B. Rao; E. S. Rubin; D. W. Keith; M. Granger Morgan (2006). Evaluation of potential cost reductions from improved amine-based CO_2 capture systems. *Energy Policy,* **34**, 3765-3772.

86 I. Adánez-Rubio; A. Pérez-Astray; T. Mendiara; M. T. Izquierdo; A. Abad; P. Gayán; L. F. de Diego; F. García-Labiano; J. Adánez (2018). Chemical looping combustion of biomass: CLOU experiments with a Cu-Mn mixed oxide. *Fuel Processing Technology,* **172**, 179-186.

87 A. Demirbas (2005). Potential applications of renewable energy sources, biomass combustion problems in boiler power systems and combustion related environmental issues. *Progress in Energy and Combustion Science,* **31**, 171-192.

88 X. Zhao; H. Zhou; V. S. Sikarwar; M. Zhao; A.-H. A. Park; P. S. Fennell; L. Shen; L.-S. Fan (2017). Biomass-based chemical looping technologies: the good, the bad and the future. *Energy & Environmental Science,* **10**, 1885-1910.

89 R. Luque (2010). Algal biofuels: the eternal promise? *Energy & Environmental Science,* 3, 245-257.

90 H. Jin; E. D. Larson; F. E. Celik (2009). Performance and cost analysis of future, commercially mature gasification-based electric power generation from switchgrass. *Biofuels, Bioproducts and Biorefining,* **3**, 142-173.

91 Y. Fan; J. G. Yao; Z. Zhang; M. Sceats; Y. Zhuo; L. Li; G. C. Maitland; P. S. Fennell (2018). Pressurized calcium looping in the presence of steam in a spout-fluidized-bed reactor with DFT analysis. *Fuel Processing Technology,* **169**, 24-41.

92 T. Mattisson; A. Lyngfelt; H. Leion (2009). Chemical-looping with oxygen uncoupling for combustion of solid fuels. *International Journal of Greenhouse Gas Control,* **3**, 11-19.

93 M. E. Boot-Handford (2015). *The Utilisation of Biomass as a fuel for Chemical Looping Combustion*. PhD thesis, Imperial College London.

94 Q. Imtiaz; D. Hosseini; C. R. Müller (2013). Review of Oxygen Carriers for Chemical Looping with Oxygen Uncoupling (CLOU): Thermodynamics, Material Development, and Synthesis. *Energy Technology,* **1**, 633-647.

95 M. Rydén; H. Leion; T. Mattisson; A. Lyngfelt (2014). Combined oxides as oxygen-carrier material for chemical-looping with oxygen uncoupling. *Applied Energy,* **113**, 1924-1932.

96 T. Mattisson, Materials for Chemical-Looping with Oxygen Uncoupling (2013). *ISRN Chemical Engineering,* **2013**, 1-19.

97 V. Frick; M. Rydén; H. Leion; T. Mattisson; A. Lyngfelt (2015). Screening of supported and unsupported Mn–Si oxygen carriers for CLOU (chemical-looping with oxygen uncoupling). *Energy,* **93**, 544-554.

98 P. Peltola; T. Tynjälä; J. Ritvanen; T. Hyppänen (2014). Mass, energy, and exergy balance analysis of chemical looping with oxygen uncoupling (CLOU) process. *Energy Conversion and Management,* **87**, 483-494.

99 F. Donat; W. Hu; S. A. Scott; J. S. Dennis (2015). Characteristics of Copper-based Oxygen Carriers Supported on Calcium Aluminates for Chemical-Looping Combustion with Oxygen Uncoupling (CLOU). *Industrial & Engineering Chemistry Research,* **54**, 6713-6723.

100 M. Arjmand; M. Keller; H. Leion; T. Mattisson; A. Lyngfelt (2012). Oxygen Release and Oxidation Rates of $MgAl_2O_4$-Supported CuO Oxygen Carrier for Chemical-Looping Combustion with Oxygen Uncoupling (CLOU). *Energy & Fuels,* **26**, 6528–6539.

101 M. Arjmand; H. Leion; T. Mattisson; A. Lyngfelt (2013). ZrO_2-Supported CuO Oxygen Carriers for Chemical-Looping with Oxygen Uncoupling (CLOU). *Energy Procedia,* **37**, 550-559.

102 G. Azimi; H. Leion; M. Rydén; T. Mattisson; A. Lyngfelt, (2013). Investigation of different Mn–Fe oxides as oxygen carrier for Chemical-Looping with Oxygen Uncoupling (CLOU). *Energy & Fuels,* **27**, 367-377.

103 G. Azimi; M. Rydén; H. Leion; T. Mattisson; A. Lyngfelt (2013). $(Mn_zFe_{1-z})_yO_x$ Combined oxides as oxygen carrier for chemical-looping with oxygen uncoupling. *AIChE Journal,* **59**, 582-588.

104 X. Wang; Z. Chen; M. Hu; Y. Tian; X. Jin; S. Ma; T. Xu; Z. Hu; S. Liu; D. Guo; B. Xiao (2017). Chemical looping combustion of biomass using metal ferrites as oxygen carriers. *Chemical Engineering Journal,* **312**, 252-262.

105 X. Wang; T. Xu; S. Liu; B. Xiao; Z. Hu; Z. Chen (2018). CuO supported on manganese ore as an oxygen carrier for chemical looping with oxygen uncoupling (CLOU). *Chemical Engineering Journal,* **343**, 340-350.

106 T. Mendiara; A. Abad; L. F. de Diego; F. García-Labiano; P. Gayán; J. Adánez (2013). Biomass combustion in a CLC system using an iron ore as an oxygen carrier. *International Journal of Greenhouse Gas Control,* **19**, 322-330.

107 Z. Zhang (2014). *The effect of Sulfur on Chemical Looping Combustion with Iron Oxides.* PhD thesis, Imperial College London.

108 H. Leion (2008). *Capture of CO_2 from Solid Fuels Using Chemical-Looping Combustion and Chemical-Looping Oxygen Uncoupling*. PhD thesis, Chalmers University of Technology.

109 A. Lyngfelt; B. Leckner (2015). A 1000MWth boiler for chemical-looping combustion of solid fuels – Discussion of design and costs. *Applied Energy,* **157**, 475-487.

110 S. A. Scott; J. S. Dennis; A. N. Hayhurst; T. Brown (2006). In situ gasification of a solid fuel and CO_2 separation using chemical looping. *AIChE Journal,* **52**, 3325-3328.

111 H. Jin; M. Ishida (2004). A new type of coal gas fueled chemical-looping combustion. *Fuel,* **83**, 2411-2417.

112 J. Adanez; A. Abad; F. Garcia-Labiano; P. Gayan; L. F. de Diego (2012). Progress in Chemical-Looping Combustion and Reforming technologies. *Progress in Energy and Combustion Science,* **38**, 215-282.

113 M. Maroto-Valer (2010). *Developments and Innovation in Carbon Dioxide (CO_2) Capture and Storage Technology*, Volume 1 - Carbon Dioxide (CO_2) Capture, Transport and Industrial Applications.

114 T. Wall; Y. Liu; C. Spero; L. Elliott; S. Khare; R. Rathnam; F. Zeenathal; B. Moghtaderi; B. Buhre; C. Sheng; R. Gupta; T. Yamada; K. Makino; J. Yu (2009). An overview on oxyfuel coal combustion – State of the art research and technology development. *Chemical Engineering Research and Design,* **87**, 1003-1016.

115 F. Sher; M. A. Pans; C. Sun; C. Snape; H. Liu (2018). Oxy-fuel combustion study of biomass fuels in a 20 kWth fluidized bed combustor. *Fuel,* **215**, 778-786.

116 M. T. Mansouri; S. M. Mousavian (2012). Exergy-based analysis of conventional coal-fired power plant retrofitted with oxy-fuel and post-combustion CO_2 capture systems. *Proceedings of the Institution of Mechanical Engineers, Part A: Journal of Power and Energy,* **226**, 989-1002.

117 R. Ben-Mansour; M. A. Habib; M. A. Nemitallah; M. Rajhi; K. A. Suara (2014). Characteristics of Oxyfuel and Air – Fuel Combustion in an Industrial Water Tube Boiler. *Heat Transfer Engineering,* **35**, 1394-1404.

118 R. H. Görke; W. Hu; M. T. Dunstan; J. S. Dennis; S. A. Scott (2018). Exploration of the material property space for chemical looping air separation applied to carbon capture and storage. *Applied Energy,* **212**, 478-488.

119 D. Sonntag (1990). Important new values of the physical constants of 1986, vapor pressure formulations based on ITS-90 and psychrometer formulae. *Zeitschrift für Meteorologie,* **70**, 340-344.

120 Q. Yang; Y. S. Lin; M. Bülow (2006). High temperature sorption separation of air for producing oxygen-enriched CO_2 stream. *AIChE Journal,* **52**, 574-581;

121 K. Wang; Q. Yu; Q. Qin; W. Duan; T. Wu (2015). Study of the sorption property of copper oxygen carrier used for chemical looping air separation. *Journal of Thermal Analysis and Calorimetry,* **120**, 1627-1633.

122 K. Shah; B. Moghtaderi; T. Wall (2012). Selection of Suitable Oxygen Carriers for Chemical Looping Air Separation: A Thermodynamic Approach. *Energy & Fuels,* **26**, 2038-2045.

123 I. Adánez-Rubio; P. Gayán; F. García-Labiano; L. F. de Diego; J. Adánez; A. Abad (2011). Development of CuO-based oxygen-carrier materials suitable for Chemical-Looping with Oxygen Uncoupling (CLOU) process. *Energy Procedia,* **4**, 417-424.

124 P. Cho; T. Mattisson; A. Lyngfelt (2004). Comparison of iron-, nickel-, copper- and manganese-based oxygen carriers for chemical-looping combustion. *Fuel,* **83**, 1215-1225.

125 H. E. Andrus; G. Burns; J. H. Chiu; G. N. Liljedahl; P. T. Stromberg; P. R. Thibeault (2008). *Hybrid Combustion-Gasification Chemical Looping Coal Power Technology Development PHASE III - FINAL REPORT*; US Power Plant Laboratories ALSTOM Power Inc. prepared for the U.S. Department of Energy: Windsor, Connecticut, U.S.

126 T. Allen; S. Bruemmer; J. Elmer; M. Kassner; A. Motta; R. Odette; R. Stoller; G. Was; W. Wolfer (2002); S. Zinkle *Higher Temperature Reactor Materials Workshop Sponsored by the Department of Energy Office of Nuclear Energy, Science, and Technology (NE) and the Office of Basic Energy Sciences (BES)*; Argonne National Laboratory operated by the The University of Chicago for the U.S. Department of Energy: Argonne, Illinois, U.S.

127 S. Bin; W. Erdorng; W. Wei (2017). Novel design of chemical looping air separation process for generating electricity and oxygen. *Energy*, **134**, 449-457.

128 K. Shah; B. Moghtaderi; J. Zanganeh; T. Wall (2013). Integration options for novel chemical looping air separation (ICLAS) process for oxygen production in oxy-fuel coal fired power plants. *Fuel,* **107**, 356-370.

129 C. Zhou; K. Shah; B. Moghtaderi (2015). Techno-Economic Assessment of Integrated Chemical Looping Air Separation for Oxy-Fuel Combustion: An Australian Case Study. *Energy & Fuels,* **29**, 2074-2088.

130 C. F. Patzschke; H. Bahzad; M. Boot-Handford; P. S. Fennell (*in press*). ASPEN simulation of a 100 MW solar powered thermo-chemical air separation system combined with an oxy-fuel power plant for BECCS. *Mitigation and Adaptation Strategies for Global Change.*

131 J. C. Abanades; M. n. Alonso; N. Rodríguez (2011). Biomass Combustion with in Situ CO_2 Capture with CaO. I. Process Description and Economics. *Industrial & Engineering Chemistry Research,* **50**, 6972-6981.

132 B. J. P. Buhre; L. K. Elliott; C. D. Sheng; R. P. Gupta; T. F. Wall (2005). Oxy-fuel combustion technology for coal-fired power generation. *Progress in Energy and Combustion Science,* **31**, 283-307.

133 J. Hong; R. Field; M. Gazzino; A. F. Ghoniem (2010). Operating pressure dependence of the pressurized oxy-fuel combustion power cycle. *Energy,* **35**, 5391-5399.

134 H. Stadler; F. Beggel; M. Habermehl; B. Persigehl; R. Kneer; M. Modigell; P. Jeschke (2011). Oxyfuel coal combustion by efficient integration of oxygen transport membranes. *International Journal of Greenhouse Gas Control,* **5**, 7-15.

135 S. Engels; F. Beggel; M. Modigell; H. Stadler (2010). Simulation of a membrane unit for oxyfuel power plants under consideration of realistic BSCF membrane properties. *Journal of Membrane Science,* **359**, 93-101.

136 M. E. Diego; M. Alonso (2016). Operational feasibility of biomass combustion with in situ CO 2 capture by CaO during 360 h in a 300 kW th calcium looping facility. *Fuel,* **181**, 325-329.

137 D. C. Ozcan (2014). *Techno-Economic Study of the Calcium Looping Process for CO_2 Capture from Cement and Biomass Power Plants*. PhD thesis, The University of Edinburgh, **2014**.

138 Z.-s. Li; T. Zhang; N.-s. Cai (2008). Experimental Study of O_2−CO_2 Production for the Oxyfuel Combustion Using a Co-Based Oxygen Carrier. *Industrial & Engineering Chemistry Research,* **47**, 7147-7153.

139 C. W. Bale; E. Bélisle; P. Chartrand; S. A. Decterov; G. Eriksson; A.E. Gheribi; K. Hack; I. H. Jung; Y. B. Kang; J. Melançon; A. D. Pelton; S. Petersen; C. Robelin; J. Sangster; M-A. Van Ende (2016). FactSage Thermochemical Software and Databases (FactSage 7.0, www.factsage.com) Calphad, **54**, 35-53.

140 T. Mattisson; A. Järdnäs; A. Lyngfelt (2003). Reactivity of Some Metal Oxides Supported on Alumina with Alternating Methane and OxygenApplication for Chemical-Looping Combustion. *Energy & Fuels,* **17**, 643-651.

141 R. Porrazzo; G. White; R. Ocone (2014). Aspen Plus simulations of fluidised beds for chemical looping combustion. *Fuel,* **136**, 46-56.

142 R. Porrazzo; G. White; R. Ocone (2016). Fuel reactor modelling for chemical looping combustion: From micro-scale to macro-scale. *Fuel,* **175**, 87-98.

143 T. M. A. Lyngfelt (2001). Capture of CO_2 using chemical-looping combustion. In *Biennial Meeting of the Scandinavian-Nordic Section of the Combustion Institute*, Department of Energy Conversion, Chalmers University of Technology.

144 O. Levenspiel (1999). *Chemical reaction engineering*. 3rd ed.; Wiley: New York Chichester.

145 P. Cho (2005). *Development and Characterisation of Oxygen-Carrier Materials for Chemical-Looping Combustion*. PhD thesis, Chalmers University of Technology.

146 M. Arjmand (2014). *Copper and Manganese-based Oxygen Carriers in Chemical-Looping Combustion (CLC) and Chemical-Looping with Oxygen Uncoupling (CLOU)*. PhD thesis, Chalmers University of Technology.

147 S. Chuang; J. Dennis; A. Hayhurst; S. Scott, Development and performance of Cu-based oxygen carriers for chemical-looping combustion. *Combustion and Flame,* **2008**, 154, 109-121.

148 F. García-Labiano; L. F. de Diego; J. Adánez; A. Abad; P. Gayán (2004). Reduction and Oxidation Kinetics of a Copper-Based Oxygen Carrier Prepared by Impregnation for Chemical-Looping Combustion. *Industrial & Engineering Chemistry Research,* **43**, 8168-8177.

149 S. Sundqvist; M. Arjmand; T. Mattisson; M. Rydén; A. Lyngfelt (2015). Screening of different manganese ores for chemical-looping combustion (CLC) and chemical-looping with oxygen uncoupling (CLOU). *International Journal of Greenhouse Gas Control,* **43**, 179-188.

150 E. M. Eyring; G. Konya; J. S. Lighty; A. H. Sahir; A. F. Sarofim; K. Whitty (2011). Chemical Looping with Copper Oxide as Carrier and Coal as Fuel. *Oil & Gas Science and Technology – Revue d'IFP Energies nouvelles,* **66**, 209-221.

151 S. C. Bayham; R. Breault; E. Monazam (2016). Particulate solid attrition in CFB systems – An assessment for emerging technologies. *Powder Technology,* **302**, 42-62.

152 J. S. Schruben; W. G. Vaux (1985). Attrition in the Bubbling Zone of a Steady-State Fluidized Bed. *Chemical Engineering Communications,* **33**, 337-347.

153 J. Werther; J. Reppenhagen (1998). *Fluidization, Solids Handling, and Processing - Industrial Applications: Chapter 7 - Attrition in Fluidized Beds and Pneumatic Conveying Lines*. William Andrew Publishing/Noyes.

154 J. Reppenhagen; J. Werther (2000). Catalyst attrition in cyclones. *Powder Technology,* 113, 55-69.

155 S. Tamjid; S. H. Hashemabadi; M. Shirvani (2010). Prediction of catalyst attrition in a regeneration cyclone. *Filtration+Separation,* 29-33.

156 M. Johansson (2007). *Screening of oxygen-carrier particles based on iron-, manganese-, copper- and nickel oxides for use in chemical-looping technologies*. PhD thesis, Chalmers University of Technology.

157 L. F. de Diego; F. García-Labiano; J. Adánez; P. Gayán; A. Abad; B. M. Corbella; J. María Palacios (2004). Development of Cu-based oxygen carriers for chemical-looping combustion. *Fuel,* **83**, 1749-1757.

158 J. Adánez; L. F. de Diego; F. García-Labiano; P. Gayán; A. Abad; J. M. Palacios (2004). Selection of Oxygen Carriers for Chemical-Looping Combustion. *Energy & Fuels,* **18**, 371-377.

159 S. Kukade; P. Kumar; P. V. C. Rao; N. V. Choudary (2016). Comparative study of attrition measurements of commercial FCC catalysts by ASTM fluidized bed and jet cup test methods. *Powder Technology,* **301**, 472-477.

160 H. M. Feilen (2014). *Attrition Rate of Oxygen Carriers in Chemical Looping Combustion Systems.* M.Sc. thesis, University of North Dakota.

161 M. Rydén; P. Moldenhauer; S. Lindqvist; T. Mattisson; A. Lyngfelt (2014). Measuring attrition resistance of oxygen carrier particles for chemical looping combustion with a customized jet cup. *Powder Technology,* **256**, 75-86.

162 M. Rydén; P. Moldenhauer; T. Mattisson; A. Lyngfelt (2014). Attrition of oxygen carrier particles in fluidized bed – basic theory and screening measurements with a customized jet cup test rig In *3rd International Conference on Chemical Looping*, Göteborg, Sweden.

163 T. A. Brown; F. Scala; S. A. Scott; J. S. Dennis; P. Salatino (2012). The attrition behaviour of oxygen-carriers under inert and reacting conditions. *Chemical Engineering Science,* **71**, 449-467.

164 F. He; W. P. Linak; S. Deng; F. Li (2017) Particulate Formation from a Copper Oxide-Based Oxygen Carrier in Chemical Looping Combustion for CO_2 Capture. *Environ Sci Technol,* **51**, 2482-2490.

165 C. R. Bemrose; J. Bridgwater (1987). A review of attrition and attrition test methods. *Powder Technology,* **49**, 97-126.

166 D. Jing; T. Mattisson; M. Ryden; P. Hallberg; A. Hedayati; J. Van Noyen; F. Snijkers; A. Lyngfelt (2013). Innovative Oxygen Carrier Materials for Chemical-Looping Combustion. *Energy Procedia,* **37**, 645-653.

167 ASTM (2001). D4179-01, Standard Test Method for Single Pellet Crush Strength of Formed Catalyst Shapes. www.astm.org: West Conshohocken, PA, United States.

168 P. Gayán; I. Adánez-Rubio; A. Abad; L. F. de Diego; F. García-Labiano; J. Adánez (2012). Development of Cu-based oxygen carriers for Chemical-Looping with Oxygen Uncoupling (CLOU) process. *Fuel,* **96**, 226-238.

169 B. Amblard; S. Bertholin; C. Bobin; T. Gauthier (2015). Development of an attrition evaluation method using a Jet Cup rig. *Powder Technology,* **274**, 455-465.

170 ASTM (1995). D5757-11: Standard Test Method for Determination of Attrition of FCC Catalysts by Air Jets. www.astm.org: West Conshohocken, PA, United States.

171 R. Cocco; Y. Arrington; R. Hays; J. Findlay; S. B. R. Karri; T. M. Knowlton (2010). Jet cup attrition testing. *Powder Technology,* **200**, 224-233.

172 C. F. Patzschke; X. Wenzhao; H. Bahzad; M. E. Boot-Handford; N. M. Dowell; P. S. Fennell (*in preparation*). Life Cycle Assessment of Oxygen Carrier Preparation, Use and Recycling or Disposal for Chemical Looping Combustion with CH_4.

173 A. Abad; T. Mattisson; A. Lyngfelt; M. Johansson (2007). The use of iron oxide as oxygen carrier in a chemical-looping reactor. *Fuel,* **86**, 1021-1035.

174 H. Leion; T. Mattisson; A. Lyngfelt (2007). The use of petroleum coke as fuel in chemical-looping combustion. *Fuel,* **86**, 1947-1958.

175 E. Jerndal; T. Mattisson; A. Lyngfelt (2006). Thermal Analysis of Chemical-Looping Combustion. *Chemical Engineering Research and Design,* **84**, 795-806.

176 A. Abad; J. Adánez; F. García-Labiano; L. F. de Diego; P. Gayán; J. Celaya (2007). Mapping of the range of operational conditions for Cu-, Fe-, and Ni-based oxygen carriers in chemical-looping combustion. *Chemical Engineering Science,* **62**, 533-549.

177 G. Samsonov (1982). *The Oxide Handbook*. Second Edition ed.; IFI/PLENUM: New York.

178 S. Sajen; S. K. Singh; P. Mungse; S. Rayalu; K. Watanabe; G. Saravanan; N. Labhasetwar (2016). Mechanically Stable Mixed Metal Oxide of Cu and Mn as Oxygen Carrier for Chemical Looping Syngas Combustion. *Energy & Fuels,* **30**, 7596-7603.

179 M. Argyle; C. Bartholomew (2015). Heterogeneous Catalyst Deactivation and Regeneration: A Review. *Catalysts,* **5**, 145-269.

180 J. A. Moulijn; A. E. van Diepen; F. Kapteijn (2001). Catalyst deactivation: is it predictable? *Applied Catalysis A: General,* **212**, 3-16.

181 M. Arjmand; A.-M. Azad; H. Leion; M. Rydén; T. Mattisson (2014). $CaZrO_3$ and $SrZrO_3$-based CuO Oxygen Carriers for Chemical-looping with Oxygen Uncoupling (CLOU). *Energy Procedia,* **51**, 75-84.

182 M. Occhiuzzi; D. Cordischi; R. Dragone (2003). Manganese ions in the monoclinic, tetragonal and cubic phases of zirconia: an XRD and EPR study. *Physical Chemistry Chemical Physics,* **5**, 4938.

183 K. Wang; Q. Yu; Q. Qin (2013). Reduction Kinetics of Cu-Based Oxygen Carriers for Chemical Looping Air Separation. *Energy & Fuels,* **27**, 5466-5474.

184 T. Simmons (2006). IPCC Methodologies for Greenhouse Gas Inventories: CO_2 emissions from stationary combustion of fossil fuels.

185 W. Xu (2017). *Techno-economic analysis of oxygen carrier production for chemical looping combustion.* M.Sc. thesis, Imperial College London.

186 E. K. Okpoko (2012). *Chemical-Looping Combustion: Investigation of Cu-Based Oxygen Carriers*. PhD thesis, Imperial College London.

187 L. F. de Diego; P. Gayán; F. García-Labiano; J. Celaya; A. Abad; J. Adánez (2005). Impregnated CuO/Al_2O_3 Oxygen Carriers for Chemical-Looping Combustion: Avoiding Fluidized Bed Agglomeration. *Energy & Fuels,* **19**, 1850-1856.

188 Y. Tanaka (2003). Water gas shift reaction for the reformed fuels over Cu/MnO catalysts prepared via spinel-type oxide. *Journal of Catalysis,* **215**, 271-278.

189 X. Huang; C. Ni; G. Zhao; J. T. S. Irvine (2015). Oxygen storage capacity and thermal stability of the $CuMnO_2$–CeO_2 composite system. *J. Mater. Chem. A,* **3**, 12958-12964.

190 D. P. Shoemaker; J. Li; R. Seshadri (2009). Unraveling atomic positions in an oxide spinel with two Jahn-Teller ions: local structure investigation of $CuMn_2O_4$. *J Am Chem Soc,* **131**, 11450-7.

191 M. Enhessari; A. Salehabadi; K. Maarofian; S. Khanahmadzadeh (2016). Synthesis and physicochemical properties of $CuMn_2O_4$ nanoparticles; a potential semiconductor for photoelectric devices. *International Journal of Bio-Inorganic Hybrid Nanomaterials,* **5**, 115-120.

192 F. Schüth; M. Hesse; K. K. Unger (2008). Precipitation and Coprecipitation. In *Handbook of Heterogeneous Catalysis*. Wiley.

193 A. Cabello; P. Gayan; M. A. Pans; C. Dueso; F. Garcia-Labiano; A. Abad; L. F. de Diego; J. Adanez (2013). Evaluation of a highly reactive and sulfur resistant synthetic Fe-based oxygen carrier for CLC using gaseous fuels. *Energy Procedia,* **37**, 580-587.

194 C. Copéret (2010). Synthesis of Solid Catalysts. Edited by Krijn P. de Jong. *ChemCatChem,* **2**, 706-706.

195 F. Schüth; K. Unger (1999). Precipitation and Coprecipitation. In *Preparation of Solid Catalysts,* 60-84.

196 G. Eriksson (1979). An algorithm for the computation of aqueous multi-component, multiphase equilibria. *Analytica Chimica Acta,* **112**, 375-383.

197 H. C. Helgeson; D. H. Kirkham; G. C. Flowers (1981). Theoretical prediction of the thermodynamic behavior of aqueous electrolytes by high pressures and temperatures; IV, Calculation of activity coefficients, osmotic coefficients, and apparent molal and standard and relative partial molal properties to 600 degrees C and 5kb. *American Journal of Science,* **281**, 1249-1516.

198 I. Puigdomenech (2015). *Spana (Medusa-Hydra)*, Royal Institute of Technology: Stockholm, Sweden.

199 J. Szekely; J. W. Evans; H. Y. Sohn (1976). *Gas-Solid Reactions*. Academic Press: New York.

200 R. M. German (2014). *Consolidation Techniques*. **1**, 237-263.

201 P. B. Narottam; R. B. Aldo (2012). *Ceramics and Composites Processing Methods*. John Wiley & Sons: Hoboken, NJ, USA.

202 N. Ingri; W. Kakolowicz; L. G. Sillén; B. Warnqvist (1967). High-speed computers as a supplement to graphical methods – V1 Haltafall, a general program for calculating the composition of equilibrium mixtures. *Talanta,* **14**, 1261-1286.

203 S. W. Sung (2009). Process identification and PID control. Lee, J.; Lee, I.-B., Eds. Wiley: Hoboken, N.J.

204 A. R. Studart; U. T. Gonzenbach; E. Tervoort; L. J. Gauckler (2006). Processing Routes to Macroporous Ceramics: A Review. *Journal of the American Ceramic Society,* **89**, 1771-1789.

205 S. Brunauer; P. H. Emmett; E. Teller (1938). Adsorption of Gases in Multimolecular Layers. *Journal of the American Chemical Society,* **60**, 309-319.

206 J. Rouquerol; D. Avnir; C. W. Fairbridge; D. H. Everett; J. M. Haynes; N. Pernicone; J. D. F. Ramsay; K. S. W. Sing; K. K. Unger (1994). Recommendations for the characterization of porous solids (Technical Report). *Pure and Applied Chemistry,* **66**, 1739-1758.

207 E. P. Barrett; L. G. Joyner; P. P. Halenda (1951). The determination of pore volume and area distributions in porous substances. I. Computations from nitrogen isotherms. *Journal of the American Chemical society,* **73**, 373-380.

208 R. M. German (2008). P. Suri; S. J. Park, Review: liquid phase sintering. *Journal of Materials Science,* **44**, 1-39.

209 Micromeritics, AccuPyc II 1340: Gas Displacement Pycnometry System. Manual.

210 P. A. Webb (1993). *PoreSizer 9320, AutoPore II 9220*; Micromeritics.

211 A. Jain, S.P. Ong, G. Hautier, W. Chen, W.D. Richards, S. Dacek, S. Cholia, D. Gunter, D. Skinner, G. Ceder, K.A. Persson (2013). The Materials Project: A materials genome approach to accelerating materials innovation APL Materials, **1**(1), 011002.

212 ICDD (2016). PDF-4+ 2016 (Database), edited by Dr. Soorya Kabekkodu, International Centre for Diffraction Data. Newtown Square, PA, USA.

213 ICDD (2019). PDF-4+ 2019 (Database), edited by Dr. Soorya Kabekkodu, International Centre for Diffraction Data. Newtown Square, PA, USA.

214 F. H. Chung (1975). Quantitative interpretation of X-ray diffraction patterns of mixtures. III. Simultaneous determination of a set of reference intensities. *Journal of Applied Crystallography,* **8**, 17-19.

215 B. D. Cullity (2001). *Elements of X-ray diffraction*. 3rd ed.; Prentice Hall: Upper Saddle River, N.J.

216 ASTM (2015). E1382-97: Standard Test Methods for Determining Average Grain. In Size Using Semiautomatic and Automatic Image Analysis, ASTM International, www.astm.org: West Conshohocken, PA, United States.

217 N. L. Johnson;; S. Kotz;; N. Balakrishnan, *Continuous Univariate Distributions*. 2nd Edition ed.; **1994**.

218 F. D. Q. I. A. A. C. R. Müller, Preventing Agglomeration of CuO-Based Oxygen Carriers for High-Temperature Chemical Looping Applications. **2018**.

219 W. Hu; F. Donat; S. A. Scott; J. S. Dennis, Kinetics of oxygen uncoupling of a copper-based oxygen carrier. *Applied Energy,* **2016**, 161, 92-100.

220 E. N. Fuller; P. D. Schettler; J. C. Giddings, New Method for Prediction of Binary Gas-Phase Diffusion Coefficients. *Industrial & Engineering Chemistry,* **1966**, 58, 18-27.

221 B. E. Poling (2007). *The properties of gases and liquids*. 5th ed., International ed. ed.; Boston, Mass. ; London : McGraw-Hill: Boston, [Mass.]; London.

222 M. Kleiber; R. Joh (2010). D1 Calculation Methods for Thermophysical Properties. *VDI Heat Atlas,* 2nd ed.

223 N. Wakao; J. M. Smith (1962). Diffusion in catalyst pellets. *Chemical Engineering Science,* **17**, 825-834.

224 C. N. Satterfield (1980). *Heterogeneous catalysis in practice*. New York ; London: McGraw-Hill.

225 Z. Zhang; T. P. Hills; S. A. Scott; P. S. Fennell (2016). Spouted bed reactor for kinetic measurements of reduction of Fe_2O_3 in a CO_2/CO atmosphere Part I: Atmospheric pressure measurements and equipment commissioning. *Chemical Engineering Research and Design,* **114**, 307-320.

226 G. Azimi; H. Leion; T. Mattisson; A. Lyngfelt (2011). Chemical-looping with oxygen uncoupling using combined Mn-Fe oxides, testing in batch fluidized bed. *Energy Procedia,* **4**, 370-377.

227 Y.Wen; Z. Li; L. Xu; N. Cai (2012). Experimental Study of Natural Cu Ore Particles as Oxygen Carriers in Chemical Looping with Oxygen Uncoupling (CLOU). *Energy & Fuels,* **26**, 3919-3927.

228 C. K. Clayton; K. J. Whitty (2014). Measurement and modeling of decomposition kinetics for copper oxide-based chemical looping with oxygen uncoupling. *Applied Energy,* **116**, 416-423.

229 R. R. G. Hill (1978). Equations for vapour pressure versus temperature: derivation and use of the Antoine equation on a hand-held programmable calculator. *Br J Anaesth,* **50**, 415.

230 P. Atkins; J. de Paula (2006). *Atkins' Physical Chemistry*. 8th ed.; W. H. Freeman and Company: New York.

231 J. Davidson; D. Harrison (1963). Fluidized particles. Cambridge University Press.

232 P. T. Clough (2017). *An investigation into H_2 production by sorbent enhanced steam reforming of biomass*. PhD thesis, Imperial College London.

233 I. H. B. Eric W. Lemmon, Marcia L. Huber, Mark O. McLinden *REFPROP Documentation*; **2018**.

234 P. S. Fennell; J. S. Dennis; A. N. Hayhurst (2009). The order with respect to oxygen and the activation energy for the burning of an anthracitic char in O_2 in a fluidised bed, as measured using a rapid analyser for CO and CO_2. *Proceedings of the Combustion Institute,* **32**, 2051-2058.

235 C. J. Tighe. Reactions of the Oxides of Nitrogen with Carbonaceous Particles. University of Cambridge, **2009**.

236 A. Savitzky; M. J. E. Golay, Smoothing and Differentiation of Data by Simplified Least Squares Procedures. *Analytical Chemistry,* **1964**, 36, 1627-1639.

237 D. Horn and J. Rieger (2001). Organic Nanoparticles in the Aqueous Phase – Theory, Experiment, and Use. *Angewandte Chemie International Edition*, **40**, 4330-4361.

238 S. Y. Chuang; J. S. Dennis; A. N. Hayhurst; S. A. Scott (2010). Kinetics of the Oxidation of a Co-precipitated Mixture of Cu and Al_2O_3 by O_2 for Chemical-Looping Combustion. *Energy & Fuels,* **24**, 3917-3927.

239 R. D. La Nauze, K. Jung (1985). *Chemical Engineering Research and Design,* 3-33.

240 T. Dogu; G. Dogu (1991). A Grain Model for Catalyst Tortuosity. *Chemical Engineering Communications,* **103**, 1-9.

241 S. Yagi; D. Kunii (1955). Studies on combustion of carbon particles in flames and fluidized beds. *Symposium (International) on Combustion,* **5**, 231-244

242 E. H. Oelkers; H. C. Helgeson (1990). Triple-ion anions and polynuclear complexing in supercritical electrolyte solutions. *Geochimica et Cosmochimica Acta,* **54**, 727-738.

243 E. L. Shock; E. H. Oelkers; J. W. Johnson; D. A. Sverjensky; H. C. Helgeson (1992). Calculation of the thermodynamic properties of aqueous species at high pressures and temperatures. Effective electrostatic radii, dissociation constants and standard partial molal properties to 1000 °C and 5 kbar. *J. Chem. Soc., Faraday Trans.,* **88**, 803-826.

244 P. T. Clough, M. E. Boot-Handford, L. Zheng, Z. Zhang, P. S. Fennell (2018). Hydrogen Production by Sorption Enhanced Steam Reforming (SESR) of Biomass in a Fluidised-Bed Reactor Using Combined Multifunctional Particles. *Materials*, **11**, 859.

245 H. E. Al-Mansour; B. H. Al-Busairi; C. G. J. Baker (2011). Energy Consumption of a Pilot-Scale Spray Dryer. *Drying Technology,* **29**, 1901-1910.

246 E. Jerndal, T. Mattisson, I. Thijs, F. Snijkers, A. Lyngfelt (2010). Investigation of $NiO/NiAl_2O_4$ oxygen carriers for chemical-looping combustion produced by spray-drying. *International Journal of Greenhouse Gas Control*, **4**, 23-35.

247 Yale University (2018). *West Campus Materials Characterization Core: XRD Principle.*" Retrieved 21 December 2018, from https://ywcmatsci.yale.edu/principle-0.